Correlaties tussen fysische en structurele eigenschappen van spinnenzijde

Correlations between Physical and Structural Properties of Spider Silk

Els Van Nimmen

Promotoren: prof. dr. ir. L. Van Langenhove, prof. dr. J. Mertens
Proefschrift ingediend tot het behalen van de graad van
Doctor in de Ingenieurswetenschappen: Materiaalkunde

Vakgroep Textielkunde
Voorzitter: prof. dr. P. Kiekens
Faculteit Ingenieurswetenschappen
Academiejaar 2005 - 2006

UNIVERSITEIT GENT

ISBN 90-8578-102-7
NUR 950
Wettelijk depot: D/2006/10.500/60

Promotors

Prof. Dr. ir. L. Van Langenhove

Universiteit Gent, FirW - Vakgroep Textielkunde

Prof. Dr. J. Mertens

Universiteit Gent, FWE – Vakgroep Biologie

Onderzoeksinstelling

Universiteit Gent, Vakgroep Textielkunde

Technologiepark 907

B-9052 Zwijnaarde

Research Institute

Ghent University, Department of Textiles

Technologiepark 907

B-9052 Zwijnaarde

ACKNOWLEDGEMENTS

I would like to thank my promotors Prof. Lieva Van Langenhove and Prof. Johan Mertens, for giving me the opportunity to perform this research.

I would especially like to thank my fellow doctoral researchers Kris Gellynck, Tom Gheysens and Domir De Bakker for their support in collecting and "milking" the spiders, for their help with the experiments and for the constructive discussions.

With respect to the experimental work, I am also indebted to the technical staff of the department. A special word of thanks goes to Lieve Van Landuyt and Katrien Ver Eecke for always be ready to help.

I further want to thank Dr. Karen De Clerck, Prof. Gustaaf Schoukens and especially Dr. Jo Verschuren, for their assistance in improving the content of this PhD-work.

My thanks are also due to the other research and administrative staff of the department for being helpful when needed.

A special word of thanks is also addressed to Prof. Erik Goormaghtigh of the ULB for the disposal of equipment for free and for his valuable comments.

I am also grateful to Prof. Robert Carleer, Dr. Peter Adriaensens, Prof. Savvas Savvides for the interesting conversations and constructive discussions.

For the financial support my sincere gratitude goes to the Research Fund of Ghent University (BOF) for the funding of the project about spider silk.

Finally, I want to thank my family and close friends for their ongoing support.

Ghent, september 2006

Els Van Nimmen

TABLE OF CONTENTS

ABBREVIATIONS AND NOTATIONS

List of amino acids and their abbreviations

3-letter code	1-letter code	Semi-long
Ala	A	Alanine
Arg	R	Arginine
Asn	N	Asparagine
Asp	D	Aspartic acid
Cys	C	Cysteine
Gln	Q	Glutamine
Glu	E	Glutamic acid
Gly	G	Glycine
His	H	Histidine
Ile	I	Isoleucine
Leu	L	Leucine
Lys	K	Lysine
Met	M	Methionine
Phe	F	Phenylalanine
Pro	P	Proline
Ser	S	Serine
Thr	T	Threonine
Trp	W	Tryptophan
Tyr	Y	Tyrosine
Val	V	Valine

Other abbrevations

AA	Amino acid
Ad-CYL	Cylindrical gland (or egg sac) silk of *Araneus diadematus*
Ad-MA	Major ampullate silk of *Araneus diadematus*
Ad-MI	Minor ampullate silk of *Araneus diadematus*
AFM	Atomic force microscopy
Avg	Average
CH_3OH	Methanol
CP	Cross polarization
CV	Coefficient of variation
DRIFTS	Diffuse reflectance infrared Fourier transform spectroscopy
DSC	Differential scanning calorimetry
dtex	decitex
FT-IR	Fourier transform infrared
FT-Raman	Fourier transform Raman
H-fibroin	Heavy chain fibroin
L-fibroin	Light chain fibroin
MA	Major ampullate
MAS	Magic angle spinning
Nc-CYL	Cylindrical gland (or egg sac) silk of *Nephila clavipes*
Nc-FL	Flagelliform gland silk of *Nephila clavipes*
Nc-MA	Major ampullate silk of *Nephila clavipes*
Nc-MI	Minor ampullate silk of *Nephila clavipes*
NMR	Nuclear magnetic resonance
NPAB	Non-poly-alanine block
NPL	Non-periodic lattice
PAB	Poly-alanine block
S.D.	Standard deviation
SEM	Scanning electron microscopy
SF	Silk fibroin
SLS	Standard linear solid

TEM	Transmission electron microscopy
TGA	Thermogravimetry
TMA	Thermal mechanical analysis

Notations

C_α	Central carbon atom (in the main chain)
C_β	Carbon atom of the CH_2 or CH_3 group in the side chain of an amino acid, linked to the central carbon atom C_α
d	Diameter
ε	Strain
E	Elastic or initial modulus
F	Force
F_v	Preload
N	Number of tests / repetitions
η	Viscosity or damping constant
ρ	Specific density
r	Strain rate
R	Correlation coefficient
σ	Stress
T_g	Glass transition temperature
T_t	Linear density, expressed in tex

SAMENVATTING

Spinnen bezitten tot zeven verschillende spinklieren die hoogperformante filamenten met uiteenlopende en opmerkelijke mechanische eigenschappen produceren. Als gevolg hiervan is er de laatste 10 jaar veel interesse in het ontwerp van deze materialen in de hoop om nieuwe proteïne-gebaseerde structurele biopolymeren te kunnen ontwikkelen. Om het ontwerp van deze materialen te kennen, is het vereist om de relaties tussen structuur en eigenschappen te verstaan. De bedoeling van dit doctoraatsonderzoek is om daartoe bij te dragen door het bestuderen van de structuur-eigenschaprelaties van twee types spinnenzijde in vergelijking met zijdes afkomstig van twee rupsen *Bombyx mori* en *Antheraea pernyi* (gekend als Tussah- of wilde zijde).

De meest bestudeerde spinnensoorten zijn *Araneus diadematus* (of kruisspin) en *Nephila clavipes.* De meest onderzochte spinnendraad is de "dragline", de draad waar de spin aan hangt bij het vallen. Informatie over structuur van deze "dragline" is echter gebaseerd op de draad van de *N. clavipes* spin. Gezien het veelvuldig voorkomen van de *A. diadematus* spin in België, werd het structuuronderzoek voornamelijk uitgevoerd op draad van deze spin, meer bepaald "dragline" en eizakspinnenzijde. Deze laatste draad werd geselecteerd omwille van de beperkte kennis van zijn eigenschappen.

Alhoewel reeds veel gekend is van de structuur en eigenschappen van de zijde van de rupsen, is een vergelijking nuttig om structurele aspecten van de spinnenzijdes te kunnen afleiden.

Dit onderzoek start met een uitgebreide studie over mechanische eigenschappen van zijdefilamenten. De verschillende type filamenten vertonen een duidelijk te onderscheiden sterkte-rekgedrag. Vooral het rek-sterktegedrag van het eizakfilament was opmerkelijk. Het vertoont geen rekverharding, m.a.w. geen verdere toename van de modulus voorbij de vloeigrens, wat toch een typische eigenschap is van textielvezels. Dit rek-sterktegedrag werd verder gekarakteriseerd met het Standaard Lineair Vast (SLS) model, een uitbreiding van het beter gekende Maxwell model. Een clusteranalyse op de parameters van dit model liet toe om twee verschillende vezelpopulaties te onderscheiden binnen een eizak. De verschillende vezelpopulaties kunnen te maken hebben met de verschillende lagen die door de spin afgezet worden bij het maken van de eizak. Anderzijds kunnen de verschillende populaties ook geproduceerd zijn door de verschillende, symmetrisch gesitueerde, tubuliforme spinklieren.

Zijdes zijn semi-kristallijne en visco-elastische materialen. Het visco-elastisch gedrag uit zich in tijdsafhankelijke fenomenen, zoals onder meer een effect van reksnelheid, hysteresis en kruipgedrag, die in dit werk dan ook bestudeerd werden. "Dragline" spinnenzijde vertoonde een duidelijk beter visco-elastisch gedrag (o.m. een kleinere permanente vervorming en lager energieverlies). Voor lagere rekken vertoont eizakspinnenzijde een vergelijkbare resiliëntie en elastisch herstelvermogen met Tussah-zijde. Bovendien hangen de mechanische eigenschappen van het eizakfilament sterk af van de reksnelheid.

Zijdefilamenten behoren tot de groep van proteïnen, ook fibroïne genoemd bij zijde. Wat betreft de structurele aspecten, werd eerst en vooral de aminozuursamenstelling bepaald. Alhoewel alle zijdes een hoog percentage aan aminozuren met kleine zijgroep (glycine, alanine, serine) bevatten, onderscheidt eizakspinnenzijde zich in de relatief hogere bijdrage van serine ter compensatie van een lager glycine gehalte. Het eizakfilament bevat bovendien een hoger percentage aan aminozuren met volumineuze zijgroepen. Dit verklaart deels hun lagere sterkte gezien deze grotere residuen de groei van compacte β-plaat- ("β-sheet") kristallen belemmeren.

De aminozuursequentie of primaire structuur van de verschillende zijdefilamenten is grotendeels beschreven in de literatuur. Herhalingen in de primaire structuur geven aanleiding tot het vormen van lokale regelmatige structuren, nl. de secundaire structuren. Deze structuren van de verschillende zijdes werden bestudeerd aan de hand van vibrationele spectroscopie en nucleair magnetische resonantie (NMR)-spectroscopie. In deze technieken kunnen bepaalde maxima in de spectra toegewezen worden aan verschillende secundaire structuren. Bovendien laat NMR-spectroscopie verder toe om de structuur van de belangrijkste aminozuren te bepalen.

Verschillende infrarood- en Raman-spectroscopische methodes werden uitgeprobeerd. De beste spectra werden gevonden door gebruik te maken van een weinig toegepaste infraroodtechniek nl. diffuse reflectie Fourier-transformatie infraroodspectroscopie (DRIFTS). Doordat een verschuiving van de maxima geobserveerd werd in de structuurgevoelige gebieden, was het noodzakelijk om via een conformationele transitie van de zijderupsproteïnen meer zekerheid te bekomen over de relatie tussen golfgetal en secundaire structuur. De conformationele transitie werd verder bevestigd via NMR-spectroscopie en differentiële scanning calorimetrie (DSC).

Uit de DRIFT- en NMR-spectra kon besloten worden dat eizakspinnenzijde bestaat uit een kleine fractie aan β-plaatstructuren die bovendien kort zijn en zowel alanine als serine bevatten. Verder werden duidelijk β-bocht- ("β-turn") structuren waargenomen. In de "dragline" spinnenzijde werden naast deze structuren ook α-helixstructuren vastgesteld.

Vervolgens werd ook het thermisch gedrag van de geselecteerde fibreuze proteïnen nagegaan via thermogravimetrie (TGA) en thermische mechanische analyse (TMA). Alle filamenten vertoonden een tweefazig degradatiegedrag. Verder werd vastgesteld dat eizakspinnenzijde en Tussah-zijde een hogere degradatietemperatuur, rond de 300 °C, vertonen dan de andere zijdefilamenten.

De thermische stabiliteit bij het strekken van de filamenten, gevonden via TMA, was hoger voor eizakspinnenzijde en *B. mori* dan voor de andere filamenten. Dit wordt toegeschreven aan de afwezigheid van α-helixstructuren die leiden tot een typische krimp in de thermische curves van Tussah- en "dragline" filamenten.

De relatief hogere thermische stabiliteit van eizakspinnenzijde wordt verklaard door de aanwezigheid van een hogere fractie aan kleine β-plaatstructuren, met naastliggende ketens die dicht bijeengepakt zijn in de amorfe gebieden en die gestabiliseerd worden door een intramoleculair netwerk van waterstofbruggen.

Deze kenmerken leiden tot een beperking van de moleculaire bewegingen van de fibroïneketens bij het opwarmen.

Vervolgens werden verdere structurele aspecten besproken die de fysische eigenschappen van zijderupsfilamenten en spinnenzijdes kunnen verklaren. Tot slot werd een structureel model voorgesteld voor eizakspinnenzijde. De structuur van het eizakfilament wordt gedomineerd door uitgestrekte amorfe gebieden die voornamelijk in serie gekoppeld zijn met een beperkt aantal smalle kristallijne domeinen. De grote fractie aan aminozuren met volumineuze zijketens verhinderen het vormen van uitgestrekte β-plaatkristallen, en blijven aldus beperkt tot β-bochtstructuren in de amorfe gebieden. Er wordt gesuggereerd dat deze β-bochtstructuren gekoppeld zijn tot helische structuren die de relatief hoge rek in dit type zijde veroorzaken. De kleine β-plaatstructuren leiden ertoe dat geen fibrillaire structuur werd waargenomen met een scanning elektronenmicroscoop (SEM) van breukoppervlakken. Op basis van deze breukanalyse wordt een kern-mantelstructuur vastgesteld.

SUMMARY

Spiders possess up to seven different spinning glands which produce high-performance fibres with various remarkable mechanical properties. As a consequence, a lot of interest has grown during the last 10 years in the design of these materials hoping to be able to develop new protein-based fibrous biopolymers. To know the design of these materials, it is required to understand the relationships between structure and properties. The aim of this doctoral research is to contribute in this by studying the structure-property relationships of two types of spider silk in comparison to silks secreted by two silkworms *Bombyx mori* and *Antheraea pernyi* (or Tussah silk).

The most studied spider species are *Araneus diadematus* (or cross-spider) and *Nephila clavipes.* Information about the structure of "dragline", the most investigated thread, is however based on the "dragline" of the *N. clavipes* spider. Considering the abundant occurrence of the *A. diadematus* spider in Belgium, the structural research is mainly performed on the threads of this spider, more specifically the "dragline" and egg sac spider silk. The latter is selected because of the limited knowledge of the characteristics of this fibre.

Although a lot is known about the structure and properties of the silkworm silks, a comparison is valuable in order to be able to derive structural aspects of spider silks.

The research starts with a detailed study of the mechanical properties of the silk fibres. The different types of fibres exhibit a clearly distinguishable stress-strain behaviour. Particularly, the tensile behaviour of the egg sac spider silk was remarkable. It shows no strain hardening, i.o.w. no further increase in modulus beyond the yield point, however, a typical feature of textile fibres. This stress-strain behaviour is further characterized with the Standard Linear Solid (SLS) model, an extension of the better known Maxwell model. A cluster analysis on the parameters of this model allowed the distinction of two different fibre populations within an egg sac. These fibre populations can be linked to the different layers that are secreted by the spider at the production of the egg sac. Otherwise, these populations can also be produced by the different, symmetrically located, tubuliform spinning glands.

Silks are semi-crystalline and visco-elastic materials. The visco-elastic behaviour leads to time-dependent phenomena such as an effect of strain rate, hysteresis and creep behaviour. These phenomena are studied in this work. "Dragline" spider silk showed a clearly better visco-elastic behaviour (a.o. a smaller permanent deformation and less energy dissipation), in spite of its higher variability in properties. For lower strain values, egg sac spider silk exhibits a comparable resilience and elastic recovery with Tussah silk. Moreover, the tensile properties of egg sac spider silk are strongly dependent on the strain rate.

Silks belong to the group of proteins, also called fibroin for silk. As far as the structural aspects are concerned, first of all the amino acid composition is determined. Although all silks contain a high percentage of amino acids with small side chain (glycine, alanine, serine), egg sac spider silk is different in the relative

higher contribution of serine in spite of a lower content of glycine. The egg sac spider silk further holds a higher percentage of amino acids with voluminous side chains. This explains partly its lower strength because these large residues hinder the growth of compact β-sheet crystals.

The amino acid sequence or primary structure of the various silk fibres is summarized based on literature. Repetitions in the primary structure lead to the formation of local regular structures, called the secondary structures. These structures of the different silks were studied with vibrational spectroscopy and nuclear magnetic resonance (NMR) spectroscopy. In these techniques certain maxima in the spectra are assigned to different secondary structures. Moreover, NMR spectroscopy allows further the determination of the structure of the most important amino acids.

Different infrared and Raman spectroscopic methods were tried. The best spectra were found by use of a less applied infrared technique, namely diffuse reflection infrared spectroscopy (DRIFTS). Because of a shift of the maxima observed in the structure-sensitive regions, it was necessary to induce a conformational transition for the silkworm silk fibroins. In this way, more certainty was obtained for the relationship between wave number and secondary structure. The conformational transition was further confirmed with NMR spectroscopy and differential scanning calorimetry (DSC).

From the DRIFT and NMR spectra, it could be concluded that the egg sac spider silk is consisting of a small fraction of "β-sheet" structures which are in addition short and contain both alanine and serine. Moreover, β-turn structures are clearly observed. In the dragline spider silk also the presence of α-helical structures was evidenced.

Subsequently, the thermal behaviour of the selected fibrous proteins was investigated by means of thermogravimetry (TGA) and thermal mechanical analysis (TMA). All fibres exhibit a two-phase degradation behaviour. Furthermore, a higher degradation temperature, about 300 °C, was observed for egg sac spider silk and Tussah silk than for the other silks.

The thermal stability when straining the fibres, found via TMA, was higher for egg sac spider silk and *B. mori* silk than for the other silk fibres. This is attributed to the absence of α-helix structures which result in a typical shrinkage in the thermal curves of Tussah and dragline silk.

The relative higher thermal stability of egg sac spider silk is explained by the presence of a higher fraction of small "β-sheet" structures, with adjacent chains tightly packed in the amorphous domains and stabilized by an intramolecular network of hydrogen bonds. These features lead to a restriction of the molecular motions of the fibroin chain after heating.

Besides a summary of the known structural models for the silkworm and spider silks, further structural aspects are discussed explaining the physical properties of the silks. Finally, a structural model is proposed for egg sac spider silk that can explain the observed physical characteristics. The structure of egg sac spider silk is dominated by extended amorphous regions which are linked mostly in series with a limited number of small crystalline domains. The large fraction of amino acids with

voluminous side chains hinder the formation of extended β-sheet crystals, and remain restricted to β-turn structures in the amorphous regions. It is suggested that these β-turn structures are linked to helical structures explaining the relative high strain observed for this type of silk. Furthermore, the small size of the β-sheet crystals explains why no fibrillar structure is observed on SEM photos of breaking surfaces. On the basis of the fractographic study, a skin-core structure is stated.

OUTLINE AND MOTIVATION

In this thesis, we address the correlations between mechanical behaviour and structural aspects of silks, with the focus on spider silks. Figure 0.1 shows a schematical representation of the outline of this thesis.

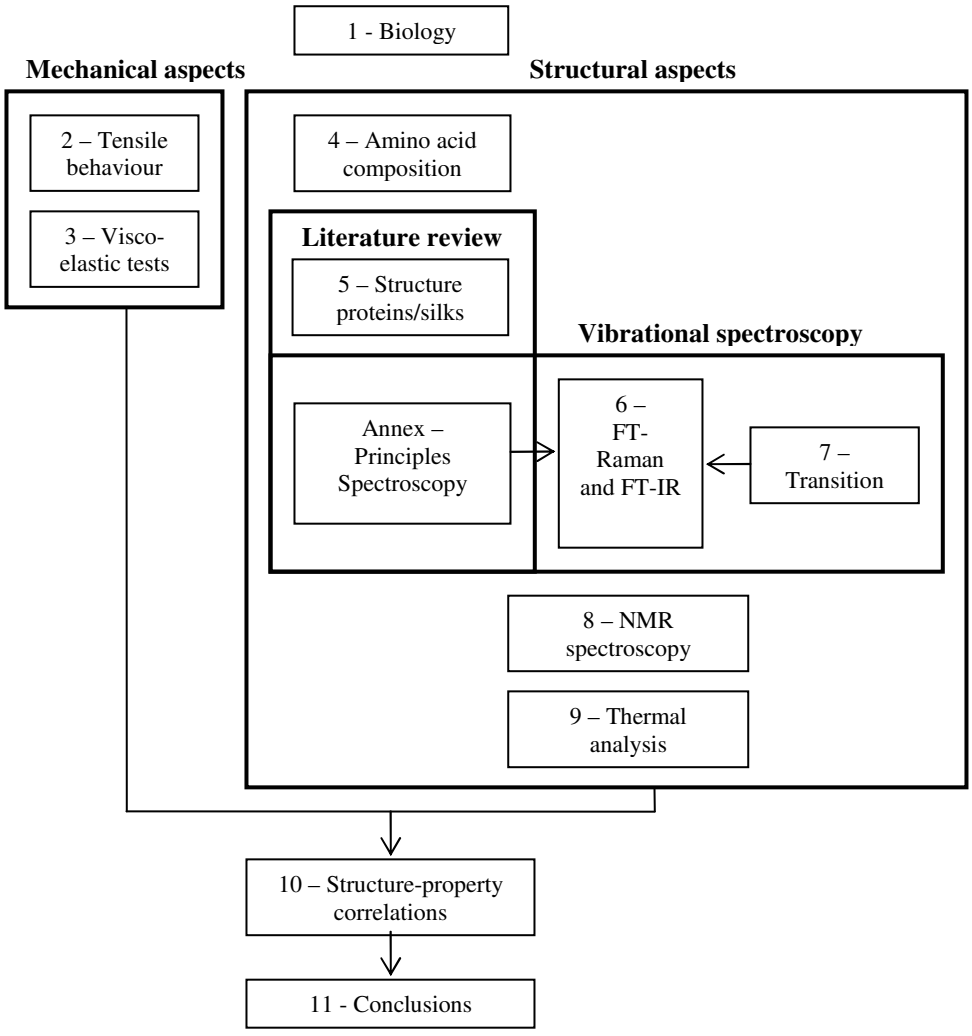

Figure 0.1 - Flowchart of the outline of this thesis

Spiders are ideal model organisms to study structure-function relationships since they possess up to seven different spinning glands, secreting fibres with different exceptional properties. Because of their remarkable properties, scientists are trying to produce spider silk artificially. The spider silk proteins are available in solution and lab-scale artificial fibres have been produced, however they lack the tenacity of native spider silk. This thesis is expected to add additional fundamental information that can help in the further understanding of the structure of spider silk and in finding the reasons for the disappointing properties of the artificial produced fibre. The analysis was limited to dragline and egg sac spider silk, mostly because of practical considerations. Dragline is produced by the major ampullate silk glands whereas egg sac spider silk is secreted by the cylindrical or tubuliform spinning glands. The study further focused on the spider *Araneus diadematus* because of its high abundance in Belgium. Furthermore, literature on structural aspects of *A. diadematus* spider silk is limited.

For reasons of comparison, *Bombyx mori* and Tussah silk were selected. *B. mori* silk is produced by the domestic silkworm *B. mori* and the structure is known to consist dominantly of β-sheet structures. Tussah silk is produced by a wild silkworm, *Antheraea pernyi*, and its structure contains β-sheet as well as α-helix structures. The difference in secondary structure between both silks is expected to help in the structural analysis.

General biological aspects of the silkworms and the spiders and their silks, such as appearance, production process, history and applications, are reviewed in Chapter 1.

The mechanical behaviour of the silks is studied in Chapter 2 and Chapter 3. In Chapter 2, uni-axial tensile testing is considered whereas in Chapter 3 visco-elastic properties are investigated.

Chapter 2 starts by describing the tensile behaviour of various silks of different spider species. From its conclusion and practical considerations, it was decided to focus this chapter further on egg sac spider silk. The limited literature on egg sac spider silk was another motivation. For egg sac spider silk, a mathematical model, based on springs and dashpots, is built to describe the stress-strain behaviour.

Silks are semi-crystalline materials of which the tensile properties are time-dependent. The visco-elastic properties that are studied in Chapter 3 include the effect of strain rate, the resilience and elastic recovery and finally the creep behaviour. It is expected that the study of the visco-elastic behaviour will result in some indirect information about the microstructure of the less-ordered or amorphous regions.

A following section, including Chapters 4 to 9, involves structural aspects of the silks. Since the secondary structure of silks is highly dependent on their chemical structure, Chapter 4 examines the amino acid composition of some silks.

Chapter 5 starts with recapitulating the most important and general structural aspects of proteins. Further on, a literature review is given on the structure of the investigated silks. With respect to spider silks, the review is extended with known structural information of other spider silk types and that of the most studied spider species *Nephila clavipes* in order to help making conclusions about the relationships between the mechanical and structural aspects in Chapter 10.

The techniques that were applied in further chapters to study secondary structure are Fourier Transform Raman spectroscopy, Fourier Transform Infrared spectroscopy, solid-state Nuclear Magnetic Resonance spectroscopy and some thermal analyses.

Since the main technique used for the study of the secondary structure was vibrational spectroscopy, in Annex the principles and sampling techniques of Fourier Transform Infrared (FT-IR) and Fourier Transform Raman (FT-Raman) spectroscopy are discussed. Furthermore, the significance of vibrational spectroscopy for obtaining information about secondary structure of proteins is reviewed in this Annex.

FT-Raman and FT-IR spectroscopy are powerful tools for studying proteins at a molecular level, because they provide information on the peptide backbone structure, as well as on conformational transitions and changes in the side chain environment.

The technique most often used in literature for the analysis of secondary structure of proteins is Raman spectroscopy. However, in Chapter 6 the application of FT-Raman spectroscopy was combined with FT-IR spectroscopy on the selected silk fibres to find the most suitable method. Different sampling methods with FT-IR spectroscopy were used and discussed, amongst others, the less known technique of diffuse reflection (DRIFT).

In order to get an idea about the reliability of the obtained DRIFT-spectra in Chapter 6 and to help in the assignment of the absorption maxima to secondary structure, a conformational transition was induced on regenerated *Bombyx mori* and Tussah silk fibroin. This study is discussed in Chapter 7.

To complement and confirm the results from the DRIFT-spectra on regenerated silk and silk fibre samples, ^{13}C Cross Polarization/Magic Angle Spinning Nuclear Magnetic Resonance spectroscopy is considered in Chapter 8. Analysis of the ^{13}C chemical shift and its relationship to protein structure shows conformation-dependent ^{13}C chemical shifts in the solid state. Especially, the local secondary structure of the most important residues (alanine, glycine, serine) can be deduced.

Chapter 9 monitors the thermal properties of some regenerated samples, as well as the silk fibres. Differential Scanning Calorimetry (DSC) is used for the confirmation of the transition induced in Chapter 7. Thermogravimetry (TGA) was applied on the silk fibres to get an idea about their thermal stability. Finally, the structural behaviour of the silks' crystalline and amorphous regions was characterized by monitoring their thermomechanical performance by means of a Thermal Mechanical Analysis (TMA).

In Chapter 10, structural models for the silks are reviewed and the relationships between the mechanical aspects and structural aspects are discussed, taking into account all experiments done and available information from literature on other spider silk types and species. More specifically, a structural model is proposed for egg sac spider silk.

Finally, the general conclusions of this work are given.

1

BIOLOGY OF SILK

Because of the origin of silks and the multidisciplinary approach of this research, this thesis starts with reviewing some biological information of the studied silks: silkworm and spider silks. Some of these aspects are important to understand why these silks are interesting for the study of structure-property relations of silks.

Furthermore, a number of previous and current applications of these silks are given with some attention to the recent trials to artificially produce silk.

1.1. DEFINITION OF SILK

Biologists and biochemists define silks differently [Craig 2003]. To a biologist, silks are secreted, fibrous materials that are deposited or spun by organisms. To a biochemist, silks are protein threads composed of repeating arrays of polypeptides that contain both discrete crystalline and noncrystalline domains that are oriented around a fibre axis.

Silk production is a characteristic of all spiders and is also known among various mites, mantids, moths, beetles, etc. Some "silks", such as the glue resin secreted by the spider aggregate glands are included in this definition, although in the strict sense they are not composed of solidified filaments.

Insects, as a group, produce many different types of silks and fibrous proteins; however, each individual produces only one silk protein. Spiders also produce a variety of silks and fibrous proteins but, in contrast to insects, an individual spider may produce as many as nine different types of silks and fibrous proteins, each of which may be composed of more than one type of protein [Kovoor 1987, Haupt & Kovoor 1993].

1.2. THE SILKWORM SILKS

1.2.1. THE DOMESTIC SILKWORM

The silk fibre is a continuous protein filament produced by various insects, especially by the larvae of a caterpillar (known as the silkworm). The silkworm is not really a worm, but a caterpillar having eyes and legs which no true worm possesses [Huber 1947].

The true silkworms belong to the order Lepidoptera, or scale-winged insects, and more specifically to the genus *Bombyx*, of which the principal species is the *Bombyx mori*, or mulberry silkworm, which produces by far the major portion of the silk used in the trade.

The silkworm has been domesticated by man some 4000 years ago. The cocoon is wrapped in a continuous silk thread whose length can exceed 1 km.

1.2.2. THE SILK PRODUCTION PROCESS

The silk production process starts with the silkworm culture which includes the proper selection and care of the eggs [Huber 1947]. Silkworm eggs are of two types: (1) those used for reproduction and (2) those used for cocoon production. By using special methods, the egg production has developed into an almost continuous process throughout the mulberry growing season.

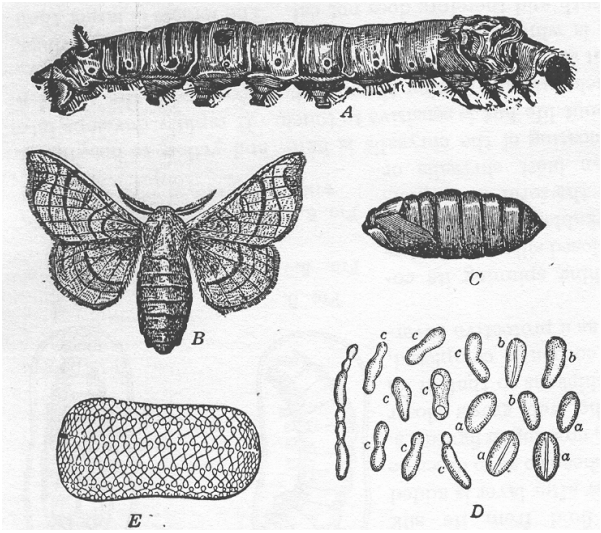

Figure 1.1 - Different stages in growth of silkworm. A: silkworm in fifth period, full size; B: moth or butterfly, C: chrysalis or pupa, D: eggs of moth, E: diagram showing cocoon and method of winding [Huber 1947]

The caterpillar, on first making its appearance, is about 3 mm long and weighs about 5 mg. Under normal conditions, there elapse 20 to 30 days between the time of the hatching of eggs and the commencement of the spinning of the cocoon [Huber 1947]. During this time the worm sheds its skin four times. The life cycle of the silkworm consists of different stages: incubation, different stages associated with shedding its skin, spinning cocoon, chrysalis or pupa and moth, as shown in Figure 1.1. Almost immediately after being hatched the worms start to devour mulberry leaves with great avidity, and continue to eat throughout the different stages of their life cycle. Though, when they are about to shed their skins, they stop eating for a time and become motionless. The silkworms increase in weight almost 10 000 fold during their short lives. When the worm has reached the limit of its growth, it ceases to eat, diminishes in weight, changes from a greenish white to a creamy white colour, and holds up its head seeking a place to anchor its silk filament. Each worm builds an oval casing or shell by extruding through its spinneret the viscous fluid from its silk glands. The silkworm has two large glands wherein the silk secretion is formed. The liquid flows through two channels to one common exit tube in the head of the worm to produce the fibroin. At this point the flow is joined by the secretion of two other symmetrically located glands, which produce the silk glue or sericin that cements together the two filaments of fibroin.

Layer after layer is spun by the mobile silkworm accelerating and decelerating its head in a figure-eight arc with attachment points at each reversal of direction [Wiedbrauck 1955, Shao & Vollrath 2002] (see Figure 1.1). Meanwhile the web grows closer and the veil thickens so that in 24 to 72 h the cocoon is completed, which serves as protective covering. After finishing spinning its cocoon, the enclosed silkworm undergoes a remarkable transformation, passing from the form of a caterpillar into an inert chrysalis or pupa. It rapidly develops into a moth, which cuts an opening through the cocoon with the aid of a fluid, which it secretes. The

entire short moth life of 1 to 4 days is for reproduction. After mating, the mother moth lays about 500 eggs, which completes her life cycle. In order to keep the continuity of the cocoon filament, the worms used for silk production, are stifled while in their chrysalis state. This is often done by steaming the cocoons.

After boiling the cocoons, they are brushed which picks up the outside end of the filament. In reeling, a sufficient number of the loose ends of the cocoon filaments to form the size of raw silk thread desired, are passed through guides [Huber 1947]. Simultaneously with the reeling some twist is given to the filaments.

The thread, or bave, consists of two fine fibroin filaments, or brins, which are covered individually and cemented together by an outer layer of a gelatin- or glue-like substance [Howitt 1953]. The outer layer substance, known as silk-gum or sericin, serves as a size during the early mechanical processing of the silk threads, and, at some appropriate stage, is removed by the process of degumming so as to leave the smooth, lustrous inner core of silk fibroin that is familiarly known as silk.

1.2.3. THE SILK SECRETION PROCESS

The silkworm digests the mulberry leaves fed to it and the proteins present in the leaves are hydrolysed by enzymes in its digestive organs to give amino acids (see Chapter 4). These amino acids, after circulating in the body to the appropriate gland, are built up into the proteins sericin and fibroin, and these two proteins are secreted into the silk gland or reservoir. The silk fibroin in the reservoir is in a water-soluble form, i.e. it is in a coiled-up form. On extrusion of the contents of the gland, the coiled-up molecules of fibroin, probably by mechanical or shearing forces [Iizuka 1966, 1985, Yamaura *et al.* 1982, 1985] due to passage through a narrow aperture, are straightened out into the extended form, orientated into the direction of spinning, and aggregated with each other so as to produce an insoluble filament of fibroin. The two fibroin filaments, that emerge simultaneously through the head of the silkworm at the rate of about 50 cm per minute, are very fine and are bound together by the protein gum sericin [Gupta 2000]. This type of spinning process is also known as liquid crystal spinning [Gupta 2000].

The mechanism for the change in conformation that accompanies spinning still remains a mystery. It has been suggested that changes in solution chemistry could cause this conformational change [Trabbic & Yager 1998 and refs herein]. Others have suggested that the hydrodynamic forces of fluid flow during fibre spinning might be responsible. Iizuka [1966, 1985] suggested that there is a critical shear rate, the value of which is altered by type and quantity of cations present, for the formation of β-sheet precipitate. He proposed that the presence of multivalent cations aids in the precipitation of fibroin through the chelation of charged residues [Iizuka 1966].

Some researchers have studied the ex vivo fibre spinning to try to understand the dramatical conformational change [Magoshi *et al.* 1985, Yamaura *et al.* 1985, Trabbic & Yager 1998]. Based on the Du Pont patented process [Lock 1993] for spinning *B. mori* fibres from 1,1,1,3,3,3-hexafluoro-2-propanol (HFIP) solutions, Trabbic & Yager [1998] used a wet spinning process to spin fibres with varying degrees of postspinning draw. Zhou and co-workers [Zhou *et al.* 2003, 2004, Zong

et al. 2004, Li *et al.* 2001] found an effect of pH and concentrations of certain cations or metal ions, such as K^+, Ca^{2+}, Cu^{2+} and Zn^{2+} ions, on the conformational transition from Silk I to Silk II in regenerated (redissolved) *Bombyx mori* silk fibroin.

No study, however, has conclusively identified the processing conditions needed to spin fibres with the correct hierarchical structure from reconstituted solutions of *B. mori* fibroin.

1.2.4. THE WILD SILKWORMS

1.2.4.1. The Tussah silkworm

Although the domesticated silkworm *Bombyx mori* is the mainstay of the silk industry, there is a considerable trade in some countries in silk produced by silkworms living "wild". The most important of these wild silks are those which are known as Tussah.

Tussah is the product of several species of silkworm of the genus *Antheraea*, particularly *Antheraea mylitta*, indigenous to India and *Antheraea pernyi* which is native to China [Huber 1947, Cook 1984].

The *A. pernyi* silk is a fairly common species, being mass-produced in north-east China for silk fibre production [Li *et al.* 2003]. The Tussah silkworm is very different from the domesticated mulberry or *B. mori* silkworm. It will feed only out of doors on oak (*Quercus serrata*) trees of shrub type which are kept at a certain height by pruning, whereas the *B. mori* silkworm feeds on mulberry leaves. On maturity, it ranges in length from 75 to 130 mm, is of soft green color, and is covered with tufts of reddish brown hair. There are two crops of cocoons produced annually. The spring crop is small and is used almost entirely for reproduction purposes for producing the autumn crop [Huber 1947].

As will be described in the further chapters, the different diet and process will result in different chemical, physical and structural properties.

1.2.4.2. Other wild silkworms

Although Tussah silk is the most important wild silk in commercial use, there are still other varieties of caterpillars which produce silk. These silks are called wild, because these worms are not capable of being domesticated and artificially cultivated. Some examples are: *Antheraea yamamai, Attacus ricini, Attacus Atlas*.

1.3. SPIDER SILK

1.3.1. INTRODUCTION

Of all the silks investigated thus far, it seems that silk from the orb-weaving spiders possess some of the most exceptional mechanical properties. The reason for this is unclear but one explanation is that a possible evolutionary adaptation has led to the

enhancement of certain properties of orb-weaver silk in comparison to other arthropods.

Orb-web weaving spiders typically have five to seven different spinning glands, each producing a specific type of silk. However, they all have several features in common. They are [Lucas 1964; Xu & Lewis 1990]

(1) composed completely of protein;

(2) undergo a transition from a soluble to an insoluble form that is virtually irreversible;

(3) composed of amino acids dominated by alanine, serine, and glycine, but, unlike silkworm silk, have substantial quantities of other amino acids, such as glutamine, tyrosine, leucine and valine; and

(4) composed of protein(s) of unknown number and molecular weight.

These silks vary in their mechanical properties over a very wide range of tensile strength and elongation. It is known that spider silk is a semicrystalline polymer, but the amount, composition, orientation, and structure of each of its phases remain the subject of debate. More details are described in the further chapters.

Because of the diversity in microstructure and properties of the different spider silks, they provide the opportunity for the development of a whole new class of biomaterials.

1.3.2. SILK PRODUCTION BY SPIDERS

1.3.2.1. Introduction

Silk production begins at the tail of the major ampullate gland, where 90% of the silk protein is produced. The silk protein is present as a dissolved high-molecular-weight polymer in the aqueous environment of the spider's silk glands. The most recent molecular weight data suggest that major ampullate gland silk fibroin has a M_n of 720.000 and a M_w/M_n of 1.03, and that its molecular weight degrades upon spinning and aging [Jackson & O'Brien 1995]. After passing and processing through the ducts, the silk protein changes from a dissolved polymer with a narrow molecular weight distribution to a very insoluble solid with about 30% lower molecular weight and greatly increased polydispersity.

The initial step of silk production involves the ingestion of proteins as prey, eventually recycling their own silk. Proteins accumulate in the silk glands and form into a liquid crystal phase that is around 50% protein by weight and yet still somewhat soluble. Synthesis of the silk protein occurs in specialised cells at the tail of the gland, and the silk protein is secreted into the lumen of the gland where it is stored in soluble form [Lucas 1964]. As the protein passes into the ducts leading to the spinnerets it is hypothesised that a phase change is induced by shearing and pressure forces resulting in an alignment of the polypeptide chains. The most interesting part of the biosynthesis for the *Nephila clavipes* spider, takes place approximately 4 mm before the protein exits the duct and involves the displacement of excess water from the proteinaceous phase to form silk filaments. By the time the

protein reaches the end of the duct, it is as insoluble as the extruded silk. The fibre diameter can be varied by virtue of a valve, regulated by muscular action, at the end of the duct, as shown in Figure 1.2 [Lucas 1964, Foelix 1996]. If the valve is almost closed, the transition of liquid to solidified silk takes place directly behind the valve. When the valve is in the "open" position, the lumen of the spigot is filled with liquid silk and a solid thread is first formed at the tip of the spigot.

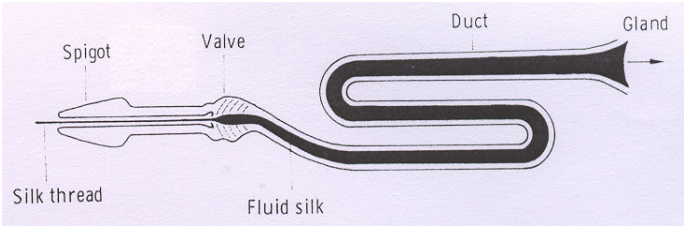

Figure 1.2 - Diagrammatic representation of dragline formation in *Araneus*. [Foelix 1996]

The transition from the water-soluble liquid form into the insoluble, solid silk thread is not yet fully understood, but apparently the molecules of the polypeptide chain change their orientation from an α-configuration (α-helices) that is soluble (with predominantly intramolecular hydrogen bonds) to the insoluble β-configuration (β-pleated sheet form with intermolecular bonds) [Foelix 1996]. It is, however, an irreversible process.

In addition, a number of studies showed that other factors, such as metal ions and pH may be involved in natural silk processing in silkworms and spiders [Knight & Vollrath 2001, Chen *et al.* 2002a,b, Ochi *et al.* 2002, Zhou *et al.* 2003]. These studies reveal successive changes in pH and the contents of the metallic ions (e.g. Na+, K+, Ca2+ and Cu2+) as silk proteins flow through the secretory pathway. pH and metallic ions have profound effects on the rheology of silk protein solutions [Chen *et al.* 2002b, Ochi *et al.* 2002]. Nemoto and co-workers [Ochi *et al.* 2002] suggested that calcium and magnesium ions may be important in silkworm silk formation, while potassium ions are thought to be important in spider dragline silk [Chen *et al.* 2002a,b,c].

1.3.2.2. The silk glands

A spider has three pairs of spinnerets on its abdomen: anterior, median and posterior, as shown in Figure 1.3. Each gland leads to a specific spinneret, which opens to the outside in the form of a tiny spigot. During the construction of a web or cocoon the spinnerets must move independently, yet must also be able to work together in a highly coordinated manner. The spinnerets can move in several ways: lifting, lowering, twisting, and also a synchronous spreading of all spinnerets can be observed [Foelix 1996]. The effective working range of the spinnerets is enhanced to a great extent by the movements of the abdomen itself.

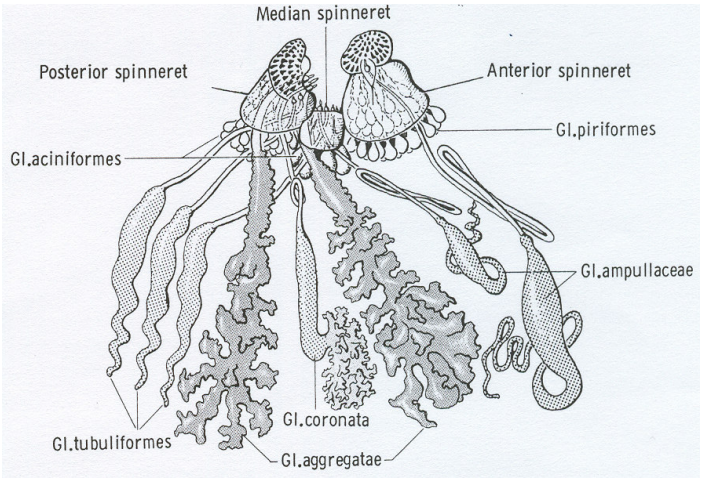

Figure 1.3 - Spinning apparatus of the golden silk spider Nephila. Only one half of the paired set of silk glands is depicted [Foelix 1996]

The following glands can be distinguished morphologically and histologically: ampullate glands, aciniform glands, cylindrical or tubuliform glands, aggregate glands, piriform glands, and flagelliform (or coronate) glands. Each spinning gland comprises the gland proper, mostly pear-shaped, and a thin duct.

1.3.2.3. The structure of an orb web

The orb web is certainly the best known of all webs. Essentially it is made up of three elements as shown in Figure 1.4 [Foelix 1996]: (1) radial threads, which converge in a central spot, (2) frame threads, which delineate the web and serve as insertion sites for the radial threads; and (3) the catching spiral. The scaffolding of the orb web is provided by the radial and frame threads; neither type is sticky. The catching spiral, in contrast, consists of a thread studded with glue droplets. The coating is hygroscopic what makes it so elastic. The orb web as a whole is thus a combination of strong frame and radial threads with a very elastic catching spiral. Frame and radii provide a mechanically stabile construction, which is also well suited for signal transmission (e.g. prey vibrations). The elastic capture thread is an adaptation to struggling prey, i.e., the impact and movements of an insect cause little damage, because the kinetic energy is largely absorbed by the yielding catching spiral [Foelix 1996 and ref. herein]. The hub usually consists of irregularly interconnected threads. Immediately surrounding the hub is the so-called "strengthening zone", but this part of the web cannot always be determined as separate from the hub itself. More important is the next part, the "free zone", which is crossed only by the radial threads. Here the spider can easily change from one face of the web to the other. The actual catching area is that part of the web covered by the sticky spiral.

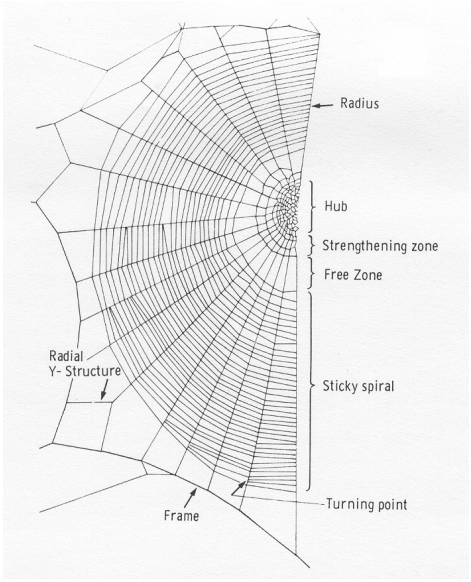

Figure 1.4 - Structure of an orb web as traced from a photograph of a web of *Araneus diadematus* [Foelix 1996]

The number of radii varies little within a particular species of orb weaver, and is often characteristic of that species. Because of the structural variation of the web between spider species, it is often possible to identify a certain spider solely by its characteristic web structure. For further structural variations in the web structure and its construction, it is referred to literature [Foelix 1996, Craig 2003].

1.3.2.4. The origin of different spider silks

Each type of gland secretes a different kind of silk with its own specific characteristics to perform a specific function. Figure 1.5 gives an overview of the different types of spider silks and their function for the orb-web weaving spider *Araneus diadematus*.

The most investigated type of spider silk is the dragline or major ampullate (MA) silk that is secreted by the major ampullate glands of the spider. The dragline is used to support the spider when constructing a web and to prevent it from falling. This function results in mechanical properties combining a high Young's modulus with a high strength. Due to its size and accessibility the major ampullate gland has been the focus of most studies.

A second important type of spider silk is the flagelliform, spiral or capture silk. This type of silk is composed of an acidific glycoprotein, secreted from the flagelliform gland, and coated with glue from the aggregate gland what makes it sticky. The glue is not regarded as silk because it is composed of glycoproteins and other amino acids. The flagelliform silk is exclusively used for the construction of the spiral components of the web. This function results in a fibre that is highly extensible and

capable of absorbing the energy of the flying prey without failure. The functional role of the glue is believed to allow for more effective capture of prey.

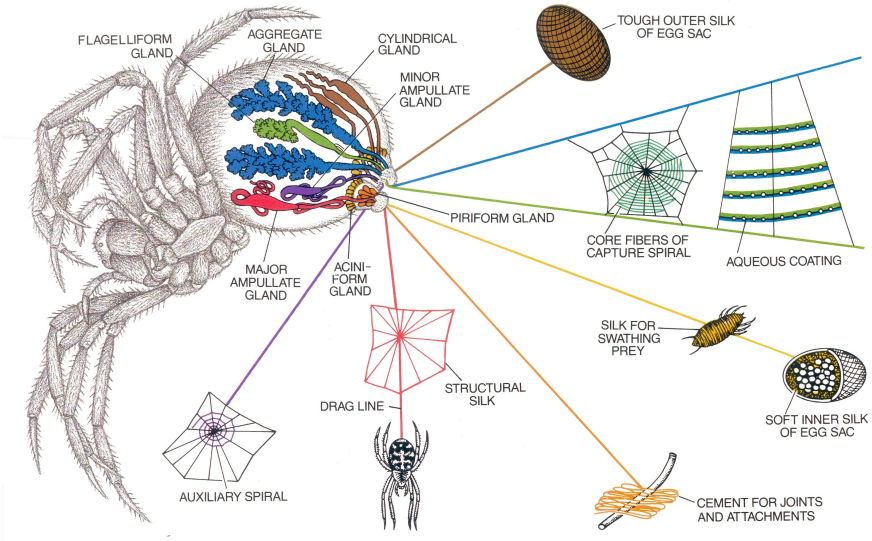

Figure 1.5 - Types and functions of spider silk of *Araneus diadematus* [Vollrath 1992, 2000]

Minor ampullate (MI) silk is the spider silk that is secreted by the minor ampullate glands and is a strong non-elastic deformably stretchable silk used in web formation [Colgin & Lewis 1998].

Another spider silk that is discussed in this text is the egg sac silk that is used to wrap eggs. Vollrath [1992, 2000] mentioned in his representation of the spinning glands (Figure 1.5) associated to its function, that the soft inner silk of the egg sac is produced by the aciniform glands whereas the tough outer silk of the egg sac is secreted by the cylindrical or tubuliform spinning glands. Viney *et al.* [2000] pretends the opposite. The tubuliform glands are only found in female spiders, what makes it more probable that the inner silk is indeed secreted by the tubuliform glands.

1.4. APPLICATIONS

1.4.1. SILKWORM SILKS

1.4.1.1. History

According to Chinese legend, silk culture dates back to the year 2640 B.C., when the Empress Si-Ling-Chi learned how to rear the caterpillars and unwind the cocoons that they made. The Empress devoted herself personally to rearing the worm, and it was largely through her encouragement that the silk industry became established in China [Cook 1984]. For three thousand years China held a monopoly in the silk industry. Then sericulture, as silk production is called, spread to Japan via Korea.

Gradually, silk production spread westwards over Asia. By the eighth century, sericulture had been carried by the Moors to Spain and Sicily, and from there it spread to Italy and France. Silk weaving began at Tours in France in 1480.

By the sixteenth century, silk was in widespread use among the wealthy nobility in Europe. For nearly 4000 years, silkworm silk was a mainstay of commerce as one of the most expensive of luxury goods, bringing wealth to traders and their communities as well as employment to the producers. The decline of traditional dress in the early years of the 20th century, coupled with the demands as well as the constraints of the Second World War, helped petrochemical fibres to gain their present strong position at the cost of natural silks. At the moment, it appears that silks, albeit now artificially made, are on the verge of a comeback [Vollrath & Knight 2003]. But to successfully copy natural silks, we must mimic the salient design features of both the feedstock dope proteins and the spinning process.

1.4.1.2. Uses

Because of its attractive properties (high strength, flexible with good water absorbing power, soft, good elastic recovery behaviour, glossiness, etc.), silk has a wide variety of uses in the apparel, drapery, upholstery and military fields.

Natural silk has a long history of use as a textile fibre, and has been used in recent years for medical sutures, blood vessels, artificial skin, tendons and for binding enzymes [Bunning *et al.* 1994, Kuzuhara *et al.* 1987].

Interest in *Antheraea pernyi* silk for biomedical applications has recently grown because *A. pernyi* SF contains the tripeptide sequence of arg-gly-asp (RGD), known as cell adhesive site for mammalian cell culture [Minoura *et al.* 1995, Pierschbacher & Ruoslahti 1984a, 1984b, Li *et al.* 2003]. Therefore, it has been investigated as a potential biomaterial such as a matrix for the enzyme immobilization and mammalian fibroblast cell culture [Kweon *et al.* 2001a, Kweon *et al.* 2001b and references herein].

1.4.2. SPIDER SILK

1.4.2.1. History

More than two centuries ago attempts were made by the French to utilize spider silk in the textile industry [Huber 1947]. With a great deal of patience a pioneer, Monsieur Bon from Languedoc, France, collected a large number of spider cocoons and from the fine gray silk, he made some stockings and gloves, which were exhibited before the Academy of Sciences in Paris in 1710. A physicist and entomologist, René Reaumur, was at that time commissioned to investigate the possibility of raising spiders for their silk. He found so many insurmountable difficulties that he was compelled to render an adverse report. The spiders were difficult to manage, became belligerent, easily excited, and cannibalistic. It was difficult to provide them with proper food and to keep them in large groups as they would fight and devour one another. Furthermore, the silk produced was small in quantity and was so delicate in quality as to be difficult to utilize in spinning.

In 1864, Dr. Wilder, an American Army surgeon, revived the idea of using spider silk in textiles. He selected the *Nephila clavipes* and proposed the milking method of reeling the filaments directly from the spider, instead of collecting the cocoons. He found the life product of about 450 spiders would be required to produce 1 yard of silk goods. Also the *Nephila madagascarensis* spiders have been used in making silk cloth. However, the large number of spiders required to produce 1 gram of silk makes the spider silk production process for textile industry impractical and not economical.

1.4.2.2. Uses

Spider silk filaments have long been used in the optical industry as crosslines in various instruments in astronomy and surveying, such as telescopes and microscopes [Huber 1947]. Their usefulness for crosslines depends on several factors such as their fineness, uniformity, strength and ability to withstand changes in humidity and temperature. Only a few spiders have been found whose silk meets the rigid requirements.

Because of their extreme properties, in the last 20 years, a lot of efforts were made to try to produce "artificial" spider silk (see further). Investigators are now developing ways to produce dragline silk in quantities sufficient for applications such as bullet-proof vests, impact sensitive composite systems, parachute cords, surgical sutures, and replacement ligaments. The spider silk's biocompatibility, biodegradability and mechanical response offer the possibility for high tensile strength sutures, prosthetic devices, artificial tendons, blood vessels, and also skin grafts could greatly benefit from the mechanical response of silks.

1.4.2.3. Artificial spinning of spider silk

Several research groups are vying to spin the first artificial spider silk, a feat that requires a three-pronged approach [Lipkin 1996]. One must determine the fibre's molecular architecture, understand the genes that yield silk proteins, and learn how to spin the raw material into thread.

Most researchers are using recombinant DNA technology to create a synthetic analogue to spider silk (mainly dragline silk, but also capture silk). The artificial genes are then inserted into yeast and bacteria, such as *Escherichia coli*, and the protein analogues are produced. The "biosilk" is then dissolved in a solvent and protein spun into fibres using spinning techniques similar to those of the spider. Several patents (see 1.6) are taken on the spinning of genetically modified spider silk proteins (a.o. Du Pont, University of Wyoming, US Army, Plant Cell Technologies and Lebensmittel Consulting, Institute for Plant Genetics & Crop Plant Research).

In a couple of years the American Chemical concern Du Pont expects to come on the market with a superstrong, elastic and comfort friendly fibre on the basis of spider rag. The company is expecting to come in mass production within 10 years at high prices. The new fibre though will be only half that heavy and will be twice as strong as the high-tech para-aramid fibre Kevlar.

As well as yeast and bacteria, plants could serve as hosts for artificial genes. It is hoped that a robust plant could express a dragline silk gene, so that perhaps silk proteins could be harvested in vast quantities, processed into a liquid polymer, and spun in factories. For the past two years, scientists at Germany's Institute for Plant Genetics & Crop Plant Research in Gatersleben [Scheller *et al.* 2001] have been inserting spider genes into potato and tobacco plants. And they have succeeded in producing and harvesting the silk protein. As a result, they predict that they can make industrial spider silk economically feasible within 5 to 7 years.

Exploiting anatomical similarities between spider silk glands and mammalian glands, Nexia Biotechnologies, Inc. in Montreal, Canada [Nexia Biotechnologies], has developed genetically modified goats whose milk contains dissolved spider silk proteins. The extracted spider silk proteins received the name Biosteel®. Recently, Nexia has decided to refocus fibre development towards biopolymer sales and specialized nano-scale fibre applications for spider silk and away from traditional fibres and yarns. This decision was prompted by the emerging interest in nanofibres and by the ongoing technical challenges of producing bulk, cost competitive spider silk fibres with superior mechanical properties, especially strength. Nexia has suspended its outsourcing of spinning micron-sized fibres with Acordis SF and stopped its in-house spinning effort. Spinning of BioSteel® proteins into nanometer diameter fibres has been achieved and Nexia is now determining the product specifications for medical and micro-electronic applications.

Researchers of the Chinese Academy of Science's Shanghai Institute for Biochemistry [Rennie 2000] successfully implanted the gene that makes the spider silk viscous into the fertilised eggs of silkworms. This way they hope to be able to mass-produce spider-strength silk.

Although silks have been sequenced and silk genes spliced into bacteria, animals and plants, synthetic silk is still not a mass-produced, high-strength technological material. The spider silk proteins in solution are available, but the problem remains the transformation from the solution state to the solid fibre. Though several different methods have been tried for spinning silk proteins artificially, the filaments lack the tenacity of natural dragline silks [Liivak *et al.* 1998, Seidel *et al.* 1998, 2000, Lazaris *et al.* 2002, Shao *et al.* 2003]. Several researchers claim that they have succeeded in producing artificial spider silk on laboratory-scale, but the further extension to industry-scale seems to be a problem.

Because of the problems encountered with the spinning of artificial silk microfibres, they are now trying to produce nano-applications, such as the production of a carbon nanotube reinforced with silk fibres (see 1.6 Patents).

1.5. REFERENCES

Bunning T.J., Jiang H., Adams W.W., Crane R.L., Farmer B., Kaplan D., In: Silk Polymers – Materials Science and Biotechnology, Kaplan D., Adams W.W., Farmer B., Viney C. (Eds.), American Chemical Society, Washington DC, ACS Symposium Series, 544:353-358 (1994)

Chen X., Knight D.P., Shao Z.Z., Vollrath F., Conformation transition in silk protein films monitored by time-resolved Fourier transform infrared spectroscopy: Effect of potassium ions on *Nephila* spidroin films, Biochemistry 41:14944-14950 (2002a) –

Chen X., Knight D.P., Vollrath F., Rheological characterization of *Nephila* spidroin solution, Biomacromolecules 3:644-648 (2002b)

Chen X., Shao Z.Z., Knight D.P., Vollrath F., Conformation transition of silk protein membranes monitored by time-resolved FTIR spectroscopy: Effect of alkali metal ions on *Nephila* spidroin membrane, Acta Chim. Sin. 60:2203-2208 (2002c)

Colgin M.A. & Lewis R.V., Spider minor ampullate silk proteins contain new repetitive sequences and highly conserved non-silk-like "spacer regions", Protein Science 7:667-672 (1998)

Cook J.G., Handbook of Textile Fibres – Natural Fibres, Merrow Publishing Co. Ltd., Durham, England, 144-165 (1984)

Craig C.L., Spiderwebs and silk – Tracing evolution from molecules to genes to phenotypes, Oxford University Press, New York, (2003)

Foelix R.F., Biology of spiders, 2nd Edition, Oxford University Press, Georg Thieme Verlag, New York, Chapter 5, 110 (1996)

Gupta V.B., Structure of textile fibres and structural dependence of their mechanical properties, In: "Progress in textiles: Science & Technology", Kothari V.K (Ed.), Vol. 2, IAFL Publications, 11-118 (2000)

Haupt J. & Kovoor J., Silk-gland system and silk production in *Mesothelae* (*Araneae*), Annales des Sciences Naturelles, Zoology, Paris 14:35-48 (1993)

Howitt F.O., Proteins – Silk, In: The structure of textile fibres, Urquhart A.R., Howitt F.O. (Eds.), The Textile Institute, Manchester, United Kingdom, Chapter V, 59-68 (1953)

Huber C.J., The silk fibers, In: Matthew's textile fibers – Their physical, microscopical and chemical properties, Mauersberger H.R. (Ed.), 5th edition, John Wiley & Sons Inc., New York, Chapter XVII, 679-729 (1947)

Iizuka E., Mechanism of fiber formation by the silkworm, *Bombyx mori* L., Biorheology 3:141-152 (1966)

Iizuka E., Silk thread – Mechanism of spinning and its mechanical properties, Appl. Polym. Symp. 41:173-185 (1985)

Jackson C. & O'Brien J.P., Molecular-weight distribution of *Nephila clavipes* dragline silk, Macromolecules 28:5975-5977 (1995)

Knight D.P. & Vollrath F., Changes in element composition along the spinning duct in a *Nephila* spider, Naturwissenschaften 88:179-182 (2001)

Kovoor J., Comparative structure and histochemistry of silk-producing organs in arachnids, In: The ecophysiology of spiders, Nentwig W. & Heimer S. (Eds.), Springer-Verlag, New York, 160-186 (1987)

Kweon H.Y., Um I.C., Park Y.H., Structural and thermal characteristics of *Antheraea pernyi* silk fibroin/chitosan blend film, Polymer, 42: 6651-6656 (2001a)

Kweon H., Woo S.O., Park Y.H., Effect of heat treatment on the structural and conformational changes of regenerated *Antheraea pernyi* silk fibroin films, J. Appl. Polym. Sci. 81:2271-2276 (2001b)

Kuzuhara A., Asakura T., Tomoda R., Matsunaga T., Use of silk fibroin for enzyme membrane, J. Biotechnl. 5:199-207 (1987)

Lazaris A., Arcidiacono S., Hunag Y., Zhou J.F., Duguay F., Chretien N., Welsh E.A., Soares J.W., Karatzas C.N., Spider silk fibres spun from soluble recombinant silk produced in mammalian cells, Science 295:472-476 (2002)

Li G., Zhou P., Sun Y., Yao W., Mi Y., Yao H., Shao Z., Yu T., The effect of metal ions on the conformation transition of silk fibroin, Chem. J. Chin. Univ. 22:860-862 (2001)

Li M.Z., Tao W., Kuga S., Nishiyama Y., Controlling molecular conformation of regenerated wild silk fibroin by aqueous ethanol treatment, Polymers for Advanced Technologies 14 (10): 694-698 (2003)

Lipkin R., Artificial spider silk, Science News, 149:152-153 (1996)

Liivak O., Blye A., Shah N., Jelinski L.W., A microfabricated wet-spinning apparatus to spin fibers of silk proteins. Structure-property correlations, Macromolecules 31:2947-2951 (1998)

Lock R.L., In: WO93/15244, E.I. Du Pont De Nemours and Company, Wilmington, DE (1993)

Lucas F., Spiders and their silks, Discovery 25:20-26 (1964)

Magoshi J., Magoshi Y., Nakamura S., Crystallization, liquid-crystal, and fiber formation of silk fibroin, J. Appl. Polym. Sci.: Appl. Polym. Symp. 41:187-204 (1985)

Minoura N., Aiba S., Gotoh Y., Tsukada M., Imai Y., Attachment and growth of fibroblast cells on silk fibroin, Biochem. Biophys. Res. Commun. 208(2):511-516 (1995)

Nexia Biotechnologies, BioSteel® Extreme Performance Fibers; http://www.nexiabiotech.com/biosteel.html

Ochi A., Hossain K.S., Magoshi J., Nemoto N., Rheology and dynamic light scattering of silk fibroin solution extracted from the middle division of *Bombyx mori* silkworm, Biomacromolecules 3:1187-1196 (2002)

Pierschbacher M.D., Ruoslahti E., Cell attachment activity of fibronectin can be duplicated by small synthetic fragments of the molecule, Nature 309:30-33 (1984a)

Pierschbacher M.D., Ruoslahti E., Variants of the cell recognition site of fibronectin that retain attachment promoting activity, Proc. Natl. Acad. Sci. USA 81:5985-5988 (1984b)

Rennie D., China Implants Spider Genes Into Silkworms, http://rense.com/general5/silk.htm (2000)

Scheller J., Gührs K.H., Grosse F., Conrad U., Production of spider silk proteins in tobacco and potato, Nat. Biotechnol. 19:573-7 (2001)

Seidel A., Liivak O., Jelinski L.W., Artificial spinning of spider silk, Macromolecules 31:6733-6736 (1998)

Seidel A., Liivak O., Sarah C., Adaska J., Ji G. Yang Z.T., Grubb D., Zax D.B., Jelinski L.W., Regenerated spider silk: Processing, properties, and structure, Macromolecules 33:775-780 (2000)

Shao Z.Z. & Vollrath F., Materials: Surprising strength of silkworm silk, Nature 418 (6899): 741-741 (2002)

Shao Z.Z., Vollrath F., Yang Y., Thogersen H.C., Structure and behavior of regenerated spider silk, Macromolecules 36:1157-1161 (2003)

Trabbic K.A. & Yager P., Comparative structural characterization of naturally- and synthetically-spun fibers of *Bombyx mori* fibroin, Macromolecules 31:462-471 (1998)

Viney C., From natural silks to new polymer fibres, J. Text. Inst., 91: 2-23 Part 3 Sp. Iss. SI (2000)

Vollrath F., Spider Webs and Silks, Scientific American 266(3):52-58 (1992)

Vollrath F., Strength and function of spiders' silks, Reviews in Molecular Biotechnology 74:67-83 (2000)

Vollrath F. & Knight D., Biology and technology of silk production, Biopolymers 8:26-46 (2003)

Wiedbrauck J.Z., Vom Spinnen bei Schmetterlingsraupen und seiner Abhängigkeit, von Metamorphosehormonen, Erpsychol. 12:176-202 (1955)

Xu M. & Lewis R.V., Structure of a protein superfiber: Spider dragline silk, Proc. Nat. Acad. Sci. USA 87:7120-7124 (1990)

Yamaura K. Okumura Y., Matsuzawa S., Mechanical denaturation of high polymers in solutions .36. Flow-induced crystallization of *Bombyx mori* L silk fibroin from the aqueous solution under a steady- state flow, J. Macromol. Sci. - Phys. B. 21:46-69 (1982)

Yamaura K. Okumura Y., Oazki A., Matsuzawa S., Flow-induced crystallization of *Bombyx mori* L silk fibroin from regenerated aqueous-solution and spinnability of its solution, Appl. Polym. Symp. 41:205-220 (1985)

Zhou L., Chen X., Shao Z.Z., Zhou P., Knight D.P., Vollrath F., Copper in the silk formation process of *Bombyx mori* silkworm, FEBS Letters 554:337-341 (2003)

Zhou P., Xie X., Deng F., Ping Z., Xun X., Feng D., Effects of pH and calcium ions on the conformational transitions in silk fibroin using 2D Raman correlation spectroscopy and C-13 solid-state NMR, Biochemistry 43:11302-11311 (2004)

Zong X.H., Zhou P., Shao Z.Z., Chen S.M., Chen X., Hu B.W., Deng F., Yao W.H, Effect of pH and copper(II) on the conformation transitions of silk fibroin based on EPR, NMR, and Raman spectroscopy, Biochemistry 43:11932-11941 (2004)

1.6. PATENTS

Basel R.M., Elion G.R., Cloning methods for high strength spider silk proteins, USA, WO9708315 (1997)

Fahnestock S.R., Novel, recombinantly produced spider silk analogs, Du Pont, USA, WO9429450 (1994)

Fahnestock S.R., Recombinantly produced spider silk, Du Pont, USA, US6268169 (2001)

Hiramatsu S., Moriyama H., Asaoka R., Morita K., Tanaka T., Yamada K., Obrien J.P., Fahnestock S.R., Silk thread containing spider thread protein and silkworm producing the silk thread, Toray Industries (Japan), Du Pont (USA), WO2005068495 (2005)

Islam S., Karatzas C., Rodenhiser A., Alwattari A., Huang Y., Turcotte C., Methods and apparatus for spinning spider silk protein, Nexia Biotechnologies Inc., Canada, WO2004090205 (2004)

Kaplan D.L., Lombardi S.J, Recombinant spider silk proteins through genetic engineering, US Army, USA, WO9116351 (1991)

Karatzas A.-L., Karatzas C., Turner J.D., Production of biofilaments in transgenic animals, Nexia Biotechnologies Inc., Canada, WO9947661 (1999)

Karatzas C., Huang Y., Turcotte C., Recovery of biofilament proteins from biological fluids, Nexia Biotechnologies Inc., Canada, GB2399820 (2003)

Ko F.K, Sukigara S., Gandhi M., Ayutsede J., Electrospun carbon nanotube reinforced silk fibers, University of Drexel, WO2005045122 (2005)

Lewis R.V., Hayashi C., Gatesy J.E., Motriuk D., Spider silk protein encoding nucleic acids, polypeptides, antibodies and method of use thereof, University of Wyoming, USA, WO03020916 (2003)

Lewis R.V., Xu M., Hinman M., Spider silk protein, University of Wyoming, USA, US5728810 (1998)

Liu T., Li W., Liu H., Zhao L., Method for the establishing an expression system of spider dragline silk gene in bombyx mori, Sichuan University Tianyou Bio, China, US2002137211 – CN1362520 (2002)

Mason S. M., Pouchkina N., Spider silk polypeptide, University of York, WO2004016651 (2004)

Mello C.M., Arcidiacono S., Butler M., Methods for the purification and aqueous fiber spinning of spider silks and other structural proteins, US Army, USA, WO0153333 (2001)

Pan Z., Xu Q., Nanometer level regenerated spider silk fiber and its preparation method, Soochow University, China, CN1670272 (2005)

Roth D.A., Lewis R.V., Expression of spider silk proteins in higher plants, University of Wyoming, USA, WO02099082 (2002)

Scheller J., Conrad U., Guehrs K.-H., Grose F., Synthetic spider silk proteins and the expression thereof in transgenic plants, IPK Institut für Pflanzengenetik, Germany, WO0194393 (2001)

Tang K., Zuo K., Sun X., Spider silk protein gene designed and synthesized by plant preference codon and its application, University Shanghai Jiaotong, China, CN1390937 (2003)

Wang Y., Li W., Niu H., Cotton fibrocyte expression vector plasmid of spider silk gene, Inst. of Genetics & Dev. Biology, China, CN1380418 (2002)

2

TENSILE BEHAVIOUR OF SILKS

Textile fibres are only partially crystalline with small crystallites which contain a number of defects; they also contain disordered or amorphous regions in which molecular packing is not as compact as in the crystalline regions. However, the molecules in the two regions are intimately connected. On the application of a tensile force, while amorphous regions, being more compliant, will make the major contribution to deformation, the crystalline regions will also take part in the deformation process. It can be expected that the tensile behaviour of silks can be correlated to the structural organisation within the fibre.

In this chapter, uni-axial tensile testing is considered. A comparison of the tensile behaviour of different silk types is made in order to find characteristic properties that can be important in relation to the structure. This is followed by a modelling of the stress-strain behaviour of egg sac spider silk since this type is the focus of this work.

2.1. STRUCTURAL BASIS OF TENSILE TESTING

Aspects of fibre structure that permit or resist polymer straightening and movement of the polymers relative to each other determine the exact shape of the stress-strain curve for each fibre [Hatch 1993]. During a tensile test, the more compliant phase, namely the amorphous phase, is the first to deform on application of load. The initial resistance to deformation, which determines its initial modulus, arises from the interchain bonds which bind the molecules in the amorphous regions, the entanglements between the chains which are present in the amorphous regions, the constraints arising from the rigid crystallites between which the amorphous regions are sandwiched and the restriction of free movement in the laterally ordered oriented amorphous regions [Gupta 2000]. In other words, the lengthening of the fibre is (1) the result of the degree to which polymers lying at angles to the fibre axis can be moved into alignment with the axis and (2) polymers with a nonlinear configuration can be straightened [Hatch 1993]. Therefore, low-modulus fibres tend to be less oriented and less crystalline than high-modulus fibres.

At the point at which permanent deformation starts to take place, called the yield point, the interchain bonds in the amorphous regions can break and the polymer chains begin to slip by each other. At that point, additional stress easily extends the fibre, resulting in a flattening of the stress-strain curve. The slope of this flattened region largely reflects the strength of intrafibre bonding: the greater the bonding strength, the greater the slope of this segment. Vollrath & Porter [2006] proposed a direct link between the glass transition temperature and the yield point in an amorphous polymer such that the amorphous fraction changes from a glass to a rubber state immediately after yield. However, the ordered (crystal) fraction does not change state and imparts the residual stiffness in a semi-crystalline polymer above the glass transition or yield point. As tensile strain increases post-yield, the rubber states are progressively converted back to glassy or crystal states because the polymer chains are forced closer together by the tensile strain. Clearly, this means that the modulus must increase as more rubber states are lost. Usually, small increments of stress in this region give rise to large deformation.

Following hardening, the internal structure of the fibre begins to give way catastrophically and the rupture point is reached. The polymers have either slipped by each other because the applied stress is greater than the intrafibre bonding force or the applied stress has surpassed the strength of the polymers themselves, causing them to rupture. With respect to the strain-at-break, fibres that are highly-oriented and crystalline and have strong intrafibre bonding and/or straight polymer configuration tend to exhibit lower strain-at-break values.

Ko [1997] offered a structural basis for the stress-strain behaviour of dragline spider silk. The structure of spider silk may be considered as a hierarchical composite consisting of a liquid crystalline phase which is organised into a well-ordered helical fibrillar reinforcement structure. The helical fibrils are embedded in a matrix which consists of a network of inter-fibril linkages formed by hydrogen bonds. The high modulus in the initial region of the stress-strain curve reflects the combined contribution of the fibrils and the inter-fibrillar network of hydrogen bonds. On rupturing of the inter-fibrillar linkages, the stress-strain curve exhibits a pseudo yield

behaviour due to re-orientation of the fibrils. As these helical fibrils are straightened a gradual increase in modulus can be seen until it reaches a maximum. This is followed by the gradual rupturing of the fibrils and eventually the failure of the spider silk. The theory of Ko [1997] emphasizes the role of a fibrillar structure on the stress-strain behaviour.

Further correlations between mechanical properties and structure are described in Chapter 10.

2.2. PROPERTIES OF DIFFERENT SILK TYPES

2.2.1. SILKWORM SILKS

The ranges of tensile properties of commercial silkworm silk from *Bombyx mori* cocoons and Tussah silk from *Antheraea pernyi* silkworms are mentioned in Table 2.1 in comparison with the spider silks.

As for spider silk, the spinning process by the silkworm determines to a large extent the mechanical properties of the silk. It is generally assumed that commercial silkworm silk is much weaker and less extensible than spider dragline silk. However, Shao & Vollrath [2002] found that artificial reeling of silk from immobilized silkworms under steady and controlled conditions produces fibres that are superior to naturally spun ones and their toughness value can even approach that of spider dragline silk. The silkworm, like the spider, produces stronger, more brittle fibres at faster spinning speeds, whereas slower speeds led to weaker, more extensible fibres. Like in spider silk, the mechanical properties of silkworm silk show considerable inter- and even intra-individual variability [Vollrath & Knight 2003].

It was shown by Meredith [1945] that tenacity, breaking extension and initial modulus of silk were related to fibre fineness. Meredith found that in general, the finer the silk, the higher the tenacity and the initial modulus and the lower the breaking extension. It has further been shown [Iizuka 1966] that X-ray crystallinity and crystallite orientation also show significant correlation with fibre fineness. Thus high crystallinity and high crystallite orientation of silk result in fairly high modulus and tenacity [Gupta 2000]. At the same time, the elongation-at-break is quite substantial due to the presence of the amorphous phase. The combined effect of these is reflected in the high toughness of silk.

2.2.2. SPIDER SILK

Table 2.1 gives a comparison of the mechanical properties of the most important spider silks with other common biological and synthetic materials. For *Araneus diadematus* and *Nephila clavipes* spider silk and for *B. mori* silk, the results of different articles were combined [De Wilde 1943, Work 1976, Denny 1980, Stauffer *et al.* 1994, Gosline *et al.* 1999, Moore & Tran 1999, Madsen *et al.* 1999, Pérez-Rigueiro *et al.* 2001].

Table 2.1- Tensile properties of spider silks and other materials (MA silk: silk from the major ampullate gland; RH: relative humidity)

Material	Modulus (GPa)	Strength (GPa)	Strain (%)	Work (MJ m^{-3})
A. diadematus MA silk	7-10	1.08-1.61	27-40	160
A. diadematus egg sac silk		0.54	24	
A. diadematus viscid silk	0.003	0.5-1.4	270-476	150
N. clavipes MA silk	20-22	1.3-1.8	10-15	80
N. clavipes egg sac silk		1.3	24	
B. mori silk	7-16	0.5-0.7	12-24	70
A. pernyi silk		0.6	35	
Tendon collagen	1.5	0.15	12	7.5
Bone	20	0.16	3	4
Wool, 100% RH	0.5	0.2	50	60
Elastin	0.001	0.002	150	2
Resilin	0.002	0.003	190	4
Synthetic rubber	0.001	0.05	850	100
Nylon	5	0.95	18	80
Kevlar 49	130	3.6	2.7	50
Carbon	300	4	1.3	25
High-tensile steel	200	1.5	0.8	6

It can be concluded that major ampullate (MA) silk is stiffer than the other polymeric biomaterials listed, although mineralised biomaterials and some synthetic materials achieve greater stiffness than this silk, as indicated by the (initial) modulus in Table 2.1. The strength of MA silk, however, is clearly superior to that of all other biomaterials in this list. Spider MA silk belongs to the stiffest and strongest polymeric biomaterials known. Although the strength and stiffness of MA silk is lower than the engineering materials, such as Kevlar, carbon and steel fibre, the large extensibility of MA silk, however, makes this silk tougher than these materials, as indicated by the work(-to-rupture) value in Table 2.1.

With respect to the different spider silks, it can be noted that MA silk shows both high strain and tensile strength. Minor ampullate silk has a comparatively lower tensile strength and lack of strain (±5%), while flagelliform or viscid silk is characterised by its extreme high strain (200-300%) and lower tensile strength (Figure 2.1), comparable with minor ampullate silk [Hayashi *et al.* 1999]. The difference between minor ampullate and major ampullate silk is also that it deforms irreversibly when stretched while major ampullate silk is elastic [Colgin and Lewis 1998] (see also in Chapter 3).

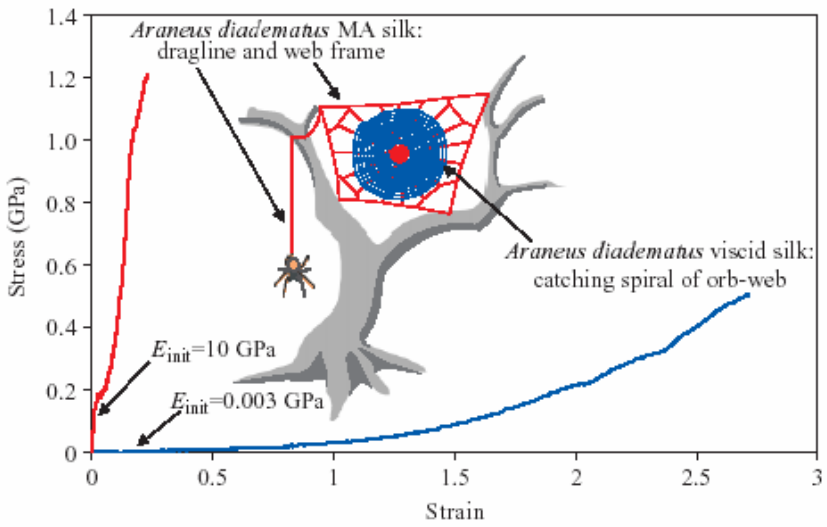

Figure 2.1 - Difference in stress-strain curve of *A. diadematus* MA and viscid silk [Gosline *et al.* 1999]

To further understand the roles that strain and toughness play in the function of MA and viscid silks, we must consider the way that these fibres are used in the normal activities of spiders. Figure 2.2 shows how the different silks are loaded taking into account their function. Gosline *et al.* [1999] concluded that fibre strain can compensate for strength when fibres are loaded normal to their long axis. The extreme toughness of both MA and viscid silks allows the spider to absorb a large amount of the prey's kinetic energy with a minimal volume of silk. Load cycle experiments by Denny [1976] indicate that 65% of the kinetic energy absorbed is transformed into heat and is not available to catapult the prey out of the web through elastic recoil.

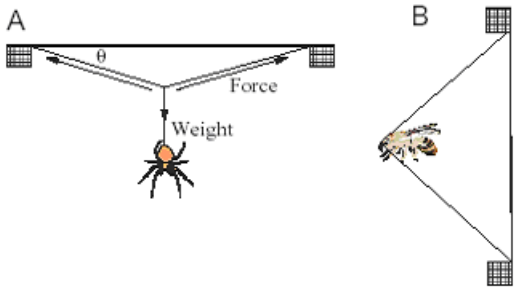

Figure 2.2 - Functional loading of *Araneus diadematus* major ampullate gland silk – A : MA silk, B: viscid silk [Gosline *et al.* 1999]

In addition, MA silk is known to exhibit the behaviour of supercontraction [Work 1977]. When MA silk is immersed in water, it shrinks by approximately 40-50%. Moreover, the initial stiffness drops by three orders of magnitude, and the material becomes rubber-like in its behaviour. Viscid silk also contracts when immersed in

water, although the effect on its mechanical properties is less dramatic [Gosline *et al.* 1994-1995]. The minor ampullate silks do not supercontract when they are immersed in water [Work 1977]. The structural implications of this phenomenon are further discussed in Chapter 10.

Spider silks are highly variable not only in mechanical properties [Cunniff *et al.* 1994, Madsen *et al.* 1999, Vollrath *et al.* 2001, Swanson *et al*. 2006] but also in chemical composition [Work & Young 1987, Lombardi & Kaplan 1999]. Some of this variability seems to be built into the genome [Hayashi & Lewis 2000, Winkler & Kaplan 2000, Swanson *et al*. 2006], and some is the outcome of production procedures [Cunniff *et al.* 1994, Hayashi *et al.* 1999, Vollrath & Knight 2003]. The condition of the spider, both external and internal, affects both silk production and mechanics. Orb webs are typically rebuilt every day and daily changes in climate (ambient temperature and humidity) or type of prey will affect the conditions under which the silk performs. The shapes of stress-strain curves vary greatly among different silks of the same spider as well as among the same type of silk in different spiders. This is due to differences in both spinning dope and spinning conditions [Vollrath & Knight 2003]. The spinning conditions are to a considerably degree under the spider's control [Cunniff *et al.* 1994, Vollrath *et al.* 2001]. The animal, for example, can vary spinning conditions by (1) adjusting its running speed when laying down silk, (2) modifying the speed in which it pulls silk with its leg, or (3) building its webs during different times of the day or night – which affects not only spinning temperature but also spinning speed in this exothermic creature.

2.3. METHODS

2.3.1. INSTRUMENT

The FAVIMAT-ROBOT (Textechno) was used to analyse the tensile properties. It is a semi-automatic single strength tester, working according to the principle of constant rate of extension (DIN 51221, DIN 53816, ISO 5079). The instrument is equipped with a balance allowing the mass to be measured at a high resolution of 0.1 mg.

The instrument includes a ROBOT, which is a fibre storage, equipped with a computer controlled transfer clamp for the transport of the single fibre to the testing position of the FAVIMAT.

Moreover, this instrument is equipped with an integrated measuring unit for linear density (in dtex = 0.1 g/km). This has the considerable advantage, certainly for natural fibres, that the fineness is determined simultaneously with the tensile properties. The linear density is measured according to the vibroscopic method (ASTM D 1577 – BISFA 1985/1989 chapter F).

The fibre is preloaded at a predefined speed. Further on, the fibre is subjected to an electro-acoustic sinusoidal vibration and the resonance frequency is detected with an opto-electronical sensor. The fibre linear density is calculated from the resonance condition, i.e. length, preload, and resonance frequency of the fibre. Suggesting a uniform mass distribution and a round cross-section, the linear density can be calculated as follows:

$$T_t = \frac{F_v \cdot 10^{11}}{4 \cdot f^2 \cdot L^2} \quad (2.1)$$

In Equation (2.1), T_t is the linear density in dtex, F_v is the preload in cN, f is the resonance frequency and L is the test length in mm.

2.3.2. TEST PARAMETERS

In literature if we look at the different results of mechanical properties of spider silk, we find that the tenacity of major ampullate (MA) spider silk varies between 0.8 GPa and 4.7 GPa and the breaking strain between 15% and 40%, independent of the spider silk species. Even within one spider species *Araneus diadematus* for tenacity results are obtained between 1.08 and 1.61 GPa and for the breaking strain between 27% and 40%. It seems very difficult to compare results, moreover often the test parameters, such as strain rate and gauge length, are not mentioned. Also the high variability within the results is rarely reported. In this section, the difference in tensile behaviour between different silks, using the same testing conditions, is investigated.

The recommended test parameters for tensile testing of different man-made fibres are given in the BISFA-standards. Often a strain rate of 50%/min is recommended except for fibres with high strain (> 8%: 100%/min). With respect to the gauge length, the preference is given to 20 mm, unless the fibres are too short. A gauge length of 10 mm increases the risk to get a break at the clamps. For the accuracy, it is recommended to take the gauge length as high as possible, although it should be taken into account that the tenacity values will be lower because of the higher probability of weak places.

Although the unit "cN/dtex" is not an S.I. unit, it is further used in this text since this unit is more accepted (historically grown) and always used in textiles, certainly for expressing tensile strength and moduli of fibres.

Since the breaking strain of spider silk is reported to be often higher than 30%, it is decided to perform the tests with the following settings: a gauge length of 20 mm, a test speed of 20 mm/min, and a pretension of 0.05 cN/dtex.

For the linear density, a test speed of 5 mm/min and a pretension of 0.08 cN/dtex were applied, as recommended by the instrument producer.

The tensile properties were tested in standardized conditions of 20 ± 2 °C and relative humidity of 65 ± 2%.

2.3.3. DEFINITION OF TENSILE PROPERTIES

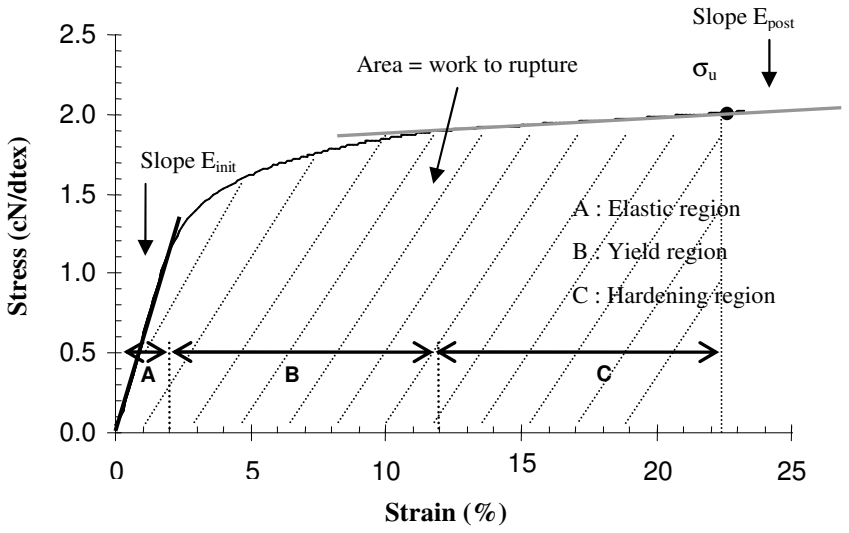

Figure 2.3 - Properties as calculated from the stress-strain curve

From the stress-strain curve, the following properties are determined (Figure 2.3):

1) **Breaking stress or tenacity** (cN/dtex): ratio of a yarn's breaking force to its linear density.

2) **Strain at break or breaking strain** (%): increase in length of a specimen produced by the breaking force, expressed as a percentage of the original nominal length.

3) **Work to rupture** (cN.cm): area contained by the force-elongation curve up to the point where the breaking force is reached, this is a measure of the toughness of a fibre. It can also be expressed in cN/dtex by dividing this value by the gauge length (in cm) and by the linear density (in dtex).

4) **Elastic Modulus** (cN/dtex): defined as the modulus in the elastic range of the diagram in which strain changes are still reversible. It is calculated from the slope of the initial straight line portion of the stress-strain curve.

5) **Post-modulus** (cN/dtex): defined as the modulus in the strain hardening zone. It is calculated from the slope of the straight line of the zone following the yield region, where the stress again is proportional to the strain values.

2.4. COMPARISON OF SILKS

2.4.1. MATERIALS

Egg sacs of the spider species *Araneus diadematus, Larinioides sclopetarius* and *Nephila clavipes* were collected in their natural habitat and tested.

Since they were collected in their natural habitat, we expect that the measured mechanical behaviour will better represent the real characteristics than if they were specially reared for this purpose. For the *A. diadematus*, 2 times 100 fibres were gently removed at random from the inside of two egg sacs (after removing the clearly visible outer cover), with care taken to stress the fibres as little as possible. For the *N. clavipes*, only one egg sac was available, 50 fibres were tested. For the *L. slopetarius*, the stress-strain curve is based on the average of tests for 25 fibres taken from one egg sac. The fibres of this species were more difficult to measure than the other spider silks.

For the dragline samples, spiders of different species were collected and kept in the laboratory under controlled conditions and the dragline filaments were manually reeled off as spiders hung freely suspended in space. The following species were selected: *A. diadematus, A. quadratus, A. marmoreus* and *N. clavipes*. From every sample, 25 (single) fibres were prepared and tested. For the *N. clavipes* fibres, because of a higher linear density (and thus less problems with testing), 50 fibres were tested. These fibres were reeled off at a controlled speed of about 6.5 cm/s with a house-made winding device.

Fibres were also tested from cocoons of the silkworms *Bombyx mori* and *Antheraea pernyi* (Tussah silk), grown at the Silk Museum of Meliskerke (The Netherlands). For these samples, the stress-strain curves were based on the average of 75 tests.

All samples were kept in a conditioned laboratory of 20 °C ± 2 °C and relative humidity of 65 ± 2 % for at least 24 hours before testing.

2.4.2. RESULTS

It should be remarked that in this study, we were mostly interested in the shape of the stress-strain curves. Because of the high variability in the results and the problems involved with testing these ultrafine fibres, it was too time-consuming and not feasible to perform sufficient tests in order to have all results in the 95% confidence range. For the dragline fibres, the simultaneous measurement of the linear density was often a problem so that some tests did not succeed.

Figure 2.4 and Figure 2.5 show the stress-strain behaviour of the egg sac spider silks and silkworm silks, and of the dragline spider silks. The average curves were stopped at the average strain-at-break values.

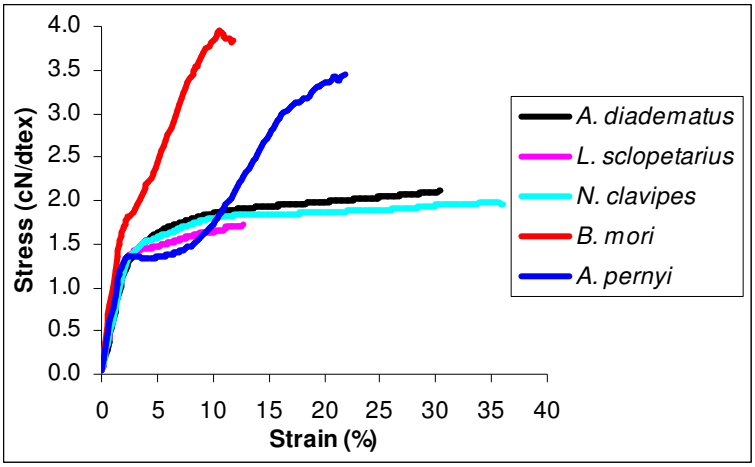

Figure 2.4 - Stress-strain curves of spider egg sac silks and silkworm silks (*B. mori* and *A. pernyi*)

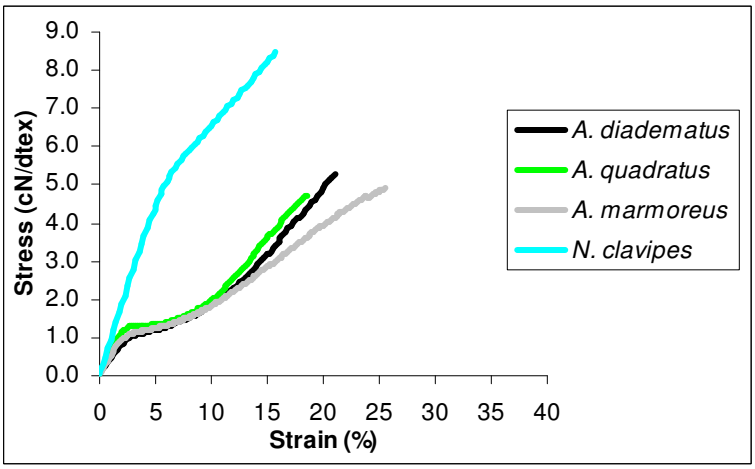

Figure 2.5 - Stress-strain curves for the dragline spider silks

It is clear that egg sac silks show a completely different stress-strain behaviour from dragline silks and even the functionally comparable silkworm cocoon silks. All stress-strain curves start with a small elastic region. For the dragline *Araneus* silks, *Bombyx mori* and *Antheraea pernyi* fibres, this region is followed by a plastic region and finally by strain hardening where the stress again linearly increases with strain. However spider egg sac silk shows a plastic-hardening region that is extremely flat. Since in this region the stress increases still linearly with strain, we will simply use the term "hardening region" to indicate this region. Further on, it should be remarked that *Nephila clavipes* dragline silk shows again a different behaviour, the initial elastic region is extended to higher strain values, and is almost directly followed by strain hardening. The plastic region is really limited.

It is also interesting to remark that the shapes of the stress-strain curves obtained for the silkworm silks show more similarities with dragline silk than with egg sac silk, even though the silkworm and spider use the former two silks for completely different functions. Since the main constituents of *B. mori* and *A. pernyi* silks are also glycine and alanine (see Chapter 4), the higher similarity in behaviour to dragline silk could be expected.

Since in further chapters, the research is focused on silks of *B. mori, A. pernyi* (Tussah) and the dragline and egg sac spider silk of *A. diadematus*, the more detailed tensile properties are summarized in Table 2.2. In this table, the values for tenacity and initial modulus are also mentioned in GPa to make it comparable with literature (Table 2.1). The conversion was made according to the following formula:

$$\rho \times 10^{-1} \times \text{Strength [cN/dtex]} = \text{Strength [GPa]} \qquad (2.2)$$

with ρ the specific density, expressed in g/cm³, this value was taken 1.30 g/cm³ [Vollrath & Knight 2001] and 1.25 g/cm³ [Cook 1984] for the spider silks and the silkworm silks, respectively.

Table 2.2 - Tensile properties of silkworm (*B. mori* and Tussah) and spider (*A. diadematus* dragline and egg sac) silks

	B. mori	**Tussah**	**Egg sac**	**Dragline**
Linear density (dtex)	1.00	2.89	0.89	0.24
SD	0.30	0.60	0.20	0.05
Strain (%)	11.86	21.91	31.50	20.66
SD	3.63	5.36	15.87	6.70
Tenacity (cN/dtex)	4.14	3.91	2.10	5.16
SD	0.66	0.74	0.42	2.35
Tenacity (GPa)	0.52	0.49	0.27	0.67
SD	0.08	0.09	0.05	0.31
Work to rupture (cN/dtex)	0.33	0.49	0.61	0.56
SD	0.13	0.15	0.33	0.36
Initial modulus (cN/dtex)	101.42	76.05	66.97	39.15
SD	14.23	6.55	6.65	10.72
Initial modulus (GPa)	12.68	9.51	8.71	5.09
SD	1.78	0.82	0.86	1.39
Strain range taken	**3-10%**	**10-17%**	**15-25%**	**10-17%**
Post-modulus (cN/dtex)	31.75	22.18	0.93	27.18
SD	30.74	41.46	38.83	8.88

For the tensile properties of the silkworm silks, slightly lower values are obtained for tenacity and strain (Table 2.1) [Denny 1980, Gosline *et al.* 1999, Pérez-Rigueiro *et al.* 2001]. Also for *A. diadematus*, for tenacity and initial modulus slightly lower values (Table 2.1) [Work 1976, Gosline *et al.* 1999, Madsen *et al.* 1999] are obtained. The different testing conditions can play a role in this.

With respect to the two different *A. diadematus* silks, a more detailed discussion of the results is mentioned further on.

2.5. IMPORTANCE OF SIMULTANEOUS MEASUREMENT OF LINEAR DENSITY

With respect to the linear density, it can be remarked that a high variation of linear density within an egg sac is observed. This promotes the importance to measure the linear density simultaneously with the tensile parameters in order to obtain a more reliable specific strength (or tenacity, in cN/dtex). Figure 2.6 and Figure 2.7 show an example of the conversion of force-strain values to stress-strain values, in which the increase in the variability of the specific strength values within an egg sac is striking.

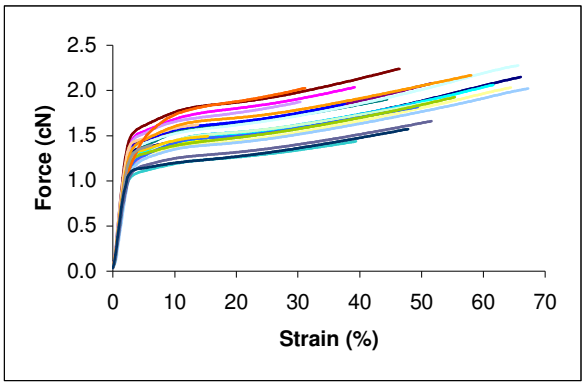

Figure 2.6 - Force-strain curves of 25 fibres taken of one egg sac

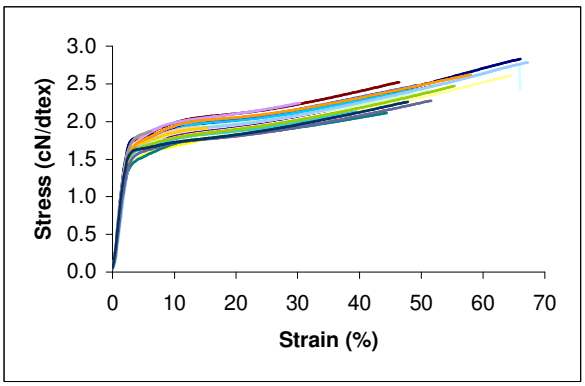

Figure 2.7 - Stress-strain curves of 25 fibres taken of one egg sac

2.6. VARIABILITY WITHIN SPIDER SPECIES

2.6.1. INTRODUCTION

Since the focus in this thesis is on the egg sac spider silk, this part is focused on the reproducibility of *A. diadematus* egg sac spider silk.

With respect to the dragline samples, too many tests did not succeed so that a further split up for the different samples was not relevant.

For the *B. mori* and *A. pernyi* samples, no individual cocoons were available.

2.6.2. EFFECT OF PREPARATION METHOD

An egg sac is randomly selected and subjected to a tensile test at a speed of 20 mm/min with a gauge length of 20 mm. A preload of 0.05 cN/dtex was used.

The linear density is simultaneously determined with the following settings: a preload of 0.08 cN/dtex and a speed of 2 mm/min and preset linear density of 0.7 dtex.

In this experiment, the fibres were consciously torn too hard to remove them from the egg sac. The egg sac fibres are clearly naturally crimped, a crimp that recovers after a limited load. It was observed that when the fibres are torn too hard, the crimp is removed after removal of the tensile force, resulting in a stiff and straight fibre. Such fibres were tested. It is clear that a plastic deformation and thus a structural transition takes place.

Figure 2.8 shows the resulting stress-strain curves.

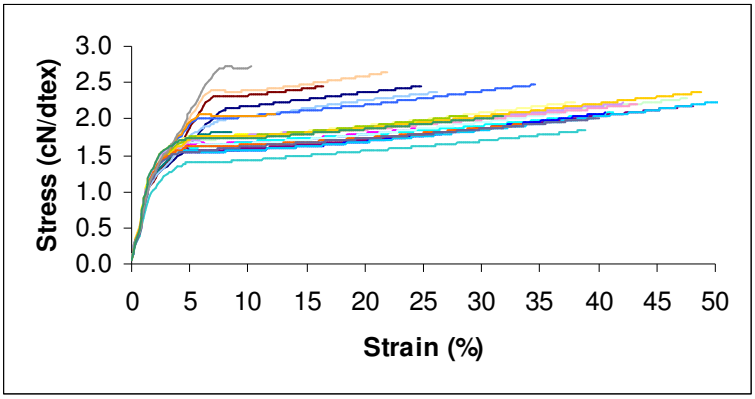

Figure 2.8 - Stress-strain curve of fibres torn too hard

First of all, a higher variability of the curves is observed. Two types of curves can be differentiated, probably depending on the size of the applied tensile force. The most occurring curve is the type that shows a lot of similarities with the shape of the curve for gently removed fibres. In the second type of curves, the less smoothed transition from elastic to plastic region is striking. The curve can in this case be

considered as a succession of three straight parts of which the slope is decreasing. It would result in a fibre with higher strength, but lower strain-at-break values.

In the further tensile tests, this result is taken into account for the preparation of samples and for skipping tests from the analysis.

2.6.3. REPRODUCIBILITY FOR *A. DIADEMATUS* SILK

2.6.3.1. Materials and methods

Five egg sacs of *Araneus diadematus* were collected in a bower in Belgium in autumn.

Since they were collected in their natural habitat, we expect that the measured mechanical behaviour will better represent the real characteristics than if they were specially reared for this purpose. The egg sacs were removed shortly after oviposition.

As published earlier [De Bakker *et al.* 2002, Foradori *et al.* 2002], the egg sac clearly consists of two layers. An outer layer is composed of some lose threads while threads of the egg sac itself are in a more tightly woven structure. Nevertheless, the fibres looked all the same in thickness along their length and were perfectly round. When looking at both layers of the egg sac with light microscopy, we see a mixture of thin and thicker threads. Since both layers could easily be distinguished and the outer layer is in most cases very thin, threads of the inner layer were selected for this study.

One hundred fibres were gently removed at random from the inside of each egg sac (after removing the clearly visible outer cover), with care taken to stress the fibres as little as possible.

For the dragline samples, some *A. diadematus* were reared in the laboratory under controlled conditions and from thirty spiders a sample of dragline thread was manually reeled off as spiders hung freely suspended in space. From every sample, ten fibres were prepared and tested.

All samples were kept in a conditioned laboratory of 20 °C ± 2 °C and relative humidity of 65 ± 2% for at least 24 hours before testing.

The FAVIMAT instrument with the settings described previously in section 2.3.1 was used.

Because of the extreme fineness of dragline spider silk and the fact that some of the threads consisted of double filaments, it was unfortunately not possible to simultaneously determine the linear density of the dragline fibres. Instead, diameters of these fibres (in µm) were measured on a large number of samples with image analysis on a light microscope. The linear density in dtex could then be calculated with the following formula [Chawla 1998]:

$$T_t = \frac{d^2 \cdot \pi \cdot \rho}{4000} \qquad (2.3)$$

In Equation (2.3), T_t is the linear density in tex, d is the diameter in µm and ρ is the specific density in g/cm³.

This formula suggests a round cross-section which is confirmed by microscopic observations and also by other authors [Huber 1947, Work 1976, Ko 1997, Poza *et al.* 2002, Pérez-Rigueiro *et al*. 2001]. As measured by Stauffer *et al.* [1994] specific density values for spider silk vary according to silk type and spider species. For *A. gemmoides* values of 1.27 and 1.26 g/cm³, whereas for *Nephila clavipes* values of 1.36 and 1.34 g/cm³ are observed for major ampullate, respectively for egg sac silk. In this study, a value of 1.3 g/cm³ is considered as is generally used in literature [Vollrath & Knight 2001].

An analysis of variance, combined with a Scheffé test for pairswise comparisons, was used where appropriate.

2.6.3.2. Results

First, it should be remarked that although 500 egg sac fibres and 300 dragline fibres were tested, not all were successful mostly due to the fineness of the fibre. For the calculation of the average stress-strain curves, for which the shape is the most important, only curves with strain-at-break values higher than 10% were considered. The curves were stopped at the average strain-at-break values of all available tests. It can be expected that the measurements show a small error since probably the weakest fibres could not be tested. However, from the histogram of the strength values, as shown in Figure 2.9, the contribution of stronger fibres is not higher than that of the weaker fibres.

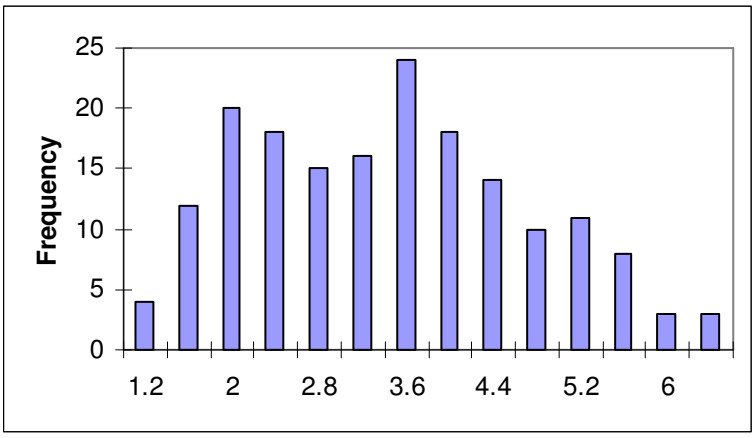

Figure 2.9 - Histogram of tenacity for dragline filaments

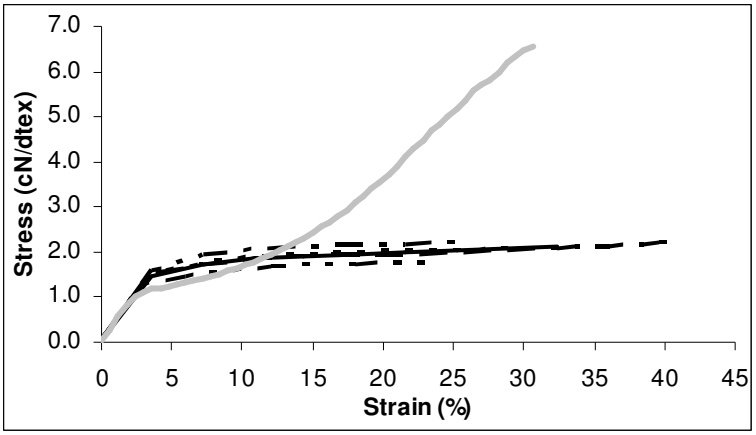

Figure 2.10 - Stress-strain curves for different egg sacs (dotted and in black) and dragline (in gray) of *A. diadematus*

The average stress-strain curves for the five egg sacs in comparison with the dragline thread of *Araneus diadematus* are shown in Figure 2.10. Three regions can be distinguished in a typical stress-strain curve for the egg sac silk of *A. diadematus*:

- A short initial linear elastic region, with a quite high initial modulus,
- A transition part where the additional force required to get additional strain decreases with increasing strain,
- A final hardening region where the curve is quite horizontal until the rupture of the fibre; a small increase of stress, results in a high increase of strain.

Another conclusion that can be made, is that the egg sacs 1 till 4 show a comparable stress-strain behaviour. Egg sac 5, on the contrary, shows a significantly lower tenacity ($p < 0.001$), a significantly lower initial modulus ($p < 0.001$) and a significantly lower work-to-rupture ($p < 0.01$). In other words, the fibres of egg sac 5 are weaker, less stiff and less tough than the other egg sac fibres.

Furthermore, although the different egg sac silks 1, 3, 4 have a significant different linear density ($p < 0.05$), the tensile properties are comparable. This indicates that the higher linear density values are compensated by higher breaking force and initial moduli values. As a consequence, coarser fibres are relatively stronger, stiffer and tougher than finer silk fibres. This is in contrast to what is observed for *B. mori* silk [Meredith 1945], probably caused by its different structure.

For dragline silk of the spider species *A. diadematus,* it can be concluded that it exhibits a complete different stress-strain behaviour than egg sac spider silk, showing:

- A short initial linear elastic region,
- A quite horizontal yield region, where little extra force is required to increase the strain,

- A final hardening region where the force is again proportionally increasing with the strain.

An overview of the average tensile properties and linear density values of the five egg sacs (1-5) and the dragline thread (6) are given in Table 2.3. In order to make a comparison possible with literature, the values are also converted in GPa using Equation (2.2).

Table 2.3 - Tensile properties of the 5 egg sacs (1-5) and the dragline (6) of *A. diadematus*

	1	2	3	4	5	All	6
Breaking strain (%)	29.87	44.71	32.98	35.38	26.00	34.07	30.51
CV	33.27	35.93	35.77	43.29	47.54	43.60	28.06
Tenacity (cN/dtex)	2.33	2.37	2.19	2.23	1.82	2.19	7.22
Tenacity (GPa)	0.30	0.30	0.28	0.28	0.23	0.28	0.92
CV	7.89	11.90	10.07	14.07	14.97	14.88	38.61
Work-to-rupture (cN/dtex)	0.61	0.89	0.63	0.68	0.42	0.65	0.13
CV	36.49	38.68	40.86	49.10	57.62	49.96	48.36
Initial modulus (cN/dtex)	71.81	70.86	68.22	66.51	59.83	67.38	50.68
Initial modulus (GPa)	9.16	9.04	8.70	8.48	7.63	8.59	6.46
CV	6.44	21.94	8.47	8.74	9.60	14.31	40.49
Linear density (dtex)	0.70	1.04	0.81	0.90	0.98	0.89	0.12
CV	18.82	14.99	17.24	25.08	14.50	22.62	

For the dragline threads, by means of image analysis on microscopic images, the average diameter of the tested draglines was determined to be 3.46 µm. This diameter allowed us to calculate the average linear density of the draglines according to Equation (2.3), namely 0.12 dtex.

As can be seen in Table 2.3, the breaking strain is not significantly different ($p > 0.1$) between egg sac spider silk and dragline spider silk, namely 30-31%. The breaking stress, however, is almost 4 times larger. The initial modulus or initial stiffness of egg sac silk is also significantly higher ($p < 0.001$) than for dragline silk.

Further on, it can be remarked that the linear density of egg sac 4 is significantly higher (± 1 dtex) compared to the other egg sacs (± 0.8 dtex).

2.6.3.3. Discussion

First of all, it should be remarked that the measured values suggest a wide experimental scatter, which can be attributed, in part, to the intrinsic variability of biological materials. In contrast to elastic modulus (a small strain property), which is significantly influenced by molecular orientation and sample morphology, fibre fracture (a large strain property) represents the response of the weakest part of the fibre and therefore shows a variable behaviour with high sensitivity to defects in the structure. A direct consequence of this is that when a number of samples of the same fibre are examined for their stress-strain behaviour, the modulus varies within narrow limits whereas breaking stress and breaking strain show considerable variation, particularly in natural fibres [Gupta 2000]. This variability is exacerbated in the case of dragline spider silk. It is suggested that the experimental difficulties to measure the fineness simultaneously with the tensile properties, play a role in this. In the case of egg sac silk, this variability may be partly due to the preparation method. The tension required for removing the fibres from the egg sac, and so the degree of permanent strain that is given, is difficult to control. Further research on the visco-elastic properties, such as elastic recovery, may reveal the influence of the preparation process.

Furthermore, it can be concluded that there is not only a high variation within the same individual egg sac, but also within different individuals of the same species. This is also observed by other authors for dragline silk [Garrido *et al.* 2002, Madsen *et al.* 1999].

Moreover, the variability seems much lower for egg sac silk than for dragline silk if we look at breaking stress and initial modulus. With respect to breaking stress, this is probably due to the characteristic quite horizontal shape of the post-yield or hardening region in the stress-strain curve. On the other hand, it should be taken into account that for dragline silk, the linear density is not simultaneously determined with the tensile properties as is the case for egg sac silk but is based on an average diameter value measured by microscopy. For egg sac silk, the variability in the force-strain curves is much higher than the variability in stress-strain curves (see Figure 2.6 and Figure 2.7). The limitations of the strength tester make it difficult to confirm this observation.

The different stress-strain behaviour is mainly due to the different amino acid composition of dragline and egg sac silk since dragline is mainly constituted of glycine and alanine, while egg sac silk consists mainly of serine and alanine, as is mentioned in Chapter 4. Since glycine is the simplest amino acid (side group H), while serine is an amino acid with a more voluminous and hydrophilic side group $-CH_2OH$, the difference in strength can be partly attributed to the more compact structure that can be built with glycine, resulting in a structure more resistant to loading. A more intensive study of the structure of egg sac silk is done in Chapters 6 to 9 to further explain the difference in behaviour.

The shapes of the stress-strain curves are similar to those that were found by Stauffer *et al.* [1994] for *Araneus gemmoides* and *Nephila clavipes*. With respect to the absolute values for strength and strain for the egg sac fibres, it should be remarked that the testing procedure and parameters (e.g. testing speed 5 mm/min) were not the same. The effect of strain rate is confirmed in a study described in

Chapter 3 [Van Nimmen *et al.* 2004]. At low testing speeds (< 20 mm/min), a lower tenacity, lower work to rupture or toughness and lower stiffness is observed than at high testing speeds. So, it is difficult to evaluate possible differences. They found for *A. gemmoides* major ampullate (MA) silk final breaking points at about 23 ±5% (n=10) with a final stress of 4.7 ± 0.5 × GPa and for egg sac silk at about 19 ±2% (n=10) with a final stress of $2.3 \pm 0.2 \times 10^9$ GPa. They obtained much higher stress values than found somewhere else for MA silk (see Table 2.1) because for the diameter measurement they take into account the ten smallest diameter points in several sections of the silks. As such, it is not useful to compare our breaking stress values with these ones. With respect to strain, we found much higher values (30% for MA silk and 31% for egg sac silk), with a much higher variability, probably due to the much higher number of tests performed. It is not clear if this difference is due to the difference in testing procedure or to the spider species. However, other published data of MA *Araneus* silk mention a strain-at-break value of 27% [Denny 1976] what makes our strain data more acceptable.

The initial modulus is a typical characteristic for fibres, and is highly dependent on the microstructure of the fibre, especially interference of molecular chains, as well as secondary bonding between chains [Singleton 1968]. The difference in initial modulus in dragline silk from data in literature [Denny 1976] (Table 2.1) may be attributed to the reeling speed [Vollrath *et al.* 2001] that was not controlled and the way the diameter is determined. It should also be mentioned that since spider silk is a visco-elastic fibre, its tensile characteristics can be highly dependent on the testing parameters, i.e. strain rate. Denny's [1976] analysis of the strain rate dependence of MA silk demonstrated that the initial stiffness increases from 9.8 to 20.5 GPa by increasing the strain rate from 0.0005 s^{-1} to 0.024 s^{-1}. This can also explain the difference in observed tensile properties of dragline thread compared with data in literature.

Moreover, Stauffer *et al.* [1994] compared the tensile properties of different silk types of *A. gemmoides*, and concluded that the initial modulus was higher for dragline than for egg sac spider silk in contrast to what it is observed here. In the experiments in this section, it can be expected that some errors are made because of incorrect measurement of the linear density of the dragline silk. However, in previous experiments comparing different spider silk species (Table 2.2), the measurement of linear density with the FAVIMAT instrument succeeded and similar values were obtained for initial modulus. It is unlikely that the observed difference in initial modulus would be incorrect.

2.7. SIMULATION OF THE STRESS-STRAIN CURVE

2.7.1. INTRODUCTION

Mechanical properties are often characterized only by breaking force, breaking strain and initial modulus. Often we are also interested in the time-dependent behaviour that is also partly included in the stress-strain curves.

In this section, a visco-elastic model, based on spring and dashpots, is described to simulate the stress-strain curve of egg sac spider silk. This simulation is not extended to dragline spider silk, because of the difficulties to measure them and as a result the higher uncertainty of the stress-strain curve.

The simulation based on visco-elastic models will also be used in further studies in order to find out the effect of strain rate on the shape of the stress-strain curve (see Chapter 3).

2.7.2. VISCO-ELASTIC MODELS

2.7.2.1. The Maxwell model

The stress-strain curve of polymers is often mathematically described by models indicating the visco-elastic behaviour of these polymers. When a material is extended by an applied force there is, besides the elastic component, a further component whose action opposes the applied force but whose magnitude depends on the speed of extension. This second component decays relatively slowly with time. When the applied force is subsequently removed, the same component also acts to resist the internal elastic forces that bring about contraction. This time dependency of polymers is also indicated as visco-elasticity (Saville 1999). Their behaviour is fitted by a visco-elastic model as the relationship between the applied stress and resultant strain contains a time-dependent element.

Most visco-elastic models consist of a combination of springs and dashpots. The spring represents the elastic solid-like behaviour where Hooke's law is valid ($F = E\varepsilon$ where F is load or force, E is elastic modulus and ε is strain), whereas the dashpot represents the time-dependent, viscous liquid-like behaviour where Newton's law is valid ($F = \eta \frac{d\varepsilon}{dt}$ where η is the viscosity or damping constant).

In the simplest Maxwell model (Tobolsky *et al.* 1951), the visco-elastic behaviour of a fibre (or yarn) is described by a spring (with elastic modulus E) and a dashpot (with damping constant or viscosity η) in series. This behaviour obeys the following equation (with ε the strain and F the force):

$$\frac{d\varepsilon}{dt} = \frac{1}{E}\frac{dF}{dt} + \frac{F}{\eta} \qquad (2.4)$$

This model is often used to describe stress relaxation, a phenomenon that is observed when a polymer is extended by a given amount and then held at that extended length. If the force required to do this is monitored, it is found to rise immediately to a maximum value and then to slowly decrease with time.

To use this model to describe stress-strain curves in tensile testing, we take into account a constant increase of strain with time, so that we can pose that $\varepsilon = r\,t$, with r a constant.

Equation (2.4) then becomes:

$$r = \frac{1}{E}\frac{dF}{dt} + \frac{F}{\eta} \tag{2.5}$$

with as starting condition $F(0)=F_v$, where F_v is the preload, from which the following solution is obtained:

$$F(\varepsilon) = F_v + \eta \cdot r \cdot \left(1 - e^{-\frac{E}{\eta \cdot r}\varepsilon} \right) \tag{2.6}$$

Equation (2.6) can be written as:

$$F(\varepsilon) = F_v + A \cdot \left(1 - e^{-B\varepsilon} \right) \tag{2.7}$$

with $A = \eta\, r$ and $B = \frac{E}{\eta \cdot r}$

This equation allows parameters A and B to be estimated by means of a non-linear regression.

2.7.2.2. The standard linear solid model

An extension of this Maxwell model is the so-called standard linear solid (SLS) model, where a linear spring in parallel is added (Figure 2.11).

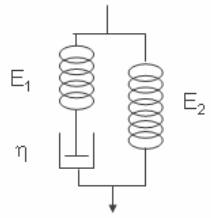

Figure 2.11 - A schematic representation of the standard linear solid model

Taking into account this spring in Equation (2.4) and by differentiating, Equation (2.7) can then be written as follows:

$$F(\varepsilon) = F_v + A \cdot \left(1 - e^{-B\varepsilon} \right) + C \cdot \varepsilon \tag{2.8}$$

with $A = \eta\, r$ and $B = \frac{E_1}{\eta \cdot r}$ and $C = E_2$

The parameters A, B and C can then be estimated by means of non-linear regression.

Figure 2.12, Figure 2.13 and Figure 2.14 show, respectively, the significance of the parameters A, B and C in the SLS model. As can be seen in Figure 2.12, parameter

A has mainly an effect on the level of the hardening zone, whereas parameter C affects the slope of this region (Figure 2.14) Finally, a change in parameter B, as shown in Figure 2.13, involves a change in the yield region.

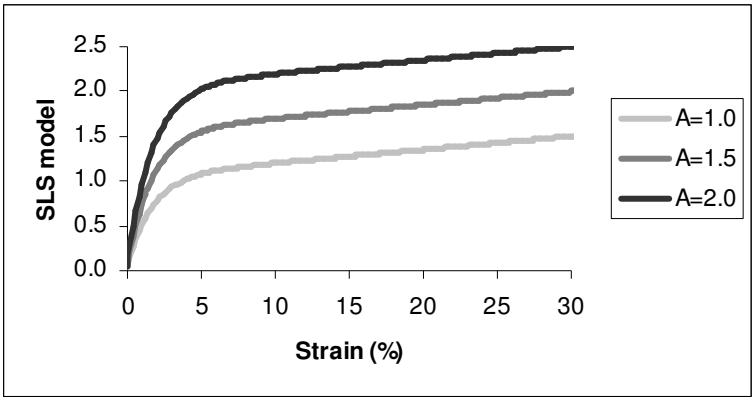

Figure 2.12 - Significance of parameter A in the SLS model

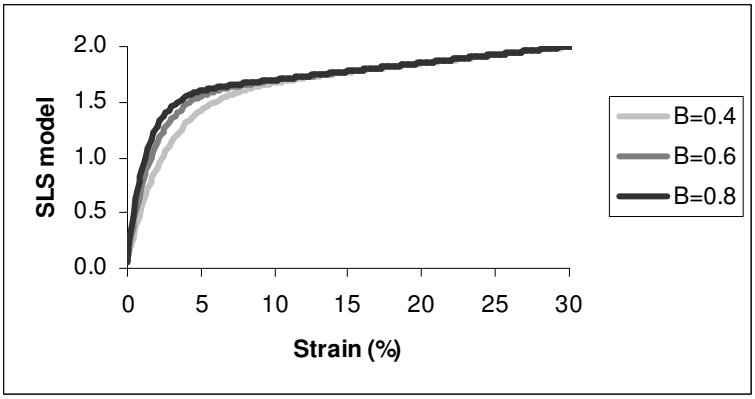

Figure 2.13 - Significance of parameter B in the SLS model

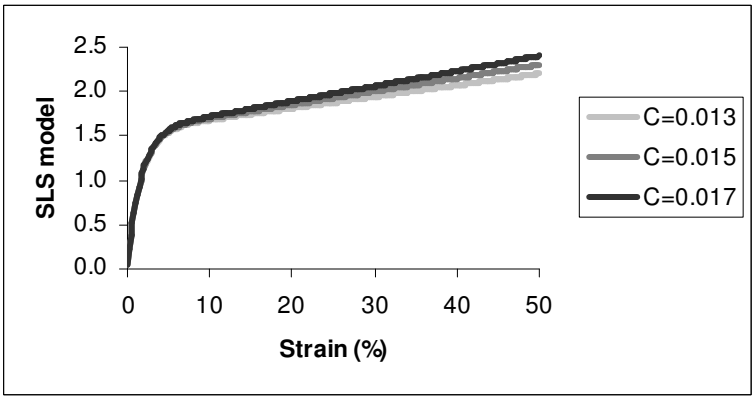

Figure 2.14 - Significance of parameter C in the SLS model

2.7.2.3. The Voigt model

Another time-dependent phenomenon is creep. If instead of a fixed extension, a fixed force is applied to the material, an initial extension of a magnitude is found that is expected from the force-strain curve followed by a further slow extension with time. For the description of creep or tensile testing under constant increase of load, the simplest model used is the Voigt model. This model consists of a spring (elastic constant E) in parallel with a dashpot (with damping constant η). The visco-elastic behaviour is then described by the following differential equation (with ε the strain and F the force):

$$F = E\varepsilon + \eta \frac{d\varepsilon}{dt} \tag{2.9}$$

Using the correct starting conditions for creep or tensile testing under constant increase of load, solutions for this equation can be found. Since these are not valuable for this study, the reader is referred to the literature (Saville 1999).

2.7.2.4. Other visco-elastic models

The models described above can be extended to more elements, such as the "four-elements model" consisting of a Maxwell element in series with a Voigt element or more generalized Maxwell and Voigt models considering a finite or infinite number of Maxwell or Voigt elements connected in parallel or in series. Since it is beyond the scope of this study, the reader is again referred to the literature for further description (Saville 1999).

2.7.3. EXPERIMENTS

2.7.3.1. Materials and methods

For this research, the stress-strain data of the five egg sacs were used, from which the average stress-strain curves shown in Figure 2.10 were produced.

The FAVIMAT tensile tester was used with the same settings as in previous studies.

2.7.3.2. Results and discussion

2.7.3.2.1. The Maxwell model

Since we were working with tensile testing with constant increase of extension, the Maxwell model as described earlier was used to describe the stress-strain behaviour. Starting from equation (2.7), the parameters A and B were estimated by means of a non-linear regression using the average stress-strain curves of the 5 egg sacs

discussed previously. For all egg sacs, correlation coefficients[1] of 94% to 99% are reached.

Figure 2.15 shows the simulation for egg sac 2 of the measured ("Meas.") stress-strain curves by means of the Maxwell model (Pred. 1). The simulation for the other egg sacs was comparable. In Figure 2.15, also a graph of the relative error, defined as:

$$\frac{F_{experimental} - F_{predicted}}{F_{experimental}} \tag{2.10}$$

is plotted. It can be concluded that the Maxwell model does not completely satisfy the simulation of the stress-strain curve for the egg sac silk fibres. In the plastic region of the stress-strain curve the measured values increase faster than the predicted values.

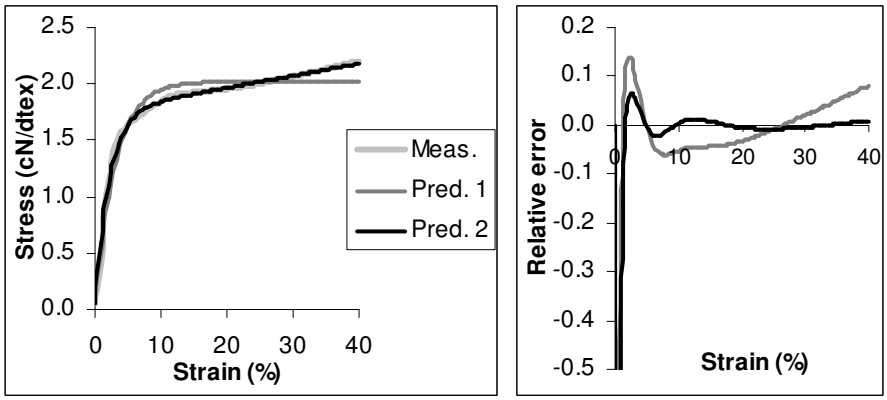

Figure 2.15 - The simulation by means of the Maxwell model (Pred. 1) and the SLS model (Pred. 2) of the stress-strain (Meas.) curves for egg sac 2

2.7.3.2.2. The standard linear solid model

In a next step we applied the standard linear solid (SLS) model, in which the 3 parameters A, B and C of Equation (2.8) were estimated by means of a non-linear regression.

With the average data of the stress-strain curves, for each egg sac a correlation of higher than 99% with a relative error smaller than 0.1% was observed, except in the initial elastic region where the maximum relative error at about 0.4-0.5% strain exceeds 0.4% to 1%. The measured versus predicted values ("Pred. 2") and the relative error for this prediction is also plotted in Figure 2.15. The results were worse for egg sac 5, although the correlation coefficient still reaches 99%. The

[1] The correlation coefficient R^2 of the regression model is defined as: 1 – Residual Sum of Squares / Corrected Sum of Squares obtained from the corresponding ANOVA-table.

deviation in the initial elastic region, is probably due to the crimp that is not fully removed by the preload before tensile testing started.

In a second step, it was tried if the prediction is improved by adding a quadratic term in Equation (2.8). The non-linear regression revealed that for three of the five egg sacs the coefficient of the quadratic term was not significantly different from zero. Moreover, for the other egg sacs the prediction was not much improved so we could conclude that the SLS model is the best model to use in further analysis.

To get an indication of the variability within the egg sac, the non-linear regression was repeated for each of the individual stress-strain curves of the 100 fibres that were tested for each of the five egg sacs. Because of the observed high variability, we performed a cluster analysis (with the statistical software SPSS) on the estimated parameters A, B and C in order to identify statistically different clusters or fibre populations.

The result of this cluster analysis is given in Table 2.4. Within the different egg sacs, two clusters (indicated as "1" and "2") of statistically different fibre populations could be detected. In this analysis, clusters of less than 10 fibre data were removed.

Table 2.4 - The average values (Mean) and the standard deviations (SD) of the parameters A, B and C of the SLS model for the 5 egg sacs of *Araneus diadematus* for 2 statistically different fibre populations ("1" and "2") as found by means of a cluster analysis (N = number of fibres within each population)

		A		B		C		
		Mean	**SD**	**Mean**	**SD**	**Mean**	**SD**	**N**
Egg sac 1	1	1.84	0.14	0.46	0.05	0.015	0.010	52
	2	2.39	0.20	0.36	0.06	-0.006	0.021	14
	Combined	1.95	0.28	0.44	0.06	0.010	0.015	66
Egg sac 2	1	1.75	0.05	0.50	0.05	0.013	0.003	33
	2	1.58	0.04	0.51	0.07	0.012	0.001	27
	Combined	1.67	0.09	0.50	0.06	0.012	0.002	60
Egg sac 3	1	1.70	0.07	0.42	0.04	0.011	0.002	31
	2	1.72	0.15	0.54	0.03	0.012	0.003	24
	Combined	1.71	0.11	0.47	0.07	0.011	0.003	55
Egg sac 4	1	1.72	0.11	0.45	0.07	0.013	0.002	43
	2	1.48	0.11	0.56	0.09	0.016	0.004	29
	Combined	1.62	0.16	0.50	0.10	0.014	0.004	72
Egg sac 5	1	1.28	0.11	0.58	0.06	0.021	0.007	19
	2	1.50	0.13	0.47	0.05	0.010	0.003	48
	Combined	1.44	0.16	0.50	0.07	0.013	0.007	67

The clusters or fibre populations for egg sac 1, egg sac 4 and egg sac 5 show completely different A, B and C values. In other words, the level of the more horizontal hardening region (indicated by A), the shape of the yield (or transition)

region (indicated by B) and the slope of the hardening region (indicated by C) of their stress-strain curves are significantly different. For egg sac 2, only the A-values of the clusters are significantly different, while the confidence regions of the parameters B and C are overlapping. With respect to egg sac 3, the B-values of the clusters are significantly different, while the confidence regions of the parameters A and C are overlapping.

Based on the cluster analysis, the stress-strain curves of the individual fibres from each egg sac were split into 2 groups and the average curve of each group was calculated. These average stress-strain curves based on the two different fibre populations for each egg sac are shown in Figure 2.16 A-E. It can be concluded that the fibre populations seem to differ mostly in the level of the relatively flat so-called hardening region and thus the breaking stress value. The initial modulus and the modulus of the hardening region, i.e. the tangent modulus at the yield point, seem to be quite equal for both fibre populations.

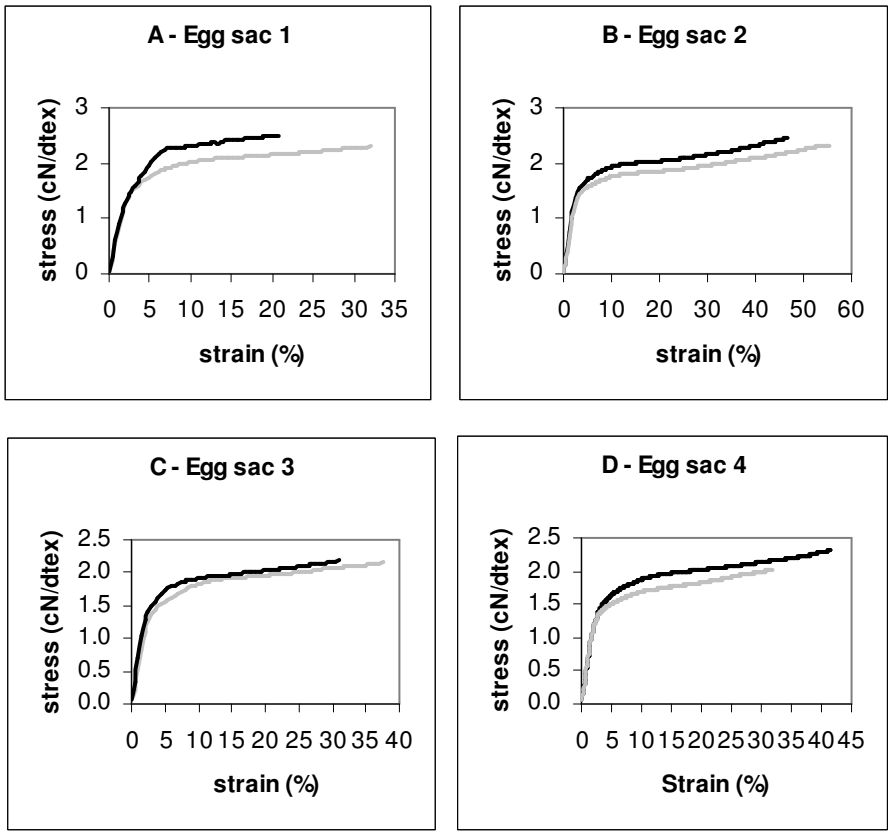

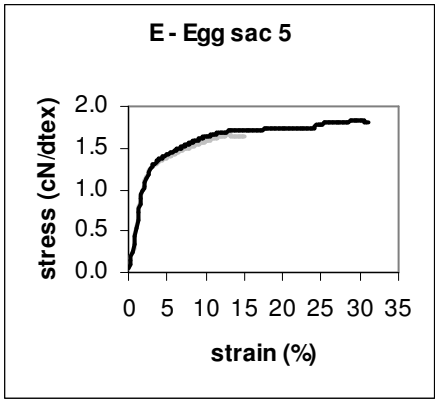

Figure 2.16 A-E - The simulation by means of the SLS model for two statistically different fibre populations found within an egg sac by means of a cluster analysis.

It is interesting to note that the different fibre populations differ mostly in the level of the hardening region, in other words the level of the region beyond the yield point and in the final breaking strain and stress values. A more detailed one-way ANOVA analysis was only performed for the egg sacs 2 and 3, because the contribution of both clusters was too much different for the other egg sacs. For these egg sacs, it is concluded that the strain-at-break, linear density and initial modulus are significantly different ($p < 0.05$) whereas no significant difference is found for the work to rupture ($p > 0.05$), tenacity and post-modulus values.

As mentioned before, the spring in the SLS model represents the solid character whereas the dashpot indicates the liquid character. By adding a (elastic) spring to the Maxwell model, an element is added that results in a linear relation between stress and strain beyond the yield point. The significance of the coefficient C indicates that there is indeed a significant, although small, increase in stress as a function of strain beyond the yield point. During post-yield extension, the long molecules tend to become oriented along the stress axis and, as a result, a structure may be obtained which approaches that of a crystalline material. This is, in fact called "strain-induced crystallization" [Wainwright *et al.* 1976] and leads to a notable increase in the value of the instantaneous elastic modulus. It is expected that the small increase of the modulus beyond the yield point compared to the other silks is attributed to the small size of the β-sheet crystals (see Chapter 6) resulting in a limited strain hardening. Also a link with the twisted non-periodic lattice (NPL) crystals demonstrated by Barghout *et al.* [1999] can be made. The twist of these regions may contribute to the flattened behaviour beyond the yield point, i.e. the lower tangent modulus at the yield point, for egg sac silk compared to dragline silk (in which the twist of the NPL crystals is not observed).

Since the fibres were randomly selected from each egg sac, the two fibre populations can probably be attributed to different layers that constitute the egg sac. Our own preliminary structural research of the egg sac of *Araneus diadematus* indeed confirms the existence of different layers, especially observed as a slight difference in colour and in the stacking of the fibres above and below the eggs [Gheysens *et al.*

2005a]. Different layers in the egg sac structure are also found for the spider *Zygiella x-notata* [Gheysens *et al.* 2005b].

However, these clusters can also be explained by a different origin, since different, symmetrically positioned, tubuliform glands are present in the spider.

2.8. CONCLUSION

The uni-axial tensile testing of the silkworm and spider silks revealed that the egg sac spider silks show a completely different stress-strain behaviour than dragline silks, and even the functionally comparable silkworm cocoon silks. The egg sac silks of different spider species all show a plastic region with little or no strain hardening, i.o.w. a flat behaviour beyond the yield point.

The breaking strain does not differ significantly between *A. diadematus* egg sac and dragline spider silks, however the breaking stress of dragline silk is three to four times higher than egg sac spider silk. The lower strength of egg sac spider silk is amongst others explained by its different amino acid composition, containing a higher fraction of serine in spite of glycine. The larger side chain of serine results in the formation of a less compact structure than expected for glycine, with hydrogen as side group. Furthermore, in further chapters a smaller size and lower fraction of β-sheet crystals is suggested for egg sac spider silk also resulting in a weaker fibre.

The stress-strain curves of the silkworm silks show more similarities with those of the dragline silks. This is explained by the presence of the same main constituents, namely alanine, glycine and a smaller fraction of serine, in both silks.

The stress-strain behaviour of egg sac spider silk is further simulated by means of a Maxwell and standard linear solid (SLS) model, which is an extended Maxwell model. The Maxwell model was proved to be insufficient to predict the stress-strain behaviour. The better prediction by means of the SLS model indicates that there is a small, however significant, strain hardening in egg sac spider silk. A further cluster analysis on the predicted results revealed that two statistically different fibre populations can be differentiated. The tensile properties of these fibre populations differ mostly in the level of the hardening region. These fibre populations are suggested to be associated to different layers that are deposited by the spider or are produced by a different tubuliform gland.

The limited strain hardening of egg sac spider silk is explained by the smaller size and fraction of β-sheet crystals (as proved in Chapter 6) which, after extensive straightening, cannot strengthen the fibre beyond the yield point in contrast to the extended β-sheet crystals in the other silks.

Further correlations with the structure are mentioned in Chapter 10.

2.9. REFERENCES

Barghout J.Y.J., Thiel B.L., Viney C., Spider (*Araneus diadematus*) cocoon silk: a case of non-periodic lattice crystals with a twist?, Int. J. Biol. Macromol. 24:211-217 (1999)

Chawla K.K., In: Fibrous materials, Cambridge University Press, UK (1998)

Colgin M.A. & Lewis R.V., Spider minor ampullate silk proteins contain new repetitive sequences and highly conserved non-silk-like "spacer regions", Protein science 7:667-672 (1998)

Cook J.G., Handbook of textile fibres – Natural fibres, 5th Edition, Merrow Publishing Co. Ltd., United Kingdom, 145-165 (1984)

Cunniff P.M., Fossey S.A., Auerbach M.A., Song J.W., Mechanical properties of major ampulate gland silk fibers extracted from *Nephila clavipes* spiders, In: Silk Polymers: Material Science and Biotechnology, ACS Symposium Series 544, Washington DC: 234-251 (1994)

De Bakker D., Gellynck K., Van Nimmen E., Mertens J., Kiekens P.; Structural analysis and differences in cocoon structure revealed by means of Scanning Electron Microscopy between several spider species; 20th European Colloquium of Arachnology, Szombathely, Hungary, 22-26 July (2002)

Denny M., The physical properties of spider's silk and their role in the design of orb-webs, J. Exp. Biol. 65:483-506 (1976)

Denny M.W., Silks - their properties and functions, Symp. Soc. Exp. Biol. 34:247-272 (1980)

De Wilde J., Some physical properties of the spinning threads of *Aranea Diadema* L., Archives Néerlandaises de physiologie de l'homme et des animaux, Tome XXVII, 118-133 (1943)

Foradori M.J., Kovoor J., Moon M.-J., Tillinghast E.K., Relation between the outer cover of the egg case of *Argiope aurantia* (*Araneae*: *Araneidae*) and the emergence of its spiderlings, J. Morphol. 252:218-226 (2002)

Garrido M.A., Elices M., Viney C., Pérez-Rigueiro, The variability and interdependence of spider drag line tensile properties, Polymer 43: 4495-4502 (2002)

Gheysens T., Van Nimmen E., Gellynck K., Beladjal L., Van Langenhove L., Mertens J. , Cocoon construction by *Araneus diadematus* in relation to the silk glands (Araneidae-Arachnida), 22 European Colloqium of Arachnology 1-6 Augustus, Blagoevgrad, Bulgaria (2005a)

Gheysens T., Beladjal L., Gellynck K., Van Nimmen E., Van Langenhove L., Mertens J., Egg sac structure of *Zygiella x-notata* (Arachnida, Araneidae), J. Arachnol. 33:549-557 (2005b)

Gosline J.M., Pollak C.C., Guerette P.A., DeMont M.E., Denny M.W., Elastomeric network models for the frame and viscid silks from the orb-web of the spider *Araneus diadematus*. In: Silk Polymers: materials science and biotechnology (Kaplan D., Adams W.W., Farmer B., Viney C., eds), Am. Chem. Soc., 329-341 (1994)

Gosline J., Nichols C., Guerette P., Cheng A., Katz S., The macromolecular design of spider silks. In: Biomimetics. Design and processing of materials (Sarikaya M., Aksay I.A., eds) AIP Press, 237-261 (1995)

Gosline J.M., Guerette P.A., Ortlepp C.S., Savage K.N., The mechanical design of spider silks: From fibroin sequence to mechanical function, J. Exp. Biol. 22(23):3295-3303 (1999)

Gupta V.B., Structure of textile fibres and structural dependence of their mechanical properties, In : Progress in Textiles: Science & Technology, Kothari V.K (Ed.), Vol. 2, IAFL Publications, India, 11-118 (2000)

Hatch K.L., Textile fibers, Chapter 8 – Fibre properties and identification, West Publishing Company, USA, 109-118 (1993)

Hayashi C.Y., Shipley N.H., Lewis R.V., Hypotheses that correlate the sequence, structure and mechanical properties of spider silk proteins, Int. J. Biol. Macromol. 24:271-274 (1999)

Hayashi C.Y. & Lewis R.V., Molecular architecture and evolution of a modular spider silk protein gene, Science 287:1477-1479 (2000)

Huber C.J., The silk fibers, In: Matthew's textile fibres – Their physical, microscopical and chemical properties, Mauersberger H.R. (Ed.), 5th edition, John Wiley & Sons Inc., New York, Chapter XVII, 679-729 (1947)

Iizuka E., Mechanism of fiber formation by the silkworm, *Bombyx mori* L., Biorheology 3(3):141-152 (1966)

Ko F.K., Spider silk, Textile Asia, April, 38-43 (1997)

Lombardi S.J. & Kaplan D.L., The amino acid composition of major ampullate gland silk (dragline) of *Nephila clavipes* (*Araneae, Tetragnathidae*), J. Arachnol. 18: 297-306 (1990)

Madsen B., Shao Z.Z., Vollrath F., Variability in the mechanical properties of spider silks on three levels: interspecific, intraspecific and intraindividual, Int. J. Biol. Macromol. 24:301-306 (1999)

Meredith R., The mechanical properties of textile fibers, J. Text. Inst. 36:T107 (1945)

Moore A.M.F. & Tran K., Material properties of cobweb silk from the black widow spider *Latrodectus hesperus*, Int. J. Biol. Macromol. 24(2-3):277-282 (1999)

Pérez-Rigueiro J., Elices M., Llorca J., Viney C., Tensile properties of *Argiope Trifasciata* drag line silk obtained from the spider's web, J. Appl. Polym. Sci. 82(9):2245-2251 (2001)

Poza P., Pérez-Rigueiro J., Elices M., Llorca J., Fractographic analysis of silkworm and spider silk, Engineering Fracture Mechanics 69(9):1035-1048 (2002)

Saville B.P., Physical testing of textiles, Woodhead Publishing Ltd. (1999)

Shao Z.Z. & Vollrath F., Materials: Surprising strength of silkworm silk, Nature 418 (6899):741-741 (2002)

Singleton R.W., Fibre testing, In: Man-Made Fibres – Science and Technology, Vol. 3, H.F. Mark, S.M. Atlas, and E. Cernia (Eds.), Interscience Publishers, 571-634 (1968)

Stauffer, S.L., Coguill, S.L., Lewis, R.V., Comparison of physical properties of three silks from *Nephila clavipes* and *Araneus gemmoides*, J. Arachnol. 22:5-11 (1994)

Swanson B.O., Blackledge T.A., Beltrán J., Hayashi C.Y., Variation in the material properties of spider dragline silk across species, Applied Physics 82(2):213-218 (2006)

Tobolsky A.V., Dunell B.A., Andrews R.D., Stress relaxation and Dynamic properties of polymers, Text. Res. J. 21:404-411 (1951)

Van Nimmen, E., Gellynck, K., Van Langenhove, L., Mertens J., The difference in tensile behaviour of different silks of the spider *A. diadematus*, In: DESIGN AND NATURE II: Comparing design in nature with science and engineering, (M.W. Collins & C.A. Brebbia, eds.), WIT Press, UK, 503-512 (2004)

Vollrath F. & Knight D., Liquid crystalline spinning of spider silk, Nature 410:541-548 (2001)

Vollrath F., Madsen B., Shao Z., The effect of spinning conditions on the mechanics of a spider's dragline silk, Proc. R. Soc. Lond. Ser. B-Biol. Sci. 268:2339-2346 (2001)

Vollrath F. & Knight D., Biology and technology of silk production, Biopolymers 8:26-46 (2003)

Vollrath F. & Porter D., Spider silk as a model biomaterial, Applied Physics 82(2):205-212 (2006)

Wainwright S.A., Biggs W.D., Currey J.D., Gosline J.M., Mechanical Design in Organisms, Edward Arnold (Publishers) Limited, London, UK (1976)

Winkler S. & Kaplan D.L., Molecular biology of spider silk, Reviews in Molecular Biotechnology 74(2):85-93 (2000)

Work R.W., The force-elongation behavior of web fibers and silks forcibly obtained from orb-web spinning spiders, Text. Res. J. 46:485-492 (1976)

Work R.W., Dimensions, birefringence and force-elongation behaviour of major and minor ampullate silk fibres from orb-web spinning spiders, Text. Res. J. 47:650-662 (1977)

Work R.W. & Young C.T., The amino acid compositions of major and minor ampullate silks of certain orb-web-building spiders (Araneae, Araneidae), J. Arachnol. 15:65-80 (1987)

3

VISCO-ELASTIC BEHAVIOUR OF SILKS

When a material is extended by an applied force there is, besides the elastic component, a further component whose action opposes the applied force but whose magnitude depends on the speed of extension. This second component decays relatively slowly with time. When the applied force is subsequently removed, the same component also acts to resist the internal elastic forces that bring about contraction. This time dependency of polymers is also indicated as visco-elasticity.

In this chapter, visco-elastic aspects are studied for the different silks. It includes the study of the resilience and elastic recovery, the creep behaviour, and finally the effect of strain rate or testing speed. The study of the visco-elastic behaviour is expected to give some information about the microstructure of the less-ordered or amorphous regions.

3.1. HYSTERESIS AND CREEP

3.1.1. LITERATURE REVIEW

3.1.1.1. Visco-elasticity of fibres

On being subjected to a tensile load, the molecules in the amorphous phase of the fibre are extended by disentanglement of the structural elements, breakage of molecular bonds and straightening of chain segments through rotation around single bonds in the main chain. As a result, the system moves to a low entropy state which would like to revert back to its original state to maximise entropy. This generates a back stress [McCrum *et al*. 1978] which, on removal of the load, results in recovery from creep. It is interesting to recall that the driving force for recovery in a cross-linked rubber is also entropic. In oriented, semi-crystalline fibres, in addition to the entanglements in the amorphous regions, the crystallites also act as cross-links and play a similar role as chemical cross-links do for lightly cross-linked rubbers which are known to have outstanding recovery characteristics. It was shown earlier that in a textile fibre, a single molecule may thread through a number of crystalline and amorphous regions. These two phases thus act in tandem and promote recovery. The recovery is also aided by secondary valence bonds, entanglements, and crystallites. The permanent deformation or secondary creep occurs mainly due to irreversible flow of polymer chains.

The superior recovery shown by wool is mainly because of the predominant role played by the crystallites, which have a spring-like helical geometry. Their participation in the deformation process during the stress-strain test ensures excellent recovery. Cotton, on the other hand, has a high density of hydrogen bonding sites and as deformation proceeds, the bonds break and reform in the new positions. This results in poor recovery. Polyamide fibres show rubber-like behaviour and thus show excellent entropy-driven recovery characteristics.

It is interesting to recall that protein fibres have a high degree of resilience which is probably related to the existence of bulky side groups on flexible backbone chains. Cellulose acetate is much more resilient than cellulose fibres as the acetate groups reduce the interaction between the chain molecules and allow them more mobility in the non-crystalline regions.

The visco-elastic nature of fibres also leads to time-dependent phenomena such as relaxation and creep of the tensile stress on the fibre when held under constant strain, respectively force. Stress relaxation and creep depend largely on the initial stress or strain level applied on the fibres. Creep behaviour also provides some indirect information on the morphology of fibres. For example, cross-linked fibres show little creep. Spider silk contains a small amount of cysteine bonds, which provide some cross-linking. Poly-p-phenylene terephthalamide (PPTA) fibres also show good creep resistance, presumably in part because of the extensive hydrogen bonding. Like PPTA, spider dragline silk has extensive hydrogen bonding.

3.1.1.2. Visco-elasticity of silks

Both visco-elasticity and irreversible deformation account for the large hysteresis of more than 50% shown by silk fibres during stretch and recovery cycles and are responsible for the great energy of dissipation of these fibres [Elices *et al.* 2005]. Hysteresis is probably produced by frictional forces among segments of protein chains [Gosline *et al*. 1994].

Denny [1976] reported hysteresis values for different silk types of *Araneus sericatus* spider. The hysteresis value is calculated as the ratio of energy dissipated to the energy absorbed and thus equals 100% minus the resilience value. For both major ampullate (MA) and viscid silks a hysteresis value of 65% is mentioned. Gosline *et al*. [1986] found a hysteresis value of 70% for *A. sericatus* frame silk.

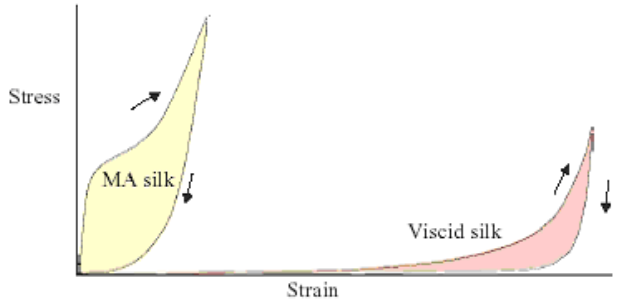

Figure 3.1 – Hysteresis of *Araneus* major ampullate and viscid silk [Denny 1976, reproduced by Gosline *et al.* 1999]

Shao & Vollrath [1999] performed loading-unloading cycles on different MA spider silks, a.o. *A. diadematus*. The elastic recovery of the four MA silks was ± 80-90%, after they had been stretched to about 70% of breaking elongation.

Shao & Vollrath [1999] envision that silks, when first under strain, take up energy because molecular chains reorient and even slip against each other when hydrogen bonds break. After starching, the molecular chain settle in stable conformations and the friction between chains and reformed hydrogen bonds induce permanent set and prevent full recovery at relaxation.

3.1.2. DEFINITIONS AND INTERPRETATION

3.1.2.1. Extensional Resilience

Elastic recovery or resilience is the extent to which a fibre becomes permanently deformed during a load-unloading cycle. It is evaluated by conducting continuous or discontinuous cyclic loading-unloading tests at various imposed strains, also called hysteresis tests.

Figure 3.2 shows the stress-strain and elastic recovery curves, used to calculate the resilience value.

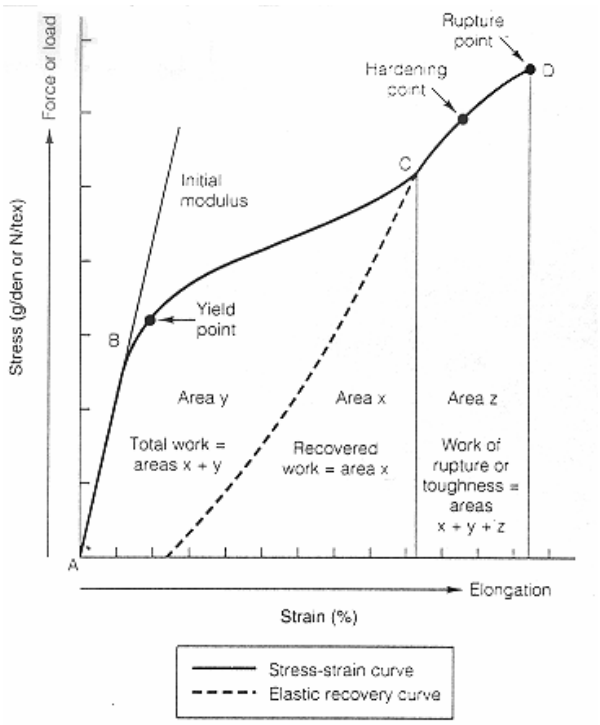

Figure 3.2 – The resilience or elastic recovery curve [Hatch 1993]

The resilience, also called work of recovery, is defined as the ratio of energy returned to the energy absorbed when a fibre is deformed and then released, it is also called work recovery.

From the elastic recovery curve (Figure 3.2), it is calculated with the following formula [Hatch 1993]:

$$\%\ \text{Resilience} = \frac{Area(X)}{Area(X+Y)} \times 100 \qquad (3.1)$$

It is often represented as a function of the strain (in %) or elongation (in mm) value.

In general, crimped fibres are more resilient than smooth, straight fibres. The presence of hydrogen bonds lowers resilience. Considerable energy is required to break the hydrogen bonds so that polymers can slide by one another; little energy is expended when the stress is released because the polymers are "locked" into their new positions by newly formed hydrogen bonds [Hatch 1993].

For some applications, such as mounting climbing rope, some hysteresis is important [Gupta 2000]. The shock load of the climber "hitting" the end of the rope travels back along the rope at the speed of sound in the rope in the form of a stress wave. This is partly reflected at the points of contact with the rock, knots, etc. A complex pattern of waves can result with the risk of failure where stress waves combine. Hysteresis losses in the rope help to attenuate these waves.

Resilience experiments are often performed following the standard DIN 53 835 Part 3. This is also done in this study.

3.1.2.2. Elastic recovery

In the initial segment AB of the stress-strain curve, the fibre behaves like an elastic spring. If the stress is removed at any point from A to B, the fibre would return to its original length because the polymers can revert to their initial positions. The elastic recovery of the fibre is therefore 100%. If the fibre is stressed beyond the yield point, but not to its hardening point and the force is then removed, the fibre will partially recover; it will attempt to return to its original length.

A model elastic recovery curve can be added to the model stress-strain curve by decreasing the force acting on the stressed model fibre and observing the amount of shortening of the fibre. This curve establishes how well a fibre can recover from different amounts of stress. The fibre contracts but not as much or as quickly as it extended when stress was increased.

It is calculated by the following equation [Farrow 1956, Hatch 1993]:

$$\% \text{ Elastic recovery} = \frac{E_{Limit} - E_{Perm}}{E_{Limit}} \times 100 \qquad (3.2)$$

With E_{Limit} the extended length or maximum elongation and

E_{Perm} the unrecovered or permanent elongation

The elastic recovery is often represented in relation to the applied stress.

Elastic recovery depends on the configuration of the polymer chains and on intrafibre bonding [Hatch 1993]. Polymers that are spiralled and folded tend to act like springs; once stress is released they attempt to return to their original configuration. When polymers are covalently crosslinked, the crosslinks work to pull the polymers back to their original positions. When polymers are hydrogen or ionically bonded, however, elastic recovery tends to decrease because new bonds form as the polymers slide by each other.

Furthermore, how much of the original length they recover depends on the force used, the length of time the force is applied, and the length of time allowed for the recovery. The % recovery decreases steadily with increasing extension of the material up to the yield point where the recovery decreased sharply.

The extent of recovery from extension is a property which is dependent on the type of material. This difference helps to account for the variation in resilience properties which are displayed by these materials in diverse applications such as the resistance to flattening of carpet tufts, the recovery of fabrics from creasing and the resistance of fabrics to abrasion.

The elastic recovery is, in this study, also calculated from the hysteresis curves, determined according to the standard DIN 53 835 Part 3. It is calculated as in Equation (3.2) in which the unrecovered elongation is taken at the preset pretension, E_{Pret}, as shown in Figure 3.3.

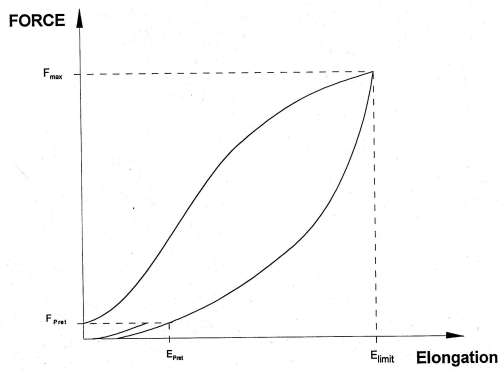

Figure 3.3 – Parameters used in the definition of elastic recovery

3.1.2.3. Stress relaxation

Another time-dependency is seen when a yarn is extended by a given amount and then held at that extended length. If the force required to do this is monitored, it is found to rise immediately to a maximum value and then slowly decrease with the passage of time; this phenomenon is known as stress relaxation [Saville 1999].

3.1.2.4. Creep

If instead of a fixed extension, a fixed force is applied to the material, there is found to be an initial extension of a magnitude that is expected from the force-extension curve followed by a further slow extension with time. This behaviour is known as creep and its magnitude is an important property to consider when assessing materials that have to be kept under load for a long period of time, such as geotextiles [Saville 1999].

As the level of force, usually expressed as a % of the tensile strength, increases, the rate of creep increases. The rate of creep also increases with increasing temperature. The level of force should be set so that the time to failure is longer than the expected life of the product.

3.1.3. RESILIENCE

3.1.3.1. Materials and methods

Two cocoon silks of silkworms, *Tussah and B. mori*, provided by the Silk Museum in the Netherlands were compared with 2 types (egg sac and dragline) of silk of the spider species *A. diadematus.* Both spider silks were obtained from reared spiders. The dragline silks were manually reeled off as for the tensile tests.

For the spider silks, 2 draglines and 2 egg sacs were selected at random and 5 tests were performed for each sample. For the *B. mori* and Tussah samples, 10 tests were done.

Special software was used on the FAVIMAT Instrument in order to evaluate the fibres with the cyclic load test according to the DIN-standard 53835-Part 3.

In this test, at first the draw of the clamp of the tensile tester approaches the programmed pretension. Then, the sample is stretched between two defined strain points and finally the pretension is approached again.

Since this test is more used for yarns, the optimal parameters for speed and pretension had to be determined. After some preliminary tests, it was decided to take the preload as small as possible. For the spider silks and *B. mori* silk the preload was set to 0.01 cN. For the coarser Tussah sample, the preload was increased to 0.05 cN because too much tests failed at the lower preload. Also the test speed had some effect on the results and was also set as small as possible at 1 mm/min. As strain points were chosen 2%, 3%, 5%, 7% and 10%. A gauge length of 20 cm was used.

The linear density values were set as measured before: *B. mori* 1.03 dtex, Tussah 2.60 dtex, egg sac 0.60 dtex and dragline 0.50 dtex.

An analysis of variance, combined with a Scheffé test for pairswise comparisons, was used where appropriate.

3.1.3.2. Results and discussion

Figure 3.4 shows the resilience values in function of the strain points for the different silks. Error bars indicate the standard deviation for each test set-up.

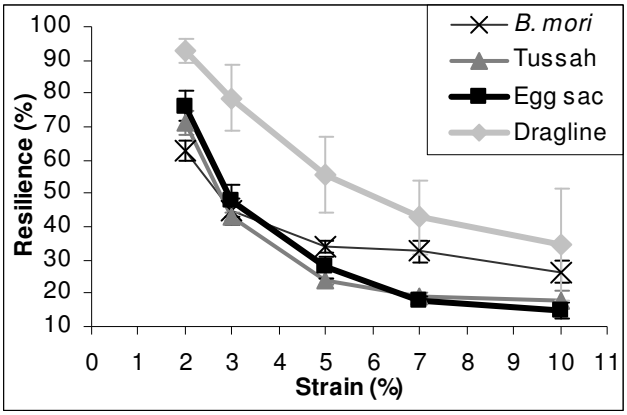

Figure 3.4 – The resilience in function of preset strain

It is clear that the variability (indicated by the error bars) for the dragline silk is much higher than for the other fibres, this is mostly due to the significant difference ($p < 0.01$) between the two selected draglines. The shape of the resilience curve in

function of the preset strain value remained, however, similar (interaction not significant).

For egg sac spider silk, the difference between the resilience of the two egg sacs was not significant ($p > 0.05$).

It is clear that the resilience is much better for dragline spider silk than for the other silks. The resilience behaviour of Tussah silk is not significantly different ($p > 0.05$) from the egg sac spider silk and at strains higher than 7%, the resilience value remains significantly constant at a value of 15 to 20%. Looking at the stress-strain curves of the different silks, Tussah silk shows in the 5-10% range, like egg sac spider silk, a relatively horizontal plastic region, the extension till the strain hardening zone is not included in these experiments. It seems that egg sac spider silk is lacking some structures, probably extended β-sheets (see also Chapter 6), responsible for the strain hardening in fibres which are certainly present in Tussah fibres. Looking at the amino acid composition of both Tussah (*A. pernyi*) and egg sac spider silk in Chapter 4, it is suggested that the presence of residues with large side chains is responsible for this behaviour.

Furthermore, for *B. mori* the resilience curve exceeds more quickly a constant value of about 30%. The different behaviour for *B. mori* is suggested to be explained by the lack of helical structures as also confirmed in further structural analysis.

Typical hysteresis curves are given in Figures 3.5 to 3.8 for the different silks.

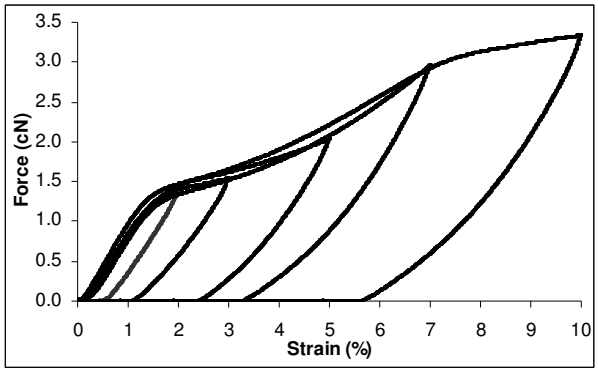

Figure 3.5 - Typical hysteresis curve for *B. mori* silk

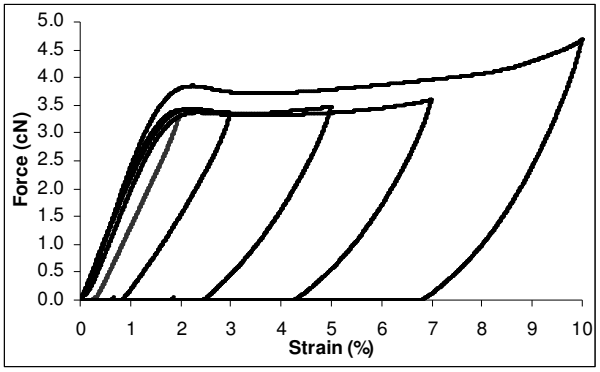

Figure 3.6 - Typical hysteresis curve for Tussah silk

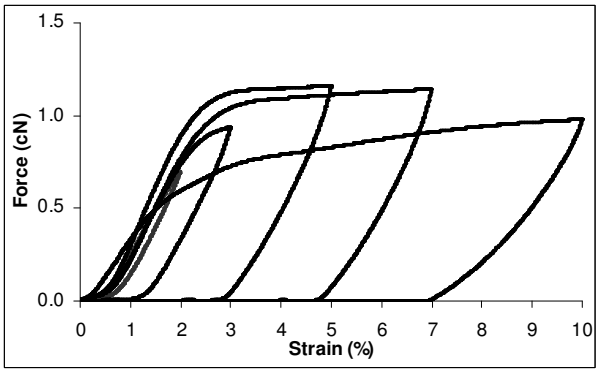

Figure 3.7 - Typical hysteresis curve for egg sac spider silk

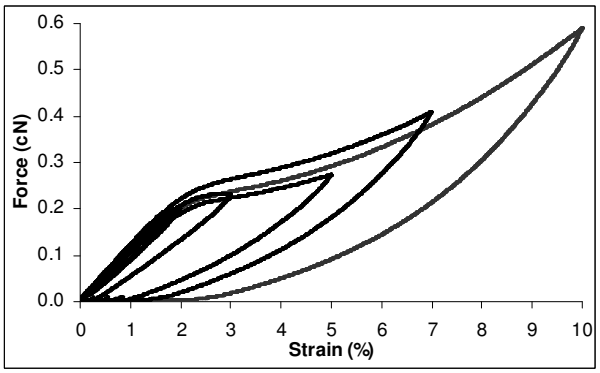

Figure 3.8 - Typical hysteresis curve for dragline spider silk

Another interesting parameter that can be calculated from the hysteresis curves is connected with the permanent unrecovered strain: the elastic recovery. The "Elastic recovery" is calculated according to Figure 3.3 and Equation (3.2).

Figure 3.9 shows the elastic recovery values in function of the preset strain values for the different silks.

In general, it can be concluded that the resilience and elastic recovery of all silks are not so high. This is explained by the high number of hydrogen bonds. As deformation proceeds, the bonds break and new bonds are formed [Gupta 2000].

It is clear that the visco-elasticity is more pronounced for Tussah and egg sac spider silk (resilience much lower). In other words, the permanent strain is much higher for Tussah and egg sac spider silk.

Carmichael *et al*. [1999] studied the effect of post-spin drawing on the microstructure of spider silk. They stated that ordered regions (NPL-crystals and also polyalanine crystallites, see Chapter 10) are degraded as a result of drawing. The chains in the remaining crystalline regions, as well as the chains that previously belonged to crystalline material, become more highly aligned. These structural changes are permanent when the fibre is allowed to relax: crystals do not reassemble in the solid state, and molecules constrained by the immediately adjacent presence of remaining crystal do not easily reorient. Amorphous material also aligns but the structural changes are temporary and recoverable.

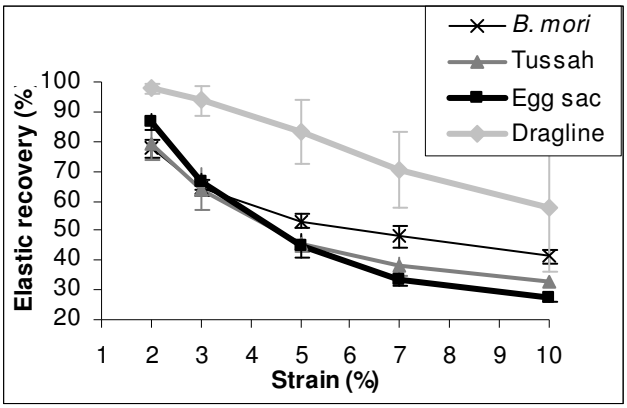

Figure 3.9 – The elastic recovery in function of preset strain

According to Gupta [2000], a higher permanent strain would indicate a low crystalline content, poor crystallite orientation, lower birefringence, and/or poor packing. In fibres, which are based on semi-crystalline polymers, the small crystallites act as cross-links. In addition, the entanglements in the amorphous regions also act as cross-links. The possibility of entanglement slippage and the weakening of intermolecular forces are likely to lead to incomplete reversibility [Gupta 2000].

The comparable elastic recovery for Tussah and egg sac spider silk is explained by the similar stress-strain behaviour below 10%. The higher crystallinity of Tussah seemed not to have an effect on the visco-elastic behaviour.

For *B. mori*, we would expect a lower elastic recovery because of its lack of helical structures. It is suggested that the cysteine bonds that are linking the different proteins (as described in Chapter 5) in *B. mori* and which are not observed for Tussah silk, are responsible for this behaviour.

Further correlations to the structure, especially for egg sac spider silk, are mentioned in Chapter 10.

3.1.4. CREEP BEHAVIOUR

3.1.4.1. Materials and methods

The same fibres as for the hysteresis tests were used to evaluate the creep behaviour of the silks. It should be remarked that the dragline fibres are wound on wooden or paper holders under some tension. It can be expected that the creep and/or relaxation phenomenon already occurred before the study. For this reason, the dragline fibres were removed from their holders at least 24 hours before the creep test was performed.

Special software was used on the FAVIMAT instrument to perform creep tests. Because of the flat behaviour of egg sac spider silk in the plastic region, it was chosen to perform the creep test as follows. At first, the draw of the clamp of the tensile tester approaches the programmed pretension (0.05 cN). Then the sample is stretched to a defined strain limit (set to 7%). The force at this defined strain is kept constant for a pre-set time, taken as 3600 seconds.

The creep test was repeated 3 to 5 times to check the reproducibility.

3.1.4.2. Results and discussion

Figure 3.10 shows typical creep curves for the silks studied.

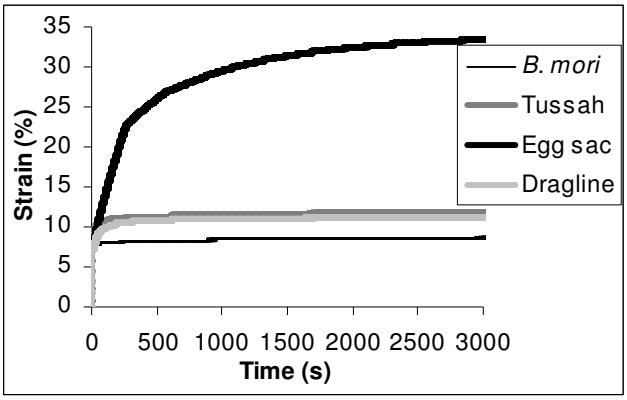

Figure 3.10 – Creep curves for different silks

B. mori silk shows a very good creep behaviour, even after 1800 s the strain only reaches a value of 8.5%.

The Tussah silk and dragline spider silk show a similar creep behaviour, in which the final strain value is reached very quickly. The strain value after 1800 s equals about 13% for Tussah and about 10% for dragline silk.

Egg sac spider silk shows a clearly non-linear creep behaviour, has a much lower stability, and thus exhibits much more creep. After 1800 s the strain reaches 31.6% and is still increasing till a value of 33.5% after 3600 s.

Looking at the stress-strain behaviour of egg sac spider silk, as shown in Chapter 2, at higher strain the force increases only slightly and also reaches a final value of about 30%. Although in the creep test, the force is kept constant, the same behaviour is observed as for the standard tensile test.

It can be expected that after an extension of 7% some hydrogen bonds are broken within the structure, the applied force prevents the structure to uncoil. In the *B. mori* and Tussah silk, it is suggested that during the time of constant force, new hydrogen bonds are immediately formed resulting in a stable structure. The higher crystalline content and possibly the available cysteine bonds, cross-linking different parts of the proteins in *B. mori* silk (as described in Chapter 5), explain the good creep behaviour of these silks.

In the case of egg sac spider silk, it is known that the crystallites are twisted [Barghout *et al*. 1999]. In the flat plastic region, apart from an alignment of the amorphous regions, also the crystallites will be oriented in the direction of the fibre axis. The hydrogen bonds responsible for the twist in the crystals are probably broken. It seems that after holding the force constant, these hydrogen bonds can not reform and possible new bonds result in a less stabile structure.

The extension observed in egg sac spider silk can be explained by the following, as also reported by Nachane & Sundaram [1995] for explaining the relaxation phenomenon of fibres. When applying a force, the segments along the same molecular chain show an overall strain along the axis of stress. This is partially due to some straightening of the molecule. The straightening takes place with the help of molecular segmental slippage due to reformed bonds at new places. When the force is held during a certain time, the fibre in the straightened out position tries to go back to the original configuration giving rise to a reduction in stress (retraction force opposite to tensile force). In order to keep the force constant, the fibre will be extended. The retraction force is clearly higher for egg sac spider silk than for the other silks, possibly caused by the smaller crystalline content (as proved in Chapter 6). The higher amount of crystallites in the silkworm silks is not able or more difficult to uncoil, so no or a smaller retraction force is produced. Moreover, it is suggested that the higher amount of β-turns found in egg sac spider silk (see Chapter 6) may cause the higher retraction force.

Further correlations to the structure, especially for egg sac spider silk, are mentioned in Chapter 10.

3.1.5. CONCLUSION

In general, it can be concluded that the resilience and elastic recovery of all silks are not so high. This is explained by the high density of hydrogen bonding sites and as deformation proceeds, the bonds break and reform in new positions.

It can be concluded that the hysteresis behaviour of dragline spider silk is much better than that of the silkworm silks and egg sac spider silk: less energy is dissipated in the loading-unloading cycle and the permanent deformation is limited.

Furthermore, egg sac spider silk shows a similar hysteresis behaviour as Tussah silk. This is explained by the similar stress-strain behaviour (flattened post-yield region) for both silks below an extension of 10%. It is suggested that the presence of a higher content of residues with larger side chain for both silks is responsible for this behaviour. However, egg sac spider silk is lacking some structures, probably extended β-sheets, that result in the strain hardening observed in Tussah silk.

As far as the creep behaviour concerned, egg sac spider silk is much more sensitive to creep than dragline spider silk and the silkworm silks. It is suggested that the smaller crystalline content, the twist observed in the β-sheet crystals and the higher content of β-turns in egg sac spider silk are responsible for the higher creep.

3.2. THE STRAIN RATE DEPENDENCY OF SILKS

3.2.1. INTRODUCTION

Apart of the strain rate, it is also known that the gauge length has an effect on the tensile properties of fibres. In this respect, the first experiments allowed, apart of looking at the strain rate dependency, also the study of the effect of gauge length.

Since these results were not giving the expected results, especially for egg sac spider silk, it was decided to extend the study for this fibre in a second set-up by adding more tensile tests and more different testing speeds, but considering only one gauge length.

3.2.2. EFFECT OF GAUGE LENGTH – LITERATURE REVIEW

The tensile strength and strain-at-break of fibres and yarns are known to depend on gauge length.

A theory about the dependence of tensile strength and strain from the gauge length has been firstly established by Peirce [1926]. He introduces the "weak-link theory", also called the "Chain of Links model" [Pickering & Murray 1999]. Fibres and yarns break at their weakest point. It is considered that a fibre can be divided into segments or "links", each containing a flaw of varying severity. Hence the fibre is considered to have failed if one of its links has failed. A longer fibre can be considered to have a larger number of links than a shorter one and therefore, there is an increased probability of encountering a more severe flaw along the fibre length. Hence longer fibres should on average have a lower strength than shorter fibres. The "weak-link theory" is confirmed by several studies on different fibres [Pickering & Murray 1999, Zhang & Wang 2001].

Several authors [Kapadia 1935, Spencer-Smith 1947, Grant & Morlier 1948, Weibull 1951, Pillary 1965, Knox & Whitwell 1971] tried to find a relationship between tensile strength and gauge length. Some find a logarithmic relation, others an exponentional one.

3.2.3. EFFECT OF STRAIN RATE – LITERATURE REVIEW

From experiments done by Charch and Moseley [1959] for nylon 66, acrylic and high density poly-ethylene (HDPE) fibres (strain rates 1%/min to 100000%/min), it was observed that in all cases, broadly speaking, the modulus and tenacity increase with an increase in strain rate while the elongation-at-break decreases.

Wang & Xia [1998, 1999] studied the strain rate and temperature dependence of the mechanical behaviour of Kevlar fibre bundles. They found that the relations between the tensile strength (GPa), elastic modulus (GPa), strain-at-break value and the log(strain rate) are approximately linear and increase over the rate change from 140 to 1350 s^{-1} for a constant temperature.

Also for MA spider silk, a strong strain rate dependency was found [Denny 1976, Gosline *et al.* 1999]. Denny's analysis [1976] of strain rate dependence of MA silk demonstrated that stiffness, strength, extensibility and toughness all increase as strain rate increases from 0.0005 s^{-1} to 0.024 s^{-1}, suggesting that the performance of MA silk may be enhanced by increasing strain rate.

Also Elices *et al*. [2005] observed for MA spider silk (*Argiope trifasciata*) that higher strain rates lead to stiffer responses and to an increment of all the relevant mechanical parameters: the initial modulus of elasticity increases by 14%, and yield stress, tensile strength, and breaking strain grow significantly.

Zhang & Wang [2001] stated that the tensile strength of visco-elastic fibres increases as the strain rate increases because of the decreasing time interval allowed for the fibres to break.

3.2.4. EFFECT OF STRAIN RATE AND GAUGE LENGTH

3.2.4.1. Materials and methods

Also for this research some spiders were collected late in autumn and reared until oviposition of the egg sac. From the collected egg sacs, 5 different egg sacs of 5 different spiders (*Araneus diadematus)* were at random selected.

The 5 egg sacs were conditioned for at least 24 hours in a climate of 20 °C ± 2 °C and R.H. 65 ± 5%. For each test, 25 fibres were gently torn out of each egg sac and tested.

The FAVIMAT single-fibre tensile tester was used to investigate the influence of gauge length and strain rate on the tensile properties of egg sac spider silk.

For each egg sac the test set-up, as mentioned in Table 3.1, was performed

The nominal linear density was for each egg sac set to a suitable value, obtained by a preliminary linear density test.

This set-up was also repeated for the silkworm silks *Bombyx mori* and Tussah (*Antheraea pernyi)*. The discussion of these studies is limited to the most important results.

For each of the tests above, the following parameters (defined in Chapter 2) were determined: tenacity (cN/dtex), strain-at-break (%), work-to-rupture (cN/dtex), linear density (dtex), initial modulus 0.6-2% (cN/dtex) and post-modulus 15-35% (cN/dtex).

Table 3.1 - Test set-up for each egg-sac

	Tensile test				Linear density test	
# fibres	Preload (cN/tex)	Gauge-length (mm)	Strain rate (%/min)	Test speed (mm/min)	Preload (cN/tex)	Test speed (mm/min)
25	0.5	10	50	5	0.2	2
25	0.5	10	100	10	0.2	2
25	0.5	10	200	20	0.2	2
25	0.5	20	50	10	0.8	3
25	0.5	20	100	20	0.8	3
25	0.5	20	200	40	0.8	3
25	0.5	30	50	15	1.3	4
25	0.5	30	100	30	1.3	4
25	0.5	30	200	60	1.3	4

3.2.4.2. Influence on tensile properties for egg sac spider silk

3.2.4.2.1. Introduction

First of all, it should be remarked that all data show high variation and a lot of outliers could be detected. The outliers were removed after an ANOVA-analysis based on a boxplot of the deleted studentized residuals[1] which is an effective method to detect outliers [Ysebaert 2004-2005].

Since for most parameters no general conclusion could be taken that is valid for all egg sacs. It is decided to take the results of all egg sacs together for performing a 3-factor Analysis of Variance (ANOVA) on the factors egg sac, gauge length and strain rate. For comparisons among pairs of means, the Tukey test was performed at p=0.05.

3.2.4.2.2. Linear density (dtex)

With respect to linear density, no significant influence of both gauge length and test speed would be expected since the fibres are at random selected from the samples. However, for different gauge lengths different preloads and test speeds for the linear density test are set, as is mentioned in Table 3.2.

---

[1] The deleted studentized residual is defined as the studentized residual, omitting the present case in the analysis. The studentized residual is defined as: $r_{ij} = e_{ij} \Big/ s_{within} \cdot \sqrt{(n_i - 1)/n_i}$ with e_{ij} the residuals defined as the measured y – predicted y, s_{within} the standard deviation within observations, n_i the number of observations

Table 3.2 - Settings for the linear density test

Gauge length (mm)	Preload (cN/dtex)	Test speed (mm/min)
10	0.2	2
20	0.8	3
30	1.3	4

These settings are in accordance with the recommendations made by the instrument manufacturer for doing linear density tests.

So, if there is some influence, then it is accidentally. Since a lot of testing parameters are divided by the linear density in order to make better comparisons between different materials, this influence should be taken into account when making some conclusions.

Figure 3.11 shows the average linear density values, averaged over all egg sacs, split up for gauge length and strain rate.

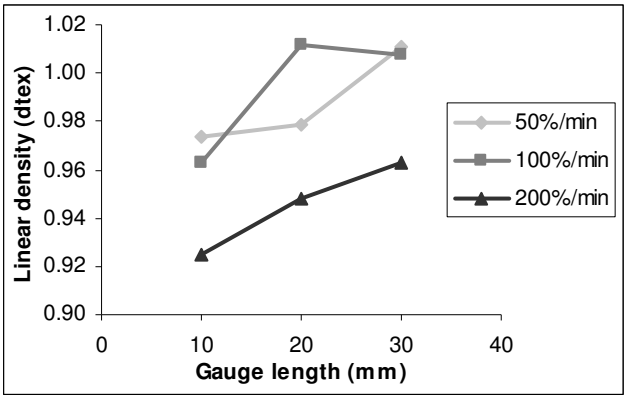

Figure 3.11 - Linear density in function of gauge length and strain rate

The 3-factor ANOVA reveals that all egg sacs have significantly different linear densities going from 0.77 dtex to 1.11 dtex.

The linear density increases significantly from 10 mm to 20-30 mm gauge length, and thus apparently with test speed, since for different gauge lengths different test speeds (and preloads) were set for the linear density test.

With respect to strain rate, the Tukey test reveals that a speed of 200%/min gives a much lower linear density than the other speeds do. Here no influence is expected, since the strain rate is used for the tensile test and not for the linear density test.

Gheysens (personal communication, not published yet) studied the way spiders are producing an egg sac and noticed that some layers can be differentiated, especially a layer deposited below the eggs and one above the eggs. Further research on these layers revealed that the egg sac fibres show significant different linear density values. As a consequence, it is possible that accidentally for the experiments at 200%/min more fibres were taken from the layer with lower linear density. The linear density of the different layers was, however, compensated by a higher

breaking force and initial modulus, so that no effect on tenacity and initial modulus was observed.

3.2.4.2.3. Strain-at-break (%)

Figure 3.12 shows the strain-at-break values for different gauge lengths and split up for different strain rates, averaged over all egg sacs.

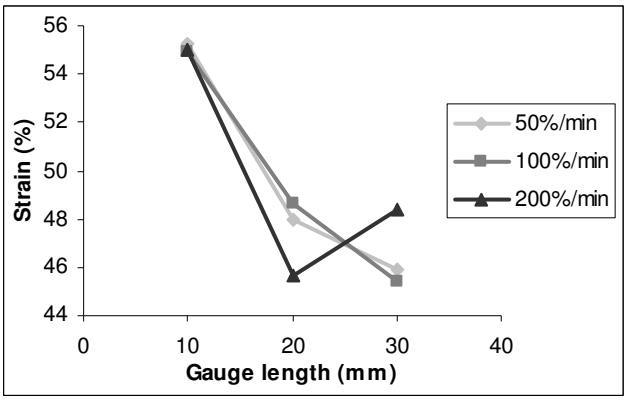

Figure 3.12 - Strain-at-break in function of gauge length and strain rate

As expected, because of the weak-link theory, the measured strain significantly decreases with gauge length. However, the Tukey test reveals that the strain values for 20 mm and 30 mm are not significantly different.

The strain rate does not have a significant influence on the strain value.

3.2.4.2.4. Tenacity (cN/dtex)

Figure 3.13 shows the tenacity, averaged over all egg sacs, in function of gauge length and strain rate.

From a 3-factor ANOVA, it can be concluded that the gauge length has a significant influence and the tenacity decreases significantly from 10 mm to 20 mm, and significantly increases to 30 mm. For the linear density, it was observed that it was statistically equal for 20 and 30 mm, and significantly lower for 10 mm. So, the much lower tenacity for 20 mm compared to that for 10 mm can be partly explained by the linear density.

We would not expect the increase for 30 mm because of the weak-link theory (tenacity significantly decreases with gauge length). Zhang & Wang [2001] concluded from experiments with wool that fibres usually break in their thinnest place (position of minimum diameter) at longer gauge length. In contrast, at shorter gauge lengths, fibres are generally more uniform and some fibres break in other positions along the fibre where structural defects or flaws might exist. Analogously for silks, we can suggest that at 30 mm, structural defects play a less significant role in the rupture process.

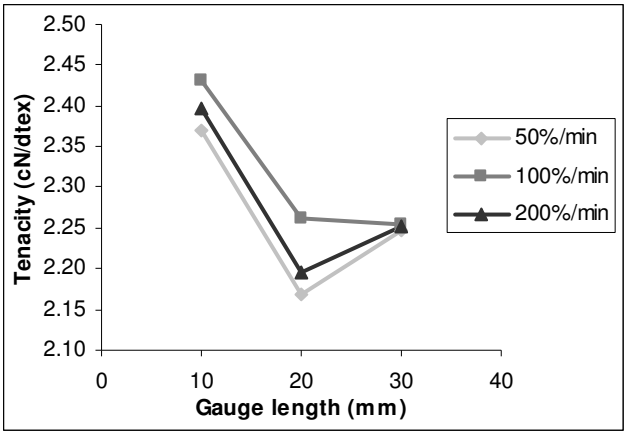

Figure 3.13 - Tenacity in function of gauge length and strain rate

With respect to strain rate, no significant influence could be detected between the values for 50%/min (2.26 cN/dtex) and 200%/min (2.28 cN/dtex). The value for a speed of 100%/min (2.32 cN/dtex) is significantly higher. The variance due to strain rate is however negligible. Also the lower linear density for a speed of 200%/min can not cause this behaviour.

3.2.4.2.5. Work-to-rupture (cN/dtex)

In order to make easier comparisons, the calculated work-to-rupture values were transformed to work-to-rupture values in cN/dtex by dividing by the linear density (dtex) and by dividing by the gauge length.

Figure 3.14 shows the work-to-rupture (expressed in cN/dtex), averaged over all egg sacs, in function of gauge length and strain rate.

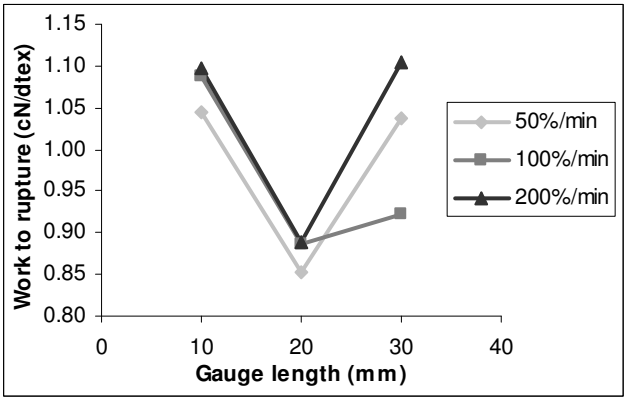

Figure 3.14 - Work-to-rupture in function of gauge length and strain rate

For the factor gauge length, the work values are not significantly different for 20 mm and 30 mm and increase significantly for 10 mm.

With respect to strain rate, no significant influence could be detected.

The work-to-rupture values are highly dependent on the strain and tenacity values and as a consequence a similar result could be expected.

3.2.4.2.6. Initial modulus 0.6-2% (cN/dtex)

The initial modulus has been determined between 0.6 and 2% in order to prevent the influence of crimp that for some fibres was not fully removed by the preload.

Figure 3.15 shows the initial modulus, averaged over all egg sacs, in function of gauge length and strain rate.

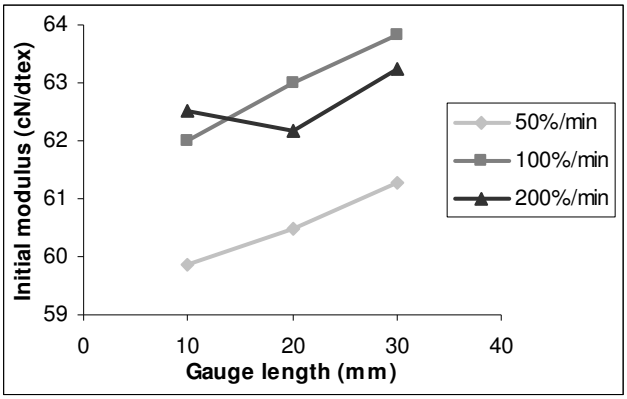

Figure 3.15 - Initial modulus in function of gauge length and strain rate

Only between the values for 10 mm and 30 mm a significant difference could be detected with the Tukey test.

Between a strain rate of 100%/min and 200%/min no significant influence could be detected. A significantly lower value is observed for a lower speed of 50%/min. From literature [Wang & Xia 1998], we would expect an increase in initial modulus with increasing speed. The effect seems negligible when using a speed higher than 100%/min.

3.2.4.2.7. Post-modulus 15-35% (cN/dtex)

Based on the shape of the stress-strain curve, it is decided to determine the post-modulus between 15 and 35%.

Figure 3.16 shows the post-modulus, averaged over all egg sacs, in function of gauge length and strain rate.

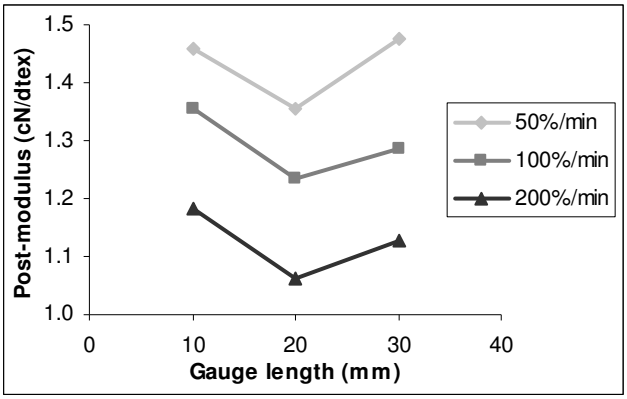

Figure 3.16 - Post-modulus (cN/dtex) in function of gauge length and strain rate

The 3-factor ANOVA for gauge length reveals that the post-modulus significantly decreases from 10 mm to 20 mm and significantly increases again from 20 mm to 30 mm.

The post-modulus significantly decreases with higher strain rates. Beyond the yield point, the chains begin to slide over each other (see Chapter 2). It can be expected that this sliding can more easily occur at lower speeds.

3.2.4.3. Influence on stress-strain curve for spider silk

3.2.4.3.1. Introduction

In order to evaluate the overall-effect of speed and gauge length on the stress-strain curves, the individual curves for each egg sac, each speed and each gauge length were simulated by means of an SLS model according to Equation (2.8) as derived in Chapter 2.

For most egg sacs, the effect of speed seems to decrease with higher gauge lengths. It is also clear from simulated graphs that the level of the hardening region and thus the breaking stress increases with strain rate. The effect of gauge length is less clear from the graphs.

In this part, the 3-factor ANOVA is described that is used to evaluate the influence of egg sac, gauge length and strain rate on the correlation coefficient and the parameters A, B and C of the SLS model.

3.2.4.3.2. The correlation coefficient

Figure 3.17 shows the correlation coefficient, averaged over all egg sacs, in function of gauge length and strain rate.

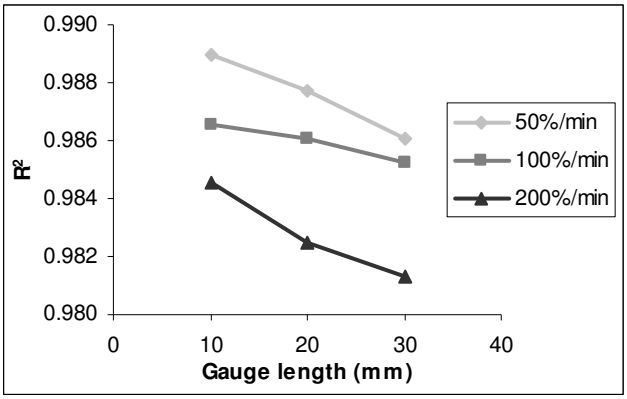

Figure 3.17 - The average of correlation coefficient in function of gauge length and strain rate

The correlation coefficient seems to increase with decreasing gauge length and decreasing strain rate; in other words, the simulation becomes worse with higher gauge length and higher strain rate. However, since the correlation coefficient still exceeds 98%, we believe that it is still useful to evaluate the parameters A, B and C.

Looking at the stress-strain curves (see also Figure 3.22 for different test speeds), it was noticed that the shape of the stress-strain curves changes in their yield region. This change is expected to be responsible for the decrease in correlation coefficient.

3.2.4.3.3. Parameter A

For the evaluation of the parameters of the SLS model, the outliers were first removed, based on a boxplot of the deleted residuals [Ysebaert 2004-2005].

Figure 3.18 shows the parameter A, averaged over all egg sacs, in function of gauge length and strain rate.

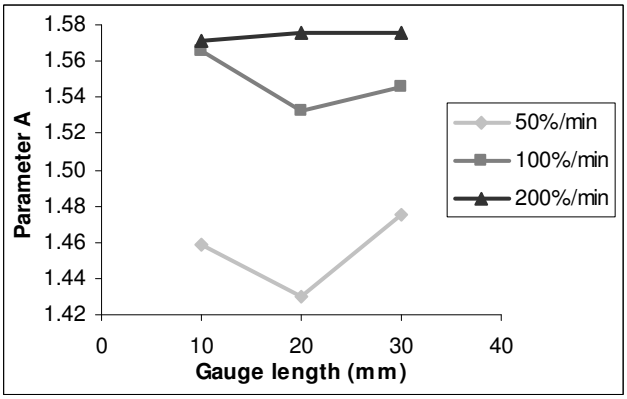

Figure 3.18 - Parameter A in function of gauge length and strain rate

The influence of gauge length on the parameter A is limited. Two overlapping homogeneous groups were selected by the Tukey criterium. With all data, no significant influence was observed.

With respect to strain rate, the value of A increases with increasing strain rate.

3.2.4.3.4. Parameter B

After removing the outliers, selected by a boxplot of the deleted residuals [Ysebaert 2004-2005], the parameter B, averaged over all egg sacs, in function of gauge length and strain rate was calculated, as shown in Figure 3.19.

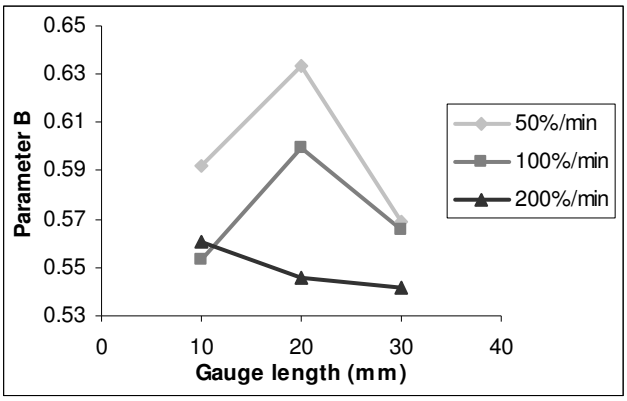

Figure 3.19 - Parameter B in function of gauge length and strain rate

With respect to gauge length, for the data of gauge length 20 mm, the parameter B is significantly higher than the other gauge lengths.

For strain rate, the value of B increases significantly with lower speeds.

3.2.4.3.5. Parameter C

Figure 3.20 shows the parameter C, averaged over all egg sacs, in function of gauge length and strain rate for the data with the outliers removed.

With respect to gauge length, it is surprising that parameter C increases significantly in the order 20 mm – 30 mm – 10 mm, in other words a minimum is observed for a gauge length of 20 mm.

With respect to strain rate, the parameter C increases significantly with decreasing strain rate.

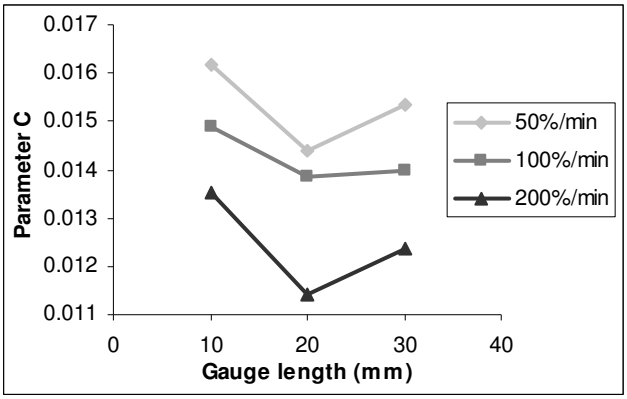

Figure 3.20 - Parameter C in function of gauge length and strain rate

3.2.4.4. Conclusion

3.2.4.4.1. Introduction

First of all, it should be remarked that there is a high variation in the data between the different egg sacs. No conclusion can be taken that is valid for every egg sac separately. But, since the variation within one egg sac is also so high, it is possible that the number of tests for each egg sac was not enough to make reliable conclusions. It was preferred to test more egg sacs with a lower number of tests than to test more fibres within one egg sac. One can expect that the more fibres are tested within one egg sac, the higher the influence of the preparation method that is not optimal. It is unavoidable that a tearing action is applied on the fibre, and so also on neighbouring fibres.

Moreover, for some parameters the basic assumptions for performing an analysis of variance (ANOVA) are not always valid, so some caution should be taken into account in the interpretation. However, because of the high number of tests that were performed and since ANOVA is quite robust against deviations from e.g. normality [Ysebaert 2004-2005], we suppose that the ANOVA analysis is still valuable.

3.2.4.4.2. Effect of gauge length

For most parameters, it is clear that the gauge length plays a significant role when testing mechanical properties of spider silk. The difference in values for 20 mm and 30 mm is not always clear, although when the gauge length is increased from 10 mm to 30 mm, one gets the following results:

- the strain decreases,
- the work-to-rupture decreases,
- the tenacity decreases,
- the initial modulus increases,

Some of these results were expected based on the weak-link theory. The longer the test length, the more chance that a weak place is included, so the fibre will break quicker resulting in a lower strain value, lower force value and lower work-to-rupture value.

It is possible that the difference between 20 and 30 cm is not high enough to make any difference. It should also be remarked that to have longer fibres, the tearing force to get the fibres out of the egg sac will be higher.

With respect to the simulation by the SLS model, firstly it should be remarked that the correlation coefficient of the model significantly decreases with gauge length. Thus, it seems that the variation that can be explained by the parameters A, B and C decreases with gauge length.

The gauge length has only a limited effect on the parameter A, and thus on the level of the hardening region. For parameter B, we again have the surprising result that it first increases followed by a decrease (for 2 egg sacs). Also for parameter C, corresponding to the slope of the hardening region, a minimum is observed for 20 mm.

Some surprising results:

- The tenacity decreases from 10 to 20 mm, followed by an increase from 20 to 30 mm. (This effect can also be seen with parameter A, however, it was not significant.)
- The post-modulus decreases from 10 to 20 mm, followed by an increase from 20 to 30 mm. As could be expected, the same is observed for parameter C.
- The parameter B increases from 10 to 20 mm, followed by a decrease from 20 to 30 mm.

Zhang & Wang [2001] observed for wool that for longer test lengths, the effect of structural defects or flaws (weak places) is smaller than for shorter lengths. A further explanation is found in the contribution of the cross-links. At higher gauge lengths, more cross-links are available which will break easier and thus the weak places will have a higher contribution to the strength and can thus result in a quicker break of the fibre. At much higher gauge lengths, the chance that stronger parts are connected with cross-links is greater which results again in more time required to break the cross-links and thus again an increase in strength. The low fraction of small crystals found in egg sac spider silk (see Chapter 6) may enforce the effect.

3.2.4.4.3. Effect of strain rate

Looking at the graphs of measured versus predicted values, it seems that the higher the test speed, the more the shape of the curve reaches the shape of dragline and normal silks. It could indicate that if it would be possible to reel off the silk from the tubuliform glands, a higher reeling speed could result in a comparable stress-strain behaviour as dragline threads, as was also observed for *B. mori* fibres [Shao & Vollrath 2002].

The strain-at-break value is not affected by strain rate. For post-modulus, it can be concluded that the value decreases significantly with strain rate.

For the other parameters, the conclusion is not always logic. In most cases, the difference between the values for 50%/min and 200%/min is lower than between the values for the strain rates 50%/min and 100%/min.

When the strain rate is increased from 50%/min to 200%/min, then:

- the strain does not differ significantly (slightly decrease),
- the work-to-rupture increases significantly (for 3 of 5 egg sacs),
- the initial modulus increases,
- the post-modulus decreases.

For the parameters work-to-rupture and initial modulus no significant influence is observed between the speeds 100%/min and 200%/min.

With increasing strain rate:

- parameter A, and thus the level of the hardening region increases;
- parameter B decreases, thus the yield point moves to higher strain values;
- parameter C decreases, and thus also the slope of the hardening region, in accordance with the results observed for post-modulus.

Some surprising result:

- The tenacity increases from 50 to 100%/min, followed by a decrease from 100 to 200%/min (2 of 5 egg sacs, for 3 egg sacs a small increase at end).

Since the effect is less clear for the increase of the strain rate from 100%/min to 200%/min, it seems that the visco-elastic effect decreases the higher the strain rate.

A further explanation of this behaviour is given in the discussion of the results of the more detailed set-up for evaluating strain rate.

3.2.4.4.4. General conclusion

Because of the surprising results that were observed at a gauge length of 20 mm and for the different speeds for egg sac spider silk, it was decided to look at the effect of strain rate more in detail by adding tensile experiments at more different speeds. Also the number of tests per egg sac was increased. This was the reason for the second set-up that was considered in section 3.2.5.

3.2.4.5. Further results for silkworm silks

3.2.4.5.1. Introduction

In this section, the results for the silkworm silks are described shortly, with attention to the differences with the egg sac spider silk.

3.2.4.5.2. Linear density

For *Bombyx mori* and Tussah silk, there was indeed no significant influence of the gauge length, when the gauge lengths 10, 20 and 30 cm were considered.

For the silkworm silks, the linear density was also unaffected by the strain rate.

The effect of strain rate for egg sac spider silk could be accidentally or due to the different layers in the egg sac silk, as described in section 3.2.4.2.2.

3.2.4.5.3. Strain-at-break (%)

For all silks, the strain-at-break value decreases significantly with gauge length, in accordance with the weak-link theory. However, the strain value decreases clearly more from 10 mm to 20 mm than from 20 mm to 30 mm.

As for egg sac spider silk, there is no significant effect of strain rate on the strain-at-break value for *Bombyx mori* silk. For Tussah silk, however, the strain value for 200%/min is significant higher than for the other speeds. This can be explained by the higher number of tests succeeded for 10 mm, having a higher strain, than for the other speeds.

3.2.4.5.4. Tenacity (cN/dtex)

For the silkworm silks, the decrease of tenacity with gauge lengths can also be observed. However, the decrease of tenacity from 20 to 30 mm is clearly smaller than from 10 mm to 20 mm.

In accordance with the weak-link theory we would expect that: when the gauge length is higher, the chance to have a weak place is higher, resulting in a lower strain-at-break and thus lower tenacity. The same explanation may be valid as for egg sac spider silk (see section 3.2.4.4.2).

A small increase of tenacity with strain rate is observed for the silkworm silks, however the increase is not significant. For visco-elastic fibres, the increase of tensile strength with strain rate is confirmed in literature [Charch & Moseley 1959, Zhang & Wang 2001, Wang & Xia 1998, 1999]. For egg sac spider silk, the value for a speed of 100%/min seems to be higher than the other speeds. Probably the result is due to the high variation in the effect for the different egg sacs. For 3 of 5 egg sacs, the tenacity is indeed slightly increasing like for the silkworm silks, for 2 egg sacs the tenacity is clearly decreasing for higher speeds than 100%/min.

3.2.4.5.5. Work-to-rupture (cN/dtex)

For all silks, the work-to-rupture values decrease significantly from 10 mm to 20 mm, what could be expected based on the weak-link theory. A further increase to 30 mm does not decrease the work-to-rupture values significantly.

The work-to-rupture values seem to increase with strain rate, although the effect is small and not always significant for the silkworm silks. For egg sac spider silk, the increase in work value from 100%/min to 200%/min is not significant. It should be remarked here that for 2 egg sacs, the work value decreases between 100%/min and 200%/min. So, here again a high variation between egg sacs exists.

3.2.4.5.6. Initial modulus (cN/dtex)

As for egg sac spider silk, only the increase of initial modulus from 20 mm to 30 mm is significant for Tussah silk. For *Bombyx mori* silk, a significant increase of initial modulus from 10 mm to 20 mm could be observed. So, the effect of gauge length seems small, although for all silks the increase from 10 to 30 mm results in a higher initial modulus. This increase is confirmed in literature [Charch & Moseley 1959, Wang & Xia 1998, 1999].

For both silkworm silks, the same behaviour is observed as for egg sac spider silk: the initial modulus seems to increase from 50%/min to 100%/min, followed by a decrease from 100%/min to 200%/min. However, the ANOVA and Tukey test revealed that the effect is small.

A further explanation is given in the more detailed study of the effect of strain rate for a gauge length of 20 mm.

3.2.5. EFFECT OF TEST SPEED

3.2.5.1. Materials and methods

For this research, some spiders were collected late in autumn and reared until oviposition of the egg sac. From the collected egg sacs, 4 different egg sacs of *Araneus diadematus* spider silk were selected at random and the eggs were carefully removed from each sample. For each test, 50 fibres were gently torn out of each egg sac.

The linear density values for the egg sacs were simultaneously determined with the tensile parameters, using following settings: a preload of 0.8 cN/tex and a speed of 2 mm/min, preset linear density 0.7 dtex.

Some hundreds of spiders *A. diadematus* were maintained under controlled conditions in the laboratory. Different samples of dragline thread were manually reeled off. Samples of three different spiders were selected and 50 fibres were taken for each test.

For this study, since we are interested in the influence of the test speed, the linear density values of the dragline threads were not determined, hence the force values (in cN) were considered.

The fibres and filaments were tested with the FAVIMAT-ROBOT using a gauge length of 20 mm, a pretension of 0.5 cN/dtex and 5 different speeds: 5 – 10 – 20 – 30 – 40 mm/min. For the dragline threads, through lack of material of the same spider taken at the same moment, only the tests for speeds of 5, 20 and 40 m/min were performed.

All fibres were kept for at least 24 hours in climatised conditions before testing.

For a further discussion of the results, the SLS model (see Chapter 2 – Equation (2.8)) is used to describe the overall stress-strain behaviour.

3.2.5.2. Results and discussion

3.2.5.2.1. Egg sac spider silk – tensile parameters

Since the linear density is used in the calculation of some tensile parameters (tenacity, modulus values, etc.), the linear density for the different egg sacs measured at different speeds is evaluated.

With respect to linear density, no significant influence of test speed would be expected since the fibres are at random selected from the samples, moreover the settings for the linear density test are the same for one gauge length (see Table 3.2).

Figure 3.21 shows the linear density values for the 4 different egg sacs in function of test speed of the tensile test, also the average linear density for all egg sacs is added ("All").

It is clear that the linear density for egg sac 4 is more variable than for the other egg sacs. Furthermore, the linear density for a speed of 20 mm/min seems also more variable. It results in a higher average linear density for this speed compared to the other speeds. It will be taken into account in the further evaluation.

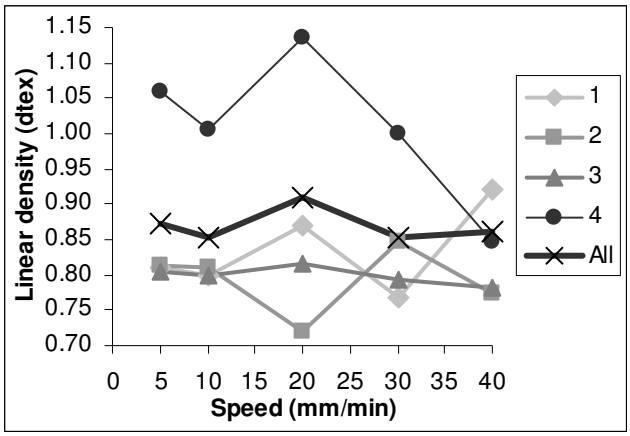

Figure 3.21 - Linear density values for different egg sacs, obtained at different tensile test speeds

A first remark that should be made is that all tensile parameters show a high variation. A boxplot of strain-at-break values reveals that a lot of extreme values in the lower range were included. The number of these extremes, however, varies between egg sacs. The egg sac silk probably shows a lot of structural defects resulting in an early rupture. It was decided to remove the outliers, based on a boxplot of the deleted studentized residuals [Ysebaert 2004-2005]. After skipping these extremes, for strain-at-break and work-to-rupture the CV-value still exceeds about 30%. For the moduli and tenacity values, the CV-value is in most cases restricted to 10-15%. The high variability (intraspecies and intraindividual) is confirmed by other authors [Madsen *et al.* 1999, Garrido *et al.* 2002] for dragline spider silk.

Figure 3.22 shows the stress-strain curves, averaged over all egg sacs, for the different speeds. It is already clear that another behaviour is observed for lower speeds (5-10 mm/min) than for higher speeds (30-40 mm/min).

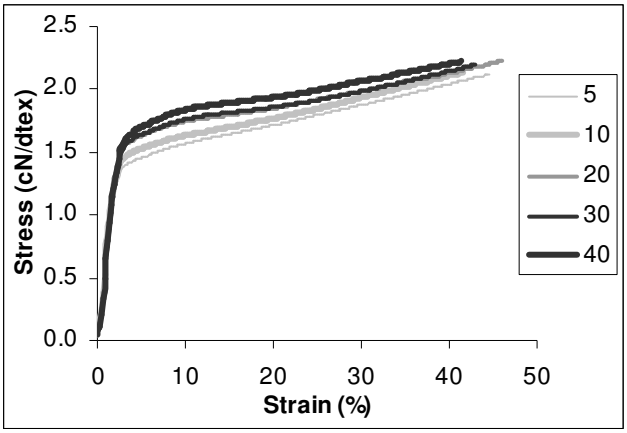

Figure 3.22 - Average stress-strain curves for different test speeds

For strain-at-break, it can be remarked that there is a high variability (CV ± 30%) within 1 egg sac and 1 test speed so that the strain-at-break varies between 40 and 52%. It should be remarked that the high variation within egg sac does not result in a reliable average value for 50 tests within a 95% confidence range. However, it was not feasible to further increase the number of tests. This variable behaviour could be expected since fibre fracture (a large strain property) represents the response of the weakest part of the fibre and therefore is very sensitive to defects in the structure.

An analysis of variance on all individual results reveals that the test speed has no significant influence ($p > 0.05$) on the measurement of strain-at-break, what could be expected from Figure 3.23.

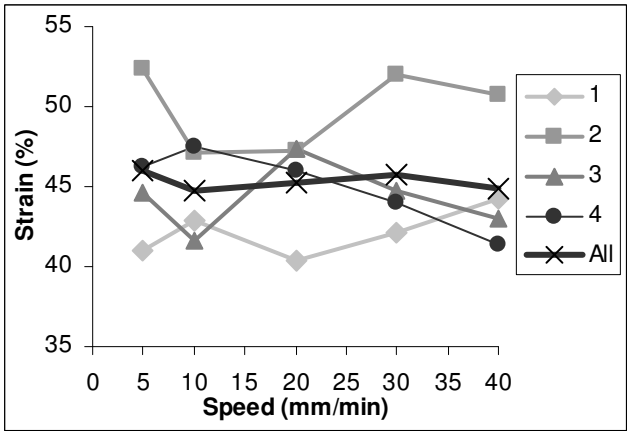

Figure 3.23 - Effect of speed on strain-at-break (%)

For tenacity values, no general conclusion can be arrived at that is valid for every egg sac. The variability within 1 egg sac and 1 test speed is lower than for the strain-at-break, probably because of the shape of the stress-strain curve. The tenacity varies between 1.9 and 2.4 cN/dtex. Moreover, it should be remarked that the high variability in linear density for egg sac 4, is not represented in the graph for tenacity. So, it is clear that the division of the force values by the linear density results in more comparable values.

If we take the results of all the egg sacs together, it can be concluded from Figure 3.24 that the tenacity increases with increasing test speed. Moreover, a significant logarithmic correlation ($R^2 = 0.98$) can be found between both parameters (Figure 3.25). This logarithmic behaviour is in accordance with strain rate dependency data found in literature for a.o. Kevlar [Wang & Xia 1998] and high performance polyethylene [Govaert & Peijs 1995] fibres.

It should be remarked that statistically this increase is only significant from 5-10 mm/min to 20-30-40 mm/min.

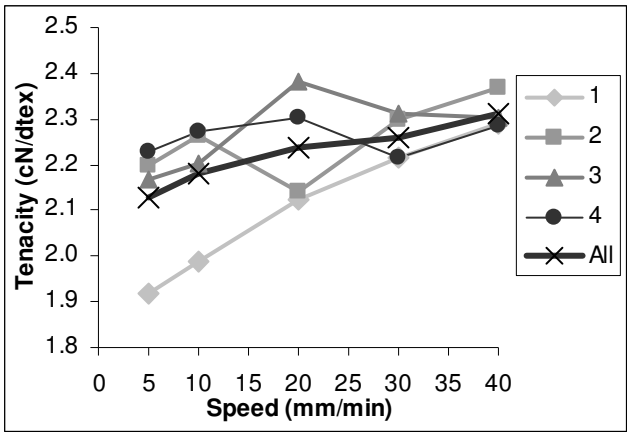

Figure 3.24 - Effect of speed on tenacity (cN/dtex)

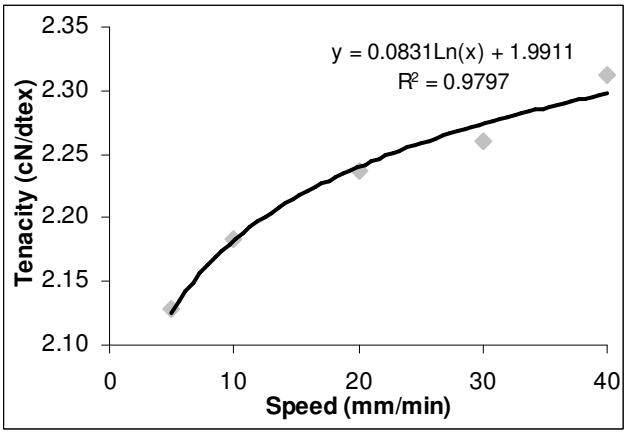

Figure 3.25 - Logarithmic relation between the average tenacity and speed

Because of the high variability of the strain-at-break, the high variability (CV = 30-40%) of work-to-rupture could be expected. The work-to-rupture varies between 1.02 cN/dtex to 1.54 cN/dtex.

Also for work-to-rupture no general conclusion can be drawn (Figure 3.26), although the biggest difference is ascribed to the value for the speed of 20 mm/min. Probably, the effect of linear density explains partly this behaviour. For the speeds 5 and 10 mm/min, resp. the speeds 30 and 40 mm/min no significant difference could be found, except for egg sac 1. The regression for work-to-rupture in function of test speed only results in a correlation coefficient of 73%, mostly because of the deviation at 20 mm/min.

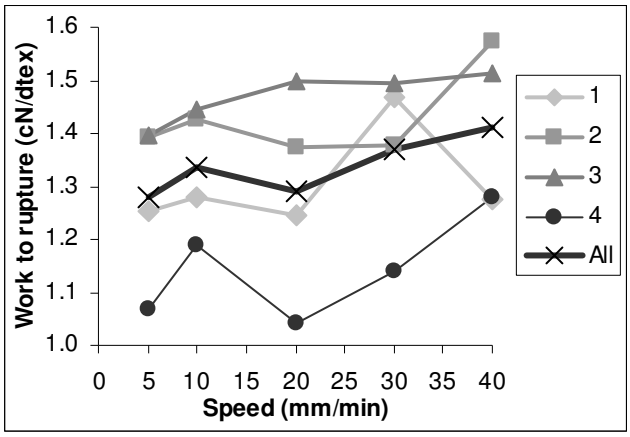

Figure 3.26 - Effect of speed on work-to-rupture (cN/dtex)

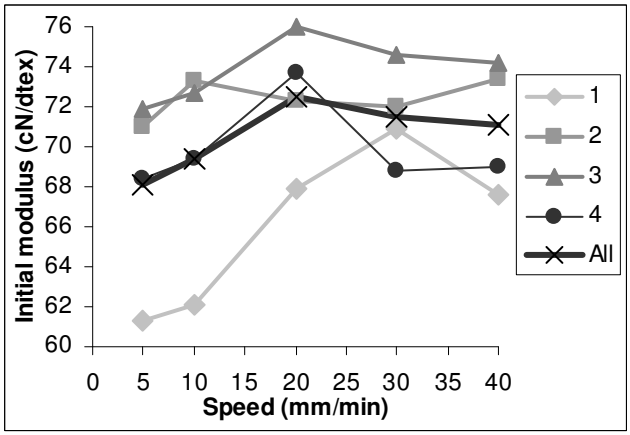

Figure 3.27 - Effect of speed on initial modulus (cN/dtex)

The initial modulus was calculated directly from the stress-strain curve as the slope of the initial straight region, where also the correlation coefficient of the regression curve was as high as possible for a minimum number of observations. The effect of crimp that is sometimes not fully removed by the preload is as such restricted to a

minimum. The effect of speed on the initial modulus for the different egg sacs is shown in Figure 3.27.

It is interesting to remark that the variability (CV) of the initial modulus within 1 egg sac and test speed is much lower than for the other parameters: in most cases below 10%. The initial modulus varies between 61 and 76 cN/dtex. The lower variability could be expected since initial modulus is significantly influenced by molecular orientation and morphology which are expected to be the same for one type of spider silk.

With respect to the influence of test speed, no significant difference can be found between 5-10 mm/min, resp. between 20-30-40 mm/min. The effect of linear density (more variable for egg sac 4, lower for 20 mm/min) is not visible.

When all egg sacs are considered together, Figure 3.28 shows the relationship between initial modulus and test speed. The initial modulus seems to increase with test speed till a speed of 20 mm/min, followed by a decrease of initial modulus with higher test speed. This observation is surprising since in literature it is often found that the elastic modulus is increasing with speed [Wang & Xia 1998]. Since the initial modulus is correlated with the microstructure of a fibre, it seems that during tensile deformation some rearrangement of the molecules in the amorphous regions occur that can relax during a longer testing time or lower test speed.

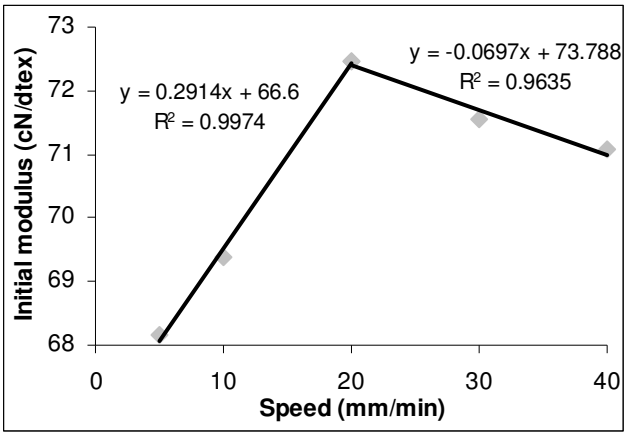

Figure 3.28 - Relation between initial modulus and speed

Also in this study, the post-modulus was determined between the strain values 10 and 35%. The variability (CV) in the post-modulus is in most cases restricted to 10-15%. The value varies between 1.0 and 1.6 cN/dtex. It is clear that the division by the linear density makes the post-modulus for the different egg sacs comparable.

For post-modulus, the decreasing trend with test speed is clear from Figure 3.29 for every egg sac. This is confirmed by a significant decrease (R^2=0.96) of post-modulus with test speed when calculating the average post-modulus for each speed, as is shown in Figure 3.30. Based on an analysis of variance, between the values at 5 and 10 mm/min no significant decrease could be detected.

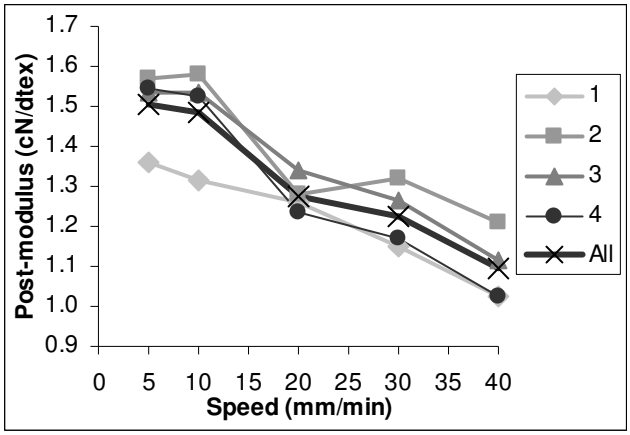

Figure 3.29 - Effect of speed on post-modulus (cN/dtex)

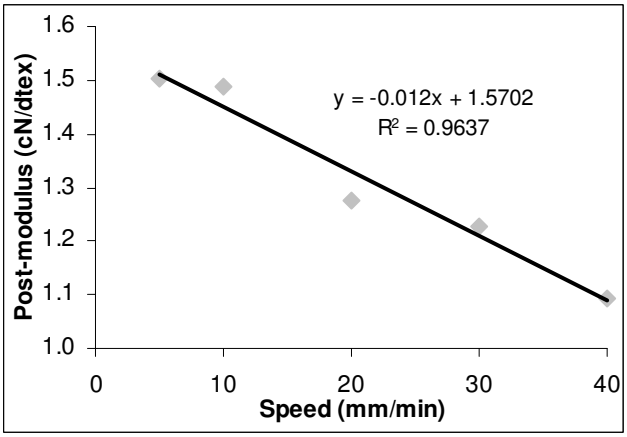

Figure 3.30 - Relation between post-modulus and speed

3.2.5.2.2. Egg sac spider silk – parameters of SLS model

Figure 3.31, Figure 3.33 and Figure 3.35 show the influence of speed on the parameters A, B and C, respectively, of the standard linear solid (SLS) model (see Equation (2.8) in Chapter 2) for the egg sacs.

As can be seen in Figure 3.32, the parameter A logarithmically increases with test speed. Since the change of parameter A results in a curve with a higher maximum level of the hardening region (quite horizontal part) (Figure 2.12), this is in accordance with the result for tenacity. Moreover, the parameter A also results in a change of initial modulus. In this respect, it should be remarked that for speeds higher than 20 mm/min, the increasing effect of A with speed is minimal, however it does not seem to decrease as is observed for initial modulus.

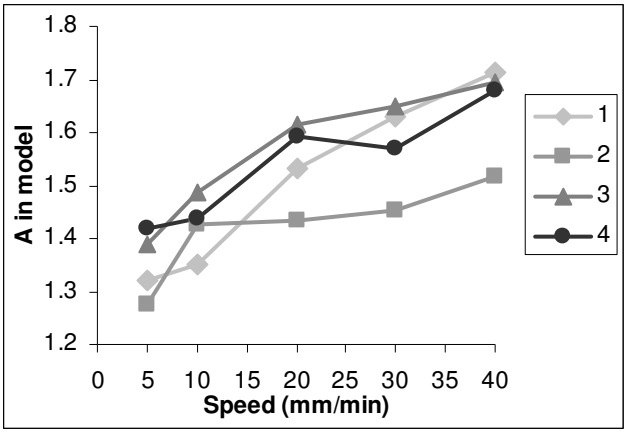

Figure 3.31 - Influence of test speed on parameter A in SLS model

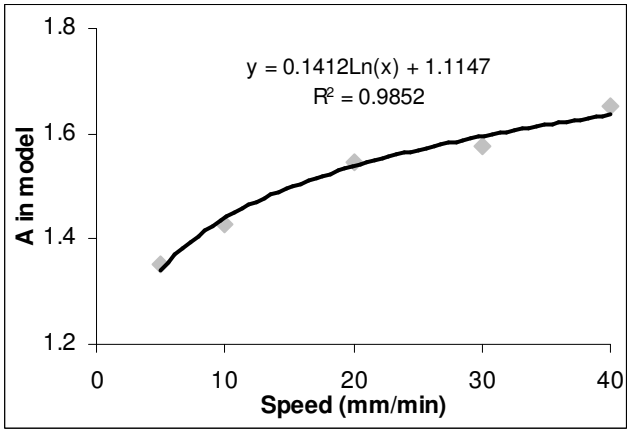

Figure 3.32 - Logarithmic relation between parameter A and test speed

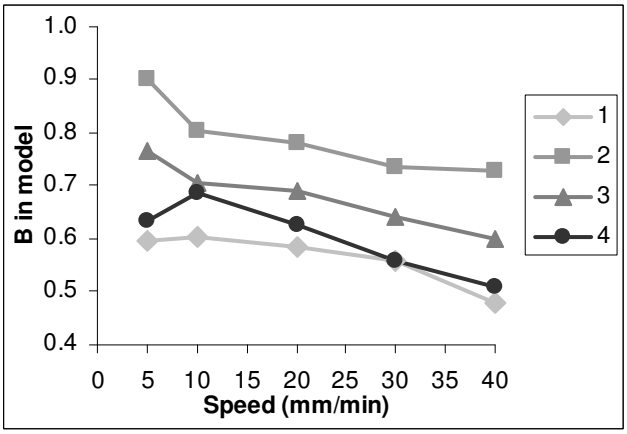

Figure 3.33 - Influence of test speed on parameter B in SLS model

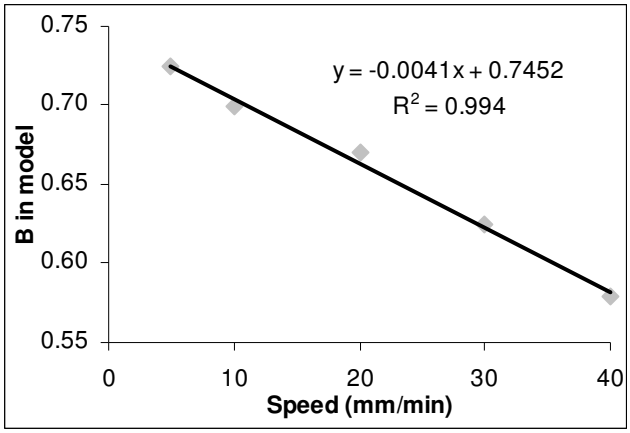

Figure 3.34 - Linear relation between parameter B and test speed

Parameter B significantly decreases linearly with test speed (Figure 3.34). The value of parameter B represents the shape of the yield region (Figure 2.13). The yield point moves to higher strains, and as a result the initial modulus decreases, as B decreases.

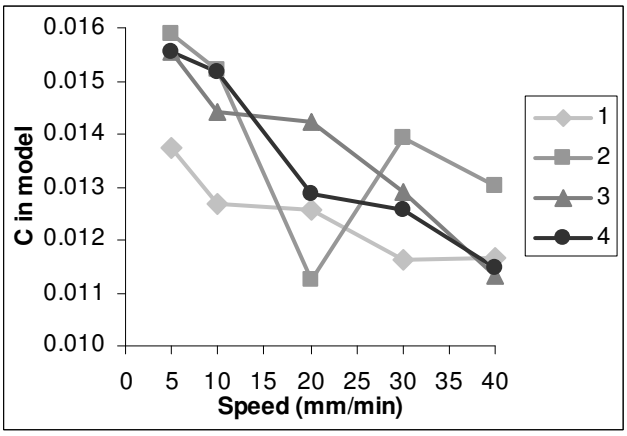

Figure 3.35 - Influence of test speed on parameter C in SLS model

Also parameter C logarithmically decreases with test speed (Figure 3.36) (R^2 was only 0.90 for a linear relation). Here as well, it should be remarked that for speeds higher than 20 mm/min, the influence of the speed on C is decreasing. An increase of C in Equation (2.8) results in a steeper slope (Figure 2.14), and thus a higher post-modulus. The influence of speed on parameter C is more or less in accordance with the result for the post-modulus.

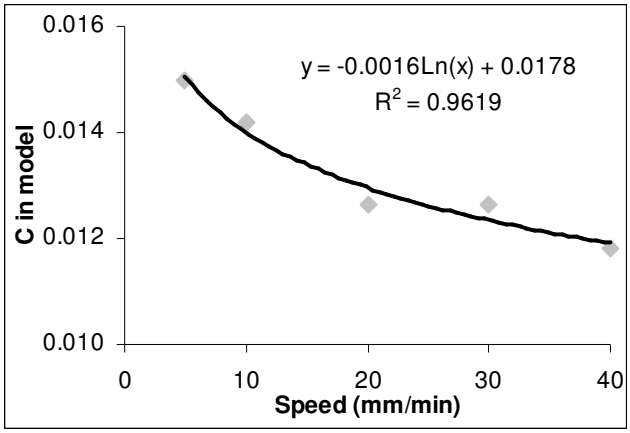

Figure 3.36 - Logarithmic relation between parameter C and test speed

3.2.5.2.3. Dragline spider silk

For draglines, no statistically significant influence of speed could be found for strain-at-break, breaking force, work-to-rupture and post-modulus (10-25%). Only for the initial modulus, the value for the speed 5 mm/min is significantly higher than for the speeds 20 and 40 mm/min, which is not in accordance to the result for egg sac silk and to the results found in literature [Wang & Xia 1998]. In summary, it can be concluded that the influence of speed is less pronounced for dragline silk than for egg sac silk.

From a more detailed study of the stress-strain curves, different shapes of curves could be observed (Figure 3.37). The Type 1 curve is in most cases the mostly occurring curve, sometimes two groups with different initial slope are observed. The Type 2 curve is the type of curve characteristic for egg sac spider silk. The Type 3 curve is an almost linear curve, but is rarely found. The reasons for these different types of curves are not clear yet:

1. Individual filaments are having different properties, it is reported that major ampullate silk is partnered with minor ampullate silk in dragline [Viney 2000]. The Type 2 curve possibly can represent the stress-strain behaviour of minor ampullate silk instead of major ampullate silk;
2. The manual "silking" at uncontrolled speeds and tensions creates different properties;
3. Some threads were torn from other spider glands than the major ampullate glands that secrete the dragline silk;
4. Some filaments are torn too hard in the preparation process before testing;
5. Filaments with variable tension are wound on a holder during a certain time, which could create some changes in structures e.g. due to creep or stress relaxation.

Recently, Garb & Hayashi [2005] stated that morphologically distinct silk glands predominately express one fibroin type, but also may express smaller amounts of fibroins primarily synthesized by other silk glands. They found that some genes

(MaSp1 and MaSp2, see Chapter 5) are expressed in both major ampullate and tubuliform glands. This confirms the 3rd option, certainly because the spiders that were used, were those that are collected late in October-November, in order to favor the conditions for egg laying.

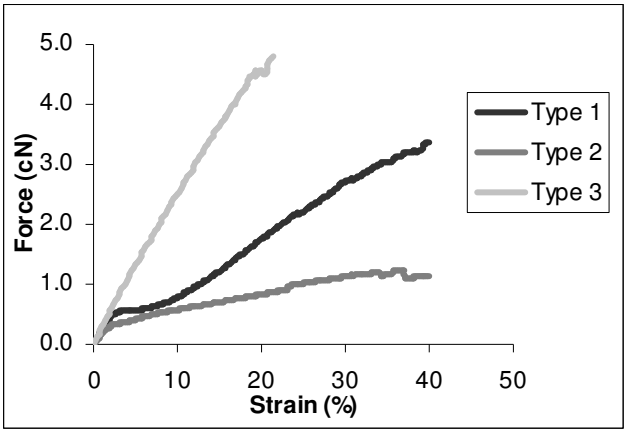

Figure 3.37 - Different types of stress-strain curves found for dragline filaments

3.2.6. CONCLUSION

Looking at the effect of the test speed for egg sac spider silk, it is proved that at low test speeds, the tenacity, the work-to-rupture or toughness and the stiffness will be lower, while the post-modulus will be higher than at high test speeds. A sort of "breaking point" occurs at a test speed of 20 mm/min. This can be explained by the fact that at lower speeds a certain amount of plastic or unrecoverable deformation takes place during the time of the test itself, due to changes in the structure, which is not the case with high test speeds.

When the stress-strain curve of egg sac silk is simulated by means of the standard linear solid (SLS, an extended Maxwell model) model, higher test speeds result in a higher level of the hardening region, in a movement of the yield region to higher strain values and in a more horizontal behaviour of the hardening region. A speed of 20 mm/min can be considered as a saturation point: at higher speeds the effect of speed decreases.

The influence of the test speed for dragline silk was clearly less pronounced than for egg sac silk. However, it should be taken into account that different shapes of stress-strain curves within each dragline were observed, possibly due to the spinning process or to the preparation process before testing.

3.3. REFERENCES

Barghout J.Y.J., Thiel B.L., Viney C., Spider (*Araneus diadematus*) cocoon silk: a case of non-periodic lattice crystals with a twist?, Int. J. Biol. Macromol. 24(2-3):211-217 (1999)

Carmichael S., Barghout J.Y.J., Viney C., The effect of post-spin drawing on spider silk microstructure: a birefringence model, Int. J. Biol. Macromol. 24:219-226 (1999)

Charch W.H. & Moseley W.W., Structure-property relationships in synthetic fibers – Part I: Structure as revealed by sonic observations, Text. Res. J. 29:525-535 (1959)

Denny M., The physical properties of spider's silk and their role in the design of orb-webs, J. Exp. Biol. 65:483-506 (1976)

Elices M., Pérez-Rigueiro J., Plaza G.R., Guinea G.V., Finding inspiration in *Argiope trifasciata* spider silk fibers, JOM, February, 60-65 (2005)

Farrow B., Extensometric and elastic properties of fibres, J. Text. Inst. 47:T58 (1956)

Garb J.E. & Hayashi C.Y., Modular evolution of egg case silk genes across orb-weaving spider superfamilies, Proc. Nat. Acad. Sci. 102(32):11379-11384 (2005)

Garrido M.A., Elices M., Viney C., Pérez-Rigueiro, The variability and interdependence of spider drag line tensile properties, Polymer 43:4495-4502 (2002)

Gosline J.M., DeMont M.E., Denny M.W., The structure and properties of spider silk, Endeavor 10(1):37-43 (1986)

Gosline J.M., Pollak C.C., Guerette P.A., DeMont M.E., Denny M.W., Elastomeric network models for the frame and viscid silks from the orb-web of the spider *Araneus diadematus*. In: Silk polymers: materials science and biotechnology, Kaplan D., Adams W.W., Farmer B., Viney C. (Eds), Am. Chem. Soc. 329-341 (1994)

Gosline J.M., Guerette P.A., Ortlepp C.S., Savage K.N., The mechanical design of spider silks: From fibroin sequence to mechanical function, J. Exp. Biol. 22(23):3295-3303 (1999)

Govaert L.E. & Peijs T., Tensile strength and work of fracture of oriented polyethylene fibre, Polymer 36(23):4425-4431 (1995)

Gupta V.B., Structure of textile fibres and structural dependence of their mechanical properties, In: Progress in Textiles: Science & Technology, Kothari V.K (Ed.), Vol. 2, IAFL Publications, India, 11-118 (2000)

Grant J.N. & Morlier O.E., Relation of specific strength of cotton fibers to fiber length and testing method, Text. Res. J. 18:481-487 (1948)

Hatch K.L., Textile fibers, Chapter 8 – Fiber properties and identification, West Publishing Company, USA, 109-118 (1993)

Kapadia D.F., Single-thread strength testing of yarns in various lengths of test specimen, J. Text. Inst. 26:T242-T260 (1935)

Knox L.J. Jr. & Whitwell J.C., Studies on breaking stress distribution. Part I: the weak-link theory and alternate models, Text. Res. J. 41:510-517 (1971)

Madsen B., Shao Z.Z., Vollrath F., Variability in the mechanical properties of spider silks on three levels: interspecific, intraspecific and intraindividual, Int. J. Biol. Macromol. 24:301-306 (1999)

McCrum N.G., Prediction of creep at long times in polymeric solids, Journal of Materials Science 13 (7):1596-1598 (1978)

Nachane R.P. & Sundaram V., Analysis of relaxation phenomena in textile fibres Part II: Inverse relaxation, J. Text. Inst. 86(1):20-32 (1995)

Peirce F.T., Tensile test for cotton yarns – The weakest link – Theorems on the strength of long and composite specimens, J. Text. Inst. 17:T355-T368 (1926)

Pickering K.L. & Murray T.L., Weak link scaling analysis of high-strength carbon fibre, Compos. Pt. A-Appl. Sci. Manuf. 30 (8):1017-1021 (1999)

Pillary K.P.R., Fiber strength at finite gauge lengths of raw and mercerized cotton: A study of bundles, Proc. Seventh Tech. Conf. ATIRA, BTRA and SITRA, Sec. A., 15-30 (1965)

Saville B.P., Physical testing of textiles, Woodhead Publishing Ltd., 1st Edition, UK (1999)

Shao Z. & Vollrath F., The effect of solvents on the contraction and mechanical properties of spider silk, Polymer 40:1799-1806 (1999)

Shao Z.Z. & Vollrath F., Materials: Surprising strength of silkworm silk, Science 418(6899):741 (2002)

Spencer-Smith J.L.S., The estimation of fiber quality, J. Text. Inst. 38:257-272 (1947)

Viney C., From Natural Silks to New Polymer Fibres, J. Text. Inst. 91:2-23 Part 3 Sp. Iss. SI (2000)

Wang Y. & Xia Y., The effects of strain rate on the mechanical behaviour of kevlar fibre bundles: an experimental and theoretical study, Compos. Pt. A-Appl. Sci. Manuf. 29(11):1411-1415 (1998)

Wang Y. & Xia Y., Experimental and theoretical study on the strain rate and temperature dependence of mechanical behaviour of Kevlar fibre, Compos. Pt. A-Appl. Sci. Manuf. 30:1251-1257 (1999)

Weibull W., A statistical distribution function of wide applicability, Journal of Applied Mechanics 18:292-297 (1951)

Ysebaert M., Analysis of Variance, Course organized by the Center for Statistics in cooperation with the Institute for Continuing Education in Science, Ghent University, 2004-2005

Zhang Y.P. & Wang X.G., The minimum diameter distribution and strength variation of top dyed wool, Wool Technology and Sheep Breeding 49(3): 212-221 (2001)

4

AMINO ACID COMPOSITION OF SILKS

Several authors believe that variation in chemical structure, especially the amino acid composition and sequence, is linked to a great extent to the mechanical performance of silks. Furthermore, silk types secreted by different spinning glands result in diverse mechanical properties. The relative proportion of the amino acids will further determine, together with the amino acid sequence, its secondary structure, as discussed in further chapters. In literature, the amino acid composition of silks is limited to certain spider species. Moreover, information on the complete amino acid composition of the spider Araneus diadematus*, the focus of this work, is restricted to one publication. By investigating dragline and egg sac silk of different spider species, it is further hoped to find the characteristic amino acids for each silk type.*

In this chapter, the chemical structure of proteins and its building blocks are recapitulated. This is followed by some experiments in which the amino acid composition of different silk types of various spider species is determined. To be complete, also the amino acid composition of the further studied silkworm silks is determined. A comparison with the amino acid compositions found in literature is made and characteristics for each silk type are identified.

4.1. THE CHEMICAL STRUCTURE

The general chemical structure of silk, and all other protein fibres, is that of a protein or, in textile terms, of a substituted nylon 2 (Figure 4.1).

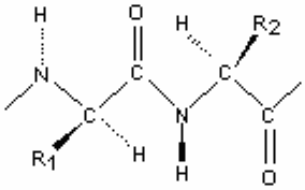

Figure 4.1 - Chemical structure of substituted nylon 2

The mole percentage, the side groups R and sequence of amino acids differentiate natural polypeptides such as silk, mohair, spider silk, and human hair.

The molecular backbone of all proteins consists of a chain of amino acids that are linked by peptide bonds to form a polypeptide chain. Figure 4.2 shows a schematic diagram of an amino acid. A central carbon atom (C_α) is attached to an amino group (NH_2), a carboxyl group (COOH), a hydrogen atom (H) and a side group (R). In a polypeptide chain (see Figure 4.3) the carboxyl group of amino acid n has formed a peptide bond, C-N, to the amino group of amino acid n + 1. One water molecule is eliminated in this process. The repeating units, which are called residues, are divided into main chain atoms and side chains. The main chain part, which is identical in all residues, contains a central carbon atom (C_α) attached to an NH group, a C=O group, and an H atom. The side chain R, which is different for different residues, is bound to the C_α atom.

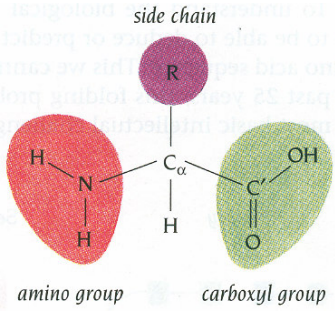

Figure 4.2 - Schematic diagram of an amino acid

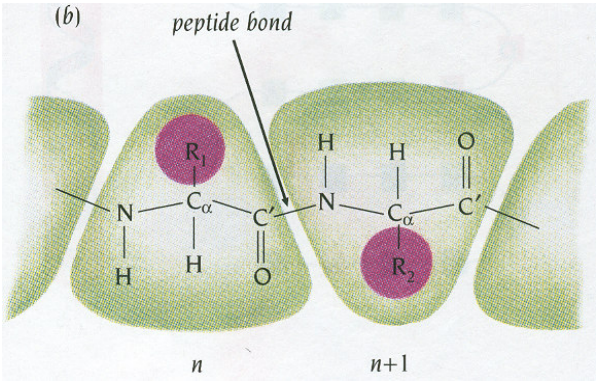

Figure 4.3 - The formation of a peptide bond from 2 amino acids

Since the peptide units are effectively rigid groups that are linked into a chain by covalent bonds at the C_α atoms, the only degrees of freedom they have are rotations around these bonds. Each unit can rotate around two such bonds: the C_α-C' and the

N-C_α bonds (Figure 4.4). By convention the angle of rotation around the N- C_α bond is called phi (ϕ) and the angle around the C_α-C' bond from the same C_α atom is called psi (ψ)

In this way each amino acid residue is associated with two conformational angles ϕ and ψ. Since these are the only degrees of freedom, the conformation of the whole main chain of the polypeptide is completely determined when the ϕ and ψ angles for each amino acid are defined with high accuracy.

Most combinations of ϕ and ψ angles for an amino acid are not allowed because of steric collisions between the side chains and main chain. The allowed combinations of angles are represented in a diagram called a Ramachandran plot (Figure 4.5) after the Indian biophysicist G.N. Ramachandran.

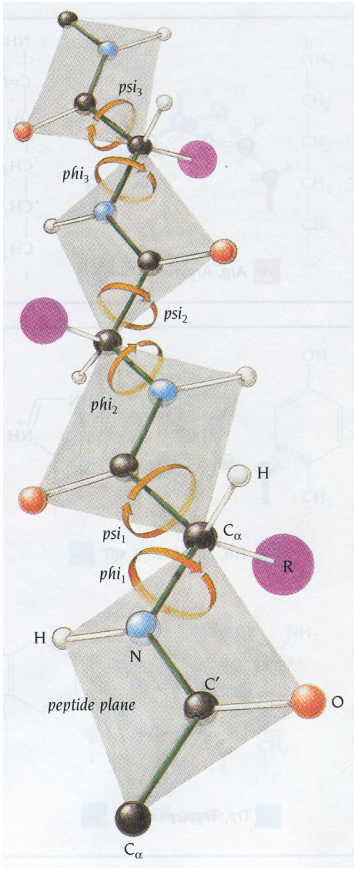

Figure 4.4 - Diagram showing a polypeptide chain where the main chain atoms are represented as rigid peptide units, linked through the C_α atoms

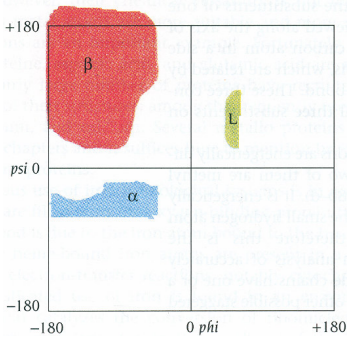

Figure 4.5 - A Ramachandran plot showing allowed combinations of the conformational angles ϕ and ψ. Coloured areas show sterically allowed regions. The areas labeled α, β and L correspond approximately to conformational angles found for the usual right-handed α-helices, β-strands, and left-handed α-helices, respectively (see also Chapter 5)

4.2. THE BUILDING BLOCKS

All of the 20 amino acids have in common a central carbon atom C_α to which are attached a hydrogen atom, an amino group (NH_2) and a carboxyl group (COOH) (Figure 4.6). What distinguishes one amino acid from another is the side chain attached to the central carbon atom C_α through its fourth valence. There are 20 different side chains specified by the genetic code; others occur, in rare cases, as the products of enzymatic modifications.

The amino acids are usually divided into three different classes defined by the chemical nature of the side chain (Figure 4.6).

(1) The first class comprises those with strictly hydrophobic side chains: alanine or Ala (A), valine or Val (V), leucine or Leu (L), isoleucine or Ile (I), phenylalanine or Phe (F), proline or Pro (P), and methionine or Met (M).

(2) The four charged residues, aspartic acid or Asp (D), glutamic acid or Glu (E), lysine or Lys (K), and arginine or Arg (R), form the second class.

(3) The third class comprises those with polar side chains: serine or Ser (S), threonine or Thr (T), cysteine or Cys (C), asparagine or Asn (N), glutamine or Gln (Q), histidine or His (H), tyrosine or Tyr (Y) and tryptophan or Trp (W).

(4) The amino acid glycine (G), which has only a hydrogen atom as a side chain and so is the simplest of the 20 amino acids, has special properties and is usually considered either to form a fourth class or to belong to the first class [Branden & Tooze 1998].

(a) Hydrophobic amino acids

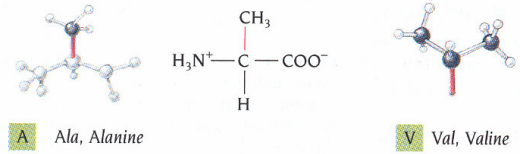

A Ala, Alanine

V Val, Valine

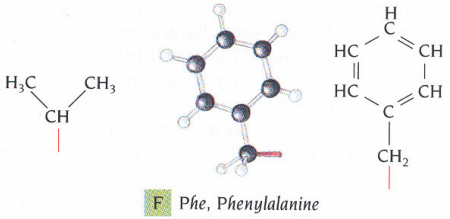

F Phe, Phenylalanine

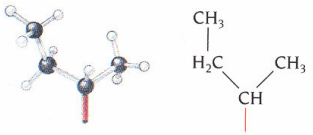

I Ile, Isoleucine

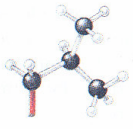

L Leu, Leucine

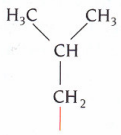

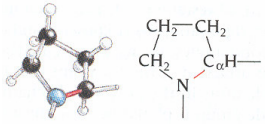

P Pro, Proline

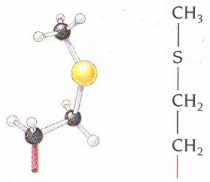

M Met, Methionine

(b) Charged amino acids

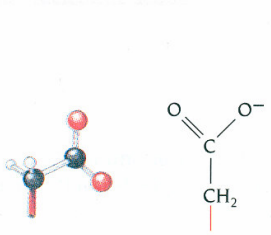

D *Asp, Aspartic acid*

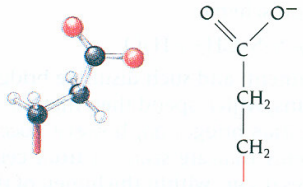

E *Glu, Glutamic acid*

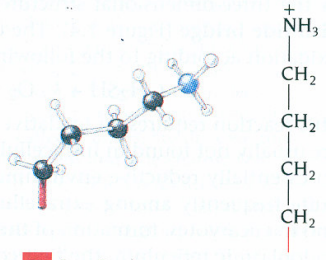

K *Lys, Lysine*

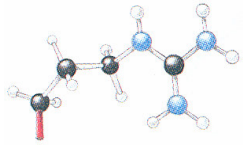

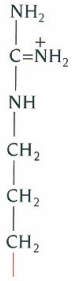

R *Arg, Arginine*

(c) Polar amino acids

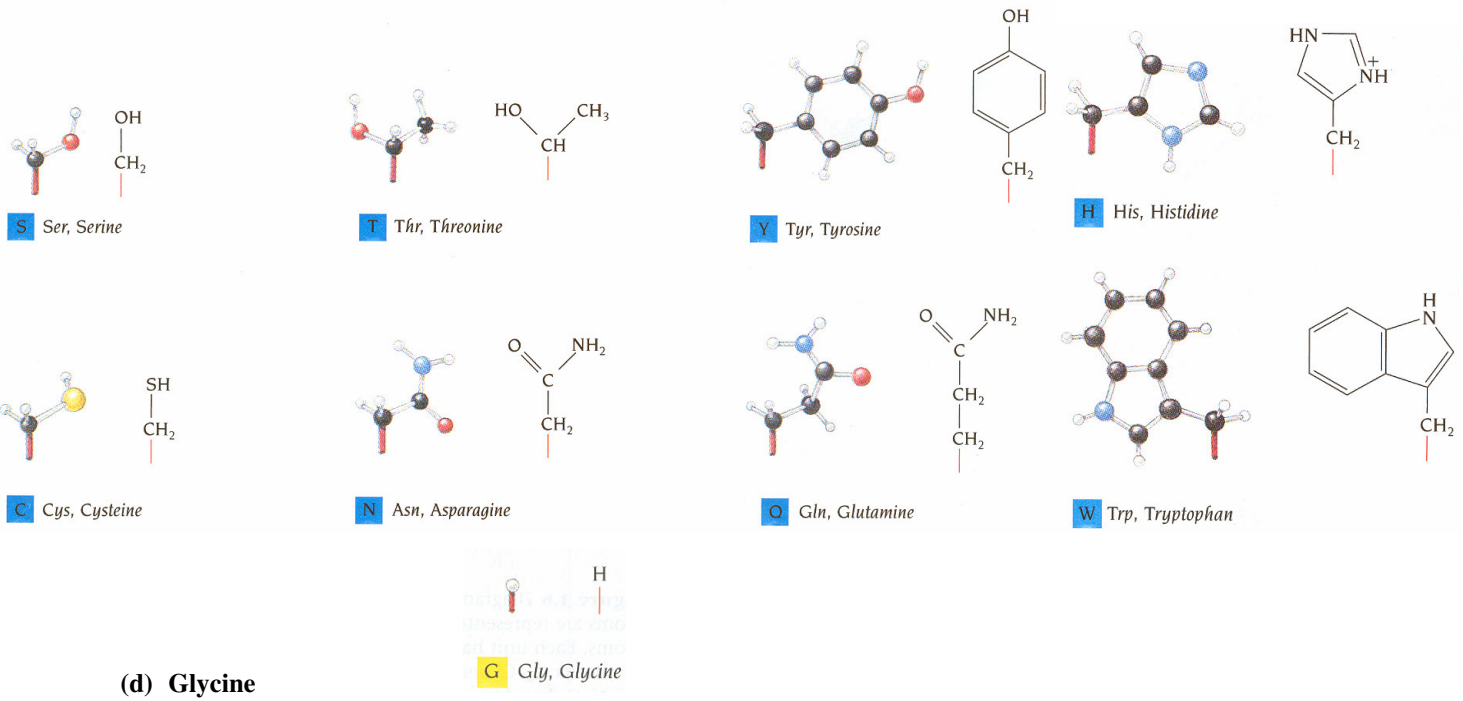

(d) Glycine

Figure 4.6 - The 20 different amino acids that occur in proteins, reproduced from Branden & Tooze [1998] (only side chains are shown, except for the first amino acid, alanine)

4.3. AMINO ACID COMPOSITION OF SILKS

4.3.1. SILKWORM SILKS

Silk fibroin, as obtained from the domestic silkworm *Bombyx mori*, contains a preponderance of small amino acid residues. Glycine, the simplest of the amino acids, comprises about 43-47% and glycine, alanine, and serine, the three simplest, 82-91% [Marsh *et al.* 1955a, 1955b, Lucas *et al.* 1960, Freddi *et al.* 1999, Zhou *et al.* 2001, Asakura & Yao 2002, Kishore *et al.* 2002, Tanaka *et al.* 2002, Fedic *et al.* 2003, Monti *et al.* 2005]. The proportions in which the glycine, alanine, and serine occur are about 3:2:1 [Marsh *et al.* 1955a].

In contrast to that of domestic silk, the amino acid composition of *A. pernyi* silk is characterized by more Ala, Asp, and Arg contents, and less Gly [Marsh *et al.* 1955b, Li *et al.* 2003]. This composition is related to the abundance of $-(Ala)_n-$ sequence, the relative abundance of basic amino acids (Arg and His) and the presence of the tripeptide Arg-Gly-Asp (RGD).

The reported amino acid compositions of both silkworm silks are further discussed in section 4.4.4.3.3.

It can be expected that the different compositions will result in structural differences. In particular, the amount of glycine in *A. pernyi* silk (26-28%) is insufficient to permit the occurrence of glycine alternate residues along the polypeptide chains, as is the case for *B. mori* (see Chapter 5). Further structure-property correlations are discussed in Chapter 10.

4.3.2. SPIDER SILKS

As shown in Table 4.1 and Figure 4.7, the seven silks secreted by the different glands of the spider all have a different amino acid composition.

It should be remarked that in addition to variations between species, there is a high degree of variation in the amino acid composition of silk produced among individuals of the same species of spider [Work and Young 1987, Vollrath 1999, Craig *et al.* 2000]. There are several factors known to affect the composition of spider dragline silk, which is secreted by the major ampullate glands: the species of the spider, the diet, the weather, the speed of silking [Craig *et al.* 2000, Vollrath & Knight 2001]. Work and Young [1987] found that there is less variability in amino acid composition for minor ampullate silk, both within species and between species, than for corresponding major ampullate silk. However, Lombardi & Kaplan [1990] showed that the variability in amino acid composition within *Nephila clavipes* can be restricted by using extremely sensitive and well-defined analytical techniques, high-quality instrumentation and the absence of contamination by other silks.

In literature, different amino acid compositions of various spider species can be found. However, a high variation within and between spider species is seen. Probably, these variations are related to the problems in handling silk samples in a reproducible manner.

Table 4.1 - Types and functions of spider silk for *Araneus diadematus* [Kaplan 1998] ([a] Small side chains = Gly + Ala + Ser, polar = Asp + Thr + Ser + Glu + Tyr + Lys + His + Arg)

Silk	Gland	Amino acids[a]
Dragline	Major ampullate	Gly (37%), Ala (18%), small side safety line chains (62%), polar (26%)
Viscid	Flagelliform	Gly (44%), Pro (21%), small side chains (56%), polar (17%)
Glue-like	Aggregate	Gly (14%), Pro (11%), polar glue (49%), small side chains (27%)
Minor	Minor ampullate	Gly (43%), Ala (37%), small side chains (85%), polar (26%)
Egg sac	Cylindrical (tubuliform)	Ser (28%), Ala (24%), small side chains (61%), polar (50%)
Wrapping	Aciniform	Ser (15%), Gly (13%), Ala (11%), small side chains (40%), polar (47%)
Attachment	Piriform	Ser (15%), small side chains (32%), polar (58%)

The different silks differentiate mostly in the different amounts of Gly, Ala, Ser and Pro they contain. For the chemical structure of these small amino acids, it is referred to Figure 4.6.

From Table 4.1 and Figure 4.7, it can be concluded that dragline, secreted by the major ampullate glands, is composed mainly of glycine (30-40%) and alanine (20-30%). Also the amount of glutamine (Glu) exceeds 10%, while the amount of proline seems to vary depending on the spider species between 5 and 15%.

Capture silk, secreted by the flagelliform gland, is constituted of mainly glycine (44%), proline (20%) and a lesser amount of alanine (10%).

With respect to egg sac silk of *A. diadematus*, secreted by the cylindrical or tubuliform gland, from Figure 4.7 we can conclude that the main amino acid constituents are alanine (25-30%) and serine (15-20%). The glycine content is restricted to about 10%. The amino acid compositions reported for egg sac silk of different spider species are more in detail discussed in section 4.4.4.3.2.

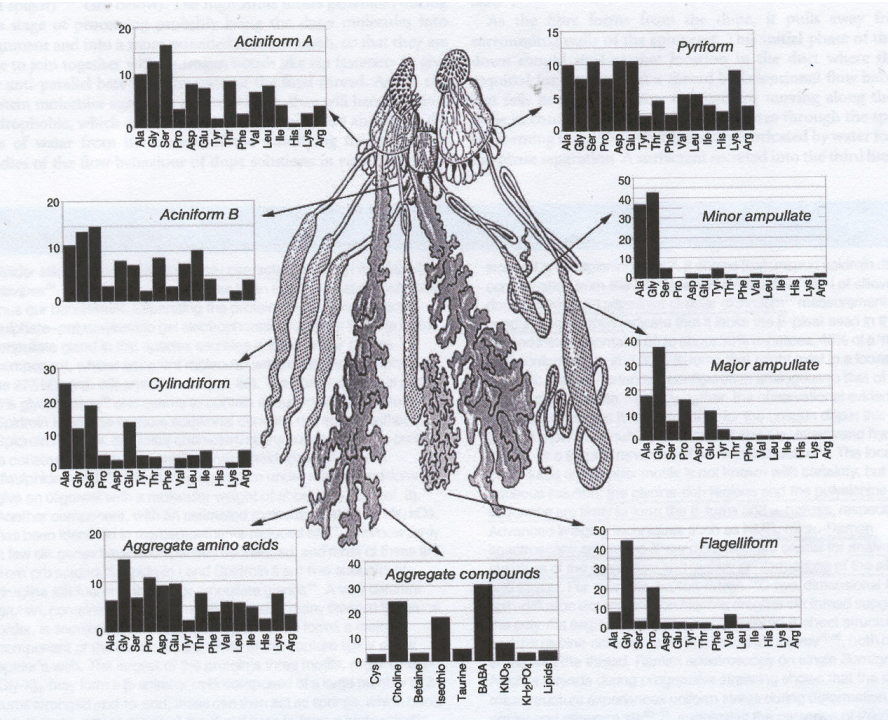

Figure 4.7 - The seven specialised glands and their different amino acid compositions of a typical Araneid orb weaver [Vollrath & Knight 2001]

4.4. EXPERIMENTAL PART

4.4.1. INTRODUCTION

The determination of the amino acid composition of the silk fibres is chosen as a first step in determining the chemical structure of the silk proteins since it can reveal chemical differences between the different silk fibres. The relative proportion of the amino acids is different for each silk protein and will determine, together with the amino acid sequence ("primary structure"), the secondary structure (see Chapter 5).

It is believed that a main part of the difference in mechanical properties of the different silk fibres can be explained by their amino acid composition. Of course, the secondary structure and the spinning process will also play an important role in the protein folding.

In literature, the amino acid composition is reported for different silk types and spider species, however often incomplete, limited to the most represented amino acids. So, in this section the complete amino acid composition of dragline (or major ampullate MA silk) and egg sac silk of different spider species is determined in order to find the characteristic composition for the different silk types. To be complete, also the silkworm silks, further considered in the next chapters, are tested.

4.4.2. MATERIALS

Draglines were manually reeled off from *Araneus marmoreus*, *A. quadratus*, *A. diadematus*, *Argiope bruennichi* and *Larinioides sclopetarius* spider species. Egg sac silk fibres were taken from *A. diadematus* and *L. sclopetarius* produced by lab-grown spiders. Furthermore, two silkworm cocoon silks, *Bombyx mori* and *Antheraea pernyi,* were provided by the Silk Museum (Meliskerke, The Netherlands) and tested. The silkworm *A. pernyi* is the one that produces the better known "Tussah" silk.

4.4.3. METHODS

To determine a spider's silk fibre composition, the secondary structure was broken and the primary peptide bonds were hydrolysed by acid hydrolysis. For one test, a fibre sample of about 10 µg was taken and washed in formic acid, rinsed with distilled water to remove adhering and interfering proteins and dried in a vacuum dryer. Several glass vials were filled with a sample and brought in a jar with hydrochlorid HCl (6N, 200 µl). The jar was flushed with argon or nitrogen before closure and heated (> 24 h, 106-110 °C). After cooling and drying, the hydrolysed amino acids were re-dissolved in 250 µl water and sonicated. 10 µl of the solution was brought in the pico-analyzer next to a reference sample. Peak heights were then recalculated to amino acid percentages.

It is noted that methionine (Met) and cysteine (Cys) are destroyed during amino acid hydrolysis. These 2 amino acids are not abundant in silk anyway. Asparagine (Asn) and glutamine (Gln) are respectively converted to aspartic acid (Asp) and glutamic acid (Glu). This means that the measured Asp and Glu are actually a sum of Asn + Asp and Gln + Glu, respectively. These sums are usually mentioned as Asx and Glx, respectively.

If possible, the procedure was repeated three to five times for each silk type.

4.4.4. RESULTS AND DISCUSSION

4.4.4.1. Introduction

In the discussion of the results, the three-letter code for the different amino acids will be used. The full name can be found in Figure 4.6 or in the list of abbreviations in the beginning of this thesis.

4.4.4.2. Dragline silk fibres

4.4.4.2.1. Results of measured composition

The amino acid composition of dragline silk of different spider species is shown in Table 4.2. The values are all measured as described above, except for the percentages for *Nephila clavipes*. Since most structural studies are focused on this spider species, the amino acid composition of this spider species is added, as found in literature [Tillinghast & Christenson 1984].

Table 4.2 - The amino acid compositions of the draglines of *Araneus marmoreus* (A.m.), *A. quadratus* (A.q.), *A. diadematus* (A.d.), *Argiope bruennichi* (A.b), *Larinioides sclopetarius* (L.s.) and *Nephila clavipes* (N.c) [Tillinghast & Christenson 1984]– N number of repetitions

Dragline	N	Gly	Ala	Ser	Tyr	Val	Pro	Glx
A.m.	4	24.0	21.1	3.9	5.3	3.6	13.3	12.1
A.d.	3	26.7	23.3	4.3	5.4	2.6	15.8	11.0
A.q.	3	26.6	21.4	3.4	5.6	2.0	17.7	13.5
A.b.	4	29.8	18.0	3.6	5.1	1.9	15.7	13.8
L.s.	5	22.8	23.4	6.0	5.5	3.2	11.4	15.5
N.c		40.3	28.4	3.0	3.1	1.5	1.7	10.1

Dragline	N	Arg	Asx	Leu	Ile	Thr	Phe	His	Lys
A.m.	4	1.6	3.8	4.2	1.8	2.1	1.2	0.0	1.3
A.d.	3	1.0	2.4	2.8	1.2	1.5	0.7	0.0	0.7
A.q.	3	1.0	2.2	2.5	1.0	1.1	0.7	0.0	0.9
A.b.	4	1.5	2.5	2.8	1.0	1.0	1.3	0.1	1.2
L.s.	5	1.0	3.3	3.9	1.2	1.0	0.7	0.1	1.0
N.c		2	1.9	4.5	0.6	1.0	0.5	0.2	0.8

It is interesting to see that the draglines of the *Araneus* and *Argiope* spider species show a comparable amino acid composition. The most important amino acids in the draglines are Gly (24-30%), Ala (18-23%), Pro (13-18%) and Glx (11-14%). The *Larinoides* species differ only slightly from the previously mentioned species, whereas *Nephila clavipes* shows some remarkable differences. The amino acid composition of *N. clavipes* (as found in literature, also started from reeled silk) is different from that of the other measured species in its higher amount of Gly and Ala, lower amount of Pro, Tyr, and Glx, as concluded from Table 4.2.

Dicko *et al.* [2004] compared the amino acid composition of major ampullate liquid silk of *Nephila* silks with those for *A. diadematus*. They stated that the ratio of Ala to Gly was higher in *Nephila* (3:4 and 3:5 resp. for *edulis* and *clavipes*) than in the *A. diadematus* (2:5). *N. edulis* showed a higher content of small side chains, about 70%, compared to *A. diadematus* and *N. clavipes*, both at about 62%. The polar chain contents showed similarities between *A. diadematus* and *N. clavipes*, resp. 26 and 29%, compared to *N. edulis* at about 21%. Another striking difference was the Pro content in MA silks, about 15% in *A. diadematus*, 1% in *N. clavipes*, and about 6% in *N. edulis*, suggesting a higher concentration of turns (see Chapter 5) in *A. diadematus* silk secondary structures. The significant higher Pro content is also observed in the measured results in Table 4.2.

4.4.4.2.2. Comparison with literature for Araneus diadematus

Since this work is focused on the spider *Araneus diadematus*, the measured amino acid composition is compared with the reported compositions in literature [Fischer & Brander 1960, Andersen 1970, Work & Young 1987], as summarized in Table 4.3.

Table 4.3 - Amino acid composition of *A. diadematus* dragline as found in literature ([1] Fischer & Brander 1960, [2] Work & Young 1987, [3] Andersen 1970)

Ref.	Gly	Ala	Ser	Tyr	Val	Pro	Glx	Arg
[1]	30.4	21.1	8.4	3.7		15.6	12.5	0.9
[1]	33.1	19.6	8.0	3.6		13.5	11.8	1.4
[1]	31.6	20.8	7.7	3.7		14.0	13.0	1.3
[2]	41.3	18.3	4.7	4.4		9.6	11.9	0.8
[3]	37.2	17.6	7.4	3.9	1.2	15.8	11.5	0.6

	Asx	Leu	Ile	Thr	Met	Phe	His	Lys
[3]	1.0	1.3	0.6	0.9	0.0	0.5	trace	0.5

The main differences between the measured composition (A.d. in Table 4.2) and the reported ones, are to be found in the less represented amino acids and especially for Ser (8% versus 4%) and Tyr (4% versus 5%). These differences can either be due to the different starting silk (e.g. liquid silk instead of silk fibre) or to the method used. By dissolution of the silk fibres, it is possible that some amino acids were lost. Hydrochlorid may act as a strong oxidizing agent. The amino acids most affected by oxidation are Cys, Met, and Tyr [Lombardi & Kaplan 1990]. Since the total amount of Cys and Met is small, these amino acids only have little influence on the secondary structure. However, Lombardi & Kaplan [1990] noted that the Tyr residue is unaffected in dragline silk hydrolysis and analysis. They also observed that for *N. clavipes* dragline silk the amino acid composition between reeled and glandular sources are very similar. So, we suggest that incomplete or imperfect dissolution of the silk fibres is the most acceptable explanation for the differences.

In spite of the differences, comparable percentages of the most important components: Ala, Gly, Pro and Glx in *A. diadematus* dragline silk are observed.

4.4.4.3. Spider egg sac and silkworm cocoon silks

4.4.4.3.1. Results of measured composition

The results for the spider egg sac and silkworm cocoon silk (*Bombyx mori* and *Antheraea pernyi*) fibres are shown in Table 4.4.

Looking at the differences between egg sac (Table 4.4) and dragline (Table 4.2) spider silk for the two tested species (*Araneus diadematus* and *Larinioides slopetarius*), similar differences are found. Egg sac spider silk contains much higher fractions of Ser, in spite of the fraction of Gly. Moreover, the higher percentage of

residues with a voluminous side chain, such as Val, Leu and Asx, is remarkable. Dragline spider silk is further characterized by a much higher fraction of Pro and Tyr.

Table 4.4 - The amino acid compositions of the cocoon or egg sac silk fibres of *Araneus diadematus* (A.d.), *Larinioides sclopetarius* (L.s.), *Bombyx mori* (B.m.) and *Antheraea pernyi* or Tussah (A.p.)

Cocoon	N	Gly	Ala	Ser	Tyr	Val	Pro	Glx
A.d.	6	4.9	31.5	13.9	0.5	10.8	0.7	8.2
L.s.	5	7.8	29.1	18.6	1.0	9.3	0.5	6.5
B.m.	1	20.5	41.8	4.7	11.0	6.1	0.3	2.6
A.p.	1	17.4	29.8	6.7	15.6	3.1	0.0	2.4

Cocoon	N	Arg	Asx	Leu	Ile	Thr	Phe	His	Lys
A.d.	6	1.6	2.6	8.0	2.3	3.5	4.1	0.0	2.2
L.s.	5	1.4	5.8	7.4	0.7	7.6	4.0	0.0	0.4
B.m.	1	0.9	5.6	1.3	1.4	1.6	1.1	0.0	1.0
A.p.	1	5.0	15.1	1.1	1.1	1.0	0.7	0.6	0.6

The results in Table 4.4 are further discussed in the next sections.

4.4.4.3.2. Comparison with literature for egg sac spider silk

Because of, in general, limited available information about egg sac spider silk, this thesis is focused on egg sac spider silk (especially *Araneus diadematus*), and thus the comparison with other egg sac silks is made more in detail. In literature, the amino acid composition of egg sac spider silk is rarely determined. Also for egg sac spider silk, the amino acid composition is mostly determined starting from liquid silk extracted from the cylindrical or tubuliform spinning glands. Table 4.5 shows the reported amino acid compositions.

As for dragline spider silk, the values for *A. diadematus* are different from those found by our method starting from spider silk fibres. However, the two main components are found to be the same, Ala and Ser, representing about 50% of the total amino acid composition.

Looking at the compositions reported in literature (Table 4.5), for most spider species, except the *Nephila* species, comparable values are found. The most represented amino acids in egg sac spider silk are Ala (23-29%), Ser (21-28%), Gly (8-11%), and Glx (7-11%). Furthermore, it is remarkable that this silk type contains high fractions of amino acids with bulky hydrophobic residues, such as Leu (6-8%) and Val (4-6%) and Phe (3-5%), and bulky polar residues, such as Asx and Thr.

It is surprising that again for the *Nephila* species, some clear differences are found, especially a smaller amount of Ser, Val and Asx.

Table 4.5 - Amino acid composition of egg sac spider silk as found by Andersen [1970] (A.d.: *Araneus diadematus*), by Casem *et al.* [1999] (L.h.f.: *Latrodectus hesperus,* based on fibre), by Dicko *et al.* [2004] (N.e.: *Nephila edulis*, based on gland content), by Garb & Hayashi [2005] (A.ar.: *Argiope argentata*, L.h.g.: *Latrodectus heperus*, based on gland content), by Foradori et al. [2002] (A.au.: *Argiope aurantia*, in.: inner layer, out.; outer layer, NA : not available, by Tian & Lewis [2006] (A.au.: *A. aurantia*, A.gem.: *Araneus gemmoides*, N.c.: *Nephila clavipes*)

Cylindrical	**Gly**	**Ala**	**Ser**	**Tyr**	**Val**	**Pro**	**Glx**	**Arg**
A.d.	8.6	24.4	27.6	1.0	6.0	0.6	8.2	1.5
A.gem.	10.8	25.9	23.9	0	6.0		11.1	1.7
A.au.in.	8.7	26.7	24.0	1.4	4.8	0.9	7.6	2.1
A.au.out.	10.3	25.8	22.4	1.8	4.2	1.3	7.3	3.1
A.au.	10.4	28.7	21.3	1.1	5.8		8.5	2.1
A.ar.	9.8	26.5	22.3	1.5	5.2	0.7	7.3	1.4
L.h.g.	8.1	25.6	22.1	1.5	5.1	1.7	10.7	1.7
L.h.f.	7.7	23.3	25.7	1.7	NA	2.0	11.0	1.3
N.c.	8.4	30.6	20.4	2.1	1.9		11.1	4.7
N.e.	8.6	27.3	20.2	2.1	2.8	0	8.6	2.2

Cylindrical	**Asx**	**Leu**	**Ile**	**Thr**	**Phe**	**His**	**Lys**	**Cys**
A.d	6.3	5.7	1.7	3.4	3.2	NA	1.8	0
A. gem.	5.7	7.0	1.9	1.7	3.4			
A.au.in.	7.0	6.6	1.7	3.6	4.0	NA	0.6	NA
A.au.out.	6.9	6.1	1.9	4.1	3.7	NA	0.6	NA
A.au.	6.9	6.7	1.9	2.1	4.8			
A.ar.	6.0	7.7	1.1	4.6	4.2	NA	0.2	1.5
L.h.g.	5.0	5.3	2.6	5.0	4.1	NA	0.2	1.3
L.h.f.	6.3	5.0	2.0	5.0	NA	NA	NA	NA
N.c.	3.9	7.5	2.0	4.7	6.7			
N.e.	3.9	7.4	2.8	5.9	3.9	0.3	1.6	0.1

Selection for physical properties has not been the only driving force in the evolution of the heavy chain fibroin. Insects are unable to synthesize the amino acids Arg, His, Ile, Leu, Lys, Met, and Thr and possibly also Phe, Tyr, and Trp [Fedic *et al.* 2003]. These essential amino acids must be obtained in the diet or supplied by symbiotic microorganisms. The high content of essential amino acids in egg sac spider silk can thus be driven by the need of easy digestion by the spiderlings. Furthermore, the presence of bulky residues is a source of high energy. It is known that spiderlings collectively create the opening to escape from the egg sac by a combination of enzymatic digestion and mastication.

4.4.4.3.3. Comparison with literature for the silkworm silks

The amino acid composition of the silkworm silks have been obtained by several investigators, some results are displayed in Table 4.6. It should be remarked that often not all amino acids are reported.

Table 4.6 - Amino acid composition of *Bombyx mori* (B.m.) and *Antheraea pernyi* (A.p.) silks as found in literature ([1] Zhou *et al.* 2001, [2] Tanaka *et al.* 2002, [3] Fedic *et al.* 2003, [4] Freddi *et al.* 1999, [5] Marsh *et al.* 1955a, [6] Marsh *et al.* 1955b, [7] Li *et al.* 2003, [8] Monti *et al.* 2005)

Ref.	Fibre	Gly	Ala	Ser	Tyr	Val	Pro	Glx	Arg	Asx
[1]	**B.m.**	45.9	30.3	12.1	5.3	1.8				
[2]	**B.m.**	42.8	32.4	14.7	11.8	3.03	0.63	1.74	0.9	1.73
[3]	**B.m.**	47.4	31.2	12.1	5.2	1.6	0.2	0.8		0.2
[4]	**B.m.**	43.7	29.3	11.5	5.3	2.2	0.67	1.37	0.62	1.65
[5]	**B.m.**	44.7	25.7	11.9	5.4	2.4	0.5	1.1	0.5	1.6
[6]	**B.m.**	44.4	30.2	11.9	4.9	2.1	0.4	0.9	0.4	1.4
[2]	**A.p.**	23.6	50.5	11.3	8.8	0.95	0.44	1.34	6.06	6.58
[6]	**A.p.**	26.6	44.2	11.8	4.9	0.6	0.3	0.8	2.6	4.7
[7]	**A.p.**	26.2	40.5	8.0	7.3	1.1	0.39	1.63	4.21	7
[8]	**A.p.**	28.3	48.6	8.9	3.7				2.6	3.9

Ref.	Fibre	Leu	Ile	Thr	Met	Phe	His	Lys	Trp	Cys
[1]	**B.m.**									
[2]	**B.m.**	0.68	0.87	1.51	0.10	1.15	0.32	0.45	0.36	0.03
[3]	**B.m.**									
[4]	**B.m.**	0.58	0.66	0.96	0.10	0.73	0.2	0.33		0.1
[5]	**B.m.**	0.5	0.6	1.0		1.6	0.2	0.4		
[6]	**B.m.**	0.5	0.5	1.0		0.6	0.2	0.3	0.2	0.1
[2]	**A.p.**	0.51	0.69	0.69	0.03	0.52	1.41	0.26	1.41	0.04
[6]	**A.p.**	0.4	0.4	0.1		0.5	0.8	0.1	1.1	0
[7]	**A.p.**	0.51	0.53	0.56		0.42	1.3	0.16		0.16
[8]	**A.p.**								0.50	

The results of *B. mori* and *A. pernyi*, as found in literature, differ a lot from the results observed in our experiments. In literature, analysis is often started from the liquid silk, obtained by dissecting the spinning glands and as a consequence these results will be more reliable than the results in Table 4.4. As suggested for dragline spider silk, some fractions of the silk may get lost by dissolution of the silk fibres. However, even the reported amino acid compositions vary significantly, certainly in the less represented residues. For *B. mori*, it is mostly the article of Tanaka *et al.* [2002] that is giving deviating values, certainly for serine and tyrosine.

It can be concluded that the main components in *B. mori* are Gly (43-47%), Ala (26-32%), Ser (±12%) and Tyr (5%). In *A. pernyi* silk (better known as Tussah silk), the same components are contributing most. However, the sum of Ala and Gly residues is in both about 75%, but the relative composition of Ala and Gly is reversed. The proportion of Gly residues is larger in *B. mori* fibroin, while the content of Ala

residues is higher in *A. pernyi* silk fibroin. Furthermore, *A. pernyi* or Tussah silk contains higher fractions of Arg (3-6% versus 0.4-0.9%) and Asx (4-7% versus 1.4-1.7%). These are the amino acids known to be present in the tripeptide sequence of Arg-Gly-Asx (RGD) in this silk (see Chapter 5), that is showing cell adhesive properties interesting for biomedical applications (see Chapter 1).

4.4.5. DIFFERENCES BETWEEN THE SILKS STUDIED

Based on Table 4.2, Table 4.5 and Table 4.6, it can be concluded that the spider and silkworm silks all have the small amino acids Ala, Gly and Ser as their main components, representing more than 85% of the total composition for the silkworm silks, and about 60% for the spider silks. However, egg sac spider silk is the only silk that shows such a high percentage of Ser, in spite of the Gly percentage. These small amino acids are said to determine the crystallinity of silks (see also in further chapters).

The spider silks differ mostly from the silkworm silks in their percentage of Glx. Furthermore, dragline spider silk is characterised by a substantial amount of Pro. Egg sac spider silk differentiates from the other silks in the higher fractions of amino acids with voluminous side groups, especially Val, Leu, and Asx and it is the only silk with a limited amount of Tyr.

As mentioned before, *Antheraea pernyi* or Tussah silk contains considerable amounts of Arg and Asx, known to be present in an RGD-sequence.

4.4.6. CONCLUSION

In all cases, the glycine, alanine and serine residues are the most abundant ones, although large differences in relative fractions can be seen between the different fibres. The sum of the percentages of these small amino acids equals more than 85% for the silkworm silks, about 60% for the spider silks.

The silkworm silks differentiate mostly in the relative content of alanine and glycine that is reversed. Moreover, *Antheraea pernyi* silk fibroin shows higher fractions of arginine (R) and aspartic acid (D) that is known to be present as an RGD sequence in the *A. pernyi* (Tussah) silk. The amino acid composition of the silkworm silks further differ from those of the spider silks in their lower content of Glx (glutamine + glutamic acid).

When the amino acid compositions of the different draglines are compared, the resemblance between the 3 *Araneus* and the *Argiope* species is remarkable. The amino acid compositions of the *Nephila* and the *Larinioides* species differ much more.

For a given spider species, it is possible to compare the dragline and the egg sac silk compositions. It is remarkable that for both *Araneus diadematus* and *Larinioides sclopetarius* the same differences are found. For both spider species, alanine, serine and amino acids with large side chains, such as valine, leucine, threonine and phenylalanine, are more abundant in the egg sac fibres, whereas glycine, tyrosine, glutamine and/or glutamic acid and proline are more available in draglines. This

means that the evolutionary division into dragline and egg sac silk happened earlier than the one between the different species, and that there is a large conservation in the fibre composition during evolutionary spider diversification.

Since further structural research is limited to the silkworm silks and the egg sac and dragline spider silk of *A. diadematus*, their amino acid composition is summarized in Table 4.7. The data give the range of values as determined in some experiments and found in literature.

Table 4.7 – Summary of amino acid composition of further studied silks

Amino acid	*B. mori*	*A. pernyi*	Egg sac	Dragline
Gly	43-47	24-28	5-9	27-41
Ala	26-32	41-51	24-32	18-23
Ser	12-15	8-12	14-28	4-8
Tyr	5-12	4-9	0.5-1.0	4-5
Val	1.6-3.0	0.6-1.1	6-11	1.2-2.6
Pro	0.2-0.7	0.3-0.4	0.6-0.7	10-16
Glx	0.8-1.7	0.8-1.6	± 8	11-13
Arg	0.4-1.5	3-6	1.5-1.6	0.6-1.4
Asx	1.4-1.9	4-7	3-6	1.0-2.4
Leu	0.5-0.7	0.4-0.5	6-8	1.3-2.8
Ile	0.5-0.9	0.4-0.7	1.7-2.3	0.6-1.2
Thr	1.0-1.5	0.1-0.7	3.4-3.5	0.9-1.5
Phe	0.6-1.2	0.4-0.5	3-4	0.5-0.7
His	0.2-0.3	0.8-1.4		trace
Lys	0.3-0.5	0.1-0.3	1.8-2.2	0.5-0.7
Met	0.1-0.2	0.03		
Cys	0.03-0.10	0-0.2		
Trp	0.2-0.5	0.5-1.4		

It is clear that the fraction of polar residues (Asx + Glx + Thr + Ser + Tyr + Lys + His + Arg) is larger for egg sac spider silk than for dragline spider silk, as is also observed by Dicko *et al.* [2004]. This can explain the different supercontraction behaviour between both silks. Also the much lower fraction of proline (cyclic imino side chain) for the egg sac silk is clear. The fraction of aliphatic, and thus hydrophobic, side chain residues (Ala + Val + Ile + Leu) is higher for the spider egg sac silk than for the dragline silk. The latter suggests the possible importance of hydrophobic interactions in egg sac spider silk.

The higher amount of large side chain residues is expected to explain the lower fraction of β-sheet structures (see Chapter 6) and thus the lower crystalline content of egg sac spider silk. These large residues prevent the formation of compact β-sheet crystals, resulting in a lower strength. Further correlations between amino acid composition, structure and mechanical behaviour are described in Chapter 10.

4.5. REFERENCES

Andersen S.O., Amino acid composition of spider silks, Comp. Biochem. Physiol. 35:705-711 (1970)

Asakura T. & Yao J., ^{13}C CP/MAS NMR study on structural heterogeneity in *Bombyx mori* silk fibre and their generation by stretching, Protein Science 11:2706-2713 (2002)

Branden C. & Tooze J., Introduction to Protein Structure, 2nd edition, Garland Publishing, Inc., New York (1998)

Casem M.L., Turner D., Houchin K., Protein and amino acid composition of silks from the cob weaver, *Latrodectus hesperus* (black widow), Int. J. Biol. Macromol. 24:103-108 (1999)

Craig C.L., Riekel C., Herberstein M.E., Weber R.S., Kaplan D., Pierce N.E., Evidence for diet effects on the composition of silk proteins produced by spiders, Mol. Biol. Evol. 17(12):1904-1913 (2000)

Dicko C., Knight D., Kenny J.M., Vollrath F., Secondary structures and conformational changes in flagelliform, cylindrical, major, and minor ampullate silk proteins. Temperature and concentration effects, Biomacromolecules 5(6):2105-2115 (2004)

Fedic R., Zurovec M., Sehnal F., Correlation between fibroin amino acid sequence and physical silk properties, J. Biol. Chem. 278(37):32255-35264 (2003)

Fischer F.G.& Brander J., Eine Analyse der Gespinste der Kreuzspinne, Hoppe-Seyler's Z. Physiol. Chem. 320:92-102 (1960)

Foradori M., Kovoor J., Moon M., Tillinghast E., Relation Between the Outer Cover of the Egg Case of *Argiope aurantia* (Araneae: Araneidae) and the Emergence of its Spiderlings, J. Morphol. 252:218-226 (2002)

Freddi G., Pessina G., Tsukada M., Swelling and dissolution of silk fibroin (*Bombyx mori*) in N-methyl morpholine N-oxide, Int. J. Biol. Macromol. 24:251-263 (1999)

Garb J.E. & Hayashi C.Y., Modular evolution of egg case silk genes across orb-weaving spider superfamilies, Proc. Nat. Acad. Sci. 102(32):11379-11384 (2005)

Kaplan D.L., Fibrous proteins-silk as a model system, Polym. Degrad. Stab. 59:25-32 (1998)

Kishore A.I., Herberstein M.E., Craig C.L., Separovic F., Solid-state NMR relaxation studies of Australian spider silks, Biopolymers 61:287-297 (2002)

Lombardi S.J. & Kaplan D.L., The amino acid composition of major ampullate gland silk (dragline) of *Nephila clavipes* (Araneae, Tetragnathidae), J. Arachnol. 18:297-306 (1990)

Li M.Z., Tao W., Lu S.Z., Kuga S., Compliant film of regenerated *Antheraea pernyi* silk fibroin by chemical crosslinking, Int. J. Biol. Macromol. 32(3-5):159-163 (2003)

Lucas F., Shaw J.T.B., Smith S.G., Comparative studies on fibroins. 1. The amino acid composition of various fibroins and its significance in relation to their crystal structure and taxonomy, J. Mol. Biol. 2:339-349 (1960)

Marsh R.E., Corey R.B., Pauling L., An investigation of the structure of silk fibroin, Biochim. Biophys. Acta 16:1-34 (1955a)

Marsh R.E., Corey R.B., Pauling L., The structure of Tussah silk fibroin, Acta Cryst. 8:710-715 (1955b)

Monti P., Freddi G., Sampaio S., Tsukada M., Taddei P., Structure modifications induced in silk fibroin by enzymatic treatments. A Raman study, J. Mol. Struct. 744:685-690 (2005)

Tanaka T., Magoshi J., Magoshi Y., Inoue S., Kobayashi M., Tsuda H., Becker M.A., Nakamura Sh., Thermal properties of *Bombyx mori* and several wild silkworm silks, J. Therm. Anal. Calorim. 70:825-832 (2002)

Tian M. & Lewis R.V., Tubuliform silk protein: A protein with unique molecular characteristics and mechanical properties in the spider silk fibroin family, Applied Physics 82(2):265-273 (2006)

Tillinghast E.K. & Christenson T., Observations on the chemical composition of the web of *Nephila clavipes* (Araneae, Araneidae), J. Arachnol. 12:69-74 (1984)

Vollrath F., Biology of spider silk, Int. J. Biol. Macromol. 24(2-3):81-88 (1999)

Vollrath F. & Knight D.P., Liquid crystalline spinning of spider silk, Nature 410:541-548 (2001)

Work R.W. & Young C.T., The amino acid compositions of major and minor ampullate silks of certain orb-web-building spiders (Araneae, Araneidae), J. Arachnol. 15(1):65-80 (1987)

Zhou C.-Z., Confalonieri F., Jacquet M., Perasso R., Li Z.-G., Janin J., Silk fibroin: Structural implications of a remarkable amino acid sequence, Proteins: Structure, Function, and Genetics 44:119-122 (2001)

5

STRUCTURE OF SILKS

The mechanical behaviour of silks, is apart of the amino acid composition, also highly dependent on the way the amino acids are combined into the overall structure. This chapter is completely based on available literature on the structure of silks.

It starts with a general description of the structure of proteins, more especially the structural hierarchy in proteins, and some of its components: the primary and secondary structure.

*This section is followed with a literature review of the structure of the silkworm silks (*Bombyx mori *and* Antheraea pernyi *or Tussah) and of spider silks. Since structural research on spider silks is mostly performed on the* Nephila clavipes *spider species, also the structure of this one is discussed, apart from the silk of the* Araneus diadematus *spider, which is the focus in this thesis.*

5.1. STRUCTURAL HIERARCHY IN PROTEINS

The structural hierarchy in proteins (Figure 5.1) was first introduced by the Danish biochemist Kai Linderstrøm-Lang [Branden & Tooze 1998].

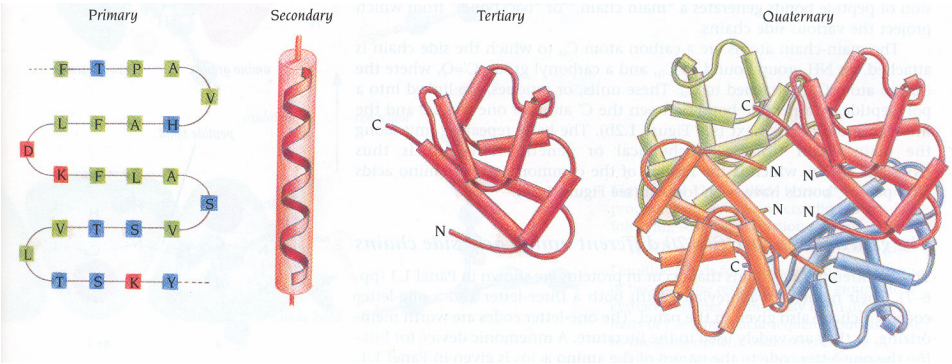

Figure 5.1 - Structural hierarchy in proteins

The information on structure in this chapter is restricted to the primary and secondary structure. Since known details on tertiary and quaternary structure of the selected silks are more related to structural models for these fibres, this information is added in Chapter 10 handling about the structure-property relations of silks.

5.2. PRIMARY STRUCTURE OF PROTEINS

The primary structure is the amino acid sequence, or, in other words, the arrangement of the amino acids along a linear polypeptide chain [Branden & Tooze 1998].

Amino acids are joined end-to-end during protein synthesis by the formation of peptide bonds when the carboxyl group of one amino acid condenses with the amino group of the next to eliminate water (see also Chapter 4). This process is repeated as the chain elongates. One consequence is that the amino group of the first amino acid of a polypeptide chain and the carboxyl group of the last amino acid remain intact, and the chain is said to extend from its amino terminus to its carboxy terminus. The formation of a succession of peptide bonds generates a “main chain”, or “backbone”, from which project the various side chains.

5.3. SECONDARY STRUCTURE OF PROTEINS

5.3.1. INTRODUCTION

Different regions of the sequence form local regular secondary structures, such as α-helices or β-strands. The formation of secondary structure in a local region of the polypeptide chain is to some extent determined by the primary structure. Certain amino acids favor either α-helices or β-strands (see next paragraphs); others favor

formation of loop regions. Simple combinations of a few secondary structure elements with a specific geometric arrangement have been found to occur frequently in protein structures. These units have been called either supersecondary structures or motifs [Branden & Tooze 1998]. Motifs are formed by packing side chains from adjacent α-helices or β-strands close to each other.

This section will be restricted to a discussion of the most important secondary structure elements and will not focus on the motifs that can be formed from them. The book of Branden & Tooze [1998] is referred to for more details.

5.3.2. THE DRIVING FORCE FOR PROTEIN FOLDING

When high-resolution studies of myoglobin became available, Kendrew *et al*. [1958, 1960] noticed that the amino acids in the interior of the protein had almost exclusively hydrophobic side chains. This was one of the first important general principle to emerge from studies of protein structure. The main driving force for folding water-soluble globular protein molecules is to pack hydrophobic side chains into the interior of the molecule, thus creating a hydrophobic core and a hydrophilic surface.

There is a major problem with creating such a hydrophobic core from a protein chain. To bring the side chains into the core, the main chain must also fold into the interior. The main chain is highly polar and therefore hydrophilic, with one hydrogen bond donor, NH, and one hydrogen bond acceptor, C=O, for each peptide unit. In a hydrophobic environment, these main-chain polar groups must be neutralized by the formation of hydrogen bonds. This problem is solved in a very elegant way by the formation of regular secondary structure within the interior of the protein molecule. Such secondary structure is usually one of two types: α-helices or β-sheets. Both types are characterized by hydrogen bonding between the main chain N-H and C=O groups, and they are formed when a number of consecutive residues have the same ϕ and ψ angles (see also Chapter 4).

5.3.3. THE α-HELIX STRUCTURE

The α-helix was first described by Pauling & Corey [1951]. α-helices in proteins are found when a consecutive residues all have the (ϕ, ψ) approximately -60° and -50° (bottom left quadrant of the Ramachandran plot, Figure 4.5 in Chapter 4). The α-helix has 3.6 residues per turn with hydrogen bonds between C=O of residue n and NH of residue n + 4 (Figure 5.2). Thus all NH and C=O groups are joined with hydrogen bonds except the first NH and the last C=O at the ends of the α-helix. As a consequence, the ends of α-helices are polar and are almost always at the surface of protein molecules.

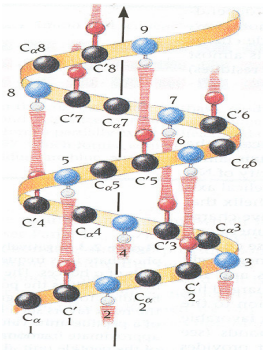

Figure 5.2 - Representation of an α-helix.

The amino acid side chains project out from the α-helix and do not interfere with it, except for proline because of its specific ring structure (see Figure 4.6 in Chapter 4). Proline fits very well in the first turn of an α-helix, but it usually produces a significant bend if it is anywhere else in the helix.

Some amino acids are more commonly found in α-helices than others. Amino acids can be divided into two kinds, those with branches at the C_β[1] and those with none. As far as the non-branched amino acids concerned, Gly is too conformationally flexible to be found with high frequency in α-helices, while Pro is too rigid. The amino acids with side chains that can H-bond (Ser, Asp, and Asn) and are not too long appear to act as competitors of main chain H bond donor and acceptors, and destabilize α-helices. The rest with no branches at the C_β can form helices. Those with branches at the C_β (Val, Ile) destabilize the α-helix due to steric interactions of the bulky side chains with the helix backbone. In general it is said that Ala, Glu, Leu and Met are good α-helix formers, while Pro, Gly, Tyr, and Ser are very poor. Such preferences were central to all early attempts to predict secondary structure from amino acid sequences, but they are not strong enough to give accurate predictions.

Variations on the α-helix in which the chain is either more loosely or more tightly coiled, with hydrogen bonds to residues n + 5 or n + 3 instead of n + 4 are called the π-helix and 3_{10} helix, respectively. The 3_{10} helix has 3 residues per turn and contains 10 atoms between the hydrogen bond donor and acceptor, hence its name. Both the π-helix and 3_{10} helix occur rarely and usually only at the ends of α-helices or as single-turn helices. They are not energetically favorable, since the backbone atoms are too tightly packed in the 3_{10} helix and so loosely packed in the π-helix that there is a hole through the middle. Only in the α-helix are the backbone atoms properly packed to provide a stable structure.

Hydrogen bonds are relatively weak, but since there are many of them in an α-helix, the total binding effect is strong and stable. The α-helix structure is known to be flexible and elastic (coiled structure like a spring).

5.3.4. THE β-SHEET STRUCTURE

The second major structural element found in proteins is the β-sheet. This structure is built up from a combination of several regions of the polypeptide chain, in contrast to the α-helix, which is built up from one continuous region. These regions, β-strands, are usually 5 to 10 residues long and are in an almost fully extended conformation with ϕ, ψ angles within the broad structurally allowed region in the upper left quadrant of the Ramachandran plot (see Figure 4.5 in Chapter 4). These β-strands are aligned adjacent to each other (see Figure 5.3 and Figure 5.5) such that hydrogen bonds can form between C=O groups of one β-strand and NH groups on

[1] The carbon atom of the CH_2 or CH_3 group in the side chain of an amino acid, linked to the central carbon atom C_α

an adjacent β-strand and vice versa. The β-sheets that are formed from several such β-strands are "pleated" with C_α atoms successively a little above and below the plane of the β-sheet.

β-strands can interact in two ways to form a pleated sheet, as shown in Figure 5.3 and Figure 5.5. Each of the two forms has a distinctive pattern of hydrogen-bonding. The antiparallel β-sheet (Figure 5.3) has narrowly spaced hydrogen bond pairs that alternate with widely spaced pairs. Parallel β-sheets (Figure 5.5) have evenly spaced hydrogen bonds that bridge the β-strands at an angle. A three-dimensional representation of both types of β-sheets are shown in Figure 5.4 and Figure 5.6. The side chains are arranged such that within a β-strand they point alternately above and below the β-sheet.

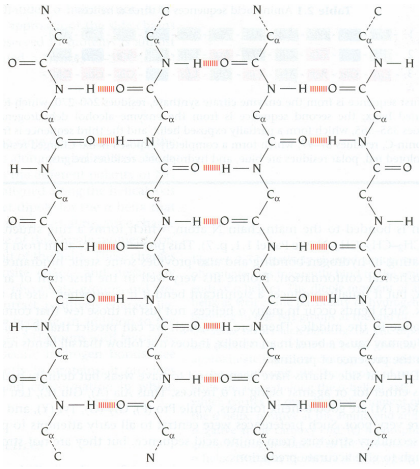

Figure 5.3 - Planar illustration of an antiparallel β-sheet

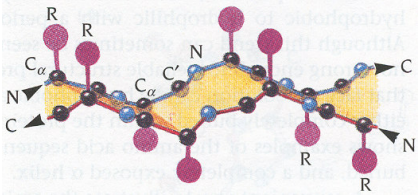

Figure 5.4 – 3-D representation of an antiparallel β-sheet

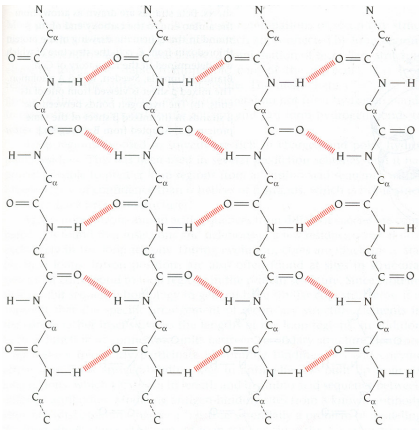

Figure 5.5 - Planar illustration of a parallel β-sheet

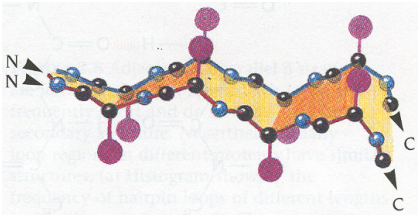

Figure 5.6 – 3-D representation of a parallel β-sheet

β-strands can also combine into mixed β-sheets with some β-strand pairs parallel and some antiparallel.

As they occur in known protein structures, almost all β-sheets have twisted strands. This twist always has the same handedness as that shown in Figure 5.7, which is defined as a right-handed twist.

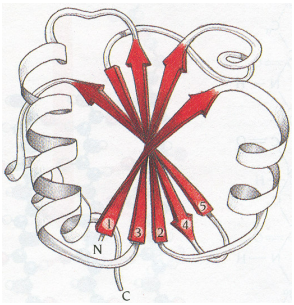

Figure 5.7 - The twist of β-sheets

Since all the peptide linkages in β-sheet structures are involved in inter-chain H bonding (in contrast to intra-chain H bonding in an α-helix), the β-sheet structure is very stable. The β-sheet structure is further flexible but inelastic.

5.3.5. THE HAIRPIN LOOP OR β-TURN STRUCTURE

Most protein structures are built up from combinations of secondary structure elements, α-helices and β-strands, which are connected by loop regions of various lengths and irregular shape. A combination of secondary structure elements forms the stable hydrophobic core of the molecule. The loop regions are at the surface of the molecule. The main chain C=O and NH groups of these loop regions, which in general do not form hydrogen bonds to each other, are exposed to the solvent and can form hydrogen bonds to water molecules.

Loop regions exposed to the solvent are rich in charged and polar hydrophilic residues. This has been used in several prediction schemes, and it has proved possible to predict loop regions from an amino acid sequence with a higher degree of confidence than α-helices and β-strands, although they have irregular structures.

Loop regions that connect two adjacent antiparallel β-strands are called hairpin loops. Short hairpin loops are usually called reverse β-turns or simply β-turns. Figure 5.8 shows two of the most frequently occurring turns: the Type I turn and the Type II turn. The type II turn usually has a glycine residue as the second of the two residues in the turn.

Long loop regions are often flexible and can frequently adopt several conformations, such as the so-called β-spiral as found in elastin [Urry 1984], making them "invisible" in X-ray structure determination and undetermined in NMR studies.

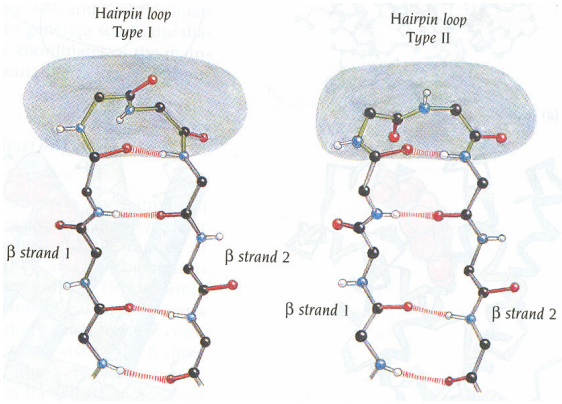

Figure 5.8 - The two most frequently occurring two-residue hairpin loops or β-turns

5.4. TERTIARY STRUCTURE OF PROTEINS

The tertiary structure is formed by packing the secondary structure elements or motifs into one or several compact globular units called domains. A domain is defined as a polypeptide chain or a part of a polypeptide chain that can fold independently into a stable tertiary structure. Often, the different domains of a protein are associated with different functions. Domains are formed by different combinations of secondary structure elements and motifs. Sequentially adjacent motifs, or motifs that are formed from consecutive regions of the primary structure of a polypeptide chain, are usually close together in the three-dimensional structure. Thus to a first approximation a polypeptide chain can be considered as a sequential arrangement of these simple motifs. The number of such combinations found in proteins is limited, and some combinations seem to be structurally favored. Thus similar domain structures frequently occur in different proteins with different functions and with completely different amino acid sequences.

The term "tertiary structure" is used as a common term both for the way motifs are arranged into domain structures and for the way a single polypeptide chain folds into one or several domains. In all cases examined so far it has been found that if there is significant amino acid sequence homology in two domains in different proteins, these domains have similar tertiary structures.

The book of Branden & Tooze [1998] is referred to for more details of combinations of domain structures.

The tertiary structure of the silkworm and certainly the spider silks is not unraveled completely. Some known features are discussed in Chapter 10.

5.5. QUATERNARY STRUCTURE OF PROTEINS

Protein molecules that have only one chain are called monomeric proteins. But a fairly large number of proteins have a quaternary structure, which consists of several

identical polypeptide chains (subunits) that associate into a multimeric molecule in a specific way. These subunits can function either independently of each other or cooperatively so that the function of one subunit is dependent on the functional state of other subunits. Other protein molecules are assembled from several different subunits with different functions.

Also with respect to the quaternary structure of the silkworm and the spider silks, known information is described in Chapter 10.

5.6. PRIMARY STRUCTURE OF SILKS

5.6.1. INTRODUCTION

A unique structural feature shared by silk protein sequences is their organisation into two types of alternating blocks or domains. One is composed of small repetitive units [Hayashi & Lewis 2000, 2001, Mita *et al.* 1994]. Often this type of block tends to be hydrophobic, especially in the lepidopteran fibroins (like silkworm silks), less so in the case of some spider silk proteins. The other type of block is non-repetitive, tends to be the most hydrophilic part of the core sequence, and is very short compared to the size of the more hydrophobic repetitive block and is referred to as a "spacer".

The size, number and hydrophilicity of the internal hydrophilic blocks within the central core region may correlate with the microenvironment within which the fibrous silk is designed to operate. For example *Bombyx* cocoon silk is designed to operate under predominantly dry conditions and has few and small internal hydrophilic blocks while spider flagelliform silk with its large internal hydrophilic blocks is designed to operate in a highly hydrated condition. This correlation may arise from the use of hydrophilic blocks to regulate the distribution of water within the spun silk and hence the degree and location of plasticization by water.

Since the function of amino and carboxy terminus (begin and end of chain) regions is not clear and is not expected to be related to the mechanical properties, for further information on these regions it is referred to literature [Beckwitt & Arcidiacono 1994, Mita *et al.* 1994, Guerette *et al.* 1996, Colgin & Lewis 1998, Sezutsu & Yukuhiro 2000, Bini *et al*. 2004].

5.6.2. PRIMARY STRUCTURE OF SILKWORM SILKS

5.6.2.1. Primary structure of *Bombyx mori*

The complete primary structure of *Bombyx mori* fibroin has been determined by Mita *et al.* [1994] and more completely by Zhou *et al.* [2000]. Silk produced by the silk moth *B. mori* is known to contain multiple repeats of the hexapeptide motif GAGAGS [Fraser *et al.* 1966, Strydom *et al*. 1977, Saito *et al*. 1984, Lombardi & Kaplan 1990] occurring in blocks of 8-10 repeats, separated by another repeating motif that is somewhat more variable. These two large sequence blocks repeat four or five times between a small, approximately 30 residues, section of non-repetitive

sequence called the "spacer" or "amorphous domain", as summarised in Figure 5.9 [Mita *et al.* 1994].

$$\{(GAGAGS)_{n=8-10} - [(GA)_{n=1-3} - GY]_{n=4-7}\}_{n=4-5} - (Spacer)$$

Figure 5.9 - Amino acid sequence of *Bombyx mori* cocoon silk fibroin (based on 324 residues) [Mita *et al.* 1994]

Based on genomic DNA analysis, Zhou *et al.* [2000] deduced a fibroin amino acid sequence that is 5263 residues long. It is made of low-complexity regions bordered by short N- and C-terminal segments of more standard amino acid composition. The bulk of the low-complexity "crystalline" domains (~90% of the fibroin) is made of repeats of a GX dipeptide motif where X is Ala in 65%, Ser in 23% and Tyr in 9% of the repeats compared with all residues in fibroin. Most of the GX dipeptide units are present as part of the two hexapeptides GAGAGS and GAGAGY which, together, account for 70% of this region. The boundary sequences (amorphous domain), contain the only tryptophan residues and 11 of 14 prolines. They also contain charged residues (Asp/Glu and Arg/Lys), which are absent in the crystalline GX-domains. For more details, it is referred to the article of Zhou *et al.* [2000].

5.6.2.2. Primary structure of *Antheraea pernyi* (Tussah)

A similar hierarchic organisation as in *B. mori* is present in the silk protein of *Antheraea pernyi*, with blocks of alternating units [Bini *et al*. 2004], but in this case the amino acid composition of each unit confers a less hydrophobic character to the block. Each unit starts with the four amino acids GSDS (except the first unit of each block, which usually starts with AAGS). This is followed by 11 to 13 hydrophobic residues and then stretches of combinations of GX, GGX and GGGX (X = A, S, Y, V, W, R, D) (hydrophilic motif). Each block contains from 3 to 11 of these units, but most consist of 5 to 6 units.

Yukuhiro and co-workers [Yukuhiro *et al.* 1997, Sezutsu & Yukuhiro 2000] found the primary repetitive motifs in *A. pernyi* silk proteins based on genomic DNA analysis. The Ap-fibroin, except for 155 residues of the amino terminus, was composed of 80 tandemly arranged polyalanine motifs. A motif was a doublet of a polyalanine block (PAB) and a nonpolyalanine block (NPAB), resulting in an alternation of hydrophobic (PAB) and hydrophilic (NPAB) regions. 78 of the 80 motifs were classified into four types (Figure 5.10 [Sezutsu & Yukuhiro 2000]) based on the differences in the NPAB sequences.

Type 1 : AAAAAAAAAAAAAGSG<u>AGG</u>XGGGYGWGDGGYGSDS

with X = S, A ,V, R

Type 2 : AAAAAAAAAAAAA.SG<u>AGG</u>A..$(GGY)_n$GGYGSDS with n = 1-3

Type 3 : AAAAAAAAAAAAAGSG<u>AGG</u>RGD……GGYGSGSS

Type 4 : AAAAAAAAAAAAA.RRAGHDRAAGS

Figure 5.10 - Motifs in *Antheraea pernyi* fibroin

The number of alanine residues in the PAB sequences ranged from 10 to 15, mostly 12 or 13.

Unlike *B. mori*, poly-alanine makes up the crystalline regions of the protein, and the noncrystalline regions are made up of a series of motifs which contain both constant and variable domains. The constant domains include $GGYGSDS(A)_{12}GSGAGG$ and $GGYGSGSS(A)_{13}SGAGG$ sequences. The variable domains include AGGGYGWGGD, $A(GGY)_n$, RGD and RRAGHDRAAGS sequences.

5.6.3. PRIMARY STRUCTURE OF SPIDER SILK

5.6.3.1. Nomenclature

The information on amino acid sequence of spider silks is mostly restricted to the spider species *Nephila clavipes* and *Araneus diadematus*. They are all based on a cloning of the genes. In literature, different nomenclature for the cloned genes of *N. clavipes* and *A. diadematus* are used and these are summarised in Table 5.1.

Table 5.1 - Different notations for the cloned genes (MA = major ampullate, Mi = minor ampullate, Flag = flagelliform, CYL = cylindrical) [Gührs *et al.* 2000]

Species	Gland	Notation System I	Notation System II	Reference
N. clavipes	MA	NCF-1	MaSp1	Xu & Lewis (1990), Beckwitt & Arcidiacono (1994)
N. clavipes	MA	NCF-2	MaSp2	Hinman & Lewis (1992)
N. clavipes	Mi		MiSp1	Colgin & Lewis (1998)
N. clavipes	Mi		MiSp2	Colgin & Lewis (1998)
N. clavipes	Flag		Flag	Hayashi & Lewis (1998)
N. clavipes	Cyl		TuSp1	Tian & Lewis (2006)
A. diadematus	Mi	ADF-1		Guerette *et al.* (1996)
A. diadematus	Cyl	ADF-2		Guerette *et al.* (1996)
A. diadematus	MA	ADF-3		Guerette *et al.* (1996)
A. diadematus	MA	ADF-4		Guerette *et al.* (1996)
A. bicentenarius	MA	ABF-1		Beckwitt *et al.* (1998)
A. gemmoides	Cyl		TuSp1	Tian & Lewis (2006)
A. aurantia	Cyl		TuSp1	Tian & Lewis (2006)

Furthermore, the nomenclatures of “Spidroin 1” and “Spidroin 2” can be found in literature for the proteins of major ampullate silks of *N. clavipes*.

In this text, it is chosen to use for the *N. clavipes* spider the notation Nc-MA, Nc-MI, Nc-FL, and Nc-CYL, where MA indicate major ampullate, MI minor ampullate, FL flagelliform silk, CYL egg sac silk produced by the cylindrical glands. For *A. diadematus* the abbreviation Ad will be used, with the same abbreviations indicating the different types of silk. The origin of the different silks is clearer with this notation, which can also be found in literature [Gosline *et al.* 1999].

In this section, only the amino acid sequence of the most studied spider species *N. clavipes* and *A. diadematus* will be discussed.

5.6.3.2. Primary structure of *Araneus diadematus* spider silk

5.6.3.2.1. Introduction

Guerette *et al.* [Guerette *et al.* 1996, Gosline *et al.* 1999] have cloned four genes (see Table 5.1: ADF-1, ADF-2, ADF-3, ADF-4) of *Araneus diadematus* coding for various types of silks: dragline silk, viscid silk and egg sac silk. Figure 5.11 gives an overview of the amino acid sequence motifs for the spider silk fibroins of *A. diadematus*.

Major ampullate gland (MA) fibroins

Ad-MA-1: ASAAAAAAGGYG**P**GSGQQG**P**GQQG**P**GGQG**P**YG**P**G

Ad-MA-2: SSAAAAAAAASG**P**GGYG**P**GSQG**P**SG**P**GGYG**P**GG**P**G

Minor ampullate gland (MI) fibroins

Ad-MI-1: GAGSGAGAGAAAAAGAGGYGQGY

Cylindrical gland (CYL) fibroin

Ad-CYL-1: AAAAAAAAGGQGGQGGYGGLGSQGAGGAGQGGYGAAGLGGQGG

Figure 5.11 - Amino acid sequence motifs for spider silk fibroins of *A. diadematus* [Guerette *et al.* 1996] (Crystal forming motifs are highlighted in gray; proline residues set in bold)

5.6.3.2.2. Major ampullate silk proteins of Araneus diadematus

The results of Guerette et al [1996] indicate that MA silk of *Araneus diadematus* (dragline) has at least two major protein constituents, both of which are rich in proline (Figure 5.11). These two proteins have similar glycine, alanine, and proline contents, but they differ in serine and glutamine content. Interestingly, a 3:2 ratio of these two proteins would have an amino acid composition that is virtually identical to that of *A. diadematus* dragline.

Ad-MA-1 shows very large transcript amounts in the major ampullate (MA) gland and modest amounts in the flagelliform gland. The amino acid composition of Ad-MA-1 fails to account for the composition of the viscid (flagelliform) silk, and therefore other viscid silk proteins remain to be cloned. Ad-MA-2 is expressed in large amounts only in the MA gland.

Ad-MA-1 encodes crystal-forming ASAAAAAA blocks (21%) and amorphous repeat blocks (79%) of GPGGQGPYGPG, GGYGPGS, and (GPGQQ)n (n = 1-8).

Ad-MA-2 contains crystal-forming ASAAAAAAAA blocks (27%) and amorphous repeat blocks of GPGSQGPS and GPGGY (73%).

5.6.3.2.3. Minor ampullate silk protein of Araneus diadematus

The silk-like protein encoded by Ad-MI-1 (Figure 5.11) is a major constituent of the minor ampullate silk, and it is likely that the sequence motif in the partial cDNA is representative of the entire gene.

Of the Ad-MI-1 protein 68% is present as $(A)_n$ (n = 5) or as $(GA)_n$ (n = 2-7) blocks; these motifs are known to form β-sheet crystals. The remaining 32% is occupied by GGYGQGY repeats, which are expected to be noncrystalline.

5.6.3.2.4. Cylindrical or egg sac silk protein of Araneus diadematus

Ad-CYL-1 is likely a constituent of egg sac silk, but because its predicted amino acid composition is quite different from that reported for this silk, Guerette *et al.* [1996] believe that other unidentified proteins must also be present. Recently, Tian & Lewis [2006] predicted the protein sequence of *Araneus gemmoides* egg sac silk from cDNA analysis of the cylindrical gland and found a much more acceptable sequence including a high amount of serine. This sequence shows similarities to the sequence found for the egg sac silk of *Nephila clavipes,* as described in Figure 5.12. They believe that Ad-CYL-1 found by Guerette *et al.* [1996] is most likely a protein expressed at a very low level in the tubuliform or cylindrical gland.

Ad-CYL-1 encoded crystal-forming poly(alanine) blocks ~ 8 residues long (19%); the remainder (81%) is formed from GGAGQGGY and GGQGGQGGYGGLGSQGA repeats, which are similar to sequences in elastin and lamprin. Repeats of this type likely contribute to the noncrystalline scattering seen in X-ray diffraction patterns of elastic proteins and silks.

The predicted sequence for egg sac silk of the spider species *A. gemmoides*, found by Tian & Lewis [2006], contained new amino acid motifs such as $(Ser)_n$, $(Ser\text{-}Ala)_n$, $(Ser\text{-}Gln)_n$, and Gly-X (X represents Gln, Asn, Ile, Leu, Ala, Val, Tyr, Phe, Asp). Moreover, *A. gemmoides* cylindrical gland fibroin shares a QQ motif with *N. clavipes* Nc-CYL-1. For the whole sequence it is referred to the article of Tian & Lewis [2006], and its reproduction in Chapter 10. Although alanine is one of the most abundant amino acids in tubuliform silk protein, the *A. gemmoides* tubuliform silk protein has very short alanine stretches, with A_3 the longest, scattered throughout the repetitive sequences.

Also in the primary structure of tubuliform gland silk of *Argiope argentata* and *Latrodectus hesperus* no A_n, $(GA)_n$ or $GPGX_n$ motifs were detected [Garb & Hayashi 2005].

5.6.3.3. Primary structure of *Nephila clavipes* spider silk

5.6.3.3.1. Introduction

Figure 5.12 gives an overview of the consensus amino acid sequence motifs for spider silk fibroins of *Nephila clavipes*.

Major ampullate gland (MA) fibroins [Xu and Lewis 1990, Hinman & Lewis 1992]

Nc-MA-1: AGAAAAAAAGGAGQGGYGGLGSQGAGRGGLGGQG

Nc-MA-2: SAAAAAAAAG**P**GGYG**P**GQQG**P**GGYG**P**GQQG**P**GGYG**P**GQQG**P**SG**P**G

Minor ampullate gland (MI) fibroins [Colgin & Lewis 1998]

Nc-MI-1: AGAGAGAAAGAGAGGYGGQGGYGAGAGAGAAAAAGAGGAGGYGRG

Nc-MI-2:
AVAGSGSAAGAGARAGSGGYGGQGGYGAGAGAGAAAGAGAGSAGGYGRG

Flagelliform gland (FL) fibroin [Hayashi & Lewis 1998]

Nc-FL-1: G**P**GGYG**P**GGSG**P**GGYG**P**GGYG**P**GGSG**P**GGYG**P**GGA

Or $(G\mathbf{P}GGX)_{N=43\text{-}63}$ – $(GGX)_{N=9\text{-}12}$ – (Spacer, 28 residues long)

Cylindrical gland (CYL) fibroin [Tian & Lewis 2006]

Nc-CYL-1: TTTTTSAARSQAASQSASSSYS----SAFAQAASSSFAISSALSR

AFSSVSSASAASSLAYSIGLSAARSLGIADATGLAGALARAVGAL

GQGATAASYGNALSTAAAQFFATAGLLNAGNASALASSFARAFSAS

AE-------SQSFAQSQAFQQASAFQQAASRSASQSAAEAGSTSSS

Figure 5.12 - Amino acid sequence motifs for spider silk fibroins of *N. clavipes* (Nc = *N. clavipes*; crystal forming motifs are highlighted in gray; proline residues set in bold)

5.6.3.3.2. Major ampullate silk proteins in Nephila clavipes

Lewis and co-workers [Xu and Lewis 1990, Hinman & Lewis 1992] identified the dragline (MA) amino acid sequences of *Nephila clavipes* from cDNA (Figure 5.12). They believe that it is only composed of two proteins.

Mello *et al.* (1994) believed that the parent protein of *N. clavipes* MA silk contain sequences derived from the first identified protein (Nc-MA-1) and one or more domains not seen in either the two identified proteins (Nc-MA-1 and Nc-MA-2).

The Nc-MA-1 protein is dominated by short runs (5-7 residues) of (hydrophobic) poly-alanine separated by approximately five repeats of a loosely conserved (less hydrophobic) Gly-Gly-X motif, where X is predominantly Gln, Tyr and Leu [Xu & Lewis 1990]. The Nc-MA-1 protein consists of two types of motifs, the hydrophobic $GAG(A)_nGGA$ (n=4-7) and the more variable less hydrophobic block $(GXG\ GXGGX)_n$ (where X = Tyr, Leu, Ala, Ser, Arg, while Pro is absent). These two motifs are reiterated over the length of the core sequence.

The most significant motifs in the second sequence, Nc-MA-2, are slightly longer runs of poly-alanine (6-10 residues). Nc-MA-2 has a glycine-rich motif that differs from the other spider silk proteins in that proline occupies every fifth residue in the glycine-rich motif, including the pentapeptides Gly-Tyr-Gly-Pro-Gly, Gly-Pro-Gly-Gly-Tyr, and Gly-Pro-Gly-Gln-Gln [Hinman & Lewis 1992]. These motifs alternate to stretches of $S(A)_n$ [Bini *et al*. 2004].

The two proteins 1 and 2 respectively are 719 and 628 residues long, each including a "tail" that is slightly more hydrophilic than the conserved regions.

In both Nc-MA-1 and Nc-MA-2 proteins, there is no spacer to separate distinct blocks, in contrast to *B. mori* and minor ampullate spider silk.

5.6.3.3.3. Minor ampullate silk proteins in Nephila clavipes

Minor ampulate silk would also be composed of only two proteins (Figure 5.12). Colgin & Lewis [1998] have found that both proteins are organised into a predominantly repetitive region and a small nonrepetitive ("spacer") carboxy terminal region [Colgin & Lewis 1998].

A typical repetitive region has ten repeat units. There are two types of motifs within a single repeat unit of Nc-MI-1, Gly-Gly-X-Gly-Gly-Y (X = Gln or Ala) motifs alternate with $(GA)_y(A)_z$ motifs, where y = 3-6 and z = 2-5. The first GGXGGY motif in the repeat is always followed by GRG and X is always alanine. The second GGXGGY motif is followed directly by the $(GA)_y(A)_z$ motif and X is always glutamine. Tyrosines (Tyr) are completely conserved in Nc-MI-1, but phenylalanine (Phe) substitutions occur in Nc-MI-2 in only 3 of 29 cases.

Like Nc-MI-1, the repeat unit of Nc-MI-2 has $(GGX)_n$ (X=Tyr, Gln, or Ala; n = 1-3) domains that alternate with GAGA motifs. The first motif is shorter than the same motif in Nc-MI-1 since Nc-MI-2 lacks the GGA present before the GGYGRG sequence. Four residues (Y,Q, R and S) in the Nc-MI-2 are highly conserved. One of the conserved residues which distinguish Nc-MI-1 from Nc-MI-2 is the serine in the GAGAGAAAGAGSA domain of Nc-MI-2.

The repetitive regions of both minor ampullate silk proteins are interrupted by non-repetitive serine-rich spacer regions. For the complete sequence, it is referred to the article of Colgin & Lewis [1998]. Although the sequences of the spacer regions differ from the repetitive regions, sequences of the spacers from different regions of the proteins are nearly identical. The 137 amino acid spacer regions are virtually identical in the two Nc-MIs and show no identity to any other known spider silk sequence. Serine (24%) and alanine (18%) are the most abundant residues in this region. Leucine (8%), asparagine (7%), threonine (7%), and valine (7%) are also present in higher percentages than in the repetitive regions. The glycine content is lower in the spacer (10%) than in the repetitive regions (17%). The spacer region is not internally repetitive, with the exception of the sequence, SSAA, which is present as a single tandem repeat.

5.6.3.3.4. Flagelliform silk fibroin of Nephila clavipes

The flagelliform silk of *Nephila* contains large blocks ranging from 259 to 385 amino acids, composed mainly of G and P residues, contained in motifs as GPGGX, GGX (where X = P, Y, A, S, V, Q, I, L, R). At the beginning and at the end of each block GGA and GGS motifs may be reiterated a number of times. The motif $(GRGGA)_n$ is found close to the end of the block and makes this region basic, while the rest of the block is slightly hydrophilic.

5.6.3.4. Cylindrical silk fibroin of *Nephila clavipes*

Tian & Lewis [2006] believes that Nc-CYL-1 (Figure 5.12) is the major component in the cylindrical gland. As seen in the cylindrical silk fibroin of *Araneus gemmoides* and *Argiope aurantia* [Tian & Lewis 2006], Nc-CYL-1 has a more complex mixture of new amino acid motifs with a high percentage of large side chain amino acids such as valine, leucine, isoleucine and phenylalanine than the other silk fibroins (Figure 5.12). The new amino acid motifs found in cylindrical silk fibroin are $(Ser)_n$, $(Ser\text{-}Ala)_n$, $(Ser\text{-}Gln)_n$, and Gly-X (X represents Gln, Asn, Ile, Leu, Ala, Val, Tyr, Phe, Asp). Moreover, *Nephila clavipes* Nc-CYL-1 shares a Gln-Gln (QQ) motif with the cylindrical gland fibroin of *A. gemmoides* and a stretch of threonine (T_5) with *A. aurantia* cylindrical gland fibroin.

5.6.3.5. Comparison *Nephila clavipes – Araneus diadematus*

There are strong similarities between the four genes cloned of *Araneus diadematus* and the genes that encode the major ampullate silk proteins of *Nephila clavipes*. All these genes encode proteins that exhibit the pattern of alternating small alanine-rich (crystal forming blocks) and larger glycine-rich amorphous blocks [Guerette *et al.* 1996].

Interestingly, different silk glands express fibroins with different proportions of crystal forming and amorphous sequence elements, imparting different tendencies for the formation of crystals in their silk fibres. For example, the two fibroins found in *A. diadematus* MA silk (Figure 5.11) have similar proportions to those produced by *N. clavipes* (Figure 5.12), with crystal forming elements occupying approximately one-quarter of the repeat block. The MI fibroin of *A. diadematus* has a much larger fraction of crystal forming blocks (68%) and very short amorphous blocks (32%), a pattern that has been documented for *N. clavipes* MI silk [Colgin & Lewis 1998].

The minor ampullate protein of *A. diadematus* (Ad-MI-1) is similar to the minor ampullate proteins of *N. clavipes* (Nc-MI-1 and Nc-MI-2) [Guerette *et al.* 1996]. However, unlike the Nc-MIs, tyrosines and glutamines are not as highly conserved in Ad-MI-1 and the length of each repeat varies.

5.7. SECONDARY STRUCTURE OF SILKS

5.7.1. SECONDARY STRUCTURE OF SILKWORM SILKS

5.7.1.1. Secondary structure of *Bombyx mori*

5.7.1.1.1. Introduction

In the solid state, *Bombyx mori* silk presents two different crystalline modifications known as Silk I and Silk II. The periodic copolypeptide poly(L-Ala-Gly) has often been used as a model of the crystalline silk fibroin sequences of *B. m*ori [Lotz &

Cesari 1979, Moore & Krimm 1976, Fossey *et al.* 1991, Anderson 1998, Asakura *et al.* 2001a, 2001b, Asakura & Yao 2002].

Valuzzi *et al*. [1997, 1999] reported the discovery of a third crystal structure of *B. mori* silk, called silk III, which has been observed in ultrathin films formed at the air-water interface of dilute (< 5%) aqueous silk solutions. The structure of the silk III form has not been fully clarified yet.

5.7.1.1.2. The structure of Silk I

The less stable Silk I forms upon desiccation of the silk gland and is considered as an intra-glandular storage form of fibroin. Silk I can also be regenerated from dissolved silk by dialysis from lithium bromide or aqueous calcium chloride in ethanol (see also Chapter 7).

Despite a long history of interest in the less stable Silk I form, its structure has remained poorly understood [Asakura *et al.* 2001b] due to the difficulty of obtaining oriented samples for studies by X-ray diffraction, electron diffraction or solid-state NMR. In fact, the silk I structure is metastable and easily converts to silk II by stretching or heating.

The study of the silk I structure was based on model building of $(Ala\text{-}Gly)_n$ and comparison of the predictions of these models with limited experimental data. Fossey and co-workers [1991, 1994] reported that the torsional angles (ϕ, ψ) of the Ala residues are (-80°, 150°), and are for the Gly residues (-150°, 80°), which are called as the out-of-register model. Since the proposed structure is composed of antipolar chains, the methyl side chains of alanyl residues in adjacent strands point to opposite sides of the sheet. The side chain distribution would thus be symmetrical in contrast to the polar silk II form, which has all alanyl residues on one side and all glycyl residues on the other (see further).

Lotz & Cesari [1979] reported two sets of torsional angles for the $(Ala\text{-}Gly)_n$ peptide: for the Ala residue, the torsional angles are (-104.6°, 112.2°) and for the Gly residues, they are (79.8°, 49.7°) or alternatively, for the Ala residue, the values are (-124.5°, 88.2°) and for the Gly residues, they are (-49.8°, -76.1°). This configuration of the $(Ala\text{-}Gly)_n$ peptide is known as the crankshaft model. In the crankshaft model of Lotz & Keith [1971], the alanyl residues are in a β-sheet conformation and the glycyl residues in a left-handed α-helical conformation.

In order to examine the validity of the proposed Silk I model, Anderson [1998] observed the WAXS pattern for recombinant silk I-like molecules. The poor agreement between the calculated WAXS pattern using Fossey's model and the observed pattern indicates that the model is inaccurate. The crankshaft model was supported from a comparison of the simulation and observation, but the agreement was still poor.

Most recently, Asakura *et al.* [2001a] proposed a silk I model on the basis of 2D spin diffusion NMR, REDOR NMR, and ^{13}C chemical shift contour plots. The torsional angle of $(Ala\text{-}Gly)_{15}$ with Silk I structure were determined as (-60°±5°, 130°±5°) and (70°±5°, 30°±5°) for Ala and Gly residues, resp. The structure of one Silk I chain is a repeated β-turn type II structure that is capable of forming

intramolecular hydrogen bonds (Figure 5.13). In addition, there are intermolecular hydrogen bonds whose direction is perpendicular to the fibre axis. All of the previous models showed only the formation of intermolecular hydrogen bonds and no intramolecular hydrogen bonds.

The β-turn type II structure is characterized by the alternating sequence of X-Gly, where X is another amino acid residue [Chou & Fasman 1977]. Especially, in the β-turn type II structure, residues other than Gly at the (i+2)th position in the Figure 5.13 will be energetically unfavorable due to steric hindrance. Thus, here is a relationship between the repeated (X-Gly) sequence and the β-turn type II structure of Silk I. Since the Silk I form of *B. mori* silk fibroin is an intermediate structure in the fibre-forming process of the silkworms, it is likely that the repeating and alternating sequence of X-Gly (where X is dominantly Ala), naturally occurring in the silkworm, arose to form β-turns that can subsequently be transformed into β-sheets.

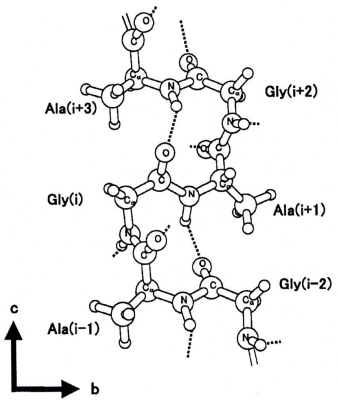

Figure 5.13 - The repeated β-turn type II

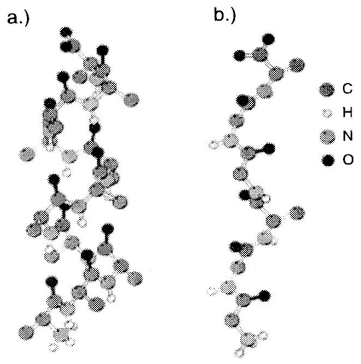

Figure 5.14 - (a) Conformation of an α-helix (b) Conformation of a 3_1-helix

Zhou *et al.* [2001] assigned the Silk I structure to a 3_1-helix-like structure based on ^{13}C solid state NMR spectra. Figure 5.14 shows the difference between an α-helix and a 3_1-helix [Kümmerlen *et al*. 1996]. The C=O bond direction is approximately along the helical axis direction in the α-helix and almost perpendicular to it in the 3_1-helix. In contrast to the α-helical structures which are stabilized by intrachain hydrogen bonds, 3_1-helices are stabilized by interchain hydrogen bonds.

Although, the conformation of Silk I is still not clear, both the repeated β-turn and the 3_1-helix structure show a comparable conformation: a 3-fold turn or helix structure, i.o.w. 3 residues are involved in 1 turn. A similar 3-fold symmetry is found for the Silk III structure, as mentioned further on.

5.7.1.1.3. The structure of Silk II

Silk II is the more stable form that is found in the natural cocoon fibre. The pseudo-unit structure of Silk II is proposed to be an antiparallel β-sheet by Marsh *et al.* [1955a] and is represented in Figure 5.15. In this drawing, the backbones of the polypeptide chains are represented as roughly elliptical; they are bonded together by hydrogen bonds to form sheets parallel to the fibre axis. The large loops between these sheets represent methyl or hydroxymethyl side chains of alanine and serine residues and the small loops represent hydrogen atoms of glycine residues.

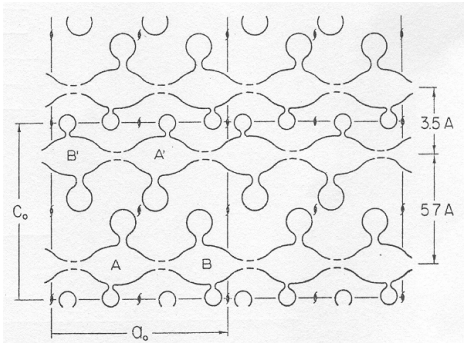

Figure 5.15 - A schematic representation of the proposed pseudo unit of structure projected along the fibre axis [Marsh *et al.* 1955a]

They proposed that a sheet is formed having chemically distinct faces. Only the hydrogen (-H) atoms of the glycine residues are protruding from the front side and the methyl ($-CH_3$) groups of the alanine residues and the methanolic ($-CH_2OH$) groups of the serine residues are protruding from the back side. Two sheets of this type can pack together efficiently either front-to-front at a distance of 3.5 Å or back-to-back at a distance of 5.7 Å. The majority of the small amino acid residues (Gly, Ala, and Ser) are arranged in accordance with the proposed pseudo unit. Marsh *et al.* [1955a] also believe that the remaining 18% of the residues (including about 5% of Tyr), which are too large to be accommodated by the pseudo unit, is nevertheless present in the crystalline component of silk fibroin and is responsible for deformations of the pseudo unit. Based on model calculations, they found that the phenyl group of Phe or Tyr can indeed pack into the proposed β-sheet structure, namely nearly parallel (angle of only 20 °) to the plane of the sheet. They concluded that the packing is determined predominantly by the Van der Waals thickness rather than the diameter of the phenyl groups.

Later, Fraser & MacRae [1973], Lotz & Keith [1971], and Fossey *et al.* [1991] supported the general features of this antiparallel β-sheet model, but some of them also noted an irregular structure to be present in the silk fibre [Fraser *et al.* 1973, Lotz & Keith 1971].

Asakura and co-workers [Asakura & Yao 2002, Asakura *et al.* 2002a] determined the relative proportions of the various components of the Silk II form of the *Bombyx mori* silk fibroin: for the 56% crystalline fraction, they found 18% distorted β-turns, 13% β-sheets (parallel alanine residues); for the remaining 44% amorphous fraction they found 22% of both distorted β-turns and distorted β-sheets.

The boundary sequences that are bordering the GX domains contain proline. Zhou *et al.* [2000] suggested that these are likely to break the β-strand, allowing the polypeptide chain to change direction and, possibly, turn back to itself into an anti-parallel β-sheet. This β-sheet would be intra- rather than interchain.

5.7.1.1.4. The structure of Silk III

Silk III is formed by crystallisation at an air/water interface. If solubilised *Bombyx mori* silk is used, the chains adopt a left-handed 3_2 helical conformation and become ordered into a slightly distorted hexagonally packed array [Valluzzi & Gido 1997]. The combination of the six residue repeating sequence poly(Gly-Ala-Gly-Ala-Gly-Ser) leads to the placement of the serine residues on one side of the helix, as can be seen in Figure 5.16 [Valluzzi & Gido 1997). One third of the cylindrical surface described by the helix is rich in serine residues. The other two thirds of the surface contain columns of vertically alternating glycine and alanine residues and are equivalent. An arrangement that clusters the bulkier more hydrophilic serine residues is also favourable in terms of energetic and packing considerations.

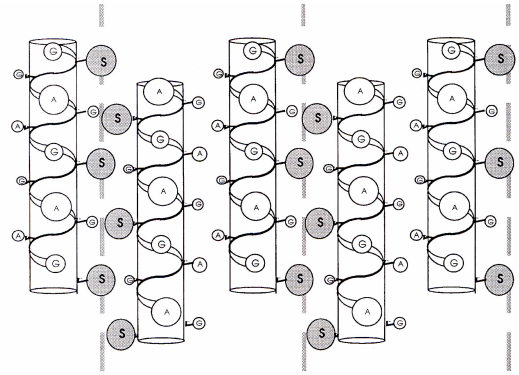

Figure 5.16 – The Gly-Ala-Gly-Ala-Gly-Ser sequence with a 3-fold helical conformation

Valuzzi *et al.* [1999] further observed that compression of the ultra-thin films results in a different orientation of these 3-fold helices.

5.7.1.2. Secondary structure of *Antheraea pernyi* (Tussah)

Marsh *et al.* [1955b] have proposed, as for *Bombyx mori*, an antiparallel β-sheet structure with a pseudo unit structure of *Antheraea pernyi* (Tussah) silk as is shown in Figure 5.17. Within each pleated sheet, adjacent polypeptide chains are held together in an antiparallel sense by linear hydrogen bonds [Pauling & Corey 1953]. The way the adjacent sheets are packed together differs from that in *B. mori* silk. In *B. mori* adjacent sheets are separated by distances alternately 3.5 and 5.7 Å, whereas in Tussah silk the sheets are spaced at equal intervals (5.3 Å). This space is occupied by the side chain atoms of the various amino acid residues. Both sides of the pleated sheets appear to be structurally equivalent.

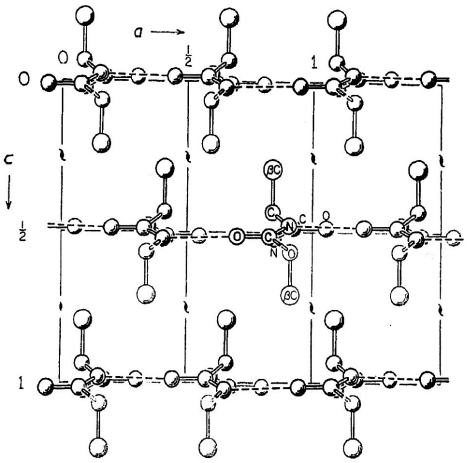

Figure 5.17 - A representation of the pseudo unit structure of Tussah silk, viewed along the fibre axis [Marsh *et al.* 1955b]

Bamford *et al.* [1954] have reported that the X-ray diffraction pattern of the β (stretched) poly-L-alanine is almost identical to that of Tussah silk. Marsh *et al.* [1955b] suggested that any distortions in the packing of sheets, as might be required by the large amino acid residues, occur that may explain the small differences in X-ray data between poly-alanine and Tussah silk.

Yukuhiro *et al.* [1997] predicted the secondary structure for the *A. pernyi* fibroin sequence with the Chou-Fasmann method and obtained results as follows:

1) each polyalanine was contained in an α-helix as a core;
2) in an individual type 1 motif more than one β-turn structure was found, and further linked Tyr, Gly and Ser residues always formed a β-turn;
3) in type 4 motifs, no β-turns were found.

As a result of the presence of the polyalanine repeats, *A. pernyi* chains can take the α-helix conformation in both aqueous solutions [Iizuka & Yang 1968] and solid-state (cast films) [Magoshi *et al.* 1977, Tsukada *et al.* 1986, 1995, 1998]. However, it has been shown that Tussah films cast from aqueous solution contain variable proportions of α-helix and random coil conformations, which can be converted into the β-sheet conformation [Tsukada *et al.* 1986, 1995, 1998] (see also Chapter 7).

5.7.2. SECONDARY STRUCTURE OF UNSPUN SPIDER SILK DOPE

NMR and ultraviolet circular dichroism measurements [Hijirida *et al.* 1996] on unspun spider dope, further also referred to as liquid silk, indicate that it lacks the β-sheet seen in the final silk and instead it contains up to about 30% α-helices, 40% of a random coil conformation, and 30% β-turns that might exist in a loose and dynamic, partially extended configuration analogous to that of the molten globule state. Taken together, the observational evidence suggests a multiple β-turn structure for the unspun dope; this might contain triple [van Raaij *et al.* 1999] or

double [van Beek *et al.* 1999] β-turns stabilised by interstrand hydrogen bonds, or a β-turn/random coil/α-helical structure [Hijirida *et al.* 1996]. The location of the β-turns and α-helix motifs is not known with certainty, but in aqueous solution the glycine-rich regions and the poly-alanine sequences are likely to form the β-turns and α-helices, respectively [Vollrath & Knight 2001].

5.7.3. SECONDARY STRUCTURE OF SPIDER SILK FIBRES

5.7.3.1. Introduction

An examination of the cDNA's and genes of the spider silks sequenced to date shows that all silks are chains of iterated peptide motifs. The consensus sequences for the repeating peptides of major and minor ampullate silks and flagelliform silk (Figure 5.11 and Figure 5.12) are repeated multiple times throughout the length of each protein.

The structure of spider silk was first proposed to consist of antiparallel sheets by Pauling & Corey [1953]. Although this has been shown to be correct there exist various other conformations and folding patterns, and a full structural elucidation is still being sought 40 years later. The difficulty arises from the slightly different peptide motifs, or repeating units, that are observed depending on species, silk type, and various other factors [Hayashi *et al.* 1999]. The interaction between adjacent motifs is directly responsible for the folding pattern of the polypeptides.

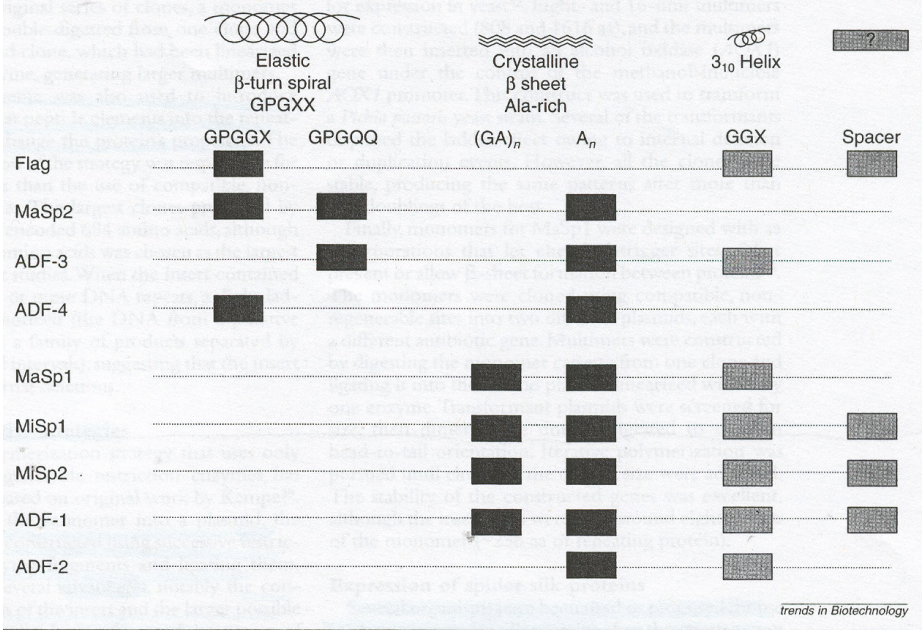

Figure 5.18 - Structural motifs found in spider silk proteins. Flag is the flagelliform silk protein. MaSp1, MaSp2, ADF-3 and ADF-4 are the proteins composing major ampullate silk. MiSp1, MiSp2, ADF-1 are the proteins composing minor ampullate silk and ADF-2 is cylindrical silk.

There is consensus that the available small peptide motifs can be grouped into four categories:

(1) Poly-Ala/poly-Gly-Ala motifs, $(GA)_n/A_n$

(2) Gly-Gly-X motif,

(3) Gly-Pro-Gly-X-X / Gly-Pro-Gly-Gln-Gln,

(4) spacers

Figure 5.18 [Hayashi *et al.* 1999] shows the categorization of silk fibres by the type of motifs that they contain, based on deduced protein sequences from *Nephila clavipes* (MiSp and MaSp) and *Araneus diadematus* (ADF).

A description of these four common silk motifs and suggested conformations are given in the next paragraphs. Furthermore, functions of some other known motifs are described.

5.7.3.2. Poly-Ala/poly-Gly-Ala motifs, $(GA)_n/A_n$

The poly-Ala motifs are present in almost all investigated spider silks, except for the flagelliform spider silk (*Nephila clavipes*). The regions of repeating alanine residues are clearly shorter in the minor ampullate silks than in the major ampullate silks, moreover they are always flanked by stretches of GA.

The sequence, GAGAGA, is common among the minor ampullate proteins [Colgin & Lewis 1998] and *Bombyx mori* silks [Mita *et al.* 1994], but is only present in one of the major ampullate silk proteins of *N. clavipes*.

Originally, based on computer predictions for major ampullate silk proteins (Nc-MAs) and physical studies of peptides in aqueous solutions, it was believed that the poly-alanine segments were likely to form α-helices [Xu and Lewis 1990, Hinman & Lewis 1992]. Moreover, detection of helix formation in silk under tension was given as evidence to support this structure.

However, the high proportion of short side amino acids (62%) [Lombardi & Kaplan 1990] in the major ampullate silk makes it more conceivable for the fibre to attain the conformational structure of the antiparallel β-pleated sheet (Figure 5.3 and Figure 5.4) with the formation of β-sheet crystals (as found earlier in Tussah silk). In later years, regions of crystalline β-sheet polymer indeed have been shown by solid-state NMR [Simmons *et al.* 1994, 1996, Hijirida *et al.* 1996, Kümmerlen *et al.* 1996] and X-Ray diffraction to correspond with the poly-Ala/poly-Gly-Ala motifs. Each individual motif forms highly aligned interlocking chains with theirselves. Moreover, the antiparallel β-sheet regions are predominantly aligned parallel to the fibre axis. The poly-Ala-Gly motif is hypothesised to interlock relatively hydrophobically compared to poly-Ala. This is due to the additional hydrophobic lysine group on the outer surface.

Moreover, Jelinski and co-workers [Simmons et al. 1996, Jelinski *et al*. 1999] found two populations of alanines differing in their degree of orientation with respect to the fibre axis. The highly oriented alanines (40% of the sample) were attributed to the poly-alanine, while the less well-oriented alanines (± 60%) were attributed to the

alanines residing in Gly-Ala-Gly sequences flanking the poly-alanines. The Gly-Ala-Gly regions are suggested to form β-sheet linkers between the highly oriented, crystalline poly-alanine regions and the presumably amorphous matrix. The glutamine residues flanking the alanine-rich runs may interfere with β-sheet formation and serve to limit crystal size.

5.7.3.3. Gly-Gly-X motif

$(GGX)_n$ motifs are present in the minor ampullate silk proteins, in one of the major ampullate (Nc-MA-1) proteins and in the cylindrical gland fibroin (Ad-CYL-1) (although not in the recent discovered sequences). Each minor ampullate protein repeat has two $(GGX)_3$ motifs and Nc-MA-1 has one $(GGX)_8$ motif per repeat. X in the GGX motif can be Gln, Ala, Tyr, Ser, or Leu. The Nc-MA-2 protein has only a GGY sequence in its structure.

A β-turn structure for the Gly-rich regions has been proposed from computer modeling to describe silk elasticity, where the pentapeptide (GPGXX) segments of the Nc-MA-2 protein are thought to form β-turns which when stretched form a β-spiral [Lewis 1992]. By fitting standard protein conformations to experimental NMR data, Jelinski *et al.* [1999] found the best fit to be either a Type I β-turn (Figure 5.8) or an α-helix conformation. Jelinski *et al.* [1999] suggested the oriented amorphous phase consists of Type I β-turns.

FT-IR data [Dong *et al.* 1991] indicated that the GGX sequences conform to a left-handed helix, likely one with three amino acids per turn. The existence of such 3_1 helices (also proposed for Silk I, see Figure 5.14) is confirmed by means of 2-D spin diffusion NMR on *Nephila madagascariensis* samples by Kümmerlen *et al.* [1996]. Their experiments do not distinguish these ordered Gly-rich regions from Gly-rich amorphous regions. It should be remarked here that the evidence of 3_1 helix for the glycine-rich segments (and ordered β-sheets for the poly-alanine segments) was based on MA silk bundles of *N. madagascariensis* of which the sequence information is not available [Thiel *et al.* 1997]. The evidence of 3_1 helices is confirmed by van Beek *et al.* [2002], however, based on 2-D solid state NMR. Van Beek *et al.* [2002] suggest that β-spirals exist in small numbers in the glycine-rich domains. Moreover, their data support the dominant presence of regular helical structures along the fibre direction, with an approximate 3-fold symmetry, suggesting a 3_1 helical structure. The 3_1-helical structure is elongated, consistent with the elongational flow of the silk dope solution during fibre spinning. The stability of these helical structures is given by the interchain hydrogen bonding. Some authors [Hayashi *et al.* 1999, Bram *et al.* 1997, Dong *et al.* 1991] furthermore suggested that these 3_1 helices form transition regions between the β-sheet and the less crystalline regions.

Even in 2002 considerable debate abounds, however, on the structure of the poly-Gly regions. Once thought to be entirely amorphous, their structure may be semi-ordered in a 3_1-helix [Kümmerlen *et al.* 1996, van Beek *et al.* 2002] and/or type 1 β-turn [Jelinski *et al.* 1999, van Beek *et al.* 2002].

5.7.3.4. Gly-Pro-Gly-X-X / Gly-Pro-Gly-Gln-Gln

Another motif (Gly-Pro-Gly-X-X), where X represents an alternating amino acid, is reported to exist in silk originating from the major ampullate and flagelliform glands [Hayashi & Lewis 1998]. In many cases, Gly-Pro-Gly-Gln-Gln is the major form.

In contrast to the loosely conserved GGX motif in the Nc-MA-1 protein, the proline containing pentapeptides characteristic of the Nc-MA-2 protein are detrimental to the formation of extended β-strands. The structure of the proline residue (Figure 4.6 in Chapter 4) forces a severe kink in an extended backbone chain [Thiel *et al.* 1997].

With regard to the Nc-MA-2 protein, different authors [Hinman & Lewis 1992, Heslot 1998, Hayashi & Lewis 1998, Hayashi *et al.* 1999] believe that the most likely conformation for these proline-rich regions is a β-turn. Under tension, the linked β-turns can form a β-turn spiral. This would be similar to the structure and elastic mechanism proposed for elastin [Urry 1984].

5.7.3.5. Gly-Leu-Gly-X-Gln-Gly motif

Another motif that can be found in the Nc-MA-1 protein is the Gly-Leu-Gly-X-Gln-Gly motif where X denotes Gly, Ser or Asn. This motif is also present in the amorphous glycine-rich domains and is believed to form a Type I β-turn (Figure 5.8) [Michal & Jelinski 1998, Jelinski *et al.* 1999].

5.7.3.6. Spacers

The structures formed by the "spacer" regions in the minor ampullate and flagelliform proteins remain unknown. While the two types of spacers differ greatly in amino acid sequence [Hayashi & Lewis 1998], they are both relative long, charged and complex. Moreover, they separate the iterated peptide motifs into clusters [Hinman *et al.* 2000].

5.7.4. DIFFERENCES BETWEEN SILKWORM AND SPIDER SILKS

5.7.4.1. Between *Bombyx mori* and spider silk

Whereas the microstructure of spider silk protein must accommodate several motifs, in general the crystalline region of *Bombyx mori* silk is dominated by one single motif, the Gly-Ala-Gly-Ala-Gly-Ser (GAGAGS) motif.

B. mori fibroin contains a preponderance of long crystal-forming blocks, which establishes a strong potential for crystal formation, and this probably accounts for the high crystal content of *B. mori* silk compared to spider silk.

The cocoon silks produced by *B. mori* are made up of tandem units of GAGAG(S) and GAGAGX (X varies between tyrosine and valine) [Zhou *et al.* 2000] and characterised by a poly-Gly-Ala crystalline organisation. This is in contrast to spider dragline silks composed of strings of alanine that result in a poly-Ala crystalline organisation. Therefore, even though their amino acid compositions are

roughly similar (see Chapter 4), the organisation of *B. mori* cocoon and spider dragline proteins is fundamentally different. [Kishore *et al.* 2002]

Silkworm silk fibroin has an occasional nonconserved tri-alanine sequence [Mita *et al.* 1994, Zhou *et al.* 2000] as well, as in the poly-alanine regions found in both major and minor ampullate spider silks.

Further structure-property relationships are discussed in Chapter 10.

5.7.4.2. Between *Antheraea pernyi* and spider silk

In contrast to *Bombyx mori* silk, the cocoon silks produced by the silkworm's sister taxa, *Antheraea pernyi*, appear to be more similar in organisation to spider dragline silks, even though they differ in relative amino acid content (see Chapter 4) [Sezutsu & Yukuhiro 2000]. The amino acid sequence of *A. pernyi* shows regular stretches of 12 or more consecutive alanine residues interrupted by glycine-rich regions, which also contain serine, alanine, tyrosine and even a few tryptophan residues.

Repeated PABs coupled with Gly-rich NPABs are also seen in spider dragline silk fibroins. However, these fibroins show some different features [Sezutsu & Yukuhiro 2000]:

- The number of alanine residues are fewer in dragline fibroin (4 to 10);
- Spider fibroins are much richer in proline but poor in serine.

Further structure-property relations are discussed in Chapter 10.

5.8. REFERENCES

Anderson J.P., Morphology and crystal structure of a recombinant silk-like molecule, SLP4, Biopolymers 45(4):307-321 (1998)

Asakura T., Ashida J., Yamane T., Kameda T., Nakazawa Y., Ohgo K., Komatsu K., A repeated β-turn structure in poly(Ala-Gly) as a model for silk I of *Bombyx mori* silk fibroin studied with two-dimensional spin-diffusion NMR under off magic angle spinning and rotational echo double resonance, J. Mol. Biol. 306:291-305 (2001a)

Asakura T., Yamane T., Nakazawa Y., Kameda T., Ando K., Structure of *Bombyx Mori* Silk Fibroin Before Spinning in Solid State Studied with Wide Angle X-Ray Scattering and 13C Cross-Polarization/Magic Angle Spinning NMR, Biopolymers 58:521-525 (2001b)

Asakura T. & Yao J., C-13 CP/MAS NMR study on structural heterogeneity in *Bombyx mori* silk fiber and their generation by stretching; Protein Science 11:2706-2713 (2002)

Asakura T., Yao J., Yamane T., Umemura K., Ulrich A.S., Heterogeneous structure of silk fibers from *Bombyx mori* resolved by C-13 solid-state NMR spectroscopy, J. Am. Chem. Soc. 124:8794-8795 (2002a)

Bamford C.H., Brown L., Elliott A., Hanby W.E., Trotter I.F., Alpha-forms and beta-forms of Poly-L-Alanine, Nature (London) 173(4392):27-29 (1954)

Beckwitt R. & Arcidiacono S., Sequence conservation in the C-terminal region of spider silk protein (Spidroin) from *Nephila clavipes* (Tetragnathidae) and *Araneus bicentenarius* (Araneidae), J. Biol. Chem. 269:6661-6663 (1994)

Beckwitt R., Arcidiacono S., Stote R., Evolution of repetitive proteins: spider silks from *Nephila clavipes* (Tetragnathidae) and *Araneus bicentenarius* (Araneidae), Insect Biochem, J. Mol. Biol. 28:121-130 (1998)

Bini E, Knight D. P., Kaplan D. L., Mapping domain structures in silks from insects and spiders related to protein assembly, J. Mol. Biol. 335(1):27-40 (2004)

Bram A., Branden C.I., Craig C., Snigireva I., Riekel C., X-ray diffraction from single fibres of spider silk, J. Appl. Crystallogr. 30:390-392 (1997)

Branden C. & Tooze J., Introduction to protein structure, 2nd edition, Garland Publishing, Inc., New York (1998)

Chou P.Y. & Fasman G.D., β-Turns in proteins, J. Mol. Biol. 115:135-175 (1977)

Colgin M.A. & Lewis R.V., Spider minor ampullate silk proteins contain new repetitive sequences and highly conserved non-silk-like "spacer regions", Protein science 7:667-672 (1998)

Dong Z., Lewis R.V., Middaugh C.R., Molecular mechanism of spider silk elasticity, Arch. Biochem. Biophys. 284:53-57 (1991)

Fossey S.A., Nemethy G., Gibson K.D., Scheraga H.A., Conformational energy studies of beta-sheets of model silk fibroin peptides. I. Sheets of poly(Ala-Gly) chains, Biopolymers 31:1529-1541 (1991)

Fossey S.A. & Kaplan D., Molecular modeling studies on silk peptides, In: Silk polymers: material science and biotechnology, ACS Symposium Series 544, Washington DC, 270-282 (1994)

Fraser R.D.B., MacRae T.P., Stewart F.H.C., Poly-l-alanylglycyl-l-alanylglycyl-l-serylglycine: A model for the crystalline regions of silk fibroin, J. Mol. Biol. 19:580-582 (1966)

Fraser R.D.B. & MacRae T.P., Conformations of fibrous proteins and related synthetic polypeptides, Academic Press, New York, USA, 293-343 (1973)

Garb J.E. & Hayashi C.Y., Modular evolution of egg case silk genes across orb-weaving spider superfamilies, Proc. Nat. Acad. Sci. 102(32):11379-11384 (2005)

Gosline J.M., Guerette P.A., Ortlepp C.S., Savage K.N., The mechanical design of spider silks: From fibroin sequence to mechanical function, J. Exp. Biol. 22(23):3295-3303 (1999)

Guerette P.A., Ginzinger D.G., Weber B.H.F., Gosline J.M., Silk properties determined by gland specific expression of spider fibroin gene family, Science 272:112-114 (1996)

Gührs K.-H., Weisshart K., Grosse F., Lessons from Nature – protein fibers, Reviews in Molecular Biotechnology 74:121-134 (2000)

Hayashi C.Y. & Lewis R.V., Evidence from flagelliform silk cDNA for the structural basis of elasticity and modular nature of spider silks, J. Mol. Biol. 275:773-784 (1998)

Hayashi C.Y., Shipley N.H., Lewis R.V., Hypotheses that correlate the sequence, structure and mechanical properties of spider silk proteins, Int. J. Biol. Macromol. 24:271-274 (1999)

Hayashi C.Y. & Lewis R.V., Molecular architecture and evolution of a modular spider silk protein gene, Science 287(5457):1477-1479 (2000)

Hayashi C.Y. & Lewis R.V., Spider flagelliform silk: lessons in protein design, gene structure, and molecular evolution, Bioessays 23(8):750-756 (2001)

Heslot H., Artificial fibrous proteins: A review, Biochimie 80:19-31 (1998)

Hijirida D., Do K.G., Michal C., Wong S., Zax D., Jelinski L.W., 13C NMR of *Nephila clavipes* major ampullate silk gland, Biophys. J. 71:3442-3447 (1996)

Hinman M.B. & Lewis R.V., Isolation of a clone encoding a second dragline silk fibroin, J. Biol. Chem. 267:19320-19324 (1992)

Hinman M.B., Jones J.A., Lewis R.V., Synthetic spider silk: a modular fiber; TIBTECH 18: 374-379 (2000)

Iizuka E. & Yang J.T., The disordered and beta conformations of silk fibroin in solution, Biochemistry 7(6):2218-28 (1968)

Jelinski L.W., Blye A., Liivak O., Michal C., LaVerde G., Seidel A., Shah N. and Yang Z., Orientation, structure, wet-spinning, and molecular basis for supercontraction of spider dragline silk, Int. J. Biol. Macromol. 24:197-201 (1999)

Kendrew J.C., Bodo G., Dintzis H.M., Parrish R.G., Wyckoff H., Phillips D.C., A three-dimensional model of the myoglobin molecule obtained by x-ray analysis, Nature 181(4610):662-666 (1958)

Kendrew, J. C., Dickerson R.E., Strandberg R.G., Hart R.G., Davies D.R., Phillips D.C., Shore V.C., Structure of Myoglobin. A Three-Dimensional Fourier Synthesis at 2 A. Resolution, Nature 185:422-27 (1960)

Kishore A.I., Herberstein M.E., Craig, C.L., Separovic F., Solid-state NMR relaxation studies of Australian spider silks, Biopolymers 61:287-297 (2002)

Kümmerlen J., van Beek J.D., Vollrath F., Meier B.H., Local structure in spider dragline silk investigated by two-dimensional spin-diffusion nuclear magnetic resonance, Macromolecules 29:2920-2928 (1996)

Lewis R.V., Spider silk: the unraveling of a mystery, Accts. Chem. Res. 25:392-397 (1992)

Lombardi S.J. & Kaplan D.L., The amino acid composition of major ampullate gland silk (dragline) of *Nephila clavipes* (Araneae, Tetragnathidae), J. Arachnol. 18:297-306 (1990)

Lotz B. & Keith H.D., Crystal structure of poly(L-ala-Gly) II. A model for silk, Int. J. Mol. Biol. 61:201-215 (1971)

Lotz B. & Cesari F.C., The chemical structure and the crystalline structures of *Bombyx mori* silk fibroin, Biochimie 61:205-214 (1979) and literature cited therein

Magoshi J., Magoshi Y., Nakamura S., Physical properties and structure of silk. III. The glass transition and conformational changes of tussah silk fibroin, J. Appl. Polym. Sci. 21(9):2405-2407 (1977)

Marsh R.E., Corey R.B., Pauling L., An investigation of the structure of silk fibroin, Biochim. Biophys. Acta 16:1-34 (1955a)

Marsh R.E., Corey R.B., Pauling L., The structure of Tussah silk fibroin, Acta Cryst. 8:710-715 (1955b)

Mello C.M., Senecal K., Yeung B., Vouros P., Kaplan D., Initial characterization of *Nephila clavipes* dragline protein, In: Silk polymers – Materials science and biotechnology; Kaplan D., Adams W.W., Farmer B., Viney C., Eds., American Chemical Society: Washington DC, 67-79 (1994)

Michal C.A. & Jelinski L.W., Rotational-echo double-resonance in complex biopolymers: a study of *Nephila clavipes* dragline silk, J. Biol. NMR 12:231-241 (1998)

Mita K., Ichimura S., James T.C., Highly repetitive structure and its organization of the silk fibroin gene, J. Mol. Evol. 38:583-592 (1994)

Moore W.H. & Krimm S., Vibrational Analysis of Peptides, Polypeptides, and Proteins. II. β-Poly(L-Alanine) and β-Poly(L-alanylglycine), Biopolymers 15: 2465-2483 (1976)

Pauling L. & Corey R. B., Branson H. R., The structure of proteins; two hydrogen-bonded helical configurations of the polypeptide chain, Proc. Natl. Acad. Sci. USA 37:205–211 (1951)

Pauling L. & Corey R.B., Two rippled-sheet configurations of polypeptide chains, and a note about the pleated sheets, Proc. Nat. Acad. Sci. USA 39:253-256 (1953)

Saito H., Tabeta R., Asakura T., Iwanaga Y., Shoji A., Ozaki T., Ando I., High-resolution ^{13}C NMR study of silk fibroin in the solid state by the cross-polarization-magic angle spinning method. Conformational characterization of Silk I and silk II type forms of *B. mori* fibroin by the conformation-dependent ^{13}C chemical shifts, Macromolecules 17:1405-1412 (1984)

Sezutsu H. & Yukuhiro K., Dynamic rearrangement within the *Antheraea pernyi* silk fibroin gene is associated with four types of repetitive units, J. Mol. Evol. 51:329-338 (2000)

Simmons A., Ray E., Jelinski L.W., Solid state 13C NMR of *N. clavipes* dragline silk establishes structure and identity of crystalline regions, Macromolecules 27:5235-5237 (1994)

Simmons A., Michal C.A., Jelinski L.W., Molecular orientation and two-component nature of the crystalline fraction of spider dragline silk, Science 271:84-87 (1996)

Strydom D.J., Haylett T., Stead R.H., The amino-terminal sequence of silk fibroin peptide CP – A reinvestigation, Biochem. Biophys. Res. Comm. 79:932-938 (1977)

Thiel B.L., Guess K.B., Viney Chr., Non-periodic lattice crystals in the hierarchical microstructure of spider (major ampullate) silk, Biopolymers 41:703-719 (1997)

Tian M. & Lewis R.V., Tubuliform silk protein: A protein with unique molecular characteristics and mechanical properties in the spider silk fibroin family, Applied Physics 82(2):265-273 (2006)

Tsukada M., Structural changes induced in tussah silk (*Antheraea pernyi*) fibroin films by immersion in methanol, J. Polym. Sci. Pt. B-Polym. Phys. 24:1227-1232 (1986)

Tsukada M., Freddi G., Monti P., Bertoluzza A., Kasai N., Structure and Molecular Conformation of Tussah Silk Fibroin Films: Effect of Methanol, J. Polym. Sci. Pt. B-Polym. Phys. 33: 1995-2001 (1995)

Tsukada M., Freddi G., Kasai N., Monti P., Structure and molecular conformation of tussah silk fibroin films treated with water-methanol solutions: Dynamic mechanical and thermomechanical behavior, J. Polym. Sci. Pt. B-Polym. Phys. 36:2717-2724 (1998)

Urry D.W., Protein elasticity based on conformations of sequential polypeptides – the biologic elastic fibre, J. Prot. Chem. 3:403-436 (1984)

Valluzzi R. & Gido S.P., The crystal structure of *Bombyx mori* silk fibroin at the air-water interface, Biopolymers 42(6):705-717 (1997)

Valluzzi R., Gido S.P., Muller W., Kaplan D., Orientation of silk III at the air-water interface, Int. J. Biol. Macromol. 24:237-242 (1999)

van Beek, J.D., Kümmerlen, D, Vollrath, F., & Meier, B.H., Supercontracted spider dragline silk: a solid-state NMR study of the local structure, Int. J. Biol. Macromol. 24:173-178 (1999)

van Beek, J.D., Hess, S., Vollrath, F., Meier, B.H., The molecular structure of spider dragline silk: Folding and orientation of the protein backbone, Proc. Nat. Acad. Sci. 99(16):10266-10271 (2002)

van Raaij M.J., Mitraki A., Lavigne G., Cusack S., A triple beta-spiral in the adenovirus fibre shaft reveals a new structural motif for a fibrous protein, Nature 401:935-938 (1999)

Vollrath F. & Knight D., Liquid crystalline spinning of spider silk, Nature 410:541-548 (2001)

Xu M. & Lewis R.V., Structure of a protein superfiber: Spider dragline silk, Proc. Nat. Acad. Sci. USA 87:7120-7124 (1990)

Yukuhiro K., Kanda T., Tamura T., Preferential codon usage and two types of repetitive motifs in the fibroin gene of the Chinese oak silkworm, *Antheraea pernyi*, Insect Mol. Biol. 6(1):89-95 (1997)

Zhou C.-Z., Confalonieri F., Medina N., Zivanovic Y., Esnault C., Yang T., Jacquet M., Janin J., Duguet M., Perasso R. and Li Z.-G., Fine organization of *Bombyx mori* fibroin heavy chain gene, Nucleic Acids Res. 28:2413-2419 (2000)

Zhou P., Li G.Y., Shao Z.Z., Pan X.Y., Yu T.Y., Structure of *Bombyx mori* silk fibroin based on the DFT chemical shift calculation, J. Phys. Chem. B 105:12469-12476 (2001)

6

VIBRATIONAL SPECTROSCOPY OF SILKS

In order to obtain information about the secondary structure of the silks, studied in previous chapters, FT-Raman and FT-infrared spectroscopy were performed.

Since both spectroscopic techniques are complementary, as discussed in Annex, the spectra obtained with these techniques are discussed simultaneously.

Furthermore, with respect to FT-infrared spectroscopy different sampling methods were compared in order to select the best one. The spectra, produced by the best method, are then further discussed for the different silkworm and spider silk samples and an evaluation of the secondary structure in these silks is made.

6.1. ASSIGNMENT OF WAVE NUMBERS TO SECONDARY STRUCTURE

As mentioned in Annex, the amide group of proteins presents characteristic vibrational modes (Amide modes) that are sensitive to the secondary structure of these proteins. Further details about spectroscopy of proteins can be found in Annex.

Table 6.1 and Table 6.2 summarize the assignments to secondary structure in the different conformation sensitive regions for FT-IR spectra and FT-Raman spectra, respectively, as found for proteins in literature.

Table 6.1 - Attribution of frequencies to secondary structure for proteins (// : IR light polarized along the fibre axis, ⊥: IR light polarized at right angles to the fibre axis, S: strong, W: weak) [Krimm & Bandekar 1986, Venyaminov & Kalnin 1990, Rathore *et al.* 2000, Griebenow *et al.* 1999, Fu *et al.* 1994, Van Dijk *et al*. 1997, Arrondo & Goni 1999, Kweon *et al.* 2001c]

Vibration	α-helix	Anti-parallel β-sheet	Parallel β-sheet	Random coil	β-turn
Amide I	1650-1660	1685-1695 W (//) 1620-1640 S (⊥)	1645 W (//) 1630 S (⊥)	1645-1656	1660-1700 or 1638-1645
Amide I' (in D_2O)	1650-1660	1675-1695 1625-1640	1625-1640	1640-1650	
Amide II	1519-1521 1548-1553	1530-1535 1563	1530 1550	1546-1553	1565 1548
Amide III	1290-1335 or 1280-1260	1215-1250	1215-1250	1250-1290	1290-1330
Amide V	610-625	695-710		650-665	570-607
Other		965-975			

Table 6.2 – Assignment of peaks to secondary structure for proteins in Raman spectra [Painter & Koenig 1976, Koenig & Sutton 1970, 1671, Xue 1994, Shao *et al.* 1995]

Conformation	Amide I (cm^{-1})	Amide III (cm^{-1})	Other
α-helix	1645-1657	1264-1310	890-945
β-sheet	1665-1680	1230-1245 1270 (weak)	1020-1060
random coil	1660-1670	1242-1250	

6.2. LITERATURE REVIEW ON SILKS

6.2.1. INTRODUCTION

With respect to FT-Raman spectroscopy, the problem of fluorescence for silks is reduced by the use of specific lasers, such as a red He-Ne laser (632.8 nm) [Shao *et al.* 1999a, 1999b, Sirichaisit *et al.* 2000] or a Nd/YAG laser (1064 nm) [Tsukada *et al.* 1995, Yang *et al.* 2004] or an Arg ion laser tuned to 514.5 nm [Trabbic & Yager 1998]. Gillespie *et al.* [1994] treated the spider silk fibres with 0.1% NaOH for 5-10 minutes. However, it appears not to solve the problem of fluorescence completely since the positively sloping baseline is still subtracted.

It is tried to identify the fluorophores responsible for the luminescence of the silk samples by means of a spectrophotometer but without any result aside from silk's own aromatic side chains [Gillespie *et al.* 1994].

6.2.2. SILKWORMS

Edwards & Farwell [1995] have recorded the FT-Raman spectra of different silks at several stages of their processing. The wave numbers and vibrational assignments of cultivated (Russian, mulberry, *Bombyx mori*) and wild (Chinese, Tussah) silk are summarized in Table 6.3.

Table 6.3 – Raman wave numbers (cm^{-1}) and vibrational assignments of silk bulk specimens (w = weak, m = medium, s = strong, v = very, br = broad, sh = shoulder)[Edwards & Farwell 1995]

Bombyx mori	Tussah	Assignment of vibrational mode
3279 m, br	3282 m, br	NH stretching; free and H-bonded
3062 m	3062 m	CH stretching of C=CH unit
3035 w	3035 w	CH aromatic stretching
2984 s	2984 s	CH_3 asymmetric stretching
2935 s	2935 s	CH_3 symmetric stretching
2878 m	2878 m	CH_2 asymmetric stretching
2856 w, sh		CH_2 symmetric stretching
2739 w	2739 w	CCH_3 aliphatic stretching
1666 ms	1666 ms	CO stretching; Amide I - β-sheet
1615 mw	1615 mw	C=C olefinic stretching (Trp, Phe, Tyr) [Tu 1982, Miura *et al.* 1988]
1605 vw	1605 vw	CC aromatic ring stretching

Bombyx mori	**Tussah**	**Assignment of vibrational mode**
	1554 w, br	CC stretching or ring vibration, Trp [Tu 1982, Miura *et al.* 1988]
1520 w		CC stretching
1451 m	1449 m	CH_2 scissoring
1404 mw	1404 mw	$C(CH_3)_2$ asymmetric bending
1370 w	1369 w	$C(CH_3)_2$ symmetric bending
1333 w	1334 mw	CH_3 bending, possibly α-helix [Koenig & Sutton 1970, 1971, Shao *et al.* 1999]
1309 w	1313 w	CH_2 bending
1260 mw	1260 mw	CN stretching, Amide III; CH_2 bending
1230 mw	1231 ms	CN stretching; CH_2 bending
	1215 w, sh	aromatic ring vibration, Tyr, Phe [Tu 1982]
1171 mw	1172 mw	CC stretching
1160 mw	1161 mw	CC stretching; C-OH bending
1085 m	1085 m	CC skeletal stretching, β-sheet [Magoshi *et al.* 1985, Zheng *et al.* 1989, Monti *et al.* 2001]
	1075 mw, sh	CC skeletal stretching
	1054 w	CC skeletal stretching
1046 w		CC skeletal stretching
1034 w	1033 w	CC skeletal stretching
1003 mw	1003 mw	CC aromatic ring stretching, Trp, Phe, Tyr [Tu 1982, Miura *et al.* 1988]
977 mw	977 mw	CH_3 rocking
946 w		CH_3 rocking
	928 vw	CH_3 rocking terminal
880 w	884 w	CH_2 rocking
854 mw	854 mw	C=CH aromatic bending, Tyr [Tu 1982]
758 w	758 w	CH_2 rocking in-phase
710 w		CH_2 rocking out-of-phase
644 mw	643 mw	Amide IV, ring deformation of Tyr [Taddei *et al.* 2004]

The attributions to secondary structure that are used in literature for silk fibroin are, as expected, mostly in agreement with those used for proteins (Table 6.1 and Table 6.2).

With respect to amino acid side chain contributions, for silk the following assignments are known:

- Bands attributable to Trp: 1595, 1550 and 1005 cm^{-1} [Tu 1982, Miura *et al.* 1988],
- Bands attributable to Phe: 1615, 1595, 1210 and 1005 cm^{-1} [Tu 1982],
- Bands attributable to Tyr: 1615, 1210, 1002, 850, 830, 642 cm^{-1} [Siamwiza *et al.* 1975, Tu 1982, Edwards & Farwell 1995, Taddei *et al.* 2004, Pellerin *et al.* 2005].
- Band attributable to Ser : 1345 [Overman & Thomas 1999]

6.2.2.1. *Bombyx mori* silk

Most infrared studies on *Bombyx mori* silk are performed on regenerated *B. mori* silk fibroin films (in transmission on film or KBr disk) in order to study the conformational transition from Silk I to Silk II structure (see Chapter 7) [Sun *et al.* 1997, Chen *et al.* 2002, Kweon *et al.* 2001b, Um *et al.* 2001, Monti *et al.* 2003]. Raman spectra of the Silk I morphological state of *B. mori* are also reported, based on the Cp Silk I fraction (after enzymatic hydrolysis with chymotrypsin) [Monti *et al.* 2001], poly(AG)II [Monti *et al.* 2003] or regenerated *B. mori* silk [Zheng *et al.* 1989, Monti *et al.* 1998]. Distinction between the Silk I and random coil is difficult to be made from FT-IR- and FT-Raman experiments [Asakura *et al.* 1985]. From these studies, IR [Magoshi *et al.* 1979, Miyazawa *et al.* 1958, 1962, Monti *et al.* 2003] and Raman [Monti *et al.* 2001, 2003, Taddei *et al.* 2004] characteristic bands for the Silk I or random coil structure were identified and summarized in Table 6.4. Monti *et al.* [2003] identified the peaks at about 1411, 1387, and 1334 cm^{-1} as IR markers for distinguishing Silk I from Silk II.

Several authors analyzed the FT-Raman spectrum [Frushour & Koenig 1975a, Edwards & Farwell 1995, Taddei *et al.* 2004] or FT-IR spectrum [Magoshi *et al.* 1979, Asakura *et al.* 1985, Sun *et al.* 1997, Um *et al.* 2001, Kweon *et al.* 2001b, Hino *et al.* 2003] of the Silk II crystalline state of *B. mori* fibres. Characteristic bands for the Silk II structure were deduced from these studies and mentioned in Table 6.4. The ranges indicate the minimal and maximal wave numbers that were found in literature.

As can be seen in Table 6.4, in the Amide III region (1200-1300 cm^{-1}) no consensus is observed between the assignments in the IR and Raman spectra. Also the assignment to the β-sheet structure in the Amide I region is different. For proteins, the IR spectra present two bands associated with the β-sheet: an intense one at about 1630 cm^{-1} and a weak one at about 1680 cm^{-1}. The intensities are opposite in the Raman spectra. For silks, the weak bands are not visible in both techniques.

Table 6.4 – FT-IR and Raman characteristic bands for the Silk I or random coil and Silk II structure

Structure	FT-IR (cm^{-1})	FT-Raman (cm^{-1})
Silk I or random coil	1654-1660 1540 1411, 1387 and 1334 1235-1240 650 and 610	1645-1659 1540 1414 1274-1276 and 1245-1246 Or 1259-1267 (random coil) 1107 954 and 928 864-865 263 and 231
Silk II (β-sheet)	1618-1630 1515-1533 1260-1265 700	1685-1693 1663-1669 1228-1236 1084-1087 977 881

With respect to the Raman bands at about 1275 and 1107 cm^{-1} [Monti *et al.* 2001], these bands were previously assigned to the presence of the α-helical conformation [Magoshi *et al.* 1985, Zheng *et al.* 1989].

N-deuterium experiments on poly(AG)II allowed the attribution of the Raman component at 1320 cm^{-1} to the Amide III mode of the β-turn type II conformation [Monti *et al.* 2003], thus confirming the results of Asakura *et al.* [2001a], who proposed a repeated β-turn type II conformation for Silk I. This is also in accordance to the results of Krimm & Bandekar [1980] who asserted that the 1290-1330 cm^{-1} range can provide a possibility for a diagnostic for β-turns.

β-poly(alanyl-glycine) is often used as model peptide to further characterize the different absorption peaks in FT-IR spectra [Moore & Krimm 1976] of *B. mori* silk. Taddei *et al.* [2004] identified some Raman bands as characteristic for the crystalline poly(AlaGly) repeating sequence with Silk I structure: 460, 420, 381, and 351 cm^{-1} based on Raman spectra of $(AG)_6$, $(AG)_9$ and $(AG)_{15}$.

Min *et al.* [2004] used attenuated total reflection infrared (ATR-FTIR) to study the conformational structure of the Silk II form of *B. mori* obtained by different methods. Taddei *et al.* [2003] reported the ATR-FTIR spectra of *B. mori* silk fibres. Chen *et al.* [1996] characterized silk films cast onto oriented PTFE substrates by means of external reflection infrared spectroscopy. The most important wave numbers found in these reflection spectra are summarized in Table 6.5.

Table 6.5 – Wave numbers in reflection spectroscopy for silks (vw: very weak, w: weak, sh: shoulder, s: strong, anti//: antiparallel)

ATR-FTIR	**Wave numbers (cm^{-1})**
Silk II	1622, 1514, 1228, 1166
Silk fibre	1616, 1509, 1445, 1336 vw, 1226, 1265 sh, 1172, 1063, 1040 sh, 988, 973
Electrospun fibre	1651, 1528 (random coil)
External reflection	**Wave numbers (cm^{-1})**
Silk films	1690 w (anti// β-sheet), 1655 (random coil), 1623 s (anti// β-sheet), 1540 w (random coil), 1522 s (anti// β-sheet)

Compared to Table 6.1 (secondary structure assignments in FT-IR), the Amide I and II bands in reflection spectroscopy are situated at the lower wave number range for the β-sheet as well as the random coil structure.

6.2.2.2. *Antheraea pernyi* (Tussah) silk

Several authors reported the FT-IR spectra of *Antheraea pernyi* (Tussah) fibre and silk fibroin films [Miyazawa & Blout 1961, Tsukada *et al.* 1994b, Tsukada *et al.* 1995, Freddi *et al.* 1997, Kweon & Park 1999, Magoshi *et al*. 2000, Kweon *et al.* 2000, 2001a, 2001c, Li *et al.* 2003a, 2003b]. The assignments are summarized in Table 6.6. The assignments for random coil structure were based on spectra found in a regenerated film from liquid silk directly obtained from the spinning glands [Magoshi *et al.* 2000].

Table 6.6 – Assignments to secondary structure for *A. pernyi* (Tussah) silk

Structure	**FT-IR (cm^{-1})**	**FT-Raman (cm^{-1})**
β-sheet	1630-1636 1516-1530 1220-1247 965 695-700	1668-1669 1241-1242 + 1230 sh 1092-1095 + 1071-1073 965 698
α-helix	1655-1660 1545-1550 1270 891-896 620-625	1657 1263 1106 908 530 and 376
Random coil	1660, 1550, 1310, 1270, 1107, 890, 650-664	

Some researchers investigated by means of Raman spectroscopy the structural changes of Tussah silk fibroin films (based on liquid silk from the glands) by a heat [Freddi *et al*. 1997] and methanol [Tsukada *et al*. 1995] or enzymatic [Monti *et al*. 2005] treatment. A similar result was obtained by Yang *et al.* [2004] for the conformational transition of the wild silk *Samia cynthia ricini* induced by stretching the liquid silk, collected from the spinning glands. From these studies, the assignments to secondary structure were deduced as summarized in Table 6.6. Again the ranges represent minimal and maximal wave numbers that were reported.

Taddei *et al.* [2003] reported the ATR-FTIR spectra of Tussah silk fibres. The spectra show absorption maxima at about 1617, 1514, 1445, 1397, 1371, 1235-1220 (broader band), 1172, 1050 (with a shoulder at lower and higher frequency), 964 and 923 cm^{-1}.

For Tussah silk, β-poly(alanine) is often used as model peptide to further characterize the different absorption bands in FT-IR spectra [Moore & Krimm 1976].

6.2.3. SPIDER SILKS

FT-IR studies of spider silks are restricted to a few publications and usually limited to the Amide I (1700-1800 cm^{-1}) and Amide III (1200-1300 cm^{-1}) regions. Raman spectroscopy is more often used for spider silk. Most FT-IR studies are involved with the conformational transition, induced by potassium [Chen *et al*. 2002, Peng *et al*. 2005] or heat [Dicko *et al*. 2004], of the liquid silk (or film) from the major ampullate silk glands of the *Nephila* genus. Dicko *et al*. [2004] extended the study (solution FT-IR-study in D_2O) with the liquid silk of the flagelliform gland, minor ampullate gland and cylindrical gland. Table 6.7 summarizes the assignments to secondary structures that were made in these studies in the Amide I region.

Table 6.7 – Assignments in the Amide I region for spider silks

IR Amide I (cm^{-1})	**Raman Amide I (cm^{-1})**	**Assignment**
	1683	monohydrogen-bonded or disordered helix
1691-1694	1667-1669	β-turns / β-sheet
1675		Anti-parallel β-sheet
1666		β-turns
1651-1658 1559 (Amide II)		α-helix
1550 (Amide II)		Helical
1657		Random coil
1655-1660 band	1652	Random coil or helical
1642-1645		Random coil
1620-1637 - 1612 + 1630 (deconvolved) 1520 (Amide II)		β-sheet [Dong *et al.* 1991]

The shoulder at 1691 cm^{-1} is usually assigned to the high frequency band of the antiparallel β-sheet structure. Chen *et al.* [2002] suggested that this shoulder may be attributed to the antiparallel β-sheet structure and the turns or bends associated with this antiparallel β-sheet structure. This was supported by their observations that the kinetics for the formation of the 1620 and 1691 cm^{-1} bands were consistently different when immersing a *Nephila* spidroin film in KCl solutions.

For the liquid silks of the spider species *Nephila edulis*, Dicko *et al*. [2004] found that all spectra were centered at about 1650 cm^{-1}, suggesting that helical and/or disordered structures dominate. It was observed that the liquid silks of the minor ampullate (MI) and cylindrical (CYL) glands have the highest helical content (57-60%) compared to major ampullate (MA) (38%) and flagelliform (FLAG) (47%) glands. All four glands had about the same composition of disordered structures (23-27%). The content of β-sheet structures was similar in MI, FLAG, and CYL (about 5%) but higher in MA (11%).

With respect to the temperature-induced transition of liquid silk of the cylindrical gland, β-turn structures were suggested for the final structure (heated to 80 °C). With increasing temperature, the MA (and MI) silk changed irreversibly to β-sheet-rich structures.

Dong *et al.* [1991] employed polarized FT-IR spectroscopy to study the structural changes in MA silk fibres of *Nephila clavipes* and *Araneus gemmoides* exposed to axial tension. They detected either the formation of α-helices or a reorientation of helices when the silk fibre is strained.

The FT-Raman studies on spider silks are also limited to the MA silks of different spider species.

Shao *et al.* [1999a] obtained Raman spectra of major ampullate dragline silks reeled from four different spiders: *Araneus diadematus, N. edulis, Latrodectus mactans* and *Euprosthenops* sp. The different spider silks differentiate in the intensity ratio of 1652 cm^{-1} to 1669 cm^{-1} and the Amide III band of *Araneus* silk splitting into a double peak at 1230 cm^{-1} and 1242 cm^{-1} in the parallel spectrum. It is concluded that *Araneus* silk contains a higher level of random coil conformation than the other spider silks.

Shao *et al.* [1999a] further noted that some of the spectral bands were highly polarized confirming that the β-sheets and partially ordered regions in all the silk fibres are highly oriented along the fibre axis. Furthermore, it was concluded that the band at 1230 cm^{-1} is more likely to be attributable to a β-sheet structure and/or other oriented backbone chains such as a 3_1-helix rather than a random coil.

Shao *et al.* [1999a, 1999b] also studied the Raman spectra of different major ampullate spider silks contracted in different solvents (methanol, water, urea). They all show that, after contraction, the β-sheet content appeared to decrease and the amount of random coil and/or α-helix structure increased, the molecular chains remaining parallel to the fibre axis.

Sirichaisit *et al.* [2000] studied the molecular deformation in spider dragline single silk (*N. edulis*) fibres subjected to stress. The Raman bands were found to be located at 854, 1095, 1230, 1450 and 1667 cm^{-1} and being particularly well resolved. The band at 1095 cm^{-1} (disordered conformation [Edwards & Farwell 1995]) and at about 1230 cm^{-1} (disordered [Edwards & Farwell 1995] or β-sheet [Xue 1994] conformation) were used to follow the molecular deformation induced by stress. Deformation of the fibre (5-15% strain) results in a shift to lower wave numbers as the strain is increased. Furthermore, they found a linear shift in band position of the peaks at 1095 cm^{-1} and 1230 cm^{-1} up to the point of fibre fracture.

Pan *et al.* [2004] recorded Raman spectra (parallel and perpendicular) of dragline silks of *A. ventricosus* spiders, raised in different containers and spun in various ways. They found an effect of container size, although the containers were composed of a different material (glass versus carton) so that the differences could also be due to the type of material, especially the roughness of the surface.

6.3. MATERIALS AND METHODS

6.3.1. MATERIALS

A few hundreds of spiders of the species *Araneus diadematus* were collected in November and fed until they laid their eggs in egg sacs. The eggs were gently removed from the egg sac fibres. After removal of some white fibres attaching, the egg sacs were used for spectral analysis.

The spiders were also used to reel off dragline samples, this was done with a speed-controlled device (Figure 6.1) at a constant speed of about 50 mm per second.

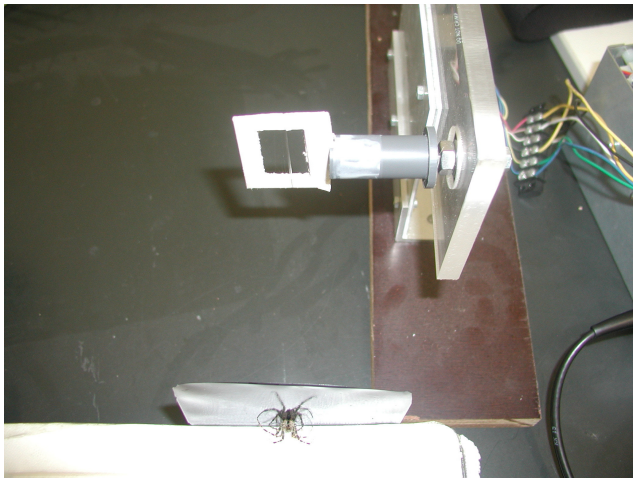

Figure 6.1 - The speed-controlled device for reeling of dragline

Fibres from cocoons of the silkworms *Bombyx mori* and *Antheraea pernyi* (Tussah silk), grown at the Silk Museum of Meliskerke (The Netherlands), were also tested.

6.3.2. METHODS

6.3.2.1. FT-IR spectroscopy

The transmission and diffuse reflection infrared measurements were performed on a Perkin Elmer GX 2000, which is a Fourier transform infrared spectrometer. A Peltier-cooled DTGS Mid-IR detector, a Mid-IR source and an extended KBr beam splitter were used. The spectrometer is also equipped with a Perkin Elmer Autoimage microscope to allow microspectroscopic measurements, as was done for obtaining the transmission spectra. A medium-band MCT detector was used with the microscope. Diffuse reflectance spectra were obtained with a Perkin Elmer DRIFTS accessory mounted in the main sample compartment.

Of the transmission methods, two techniques were explored: direct transmission microscopy and potassium bromide (KBr) disks. In transmission microscopy, by focusing the IR beam, the transmission signal in air through a single fibre (or if too fine through a limited number of neatly adjacent fibres) was obtained. In the KBr-disk method, the silk fibres were finely cut and blended to a 1% concentration with KBr prior to pelletizing. The main sample compartment was used to record transmission spectra of the KBr pellets. In both methods, a background spectrum was recorded without any sample holder in the sample compartment.

Of the reflection methods, diffuse reflection (DRIFTS) as well as attenuated total reflection infrared (ATR-FTIR) spectroscopy, were performed. The DRIFT spectra were recorded from aligned fibre bundles, as well as from fibre sections in random orientation ("cup-method"). Before recording a DRIFT spectrum, a background spectrum was recorded with the provided sandpaper standard samples. This background spectrum allows amongst others the correction for atmospheric H_2O and CO_2 bands. The sample is focused and the energy is monitored.

The spectra of the fibres in random orientation are recorded by finely cutting the fibres and putting them in a small cup. As the addition of KBr did not improve the spectra, it was decided to work on pure silk. A background spectrum is recorded with pure KBr.

All the experiments are performed with 16 scans and a resolution of 4 cm^{-1} in the spectral range 400-4000 cm^{-1} with a data interval of 1 cm^{-1}. For DRIFTS experiments, the spectra of 10 different samples are averaged. For *A. diadematus* dragline, average was limited to 5 samples due to the limited amount of material available. The transmission as well as diffuse reflection measurements, were performed in a conditioned atmosphere of 20 °C and 65% R.H.

6.3.2.2. ATR-FTIR spectroscopy

The ATR-experiments were done at the Université Libre de Bruxelles (ULB). The ATR-FTIR spectra were obtained on a Bruker IFS55 FT-IR spectrophotometer (Ettlingen, Germany) equipped with a mercury-cadmium-telluride detector (broad band 12000-420 cm^{-1}, liquid nitrogen cooled) with an aperture of 3.5 mm. The internal reflection element was a "Golden Gate" single pass diamond ATR. The measurements were performed at room temperature (21 °C). The spectra were

recorded with a nominal resolution of 2 cm^{-1} by co-adding 512 scans. For all types of silk fibres, 4 different samples were averaged.

6.3.2.3. FT-Raman spectroscopy

The Perkin-Elmer Spectrum GX 2000 spectrometer was equipped with a Raman sample accessory. A diode-pumped YAG near infrared laser (1064 nm, variable power from 10 mW to 2000 mW), and InGaAs detector and a Raman beamsplitter was used.

The measurements were performed in back-scattering mode (180° excitation optics) with 16 scans, a resolution of 4 cm^{-1} with a data interval of 1 cm^{-1}. For a clear presentation of the different spectra, the area of the total spectrum from 3500 to 150 cm^{-1} was normalized.

With respect to egg sac spider silk, it was only possible to get acceptable spectra after drawing and aligning the fibres. This is probably due to the effect of the direction of the incident light versus the fibre axis, caused by the anisotropy of the fibres. Also the crimp of the fibres can play a role. Because of the low resolution, for egg sac spider silk an average of 3 spectra was taken.

In order to obtain improved spectra with a lower effect of fluorescence, the fibres selected above were also recorded on a FT-Raman spectroscope connected with a microscope. However, no improved spectra were obtained.

6.3.2.4. Processing

For the clearness of the graphs, all spectra are always area normalized over the selected region. To interpret spectra, ratios of intensities are taken into account.

In order to allow a comparison between the reflection and transmission methods, the transmittance values in the transmission spectra were converted to absorbance values. As recommended for DRIFT spectra, the spectra were maintained as recorded in KM units, defined as $(1-R^2)/2R$, with R the reflectance value. The ATR-FTIR spectra are converted to absorbance values (Absorbance = log 1/Reflectance[1]). Moreover, all spectra were area normalized to 1000 between 1800 and 800 cm^{-1}. All spectra were obtained from the average of at least three samples.

Figure 6.2 indicates the difference of absorbance and Kubelka-Munk units in function of reflectance.

The KM spectra tend to slightly lower weak absorptions (reflectance R higher than 0.44) and highly increase strong absorptions (reflectance lower than 0.44) [Verschuren 2005].

[1] The "Reflectance" value indicates the intensity of the reflected light after calibration with a background spectrum.

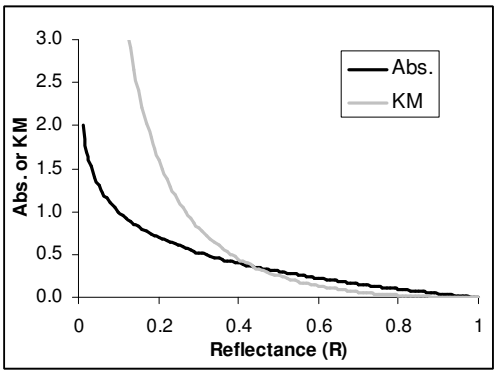

Figure 6.2 - Absorbance (Abs.) and Kubelka-Munk (KM) as function of Reflectance R

6.4. COMPARISON OF DIFFERENT FT-IR SAMPLING TECHNIQUES

6.4.1. RESULTS AND DISCUSSION

Figure 6.3 and Figure 6.4 show the spectra obtained according to the different FT-IR techniques for the silkworm silks. Figure 6.5 and Figure 6.6 show the spectra for the spider silks.

As can be seen in Figures 6.3 to 6.6, the peak maxima in the Amide I and Amide II region are always shifted to higher wave numbers for the spectra recorded with diffuse reflection (DRIFTS). However, the transmission spectra ("Transmission" and "KBr disk") resulted in broad Amide I and II bands that were not repeatable. The intensity of the Amide I band is much higher due to the feature of DRIFT spectra, expressed in KM units, that stronger absorptions are extra enlarged compared to absorbance values (=-log R) (see Figure 6.2). In order to explain the shift, the effect of background, built-in H_2O/CO_2 correction, water absorption and sample variation were investigated. Although water absorption has some effect in the intensity of the absorption bands, the effect was negligible compared to the effect of sample variation. No explanation of the shift in the Amide I and II bands was found from these experiments. It is suggested that specular reflection plays a role in this.

Also in the Amide III region, some differences are observed, although much smaller than in the Amide I and II regions. In the other regions, similar peaks are found for all techniques. The assignment of the peak maxima for the DRIFT spectra to functional groups and/or secondary structure is summarized in Table 6.8.

Within the DRIFT spectra, the highest difference is observed in the intensity and peak positions of the Amide I and II bands. The differences are attributed to the differences in alignment of the fibre parts in the aligned fibres and cut fibres ("cup-method") with respect to the direction of the incident light, resulting in a polarizing effect (see Annex). It was observed that the direction of the aligned fibres had

indeed an effect on the spectra. For all silk fibres, the Amide I band was showing a broader tail to lower wave numbers in the perpendicular direction than in the parallel direction. Furthermore, the maximum at about 1692 cm^{-1} clearly decreases in the perpendicular spectrum. Also in the ATR-spectra, the effect of alignment of the fibres with respect to the incident beam was clearly seen as an increase of the Amide I band (± 1620 cm^{-1}) in the perpendicular spectrum. It was also clear that for egg sac spider silk, the effect of polarization was less pronounced. This is in agreement with Parkhe *et al.* [1997] who found no orientation of the β-sheet crystals in egg sac spider silk.

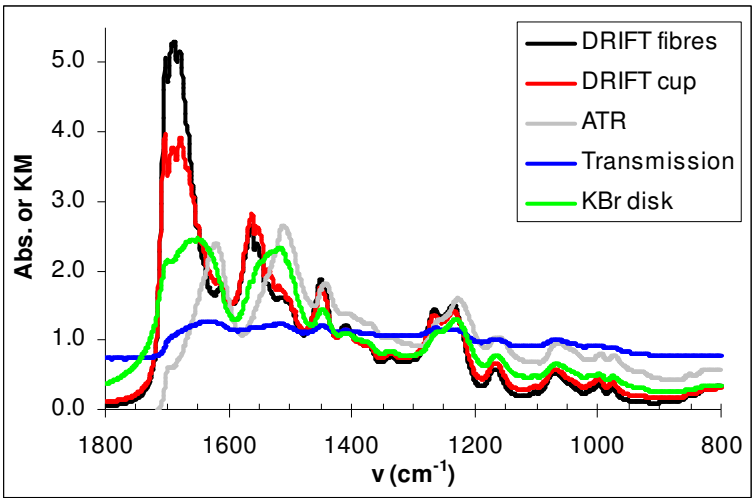

Figure 6.3 - Difference in FT-IR techniques for *B. mori* fibres

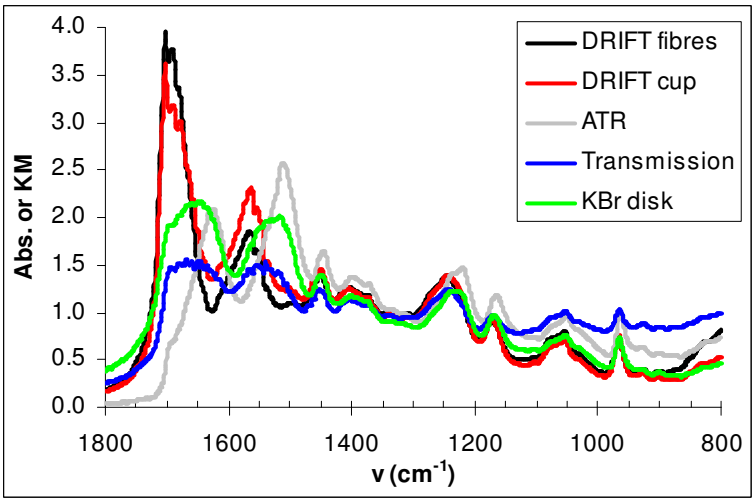

Figure 6.4 - Difference in FT-IR techniques for Tussah fibres

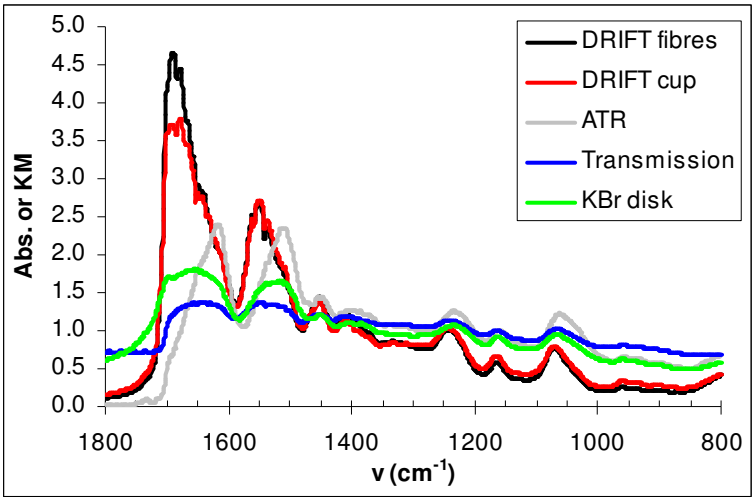

Figure 6.5 - Difference in FT-IR techniques for egg sac spider silk

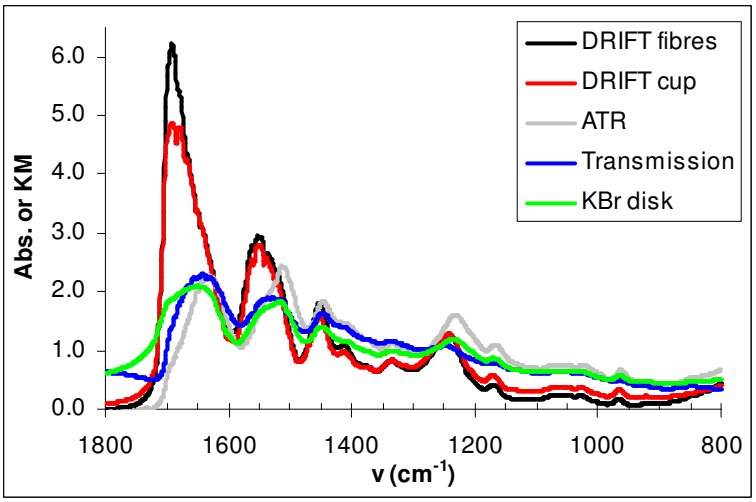

Figure 6.6 - Difference in FT-IR techniques for dragline spider silk

In ATR-spectroscopy, it is known that the molecules of the first layers contribute more than the molecules located further away from the reflecting surface [Goormaghtigh *et al*. 1999]. We would expect that both DRIFTS as ATR-FTIR are techniques in which the beam penetrates only over a small depth into the sample, so they can both be considered as surface techniques. However, weak absorbers result in a very deep penetration in DRIFTS [Milosevic & Berets 2002], as indicated by Equation (8) in Annex. Because of the shear forces during the spinning process of the silks, the skin of these fibres may not be uniform. The different penetration depth together with the specular reflection in DRIFTS measurements probably results in this behaviour. The ATR spectra show another feature that differentiates them from both the transmission and DRIFT spectra, namely that most absorption

peaks are shifted to lower wave numbers. These differences probably are due to the particular nature of the reflection spectrum. The calculation of the absorbance in ATR as the negative logarithm of reflectance results in differences in band shape and intensity compared to pure absorbance spectra as recorded in transmission spectroscopy [Goormaghtigh *et al*. 1999]. How much band shape and intensity are affected depends on experimental conditions. For *B. mori*, similar ATR absorption maxima were found as observed by Min *et al.* [2004]. Moreover, the base line between 2400 and 1800 cm^{-1} is more flat for the DRIFT spectra than for the spectra recorded with the other techniques. This is typical for DRIFT spectra, recorded in KM units, that small absorptions are reduced. The KBr-disk method is not an interesting method for the silk fibres, because it is very difficult and time-consuming to get the fibres fine enough in order to homogeneously blend them with the KBr.

The much higher resolution for DRIFTS compared to transmission measurements can be explained by the fact that silk fibres are probably weak absorbers, resulting in a higher penetration depth and thus a higher sensitivity [Milosevic & Berets 2002].

Since the spectra were most repeatable and the best resolved (different maxima can be clearly detected) in the Amide I and II region by using DRIFTS, the technique of diffuse reflection, especially on aligned fibres, is further used for a detailed discussion of the secondary structure of the silk fibres. We are expecting that the Amide I and II regions in DRIFT spectra may reveal more details than the other techniques allow. The ATR-FTIR spectra will be used to help in the assignment of peaks to secondary structure.

Moreover, the FT-Raman spectra will be compared with the DRIFT spectra in order to deduce complementary information from both techniques.

6.5. FT-IR DIFFUSE REFLECTION SPECTRA

6.5.1. INTRODUCTION

The discussion of the spectra is mainly focused on aspects related to the difference in structure. For further assignments, it is referred to Chapter 7 or Table 6.8 giving a summary of the assignments, as mainly found in literature.

6.5.2. REGION 3800-2400 CM^{-1}

Figure 6.7 shows the DRIFT spectra in the 2400-3800 cm^{-1} region for the different silks.

In this region, the absorption maxima are not related to the structure of the silk proteins. The assignment of the maxima in this region, mainly based on literature, is summarized at the end in Table 6.8.

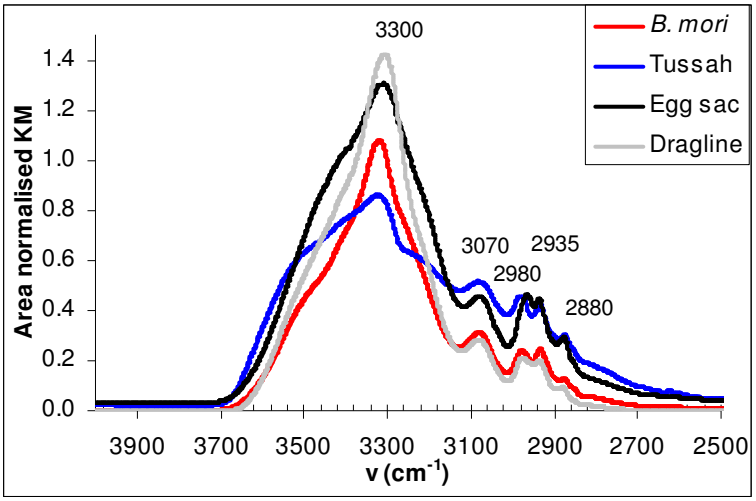

Figure 6.7 - DRIFT spectra in the 2400-3800 cm^{-1} region

The wave number of the Amide A vibration (±3300 cm^{-1}) is connected with the hydrogen bonding strength: a higher value of this frequency can be attributed to lower hydrogen bond strengths within the protein [Krimm & Bandekar 1986]. For the different silks, this means that the hydrogen bonds seem strongest in spider silk dragline (3300 cm^{-1}), followed by egg sac spider silk (3310 cm^{-1}) and the silkworm silks (3321-3327 cm^{-1}). The shoulder at higher wave number could be attributed to the OH functional group available in serine, although also the CO_2^- of glutamic acid and aspartic acid can be responsible for it.

Figure 6.8 shows the FT-Raman spectra in the Amide A and B region for the selected silks.

From the Raman spectra, it can be further concluded that, although the intensity is completely different, bands at about the same wave numbers are found as in the DRIFT spectra.

In the Raman spectra, egg sac spider silk differentiates from the other silks in the lower intensity of the maximum at about 2935 cm^{-1} relative to the maximum at about 2980 cm^{-1}. It can be explained by its different amino acid composition (see Chapter 4): the two major amino acid residues in egg sac spider silk are alanine and serine, whereas in the other silks these are alanine and glycine. Furthermore, the content of leucine and valine residues, both containing two CH_3 groups in their side chain, is much more represented in egg sac spider silk than in the other silks. The vibration of these more voluminous amino acid residues is possibly different from that of alanine, with only one methyl ($-CH_3$) group.

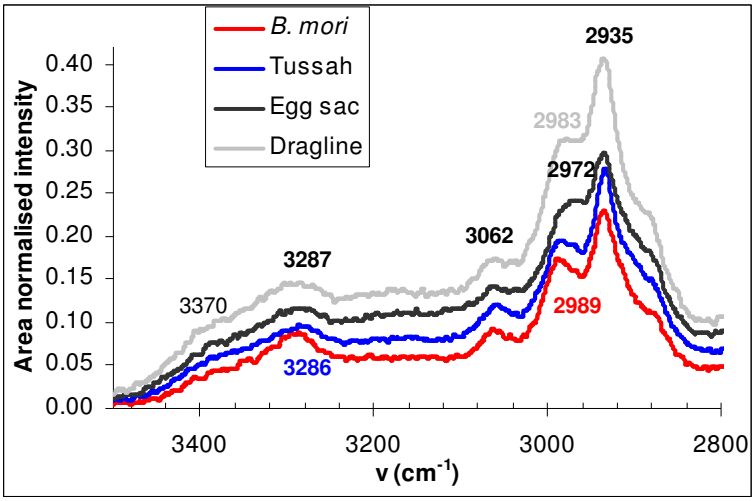

Figure 6.8 - FT-Raman spectra in the Amide A-B region for the different silks

6.5.3. AMIDE I REGION - 1600-1700 CM^{-1}

Figure 6.9 shows the DRIFT spectra in the 1800-1450 cm^{-1} for the different silks. In these spectra, normalizing was done on the maximum at about 1692 cm^{-1}.

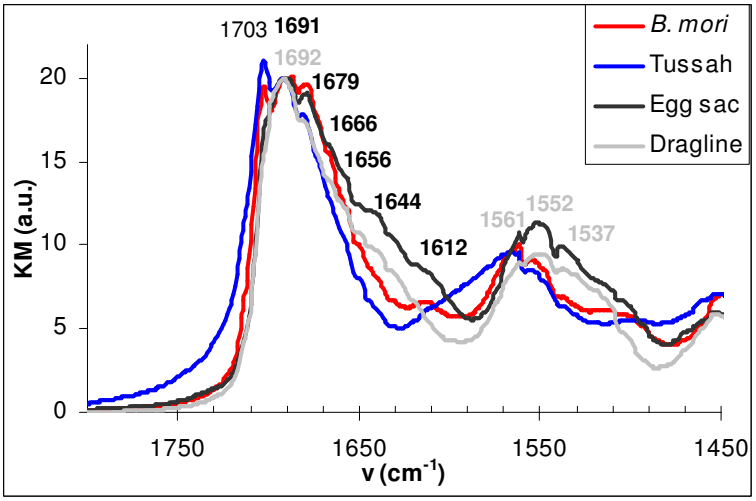

Figure 6.9 - DRIFT spectra in the 1800-1450 cm^{-1} region (a.u. = arbitrary units)

It seems that for silks different peaks can be identified: 1700-1703 cm^{-1}, 1691-1692 cm^{-1}, ±1687 cm^{-1}, 1678-1679 cm^{-1}, 1666-1667 cm^{-1} (shoulder), ±1656 cm^{-1} (shoulder), ±1649 cm^{-1} (shoulder), ±1644 cm^{-1} (especially for egg sac), ±1612 cm^{-1} (shoulder - weak band for *Bombyx mori*).

These frequencies are all higher than those found in literature (mainly transmission spectra). The assignment to a specific secondary structure, seen mostly for proteins in solution, is mentioned in Table 6.1. In short, it can be concluded that the sequence in secondary structure assignment with increasing wave number is: β-sheet (parallel/antiparallel), random coil / α-helix, beta-turns and finally anti-parallel β-sheet.

Taking into account the higher frequency of the DRIFT spectra and the relative positions of the characteristic frequencies of the different secondary structures, we expect that the peak at 1700-1703 cm^{-1} is the high-frequency peak of the anti-parallel β-sheet. Since the known structure for *B. mori* and Tussah is the antiparallel β-sheet structure, it is surprising that the low-frequency peak is not observed. Moreover, in transmission spectra, it is the low-frequency peak that has the highest intensity, whereas the high-frequency peak is weak and sometimes not even observed. It is probably characteristic for this sampling mode.

In order to estimate the resolving power of the DRIFT spectra to estimate the secondary structure and to get a confirmation of the peaks attributed to the β-sheet structure, regenerated *B. mori* silk was produced that is expected to contain a high proportion of random coil and/or Silk I structures. With a treatment with a methanol solution, it is known that the conformational transition is induced from random coil structure to a β-sheet conformation. This is discussed in detail in Chapter 7. The assignment of the peak at 1700-1703 cm^{-1} is confirmed by this experiment.

It is suggested that the maximum at 1678-1679 cm^{-1} is attributed to the random coil conformation, whereas the maxima at 1691-1692 cm^{-1} and ±1687 cm^{-1} are associated with β-turn structures. The shoulders at 1666-1667 cm^{-1} and ±1656 cm^{-1} are attributed to the α-helical conformation. The experiment with the methanol treatment of the regenerated *B. mori* reveals that after methanol treatment the former peaks decrease considerably relative to the maxima at about 1700 cm^{-1}, whereas the relative intensity of the latter peaks does not considerably change.

The assignment of the shoulder at 1644 cm^{-1}, only clearly observed for egg sac spider silk, is not clear. Some authors associated a band at about 1640 cm^{-1} with β-turn structures [Hollosi *et al.* 1994, van Dijk *et al*. 1997]. A peak at about 1640 cm^{-1} is also observed for the absorption of liquid water [Smith 1999]. In the Raman spectra, as shown in Figure 6.10, however, this peak is also observed for the spider silks. Since Raman spectra are insensitive to water absorption, the peak at about 1640 cm^{-1} cannot be associated with water. From the experiments with methanol (Chapter 7), it was suggested that this peak is associated with the side chain vibration of possibly glutamine because of the high abundance of glutamine and glutamic acid in the spider silks compared to the silkworm silks (Chapter 4).

A peak at about 1612 cm^{-1} in the DRIFT spectra has been assigned to protein side chains, especially amide or aromatic groups [Tso *et al.* 2005]. In Raman spectra peaks at about 1615-1550 cm^{-1} are better visible and are due to vibrations of phenylalanine (Phe) and tyrosine (Tyr) [Tu 1982, Miura *et al.* 1988, Taddei *et al.* 2004, Zheng *et al.* 2004, Pellerin *et al.* 2005]. The differences in peak heights can be partly explained by the different relative abundance of these aromatic amino acids in the different silks (see Chapter 4). The phenylalanine residues in egg sac spider silks are also identified by the strong peak at about 1001 cm^{-1} [Tu 1982]. The

tyrosine residues are also detectable in the peaks at about 850, 830 and about 640 cm^{-1} [Tu 1982, Edwards & Farwell 1995, Taddei *et al.* 2004, Pellerin *et al.* 2005], as seen in Figure 6.14

Based on the suggested assignments in the Amide I region, we can conclude that the β-sheet content seems limited for egg sac and dragline spider silk. The spider silks seem to show a higher fraction of β-turn conformations. The random coil content seems the highest for egg sac and *B. mori* silk. The higher intensity at lower wave number is probably due to the contribution of side chain vibrations, although a higher content of helical structures is also possible.

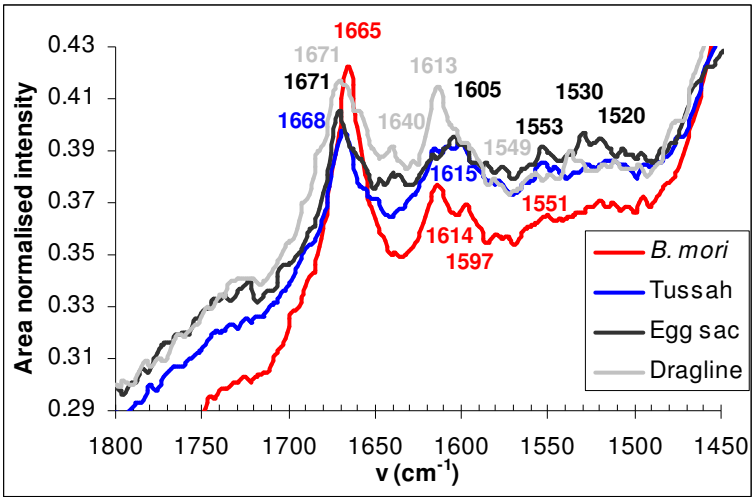

Figure 6.10 - Raman spectra in the 1800-1450 cm^{-1} region for the different silks

With respect to the Raman spectra (Figure 6.10), the maxima at about 1665-1670 cm^{-1} indicate that the structures are dominated by the antiparallel β-sheet structure, as found for the Silk II structure [Frushour & Koenig 1975a, Edwards & Farwell 1995, Taddei *et al.* 2004]. The dragline and egg sac spider silk show a much broader band and at a higher wave number of 1671 cm^{-1}, it may result from the higher contribution of β-turn structures, as also suggested for the DRIFT spectra. The dragline and egg sac fibre also show a clear shoulder at about 1660 cm^{-1} and a clear peak at about 1640 cm^{-1}. In the spectra of Tussah, a shoulder is observed at 1650-1655 cm^{-1}, assigned to the α-helical structure (Table 6.2) and confirmed by Tsukada et al. [1995]. The shoulder at about 1660 cm^{-1} is suggested to be due to the presence of random coil or Silk I conformation [Monti *et al*. 2001, 2003, Zhou *et al*. 2004, Taddei *et al*. 2004] or even helical (Table 6.2), whereas the assignment of the peak at about 1640 cm^{-1} is, as suggested previously, due to a side chain vibration.

6.5.4. AMIDE II REGION – 1510-1580 CM^{-1}

In this region (Figure 6.9), for the different silks, three broad bands can be detected in DRIFT spectra: 1566-1561 cm^{-1}, 1556-1552 cm^{-1}, 1540-1537 cm^{-1}.

The assignment to secondary structure as found in literature is summarized in Table 6.1. The sequence in assignment with increasing wave number is: β-sheet (parallel/antiparallel), random coil/α-helix, β-turn and/or antiparallel β-sheet.

Taking into account this sequence, the band at 1566-1561 cm^{-1} could be assigned to β-turn or anti-parallel intermolecular β-conformation [Venyaminov & Kalnin 1990] and the band at 1556-1552 cm^{-1} to random coil or α-helix and finally the band at 1540-1537 cm^{-1} to β-sheet. However, the low intensity of the band at about 1537 cm^{-1} for Tussah and *Bombyx mori* makes the last assignment incorrect.

Based on the experiments in which the conformational transition is induced in regenerated *B. mori* (see Chapter 7), the following assignment is suggested: 1566-1561 cm^{-1} to β-sheet, 1556-1552 cm^{-1} to β-turn and a side chain vibration to 1540-1537 cm^{-1}.

The assignment of the very weak shoulder at ±1520 cm^{-1} is not certain. Wilson *et al.* [2000] found peaks at about 1550 cm^{-1} and 1515 cm^{-1} for a synthesized protein containing poly-(Ala-Gly-Gly) blocks. Both peaks are best observed for the spider silks, this can confirm the presence of p-AGG motifs in both silks. Peaks at about 1515 cm^{-1} are often associated with out-of-phase vibrations of adjacent amide groups involved in an antiparallel β-sheet structure [Chen *et al.* 1996, Freddi *et al.* 1997, 1999, Wilson *et al.* 2000, Min *et al.* 2004, Ha *et al.* 2005]. Furthermore, a resolved sharp line at about 1515 cm^{-1} has been assigned to tyrosine ring absorptions [de Jongh *et al.* 1996]. Also the experiment with methanol did not allow the assignment of this peak, so a side chain vibration is suggested.

The low resolution of the Amide II region in the Raman spectra (Figure 6.10) does not allow the deduction of complementary information.

6.5.5. THE 1500-1100 CM^{-1} REGION

Figure 6.11 and Figure 6.12 show the DRIFT, respectively, FT-Raman spectra in the 1500-1100 cm^{-1} region for the different silks.

The band at 1450-1453 cm^{-1} is a characteristic band for polypeptides and is assigned to asymmetric methylene (CH_2) and methyl (CH_3) bending [Krimm & Bandekar 1986]. Methyl groups are particularly abundant in these silks, since the alanine content is estimated at about 20-24% for spider silks, at about 40-50% for Tussah silk and at about 30% for *Bombyx mori* silk of the total amino acid content. This band is often used as a standard for normalization in vibrational spectra of proteins. The experiments with the regenerated *B. mori* (Chapter 7) reveal that it may not be correct to do this due to an observed shoulder at higher wave number.

The peak/band at ±1410 cm^{-1} in the DRIFT and Raman spectra is attributed to side chain vibrations (Tyr, Glu or Asp) [Pellerin *et al.* 2004]. All silks contain a considerable amount of Tyr, Glu and/or Asp residues (Chapter 4), what makes this

assignment acceptable. Glu and Asp residues are thought to be located in the β-bends found between the antiparallel β-sheets in *B. mori* silk [Zhou *et al.* 2000, Pellerin *et al.* 2004]. In the Raman spectra, the region 1420-1350 is less resolved, but clearly shows some different bands for the silks, probably associated with the different relative contributions of these amino acids in the different silks.

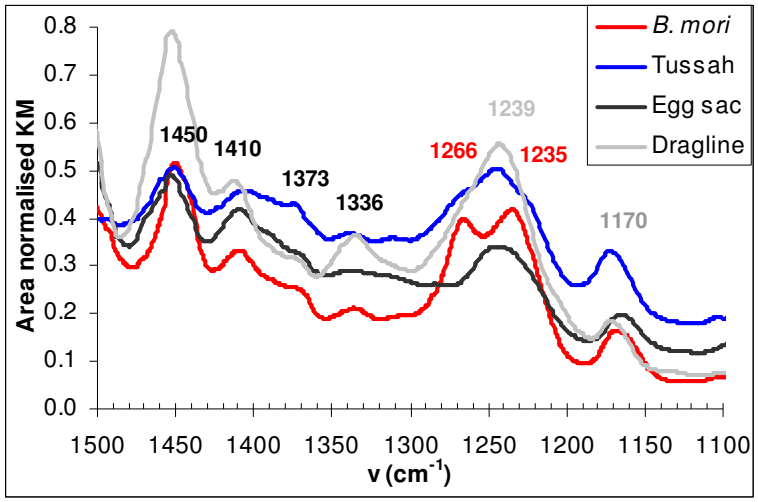

Figure 6.11 - DRIFT spectra in 1500-1100 cm^{-1} region

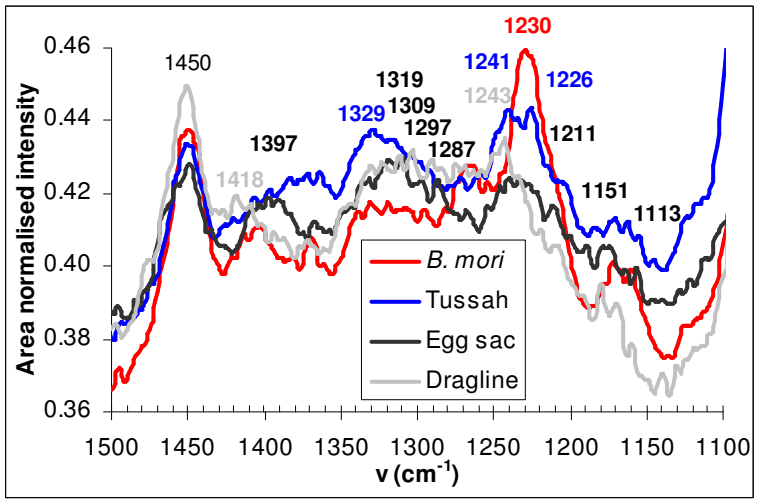

Figure 6.12 - FT-Raman spectra in the 1500-1100 cm^{-1} region

With respect to the Amide III region, in the Raman spectra, this region is less resolved than in the DRIFT spectra.

At ±1373 cm^{-1} a weak maximum (or shoulder) is observed in the DRIFT spectra for all silks, and most clearly for Tussah silk. In literature [Krimm & Bandekar 1986], a medium peak at 1370 cm^{-1} is observed for Pro-Leu-Gly-NH_2 (Type II β-turn), while

a medium weak maximum at 1372 cm^{-1} is observed for β-poly(L-alanine) (β-sheet) and a strong peak at about 1380 cm^{-1} for α-poly(L-alanine) (α-helix). So, this 1373 cm^{-1} maximum may indicate the presence of poly(Ala) since it is a known, highly repeated, motif for Tussah silk. Although the length of this motif changes for the different silks, the motif is also found for *A. diadematus* dragline silk (n = 6-8) [Guerette *et al.* 1996], *A. diadematus* egg sac silk (n ≤ 8), and Tussah silk (n = 10-15) (see also Chapter 5). The length of the A_n chain in *B. mori* is restricted to 2 or 3 and is not really identified as a motif in this silk type. It seems that the height of the peak can be considered as a measure for the repeat length of the poly-alanine motif.

In the region 1350-1330 cm^{-1} a broad maximum at about 1336 cm^{-1} can be observed in the DRIFT spectra. In the Raman spectrum, the band is extended to lower wave numbers and shows much more noise. Monti *et al.* [2003] observed peaks at 1334 cm^{-1}, 1387 cm^{-1} and 1411 cm^{-1} for a poly-alanylglycine peptide and assigned these peaks to the Silk I structure. This combination is more or less found for all these silks, so it should point out the presence of a poly-Ala-Gly motif and a Silk I structure. The AG-motif is known to be markedly present in *B. mori* (see Chapter 5) whereas in the other silks the AG sequence is present in the known GX-motifs, but is as such not necessarily repeated.

In literature, the assignment to secondary structure of the Amide III region (1300-1200 cm^{-1}) can be found [Griebenow *et al.* 1999, Krimm & Bandekar 1986, Fu *et al.* 1994] as was reported in Table 6.1. With respect to the assignment to α-helix, no consensus in literature could be found. There is also a large overlap between the regions assigned to α-helix and random coil, which makes it difficult to differentiate between both.

Taking into account Table 6.1, for our silk spectra, we can conclude that the weak band at about 1300 cm^{-1} in the DRIFT spectra can be assigned to the β-turn structures present in all silks. In the Raman spectra, this peak is more difficult to detect.

In the Amide III region of the DRIFT spectra of Tussah silk, three components can be differentiated. This is in agreement with the structure of Tussah containing both β-sheet, α-helical and random coil structures. *B. mori* shows a real splitting in two peaks at about 1266 cm^{-1} and 1236 cm^{-1} in the DRIFT spectra in agreement with the combination of β-sheet and random coil conformation found in *B. mori*. The component at about 1244 cm^{-1} is then suggested to be associated with the α-helical structure. The assignment to β-sheet and random coil structure is less clear from these experiments and taking into account the literature for silk (Table 6.4 and Table 6.6).

From the experiments with the regenerated samples (Chapter 7), we could conclude that the maxima at about 1265 cm^{-1} and 1235 cm^{-1} are assigned to the β-sheet and random coil structure, respectively.

Then we can conclude that the structure of the dragline is dominated by the α-helical structure, with some small fractions of β-sheet and random coil conformation. Furthermore, we would expect egg sac spider silk to contain mostly α-helical and random coil structures, since the shoulder at about 1266 cm^{-1} is not observed for this

type of silk (neither in DRIFT nor in Raman). These results are in agreement with the proposed structure for the spider silks based on the Amide I region.

All silks also show a peak around 1170 cm^{-1} in the DRIFT spectra. Edwards & Farwell [1995] associated peaks at about 1171-1172 cm^{-1} to C-C stretching, whereas peaks at about 1160-1166 cm^{-1} to a combination of C-C stretching and C-OH bending. Peaks at about 1172-1173 cm^{-1} (sometimes in combination with a peak at 1208 cm^{-1}) were attributed to vibrations of the side chain of the tyrosine (Tyr) residue [Takeuchi *et al.* 1989, Monti *et al.* 2005]. However, also α-poly-alanine and β-poly-alanine show this peak [Krimm & Bandekar 1986], what makes the assignment to the tyrosine residue less probable. The intensity seems the highest for Tussah silk, what could be expected because of the longer repeats of the $(Ala)_n$ motif. For Tussah and dragline spider silk, this peak is found at a higher frequency (1173, resp. 1172 cm^{-1}) than for *B. mori* and egg sac spider silk (1168, resp. 1165 cm^{-1}). Possibly, a link to a different secondary structure for the poly-alanine repeats can be made. However, the experiment with methanol reveals that this peak was situated at almost the same wave number (1170-1171 cm^{-1}) before the treatment and after the conformational transition. At lower methanol concentrations, the peak broadened and shifted to a higher wave number (1173-1175 cm^{-1}) attributed to the formation of the Silk III structure (3_2 helical structure). The untreated and methanol treated Tussah samples showed maxima at 1173-1174 cm^{-1}. A shift to a somewhat higher wave number can possibly indicate a more helical structure for the poly-alanine motif situating in the more amorphous regions, since the crystalline regions (characterized by the β-sheet structure) are not affected by a methanol treatment.

6.5.6. THE 1100-450 REGION

Finally, Figure 6.13 and Figure 6.14 respectively show the DRIFT and Raman spectra in the 1100-500 cm^{-1} region for the different silks.

The Amide IV region of the studied silks is characterized by the region 1100-1050 cm^{-1} where in fact in the DRIFT spectra some overlapping peaks can be found, around 1071 cm^{-1}, 1055 cm^{-1}, and 1028 cm^{-1}. The peak at 1055 cm^{-1} is only clearly observable for Tussah and dragline, in contrast to *Bombyx mori* and egg sac spider silk for which this peak is hardly visible as a shoulder. It is clear that for these latter silks, the intensity at 1071 cm^{-1} is higher. For Tussah, however, the shoulder at 1071 cm^{-1} is clearly observable. For dragline, the intensities of both peaks seem comparable.

The peak at 1071 cm^{-1} is mainly attributed to C^{α}-C^{β} stretching, and Raman peaks at the same frequency are also found for *Nephila edulis* and *Samia cynthia ricini* [Rousseau *et al.* 2004]. The Raman peak is shifted to 1083-84 cm^{-1} for *B. mori*, and to 1094 cm^{-1} for Tussah [Monti *et al*. 2005, Tsukada *et al*. 1995] and was assigned to β-sheet. This is in accordance with the maxima found in the recorded Raman spectra on *B. mori* and Tussah silk (Figure 6.14).

A shoulder at 1028 cm^{-1} is observed for all silks, except for dragline, where it is a weak peak. Zheng *et al*. [2004] attributed a peak at about 1032 cm^{-1} to a side chain vibration of phenylalanine. However, the phenylalanine content is the highest for egg sac spider silk (±3%) and is not observed for this silk. A medium peak at this

frequency is also observed for poly-glycine II that is known to form a threefold 3_1 helix. This peak points out the availability of poly-Gly motifs in all these silks. For spider silk and Tussah, the sequence of GG is restricted to 2 or 3. In *B. mori* the availability of a G_n motif is not clear. It may be a confirmation of the available 3_1 helical structure in the Gly-rich motifs in dragline and egg sac spider silk for the Gly-rich motifs.

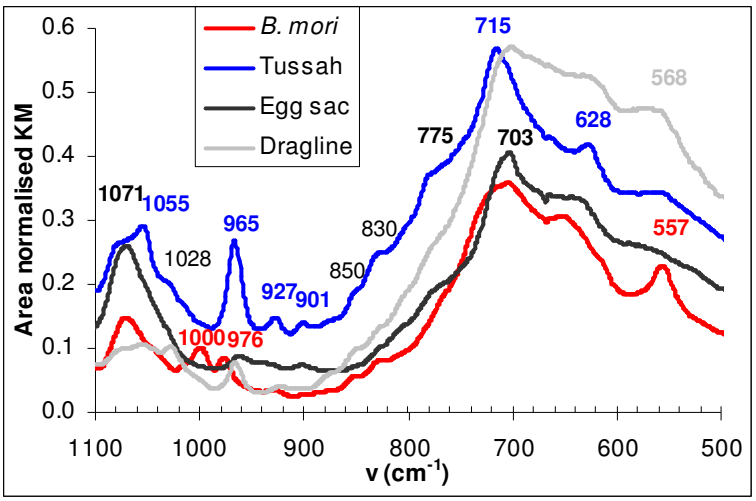

Figure 6.13 - DRIFT spectra in the 1100-450 cm^{-1} region

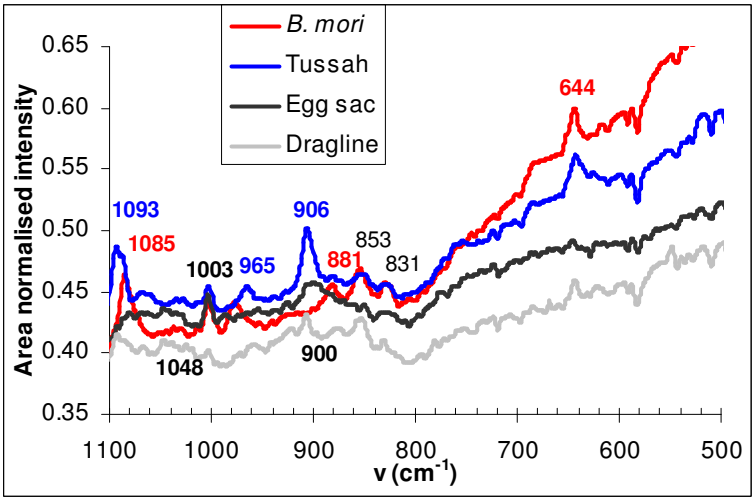

Figure 6.14 - FT-Raman spectra in the 1100-500 cm^{-1} region

Taking into account the known structure of *B. mori* and Tussah silk, we conclude that the peak at about 1055 cm^{-1} is attributed to the α-helical structure. In the experiment with regenerated *B. mori* (Chapter 7), the untreated sample showed a maximum at about 1057 cm^{-1}, with a shoulder at about 1070 cm^{-1}. This shoulder is possibly attributed to β-sheet or β-turn structures that are not completely dissolved

what confirms the presence of small β-sheet or β-turn structures in egg sac spider silk. Since random coil and α-helical structures are often difficult to differentiate in FT-IR spectroscopy, it is indeed possible that the assignment of the peak at about 1055-1060 cm^{-1} is a random coil structure for *B. mori* regenerated silk and an α-helical structure for Tussah and dragline silk.

Based on this assignment, for the spider silks, the same conclusions can be made as those concluded from the Amide III region. Egg sac spider silk is dominated by the β-sheet or β-turn structures with some contribution of a helical structure, whereas in dragline spider silk, the structure seems dominated by a helical, possibly 3_1 helix, structure with equal contributions of β-sheet and random coil structures.

A shift to smaller frequency, to about 1016 cm^{-1}, is observed for polyglycine II that is known to be an antiparallel-chain rippled β-sheet. However, even for α-poly-alanine, known to form an α-helical structure, the weak IR-peak is observed at 1016 cm^{-1}. So, the assignment of a possible shoulder at this wave number is not clear. In regenerated *B. mori* silk, in this region only at this wave number a peak is observed, so it seems a marker for the random coil or Silk I structure (possibly β-turn).

Only *B. mori* silk shows the maxima at 1000 cm^{-1} and 976 cm^{-1}. For Raman spectra, a peak at 1001-1003 cm^{-1} was attributed to aromatic ring bridge vibrations in phenylalanine and tyrosine [Pellerin et al. 2005, Rousseau *et al.* 2004] and was indeed observed in *B. mori* and *N. edulis*, however it was not observed in a wild silkworm silk *S.c. ricini* [Rousseau *et al.* 2004]. Since the tyrosine and phenylalanine content of *B. mori* is comparable with that in Tussah, it does not explain the marked peak for *B. mori*. The assignment of the peak at 976 cm^{-1} therefore remains unclear. A possible explanation is a split-up of a band at about 966 cm^{-1} in two bands as is found in the Amide III region, so that the β-sheet peak is shifted to higher frequencies. They can also be considered as characteristic markers for the GAGAGS sequence that is known to form a β-sheet structure in *B. mori*.

A peak at 965-970 cm^{-1} is attributed to the poly-alanine chain and is consequently assigned to β-sheets by several authors [Tsukada *et al*. 1995, Kweon & Park 1999, Kweon *et al.* 2000, 2001, Freddi *et al.* 1997, Magoshi *et al.* 1977, Taddei *et al.* 2003]. Thus, the presence of the peak at ±966 cm^{-1} should point out the existence of poly-Ala motifs in spider silks and clearly in Tussah silk. This motif is indeed found for dragline (n=6-8), *Araneus diadematus* egg sac silk (n≤8), and Tussah silk (n=10-15). The length of the A_n chain in *B. mori* is restricted to 2 or 3 and is not really identified as a motif in this silk type. Here, it seems that the height of the peak is a measure for the length of the A_n chain, similarly as for the peaks at about 1373 cm^{-1} and 1170 cm^{-1}. The relative intensities of this peak are comparable for DRIFT and Raman spectra: the intensity is much lower for the spider silks.

Also in the region 900-930 cm^{-1} the different silks can be distinguished. For Tussah silk, the peaks at 927 cm^{-1} and 901 cm^{-1} are markedly visible compared to the other silks. Peaks at about 900 cm^{-1} have been associated with the Ala_n chain [Krimm & Bandekar 1986, Kweon *et al.* 2000, Freddi *et al.* 1997]. The height of this peak for Tussah is also in agreement with the much higher length of the Ala_n chain, compared to the other silks. Some researchers assigned this peak to an α-helical conformation [Kweon *et al.* 2000, Freddi *et al.* 1997]. However, Krimm & Bandekar [1986]

found a peak at about 910 cm^{-1} for polyalanine in both β-sheet structure and α-helical structure. Also dragline shows observable peaks at resp. 908 cm^{-1} and 922 cm^{-1}. Egg sac spider silk, however, shows an observable peak only at 902 cm^{-1} and a weak shoulder (to the peak at about 960 cm^{-1}) at about 930 cm^{-1} whereas *B. mori* shows one only at 929 cm^{-1}. Possibly, it can indicate that in Tussah, dragline and possibly egg sac spider silk polyalanine is present in different conformational states, whereas in *B. mori* only one conformational state is detected.

It is known from literature that the (weak) features at ±850 and ±830 cm^{-1} make a doublet attributed to Fermi resonance of the aromatic side chain of the tyrosine residue. It is well-known that the relative intensity of the tyrosine doublet (R_{Tyr} = I_{850}/I_{830}) can be used as a spectral marker of the environment of the hydroxyl groups and the strength of hydrogen bonds involving these groups [Siamwiza *et al.* 1975, Monti *et al.* 1998, Shao *et al.* 1999, Taddei *et al.* 2004, Rousseau *et al.* 2004]. If this ratio is compared for the different techniques, as shown in Figure 6.15, this ratio seems comparable for *B. mori*, Tussah and egg sac spider silk and somewhat higher for dragline spider silk. The tyrosine residues normally exist in the amorphous regions, which contain most of the amino acids with bulky and polar side chains. An increase in R_{Tyr} leads to the conclusion that the hydrogen bonds involving the tyrosine residues are weaker, and consequently the mobility of the tyrosine residues is higher [Monti *et al.* 1998] in dragline spider silk compared to the other silks.

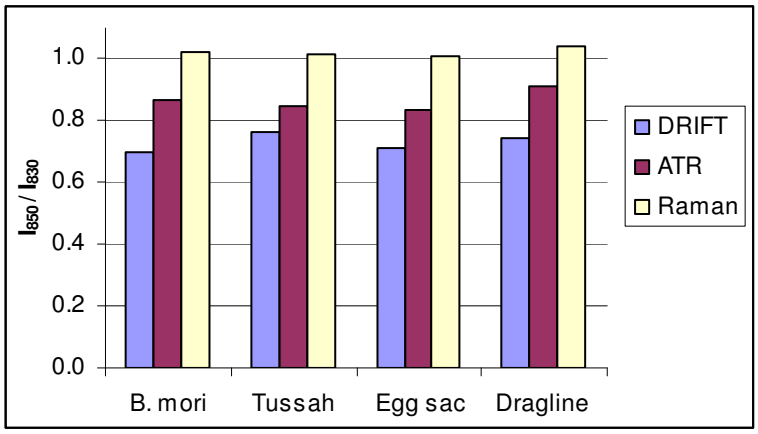

Figure 6.15 - The intensity ratio I_{850}/I_{830} for the different silks

The aromatic side chain of the tyrosine residue gives also rise to symmetrical vibrations, detectable by Raman, at 642 cm^{-1} and 1002 cm^{-1}. This explains partly the broad band observed at the Amide V region between 600 and 700 cm^{-1} in the DRIFT spectra.

At about 775 cm^{-1} a shoulder is clearly observable for Tussah and for egg sac spider silk. The assignment of this peak is not clear.

In literature, the assignment to secondary structure of the Amide V region in FT-IR spectra can be found [Krimm & Bandekar 1986, Fu *et al.* 1994] and is summarized in Table 6.1.

At about 700 cm^{-1}, for all silks a broad band is observed. However, for Tussah this band is shifted to a higher frequency of 715 cm^{-1}. According to literature, this band can point out the presence of an anti-parallel pleated β-sheet [Krimm & Bandekar 1986, Kweon *et al.* 2000, Freddi *et al.* 1997, Magoshi *et al.* 1977]. The shift to a higher frequency for Tussah could be due to the longer length of the β-sheet.

In this region, it seems that there is an overlapping band at about 665 cm^{-1} that is found for all silks. For most silks, except for *B. mori*, there is also a band (or shoulder) at about 630 cm^{-1}. According to Krimm & Bandekar [1986], the combination of these two bands can be associated with an α-helical conformation. Although, other authors [Kweon *et al.* 2000, Freddi *et al.* 1997] assign a band at about 660-664 cm^{-1} to a random coil conformation. *B. mori* shows only one band at about 653 cm^{-1}, probably this can be attributed to random coil conformation. An absorption at 610 cm^{-1} has also been mentioned as characteristic for the Silk I or β-turn structure [Magoshi *et al.* 1979]. So indeed, it seems that the *B. mori* silk fibre consists of a combination of β-sheet and random coil whereas in the other fibres also a small contribution of helical conformations and/or β-turn structures can be found.

With respect to the peak/band at about 560 cm^{-1}, in the experiments with the regenerated *B. mori*, even the methanol treated samples show clear peaks at this position. The assignment of this peak is not clear. It is remarked that the maximum of this band is considerably higher for the spider silks, possibly indicating a lower strength of the hydrogen bonds or a longer structure.

From the spectral analysis of the Amide V region, we would expect that the β-sheet content is the highest for Tussah silk, followed by spider egg sac silk. However, the much lower wave number (703 cm^{-1} versus 715 cm^{-1}) of the maximum can indicate a different conformation: smaller in size or β-turn structure.

It is clear that in this last region, limited information can be deduced from the Raman spectra (Figure 6.14).

6.5.7. SUMMARY OF DIFFERENCES BASED ON DRIFT SPECTRA

Table 6.8 gives a summary of the observed maxima in DRIFT spectra of the different silks, and the proposed assignment to motif and/or secondary structure. Remarkable differences between the silks are indicated in bold.

The assignments for which no reference is indicated, are based on the performed experiments.

Table 6.8 - Summary of absorption maxima and their assignment for DRIFT spectra of silks

B. mori	Tussah	Egg sac	Dragline	Assignment	Reference
				Amide A-B regions	
3500 sh	3500 sh	3500 sh	3500 sh	OH, CO_2^- functional groups	Krimm & Bandekar 1986
3321 vs	3327 s	3315 vs	3303 vs	Amide A, NH stretching	Krimm & Bandekar 1986
3081 m	3083 m	3083 m	3082 m	Amide B	Krimm & Bandekar 1986
2979 m	2981 m	**2965 m**	2977 m	CH_2 or CH_3 symmetrical stretching	Krimm & Bandekar 1986, Edwards & Farwell 1995
2934 m	2934 m	2936 m	2936 m	CH_2 or CH_3 asymmetrical stretching	Krimm & Bandekar 1986, Edwards & Farwell 1995
2877 w	2875 w	2877 w	2880 w	$C^{\alpha}H^{\alpha}$ stretching, poly(L-alanine) or CH_2 asymmetrical stretching	Taddei *et al.* 2003, Edwards & Farwell 1995
				Amide I region	
1703 s	**1703 s**	1700 sh	1700 sh	β-sheet	
1691 s	1692 m	1691 s	1692 vs	β-turn	
1687 s	1687 sh	1687 s	1687 sh	β-turn	
1680 s	1679 sh	**1680 s**	1680 sh	random coil	
		1666 sh	1666 sh	α-helix	
		1656 sh	1651 sh	α-helix	
		1644 sh	1644 sh	side chain vibration	
1612 vw		1612 sh		side chain vibrations (Tyr, Phe)	Zheng *et al.* 2004, Tso *et al.* 2005

B. mori	**Tussah**	**Egg sac**	**Dragline**	**Assignment**	**Reference**
				Amide II region	
1562 w	1562 w	1561 w	1561 w	β-sheet	
1556 vw	1556 vw	**1552 w**	**1552 w**	β-turn, AGG motif	
1538 sh	1537 sh	**1538 vw**	1538 sh	side chain vibration	
1515sh		1515 sh	1515 sh	AGG motif	
1504 vw	1493 vw	1500 sh	1500 sh	Side chain vibration	
	1459 sh	**1459 sh**			
1450 m	1451 m	1454 m	1452 m	CH_2 and CH_3 bending	Krimm & Bandekar 1986
				Amide III region	
1409 w	1407 w	1409 w	1413 w	Silk I	Monti *et al.* 2003
1377 w	1373 w	1373 sh	1373 sh	CH_3 symm. stretching, Silk I	Moore & Krimm 1976, Monti *et al.* 2003
1336 w	1338 vw	1335 w	1335 m	CH_3 symm. bending, Silk I	Moore & Krimm 1976, Edwards & Farwell 1995, Monti *et al.* 2003
1310 sh	1312 vw	1284 vw		β-turn	Monti *et al.* 2003
1266 m	**1266 sh**		**1266 sh**	β-sheet	Bhat & Nadiger 1978, Sun *et al.* 1997, Um *et al.* 2001, Kweon *et al.* 2001, Ayutsede *et al.* 2005
	1244 m	**1244 m**	**1243 m**	α-helix	
1235 m	**1235 sh**			random coil	Bhat & Nadiger 1978, Sun *et al.* 1997, Um *et al.* 2001, Kweon *et al.* 2001, Ayutsede *et al.* 2005

B. mori	**Tussah**	**Egg sac**	**Dragline**	**Assignment**	**Reference**
1168 m	1173 m	**1165 m**	1172 m	NC^{α} stretching, H^{α} bending, p-Ala motif	Taddei *et al.* 2003
1102 vw	1103 vw			p-Ala motif, α-helix or Silk I	Tsukada *et al.* 1994, Edwards & Farwell 1995, Taddei *et al.* 2003, Monti *et al.* 2003
Skeletal stretch or Amide IV mode					
1071 m	**1071 sh**	**1071 m**	**1071 sh**	(1063) CH_3 rocking, β-sheet	Moore & Krimm 1976, Tsukada *et al.* 1994
	1054 m		**1055 w**	random coil / α-helix	
	1028 sh		**1028 w**	p-Gly, helical structure	
1000 w				GAGAGS motif, β-sheet	
977 w				GAGAGS motif , β-sheet	
	967 s	**962 vw**	966 w	β-sheet, p-Ala motif	Tsukada *et al.* 1994, Monti *et al.* 2005
929 vw	**927 w**	927 sh	922 vw	α-helix or Silk I	Monti *et al.* 2003, Zheng *et al.* 2004
	901 w	902 vw	908 vw	α-helix, p-Ala motif	Tsukada *et al.* 1994, Monti *et al.* 2005
850 vw	850 sh	850 sh	850 sh	Fermi resonance of Tyr side chain	Siamwiza *et al.* 1975, Rousseau *et al.* 2004

B. mori	**Tussah**	**Egg sac**	**Dragline**	**Assignment**	**Reference**
826 vw	827 sh **775 sh**	827 sh **775 sh**	827 sh	Fermi resonance of Tyr side chain	Siamwiza *et al.* 1975, Rousseau *et al.* 2004
			Amide V mode		
704 s	**715 vs**	703 s	702 vs	β-sheet	Bhat & Nadiger 1978, Tsukada *et al.* 1994, Kweon *et al.* 2000, 2001
	665 vw	664 vw	666 sh	random coil or Silk I	Tsukada *et al.* 1994, Freddi *et al.* 1997, Kweon & Park 1999, Kweon *et al.* 2000, 2001, Monti *et al.* 2003
653 m	645 vw	643 vw	646 w	(643) Tyr side chain, Amide IV, random coil or Silk I	Bhat & Nadiger 1978, Asakura *et al.* 1985, Magoshi *et al.* 1979, Takeuchi *et al.* 1989, Edwards & Farwell 1995, Monti *et al.* 2003, Zheng *et al.* 2004, Monti *et al.* 2005
	628 m	630 sh	633 m	(621) Phe side chain, α-helix	Tsukada *et al.* 1994, Kweon & Park 1999, Kweon *et al.* 2001, Zheng *et al.* 2004
557 m	561 w	567 sh	568 m	CCC or CCN stretching, Amide IV	Edwards & Farwell 1995

6.6. FT-IR ATTENUATED TOTAL REFLECTION (ATR) SPECTRA

6.6.1. THE AMIDE A AND B REGIONS

Figure 6.16 shows the Amide A and B regions in the ATR spectra for the different silks.

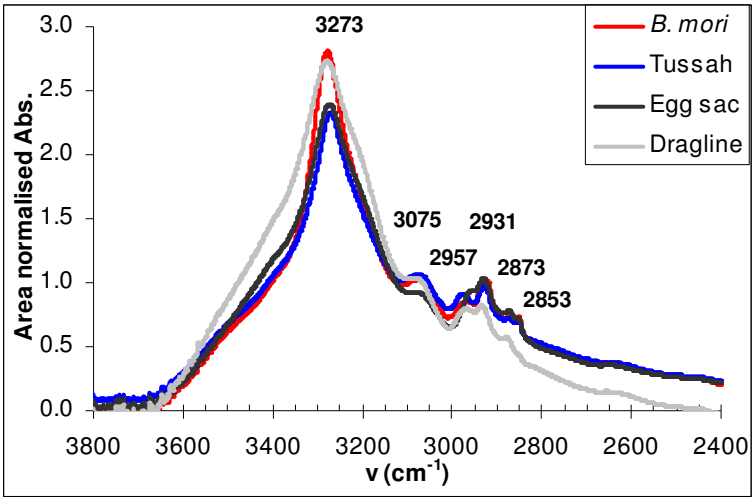

Figure 6.16 - Amide A and B regions in ATR spectra

In the ATR spectra the spectral variation is less pronounced as compared to the DRIFT spectra. Maxima are observed at about the same wave number as in those obtained with DRIFTS. The peak assigned to CH_3 asymmetrical stretching is shifted to lower wave numbers (about 2970 cm^{-1}) than in DRIFT spectra (at about 2980 cm^{-1}). It is noted that similar to the DRIFT spectra, the peak at the higher wave number (about 2970 cm^{-1}) is shifted to a lower wave number (2957 cm^{-1}) for egg sac spider silk.

The peak assigned to the CH_2 symmetrical stretching (at about 2853 cm^{-1}) [Edwards & Farwell 1995] is clearly observed in ATR-FTIR in contrast to DRIFTS, where this peak was not visible.

The difference between the silks is seen mostly in the relative intensity of the peaks at about 2960 cm^{-1} and 2930 cm^{-1} assigned respectively to CH_3 asymmetrical and symmetrical stretching. Figure 6.17 shows the intensity ratio of the peaks assigned respectively to CH_3 asymmetrical (2980-2970 cm^{-1}) and symmetrical stretching (about 2930 cm^{-1}) for the DRIFTS and ATR spectra. The same trend is followed for the spectra obtained with both techniques. It is suggested that there is an invisible band overlapping with one of these bands, which is varying with the type of silk.

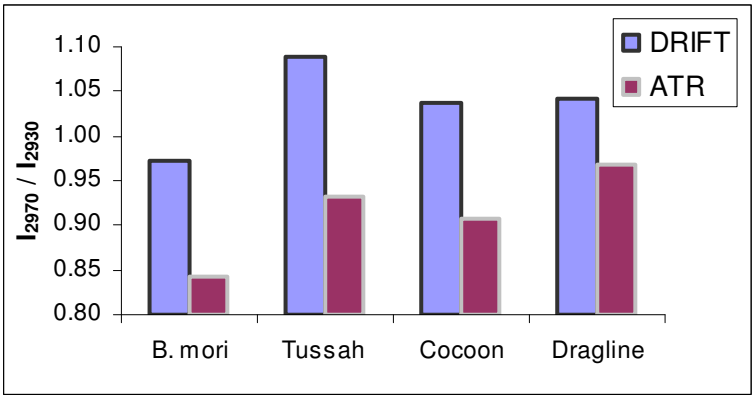

Figure 6.17 - Intensity ratio of maxima at ±2980-2970 cm^{-1} to ±2930 cm^{-1} for DRIFT and ATR spectra

6.6.2. THE AMIDE I AND II REGIONS

Figure 6.18 shows the Amide I and II regions in the ATR spectra of the different silks.

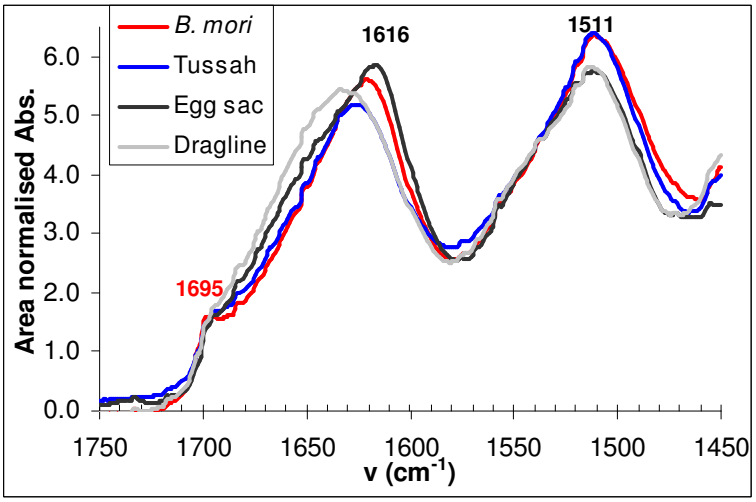

Figure 6.18 - The Amide I-II region in ATR spectra

The Amide I and II regions clearly show fewer details than in the DRIFT spectra. The *Bombyx mori*, Tussah and egg sac spider silk samples contain some antiparallel β-sheet, as is confirmed by the strong absorption at about 1620-1630 cm^{-1} and the weak shoulder at about 1695 cm^{-1} [Byler & Susi 1986, Venyaminov & Kalnin 1990, Dong *et al.* 1990, Haris & Chapman 1992]. For dragline spider silk the maximum is shifted to 1634 cm^{-1}, which is still to be associated with the β-sheet structure. The high-frequency peak of the anti-parallel β-sheet structure (1695 cm^{-1}) has, however, decreased to a shoulder.

Taking into account the experiment with methanol (Chapter 7), we would expect a high amount of random coil structure for dragline. The shoulder observed for egg sac spider silk may also indicate the random coil fraction, although a type of helical structure is also a possibility since the distinction between random coil and Silk III (3_2 helical) structure could not be made with ATR-spectroscopy in the experiment with methanol. Moreover, also in the spectrum of the Tussah sample, apart from a shift to a lower wave number, no indication of an α-helical structure is found. Further NMR experiments (Chapter 8) were performed to confirm the presence of the α-helical structure, however, even with this technique the detection was difficult.

The Amide II region is characterised by a strong absorption band at 1511-1514 cm^{-1} for all silk fibres. All fibres also show a weak shoulder at about 1557 cm^{-1}. With the assignments as given by literature [Byler & Susi 1986, Venyaminov & Kalnin 1990, Dong *et al.* 1990, Haris & Chapman 1992] (Table 6.1), the Amide II region of the ATR spectra does not clarify which conformation is present in the silk fibres. Also the ATR-experiments on the methanol treated samples reveal no more details from the Amide II region.

6.6.3. THE REGION 1500-1100 CM^{-1}

Figure 6.19 shows the 1500-1100 cm^{-1} region in the ATR-spectra for the different silks.

In this region, apart from the Amide III region, the same conclusions can be made as in DRIFT spectra. In the Amide III region (1300-1200 cm^{-1}), the maxima are shifted to lower wave numbers. For *B. mori*, the peaks at 1255 cm^{-1} and at 1227 cm^{-1} are clearly different in intensity, in contrast to what is observed in the DRIFTS spectrum. In both spectra of egg sac spider silk fibre, the shoulder at 1266 cm^{-1} is not observed. To the contrary for Tussah fibre, this shoulder is seen in the DRIFTS spectrum, but not in the ATR spectrum. The intensities of the peaks and shoulders are also clearly different in the ATR spectrum.

Also the experiment with regenerated *B. mori* (Chapter 7) does not allow an assignment to a secondary structure.

Looking at the transmission spectra, an analogous Amide III spectrum is observed for *B. mori*, a split into two peaks with comparable intensity. Also for Tussah fibre, an overlap of 3 peaks can be identified in the transmission spectra, as is seen in the DRIFT spectra. Also for the other fibres, the transmission spectra are more similar to the DRIFT spectra than to the ATR spectra. So, it seems difficult to make conclusions about the conformation based on the Amide III region. Possibly side chain vibrations also play a role in this.

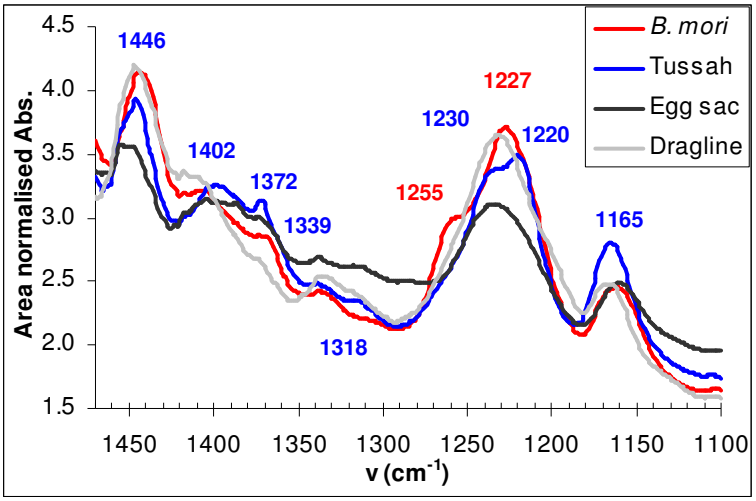

Figure 6.19 - The ATR spectral region between 1500 and 1100 cm^{-1}

6.6.4. THE REGION 1100-400 CM^{-1}

Figure 6.20 shows the 1100-400 cm^{-1} region in the ATR-spectra for the different silks.

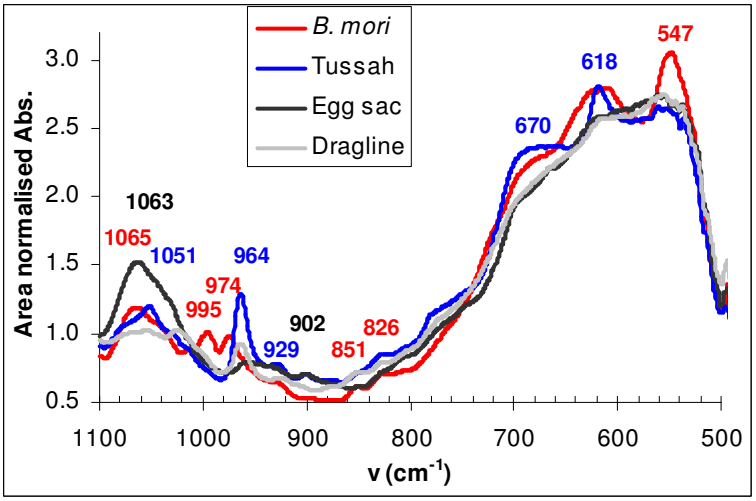

Figure 6.20 - The ATR spectral region between 1100 and 400 cm^{-1} (based on 2 spectra for each sample)

In this region as well, except for the Amide V region, spectra are obtained that are similar to those recorded with the other FT-IR spectroscopic techniques. In the Amide V region (750-500 cm^{-1}), which is also sensitive to structural conformation, the peaks are more pronounced than in DRIFT spectra (Figure 6.13). However, the

peaks at about 700 cm^{-1}, associated with a β-sheet conformation, are not seen, although it is known that Tussah and *B. mori* silks indeed contain a high proportion of β-sheet structure. Based on the ATR-experiments with methanol, the shoulder at 670 cm^{-1} and the peak at about 620 cm^{-1} can indeed confirm the β-sheet structure present in *B. mori* and Tussah fibres.

6.7. CONCLUSION

DRIFT spectroscopy can be considered as a reliable technique to study the secondary structure of silk fibres, and more in general of proteins in solid state.

The DRIFTS measurements agree quite well with the transmission measurements, apart from the Amide I and Amide II regions. In the Amide I and II regions (1500-1800 cm^{-1}), the peaks are shifted to higher wave numbers for all silks, probably due to the effect of specular reflection.

DRIFT spectra of silk fibres confirm peaks found in standard FT-IR-spectra from literature but seem to give complementary information in the 1500-1800 cm^{-1} region, where the peaks are clearly visible, without much noise. Although ATR-FTIR spectroscopy seems to result in reliable spectra in the 1500-1800 cm^{-1} region, differences with transmission and DRIFT spectra are found in the Amide III and V regions, which are also sensitive to structural conformations.

Because of the observed shifts, in Chapter 7 a conformational transition was induced for *Bombyx mori* and Tussah silk fibroin in order to make more reliable conclusions with respect to the assignments to secondary structure. The results of Chapter 7 were taken into account in the assignments to the secondary structure in this chapter.

Raman spectroscopy is not found to be a reliable technique to estimate the secondary structural components in the different silks because of fluorescence. It could also be expected that the alignment of the fibres play a role in this. With the used instruments, it was even difficult to obtain comparable spectra as found in literature for Tussah and *B. mori* silk.

Even from the Raman spectra, we conclude for egg sac spider silk that the β-sheet fraction is very limited. Because of the low resolution of the spectra, it was difficult to detect α-helix, β-turn and random coil structures in the different silks.

The general structure of *Bombyx mori* and Tussah silk is confirmed. For *B. mori*, β-sheet and random coil structures can be detected, whereas the α-helical structure is an extra structure found in Tussah. This difference allowed the identification of the secondary structure of the spider silks.

Absorption peaks in the Amide I, Amide II, Amide IV and Amide V regions reveal that egg sac spider silk of *Araneus diadematus* shows only limited amounts of β-sheet structures and seems dominated by β-turn structures in combination with random coil and helical conformations. The presence of β-turn structures is suggested not to take part in extended β-sheet structures. The linked β-turns possibly form a β-turn spiral. Furthermore, the twist in the β-sheet crystals [Barghout *et al.* 1999] (see Chapter 10 – Figure 10.14) is only possible when the β-

turns, connecting different β-strands, are longer at the outside than in the inner side. This can be confirmed by the clearly observed different maxima associated with β-turn structures.

It is further suggested that the β-sheet crystals present in egg sac spider silk are much smaller than those in the silkworm silks.

The investigated dragline spider silk seems to be dominated by β-turn structures as well, although the Amide III, Amide IV and Amide V peaks also show evidence of helical structures.

6.8. REFERENCES

Arrondo J.L.R., Goni F.M., Structure and dynamics of membrane proteins as studied by infrared spectroscopy, Prog. Biophys. Mol. Biol. 72:367-405 (1999)

Asakura T., Kuzuhara A., Tabeta R., Saito H., Conformation characterization of *Bombyx mori* silk fibroin in the solid-state by high-frequency C-13 cross polarization magic angle spinning NMR, X-Ray-diffraction, and infrared-spectroscopy, Macromolecules 18:1841-1845 (1985)

Asakura T., Ashida J., Yamane T., Kameda T., Nakazawa Y., Ohgo K., Komatsu K., A repeated β-turn structure in poly(Ala-Gly) as a model for silk I of *Bombyx mori* silk fibroin studied with two-dimensional spin-diffusion NMR under off magic angle spinning and rotational echo double resonance, J. Mol. Biol. 306:291-305 (2001a)

Ayutsede J., Gandhi M., Sukigara S., Micklus M., Chen H.E., Ko F., Regeneration of *Bombyx mori* silk by electrospinning - Part 3: Characterization of electrospun nonwoven mat, Polymer 46:1625-1634 (2005)

Barghout J.Y.J., Thiel B.L., Viney C., Spider (*Araneus diadematus*) cocoon silk: a case of non-periodic lattice crystals with a twist?, Int. J. Biol. Macromol. 24:211-217 (1999)

Bhat N.V. & Nadiger G.S., Effect of Nitrogen Plasma on the Morphology and allied Textile Properties of Tasar Silk Fibres and Fabrics, Text. Res. J., Dec., 685-691 (1978)

Byler D.M. & Susi H., Examination of the secondary structure of proteins by deconvolved FTIR spectra, Biopolymers 25:469-487 (1986)

Chen C.C., Riou S., Hsu S.L., Stidham H.D., Characterization of silk crystallization behavior on highly oriented substrates, Langmuir 12:1035-1039 (1996)

Chen X., Knight D.P., Shao Z.Z., Vollrath F., Conformation transition in silk protein films monitored by time-resolved Fourier transform infrared spectroscopy: Effect of potassium ions on *Nephila* spidroin films, Biochemistry 41(50):14944-14950 (2002)

de Jongh H.H.J., Goormaghtigh E., Ruysschaert J.-M., The different molar absorptivities of the secondary structure types in the Amide I region: An attenuated total reflection Infrared study on globular proteins, Analythical Biochemistry 242(1):95-103 (1996)

Dicko C., Knight D., Kenny J.M., Vollrath F., Secondary structures and conformational changes in flagelliform, cylindrical, major, and minor ampullate silk proteins. Temperature and concentration effects, Biomacromolecules 5(6):2105-2115 (2004)

Dong Z., Lewis R.V., Middaugh C.R., Molecular mechanism of spider silk elasticity, Arch. Biochem. Biophys. 284:53-57 (1991)

Edwards H.G.M. & Farwell D.W., Raman spectroscopic studies of silk, J. Raman Spectrosc. 26:901-909 (1995)

Freddi G, Monti P, Nagura M, Gotoh Y, Tsukada M , Structure and molecular conformation of Tussah silk fibroin films: Effect of heat treatment, J. Polym. Sci. Pt. B-Polym. Phys. 35(5):841-847 (1997)

Frushour B.G. & Koenig J.L., In: Advances in Infrared and Raman Spectroscopy, Vol. 1, Clark R.J.H., Hester R.E. (Eds.), Heyden, London, 35 (1975a)

Fu F.-N., De Oliviera D.B., Trumble W.R., Sarkar H.K., Secondary Structure Estimation of Proteins Using the Amide III Region of Fourrier Transform-Infrared Spectroscopy: Application to Analyze Calcium Binding-Induced Structural Changes in Calsequestrin, Applied Spectroscopy 48(11):1432-1441 (1994)

Gillespie D.B., Viney Chr., Yager P., Raman spectroscopic analysis of the secondary structure of spider silk fiber, In: Silk polymers: material science and biotechnology, ACS Symposium Series 544, Washington DC, 155-167 (1994)

Goormaghtigh E., Raussens V., Ruysschaert J.-M., Attenuated total reflection infrared spectroscopy of proteins and lipids in biological membranes, Biochim. Biophys. Acta 1422:105-185 (1999)

Griebenow K., Santos A.M., Carrasquillo K.G., Secondary structure of proteins in the amorphous dehydrated state probed by FTIR spectroscopy – Dehydration-induced structural changes and their prevention, The Internet Journal of Vibrational Spectroscopy 3(1):1-60 (1999)

Guerette P.A., Ginzinger D.G., Weber B.H.F., Gosline J.M., Silk properties determined by gland-specific expression of a spider fibroin gene family, Science 272(5258):112-115 (1996)

Ha S.-W., Tonelli A.E., Hudson S.M., Structural studies of *Bombyx mori* silk fibroin during regeneration from solutions and wet fiber spinning, Biomacromolecules 6:1722-1731 (2005)

Haris P.I. & Chapman D., Does Fourier-transform infrared spectroscopy provide useful information on protein structures?, TiBS 17:328-332 (1992)

Hino T., Tanimoto M., and Shimabayashi S., Change in secondary structure of silk fibroin during preparation of its microspheres by spray-drying and exposure to humid atmosphere, J. Colloid Interface Sci. 266:68-73 (2003)

Hollosi M., Majer ZS., Ronai AZ., Magyar A., Medzihradszky K., Holly S., Perczel A., Fasman G.D., CD and Fourier transform IR spectroscopic studies of peptides. II. Detection of beta-turns in linear peptides, Biopolymers 34:177-185 (1994)

Koenig J.L. & Sutton P., Raman spectra of poly-L-lysine, Biopolymers 9:1229-1237 (1970)

Koenig J.L. & Sutton P., Raman scattering of some synthetic polypeptides, poly(gamma-benzyl L-glutamate), poly-L-valine and poly-L-serine, Biopolymers 10:89-106 (1971)

Krimm S. & Bandekar J., Vibrational analysis of peptides, polypeptides, and proteins. Ⅵ. Assignment of β-turn modes in insulin and other proteins, Biopolymers 19:1-29 (1980)

Krimm S. & Bandekar J., Vibrational spectroscopy and conformation of peptides, polypeptides, and proteins, Advances in Protein Chemistry 38:181-364 (1986)

Kweon H.Y. & Park Y.H., Structural and conformational changes of regenerated *Antheraea pernyi* silk fibroin films treated with methanol solution, J. Appl. Polym. Sci. 73:2887-2894 (1999)

Kweon H.Y., Um I.C., Park Y.H., Thermal behavior of regenerated *Antheraea pernyi* silk fibroin film treated with aqueous methanol, Polymer 41(20):7361-7367 (2000)

Kweon H.Y., Um I.C., Park Y.H., Structural and thermal characteristics of *Antheraea pernyi* silk fibroin/chitosan blend film, Polymer 42:6651-6656 (2001a)

Kweon H., Ha H.C., Um I.C., Park Y.H., Physical properties of silk fibroin/chitosan blend films, J. Appl. Polym. Sci. 80:928-934 (2001b)

Kweon H., Woo S.O., Park Y.H., Effect of Heat Treatment on the Structural and Conformational Changes of Regenerated *Antheraea pernyi* Silk Fibroin Films, J. Appl. Polym. Sci. 81:2271-2276 (2001c)

Li M., Tao W., Lu S., Kuga S., Complaint film of regenerated *Antheraea pernyi* silk fibroin by chemical crosslinking, Int. J. Biol. Macromol. 32 :159-163 (2003a)

Li M.Z., Tao W., Kuga S., Nishiyama Y., Controlling molecular conformation of regenerated wild silk fibroin by aqueous ethanol treatment, Polymers for Advanced Technologies 14 (10): 694-698 (2003b)

Magoshi J., Magoshi Y., Nakamura S., Physical properties and structure of silk. III. The glass transition and conformational changes of Tussah silk fibroin, J. Appl. Polym. Sci. 21:2405-2407 (1977)

Magoshi J., Mizuide M., Magoshi Y., Takahashi K. Kubo M., Nakamura S., Physical properties and structure of silk. VI. Conformational changes in silk fibroin induced by immersion in water at 2 to 130 °C, J. Polym. Sci. Pt. B-Polym. Phys. 17:515-520 (1979)

Magoshi J., Magoshi Y., Nakamura S., Polym. Commun. 26:309-311 (1985)

Magoshi J., Magoshi Y., Becker M.A., Kato M., Han Z., Tanaka T., Inoue S., Nakamura S., Crystallization of silk fibroin from solution, Thermochimica Acta 352:165-169 (2000)

Milosevic M. & Berets S.L., A review of FTIR diffuse reflection sampling considerations, Applied Spectroscopy Reviews 37(4):347-364 (2002)

Min B.-M., Jeong L., Nam Y.S., Kim J.-M., Kim J.Y., Park W.H., Formation of silk fibroin matrices with different texture and its cellular response to normal human keratinocytes, Int. J. Biol. Macromol. 34: 281-288 (2004)

Miura T., Takeuchi H., Harada I., Characterization of individual tryptophan side chains in proteins using Raman spectroscopy and hydrogen-deuterium exchange kinetics, Biochemistry 27:88-94 (1988)

Miyazawa T., Shimanouchi T., Mizushima S., Normal vibrations of N-methyl acetamide, J. Chem. Phys. 29:611-616 (1958)

Miyazawa T. & Blout E.R., The infrared spectra of polypeptides in various conformations: amide I and amide II bands, J. Am. Chem. Soc. 83:712-719 (1961)

Miyazawa T., Masuda Y., Fukushima K., Chain conformation and amide V band of polypeptides, J. Polym. Sci. 62(174):S62-S64 (1962)

Monti P., Freddi G., Bertoluzza A., Kasai N., Tsukada M., Raman spectroscopic studies of silk fibroin from *Bombyx mori*, J. Raman Spectrosc. 29(4):297-304 (1998)

Monti P., Taddei P., Freddi G., Asakura T., Tsukada M., Raman spectroscopic characterization of *Bombyx mori* silk fibroin: Raman spectrum of Silk I, J. Raman Spectrosc. 32 (2):103-107 (2001)

Monti P., Taddei P., Freddi G., Ohgo K., Asakura T., Vibrational 13C-Cross-Polarization/Magic Angle Spinning NMR Spectroscopic and thermal characterization of poly(alanine-glycine) as model for Silk I *Bombyx mori*, Biopolymers (Biospectroscopy) 72:329-338 (2003)

Monti P., Freddi G., Sampaio S., Tsukada M., Taddei P., Structure modifications induced in silk fibroin by enzymatic treatments. A Raman study, J. Mol. Struct. 744:685-690 (2005)

Moore W.H. & Krimm S., Vibrational analysis of peptides, polypeptides, and proteins. II. β-poly(L-alanine) and β-poly(L-alanylglycine), Biopolymers 15: 2465-2483 (1976)

Overman S.A. & Thomas G.J., Jr., Raman markers of nonaromatic side chains in an α-helix assembly: Ala, Asp, Glu, Gly, Ile, Leu, Lys, Ser, and Val residues of phage fd subunits, Biochemistry 38:4018-4027 (1999)

Painter P.C. & Koenig J.L., Raman spectroscopy of polypeptides and proteins, In: Handbook of biochemistry and molecular biology, Fasman G.D. (Ed.) 3rd edition, 575-587 (1976)

Pan Z.J., Li C.P., Xu Q., Active control on molecular conformations and tensile properties of spider silk, J. Appl. Polym. Sci. 92:901-905 (2004)

Parkhe A.D., Seeley S.K., Gardner K., Thompson L., Lewis R.V., Structural studies of spider silk proteins in the fiber, J. Mol. Recognit. 10:1-6 (1997)

Pellerin Chr., Rousseau M.-E., Côté M., Pézolet M., Study of molecular orientation by vibrational spectroscopy: From polymers to silk, Macromolecular Symposia 220:85-98 (2005)

Peng X., Shao Z., Chen X., Knight D.P., Wu P., Vollrath F., Further investigation on potassium-induced conformation transition of *Nephila* spidroin film with two-dimensional Infrared correlation spectroscopy, Biomacromolecules 6:302-308 (2005)

Rathore O., Winningham M.J., Sogah D.Y., A novel silk-based segmented block copolymer containing GlyAlaGlyAla beta-sheets templated by phenoxathiin, J. Polym. Sci. Pol. Chem. 38(2):52-366 (2000)

Rousseau M.-E., Lefèvre T., Beaulieu L., Asakura T., and Pézolet M., Study of protein conformation and orientation in silkworm and spider silk fibers using Raman microspectroscopy, Biomacromolecules 5:2247-2257 (2004)

Shao Z.Z., Wu D., Li G.X., Peng L.W., Yu T.Y., Zheng S.D., Chin. J. Light Scattering 7:2 (1995)

Shao Z., Vollrath F., Sirichaisit J. and Young R.J., Analysis of spider silk in native and supercontracted states using Raman spectroscopy, Polymer 40(10):2493-2500 (1999a)

Shao Z., Young R.J., Vollrath F., The effect of solvents on spider silk studied by mechanical testing and single-fibre Raman spectroscopy, Int. J. Biol. Macromol. 24:295-300 (1999b)

Siamwiza M.N., Lord R.C., Chen M.C., Takamutsa T., Harada I. Matsura H., Shimanouchi T., Interpretation of doublet at 850 and 830 cm^{-1} in Raman spectra of tyrosyl residues in proteins and certain model compounds, Biochemistry 14:4870-4876 (1975)

Sirichaisit J., Young R.J., Vollrath F., Molecular deformation in spider dragline silk subjected to stress, Polymer 41:1223-1227 (2000)

Smith B.C., Infrared spectral interpretation – A systematic approach, CRC Press, Boca Raton, Florida (1999)

Sun Y.Y., Shao Z.Z., Hu P., Yu T.Y., Hydrogen bonds in silk fibroin poly(acrylonitrile-co-methyl acrylate) blends: FTIR study, J. Polym. Sci. Pt. B-Polym. Phys. 35(9):1405-1414 (1997)

Taddei P., Monti P., Freddi G., Arai T., Tsukada M., IR study on the binding mode of metal cations to chemically modified *Bombyx mori* and Tussah silk fibres, J. Mol. Struct. 651:433-441 (2003)

Taddei P., Asakura T., Yao J., Monti P., Raman study of poly(alanine-glycine)-based peptides containing tyrosine, valine, and serine as model for the semicrystalline domains of *Bombyx mori* silk fibroin, Biopolymers 75(4):314-324 (2004)

Takeuchi H., Watanabe N., Satoh Y., Harada H., Effects of hydrogen-bonding on the tyrosine Raman bands in the 1300-1150 cm^{-1} region, J. Raman Spectrosc. 20(4):233-237 (1989)

Trabbic K.A. & Yager P., Comparative structural characterization of naturally- and synthetically-spun fibers of *Bombyx mori* fibroin, Macromolecules 31:462-471 (1998)

Tso I.M., Wu H.C., Hwang I.R., Giant wood spider *Nephila pilipes* alters silk protein in response to prey variation, J. Exp. Biol. 208: 1053-1061 (2005)

Tsukada M., Freddi G., Gotoh Y, Kasai N, Physical and Chemical Properties of Tussah Silk Fibroin Films, J. Polym. Sci. Pt. B-Polym. Phys. 32 (8):1407-1412 (1994b)

Tsukada M., Freddi G., Monti P., Bertoluzza A., Kasai N., Structure and molecular conformation of Tussah silk fibroin films: Effect of methanol, J. Polym. Sci. Pt. B-Polym. Phys. 33:1995-2001 (1995)

Tu A.T., In: Raman spectroscopy in biology: Principles and applications, John Wiley & Sons, Chichester, 65 (1982)

Um I.C., Kweon H.Y., Park Y.H., Hudson S., Structural characteristics and properties of the regenerated silk fibroin prepared from formic acid, Int. J. Biol. Macromol. 29:91-97 (2001)

Van Dijk A., Van Wijk L., Van Vliet A., Haris P., Van Swieten E., Tesser G., Robillard G., Structure characterization of the central repetitive domain of high molecular weight gluten proteins. I. Model studies using cyclic and linear peptides, Protein Science 6:637-648 (1997)

Venyaminov S.Y. & Kalnin N.N., Quantitative IR spectrophotometry of peptide compounds in water (H_2O) solutions. II. Amide absorption bands of polypeptides and fibrous proteins in alpha-coil, beta-coil, and random coil conformations, Biopolymers 30(13-14):1243-57 (1990)

Verschuren J., De plasmabehandeling van textielproducten, rekening houdend met hun specifieke eigenschappen (The plasma treatment of textile products, taking into account their specific properties), Doctoral thesis (2005)

Wilson D., Valluzzi R., Kaplan D., Conformational transitions in model silk peptides, Biophys. J. 78(5):2690-2701 (2000)

Xue G., Laser Raman spectroscopy of polymeric materials, Progr. Polym. Sci. 19:317-388 (1994)

Yang M., Yao J., Sonoyama M., and Asakura T., Spectroscopic characterization of heterogeneous structure of *Samia cynthia* silk fibroin induced by stretching and molecular dynamics simulation, Macromolecules 37:3497-3504 (2004)

Zheng S., Li G., Yao W., Yu T., Raman spectroscopic investigation of the denaturation process of silk fibroin, Applied Spectroscopy 43:1269-1272 (1989)

Zheng R., Zheng X., Dong J., Carey P.R., Proteins can convert to beta-sheet in single crystals, Protein Science 13:1288-1294 (2004)

Zhou C.-Z., Confalonieri F., Medina N., Zivanovic Y., Esnault C., Yang T., Jacquet M., Janin J., Duguet M., Perasso R. and Li Z.-G., Fine organization of *Bombyx mori* fibroin heavy chain gene, Nucleic Acids Res 28:2413-2419 (2000)

Zhou P., Xie X., Deng F., Ping Z., Xun X., Feng D., Effects of pH and calcium ions on the conformational transitions in silk fibroin using 2D Raman correlation spectroscopy and C-13 solid-state NMR, Biochemistry 43:11302-11311 (2004)

7

METHANOL-INDUCED CONFORMATIONAL TRANSITION

By comparing different FT-IR techniques, it was concluded that the resolution and the repeatability, especially in the Amide I and II region, were the best for DRIFT spectra. Unfortunately, literature on DRIFT spectra of polymers is limited, moreover not existing for silk fibres. Furthermore, some spectral differences are observed as compared to the more often applied transmission FT-IR spectroscopy, especially in the Amide I and II regions. The FT-IR spectra contain some regions that are sensitive to conformational changes in secondary structure. In these regions, the assignment of peaks to secondary structure is quite well known for transmission spectra of proteins.

In an attempt to assign peaks to secondary structure in the DRIFT spectra, a conformational transition of silk fibroin from domestic Bombyx mori *silkworm and wild* Antheraea pernyi *(Tussah) silkworm was induced by a methanol treatment.*

7.1. CONFORMATIONAL TRANSITION OF SILK

Silk fibroin (SF) films can be prepared by casting the liquid silk from the gland of mature silkworm. Similar films can also be prepared by dissolution-regeneration of silk fibres, and this method is clearly more suited for practical production than collecting glandular silk. The native liquid silk is obtained by collecting it from the posterior region of the silkworm gland [Tsukada *et al.* 1994a, 1994b, 1995, Freddi *et al.* 1997, Monti *et al.* 2005]. The "regenerated" silk fibroin is obtained after degumming and dissolving the silk fibres. The solvents mostly used for *Bombyx mori* fibres are 9.3 M lithium bromide (LiBr) [Trabbic & Yager 1998, Chen *et al.* 2001, Asakura *et al.* 2002a, 2002b, Kim *et al.* 2004, Tsukada *et al.* 1994b, Liang & Hirabayashi 1992, Monti *et al.* 2005] and a ternary solvent system of aqueous calcium chloride in ethanol $CaCl_2/CH_3CH_2OH/H_2O$ in 1:8:2 molar ratio for 30 min. at 85 °C [Kweon *et al.* 2001b, Um *et al.* 2001, 2003, Hino *et al.* 2003]. With respect to *Antheraea pernyi*, concentrated lithium thiocyanate LiSCN [Tsukada *et al.* 1994b, Li *et al.* 2003a, 2003b] or calcium nitrate $Ca(NO_3)_2$ hydrate at about 100 °C for 3-5 h [Kweon & Park 1999, Kweon *et al.* 2000, 2001a, 2001b, 2001c, Ha *et al.* 2005] or aqueous calcium chloride [Hino *et al.* 2003] are used.

The solution is then dialyzed in a cellulose tube against distilled water for 3 to 4 days at room temperature. During the dialysis, salt (calcium or lithium) molecules are removed and an aqueous SF solution is prepared.

In order to obtain samples suitable for transmission FT-IR, the aqueous solution obtained after dialysis is then cast onto polystyrene or polyethylene plates to obtain a film of the required thickness and the films are air-dried. Li *et al.* [2001a] used the technique of freeze-drying to quickly dry the sample.

The native liquid silk and regenerated silk fibroin of *B. mori* are thought to consist of a Silk I conformation. Despite a long history of interest in the less stable Silk I form, it has remained poorly understood [Asakura *et al.* 2001a]. The structure has long been considered as a random coil conformation. Different models were proposed [Asakura *et al.* 2001a]: the out-of-register model [Fossey *et al.* 1991], later a crankshaft model [Lotz & Cesari 1979]. More details of these models are given in Chapter 5. Most recently, Asakura *et al.* [2001b] proposed a repeated β-turn Type II structure as model for Silk I.

Most studies, however, support the idea that aqueous solutions of *B. mori* silk fibroin consist mainly of random coil conformations [Magoshi *et al.* 1979, Venyaminov & Kalnin 1990, Trabbic & Yager 1998] and they may also contain some fraction of Silk I structure [Yoshimizu & Asakura 1990, Zheng *et al.* 1989, Tsukada *et al.* 1994b, Canetti *et al.* 1989].

The presence of β-turns in the native or regenerated Silk I structure has been confirmed recently by Asakura *et al.* [2002a,b] using NMR studies. However, apart of a random coil structure, also some small fractions of β-sheet were found [Trabbic & Yager 1998]. Magoshi *et al.* [1994] reported that a random coil conformation is obtained for fibroin molecules in dilute aqueous solutions by extremely rapid freezing. This agrees with the result of Li *et al.* [2001a] who reported that lyophilized or freeze-dried silk fibroin was mainly amorphous when the freezing

temperature was below -20 °C, while Silk I was prepared when the temperature was above -20 °C.

The Silk I structure is fundamentally different from that of the native silk fibre after spinning, called Silk II. As described in Chapter 5, there is consensus that the structure of Silk II corresponds to an antiparallel β-sheet conformation.

The silk II structure may be regenerated by treatment with formic acid [Asakura *et al.* 2002a, Um *et al.* 2001, 2003, Kweon *et al.* 2001b] or methanol [Magoshi *et al.* 1979, Iizuka & Yang 1968, Venyaminov & Kalnin 1990, Yoshimuzi & Asakura 1990] or ethanol [Chen *et al.* 2001] or water-dioxane (2:1 v/v) solution [Venyaminov & Kalnin 1990]. Also a heat treatment or blending with other polymers, such as chitosan [Chen *et al.* 1997, Kweon *et al.* 2001a, 2001b] and sodium alginate [Liang & Hirabayashi 1992], results in the conformational transition to a Silk II (supposed to be dominantly β-sheet) structure.

Asakura *et al.* [2001] stated that the Silk I form of *B. mori* silk fibroin is an intermediate structure in the fibre-forming process of the silkworms, it is likely that the repeating and alternating sequence of X-Gly (where X is dominantly Ala), naturally occurring in the silkworm, arose to form β-turns that can subsequently be transformed into β-sheets. Peng *et al*. [2005] reported a similar model for the assembly of spider silk nanofibrils in which also β-turn structures are proposed as intermediate structures in the conformational transition of random coil and/or α-helix structures to β-sheet crystals. Asakura *et al.* [2001] speculated about the mechanism of structural transition from silk I to silk II using this silk I model. The network of hydrogen bonds present in the structure of silk I makes it extremely stable to heat treatment [Nakamura *et al.* 1994]. However, the silk I structure is unstable upon mechanical deformation. It is highly probable that mechanical deformation of the silk I structure would disrupt the network of hydrogen bonds and convert intramolecular hydrogen bonds to intermolecular bonds, to form anti-parallel β-sheets that are characteristic of the silk II form. The role of water seems very important in the appearance of the silk I structure, and in the transition from the silk I to the silk II form. Since the silk I form exists in aqueous solutions and is obtained from the silk glands of silkworms while dried without disturbance at room temperature, there remains a lot of water around the silk fibroin chains [Asakura & Yamaguchi 1987]. In addition, the transition from silk I to silk II occurs easily in the presence of water. In the biological spinning process, the mature larva of the silkworm stretch the silk fibroin chain by performing head movements depicting the number eight (see Chapter 1).

With respect to *A. pernyi* (Tussah) silk, there is consensus that the native and liquid SF film consist of α-helical and random coil components [Tsukada *et al.* 1994b, 1995, 1998, Freddi *et al.* 1997, Kweon & Park 1999, Kweon *et al*. 2000, 2001c].

The conformational transition of native liquid and regenerated *A. pernyi* silk to β-sheet induced by heat [Freddi *et al.* 1997, Tsukada *et al.* 1994b, Tsukada *et al.* 1998, Kweon *et al.* 2001c] or methanol [Kweon & Park 1999, Kweon *et al.* 2000, Tsukada *et al.* 1995] or ethanol [Li *et al.* 2003b] treatment has been reported by several authors.

Alcohols such as methanol and ethanol are well known as a crystallization agent for silk fibroin (SF) molecules. The crystallization mechanism, as proposed by Um *et al.* [2003], is that alcohols attract the water from the SF molecules due to their polar character and this promotes the aggregation of hydrophobic amino acids, such as Ala and Gly. Since these amino acids are the main components of the crystalline region and the Gly-Ala sequence is a unit dimension of the SF crystal structure, the alcohols may cause to induce the β-sheet crystallization of SF, accompanied with the exclusion of hydrophobic amino acids.

Some authors [Tsukada *et al.* 1995, Kweon & Park 1999] stated that water might be necessary to induce swelling in order to allow the diffusion of methanol into the structure. The rate of diffusion into the film, as well as the effectiveness in inducing swelling and rearrangement of the inter-/intramolecular hydrogen bonds, might thus depend on the composition of the water-methanol solution. In fact, both water and methanol molecules give rise to structures stabilised by hydrogen bonds, the size of these structures being dependent on the steric hindrance of H and CH_3 side groups involved in their formation. For *A. pernyi* silk fibroin, crystallization is likely to proceed through conformational transition from both α-helix to β-sheet (confirmed by X-ray and Raman spectroscopy), and random coil to β-sheet structure (as shown by IR-spectra) [Tsukada *et al.* 1995].

Research on the structure of major ampullate silk before and after spinning of silk fibroin of *Nephila* spiders is also performed. The silk before spinning is always obtained by dissecting the major ampullate glands and collecting the liquid silk [Hijirida *et al.* 1996, Chen *et al.* 2002, Dicko *et al.* 2004, Peng *et al.* 2005].

In this chapter, the conformational transition to β-sheet structure is obtained for regenerated *B. mori* and *A. pernyi* silk fibroin by a treatment with different methanol concentrations in water.

7.2. MATERIALS AND METHODS

7.2.1. PREPARATION OF THE REGENERATED SILK FIBROIN

In order to obtain the regenerated *Bombyx mori* silk fibroin, a fabric made of *B. mori* silk was dissolved in 9.3 M lithium bromide (LiBr) at room temperature for 3-4 days. The LiBr molecules break hydrogen bonds of the chains and then a "Silk I" structure with a new type of hydrogen bonding can be formed after dialysis against water [Asakura *et al.* 2001].

After filtration the aqueous LiBr-solution is dialysed in a cellulose tube (molecular cut-off: 12-14000 kDa, serva) against distilled water for 3-4 days in order to remove the salts. This was followed by freeze-drying the sample. Freeze-drying is used as a gentle dehydration method to dry materials sensitive to heat. Most materials, including dissolved sugars in water, biomaterials, etc. do not crystallize during freezing. In the course of freezing, water is removed by sublimation, and the freeze-concentrated solution is amorphous. The freeze-drying process resulted in a silk fibroin foam that is supposed to show the Silk I structure (random coil and/or β-turn). It was hoped that neither β-sheet crystals nor α-helix conformations are present.

In order to check the reproducibility of the method, and to check the method for the *B. mori* fibres that were used in previous analysis (mechanical tests, FT-IR and Raman spectra), this procedure was repeated a second time on the fabric (1 g) and silk fibres (1 g).

For obtaining a regenerated sample from *Antheraea pernyi* (Tussah) silk, lithium thiocyanate (LiSCN) was chosen as solvent. One gram of *A. pernyi* (Tussah) fibres was dissolved in 9.3 M LiSCN (11.70 g in 20 ml) at room temperature for 3-4 days. The further procedure was the same as for *B. mori*.

7.2.2. FT-IR SPECTROSCOPY

The regenerated silk fibroin was placed in a cup for DRIFTS measurements. After recording the untreated sample, a few drops of methanol solution were dripped on the cup. After drying the treated sample for at least 24 hours, the DRIFT spectra were recorded. The selected concentrations of methanol were 0% (100% water, if possible), 20% (if possible), 40%, 60%, 80% and 100%.

A Perkin Elmer GX 2000 spectrophotometer, like in the DRIFT experiments in Chapter 6, was used for recording the spectra. For each DRIFTS measurement, 16 interferograms were co-added to yield spectra with a nominal resolution of 4 cm^{-1}, and interpolated to a wave number scale of 1 cm^{-1}.

Each spectrum was collected over the 4000-400 cm^{-1} range. Before recording a spectrum, the spectrum of KBr (dried at 45 °C, pre-grinded) was recorded as background to correct for H_2O and CO_2 bands. Moreover, before the measurement the sample is focused and the energy optimized.

For each methanol treatment, the final spectrum of the dry sample was calculated from the average of 10 spectra (20 spectra for the 1st prepared *Bombyx mori* samples). The *Antheraea pernyi* (Tussah) samples were first oven dried for at least 24 h at 40 °C before recording the spectra. The effect of oven drying was checked for some *B. mori* samples and resulted in negligible differences, so oven drying was not performed for the samples. The area of several regions within the spectra was normalized to 100 or 1000 depending on the size, and separately plotted for each region. It was not possible to normalize on a peak maximum because of the shift of some bands in the spectra of the methanol treated samples.

For instrument specifications of the ATR FT-IR experiments it is referred to Chapter 6.

7.3. SPECTRA OF THE FREEZE-DRIED SILK FIBROIN SAMPLES

7.3.1. INTRODUCTION

First of all, it should be noted that for *Bombyx mori* the regenerated silk fibroin (SF) is obtained as a foam, whereas for Tussah the regenerated sample has less coherence and looks more like a powder.

The spectra of the freeze-dried SF samples are obtained by averaging all spectra of the dry samples (before methanol treatment) after normalizing the area (to 1000) of the spectra over the whole region 4000-400 cm^{-1}. In the figures, the regenerated *B. mori* sample obtained from the fibres is indicated as "MoriFib", those obtained from the fabric as "MoriFab 1-2", the number stands for the 1st, resp. 2nd time that the sample was prepared. The regenerated *Antheraea pernyi* (Tussah) sample is indicated by "Tussah".

Since the aim of this chapter is to assign absorption maxima to secondary structure for DRIFT spectra, in this chapter the discussion is restricted to information that is related to the secondary structure of the silk fibroins. For assignments of maxima that are not mentioned here, it is referred to Chapter 6.

7.3.2. DISCUSSION OF THE SPECTRA

The mode of vibration between 3800-2400 cm^{-1} (Amide A-B region) does not depend on the backbone conformation but is very sensitive to the strength of hydrogen bonds.

As is shown in Figure 7.1, the spectra of regenerated *Bombyx mori* in the Amide A-B region mostly differ in their intensity. If the spectra of regenerated *B. mori* and Tussah are compared, it can be seen that the Amide A band, associated with NH stretching, is shifted to lower wave numbers for Tussah (3299 cm^{-1}) SF. This implies that stronger intermolecular hydrogen-bonding networks are formed between the NH groups of the molecules in the silk fibroin particles, also seen in the conformational transition of glutamic acid benzyl esters to a β-sheet structure [Okabayashi *et al.* 2002]. It can be a confirmation that β-sheet crystals are formed. We also note, in this respect, the small shift seen for *B. mori*, prepared the second time (3321-3323 cm^{-1}), compared with the *B. mori* samples firstly prepared (3315 cm^{-1}).

Another clear difference in this region between *B. mori* and Tussah regenerated silk is the difference in relative intensities of the peaks at about 2980 cm^{-1} and about 2940 cm^{-1}. These bands are associated with CH_3 asymmetric and symmetric stretching, respectively [Edwards & Farwell 1995, Krimm & Bandekar 1986, Moore & Krimm 1976]. The ratio I_{2980}/I_{2940} equals 1.10 for regenerated Tussah compared to a value of 0.92 for regenerated *B. mori* fabric and 0.91 for regenerated *B. mori* fibres. For the *B. mori* and Tussah fibres, this ratio equals 0.97, resp. 1.09 for the spectra shown in Chapter 6. The similar value of the ratios for the regenerated Tussah and the Tussah fibres suggests that the regenerated Tussah already consists of a considerable amount of β-sheets.

In general, it seems that all bands in the Amide A-B regions are shifted to lower wave numbers for regenerated Tussah compared to *B. mori* indicating that stronger or more (intermolecular) hydrogen bonds are formed.

The Amide I region of proteins is known to be very sensitive to the structural conformation of the proteins. It is clear from the spectra (Figure 7.2) of this region, that the samples of *B. mori*, both obtained from the fabric, show a different structure. However, the sample obtained from the *B. mori* fibres seems to show a similar

structure as that obtained from the fabric, prepared at the same time using the same procedure.

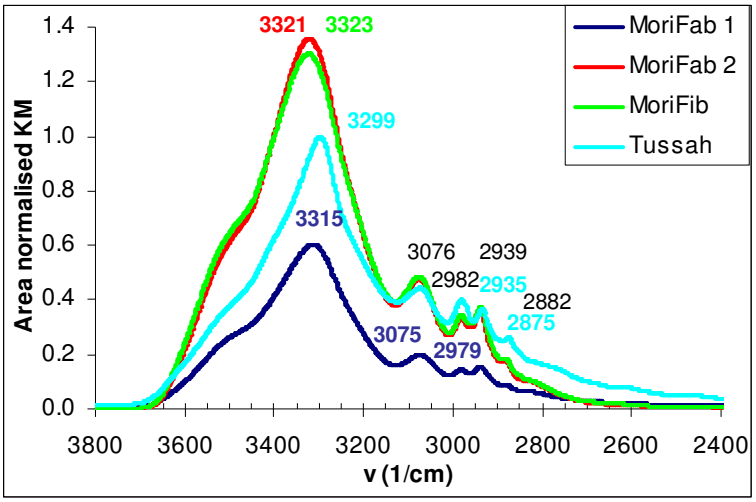

Figure 7.1 - Amide A-B regions for regenerated *B. mori* (fabric: MoriFab 1-MoriFab 2; fibres: MoriFib) and *A. pernyi* (Tussah)

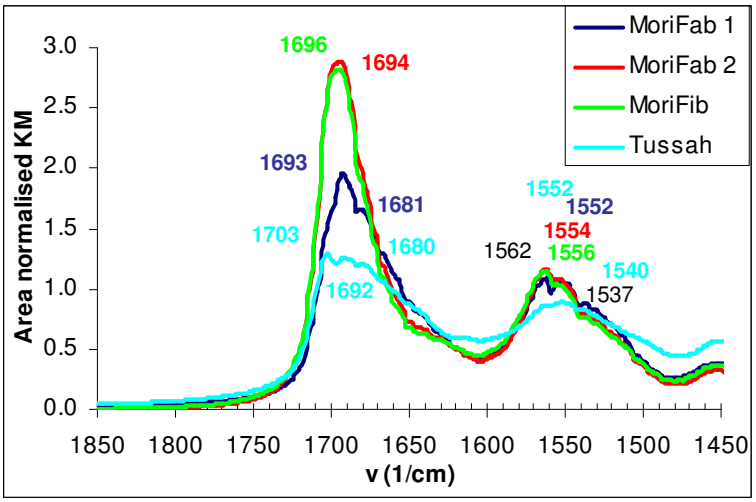

Figure 7.2 - Amide I-II regions for regenerated *B. mori* (fabric: MoriFab 1-MoriFab 2; fibres: MoriFib) and *A. pernyi* (Tussah)

Tussah shows a completely different spectrum in the Amide I and more similar to the spectrum of Tussah silk fibres, as recorded in Chapter 6. It is suggested that this is due to the presence of β-sheet crystals that were not completely dissolved in LiSCN.

In the Amide II region (Figure 7.2), the relative intensity of the bands at about 1562 cm^{-1} and at about 1552 cm^{-1} is clearly different between the regenerated *B. mori*

prepared the 1st time (I_{1562}/I_{1552} = 1.02) and that prepared the 2nd time (I_{1562}/I_{1552} = 1.07-1.10). The same is valid for the ratio of intensities at 1562 cm^{-1} to 1357 cm^{-1} (I_{1562}/I_{1537} = 1.24 versus 1.46-1.50). It indicates that the secondary structure of both samples is slightly different. For Tussah, no clear maximum is observed at about 1562 cm^{-1} and the band is shifted to lower frequencies. The relative intensities I_{1562}/I_{1552} and I_{1562}/I_{1537} are clearly lower for regenerated Tussah (0.98 and 1.05, respectively) compared to regenerated *B. mori*. Further assignments to secondary structure are mentioned in the next section 7.4.

Since the DRIFT-peaks in the Amide I and Amide II regions are shifted compared to the spectra that can be found in literature, it is too early to associate the different peaks with different secondary structures.

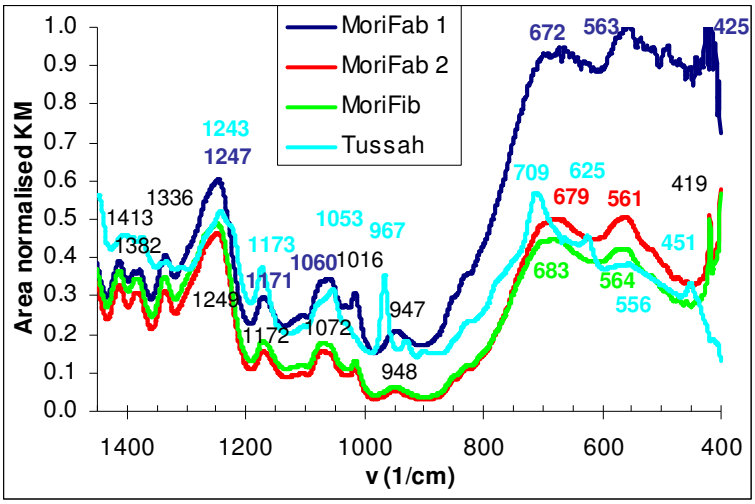

Figure 7.3 - 1450-400 cm^{-1} region for regenerated *B. mori* (fabric: MoriFab 1-MoriFab 2; fibres: MoriFib) and *A. pernyi* (Tussah)

Figure 7.3 shows the DRIFT spectra in the 1450-400 cm^{-1} region for the regenerated silk samples. Fortunately, the peaks in the region 1450-400 cm^{-1} are comparable with the peaks found in FT-IR transmission spectra in literature. It is expected that this region can help to have a confirmation of the secondary structural components present in the sample.

The peaks at 1411, 1387, 1334 cm^{-1} are reported to be markers for the Silk I structure [Monti *et al.* 2003]. Peaks at about these positions are indeed observed for all regenerated *B. mori* samples, resp at 1413, 1380-1382, and 1336-1337 cm^{-1}. For the regenerated Tussah, the first two peaks are shifted to lower wave numbers, to resp. 1406 and 1375 cm^{-1}.

The Amide III region is also a region that is sensitive to structural conformation, however, some side chain vibrations would also be situated in this region. As mentioned in Chapter 6, the association to secondary structure in the region 1260-1265 is not clear from literature of silk. The maximum in this region for the firstly prepared sample ("MoriFab1") is at 1247 cm^{-1}, whereas for the secondly prepared samples ("MoriFab2" and "MoriFib") it is shifted to 1249 cm^{-1}. This small shift can

indicate the slightly different secondary structure of these samples. Moreover, the samples show a clear shoulder at higher wave number. Although the maximum is found at 1243 cm^{-1} for the Tussah sample, shoulders at lower and higher wave numbers can be observed, probably indicating at least 3 different secondary structural components.

Itoh *et al.* [1978] and Monti *et al.* [2003] reported the peaks at 1274-1276 and 1245 cm^{-1} associated with Silk I structure. This can confirm again that regenerated *B. mori* contains a high amount of Silk I structure.

The region 1100-1020 cm^{-1} is also expected to be sensitive to the secondary structure. The peaks at about 1110 and 1050 cm^{-1} are associated with motion of the alanyl residue [Taddei *et al.* 2003]. Peaks in the region 1073-1095 cm^{-1} are attributed to the β-sheet conformation, 1100-1106 cm^{-1} to α-helix conformation for Tussah silk [Tsukada *et al.* 1994], whereas also the Silk I structure is reported for wave numbers 1105-1107 cm^{-1} [Monti *et al.* 2003]. Though, the maxima in this region are clearly different for the different samples: 1060 (MoriFab 1), 1072 (Mori Fab 2 – MoriFib), 1055 (Tussah) cm^{-1}, it is difficult to make conclusions. It again indicates that the procedure that was used for *B. mori* the second time resulted in a different secondary structure.

The peaks at about 998 and 975 cm^{-1} in *B. mori* silk fibre are associated with the Gly-Ala repeats [Asai *et al.* 1955, Freddi *et al.* 1999], probably the GAGAGS motif that is known to form an antiparallel β-sheet structure. These peaks are not observed for the regenerated samples, confirming a different structure than the β-sheet rich *B. mori* fibre. Instead a single peak at about 950 cm^{-1} is observed.

The weak doublet at about 850 and 827 cm^{-1} is due to Fermi resonance between a ring breathing vibration and the overtone of an out-of-plane ring-bending vibration of the tyrosine (Y) residue [Siamwiza *et al.* 1975, Takeuchi *et al.* 1989]. This doublet is sensitive to the hydrogen-bonding state of the tyrosine (Y) phenoxyl group and has been intensively used [Taddei *et al.* 2004] as an indicator of Y interactions in globular proteins, their assemblies, and their degree of exposure to water. The significance of this ratio is further described in Annex.

For the freeze-dried samples the intensity ratio $\mathbf{I_{850} / I_{827}}$ is comparable for all samples (for MoriFab 1 0.84, MoriFab 2 0.75, MoriFib 0.77 and for Tussah 0.81). It is possible that the tyrosine residue is deprotonated since the intensity ratio is near 0.7. The significant difference in intensity ratio between the samples firstly and secondly prepared indicates a different environment for the tyrosine residues, situated in the amorphous regions.

A band at about 650-665 cm^{-1} is characteristic for random coil and/or Silk I structure [Kweon *et al.* 2000, 2001a, Tsukada *et al.* 1994, Freddi *et al.* 1997, Monti *et al.* 2003]. These bands, although at somewhat higher wave number, can be clearly seen in the spectra of the regenerated *B. mori* SF.

A peak at 425 cm^{-1} is also observed by Magoshi *et al.* [1979] when immersing regenerated SF films in random coil form in water at a temperature above 70 °C, expecting to form β-sheet crystals. However, no association to secondary structure is made. The regenerated *B. mori* samples also show peaks at about this wave number: 425 cm^{-1} and 419 cm^{-1}. The Tussah sample, however, does not display a

clear peak at this wave number, but at a much higher wave number 451 cm^{-1}, also found by Krimm & Bandekar [1986] for poly-L-alanine in the β-form.

The Tussah regenerated sample shows strong absorption bands at 709 cm^{-1}, 967 cm^{-1}, and a shoulder at about 1220 cm^{-1} associated with the β-sheet structure [Kweon *et al.* 2000, 2001a, Tsukada *et al.* 1994, Freddi *et al.* 1997, Magoshi *et al.* 1979]. Moreover, also peaks associated with the α-helical structure are clearly visible in the spectra of regenerated Tussah: a shoulder at 1270 cm^{-1}, 900 cm^{-1} and 625 cm^{-1} [Kweon *et al.* 2001c]. However, also a very weak peak is observed at 664 cm^{-1}, associated with a random coil conformation [Kweon *et al.* 2001c]. Also the peak at about 930 cm^{-1} should be noted that, together with 950 cm^{-1}, has been associated with the Silk I structure [Monti *et al.* 2003].

7.3.3. CONCLUSION FOR FREEZE-DRIED SAMPLES

To conclude, in the case of the *Bombyx mori* samples there is no clear indication that β-sheet crystals are present. However, the samples made at different times seem to contain different structural components. It is suggested that the reason for the different structure is mainly to be sought in the applied procedure for freeze-drying. For the first sample ("MoriFab1"), the dialysed solution was first frozen in liquid nitrogen (T < -20 °C) before freeze-drying. In a second time, the procedure was repeated for the *B. mori* fabric and *B. mori* fibres with a pre-freezing in a freezer (T > -20 °C). Li *et al.* [2001a] reported that lyophilized silk fibroin was mainly amorphous if the freezing temperature was below -20 °C, while Silk I was prepared at a temperature above -20 °C. Also a longer dialysis time can be an explanation of the different structure. During the dialysis, salt (calcium or lithium) molecules are removed and aqueous SF solution is prepared. Since SF is composed of mostly hydrophobic amino acids, fibroin molecules in aqueous solution tend to aggregate and get entangled by hydrophobic interactions.

We suppose that the regenerated *B. mori* samples, prepared the 2nd time, contain a higher amount of Silk I, probably, β-turns apart from random coil components. β-turns, as intermediate structure in the conformational transition from random coil to β-sheet structure, are also suggested by Asakura *et al.* [2001b] for *B. mori*, Peng *et al.* [2005] for *Nephila* spidroin film and Okabayasi *et al.* [2002] for oligomeric benzyl esters. If this theory is followed, it is assumed that a β-turn configuration is associated with a peak at about 1693-1695 cm^{-1}, and the peaks at about 1687 and 1681 cm^{-1}, mostly observed for the 1st prepared *B. mori* sample, with random coil conformation. The band at 670-680 cm^{-1} confirms the existence of a random coil conformation for all *B. mori* samples.

Moreover, it seems that the regeneration of Tussah fibres was not so successful as the sample already contains a certain amount of β-sheet. However, the assumed random coil peaks at about 1687 and 1681 cm^{-1} are also observed in the spectrum. Moreover, the existence of random coil and α-helical structures is proved by the band in the Amide V region (625 cm^{-1} and 664 cm^{-1}).

7.4. EFFECT OF METHANOL TREATMENT

7.4.1. INTRODUCTION

It is chosen to select the more amorphous sample of regenerated *Bombyx mori* for a detailed discussion of the methanol (CH_3OH) treatment. The spectra of the other samples will be discussed if required for confirmation of the conclusions.

A CH_3OH concentration of 20% resulted already in partial dissolution of the selected regenerated *B. mori* sample (firstly prepared), which makes the FT-IR spectra less reliable because of the high contribution of absorption of water. This behaviour is another indication that the components in random coil conformations are highly represented in this freeze-dried sample [Kweon & Park 1999]. For the regenerated *B. mori* samples that were prepared the second time, even the spectrum for a treatment with pure water was recordable.

Moreover, it was observed that the spectra of treated samples with CH_3OH concentrations of 40% and 60% were different from spectra of treatments with 80% and 100% CH_3OH.

Because of the partial dissolution of the regenerated sample treated with 20% CH_3OH and the different behaviour for lower and higher CH_3OH concentrations, it was decided to add a treatment with CH_3OH concentrations of 30% and 70% for this regenerated sample (1^{st} prepared).

As a result of the partial dissolution of the sample at 20% and 30%, the normalized spectra of the samples (e.g. peak at about 1450 cm^{-1} set to 1, intensity at 2000 cm^{-1} set to 0) treated with different CH_3OH concentrations were difficult to compare. So, it was chosen to split the spectra in different regions and to normalize the area of the separate regions.

Figures 7.4, 7.5, 7.9, 7.12, 7.13 and 7.16 give the average spectra of the CH_3OH treated samples after drying (firstly prepared). The untreated sample is indicated in the figures as “Before”. First of all, it can be concluded that two groups of similar spectra for the treated samples can be considered: the spectra of samples treated with CH_3OH concentrations of 20 to 60% and the spectra of CH_3OH concentrations of 70% and higher. Furthermore, the spectra of the samples treated with a CH_3OH concentration higher than 60% are similar to the spectrum of *B. mori* fibre as discussed in Chapter 6. It is suggested that the samples treated with lower CH_3OH concentrations have another structure than those treated with higher concentration. Because of the higher water content in those samples, the Silk III or 3_2 helical structure [Viney 2000], as detected at the air water interface by Valluzzi *et al.* [1997, 1999], is proposed.

The FT-IR spectrum of methanol shows absorption peaks at 3336-3347, 2945, 2833, 2522, 2046, 1460, 1116, 1030 and 662 cm^{-1}. The peak at 2833 cm^{-1} visible in the spectra of methanol can be detected in all spectra as a relatively broad but weak band. The small peak at 2046 cm^{-1} in all spectra available in the methanol spectrum can be the reason for the deviation from zero around 2000 cm^{-1} (not shown in Figure 7.4). The spectra of methanol show clear peaks at 1116 and at 1030 cm^{-1} (C-OH stretch), these peaks are hardly visible, confirming that most methanol is evaporated for all samples.

7.4.2. THE AMIDE A-B REGION (3800-2400 CM^{-1})

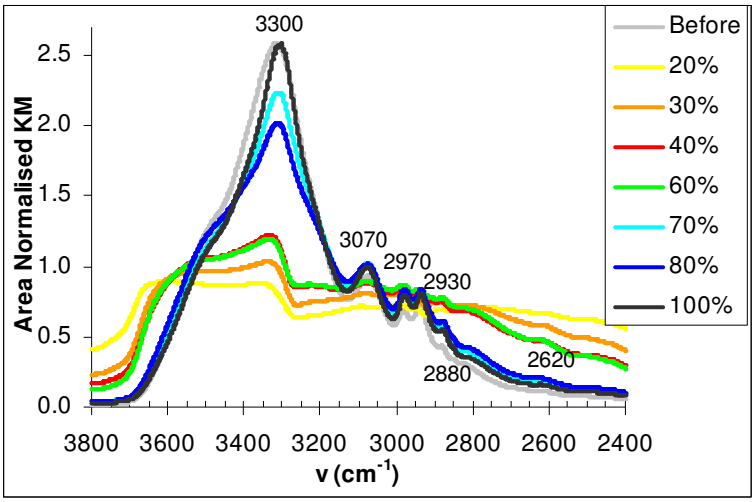

Figure 7.4 - The Amide A and B region in the spectra for the samples treated with different CH_3OH concentrations

The mode of vibration between 3800-2400 cm^{-1} does not depend on the backbone conformation but is very sensitive to the strength of the hydrogen bond. Although these regions are not important for structural characterization of proteins, they confirm the presence of water and methanol.

As shown in Figure 7.4, all samples show the same absorption maxima, for the assignment it is referred to Chapter 6.

For lower concentrations of CH_3OH (up to 60%), a broad band at 3650-3340 cm^{-1} can be observed. This band is associated with bonded OH stretch. Since the band evolves to a shoulder for higher CH_3OH concentrations, this band is probably related to the effect of water in which the OH groups are easily hydrogen bonded. So, it confirms that these samples (up to 60% CH_3OH) contain a higher water content than the other samples. Similar shapes of the Amide A and B bands were observed for the other treated samples.

7.4.3. THE AMIDE I REGION (1600-1800 CM^{-1})

Figure 7.5 shows the effect of the methanol treatment on the Amide I mode in the spectra.

As can be seen from Figure 7.5, different groups can be observed. The spectrum of the regenerated *Bombyx mori* ("Before") shows a maximum at a lower wave number (1693 cm^{-1}) than any other spectrum.

After the CH_3OH treatment, a new peak is observed at ±1703-1707 cm^{-1}. Even without any deconvolution or curve-fitting procedure, it is clear that this peak,

compared to the other peaks, is relatively higher and shifted to higher wave number (1707 cm^{-1}) for CH_3OH concentrations of 20, 30, 40 and 60%. As suggested in the introduction, a Silk III structure is proposed for the samples treated with lower CH_3OH concentrations.

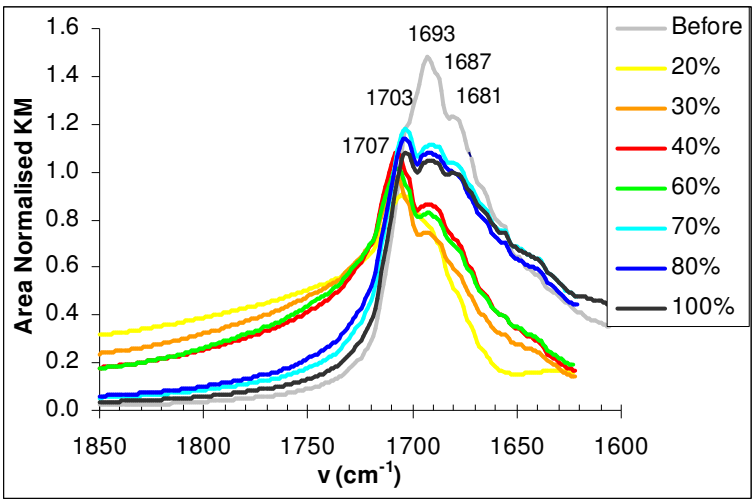

Figure 7.5 - The Amide I mode in the spectra for the samples treated with different CH_3OH concentrations

We expect a conformational transition from Silk I/random coil to a β-sheet structure for *B. mori*. A comparison with the spectra of the *B. mori* fibre (Chapter 6) let us suggest that the peak at ±1703 cm^{-1} can be associated with the formation of β-sheet crystals.

Based on theoretical work, Nevskaya & Chirgadze [1976] calculated that the frequency of the α-helix depends on the length of the helix. Moreover, the central and terminal regions of an α-helix could yield different spectra. Any distortion of the α-helix would also shift the frequency of the Amide I-associated band. Such distortions have been recently described in protein crystals [Blundell *et al.* 1983]. Also Reisdorf & Krimm [1994] found a relationship between band position in FT-IR spectra and the length of a 3_{10} helix. Longer 3_{10} helices segments would have their signals displaced to lower wave numbers. Similarly, we could assume that the shift to a slightly higher wave number is due to either an increase of chain length of the β-sheet crystals, or to a distortion of the β-sheet structure.

Experimental evidence indicates that, depending on the protein, the α-helix or the β-sheet components can be very broad [Chirgadze *et al.* 1976] and split into several subcomponents. Surewicz *et al.* [1987] also stated that bands at different positions (e.g. 1703 and 1707 cm^{-1}) can be attributed to β-type segments with a slightly different pattern of hydrogen bonding. As a result, it is also possible that the contribution of β-sheet subcomponents varies for the different treatments, resulting in a shift of the maximum intensity.

However, the finding of a different structure by Valluzzi *et al*. [1997, 1999] for silk fibroin at the air-water interface of dilute aqueous silk solutions makes it more reasonable to assign the slightly higher wave number at about 1707 cm^{-1} found for lower CH_3OH concentrations to the Silk III structure.

The second derivative of the spectra (Figure 7.6) in the region of the Amide I band is useful in obtaining an indication of the number of components when overlapping bands are present and in determining their real position. This method is generally used on resolving Amide I into the bands due to different secondary structures. Although a peak at about 1705 cm^{-1} is observed for all samples, the 2nd derivatives of the spectra of lower concentrations (30-60%) seem to display a shoulder at somewhat higher wave number. So, it is suggested that there is a contribution of an extra component for these concentrations. It confirms the different structure associated with the samples treated with lower CH_3OH concentrations.

Considering the peak at about 1703 cm^{-1} attributable to β-sheet structure, the transition into β-sheet conformation can be represented by the ratios of the β-sheet peak to all other observable peaks. The effect of CH_3OH concentration on the transition into β-sheet conformation for the regenerated *B. mori* sample (1st prepared) is shown in Figure 7.7. It should be remarked that for the samples treated with lower CH_3OH concentration, the intensity at 1707 cm^{-1} is used instead of 1703 cm^{-1}.

For most peaks the same behaviour is observed. However, some differentiation can be made in the degree of decrease: the peak at 1644 cm^{-1} shows the highest effect, followed by the peaks at 1693-1687-1681 cm^{-1} and the lowest effect for the peaks at 1671-1666-1660-1651 cm^{-1}. This may indicate a similar secondary structure for the wave numbers in these groups.

Compared to the untreated sample ("Before"), it is clear that the ratios for 1693-1687-1681 cm^{-1} are considerably higher whereas for 1671-1666-1660-1651 cm^{-1} the intensity ratios are comparable with the untreated one (only looking at 70-100% CH_3OH). The increase in intensity compared to the untreated sample implies that random coil or β-turn conformation is transformed to β-sheet conformation. We can conclude that the maxima at about 1693, 1687, and 1681 cm^{-1} are associated with the random coil or β-turn structure.

The peak at 1693 cm^{-1}, the highest peak observed in the untreated sample, is also visible in the spectra of the treated samples, but has significantly decreased relative to the peak at about 1703 cm^{-1}. Moreover, the untreated *B. mori* samples, prepared the 2nd time, also displayed a maximum at about this wave number. It is assumed that this peak is associated with an intermediate structure, a β-turn structure as is also reported by Asakura *et al.* [2001, 2002a,b] for *B. mori*, Okabayashi *et al.* [2002] for benzyl esters, and Peng *et al.* [2005] for *Nephila* spidroin. Several authors [Bandekar & Krimm 1979, Peng *et al.* 2005] assigned a peak near 1690 cm^{-1} to a β-turn conformation.

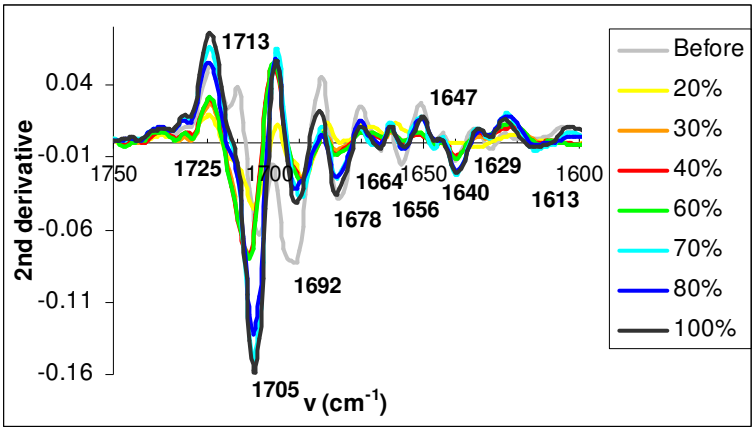

Figure 7.6 - Second derivative (based on 13 datapoints) of the Amide I region

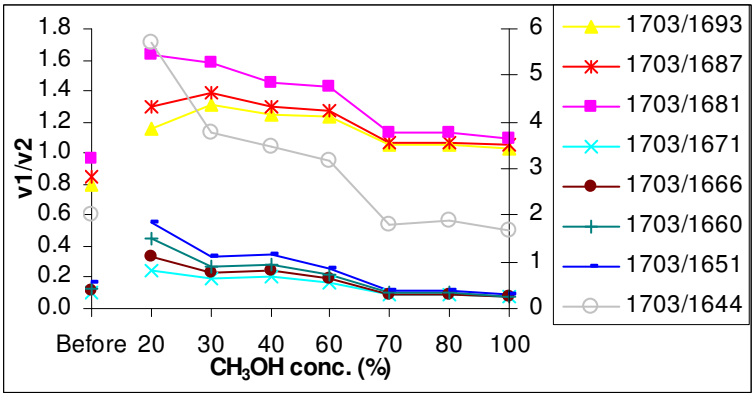

Figure 7.7 - The effect of CH_3OH concentration on β-sheet formation for regenerated *B. mori* (ratio with 1644 on secondary axis)

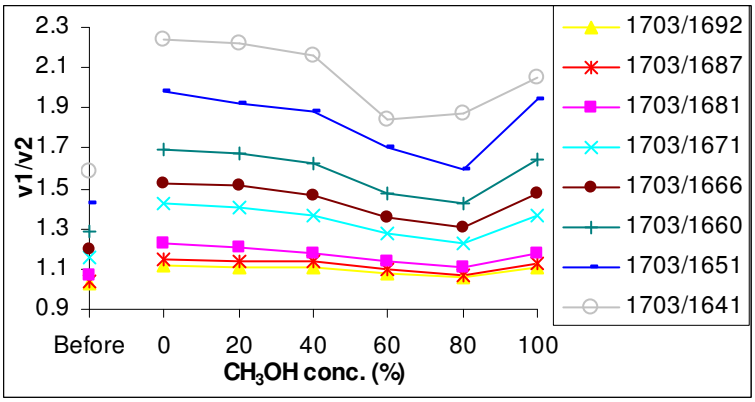

Figure 7.8 - The effect of CH_3OH concentration on β-sheet formation for regenerated Tussah

A shoulder at 1687 cm^{-1} is observed for all spectra. Also this shoulder seems to decrease for increasing CH_3OH concentrations up to 60%. The weak peak at 1681 cm^{-1}, clearly visible in the original spectrum and the spectra for higher CH_3OH concentrations, is hardly detectable in the spectra for lower CH_3OH concentrations. The peaks at 1687 cm^{-1} and 1681 cm^{-1} can thus be attributed to the random coil or β-turn conformation. The more deviating behaviour and higher ratio for the maximum at 1681 cm^{-1} let suggest that this maximum is associated with the random coil conformation whereas the peaks at 1687 cm^{-1} and 1693 cm^{-1} are linked to the β-turn conformation. We do not expect that an α-helix conformation is present in *B. mori*. The peaks at 1681 cm^{-1} and 1687 cm^{-1} are also present in regenerated Tussah, however the wave numbers are too high for the assignment to an α-helical structure (see Table 6.1 in Chapter 6).

For an assignment of the maxima at about 1671-1666-1660-1651 cm^{-1}, we consider the intensity ratios for the Tussah sample as shown in Figure 7.8. In the Tussah sample, we do not observe the shifts for lower CH_3OH concentrations, suggesting that the Silk III structure is not existing in Tussah silk fibroin. Since the arrangement of the serine residue in the GAGAGS sequence (not available in Tussah) results in this structure, it could be expected. We also observed that the untreated Tussah sample already contains a large fraction of β-sheet structure (as confirmed by the maxima at about 1703 cm^{-1} in Figure 7.2). From literature [Tsukada *et al*. 1995], we know that the conformational transition to the β-sheet structure occurs in two phases: firstly the random coil conformation is converted, followed by a transition of the α-helical structure. As a consequence for our sample, we expect that the transition of random coil to β-sheet structure is almost complete in the untreated sample. From Figure 7.8, we can conclude that the suggested assignments for the maxima at about 1692, 1687, and 1681 cm^{-1} are in agreement with this. For the assignment of 1671 to 1651, we suggest an assignment to a helical structure, probably α-helix.

The peak at about 1640 cm^{-1} behaves differently for the *B. mori* sample. A peak at about 1640 cm^{-1} is also observed in Raman spectroscopy for the spider silks, so the association to liquid water absorption is not probable. Some authors associated a band at about 1640 cm^{-1} with β-turn structures [Hollosi *et al.* 1994, van Dijk *et al*. 1997]. Also some contributions of side chain residues are possible (see Annex), especially lysine, glutamine, asparagine or arginine. Furthermore, it is surprising that in the spectra of the silk fibres, only the spider silks show clearly absorption maxima at about 1640 cm^{-1}.

The contribution of lysine, asparagine and arginine is for the dragline spider silk too small to expect it visible in the FT-IR spectra. However, when we look at the amino acid composition of all silks (see Chapter 4), the main difference between silkworm silks and the spider silks is to be found in the contribution of glutamine and glutamic acid (Glx).

Furthermore, it is clearly seen in Figure 7.7 that the ratio 1707/1644 for CH_3OH concentrations up to 60% is much higher than that for the untreated sample, whereas for higher CH_3OH concentrations the ratio 1703/1644 seems comparable to the untreated sample.

It is suggested that some polar side chain residues, like serine or glutamine, result in the Silk III folding behaviour what can explain the (weak) absorption maximum at about 1640 cm^{-1} for the spider silks (see spectra in Chapter 6) as a side chain vibration of glutamine. The contribution of these polar side chain residues in the Silk III structure could explain the effect on the maxima at about 1707 cm^{-1} whereas the side chain absorption has no effect on the β-sheet structure, represented by the peak at about 1703 cm^{-1}.

It seems that the effect of the water and/or methanol makes the side chain absorption at about 1644 cm^{-1} more visible in the *B. mori* and Tussah SF, whereas in the silk fibres, the peak remains invisible.

7.4.4. THE AMIDE II REGION (1480-1610 CM^{-1})

Figure 7.9 and Figure 7.10 show the effect of the CH_3OH treatment on the Amide II mode in the spectra for resp. *Bombyx mori* and *Antheraea pernyi*. For this region, more comparable spectra were obtained by normalizing on the maximum at about 1562 cm^{-1}.

The amorphous sample shows a sharp peak at 1562 cm^{-1}, a broader moderate band at 1552 cm^{-1} and a weaker shoulder at 1537 cm^{-1}. With increasing CH_3OH concentration, the peak at 1562 cm^{-1} becomes broader with a maximum at about 1566 cm^{-1} up to 60% CH_3OH concentration. However, for higher CH_3OH concentrations, this band again becomes smaller and the maximum shifts again to 1562 cm^{-1}.

The peaks at 1553 cm^{-1} and 1537 cm^{-1} clearly decrease and become a shoulder. For concentrations higher than 60%, these maxima again increase but remain weaker than in the untreated sample.

In Table 6.1 in Chapter 6, the assignments to secondary structure of peaks in the Amide II region were summarized.

It is suggested that the maximum at 1562 cm^{-1} can confirm the existence of β-sheet structures in all samples. Figure 7.11 shows the intensity of the maximum at 1562 cm^{-1} relative to the intensities of 1566 cm^{-1}, 1553 cm^{-1} and 1537 cm^{-1}.

We suppose that the bands at 1566-1568 cm^{-1} are associated with the presence of the Silk III structure, a type of helical structure, for the CH_3OH treated samples (20-60%). It can be expected that bands at different positions (e.g. 1566 and 1568 cm^{-1}) can be attributed to helical segments with a slightly different pattern of hydrogen bonding [Surewicz *et al.* 1987]. The assignment to a helical structure is also in agreement with the shoulder at higher wave number observed for the Tussah samples and the Tussah fibres (see Chapter 6).

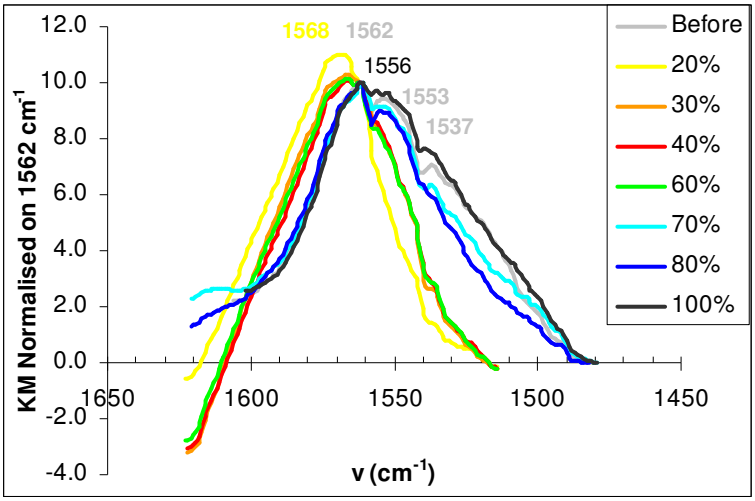

Figure 7.9 - The Amide II mode in the spectra for the CH_3OH treated samples

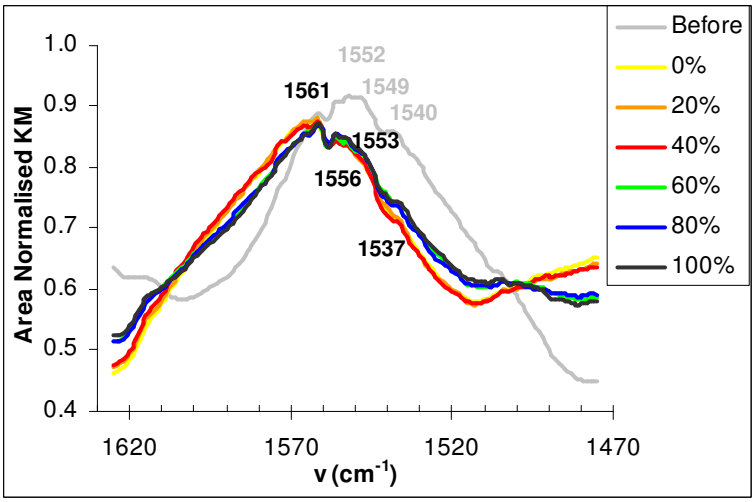

Figure 7.10 – Effect of CH_3OH in the Amide II region for the Tussah sample

With respect to the band at 1553-1556 cm^{-1}, it should be noted that although the untreated sample here shows a maximum at 1553 cm^{-1}, the maximum is shifted to 1556 cm^{-1} for the other untreated samples (*Bombyx mori* prepared 2nd time) as is also observed for the treated samples. For the Tussah sample, as shown in Figure 7.10, maxima at both wave numbers are observed for almost all samples (untreated and treated ones), however the intensity ratio I_{1562}/I_{1556} was comparable to the intensity ratio I_{1562}/I_{1553}. The decrease of this band and the shift to 1556 cm^{-1} for the other *B. mori* samples (see also Figure 7.11) can be an indication that the band at 1553-1556 cm^{-1} is attributed to a β-turn structure rather than to a random coil conformation. This is confirmed by the limited effect for the Tussah sample of which the untreated sample is proved to consist already mainly of β-sheet structures. The assignment to

β-turn and β-sheet structures are in agreement with the assignments in Table 6.1 (Chapter 6).

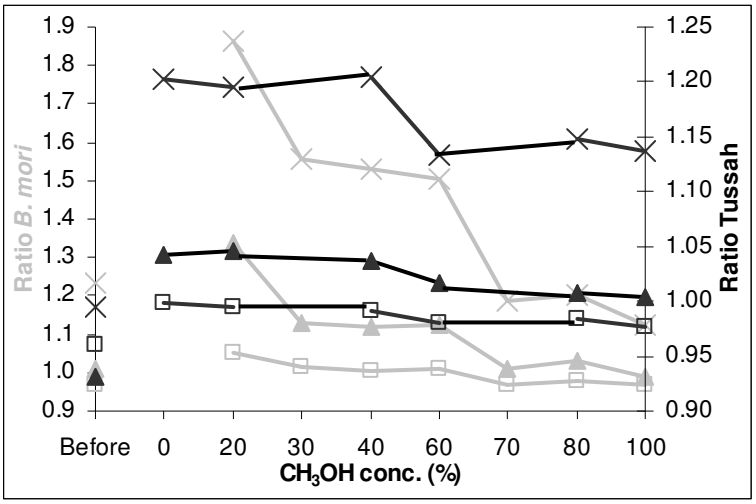

Figure 7.11 - The intensity ratios I_{1562}/I_{1566} (□), I_{1562}/I_{1553} (▲), I_{1562}/I_{1537} (×) for the regenerated *B. mori* fabric (black line) and the regenerated Tussah sample (gray line)

Like in the Amide I region, it seems that the low-wave number peak of the anti-parallel β-sheet structure is not visible whereas the high-wave number peak is considerably strengthened, contrary to what is observed in transmission FT-IR spectra.

These assignments are also in agreement with the more constant character of the intensity ratio I_{1562}/I_{1566} (indicated by □) and I_{1562}/I_{1553} (indicated by ▲). For the formation of β-turns, it can be expected that each treatment in *B. mori* is accompanied with two transition processes: the transition from random coil to β-turn and the transition from β-turn to β-sheet, as the β-turn structure is considered as an intermediate structure by several authors [Asakura *et al.* 2001, 2002a,b, Okabayashi *et al.* 2002, Peng *et al.* 2005].

A peak at 1540 cm^{-1} has been associated with the Silk I structure by Monti *et al.* [2003]. The ratio I_{1562}/I_{1537} is affected mostly by the CH_3OH treatment, as shown in Figure 7.11. A random coil conformation is not possible since the ratio 1562/1537 is comparable or even lower for the untreated *B. mori* sample and the *B. mori* samples treated with high CH_3OH concentration. In the experiment with the Tussah silk fibroin (Figure 7.10), however, the ratio is much higher in the treated samples than in the untreated one. Moreover, in the spectra of the silk fibres (Chapter 6), it is observed that the shoulder at about 1537 cm^{-1} is much weaker for the silkworm silks than for the spider silks. This again lets us suggest the assignment of the shoulder at 1537 cm^{-1} to a polar side chain residue, probably glutamine.

7.4.5. THE 1500-1300 CM^{-1} REGION

Figure 7.12 shows the region between 1500 and 1300 cm^{-1}.

The amorphous sample shows clear peaks at 1454, 1414, 1389, 1379 and 1336 cm^{-1}. With increasing CH_3OH concentrations up to 60%, the following transitions occur:

- The peak at 1454 cm^{-1} is transformed to a peak at somewhat lower frequency combined with a shoulder at about 1460 cm^{-1};
- The peak at 1414 cm^{-1} is broadened and shifted to somewhat higher frequency (± 1420 cm^{-1});
- The peak at 1389 cm^{-1} is clearly broadened and decreases;
- The peak at 1336 cm^{-1} clearly increases and shifts to somewhat higher frequency (±1340 cm^{-1}), whereas the peak at 1379 cm^{-1} becomes a shoulder of this increased peak.

When the CH_3OH concentrations is further increased to 100%, then:

- The shoulder at about 1460 cm^{-1} again decreases and a sharp peak at about 1450 cm^{-1} is observed;
- The band at 1414 cm^{-1} before CH_3OH treatment returns from ±1420 cm^{-1} back to ±1415 cm^{-1};
- The band at about 1340 cm^{-1} with its shoulder is again split up in a broader band with maximum at 1371-1375 cm^{-1} and a smaller band with maximum at 1335 cm^{-1} with a shoulder at somewhat higher frequency.

Peaks at about 1414, 1387 and 1334 cm^{-1} have been identified as Silk I markers [Monti *et al.* 2001, 2003]. The decrease in these peaks (and/or shift to higher wave number) suggests that some Silk I structures are indeed transformed. The proposed Silk III structure present in the samples treated with lower CH_3OH concentration may explain the shift observed for these samples.

Moore & Krimm [1976] reported that a peak at 1336 cm^{-1} is attributed to CH_3 symmetric stretching. The change in this peak is in accordance with the change in the Amide B peak at 2930 cm^{-1} of CH_3 symmetric stretching (Figure 7.4). The shifts to higher wave numbers can also be attributed to stronger H-bonds due to the presence of water and/or methanol.

The peak at ±1450 cm^{-1} is often used as standard in normalizing the spectra. From this study, it can be concluded that this peak is affected by an induced transformation from random coil to β-sheet and is, in our case, not useful for normalizing. The effect of water vapour, released during the experiment, can play a role in this.

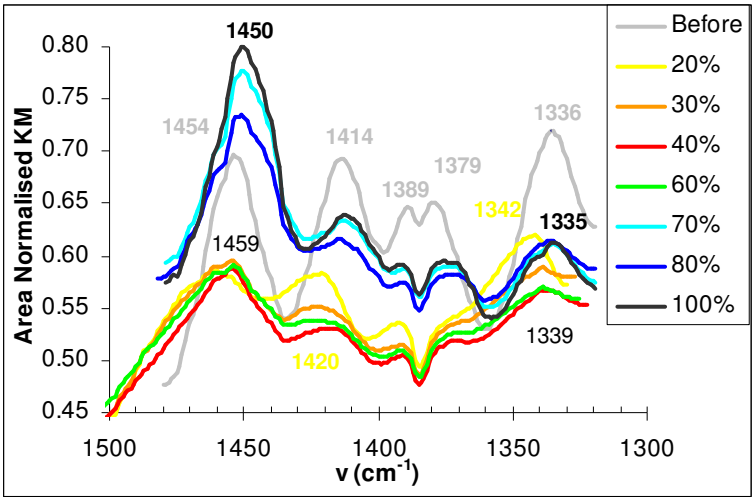

Figure 7.12 - The 1500-1300 cm^{-1} region in the spectra for the CH_3OH treated samples

7.4.6. THE AMIDE III MODE (1320-1180 CM^{-1})

The Amide III mode (1200-1300 cm^{-1}) is represented in Figure 7.13. With respect to this region, for silk no consensus is found in literature for the assignment of the different maxima, as described in Chapter 6.

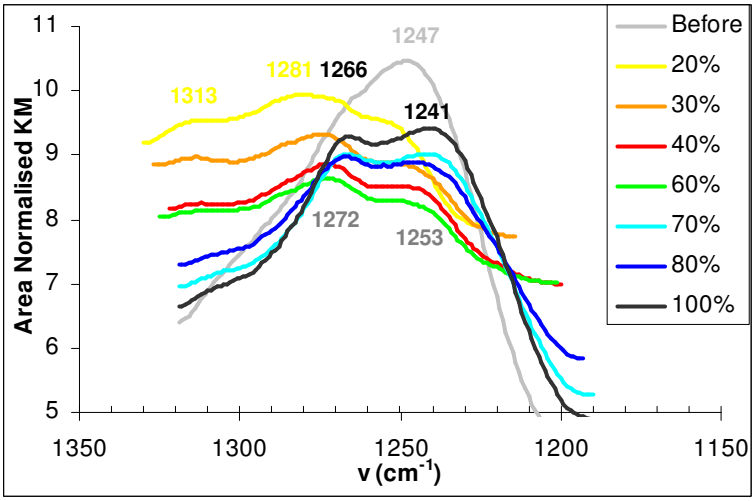

Figure 7.13 – The Amide III mode in the spectra of the treated samples

From Figure 7.13, it is clear that the broad peak at 1247 cm^{-1} is split in two peaks at ±1266 cm^{-1} and 1241 cm^{-1} for the samples treated with higher CH_3OH. Here again a shift to slightly higher wave numbers of the band at 1266 cm^{-1} is observed for concentrations of 60% and lower. Maxima at about 1281-1272 cm^{-1} can thus be

related to the Silk III structure. For the silk I conformation, several authors [Frushour & Koenig 1975, Itoh *et al.* 1978, Ishida *et al.* 1990, Monti *et al* 2001, 2003] found two maxima at about 1273-1276 cm^{-1} and 1243-1245 cm^{-1} for silk fibroin with Silk I (or β-turn) conformation. The observed maxima in our spectra are shifted too much to higher wave number to make this assignment acceptable for the combined peaks of about 1272 cm^{-1} and 1253 cm^{-1}.

From the difference in the Amide III region for *Bombyx mori* and Tussah, it was concluded in Chapter 6 that the maximum at about 1240 cm^{-1} is associated with the α-helical structure. In order to verify this assignment, Figure 7.14 shows the Amide III region for the Tussah sample. The peak maxima at about 1250 and 1225 cm^{-1} decrease similarly relative to the maxima at about 1265 cm^{-1}. Since we expect an increase of the β-sheet content and a decrease of the α-helix content and random coil content, we would associate the β-sheet structure with the maxima at ± 1265 cm^{-1}. The slight shift to higher wave number (1249 cm^{-1} compared to 1247 cm^{-1}) for the different untreated *B. mori* samples (Figure 7.3) confirms this assignment. However, this assignment is not in agreement with Table 6.1 in Chapter 6 reporting a lower wave number range for β-sheet than for random coil conformation. This is explained as follows. In the Amide I region, most spectra of proteins show a weak high wave number band (1685-1695 cm^{-1}) and a strong low wave number band (1620-1640 cm^{-1}). In DRIFT spectroscopy, the low wave number band in the Amide I and II regions is not observed and the high wave number band is clearly strengthened. We suggest that the same is valid in the Amide III region in the DRIFT spectra.

Furthermore, the maximum at about 1243-1249 cm^{-1} is then associated with the α-helix structure. This is in accordance with the assignment of the Silk III structure, a type of helical structure, to a maximum at about 1250 cm^{-1}. The maximum at about 1225 cm^{-1} in the Tussah spectra and at about 1240 cm^{-1} in the *B. mori* spectra are then attributed to the random coil structure.

Bhat and Nadiger [1980] suggested the method for calculating the crystallinity index of SF with the intensity ratio of the IR absorption bands at 1265 and 1235 cm^{-1}. Similarly, the ratio of the peak intensity attributed to β-sheet / Silk III (1281-1266 cm^{-1}) versus the peak intensity attributed to random coil (1240-1251 cm^{-1}) conformation is calculated and represented for all regenerated *B. mori* and Tussah samples in Figure 7.15. For all CH_3OH treated samples the β-sheet content seems to increase compared to the untreated samples ("Before"). The β-sheet content seems to decrease with the increase of CH_3OH concentration. It is clear that this "crystallinity index" is much higher for the group 20%-30%-40%-60%, and will be near 1 for higher concentrations, and much lower than 1 for the untreated sample. However, it should be remarked that in the case of lower CH_3OH concentration, the increase in this ratio represents the formation of the Silk III structure and not β-sheet formation.

After CH_3OH treatment, an extra weak peak at ±1313 cm^{-1} is also observed. Krimm & Bandekar [1986] computed the complete normal mode spectrum of β-turn type II and predicted all the Amide III modes in the 1290-1330 cm^{-1} range; because this region is at a significantly higher frequency than the Amide III modes associated with β-sheets and α-helices, these authors asserted that this spectral range can

provide a diagnostic for β-turns, although they advised it must be used with caution because of its sensitivity to side chain composition and backbone conformation. The peak at about 1313 cm^{-1} then confirms the presence of β-turns type II, in agreement with the repeated turns type II model recently proposed for the Silk I peptides by Asakura *et al.* [2001].

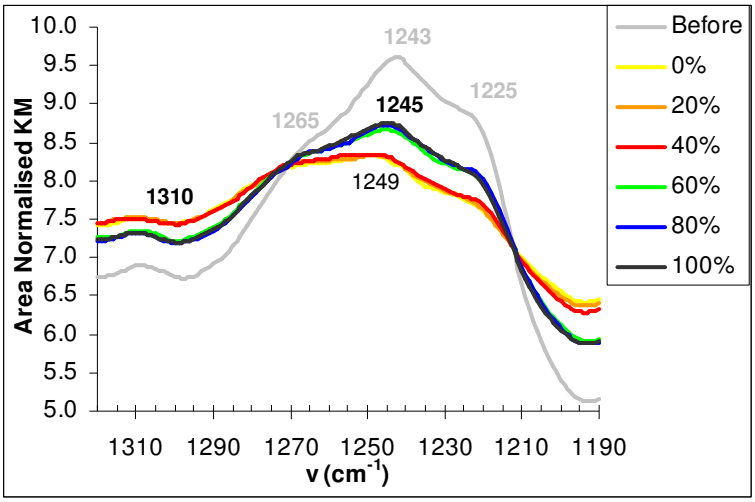

Figure 7.14 – The effect of CH_3OH concentration in the Amide III region for the Tussah sample

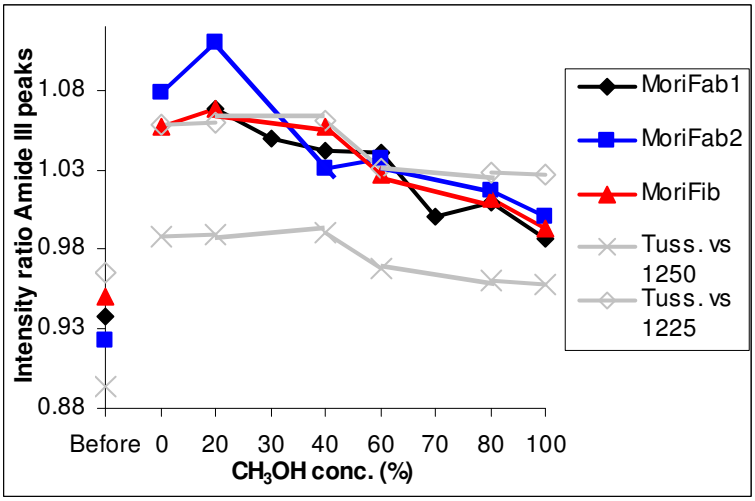

Figure 7.15 – The "crystallinity index" for *B. mori* and for Tussah ("Tuss. vs 1250" – "Tuss. vs. 1225")

7.4.7. THE 1220 – 920 CM^{-1} REGION

As can be seen in Figure 7.16, there are some clear differences in the spectra of the CH_3OH treated samples in comparison with the untreated one.

The untreated sample is characterized by the peaks at 1171 cm^{-1}, overlapping peaks at 1057 cm^{-1} and 1068 cm^{-1}, a weak peak/shoulder at 1105 cm^{-1}, a sharp peak at 1015 cm^{-1} and a broad band at 946 cm^{-1}. The CH_3OH treatment induces the following changes:

- A broadening and shift of the peak at 1171 cm^{-1} for lower CH_3OH concentrations;
- A shift to ±1080 cm^{-1} and even higher to 1086 cm^{-1} for 20% CH_3OH treated sample, to about 1070 cm^{-1} for higher CH_3OH concentrations with a shoulder at 1060-1045 cm^{-1};
- A new shoulder at ±1002 cm^{-1} and a clear new peak at 977 cm^{-1} for higher CH_3OH concentrations;
- A disappearance of the band at 946 cm^{-1} and appearance of a new maximum at about 930 cm^{-1}.

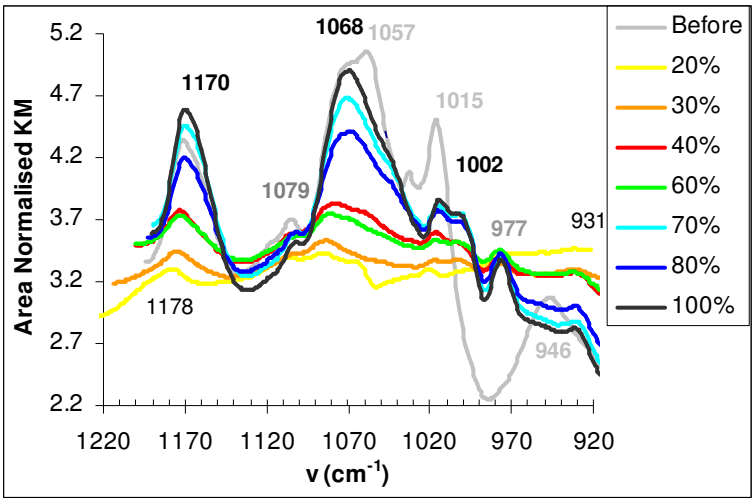

Figure 7.16 - The 1220-920 region in the spectra of the CH_3OH treated samples

Peaks at about 1172-1173 cm^{-1} were suggested in Chapter 6 to be attributed to the poly-alanine motif. Figure 7.17 shows the shift of the band at about 1172 cm^{-1} for the different samples. It is clear that for low CH_3OH concentrations, a shift to higher wave numbers is observed. The effect seems to decrease with β-sheet or β-turn content originally present in the regenerated untreated sample. We accept the assignment to a poly-alanine sequence, probably situating in a more amorphous region since the peak is not or only slightly shifted after the conformational transition ("Before" versus "70-100%"). A more helical structure possibly can shift the wave number of this peak to higher values.

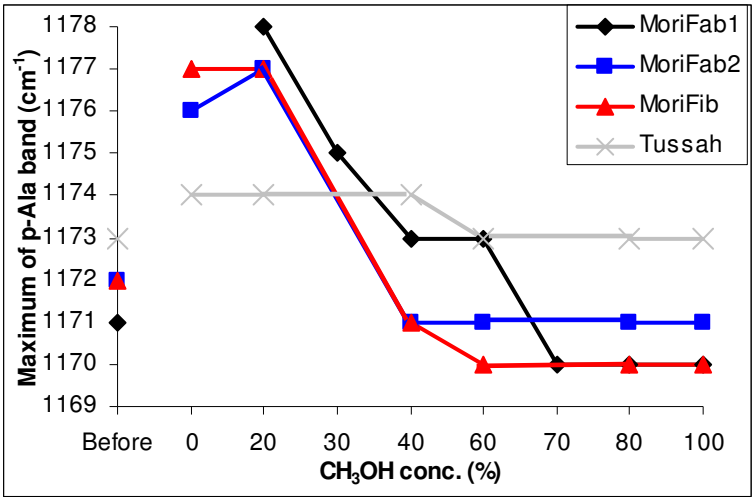

Figure 7.17 - Shift of poly-alanine band (± 1172 cm^{-1})

Peaks at about 1073-1095 cm^{-1} are assigned to a β-sheet conformation [Tsukada *et al.* 1995, Edwards & Farwell 1995]. They are usually attributed to vibrations of Ala-rich segments of the fibroin chain [Frushour & Koenig 1974, Moore & Krimm 1976, Monti *et al.* 2005]. Since the poly-alanine motif is not present in *Bombyx mori*, it could also be associated with the GAGAGS motif that is known to form an antiparallel β-sheet in *B. mori*. Figure 7.18 represents the shift of the peak at about 1057-1072 cm^{-1} by increasing CH_3OH concentrations for different samples. We suppose that the chain length of the β-sheet structure and the presence of Silk I and/or Silk III structures play a role in this shift.

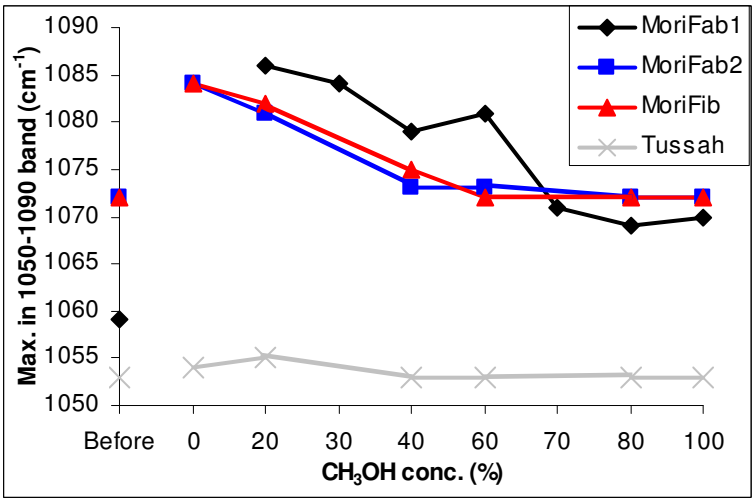

Figure 7.18 - Effect of CH_3OH on band at about 1072 cm^{-1}

Taking into account the spectrum of the untreated samples, the following assignments are suggested in this region:

- 1079-1086 cm^{-1} : Silk I (or β-turn) structure
- 1068-1075 cm^{-1} : β-sheet structure
- 1057-1060 cm^{-1} : random coil structure
- 1030 cm^{-1} : α-helix structure (only observed for Tussah)

The peak at about 1015 cm^{-1} has been assigned to the Gly-Gly linkage, characteristic for the amorphous region in silk fibroin [Asai *et al.* 1955, Bhat & Nadiger 1978, Freddi *et al.* 1999]. In spider silk, the Gly-Gly-X motif is found to be involved in either a β-turn structure or a 3_{10} helical structure. Some authors [Asakura *et al.* 2001, 2002a,b, Okabayashi *et al.* 2002, Peng *et al.* 2005] believe that the β-turn structure is an intermediate structure in the conformational transition from random coil to β-sheet structure. With the assignment of 1015 cm^{-1} to the β-turn structure, this theory is confirmed with the decrease of the intensity of this peak.

Peaks at about 998 cm^{-1} and 975 cm^{-1} have been assigned to Gly-Ala repeats in *B. mori* [Asai *et al.* 1995, Freddi *et al.* 1999] and are considered as characteric peaks indicating a β-sheet structure [Magoshi *et al.* 1979, Freddi *et al.* 1999]. For Tussah silk, the β-sheet peak is observed typically at 965 cm^{-1} [Freddi *et al.* 1997, Kweon *et al.* 2000]. Again a confirmation is obtained for the formation of β-sheet crystals when regenerated *B. mori* silk is treated with CH_3OH.

A peak at 923 cm^{-1} has been associated with the motion of the alanyl residue [Taddei *et al.* 2003] in Tussah fibres, usually involved in an α-helical structure. Monti *et al.* [2003] associated the peaks at about 930 cm^{-1} and 950 cm^{-1} with the Silk I structure, whereas Zheng *et al.* [2004] attributed a peak at about 936-946 cm^{-1} to an α-helical structure in certain proteins. We do not expect any helical structure in *B. mori* so we rather follow Monti *et al.* [2003] that both peaks are associated with a Silk I structure, probably a β-turn structure. If all regenerated *B. mori* samples are compared, only a band at about 950 cm^{-1} is observed, whereas for the Tussah sample the band is observed at 930 cm^{-1}. So, the assignment of the peak at about 950 cm^{-1} will be rather random coil, whereas for the assignment of the peak at about 930 cm^{-1} the Silk I or β-turn structure is suggested.

7.4.8. THE 920-400 CM^{-1} REGION

Finally, the region between 900 and 400 cm^{-1} (Figure 7.19) is characterized by some broad but strong bands in the 700 cm^{-1} region (Amide V), a band at about 660 cm^{-1} and at about 560 cm^{-1} (Amide VI).

The broad band in the 700 cm^{-1} region shifts from 715 cm^{-1} to 734-737 cm^{-1} for CH_3OH concentrations of 20% to 60%, and returns to a lower wave number of 723-724 cm^{-1} for higher CH_3OH concentrations. The shift to a higher wave number for lower concentrations is attributed to the presence of the Silk III structure in these samples, as stated before. As for the β-sheet peak in the Amide I peak, also a correlation with the size of the crystal is suggested.

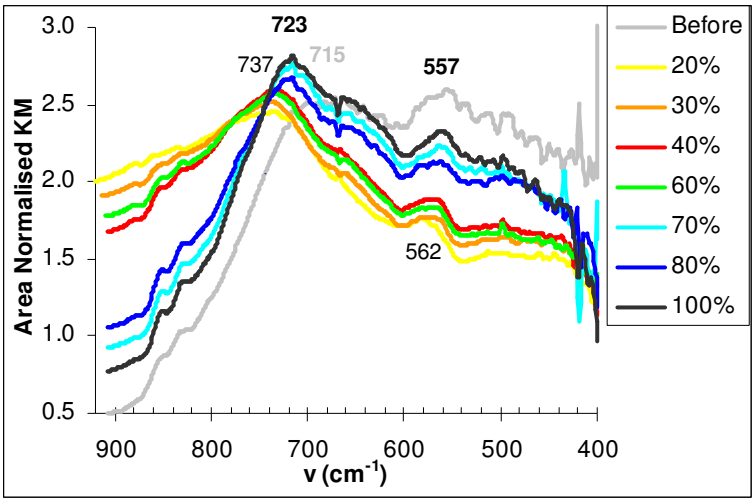

Figure 7.19 - The 920-400 region in the spectra of the CH_3OH treated samples

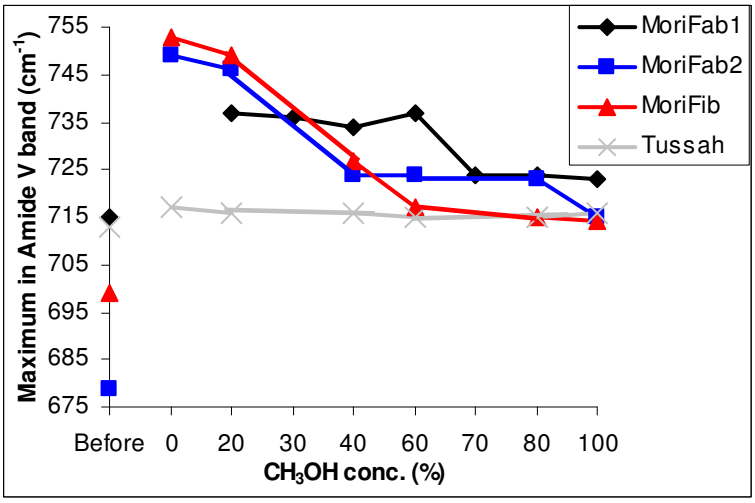

Figure 7.20 - Shift of the 700 cm^{-1} band for CH_3OH treated samples

The shift in this region is shown in detail in Figure 7.20 for the different samples. A shift to higher wave numbers is clearly observed with CH_3OH concentrations up to 60%. A further increase in CH_3OH concentration has little further effect on peak shift. It is also possible that at low CH_3OH concentrations the broad band at about 750 cm^{-1} is affected a lot by the high water content, having a high hydrogen bonding potential, making the structure less stabilized and thus more difficult to measure with infrared spectroscopy. It is known that the Amide V band is also affected by the strength of the hydrogen bonds [Krimm & Bandekar 1986]. A shift to lower wave numbers indicates that stronger hydrogen bonds are formed. This can be an

explanation for the shift to lower wave numbers for higher CH_3OH concentrations, since we expect these samples to contain a higher β-sheet content.

From the experiments with the Tussah sample, it is clear that the peaks at about 900 cm^{-1} and 624 cm^{-1} are associated with the α-helical conformation.

It is known that the doublet at 830 and 850 cm^{-1} is due to Fermi resonance between a ring breathing vibration and the overtone of an out-of-plane ring-bending vibration of the tyrosine (Tyr) residue [Siamwiza *et al.* 1975, Takeuchi *et al.* 1989]. For details, we refer to Annex about the contribution of side chain modes to vibrational spectra. In *Bombyx mori*, the tyrosine residues are normally situated in the amorphous regions, which contain most of the amino acids with bulky and polar side chains [Lucas 1958]. Monti *et al.* [1998] observed that the R_{Tyr} decreases from 1.8 to 1.5 on going from lyophilized powder (obtained from liquid silk collected from glands) to fibre. They concluded that the hydrogen bonds involving the tyrosyl residues are stronger in the fibre than in the lyophilized powder and, consequently, the mobility of tyrosine residues is higher in the latter. Compared to the detailed study of Siamwiza *et al.* [1975], who found values between 0.3 and 1.25, the values obtained by Monti *et al*. [1998] are very high.

In our study, the ratio of 850 to 828 cm^{-1} is increased compared to the untreated samples and is situated always between 0.85 and 1.00. We can expect that the phenolic OH group acts as both donor and acceptor for the hydrogen bonds. [Siamwiza *et al.* 1975]. Moreover, we would conclude that the hydrogen bonds involving the tyrosyl residues are stronger in the regenerated sample than in the CH_3OH treated sample and, consequently, the mobility of tyrosine residues is higher in the latter. We would expect the opposite. It is suggested that the presence of remaining fractions of CH_3OH residues, as H acceptors, plays a role in this.

7.5. ATR-FTIR SPECTROSCOPY

The untreated and CH_3OH treated samples of regenerated *B. mori* fibres (prepared the 2nd time) were also analysed by means of ATR-FTIR spectroscopy. ATR-FTIR spectroscopy of the CH_3OH treated Tussah sample was not possible because the pression on the samples results in disintegration. For the Amide I and II region, the spectra are shown in Figure 7.21.

The regenerated *B. mori* sample shows an absorption maximum at 1636 cm^{-1} in the Amide I region, and a maxima at 1515 cm^{-1} with a shoulder at about 1530 cm^{-1} in the Amide II region, indicating a high amount of random coil structure.

The decreasing shoulder at about 1640 cm^{-1} indicates the decreasing amount of random coil and/or Silk III conformation with increasing CH_3OH concentrations, whereas the increasing intensity of the band at 1620 cm^{-1} confirms the formation of β-sheet crystals. Also in the Amide II region, the decreasing shoulder at about 1530 cm^{-1} combined with the increase of the intensity of the maxima at about 1513 cm^{-1} indicates the conformational transition into β-sheet structures. The conformational transition from random coil to β-sheet conformation is clearly confirmed by this technique.

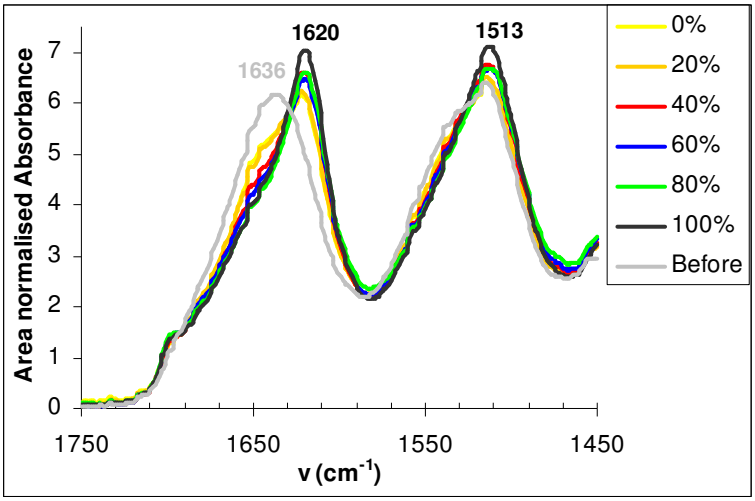

Figure 7.21 - ATR-FTIR spectra in Amide I and II region for untreated and treated regenerated *B. mori* fibres

The ATR spectra (Figure 7.21) clearly shows an increase of the intensity of the maximum at about 1512 cm^{-1}, thus associated with the β-sheet structure, and a decrease of the shoulder at about 1540 cm^{-1}, assigned to the random coil structure. The differentiation between random coil and Silk III structure cannot be observed.

The ATR spectrum in the range 1400-500 cm^{-1} for the regenerated sample ("Before") and the CH_3OH treated samples is shown in Figure 7.22. The absorption maxima are indicated.

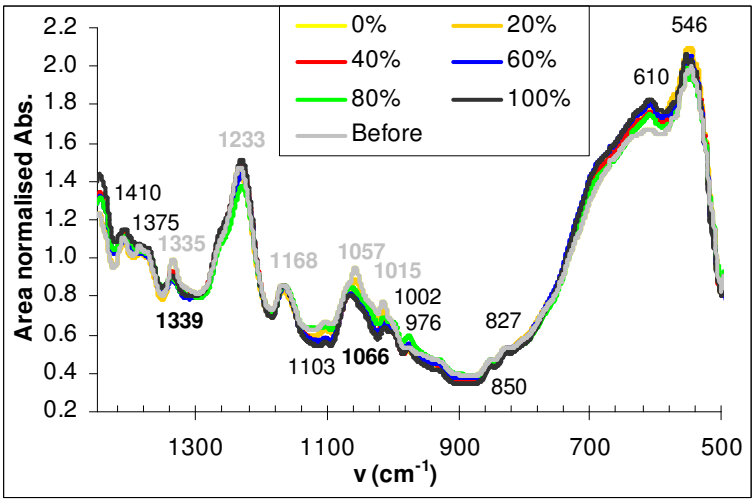

Figure 7.22 - ATR-FTIR spectra of the untreated and treated *B. mori* samples

As in the DRIFT spectra, the transition is visible in the region 1420-1320 cm^{-1}, in the region 1300-1200 cm^{-1} (Amide III), the region 1100-950 cm^{-1} and the region 700-600 cm^{-1} (Amide V).

In the region 1420-1320 cm^{-1}, the intensity of the maxima at about 1410, 1375 and 1335 cm^{-1} is decreased confirming the decrease in the amount of Silk I or random coil structure. Also the shift to higher wave number of the maxima at 1335 cm^{-1} for the untreated sample to 1339 cm^{-1} for the CH_3OH (60% and higher) treated samples, as observed in the DRIFT spectra, should be remarked.

In the Amide III region, mostly the increase of the shoulder at about 1265 cm^{-1} is visible compared to the spectrum of the untreated sample. It confirms the assignment to the β-sheet structure.

The conformational transition is best observed in the region 1100-950 cm^{-1}. First of all, the intensity of the peak at about 1057 cm^{-1} decreases significantly. In the CH_3OH treated samples, the maximum is shifted to 1066 cm^{-1}, accompanied with a weak shoulder at about the maximum observed in the untreated sample. This indicates clearly that the peak at about 1057 cm^{-1} is assigned to the random coil structure and the peak at about 1066 cm^{-1} to the formation of the β-sheet crystals. At somewhat lower wave numbers, the peak at about 1015 cm^{-1} clearly decreases, whereas the peak at about 976 cm^{-1} clearly increases in the CH_3OH treated samples compared to the untreated one. For the 60-80-100% CH_3OH treated samples, the shoulder observed at about 1002 cm^{-1} becomes a weak peak. It confirms the assignment of the combined peaks at about 1000 and 976 cm^{-1} to the β-sheet structure.

Furthermore, in the Amide V region, compared to the untreated sample a shoulder at about 675 cm^{-1} and the peak at about 610 cm^{-1} are clearly increasing. This region is, however, completely different than in the DRIFT spectra.

7.6. CONCLUSION

It was indeed possible to visualize structural differences in the spectra after the treatment of regenerated samples with methanol. Moreover, for the *Bombyx mori* sample the highest effect was obtained at 70% methanol concentration. Further increase of the concentration has a limited effect.

DRIFT spectroscopy allows a more detailed description of the conformational transition than transmission FT-IR spectroscopy, which is always used in literature. It is confirmed that the β-turn structure can be considered as an intermediate structure that is formed during the conformational transition from random coil to β-sheet structure.

Also compared to the studied ATR spectroscopy, DRIFT spectroscopy reveals more details. However, the conformational differences observed in ATR confirm the transition from random coil to β-sheet structure.

It is clear that the spectra for methanol concentrations 20-60% show another behaviour than those for higher methanol concentrations. This is attributed to the higher water content in the samples, resulting in a different structure. A Silk III

structure (probably a 3_1 helix, see Chapter 5) for silk fibroin at the air-water interface, is suggested for the samples treated with low methanol concentrations (up to 60%). This study allowed the identification of some Silk III spectral markers.

In Table 7.1 the suggestions for the assignment to secondary structure are reported.

Table 7.1 – Suggested assignments to secondary structure in DRIFTS

Wave number	Assignment to structure
1703 (Amide I) 1561-1563 (Amide II) 1265-1266 (Amide III) 1068-1075 (Amide IV) 965-977 715-725 (Amide V) 557-562	β-sheet
1681 (Amide I) 1225-1240 (Amide III) 1057-1060 (Amide IV) 950 660 (Amide V)	Random coil
1693-1687 (Amide I) 1553-1556 (Amide II) 1414-1420 1389 1336 1313-1320 (Amide III) 1079-1086 1015 930	Silk I (β-turn)
1671-1651 (Amide I) 1243-1249 (Amide III) 1053-1055 (Amide IV) 900 624	α-helix
1707 (Amide I) 1566-1568 (Amide II) 1281-1272 (Amide III) 1173-1178 (Amide IV) 1086-1079 (Amide IV) 734-737 (Amide V)	Silk III or 3_2 helical structure
1640-1645 1537-1540 (Amide II)	Side chain vibration

To estimate the content of the different secondary structures, a curve fitting procedure was tried. Although this procedure is often used in literature for proteins,

it was not possible to get repeatable results for the silk proteins. The theoretical background of the spectra is still badly understood. Furthermore, the number of bands within these regions, the width, height and overall shape of the absorption bands of the different functional groups are not known beforehand, what makes the degrees of freedom in this procedure and thus the number of possible solutions very high. A further optimization of the procedure is required in order to quantify the secondary structure of the silk proteins.

7.7. REFERENCES

Asakura T. & Yamaguchi T., Proposal of new model for silk I structure of *B. mori* silk fibroin, J. Seric. Sci. Jpn. 56:300-304 (1987)

Asakura T., Yamane T., Nakazawa Y., Kameda T., Ando K., Structure of *Bombyx mori* silk fibroin before spinning in solid state studied with Wide Angle X-Ray Scattering and 13C Cross-Polarization/Magic Angle Spinning NMR, Biopolymers 58:521-525 (2001a)

Asakura T., Ashida J., Yamane T., Kameda T., Nakazawa Y., Ohgo K. And Komatsu K., A repeated beta-turn structure in poly(Ala-Gly) as a model for Silk I of *Bombyx mori* silk fibroin studied with two-dimensional spin-diffusion NMR under Off Magic Angle Spinning and Rotational Echo Double Resonance, J. Mol. Biol. 306:291-305 (2001b)

Asakura T., Yao J., Yamane T., Umemura K., Ulrich A.S., Heterogeneous structure of silk fibers from *Bombyx mori* resolved by ^{13}C solid-state NMR spectroscopy, J. Am. Chem. Soc. 124(30):8794-8795 (2002a)

Asakura T. & Yao J., 13C CP/MAS NMR study on structural heterogeneity in *Bombyx mori* silk fiber and their generation by stretching, Protein Science 11:2706-2713 (2002b)

Asai M., Tsuboi H. Shimanouchi T., Mizuchima S., Infrared spectra of polypeptides and related compounds. I, J. Phys. Chem. 59:322-325 (1955)

Bandekar J. & Krimm S., Vibrational analysis of peptides, polypeptides, and proteins: Characteristic amide bands of β–turns, Proc. Nat. Acad. Sci. USA 76(2):774-777 (1979)

Bhat N.V. & Nadiger G.S., Effect of nitrogen plasma on the morphology and allied textile properties of Tasar silk fibres and fabrics, Text. Res. J., Dec, 685-691 (1978)

Bhat N.V. & Nadiger G.S., Crystallinity in silk fibers – Partial acid hydrolysis and related studies, J. Appl. Polym. Sci. 25(5):921-932 (1980)

Blundell T., Barlow D., Borkakoti N., Thornton J., Solvent-induced distortions and the curvature of alpha-helices, Nature 306:281-283 (1983)

Canetti M., Seves A., Secundo F., Vecchio G., CD and small-angle X-Ray scattering of silk fibroin in solution, Biopolymers 28:1613-1624 (1989)

Chen X., Li W., Yu T., Conformation transition on silk fibroin induced by blending chitosan, J. Polym. Sc. Polym. Phys. 35:2293-2296 (1997)

Chen X., Shao Z.Z., Marinkovic N.S., Miller L.M., Zhou P., Chance M.R., Conformation transition kinetics of regenerated *Bombyx mori* silk fibroin membrane monitored by time-resolved FT-IR spectroscopy, Biophys. Chem. 89:25-34 (2001)

Chen X., Knight D.P., Shao Z.Z., Vollrath F., Conformation transition in silk protein films monitored by time-resolved Fourier transform infrared spectroscopy: Effect of potassium ions on Nephila spidroin films, Biochemistry 41(50):14944-14950 (2002)

Chirgadze Y.N., Brazhinikov E.V., Nevskaya N.A., Intramolecular distortion of alpha-helical structure of polypeptides, J. Mol. Biol. 102(4):781-792 (1976)

Dicko C., Knight D., Kenny J.M., Vollrath F., Secondary structures and conformational changes in flagelliform, cylindrical, major, and minor ampullate silk proteins. Temperature and concentration effects, Biomacromolecules 5(6):2105-2115 (2004)

Edwards H.G.M. & Farwell D.W., Raman spectroscopic studies of silk, J. Raman Spectrosc. 26: 901-909 (1995)

Fossey S.A., Nemethy G., Gibson K.D., Scheraga H.A., Conformational energy studies of β-sheets of model silk fibroin peptides. I. Sheets of poly(Ala-Gly) chains, Biopolymers 31(13):1529-1541 (1991)

Freddi G., Monti P., Nagura M., Gotoh Y., Tsukada M., Structure and molecular conformation of tussah silk fibroin films: Effect of heat treatment, J. Polym. Sci. Pt. B-Polym. Phys. 35(5):841-847 (1997)

Freddi G., Pessina G., Tsukada M., Swelling and dissolution of silk fibroin (*Bombyx mori*) in N-methyl morpholine N-oxide, Int. J. Biol. Macromol. 24:251-263 (1999)

Frushour B.G. & Koenig J.L., Raman spectroscopic study of mechanically deformed poly-L-alanine, Biopolymers 13:455-474 (1974)

Frushour B.G. & Koenig J.L., In: Advances in Infrared and Raman spectroscopy, Vol. 1, Clark R.J.H., Hester R.E. (Eds.), Heyden, London, 35 (1975)

Ha S.-W., Tonelli A.E., Hudson S.M., Structural studies of *Bombyx mori* silk fibroin during regeneration from solutions and wet fiber spinning, Biomacromolecules 6:1722-1731 (2005)

Hijirida D.H., Do K.G., Michal C., Wong S., Zax D., Jelinski L.W., 13C NMR of *Nephila clavipes* major ampullate silk gland, Biophys. J. 71(6):3442-3447 (1996)

Hino T., Tanimoto M., Shimabayashi S., Change in secondary structure of silk fibroin during preparation of its microspheres by spray-drying and exposure to humid atmosphere, J. Colloid Interface Sci. 266:68-73 (2003)

Hollosi M., Majer Z.S., Ronai A.Z., Magyar A., Medzihradszky K., Holly S., Perczel A., Fasman G.D., CD and Fourier Transform IR spectroscopic studies of peptides. II. Detection of beta-turns in linear peptides, Biopolymers 34:177-185 (1994)

Iizuka E. & Yang J.T., The disordered and beta conformations of silk fibroin in solution, Biochemistry 7(6):2218-2228 (1968)

Ishida M., Asakura T., Yokoi M., Saito H., Solvent- and mechanical-treatment-induced conformational transition of silk fibroins studied by high-resolution solid-state 13C NMR spectroscopy, Macromolecules 23:88-94 (1990)

Itoh K., Magoshi J., Magoshi Y., Nakamura S., in: Proceedings of the 6th International Conference on Raman Spectroscopy, Heiden, London, Vol. 2, 290-291 (1978)

Kim U.-J., Park J., Li C., Jin H.-J., Valluzzi R., Kaplan D.L., Structure and properties of silk hydrogels, Biomacromolecules 5:786-792 (2004)

Krimm S. & Bandekar J., Vibrational spectroscopy and conformation of peptides, polypeptides and proteins, Advances in Protein Chemistry 38:181-364 (1986)

Kweon H.Y. & Park Y.H., Structural and conformational changes of regenerated *Antheraea pernyi* silk fibroin films treated with methanol solution, J. Appl. Polym. Sci. 73:2887-2894 (1999)

Kweon H.Y., Um I.C., Park Y.H., Thermal behavior of regenerated *Antheraea pernyi* silk fibroin film treated with aqueous methanol, Polymer 41(20):7361-7367 (2000)

Kweon H.Y., Um I.C., Park Y.H., Structural and thermal characteristics of *Antheraea pernyi* silk fibroin/chitosan blend film, Polymer 42:6651-6656 (2001a)

Kweon H., Ha H.C., Um I.C., Park Y.H., Physical properties of silk fibroin/chitosan blend films, J. Appl. Polym. Sci. 80:928-934 (2001b)

Kweon H., Woo S.O., Park Y.H., Effect of heat treatment on the structural and conformational changes of regenerated *Antheraea pernyi* silk fibroin films, J. Appl. Polym. Sci. 81:2271-2276 (2001c)

Li M., Lu S., Wu Z., Yan H., Mo J., Wang L., Study on porous silk fibroin materials. I. Fine structure of freeze dried silk fibroin, J. Appl. Polym. Sci. 79(12):2185-2191 (2001a)

Li M.Z., Tao W., Lu S.Z., Kuga S., Compliant film of regenerated *Antheraea pernyi* silk fibroin by chemical crosslinking, Int. J. Biol. Macromol. 32(3-5):159-163 (2003a)

Li M.Z., Tao W., Kuga S., Nishiyama Y., Controlling molecular conformation of regenerated wild silk fibroin by aqueous ethanol treatment, Polymers for Advanced Technologies 14 (10):694-698 (2003b)

Liang C.X. & Hirabayashi K., Mechanical properties of fibroin-chitosan membrane, J. Appl. Polym. Sc. 45:1937-1943 (1992)

Lotz B. & Cesari F.C., Chemical structure and the crystalline structures of *Bombyx mori* silk fibroin, Biochimie 61(2):205-214 (1979)

Lucas F., Shaw J.T.B., Smith S.G., The silk fibroins, Adv. Protein Chem. 13:107-242 (1958)

Magoshi J., Mizuide M., Magoshi Y., Takahashi K. Kubo M., Nakamura S., Physical properties and structure of silk. VI. Conformational changes in silk fibroin

induced by immersion in water at 2 to 130°C, J. Polym. Sci. Pt. B-Polym. Phys. 17:515-520 (1979)

Magoshi J., Magoshi Y., Nakamura S., Mechanism of fiber formation of silkworm, In: Silk polymers: Material science and biotechnology, ACS Symposium Series 544, Washington DC, 292-310 (1994)

Monti P., Freddi G., Bertoluzza A., Kasai N., Tsukada M., Raman spectroscopic studies of silk fibroin from *Bombyx mori*, J. Raman Spectrosc. 29(4):297-304 (1998)

Monti P., Taddei P., Freddi G., Asakura T., Tsukada M., Raman spectroscopic characterization of *Bombyx mori* silk fibroin: Raman spectrum of Silk I, J. Raman Spectrosc. 32 (2):103-107 (2001)

Monti P., Taddei P., Freddi G., Ohgo K., Asakura T., Vibrational 13C-Cross-Polarization/Magic Angle Spinning NMR spectroscopic and thermal characterization of poly(alanine-glycine) as model for Silk I *Bombyx mori*, Biopolymers (Biospectroscopy) 72:329-338 (2003)

Monti P., Freddi G., Sampaio S., Tsukada M., Taddei P., Structure modifications induced in silk fibroin by enzymatic treatments. A Raman study, J. Mol. Struct. 744:685-690 (2005)

Moore W.H. & Krimm S., Vibrational analysis of peptides, polypeptides, and proteins. II. β-poly(L-alanine) and β-poly(L-alanylglycine), Biopolymers 15(12):2465-2483 (1976)

Moore W.H. & Krimm S., Vibrational analysis of peptides, polypeptides, and proteins. I. Polyglycine I, Biopolymers 15(12):2439-2464 (1976)

Nevskaya N.A. & Chirgadze Y.N., Infrared spectra and resonance interactions of amide-I and II vibration of alpha-helix, Biopolymers 15(4):637-648 (1976)

Nakamura S., Magoshi J., Magoshi Y., Thermal properties of silk proteins in silkworms, In: Silk polymers: Material science and biotechnology, ACS Symposium Series 544, Washington DC, 210-221 (1994)

Okabayashi H., Ishida M., Tamaoki H., Masuda H., O'Connor C.J., Fourier transform IR study of aggregational behavior of N-acetyl-L- and N-butyloxycarbonyl-L-glutamic acid oligomeric benzyl esters in dioxane and benzene: beta-turn -> antiparallel beta-sheet transition, Biopolymers 65:81-88 (2002)

Peng X., Shao Z., Chen X., Knight D.P., Wu P., Vollrath F., Further investigation on potassium-induced conformation transition of *Nephila* spidroin film with two-dimensional Infrared correlation spectroscopy, Biomacromolecules 6:302-308 (2005)

Reisdorf Jr. W.C. & Krimm S.; Protein normal modes: calculation of spectroscopically reliable infrared bands, Biophys. J. 66(2):A373 Part 2 (1994)

Reisdorf Jr. W.C. & Krimm S., Infrared dichroism of amide I and amide II modes of alpha I- and alpha II-helix segments in membrane proteins, Biophys. J. 69:271-273 (1995)

Siamwiza M.N., Lord R.C., Chen M.C., Takamutsa T., Harada I. Matsura H., Shimanouchi T., Interpretation of doublet at 850 and 830 cm^{-1} in Raman spectra of tyrosyl residues in proteins and certain model compounds, Biochemistry 14:4870-4876 (1975)

Surewicz W.K., Moscarello M.A., Mantsch H.H., Secondary structure of the hydrophobic myelin protein in a lipid environment as determined by Fourier-transform Infrared spectrometry, J. Biol. Chem. 262(8):8598-8602 (1987)

Taddei P., Monti P., Freddi G., Arai T., Tsukada M., IR study on the binding mode of metal cations to chemically modified *Bombyx mori* and Tussah silk fibres, J. Mol. Struct. 651:433-441 (2003)

Taddei P., Asakura T., Yao J., Monti P., Raman study of poly(alanine-glycine)-based peptides containing tyrosine, valine, and serine as model for the semicrystalline domains of *Bombyx mori* silk fibroin, Biopolymers 75(4):314-324 (2004)

Takeuchi H., Watanabe N., Satoh Y., Harada H., Effects of hydrogen-bonding on the tyrosine Raman bands in the 1300-1150 cm^{-1} region, J. Raman Spectrosc. 20(4):233-237 (1989)

Trabbic K.A. & Yager P., Comparative structural characterization of naturally- and synthetically-spun fibers of *Bombyx mori* fibroin, Macromolecules 31:462-471 (1998)

Tsukada M., Freddi G., Kasai N., Physical properties and phase separation structure of *Antheraea pernyi*/*Bombyx mori* silk fibroin blend films, Journal of Polymer Science, Part B: Polymer Physics, 32:1175-1182 (1994a)

Tsukada M., Freddi G., Gotoh Y, Kasai N, Physical and chemical properties of Tussah silk fibroin films, J. Polym. Sci. Pt. B-Polym. Phys. 32 (8):1407-1412 (1994b)

Tsukada M., Freddi G., Monti P., Bertoluzza A., Kasai N., Structure and molecular conformation of Tussah silk fibroin films: Effect of methanol, J. Polym. Sci. Pt. B-Polym. Phys. 33: 1995-2001 (1995)

Tsukada M., Freddi G., Kasai N., Monti P., Structure and molecular conformation of Tussah silk fibroin films with water-methanol solutions: Dynamic mechanical and thermomechanical behavior, J. Polym. Sci. 36:2717-2724 (1998)

Um I.C., Kweon H.Y., Park Y.H., Hudson S., Structural characteristics and properties of the regenerated silk fibroin prepared from formic acid, Int. J. Biol. Macromol. 29:91-97 (2001)

Um I.C., Kweon H.Y., Lee K.G., Park Y.H., The role of formic acid in solution stability and crystallization of silk protein polymer, Int. J. Biol. Macromol. 33(4-5):203-231 (2003)

Valluzzi R. & Gido S.P., The crystal structure of *Bombyx mori* silk fibroin at the air-water interface, Biopolymers 42(6):705-717 (1997)

Valluzzi R., He S.J., Gido S.P., Kaplan D., *Bombyx mori* silk fibroin liquid crystallinity and crystallization at aqueous fibroin-organic solvent interfaces, Int. J. Biol. Macromol. 24:227-236 (1999)

Van Dijk A., Van Wijk L., Van Vliet A., Haris P., Van Swieten E., Tesser G., Robillard G., Structure characterization of the central repetitive domain of high molecular weight gluten proteins. I. Model studies using cyclic and linear peptides, Protein Science 6:637-648 (1997)

Venyaminov S.Y. & Kalnin N.N., Quantitative IR spectrophotometry of peptide compounds in water (H2O) solutions. II. Amide absorption bands of polypeptides and fibrous proteins in alpha-, beta-, and random coil conformations, Biopolymers 30:1259-1271 (1990)

Viney C., From natural silks to new polymer fibres, J. Text. Inst. 91:2-23 Part 3 Sp. Iss. SI (2000)

Yoshimizu H. & Asakura T., The structure of *Bombyx mori* silk fibroin membrane swollen by water studied with ESR, carbon-13 NMR and FT-IR spectroscopies, J. Appl. Polym. Sc. 40:1745-1756 (1990)

Zheng S., Li G., Yao W., Yu T., Raman spectroscopic investigation of the denaturation process of silk fibroin films, Applied Spectroscopy 43:1269-1272 (1989)

Zheng R., Zheng X., Dong J., Carey P.R., Proteins can convert to beta-sheet in single crystals, Protein Science 13:1288-1294 (2004)

8

NUCLEAR MAGNETIC RESONANCE SPECTROSCOPY OF SILKS

Since some doubts remain to exist in the analysis of the secondary structure of the silks by means of the infrared and Raman spectroscopic techniques, it is chosen to add some NMR experiments, especially solid-state ^{13}C Cross-Polarization / Magic Angle Spinning (CP/MAS) NMR spectroscopy.

Analysis of the ^{13}C chemical shift and its relationship to protein structure in silkworm silk shows conformation-dependent ^{13}C chemical shifts in the solid state. Especially, the local secondary structure of the most important residues (alanine, glycine, serine) can be deduced.

In this chapter, NMR spectroscopy is used to get a confirmation of the results in Chapter 7 with respect to the conformational transition of Bombyx mori *silk. Furthermore, this technique is applied on the different silkworm silks and spider silks of the spider* Araneus diadematus *to confirm the secondary structure as found with the DRIFT spectra in Chapter 8.*

8.1. BASIC CONCEPTS OF NMR

Some atomic nuclei have a nuclear spin (I), and the presence of a spin makes these nuclei behave rather like bar magnets [Williams & Fleming 1996]. In the presence of an applied magnetic field the nuclear magnets can orient themselves in 2I + 1 ways. In the application of Nuclear Magnetic Resonance (NMR) spectroscopy, ^{1}H and ^{13}C are the most important nuclei, and both have spins of 1/2. These nuclei, therefore, can take up one of only two orientations, a low energy orientation aligned with the applied field and a high energy orientation opposed to the applied field. The difference in energy is given by:

$$\Delta E = h \nu \tag{8.1}$$

The frequency ν in Hz, the resonance frequency, is given by:

$$\nu = \gamma B_0 / 2 \pi \tag{8.2}$$

where h is the Planck constant, γ is the magnetogyric ratio (a proportionality constant, differing for each nucleus, which essentially measures the strength of the nuclear magnets) and B_0 is the strength of the applied magnetic field. The frequency is therefore dependent upon both the applied field strength and the nature of the nucleus in question.

Equation (8.1) becomes:

$$\Delta E = h \gamma B_0 / 2 \pi \tag{8.3}$$

The ratio between the number of nuclei in the low energy state (N_α) and the number in the high energy state (N_β) is given by the Boltzmann distribution:

$$N_\beta / N_\alpha = \exp(-\Delta E/kT) \tag{8.4}$$

with T being the measuring temperature and k the Boltzmann constant.

When a radio frequency signal is applied to the system, this distribution is changed if the radio frequency matches the frequency at which the nuclear magnets naturally precess in the magnetic field B_0: some of the N_α nuclei are promoted from the low energy state to the high energy state, and N_β increases.

The spectrum is measured in one of two ways [Williams & Fleming 1996]. In the traditional continuous wave (CW) method, a small proportion of the applied signal is absorbed in promoting some of the N_α nuclei to the higher energy state, and this response is picked up in a receiving coil. The frequency range being studied is scanned steadily from one extreme to the other, either by varying the frequency of the transmitter or by varying the magnetic field. The spectrum is then plotted directly, as it is being taken, as absorption (upwards) against frequency (increasing towards the left); the whole process taking a few minutes. Alternatively, the radio frequency signal is applied as a single powerful pulse, which effectively covers the whole frequency range and lasts for a time (t_p) typically of a few microseconds. This pulse generates an oscillating magnetic field (B_1) along the x-axis, at right angles to the applied magnetic field (B_0), which is defined as being along the z-axis (Figure 8.1). Because of the small

difference between N_α en N_β, the sample being investigated has a net magnetization (M), which is initially aligned in the direction of the applied field.

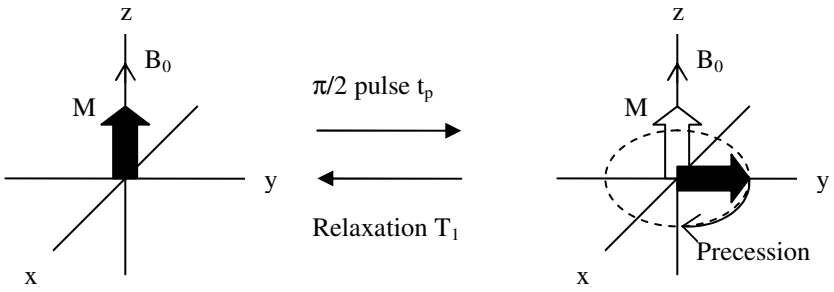

Figure 8.1 - Principle of recording FT spectrum

The effect of the pulse is to tip the magnetization through an angle given by:

$$\Theta = \gamma B_1 t_p \qquad (8.5)$$

Commonly, the time (t_p) is chosen so that Θ is 90°, such pulses are also called $\pi/2$ pulses. The magnetization, disturbed from its orientation along the z-axis, precesses in the xy plane, just as a gyroscope precesses when it is tipped out of the axis of the gravitational field. A receiver coil is placed to detect magnetization orientated along the y-axis. Thus, after the pulse has been applied, the detection signal starts along the +y (positive signal), precesses to the x axis (zero signal), then to –y (negative signal), and so on. The signal is detected typically for times of the order of a second. The frequency of oscillation detected is the difference between the NMR resonance frequency and the excitation frequency. Let us suppose that we are recording an NMR spectrum which consists of two resonance lines, which differ in frequency from the excitation energy by 5 and 7.5 Hz. The magnetization in the xy plane due to excitation of the resonance frequency differing by 5 Hz from the excitation energy oscillates from positive to negative (and back to positive) 5 times per second. As it does so, it decays exponentially as relaxation gradually allows the signal to return back to the equilibrium direction along the z axis. The signal is therefore an exponentially decaying cosine of frequency 5 Hz. That due to the frequency differing from the excitation energy by 7.5 Hz similarly gives a decaying signal which oscillates 7.5 times per second. By the mathematical manipulation of Fourier transformation (FT), these decaying cosine waves (said to be in the time domain) can be converted into frequency signals (said to be in the frequency domain). In doing this, the excitation frequency has conveniently been taken as the reference frequency, 0 Hz. If the two NMR frequencies are simultaneously excited, then the two decaying cosine waves interfere, but the information necessary to extract both line frequencies is still present. The so-called interferograms or free induction decays (FIDs) of real NMR spectra are of course much more complicated since spectra typically contain many NMR resonances over a larger range of higher frequency differences. After Fourier transformation, the spectrum is then plotted in exactly the same form as a CW spectrum.

In the CW method, the resonances can only be excited sequentially, whereas in the FT method they can all be excited simultaneously. Hence, FT-NMR is enormously more sensitive than CW NMR in terms of the signal-to-noise ratio (S/N) for a given expenditure of time. Also in FT-NMR, a large number of successive pulses can be applied (each followed by an acquisition period), and the interferograms in digital form added together in a computer, followed by Fourier transformation on the sum. Not only is the absorption intensified by this procedure but noise, which is random, is largely cancelled out. The accumulation of n spectra improves the S/N ratio by $\sqrt{n}$ relative to that obtained in a single spectrum.

It is convenient instead to measure the difference of the frequency (ν_s) of the peak from some internal standard and to divide this by the operating frequency to obtain a field-independent number. The internal standard almost always used is tetramethylsilane (TMS), and the chemical shift scale δ is then defined by:

$$\delta = \nu_s \text{ (Hz)} - \nu_{TMS} \text{ (Hz)} / \text{ operating frequency (MHz)} \qquad (8.6)$$

The parameter δ has no units and is expressed as fractions of the applied field in parts per million (ppm).

In ^{13}C spectra, the range of frequencies is a small segment of about 5000 Hz in the neighbourhood of the resonance frequency. This range is wide enough to bring each of the different ^{13}C atoms in most organic compounds successively into resonance. The precise frequency at which each carbon atom comes into resonance is determined not only by the applied field, B_0, but also by minute differences in the magnetic environment experienced by each nucleus. These minute differences are caused largely by the variation in electron density in the neighbourhood of each nucleus, with the result that each chemically distinct carbon atom in a structure, when it happens to be a ^{13}C, will come into resonance at a slightly different frequency from all the others. The electrons affect the microenvironment because their movement creates a magnetic field.

8.2. SOLID-STATE NMR SPECTROSCOPY

8.2.1. NUCLEAR SPIN INTERACTIONS IN THE SOLID PHASE

8.2.1.1. Chemical shift anisotropy

Chemical shift anisotropy (CSA) means orientation dependence of the chemical shift, and arises due the fact that in a nucleus, the charge distribution is rarely spherically symmetrical. The degree to which electron density affects resonance frequency (also known as shielding) of a nucleus depends on the orientation of the electron cloud.

Anisotropic interactions are often attributed to a line-broadening effect in NMR spectra. However, there is a range of situations when their presence can either not be avoided, or is even particularly desired, as they encode structural parameters, such as orientation information, on the molecule of interest.

The CSA is dependent on 1 - 3 $\cos^2 \theta$ where θ is the angle between the long axis of the ellipsoid (electron cloud) with the field B_0. By spinning the sample at θ_m=54.74°, called the magic angle, the effect of CSA is eliminated (see further MAS).

8.2.1.2. Chemical shielding

The chemical shielding is a local property of each nucleus, and depends on the external magnetic field. Specifically, the external magnetic field induces currents of the electrons in molecular orbitals. These induced currents create local magnetic fields that often vary accross the entire molecular framework such that nuclei in distinct molecular environments usually experience unique local fields from this effect.

Under sufficiently fast magic angle spinning (see 8.2.2), or in solution-state NMR, the directionally dependent character of the chemical shielding is removed, leaving the isotropic chemical shift.

8.2.1.3. Dipolar coupling

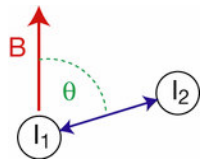

Figure 8.2 - Dipolar coupling vectors

Nuclear spins exhibit a dipole moment, which interacts with the dipole moment of other nuclei (dipolar coupling). The magnitude of the interaction is dependent on the spin species, the internuclear distance, and the orientation of the vector connecting the two nuclear spins with respect to the external magnetic field B (Figure 8.2). The dipolar coupling is, like CSA, also proportional to 1 - 3 $\cos^2 \theta$ and hence is dependent on the orientation of the dipoles.

Consequently, two nuclei with a dipolar coupling vector at an angle of θ_m=54.74° (magic angle) to a strong external magnetic field, makes the dipolar coupling zero (see further MAS).

8.2.1.4. J-coupling (scalar coupling)

The J-coupling or scalar coupling describes the interaction of nuclear spins through chemical bonds, in other words, it exists through the electrons in the bonds. The scalar coupling leads to a splitting of resonance lines. The effect is mediated via the electrons and its magnitude therefore rapidly decreases when the number of intervening bonds increases.

8.2.1.5. Other interactions

Some nuclei exhibit quadrupolar interactions (spin > 1/2).

8.2.2. ^{13}C CROSS-POLARIZATION MAGIC ANGLE NMR

A fundamental RF pulse sequences and building block in most solid-state NMR experiments is cross-polarization (CP) [Pines 1973, Laws *et al*. 2002]. The process involves transferring polarization from the abundant nuclei (high gyromagnetic ratio, ^{1}H) to the "sparse" nuclei (low gyromagnetic ratio, like ^{13}C, ^{15}N) by bringing them into a dipolar thermal contact, and then detecting the sparse spins. As such the signal of nuclei with a low gyromagnetic ratio (e.g. ^{13}C, ^{15}N) is enhanced.

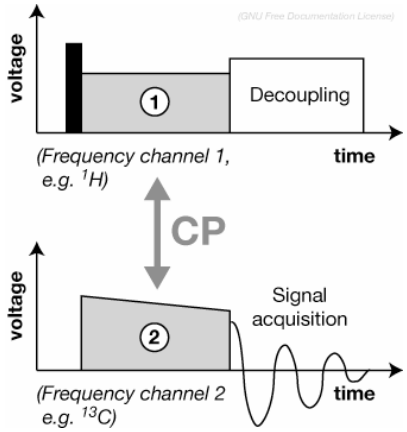

Figure 8.3 - Cross-polarization (CP) pulse scheme in solid-state NMR spectroscopy

In the ^{1}H-^{13}C process (Figure 8.3), the ^{1}H magnetization is brought into the *xy* plane by a $\pi/2$ pulse. Radio frequency fields are then applied to ^{1}H (protons) and ^{13}C spins (carbons) for a period of t_{cp}. When the mutation frequencies of ^{1}H and ^{13}C spins are equal, an energy conserving dipolar contact is created and the Hartmann–Hahn condition is achieved - $B_{1H}\gamma_H = B_{1C}\gamma_C$. It is through this contact that polarization is transferred from ^{1}H spins to ^{13}C spins. When the Hartmann-Hahn (contact) pulse is turned off, the ^{1}H radio frequency is left on during the ^{13}C data acquisition in order to provide ^{1}H decoupling. The ^{13}C spins are detected while the ^{1}H spins are decoupled. The increase in ^{13}C-spin magnetization during CP mix time depends on the ^{1}H-^{13}C dipolar coupling strength and the maximal signal enhancement can be γ_H / γ_C.

Nuclear spin interactions need to be removed (decoupled) in order to increase the resolution of NMR spectra, and to isolate spin systems. A technique that can substantially reduce or remove the chemical shift anisotropy and the dipolar coupling is sample rotation (most commonly called magic angle spinning).

By spinning the sample (1-40 kHz) at the magic angle θ_m (ca. 54.74°, where $\cos^2\theta_m=1/3$) with respect to the direction of the magnetic field, the normally wide

lines narrow, therefore increasing the resolution for better identification and analysis of the spectrum.

In any condensed phase, a nuclear spin experiences a great number of interactions. The main three interactions (dipolar, chemical shift anisotropy, quadrupolar) often lead to very broad and featureless lines. However, these three interactions in solids are time-dependent and can be averaged by MAS. The nuclear dipole-dipole interaction, between magnetic moments of nuclei averages to zero. The chemical shift anisotropy, a nuclear-electron interaction, averages to a non-zero value. And the quadrupolar interaction is only partially averaged by MAS leaving a residual secondary quadrupolar interaction. In liquids, e.g. a solution of an organic compound, most of these interactions will average out because of the rapid time-averaged molecular motion that occurs. This orientation averaging in solution is mimicked by MAS of a solid. This causes the signal to become much narrower giving rise to the isotropic value which is of interest for structural determination of solid materials and compounds.

The physical spinning of the sample is achieved via an air turbine mechanism. These turbines (or rotors) come in a variety of diameters (2.0-15.0 mm), and are usually spun on air or nitrogen gas. The cylindrical rotors are axially symmetric about the axis of rotation. Samples are packed into the rotors and these are then sealed with a single or double end cap.

"Magic angle spinning" (MAS) is often combined with "Cross polarisation" (CP) resulting in CP/MAS NMR.

8.3. SOLID-STATE NMR OF SILKS

Several researchers performed solid-state ^{13}C CP/MAS NMR spectroscopy on *Bombyx mori* fibres and regenerated films of these fibres [Asakura *et al.* 1997, Asakura *et al.* 2001a, 2001b, Asakura *et al.* 2002, Asakura & Yao 2002, Zhao *et al.* 2003, Kim *et al.* 2003 (regenerated SF, electrospun, dissolved in), Ohgo *et al.* 2003 (electrospun, dissolved in 9 M LiBr)].

Nakazawa & Asakura [2002] studied the structure of silk fibroin prepared from the silk glands of *A. pernyi* with ^{13}C CP/MAS NMR, before and after methanol treatment.

With respect to spider silk, ^{13}C CP/MAS NMR spectra were taken for *Nephila edulis* (egg sac + MA silk) [Kishore *et al.* 2002], *Nephila clavipes* (MA + minor ampullate) [Hijrida *et al.* 1996, Parkhe *et al.* 1997, Liivak *et al.* 1997, Asakura *et al.* 2004] and *Argiope keyserlingi* (egg sac + MA silk) [Kishore *et al.* 2002].

In literature, the ^{13}C CP/MAS NMR spectra of these silks are not discussed in detail. The spectra of dragline and egg sac spider silk are noted to be similar [Kishore *et al.* 2002], although some differences are clearly seen in the spectra and are to be expected because of their different amino acid composition (see Chapter 4).

In this thesis, solid-state NMR spectroscopy was used to confirm the structural transition induced by methanol, as studied in Chapter 7. The spectra of the

regenerated samples will also help to assign the observed maxima to the correct secondary structure.

Furthermore, this technique is used to identify the local secondary structure of the most important amino acids present in the silks: alanine, glycine and serine. In this way, apart from a confirmation of the results of the DRIFTS experiments, complementary information on secondary structure of the studied silks will be obtained.

8.4. ASSIGNMENT OF PEAKS TO SECONDARY STRUCTURE

Saito & Ando [1989] summarize the conformation-dependent ^{13}C chemical shifts of polypeptides and proteins, and showed the usefulness of these chemical shifts in the conformational characterization of proteins. Among the ^{13}C peaks, the broad Ala C_β peak is most sensitive to both the conformation and intermolecular arrangement. This peak is often used in a curve fitting procedure in order to quantify the secondary structure [Zhao *et al.* 2003, Zhou *et al.* 2004].

The diagnostic peaks to identify the secondary structure in CP/MAS NMR spectra are given in Table 8.1 [Asakura *et al.* 2002, Asakura & Yao 2002, Zhao *et al.* 2003, Hronska *et al*. 2004]:

Table 8.1 - Chemical shift (ppm) distributions for C_α and C_β in secondary structure elements for particular amino acids [reproduced from Hronska *et al.* 2004]

		Ala	Gly	Leu	Ser	Tyr
C_α	β-sheet	49.6-52.1	42.4-44.9	52.4-54.9	55.5-58	55.4-57.9
C_α	helix	54.4-56.4	47.2-49.2	57.2-59.2	60.3-62.3	60.2-62.2
C_α	random coil	50.8-53.1	43.5-45.3	52.8-55.6	56.6-58.5	55.8-57.7
C_β	β-sheet	19.3-23.1		42.6-46.4	63.5-67.3	39.1-42.9
C_β	helix	17.8-19.5		41.1-42.8	62.0-63.7	37.6-39.3
C_β	random coil	17.7-19.0		40.5-42.4	62.3-63.8	37.0-39.1

In this table, the C_α refers to the carbon atom in the main chain, whereas C_β refers to the carbon atom of the CH_2 or CH_3 group in the side chain of these amino acids, linked to the central carbon atom C_α.

As can be seen in Table 8.1 for amino acid residues, the chemical shift of the C_α peaks shifts upfield when the residue is in a β-sheet conformation and shifts downfield when the conformation is α-helical [Liivak *et al*. 1997]. The trend for the C_β chemical shifts is opposite.

From studies on silk fibroin in solution and/or solid state, characteristic chemical shifts for the different secondary structures found in silk fibroin are summarized in Table 8.3.

It should be remarked that for the Silk I structure of *Bombyx mori* and for β-turn structures often peaks at the same chemical shift values are observed [Asakura *et al.* 1997, 2001, Zhou *et al.* 2001, Monti *et al.* 2003]. This may indicate that the Silk I structure of *B. mori* indeed contains some β-turns, and not only random coil conformation.

All the chemical shift values for the different secondary structure of silk fibroin (Table 8.3) are considerably lower than those mentioned by Hronska *et al.* [2004] in Table 8.1 for proteins. The latter table is mainly based on NMR information in liquid state, whereas silks are fibrous proteins tested in solid state. It is suggested that this explains the difference. So, some caution should be taken when comparing spectroscopy of globular proteins with fibrous proteins.

However, the order of assignment to different secondary structures is similar: for C_α β-sheet - random coil - α-helix, for C_β random coil - α-helix - β-sheet. Although in Table 8.1 the ranges for random coil and α-helix are overlapping to a great extent.

Ando *et al.* [1998] studied the structure of solid peptides by solid-state ^{13}C CP/MAS NMR. The chemical shift values for the carbon atoms of the alanine residues, associated with different secondary structures, are mentioned in Table 8.2.

Table 8.2 – Chemical shifts for the Ala residues for solid peptides from ^{13}C CP/MAS NMR experiments [reproduced from Ando *et al.* 1998]

	Chemical shift (ppm)		
Sample	**Ala C_α**	**Ala C_β**	**Secondary structure**
$(Ala)_n$	53.0	15.5	α-helix (right-handed)
	48.7	21.0	β-sheet
$(D,L\text{-}Ala)_n$ [a]	50.1	15.9	α-helix (left-handed)
$(Ala\text{-}Gly\text{-}Gly)_n$ I	49.7	22.6	β-sheet
$(Ala\text{-}Gly\text{-}Gly)_n$ II	49.7	18.4	3_1-helix
$(Ala\text{-}Ala\text{-}Gly)_n$	50.1	21.4	β-sheet
$(Ala\text{-}Gly)_n$ I [b]	49.5	21.0	β-sheet
$(Ala\text{-}Gly)_n$ II [c]	51.5	17.6	Unknown (Silk I)
$(Pro\text{-}Ala\text{-}Gly)_n$	49.3	18.6	Triple-helix

[a] (D,L-Ala)n denotes copolymer of D- and L-alanine.
[b] $(Ala\text{-}Gly)_n$ form I is a model compound for silk II
[c] $(Ala\text{-}Gly)_n$ form II is a model compound for silk I

The different chemical shift values that are obtained for a similar secondary structure make it difficult to assign a secondary structure with certainty.

Table 8.3 – Chemical shifts found in literature for silk fibroin (br = broad, s = sharp)

	Chemical shift (ppm)	Structure	References
Gly C=O	169.9	Silk I	Saito *et al*. 1984a, Asakura *et al.* 2001, Zhou *et al.* 2001, 2004, Monti *et al.* 2003
	171.3	Random coil	Nakazawa & Asakura 2002, Yang & Asakura 2005
Ala C=O	172.2	Silk II or β-sheet	Saito *et al*. 1984a, Kümmerlen *et al.* 1996, Asakura *et al.* 1997, Asakura & Yao 2002, Zhao *et al.* 2003, Ha *et al.* 2005
	175.5	Random coil	Nakazawa & Asakura 2002, Yang & Asakura 2005
	176.4-176.5	α-helix	Hijirida *et al*. 1996, Nakazawa & Asakura 2002, Zhao *et al.* 2003, Asakura *et al.* 2004, Yang & Asakura 2005
	176.8 s	Silk I or β-turn	Saito *et al*. 1984a, Asakura *et al.* 2001, Zhou *et al.* 2001, 2004, Monti *et al.* 2003
Ser C_β	61.3	Random coil	Nakazawa & Asakura 2002, Yang & Asakura 2005
Ser C_α	55.6-55.9	Random coil	Nakazawa & Asakura 2002, Yang & Asakura 2005
	59.2	α-helix	Zhao *et al.* 2003, Asakura *et al.* 2004, Yang & Asakura 2005
Ala C_α	48.5-48.9	Silk II or β-sheet	Saito *et al*. 1984a, Kümmerlen *et al.* 1996, Asakura *et al.* 1997, Asakura & Yao 2002, Zhao *et al.* 2003, Ha *et al*. 2005
	48.7-48.9	3_1-helix	Saito *et al*. 1984b, Hijirida *et al*. 1996, Asakura *et al.* 2004
	50.0-50.4	Random coil	Nakazawa & Asakura 2002, Zhao *et al.* 2003, Ha *et al.* 2005, Yang & Asakura 2005
	50.7–50.8 s	Silk I or β-turn	Saito *et al*. 1984a, Asakura *et al.* 2001, Zhou *et al.* 2001, 2004, Monti *et al.* 2003
	52.0-52.5	α-helix	Hijirida *et al*. 1996, Nakazawa & Asakura 2002, Zhao *et al.* 2003, Asakura *et al.* 2004, Yang & Asakura 2005
	52.4	3_{10}-helix	Zhao *et al.* 2003

	Chemical shift (ppm)	**Structure**	**References**
Gly C_α	42.7	Random coil	Nakazawa & Asakura 2002, Yang & Asakura 2005
	43.2	Silk I	Saito *et al*. 1984a, Asakura *et al.* 2001, Zhou *et al.* 2001, 2004, Monti *et al.* 2003
	44	α-helix	Zhao *et al.* 2003, Asakura *et al.* 2004, Yang & Asakura 2005
Tyr C_β	36.1	Random coil	Nakazawa & Asakura 2002, Yang & Asakura 2005
Ala C_β	15.0 ± 0.5	Random coil	Zhou *et al.* 2004
	15.1-15.8	α-helix	Hijirida *et al*. 1996, Nakazawa & Asakura 2002, Zhao *et al.* 2003, Asakura *et al.* 2004, Yang & Asakura 2005
	15.2	3_{10} helix	Zhao *et al.* 2003
	16.5	Silk I	Saito *et al*. 1984a, Asakura *et al.* 2001, Zhou *et al.* 2001, 2004, Monti *et al.* 2003
	16.5-16.7 br	Distorted β-turn	Zhao *et al.* 2003, Asakura & Yao 2002
	16.6-16.9	Random coil	Nakazawa & Asakura 2002, Zhao *et al.* 2003, Ha *et al.* 2005, Yang & Asakura 2005
	17.0-17.4	3_1-helix	Saito *et al*. 1984b, Hijirida *et al*. 1996, Zhou *et al*. 2004, Asakura *et al.* 2004
	19.6-19.9	Polar anti// β-sheet	Asakura *et al.* 2002, Ha *et al.* 2005
	+ 21.9	Antipolar anti// β-sheet	Asakura *et al.* 2002, Ha *et al.* 2005
	20.0 ± 0.5	Silk II or β-sheet	Zhou *et al.* 2001, 2004
	21.5 ± 0.5	distorted β-sheet	Zhou *et al.* 2004

8.5. MATERIALS AND METHODS

The ^{13}C CP/MAS NMR spectra were recorded at the University of Hasselt at the Laboratory of Applied Chemistry. The solid state ^{13}C NMR spectra were recorded at room temperature on a Varian Inova 200 MHz spectrometer at 50.3 MHz and/or Varian VNMRS 400 MHz spectrometer at 100.6 MHz. Magic angle spinning was performed at 6 and/or 9 kHz, making use of ceramic Si_3N_4 rotors. The Hartmann-Hahn condition ($\omega_H = \gamma_H.B_{1H} = \gamma_C.B_{1C} = \omega_C$) for cross polarization was set using the aromatic signal of hexamethylbenzene. The chemical shift of this signal at 132.1 ppm from TMS was applied as a standard. The contact time and preparation delay was set to 1.5 ms and 3 s respectively. The number of scans was function of the amount of material. An optimal signal-to-noise ratio is aimed at.

Apart from the *Bombyx mori*, *Antheraea pernyi* (Tussah), *Araneus diadematus* egg sac and dragline fibres, spectra were also taken on regenerated *B. mori* samples as were also used for the DRIFT spectroscopy in Chapter 7. "MoriFab1" stands for the sample based on the *B. mori* fabric that was prepared with lower freezing temperature in the freeze-drying process. "MoriFib" is the sample, prepared by dissolving the *B. mori* fibres and freezing in a lesser extent in freeze-drying.

For comparison of spectra, the area of the spectra was normalized to 1000.

8.6. RESULTS

8.6.1. *BOMBYX MORI* IN DIFFERENT STATES

Figure 8.4 shows the ^{13}C CP/MAS solid-state NMR spectra for *Bombyx mori* fibroin in fibre and regenerated foam ("MoriFab1", "MoriFib").

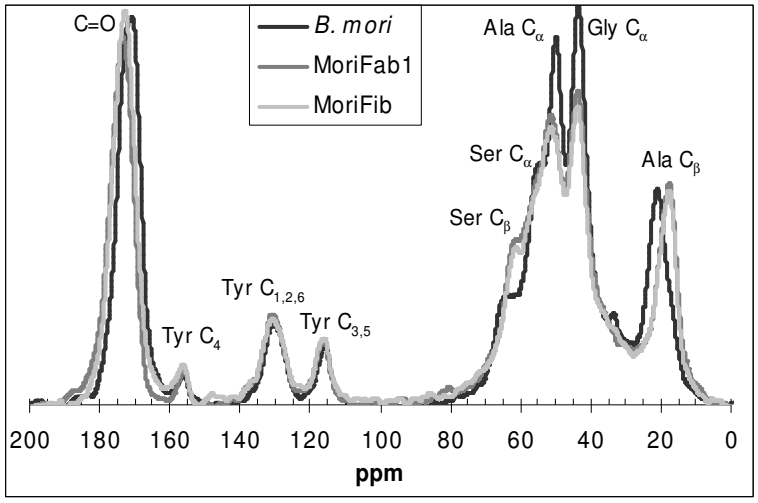

Figure 8.4 - NMR spectra of *B. mori* fibroin in different states

Table 8.4 summarizes the ppm-values of the observed maxima in the ^{13}C CP/MAS solid-state NMR spectra.

Table 8.4 - ppm-values of the maxima in the NMR spectra for *B. mori* fibroin in different states and their assignment (s: strong, m: medium, w: weak, v: very, sh: shoulder, b: band)

	Fibre	**MoriFab1**	**MoriFib**
C=O	170.8 vs	173.5 vs	172.7 vs
Tyr C_4	156.1 w	156 w	148 w
Tyr $C_{1,2,6}$	130.5 m	131 m	131 m
Tyr $C_{3,5}$	116 m	116.2 m	116 m
	78.2 vvw	80.4 vw	86 vw
Ser C_β	63.9 vw	61.4 vw	61.4 vw
Ser C_α	54.3 sh	55.5 sh	55.9 sh
Ala C_α	49.9 vs	51.3 vs	51.3 vs
Gly C_α	43.5 vs	43.8 vs	43.8 vs
Val C_β	33.6 w	29.1 vw	
Ala C_β	21.1 s	± 21 sh	± 21 sh
	± 17.5 sh	17.7 s	17.7 s

With respect to the carbonyl peaks in the region 170-180 ppm, it should be remarked that the Gly C=O, Ala C=O and Ser C=O are all superimposed on each other resulting in only one observable peak. The resolution for the conformation dependent ^{13}C chemical shifts for carbonyl carbons is too low to determine the protein structure. Furthermore, it should be remarked that all Ala and Gly peaks are shifted to higher ppm (± 1 ppm) than is observed in literature for Silk II (β-sheet in fibre) and random coil or Silk I structure (see Table 8.3). It is suggested that this shift is caused by the isotope labelling of the silk proteins that is usually done in literature. In these studies, the spiders are fed with a ^{13}C-labeled amino acid solution [Hijirida *et al*. 1996, Kümmerlen *et al*. 1996, Parkhe *et al*. 1997, Nakazawa & Asakura 2002, Hronska *et al*. 2004]. A lot of studies are also performed in solution state on the liquid silk obtained from the spinning glands of the spiders what can explain the somewhat deviating results. In the solution state, the NMR chemical shift of proteins with possible rotation around the bonds becomes the averaged value for all rotations because of rapid rotation around the N-C_α and C_α-C(=O) peptide bonds (dihedral angles ϕ, ψ, see Chapter 5) in the NMR time scale. In the solid state, however, the chemical shift is characteristic of specific conformations because the internal rotation around the peptide bonds is fixed.

The regenerated samples show a carbonyl peak at about 173 ppm, somewhat higher for "MoriFab1". For the *B. mori* fibre, this peak is shifted to lower ppm values at

about 170.8 ppm, indicating the Silk II-related structure versus the Silk I-related structure.

The bands at about 160 ppm, 130 ppm and 117 ppm are assigned to the chemical shifts of the aromatic carbon groups of the tyrosine residues [Kümmerlen *et al*. 1996, Asakura *et al*. 2001a, Hronska *et al*. 2004]. Since no shifts can be observed between the regenerated and fibre samples, it can be deduced that the Tyr residues indeed reside in the amorphous regions of the fibre.

The differences in the spectra of the regenerated samples ("MoriFab1", "MoriFib") are small. For "MoriFib", a shift to lower ppm is observed for the C=O peak, which may indicate a higher content of Silk II structure since the Ala C=O peak is much lower for Silk II (about 172.2 ppm) than for Silk I (176.8 ppm). The Ser C_α peak is somewhat shifted and the intensity of the Ser C_β peak is somewhat higher for *B. mori* "MoriFib", what can indicate indeed some structural differences in both regenerated samples, as found in DRIFT spectroscopy. Furthermore, in the spectrum of the regenerated *B. mori* ("MoriFib ") fibres, a shoulder at lower ppm for the Ala C_α peak seems much more visible than in the other regenerated sample. This again confirms the higher abundance of β-sheet or β-turn structures (Ala C_α peak at about 48.5-48.9 ppm as observed in Silk II) in "MoriFib " than in "MoriFab1".

Taking into account the Ala C_β peak, a semi-quantitative evaluation of the β-sheet content can be made by taking the ratio of the intensity at 21.1 ppm (β-sheet) to the intensity at 17.7 ppm (non-β-sheet). If this is done for "MoriFab1" and "MoriFib", a slightly higher value is found for "MoriFib" (0.59) than for "MoriFab1" (0.58), indicating only a small difference in β-sheet content between both samples. For the *B. mori* fibre, this ratio equals 1.82 indicating the well-known β-sheet formation in this silk.

The *B. mori* fibre shows an Ala C_β peak at about 21 ppm combined with a shoulder at lower ppm, a Gly C_α peak at about 43.5 ppm, an Ala C_α peak at about 50 ppm, a Ser C_α shoulder at about 54.3 ppm and a Ser C_β peak at about 64 ppm. The small peak at about 33.6 ppm is possibly attributed to the Val C_β [Asakura & Yao 2002, Zhao *et al*. 2003]. The Tyr C_β peak is weakly visible at about 37 ppm [Asakura *et al*. 2001a, 2004, Nakazawa & Asakura 2002, Hronska *et al*. 2004]. Taking into account Table 8.3 and the observed shift of ± 1 ppm, all these peaks indicate indeed that the antiparallel β-sheet structure is dominated in the *B. mori* fibre. Furthermore, chemical shift values are obtained that are more in accordance with Table 8.1 for the assignment of proteins.

The shifts that are observed for the silk fibre compared to the regenerated fibroins, indicate that Ala, Ser and Gly are all involved in the formation of β-sheets. It is known from literature that it is indeed the Gly-Ala-Gly-Ala-Gly-Ser-sequence that shows the β-sheet formation.

8.6.2. SILK FIBRES

Figure 8.5 shows the ^{13}C CP/MAS NMR solid-state spectra of the silkworm silks (*Bombyx mori* and Tussah) and the spider silks (egg sac and dragline), taken on a 400 MHz spectrometer.

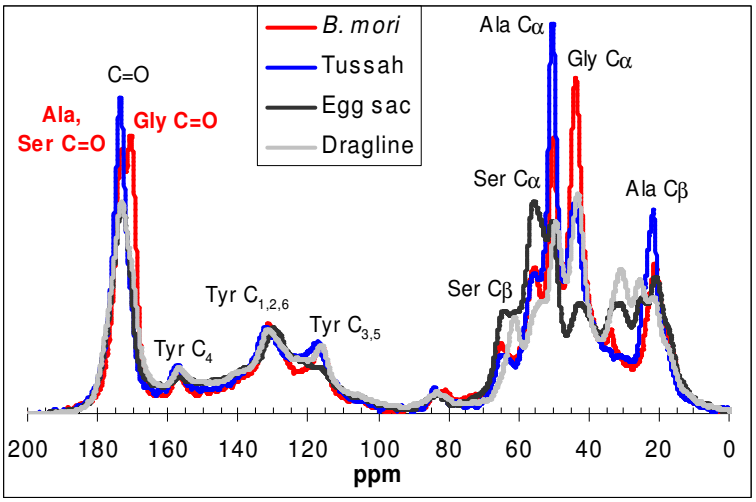

Figure 8.5 - ^{13}C CP/MAS NMR solid-state spectra of the different silks

It is clear that the different silk fibres can be differentiated based on the NMR spectra. The NMR spectrum of egg sac spider silk is comparable with the spectra obtained by Kishore *et al*. [2002] for *Nephila edulis* and *Argiope keyserlingi* egg sac silks, although more resolved bands are observed with the instrument we used (400 MHz compared to 300 MHz). The NMR spectra of dragline spider silks, recorded by Kishore *et al.* [2002], showed some variation between varieties. Also the relative intensities of the peaks in the region 100-0 ppm in our spectrum of *A. diadematus* are deviating from the ones recorded by Kishore *et al.* [2002] (*N. edulis* and *A. keyserlingi*), by Kümmerlen *et al*. [1996] (*N. madagascariensis*), by Hijirida *et al.* [1996] (*N. clavipes*) and by Parkhe *et al.* [1997] (*N. clavipes*). It is explained by the different amino acid composition of dragline silk of different spider varieties. Probably, the variability in amino acid composition between the varieties of egg sac spider silk is less than in the case of dragline silk.

The NMR spectrum of *B. mori* fibre is comparable as those found in literature [Saito *et al*. 1984a, Kümmerlen *et al*. 1996, Asakura & Yao 2002, Zhao *et al.* 2003]. For Tussah (*A. pernyi*) silk fibres, no solid-state NMR spectra are available from literature. However, the spectrum is comparable with the NMR spectrum found for *A. pernyi* silk fibroin films (obtained from liquid silk of the glands) treated with a 60% methanol-water mixture (known to induce β-sheet formation, see Chapter 7) [Nakazawa & Asakura 2002].

Table 8.5 summarizes the observed peaks in the NMR spectra and their assignment, if known from literature.

With respect to the carbonyl peaks in the region 170-180 ppm, it should be remarked that the Gly C=O, Ala C=O and Ser C=O are still, even with the 400 MHz instrument, for most silks, superimposed on each other resulting in only one observable peak. For *B. mori* a splitting in two peaks (Gly C=O and Ala C=O + Ser C=O, see Figure 8.5) is seen, as also observed in literature [Kümmerlen *et al*. 1996, Asakura & Yao 2002, Zhao *et al*. 2003], even with a 100 MHz instrument.

Table 8.5 - Observed ppm-values of peaks in NMR spectra (s: strong, m: medium, w: weak, v: very, sh: shoulder, b: band)

	B. mori	**Tussah**	**Egg sac**	**Dragline**
C=O	173.4 vs	173.6 vs	173.3 vs	173.2 vs
	170.7 sh vs			
Tyr C_4	156.6 w	157.1 w	157.0 vw	157.0 w
Tyr $C_{1,2,6}$	131.5 m	132.1 w	130.0 m	131.9 m
Tyr $C_{3,5}$	116.5 m	117.3 w	116.6 sh	116.4 m
	80.9 vw b	84.2 vw b	83.2 vw b	83.5 vw b
Ser C_β	65.2 w	64.5 w	64.3 sh	
Pro C_α				61.3 m
Ser C_α	55.4 w	55.4 sh	55.7 vs	56 sh
Leu C_α			54 sh	54 sh
Ala C_α	50.1 s	50.5 vs	50.5 s	49.6 s
Gly C_α	43.8 vs	44.3 s	42.7 m	43.2 vs
Val C_β	33.8 vw		33.5 sh	
Gln $C\gamma$ / Pro C_β			31.2 m	31.0 s
Gln C_β / Leu $C\gamma$			25.0 w	25.6 m
Ala C_β	21.1 m	21.6 s	20.8 m	21.6 w
Ala C_β	17.6 sh	18.2 sh	17.7 sh	18.1 sh

The bands at about 160 ppm, 130 ppm and 117 ppm are assigned to the chemical shifts of the aromatic carbon groups of the tyrosine residues [Kümmerlen *et al*. 1996, Asakura *et al*. 2001a, Hronska *et al*. 2004]. The much lower contribution of tyrosine residues in egg sac spider silk is only confirmed by the peak at about 117 ppm.

In all fibres, the Ala residues make part of the antiparallel β-sheet structure as is confirmed by the Ala C_α peak at about 50 ppm and the maximum of the peak for the alanine methyl carbon (Ala C_β) at about 21 ppm and the assignments in Table 8.1. This is in accordance with what is known about the structure of poly-Ala runs in

Tussah and dragline fibres and the structure of the Gly-Ala-Gly-Ala-Gly-Ser sequence in *B. mori* fibres (see Chapter 5 reviewing the structure of silks).

Asakura *et al.* [2004] deconvoluted the Ala C_β band into three components: 23.0, 20.4, 16.6 ppm but did not assign the components. The Tussah fibres show a shoulder at higher ppm-values (Figure 8.6). The assignment to some helical structure is not likely, since this is not in accordance with Table 8.1 and Table 8.3, more especially the observed shift upfield (lower ppm) for an α-helical conformation. We suggest that the shoulder in the Tussah spectrum is associated with the Arg Cγ peak as was also identified by Asakura *et al*. [2004] for a peak at about 24 ppm. Since the Arg content in *A. pernyi* silk is estimated to be around 6%, compared to about 1% for the other fibres (see Chapter 4), this is an acceptable assignment.

The peak at 20.4 ppm is suggested to be assigned to the β-sheet structure and the peak at about 16.6 ppm to random coil or silk I (β-turn) structure as the maxima observed for the regenerated samples is also at this ppm. In literature, comparable ppm-values (17.6 ppm) are found for non-β-sheet structures versus 20.4 ppm for β-sheet structures in regenerated and methanol treated *B. mori* silk fibroin [Kim *et al.* 2003]. Asakura and co-workers [Asakura *et al.* 2002, Asakura & Yao 2002, Zhao *et al*. 2003] assigned the component at about 16.5 ppm to a distorted β-turn in *B. mori* fibre. The shoulder that is observed in the Ala C_β band at about 18 ppm can thus be assigned to the β-turn or random coil structure. In this case, the fraction of β-turn structure is the highest for egg sac spider silk. Moreover, because of the lower value of the maximum in the Ala C_β band for egg sac spider silk, it may indicate that a higher percentage of the Ala methyl groups is pointing in opposite directions (antipolar) in the available β-sheet structures than in the other silks [Asakura *et al.* 2002], although the split-up in two is not clear from the spectra. We would expect for Tussah and dragline fibres a shoulder at lower ppm value (15-16 ppm), but this is not clearly visible in the spectra. It indicates that most alanine residues are in β-sheet conformation, also in these silks.

Because of the different shapes of the Ala C_β band and the superposition of another band at about 25 ppm for spider silk and Tussah, the curve fitting was not considered as useful.

The assignment of the Val C_β peak at about 34 ppm is confirmed since it is also clearly visible for egg sac spider silk that contains a much higher content of Val residues (about 6%, see Chapter 4). The value is too low to be assigned to the Tyr C_β (normal value at about 36-37 ppm [Nakazawa & Asakura 2002, Zhao *et al.* 2003, Asakura *et al.* 2004, Hronska *et al.* 2004]).

The spider silks differentiate from the silkworm silks in the clearly visible Gln carbon peak at about 31 ppm [Hijirida *et al.* 1996, Kümmerlen *et al.* 1996, Kishore *et al.* 2002].

The peaks at about 25 ppm and about 31 ppm are suggested to be assigned to resp. Gln C_β and Gln Cγ as reported by Hijirida *et al.* [1996] and Asakura *et al*. [2004] for *N. clavipes* major ampullate silk fibroin for dragline spider silk. Another possible assignment is the Leu Cγ peak as was also detected by Hronska *et al.* [2004] on *N. edulis* silk dope and by Asakura *et al.* [2004] on a synthesized *N. clavipes* fibroin.

Because of the relatively high contribution of Leu in egg sac spider silk (about 6%) compared to dragline spider silk (about 1%) (see also Chapter 4), it is suggested that for egg sac spider silk the peak at about 25 ppm is the superposition of both Leu Cγ and Gln C_β peaks. It also explains the shift downfield.

The somewhat lower chemical shift for the Gly C_α peak found for egg sac and dragline spider silk may indicate that the Gly residues make part of the silk I structure or β-turn structure, since a chemical shift of 43.2 ppm was found for this structure by several authors [Asakura *et al.* 2001, Zhou *et al.* 2001, 2004, Monti *et al.* 2003]. The broader band for egg sac is probably due to the supercomposition of the Leu C_β peak [Hronska *et al*. 2004, Asakura *et al*. 2004] that is superimposed on the Gly C_α, since Leu residues contributes about 6% of the total amino acid composition (see Chapter 4). For the other silks, the Leu content is much lower (1-3%) and probably not detectable in the NMR spectra. For Tussah, the higher chemical shift at about 44.3 ppm may indicate the presence of the α-helical formation.

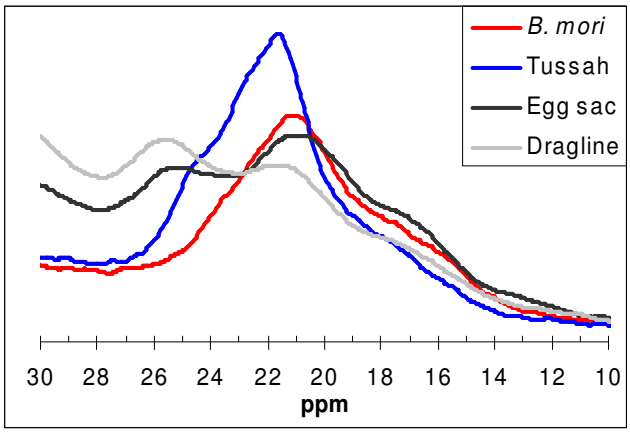

Figure 8.6 - The Ala C_β band as detail of the NMR spectra for the silks

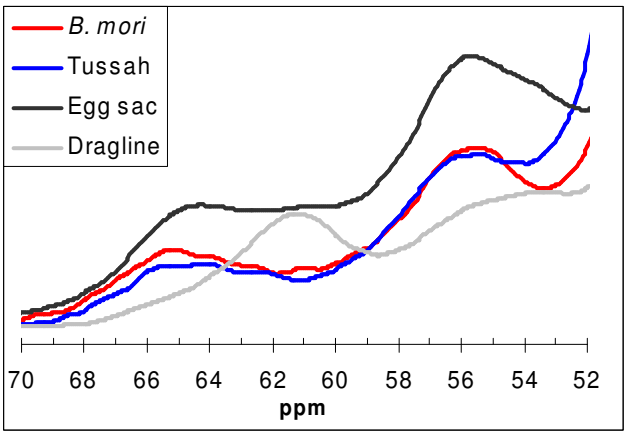

Figure 8.7 - The Ser C_β and C_α peaks in the NMR spectra of silks

From the NMR spectra, the increasing content of serine can be observed from the intensity of the Ser C_α peak (about 55 ppm [Kümmerlen *et al.* 1996, Asakura *et al.* 1997, Asakura & Yao 2002, Zhao *et al.* 2003]), the highest for egg sac spider silk, followed by *B. mori* (GAGAGS motif), Tussah and finally dragline spider silk.

At about 62-65 ppm, all silks show a band (Figure 8.7). For egg sac spider silk, because of the known high proportion of serine residues in its structure, it is clear that this band is the Ser C_β peak. Also for *B. mori* and Tussah the assignment to Ser C_β is suggested. Dragline silk shows a band that is significantly lower than for the other silks, the assignment to Pro C_α, as was also found for *Nephila clavipes* [Liivak *et al*. 1997], which is acceptable since dragline silk contains a much higher proline content than the other silks (Chapter 4).

Based on the Ser C_β peaks and Table 8.1 [Hronska *et al*. 2004], we can conclude that for *B. mori* and egg sac silk, also the Ser residues take part of the β-sheet and/or β-turn structure. For *B. mori*, it is indeed known that the GAGAGS-structure takes the β-sheet conformation (see Chapter 5).

With respect to the Ser C_α peaks, a chemical shift value of 55-56 ppm is found for all fibres. Nakazawa & Asakura [2002] assigned a component at about 55.6 ppm to random coil, 59.2 ppm to α-helix and 54.9 ppm to β-sheet structure for regenerated silk fibroin films of *A. pernyi* (untreated and treated with methanol). Also from Table 8.1 [Hronska *et al*. 2004], it is clear that none of the serine residues in the different silks are in the α-helical conformation. Considering Table 8.1 [Hronska *et al*. 2004], the value of 55.7 ppm found for egg sac spider silk is too low to deduce a random coil conformation for the serine residues. It is rather suggested that the serine residues in the egg sac spider silk are mostly involved in a β-sheet related conformation.

For the spider silks, a shoulder at the Ser C_α peak is observed at about 54 ppm (Figure 8.7). Because of the higher content of Leu for the spider silks, compared to the silkworm silks, an association to the Leu C_α carbon is suggested [Hronska *et al.* 2004].

Unfortunately, the α-helical conformation, that is known to be available in Tussah silk and suggested to be available in the spider silks, was difficult to confirm from the NMR spectra.

8.7. CONCLUSION

First of all, it should be remarked that less resolved spectra were obtained than found in literature, probably because of isotope labelling of the silk fibroins that is often used. Unfortunately, in this study this was not feasible because of practical considerations. Furthermore, some shifts are observed compared to literature that are attributed to the state of the silk fibroins (liquid versus solid state) or also to the isotope labelling.

With respect to the regenerated *B. mori* silk fibroin samples, it can be concluded that indeed the samples, made according to different procedures, are different in the β-sheet content and possibly the content of β-sheets of limited lengths or β-turns. In

comparison to the silk fibre, it is clear that most of the β-sheets are indeed dissolved by the procedure. The results are in agreement with the infrared spectroscopic observations in Chapter 6.

The structures of *B. mori* and Tussah silk as found from the solid-state NMR spectra are in accordance with literature, although the α-helical structure for Tussah is difficult to confirm. The latter is also valid for dragline spider silk. The resolution of the instrument was probably not high enough to detect the smaller fractions of α-helical structure.

For egg sac spider silk, it is suggested that the alanine residues, as well as the serine residues, are involved in a β-sheet related conformation. Also a high amount of β-turn structures, as detected in FT-IR spectroscopy, is confirmed.

8.8. REFERENCES

Ando I., Kameda T., Asakawa N., Kuroki S., Kurosu H., Structure of peptides and polypeptides in the solid state as elucidated by NMR chemical shift, J. Mol. Struct. 441(2-3):213-230 (1998)

Asakura T., Demura M., Date T., Miyashita N., Ogawa K., Williamson P.W., NMR study of Silk I structure of *Bombyx mori* silk fibroin with 15N- and 13C-NMR chemical shift contour shifts, Biopolymers 41:193-203 (1997)

Asakura T., Yamane T., Nakazawa Y., Kameda T., Ando K., Structure of *Bombyx Mori* silk fibroin before spinning in solid state studied with Wide Angle X-Ray scattering and ^{13}C Cross-Polarization/Magic Angle Spinning NMR, Biopolymers 58:521-525 (2001a)

Asakura T., Ashida J., Yamane T., Kameda T., Nakazawa Y., Ohgo K. And Komatsu K., A repeated beta-turn structure in poly(Ala-Gly) as a model for Silk I of *Bombyx mori* silk fibroin studied with two-dimensional spin-diffusion NMR under Off Magic Angle Spinning and Rotational Echo Double Resonance, J. Mol. Biol. 306:291-305 (2001b)

Asakura T. & Yao J., ^{13}C CP/MAS NMR study on structural heterogeneity in *Bombyx mori* silk fiber and their generation by stretching, Protein Science 11:2706-2713 (2002)

Asakura T., Yao J., Yamane T., Umemura K., Ulrich A.S., Heterogeneous structure of silk fibers from *Bombyx mori* resolved by ^{13}C solid-state NMR spectroscopy, J. Am. Chem. Soc. 124(30):8794-8795 (2002)

Asakura T., Yang M., Kawase T., Structure of characteristic sequences in *Nephila clavipes* dragline silk (MaSp1) studied with ^{13}C solid state NMR, Polymer Journal 36(12):999-1003 (2004)

Ha S.-W., Tonelli A.E., Hudson S.M., Structural studies of *Bombyx mori* silk fibroin during regeneration from solutions and wet fiber spinning, Biomacromolecules 6:1722-1731 (2005)

Hijirida D.H., Do K.G., Michal C., Wong S., Zax D., Jelinski L.W., ^{13}C NMR of *Nephila clavipes* major ampullate silk gland, Biophys. J. 71(6):3442-3447 (1996)

Hronska M., van Beek J.D., Williamson P.T.F., Vollrath F., Meier B.H., NMR characterization of native liquid spider dragline silk from *Nephila edulis*, Biomacromolecules 5:834-839 (2004)

Kim S. H., Nam Y.S., Lee T.S., Park W.H., Silk fibroin nanofiber. Electrospinning, properties, and structure, Polymer Journal 35(2):185-190 (2003)

Kishore A.I., Herberstein M.E., Craig C.L., Separovic F., Solid-state NMR relaxation studies of Australian spider silks, Biopolymers 61:287-297 (2002)

Kümmerlen J., van Beek J.D., Vollrath F., Meier B.H., Local structure in spider dragline silk investigated by two-dimensional spin-diffusion nuclear magnetic resonance, Macromolecules 29(8):2920-2928 (1996)

Laws D.D., Bitter H.M.L., Jerschow A., Solid-state NMR spectroscopic methods in chemistry, Angew. Chem. Int. Ed. 41(17):3096-3129 (2002)

Liivak O., Flores A., R. Lewis, Jelinski L.W., Conformation of the polyalanine repeats in minor ampullate gland silk of the spider *Nephila clavipes*, Macromolecules 30:7127-7130 (1997)

Monti P., Taddei P., Freddi G., Ohgo K., Asakura T., Vibrational ^{13}C-Cross-Polarization/Magic Angle Spinning NMR spectroscopic and thermal characterization of poly(alanine-glycine) as model for Silk I *Bombyx mori* fibroin, Biopolymers (Biospectroscopy) 72:329-338 (2003)

Nakazawa Y. & Asakura T., High-resolution ^{13}C CP/MAS NMR study on structure and structural transition of *Antheraea pernyi* silk fibroin containing poly(L-alanine) and Gly-rich regions, Macromolecules 35(6):2393-2400 (2002)

Ohgo K., Zhao C., Kobayashi M., Askura T., Preparation of non-woven nanofibers of *Bombyx mori* silk, *Samia cynthia ricini* silk and recombinant hybrid silk with electrospinning method, Polymer 44:841-846 (2003)

Parkhe A.D., Seeley S.K., Gardner K., Thompson L., Lewis R.V., Structural studies of spider silk proteins in the fiber, J. Mol. Recognit. 10(1):1-6 (1997)

Pines A., Gibby M.G., Waugh J.S., Proton-enhanced NMR of dilute spins in solids, J. Chem. Phys. 59:569-90 (1973)

Saito H., Tabeta R., Asakura T., Iwanaga Y., Shoji A., Ozaki T., Ando I., High-resolution ^{13}C NMR study of silk fibroin in the solid state by the Cross-Polarization-Magic Angle Spinning method. Conformational characterization of Silk I and Silk II type forms of *Bombyx mori* fibroin by the conformation-dependent ^{13}C chemical shifts, Macromolecules 17:1405-1412 (1984a)

Saito H., Tabeta R., Shoji A., Ozaki T., Ando I., Miyata T., A high-resolution C-13-NMR study of collagenlike polypeptides and collagen fibrils in solid-state studied by the Cross-Polarization Magic Angle-Spinning method – Manifestation of conformation-dependent C-13 chemical-shifts and application to conformational characterization, Biopolymers 23(11):2279-2297 (1984b)

Saito H. & Ando I., High resolution solid state NMR studies of synthetic and biological macromolecules, Annual Reports of NMR Spectroscopy, Academic Press, London, 21:209-290 (1989)

Williams D.H. & Fleming I., Spectroscopic methods in organic chemistry, McGraw-Hill, New York, 5th Edition, ISBN 0-07-709147-7 (1996)

Yang M. & Asakura T., Design, expression and solid-state NMR characterization of silk-like materials constructed from sequences of spider silk, *Samia cynthia ricini* and *Bombyx mori* silk fibroins, Journal of Biochemistry 137:721-729 (2005)

Zhao C., Yao J., Masuda H., Kishore R., Asakura T., Structural characterization and artificial fiber formation of *Bombyx mori* silk fibroin in hexafluoro-iso-propanol solvent system, Biopolymers 69:253-259 (2003)

Zhou P., Li G.Y., Shao Z.Z., Pan X.Y., Yu T.Y., Structure of *Bombyx mori* silk fibroin based on the DFT chemical shift calculation, J. Phys. Chem. B 105:12469-12476 (2001)

Zhou P., Xie X., Deng F., Ping Z., Xun X., Feng D., Effects of pH and calcium ions on the conformational transitions in silk fibroin using 2D Raman correlation spectroscopy and C-13 solid-state NMR, Biochemistry 43:11302-11311 (2004)

9

THERMAL BEHAVIOUR OF SILKS

Silks are thermoset polymers, i.o.w. they degrade prior to melting. A reason for this is to be found in the extensive hydrogen bonding. When heated, the primary bonds (covalent bonds eg. C-C, C-H, C=O, N-H, O-H) break before all the hydrogen bonds can be eliminated. Secondary bonds (e.g. hydrogen bonds) can be reformed many times whereas covalent bonds are permanent.

In this chapter, the thermal behaviour of the different silks is analysed. It is expected that the effect of heat will also give some information about the structure of these materials. The techniques used are differential scanning calorimetry (DSC), thermogravimetry (TGA) and thermal mechanical analysis (TMA). The DSC experiments were added to confirm the DRIFTS results of the methanol-induced transformation.

9.1. DIFFERENTIAL SCANNING CALORIMETRY

9.1.1. PRINCIPLE OF DIFFERENTIAL SCANNING CALORIMETRY

Differential Scanning Calorimetry (DSC) measures the amount of energy (heat) absorbed or released by a sample as it is heated, cooled, or held at a constant temperature.

In practice, the DSC instrument measures the energy necessary to establish a nearly zero temperature difference between a substance and an inert reference material, as the two specimens are subjected to identical temperature regimes in an environment heated or cooled at a controlled rate.

The basic principle underlying this technique is that, when the sample undergoes a physical transformation such as phase transitions, more (or less) heat will need to flow to it than to the reference to maintain both at the same temperature. Whether more or less heat must flow to the sample depends on whether the process is exothermic or endothermic. For example, as a solid sample melts to a liquid it will require more heat flowing to the sample to increase its temperature at the same rate as the reference. This is due to the absorption of heat by the sample as it undergoes the endothermic phase transition from solid to liquid. Likewise, as the sample undergoes exothermic processes (such as crystallization) less heat is required to raise the sample temperature. By observing the difference in heat flow between the sample and reference, differential scanning calorimeters are able to measure the amount of energy absorbed or released during such transitions.

Typical applications include determination of melting point temperature and the heat of melting; measurement of the glass transition temperature, curing and crystallization studies, and identification of phase transformations.

9.1.2. LITERATURE REVIEW

Several researchers performed DSC on liquid or regenerated silk of *Bombyx mori* [Magoshi *et al*. 1979, 2000, Nakamura *et al*. 1994, Freddi *et al*. 1999, Um *et al*. 2001, Tanaka *et al*. 2002] and *Antheraea pernyi* (Tussah) [Tsukada *et al*. 1994a, 1994b, 1994c, Freddi *et al*. 1997, Kweon *et al.* 2000, 2001a, 2001b, Tanaka *et al*. 2002, Motta *et al*. 2002, Li *et al*. 2003] and looked at the conformational transition induced by heat, water, methanol or formic acid or to the blending effect [Tsukada *et al.* 1994a, 1994b, Kweon *et al.* 2001a].

All samples show an endothermic peak at about 100 °C due to the evaporation of water. Some authors attributed a broad exothermic peak at about 70 °C for liquid or regenerated Tussah fibroin film to the crystallization (irreversible phase transition) from α-helix to β-sheet [Magoshi *et al*. 2000, Tanaka *et al*. 2001].

For *B. mori*, an endothermic shift is observed at about 175 °C, due to the glass transition of the amorphous parts of fibroin [Magoshi *et al.* 1979, Tsukada *et al.* 1994b, Nakamura *et al.* 1994, Motta *et al.* 2002]. For Tussah fibres, this

endothermic shift is observed at a higher temperature of about 190 °C [Tsukada *et al.* 1994b, 1994c]. However, this endothermic shift is not always visible.

The DSC curve of regenerated or liquid *B. mori* and Tussah fibroin film is further characterized by an endotherm-exotherm combination at about 205 °C / 220 °C for *B. mori* and about 215 °C / 230 °C or 230 °C / 240 °C for Tussah. Several authors [Tsukada *et al.* 1994c, Kweon *et al*. 2001b, Li *et al*. 2001, 2003] associated the endotherm at about 230 °C with the intensive molecular motion within α-helix crystals. The sharp exotherm is attributed to the crystallization of amorphous fibroin in the random coil conformation with the formation of β-sheet crystals (random coil → β-sheet transition) [Tsukada *et al*. 1994c, Freddi *et al*. 1997, Kweon *et al*. 2000, 2001b, Li *et al*. 2001, 2003].

Finally, a sharp endothermic peak is observed at about 280 °C for *B. mori* and at about 360 °C for Tussah silk fibroin due to thermal decomposition of the silk fibroin with unoriented β-sheets. A well-oriented β-sheet structure in *B. mori* silk is having a decomposition temperature above 300 °C [Tsukada *et al*. 1996].

Tsukada *et al.* [1996] investigated the thermal behaviour of *B. mori* silk fibres, differing in fibre size. The DSC thermograms were characterized by a broad endothermic transition at 306-312 °C due to thermal decomposition of silk fibroin.

Li *et al*. [2001, 2003] reported the DSC curves of *A. pernyi* silk fibroin fibre. Thermal degradation of fibroin was observed as one large endothermic peak at about 372 °C.

With respect to spider silk, Guess & Viney [1998] performed a DSC analysis on major ampullate silk of *Nephila clavipes* to prove that fibres contain bound moisture even after drying in a desiccator.

9.1.3. DSC OF REGENERATED *B. MORI* SAMPLES

9.1.3.1. Introduction

In Chapter 7, *Bombyx mori* and Tussah silk fibres were dissolved, dialysed and freeze-dried in order to obtain "amorphous" samples, in this chapter DSC was used to find out if these experiments were succeeded.

Since DSC of the fibres only would result in an idea of the thermal degradation temperature, thermogravimetry (TGA) was considered as a more valuable tool in this respect.

9.1.3.2. Materials and methods

The regenerated *Bombyx mori* samples, based on fabric and fibres (samples indicated as "MoriFib", "MoriFab 1", and "MoriFab 2"), were analysed. These samples were the same as those investigated in Chapter 7. To evaluate the conformational transition, the regenerated *B. mori* samples, treated with 60% and 100% methanol, were also tested. For the "MoriFab 2" sample also a treatment with 20% methanol was considered.

The samples were maintained in climatized conditions for at least 24 hours prior to testing.

Conventional DSC measurements were performed in non-hermetic pans using a TA Instruments DSC 2920. The temperature was calibrated with gallium, indium and tin. Indium was used for enthalpy calibration. The purge gas was nitrogen (25 ml/min.). The samples, about 5 à 8 mg, were first equilibrated at 50 °C for 10 minutes, followed by an equilibration at 20 °C. The temperature was then increased to 270 °C at a ramp of 10 °C/min.

9.1.3.3. Results and discussion

Figure 9.1 shows the DSC plots for the different *Bombyx mori* samples. The regenerated samples, produced with the same procedure ("MoriFab 2" and "MoriFib"), showed the same thermal behaviour with DSC. Only "MoriFab 2" is kept in Figure 9.1.

The region below 50 °C represents the prior equilibration at 50 °C and 20 °C and is not important for this analysis.

At about 100-110 °C, a broad endothermic peak is observed associated with the evaporation of water.

For the regenerated untreated samples ("MoriFab 1" and "MoriFab 2"), a weak broad exotherm is clearly seen at about 170 °C. This peak is the consequence of an overlap of the water evaporation peak and the endothermic shift due to the glass transition temperature (at about 175 °C [Magoshi *et al.* 1979, Tsukada *et al.* 1994, Nakamura *et al.* 1994, Motta *et al.* 2002]). The higher crystallinity (and disappearance of the amorphous fraction) of the methanol treated samples made the glass transition of the still residual amorphous regions less visible and probably shifted to higher temperatures [Magoshi *et al.* 1979, Motta *et al*. 2002]. To validate this further, additional measurements by means of modulated DSC could be useful. With this technique, it is expected that the water evaporation peak and the endothermic shift are separated.

However, the much higher exotherm for "MoriFab 1" confirms the higher amorphous content in "MoriFab 1" than in "MoriFab 2".

The exotherm peak occurring in the range 200-230 °C has been associated with specific structural changes of the amorphous silk fibroin during heating. The most relevant thermal changes induced by heating and appearing just above 200 °C have been attributed to conformational transitions (random coil - β-sheet, α-helix - β-sheet) accompanying the crystallization of amorphous silk fibroin to β-sheet crystals [Tsukada *et al.* 1994b]. The shift of the exotherm from about 216 °C for "MoriFab 2" to about 232 °C for "MoriFab 1" may indicate the different secondary structure for both samples, in agreement with what is observed in Chapter 7.

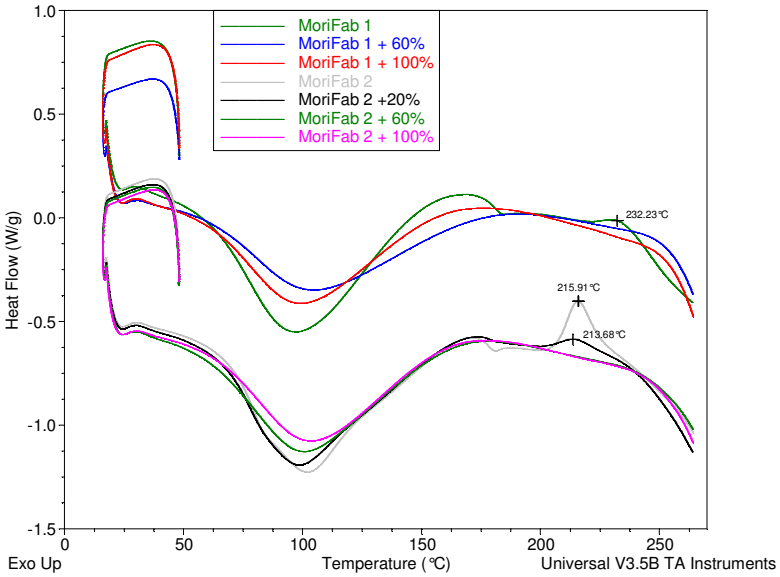

Figure 9.1 – DSC curves of untreated and methanol treated regenerated *B. mori* samples

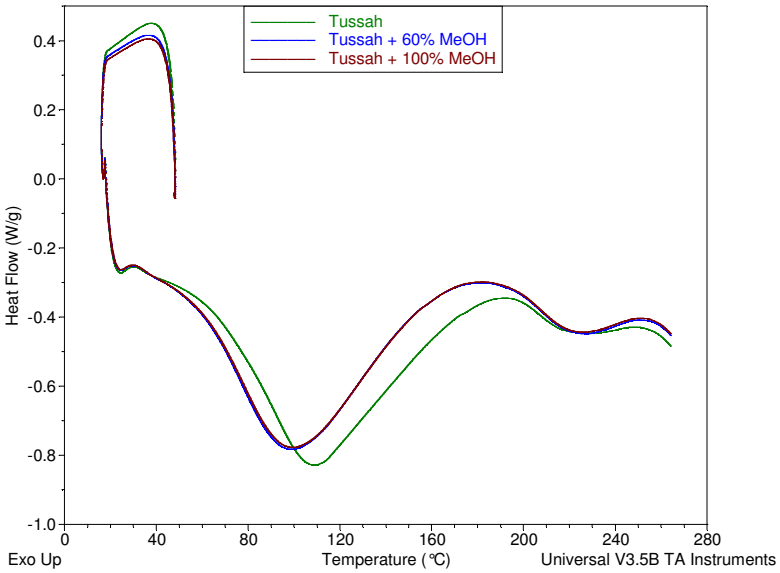

Figure 9.2 - DSC curves of untreated and methanol treated regenerated Tussah samples

By a treatment of methanol, the combination of exotherm and endotherm peaks in the region 200-230 °C disappeared indicating that the conformational transition from random coil to β-sheet structure indeed took place. As observed in the DRIFT

spectra (Chapter 7), the differences between a 60% methanol and 100% methanol treatment are minimal. However, the 20% methanol treated sample still shows a small exotherm at about 214 °C, indicating that the sample is not completely crystallized. Moreover, the decrease of the water peak at about 100 °C and the higher temperature of this peak, for this sample, can indicate a reduction of the quote of the amorphous regions [Motta *et al*. 2002].

For the Tussah sample, the DSC curve is represented in Figure 9.2. The broad exothermic peak at about 70 °C, assigned to the crystallization from α-helix to β-sheet in some literature [Magoshi *et al*. 2000, Tanaka *et al*. 2001], is not visible. It can be the reason for the shift of the DSC curve of the regenerated compared to the methanol treated samples. The relatively small difference that can be observed after the methanol treatment is in agreement with the DRIFTS results. Although, the different methanol concentrations (60% and 100%) resulted in a different contraction of the sample, DSC seems not appropriate to visualize the difference.

A broad exotherm is observed at about 190 °C, attributed to the glass transition of the amorphous parts [Tsukada *et al.* 1994b, 1994c]. The temperature of this exotherm is indeed higher than for *B. mori*.

Compared to DSC experiments in literature [Kweon *et al*. 2000, Motta *et al.* 2002] on regenerated Tussah samples, the endo-exotherm combination is not seen. The used procedure for obtaining an amorphous Tussah sample was unfortunately not successful. It is known from literature that it is more difficult to solve this silk compared to *B. mori* silk. The more complex structure of Tussah silk (apart from β-sheet crystals, also α-helical structures) is suggested to play a role in this. Moreover, Tussah silks shows a higher fraction of charged amino acids (especially Arg and Asp, see chapter 4) that possibly results in ionic interactions that are more difficult to break.

9.2. THERMOGRAVIMETRY

9.2.1. PRINCIPLE OF THERMOGRAVIMETRY

In thermogravimetry (TGA), the change in weight is continuously recorded as a function of a combination of temperature with time. The commonly investigated processes are: thermal stability and decomposition, dehydration, oxidation, determination of volatile content and other compositional analysis, binder-burnout, high-temperature gas corrosion etc.

9.2.2. LITERATURE REVIEW

Different authors performed thermogravimetry on regenerated or liquid *Bombyx mori* [Tsukada *et al*. 1994b, Motta *et al*. 2002] and/or *Antheraea pernyi* (Tussah) [Tsukada *et al*. 1994b, 1994c, Kweon *et al*. 2000, 2001a] films to study the conformational transition induced by heat or a methanol treatment or the effect of blending [Kweon *et al*. 2001a, Tsukada *et al*. 1994a, 1994b].

In the TGA curves of regenerated *B. mori* fibroin films, three regions can be observed: a first region (< 150 °C) due to the loss of water, a second region (170-250 °C) characterized by a very low weight loss attributed to the loss of other low temperature volatile species, and a third region of abrupt weight loss due to thermal degradation of the fibroin [Tsukada *et al*. 1994b, Motta *et al*. 2002, Um *et al*. 2001]. This last weight loss is associated with the breakdown of side chain groups of amino acid residues as well as the cleavage of peptide bonds [Um *et al*. 2001]. Regenerated Tussah fibroin films are thermally more stable, resulting in a shift of the second (220-300 °C) and third region (300-400 °C) to higher temperatures [Tsukada *et al*. 1994b, Kweon *et al*. 2000].

In the TGA curves of *B. mori* fibres, as observed by Tsukada *et al*. [1996], the percentage of weight decreased sharply beyond 300 °C, due to thermal degradation.

It is reported that silk fibre pyrolizes before the β-sheet crystals melt [Magoshi & Nakamura 1975, Nakamura *et al*. 1994].

No thermogravimetric information was found for spider silk fibres in literature.

9.2.3. MATERIALS AND METHODS

The different silk fibres (*Bombyx mori*, Tussah, egg sac and dragline *Araneus diadematus* spider silk) were all analysed by means of thermogravimetry (TGA).

2 to 3 mg of fibres was heated at a scanning speed of 10 °C/min from 20 to 800 °C under the flow of nitrogen gas.

9.2.4. RESULTS

The TGA curves of the different silk fibres are shown in Figure 9.3.

All the samples exhibited an initial weight loss below 100 °C, which is essentially due to the evaporation of water induced by heating. The initial weight loss is clearly the lowest for egg sac spider silk.

Then, the samples remained stable until about 260 °C, when a sharp drop of the TGA curves indicated the beginning of the thermal decomposition accompanied by a greater weight loss. *B. mori* and dragline spider silk show a faster degradation curve than the Tussah and egg sac spider silk, indicating a lower thermal stability. The degradation temperatures are indicated in Figure 9.3, as maxima in the 1st derivative of the TGA curves. The temperatures at which *B. mori*, Tussah, egg sac and dragline spider silk exhibit a 20% weight loss, used for the evaluation of the thermo-oxidative stability, were 279, 302, 300, and 281 °C, respectively. The higher thermal stability for *A. pernyi* (Tussah) compared to *B. mori* is confirmed [Tsukada *et al.* 1994b]. Also a higher thermal stability for egg sac spider silk, compared to dragline spider silk was found, in both nitrogen and air atmosphere.

For all silks, except of dragline silk, two deflection points are observed, as indicated in the 1st derivative of the TGA curves shown as dotted lines in Figure 9.3. It indicates that the degradation occurs in two steps. The first step occurs at a higher rate than the second step, as estimated by the slopes. It should be remarked that

when the weight is recorded in air also dragline shows a two-phase degradation behaviour.

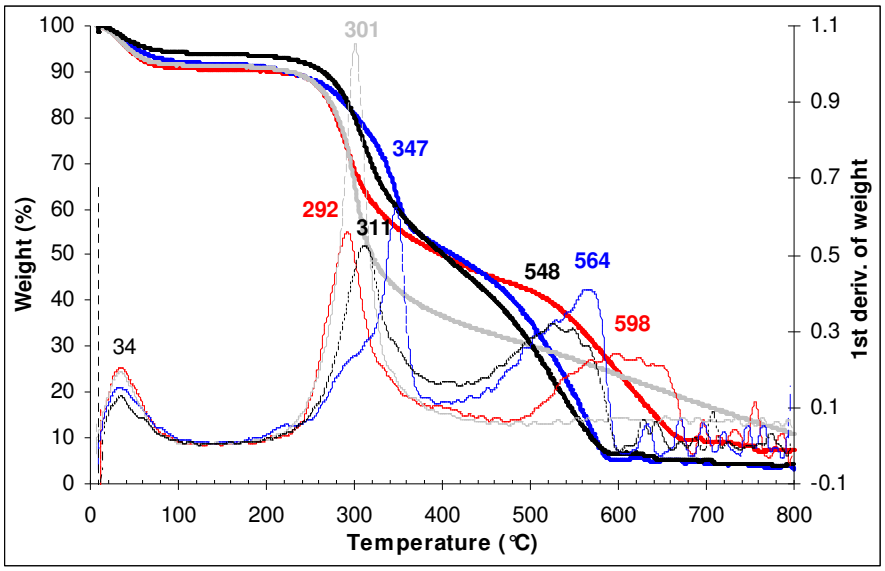

Figure 9.3 – Weight (in bold) and 1st derivative (dashed lines) of weight in function of temperature for the different silks (in red: *B. mori,* in blue: Tussah, in grey: dragline, in black: egg sac)

A further explanation of the higher thermal stability of egg sac spider silk in relation to its structure is given in Chapter 10.

9.3. THERMAL MECHANICAL ANALYSIS

9.3.1. PRINCIPLE OF THERMAL MECHANICAL ANALYSIS

An instrument for "thermal mechanical analysis" (TMA) permits the measurement of dimensional and viscoelastic changes as a function of temperature or time.

With TMA, the dimensional properties of a sample are measured as the sample is heated, cooled or held under isothermal conditions. The loading or force can be varied.

Melting of the crystalline phase results in a discontinuous and rapid decrease in the mechanical performance of the material over a narrow temperature range. Softening of the amorphous phase, however, results in a continuous, slow decrease in fibre mechanical properties over a wider temperature range. It is therefore possible to characterize the structural behaviour of a material's crystalline and amorphous regions by monitoring its thermomechanical performance [Cao & Bhoyro 2001].

Thermal shrinkage can give an indication of orientation [McCrum *et al.* 1997]. Since molecular orientation is "frozen-in", it follows that it can be "unfrozen" by raising the temperature. An oriented amorphous polymer on being heated through

its glass transition re-enters the rubbery state. The low mobile molecules recoil to random configurations, losing their orientation, and the polymer is seen to shrink back to approximately its original dimensions. Similar thermal shrinkage occurs on heating an oriented crystalline polymer, but in this case it is necessary to melt crystals before constraint on the amorphous fraction is totally released and complete shrinkage is obtained.

9.3.2. LITERATURE ON SILK

Tsukada *et al*. [1998] studied the thermal response by means of TMA of Tussah (*Antheraea pernyi*) silk fibroin films treated with different water-methanol solutions.

A gradual contraction starting from room temperature, which was essentially due to moisture release, characterized the thermomechanical behaviour of tussah films treated with water-methanol solutions for 2 min. At above 200 °C the TMA pattern changed as a function of the treatment conditions. The film treated with 100% methanol showed a rapid shrinkage, which attained its maximum at 211 °C, prior to the final extension leading to sample failure. This behavior is similar to that reported for untreated tussah films with random coil and α-helix conformation. The film treated with 80% methanol exhibited almost the same trend, but instead of breaking after the sharp shrinkage at 212 °C, it continued extending in response to the applied tension. Then, it underwent a final contraction (peak at 335 °C), followed by film failure due to thermal degradation.

Typical α-helix features in TMA are a strong loss peak at lower temperature and a TMA shrinkage beyond 200 °C. However, the shift of the major loss peak to higher temperatures (219-220 °C) and the appearance of a new loss component at around 230 °C, as well as the weakening of the TMA contraction and subsequent extension phases beyond 200 °C, lead to conclude that the methanol treatment resulted in local conformational transitions, with formation of nuclei of β-sheet structure [Tsukada *et al.* 1998]. The presence of nuclei of β-sheet crystallization acted as high-strength intermolecular junctions between adjacent random coil and α-helix domains.

Tsukada *et al*. [1994b] performed TMA on blend films of *A. pernyi* and *Bombyx mori* liquid silks. They found that the thermal expansion and contraction properties can be modulated by varying the amount of the two components of the blend. The higher thermal stability of *A. pernyi* silk fibroin films compared to *B. mori* films was confirmed. Tsukada *et al*. [1994] also compared the thermal behaviour, a.o. TMA, of different types of regenerated *A. pernyi* silk film, the first one obtained directly from the spinning glands of the silkworm, the second one obtained by dissolution of the silk fibre in LiSCN (solution-cast), followed by casting of the concentrated solution. It was concluded that the solution-cast regenerated silk fibroin exhibited higher thermal stability than that of the native silk fibroin film.

Cao & Bhoyro [2001] compared the TMA curve of wool yarns with that of a silk yarn. They found the silk (probably *B. mori*) yarn to remain stable below 300 °C.

Tsukada *et al*. [1996] performed TMA to investigate the effect of fibre size. The TMA profiles were characterized by an initial region of shrinkage (to 100 °C, due to

loss of moisture), followed by a region of slight but continuous extension until about 300 °C. A final abrupt extension (thermal degradation) occurred at 302-306 °C.

No TMA-experiments were found for spider silk fibres in literature.

9.3.3. MATERIALS AND METHODS

The same silk samples, as studied by the other techniques, were analysed by TMA: *Bombyx mori* silkworm silk, Tussah (*Antheraea pernyi*) silkworm silk, *Araneus diadematus* egg sac and dragline spider silk. For egg sac spider silk, two different egg sacs were tested. For dragline spider silk, also a sample of *Nephila clavipes* dragline was added.

All fibres were measured as fibre bundles. The bundles were clamped between two leaden bolls with a mass of about 0.1 g. These samples were maintained in climatized conditions for at least 24 hours prior to testing.

A preload force of 0.005 N was applied. During the measurement, the bundle was subjected to three different forces: low, moderate and high, ranging between 0.001 and 0.5 N. The gauge length was taken as 20 ± 5 mm for all the silks.

The temperature of the instrument was calibrated with indium and tin (in penetration mode). This was followed by a calibration of the probe and the force of the instrument. The measurements were performed under a nitrogen N_2 atmosphere to prevent degradation. The thermal expansion/shrinkage is recorded with a speed of 10 °C/min from 40 °C to 320 °C.

9.3.4. RESULTS AND DISCUSSION

Figure 9.4, Figure 9.5, Figure 9.6, and Figure 9.7 show the TMA curves for the different silk fibres with 3 different forces applied. For the *B. mori* and Tussah samples, also the derivative of dimensional change is displayed (curves grouped below).

It is clear that the force applied has a large effect on the dimensional change, certainly at higher temperatures. The dimensional change at higher temperature is increasing with force.

B. mori silk and egg sac spider silk are dimensionally more stable during heating than Tussah and dragline spider silk. The thermal stability of *B. mori* silk bundles is in agreement with the results found in literature [Magoshi & Nakamura 1975, Nakamura *et al*. 1994, Freddi *et al*. 1995, Tsukada *et al*. 1994d, Cao & Bhoyro 2001] for silk fibres and yarns. A steep length increase below 350 °C results from melting of β-sheet crystallites. A strong contraction starting at about 300 °C indicated that the silk yarn experienced pyrolysis, as observed for the smallest force. It is reported that *B. mori* silk fibre pyrolizes before the β-sheet crystallites melt [Magoshi & Nakamura 1975, Nakamura *et al*. 1994]. From our experiments, it can be concluded that it depends on the force applied.

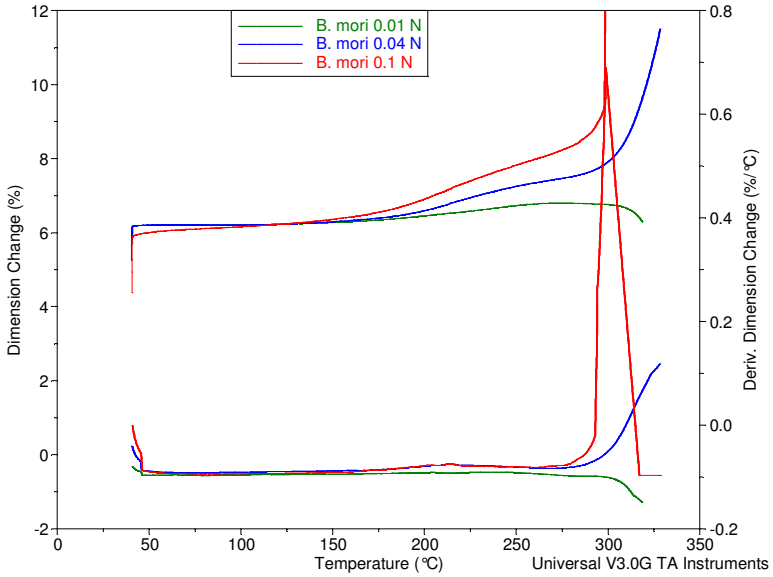

Figure 9.4 – TMA curve of *B. mori* fibre bundles

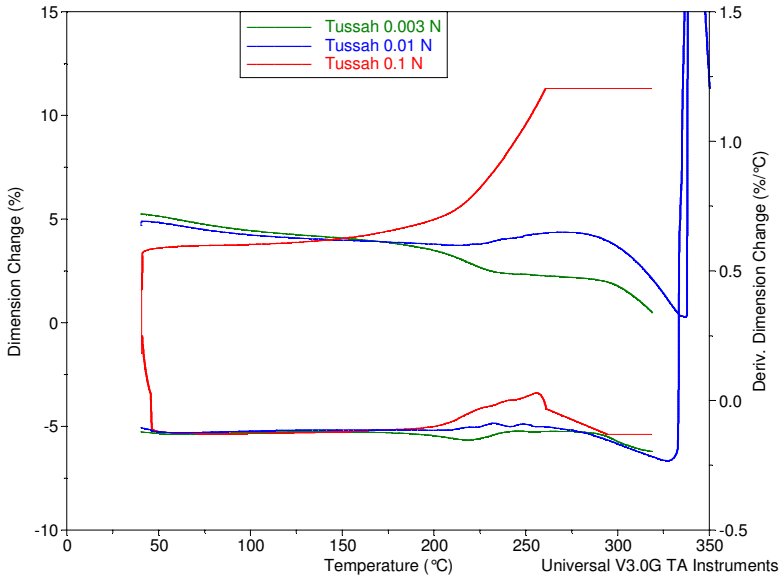

Figure 9.5 – TMA curve of Tussah fibre bundles

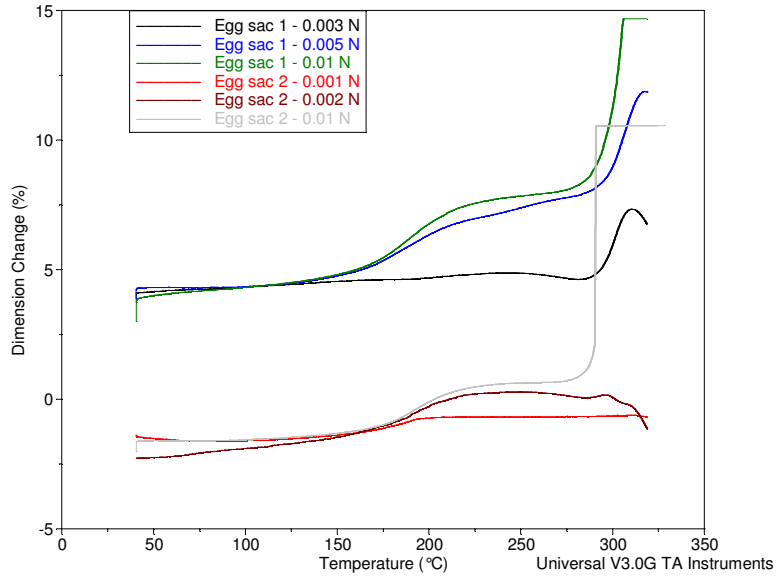

Figure 9.6 – TMA curve for fibre bundles from 2 egg sacs

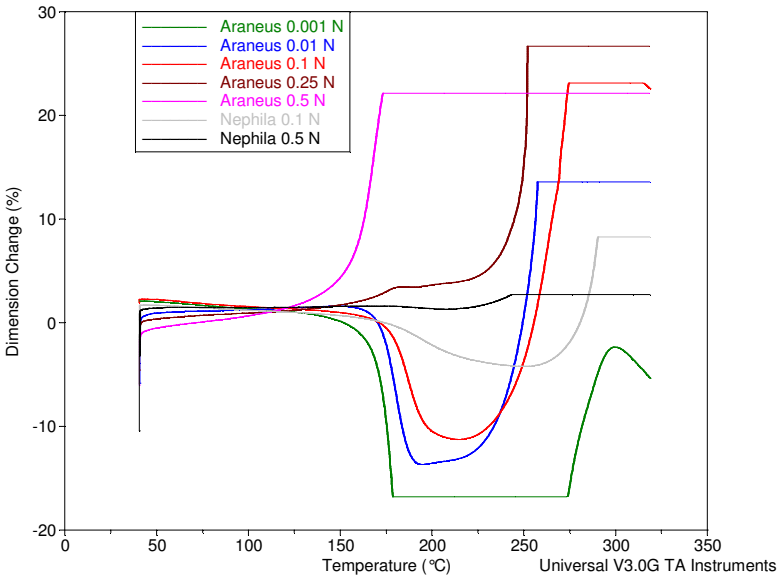

Figure 9.7 – TMA curve for fibre bundles of *A. diadematus* ("Araneus") and *N. clavipes* ("Nephila") dragline silk

For the dragline and Tussah silk at about 180-200 °C a significant shrinkage occurs for lower forces applied. Moreover, the dragline silk first shrinks where after it extends enormously at a temperature of about 230 °C. The onset temperature of shrinkage shifts to higher temperatures, the higher the load applied.

Dragline silk shows a comparable behaviour as found in literature for regenerated Tussah silk film treated with 100% methanol [Tsukada *et al*. 1998] and also wool yarns [Cao & Bhoyro 2001]. The TMA shrinkage beyond 200 °C was attributed to the typical α-helix conformation and, especially, local conformational transitions, with formation of nuclei of β-sheet structure. The TMA shrinkage indeed indicates the presence of an α-helical structure in dragline spider silk.

Tussah and dragline spider silk, known to contain a considerable amount of α-helical structures, show a clear shrinkage when heated under an applied force. Even for the smallest possible (limited by the instrument) load applied, no shrinkage is observed for both egg sacs and *B. mori*. This result confirms that the α-helical content in egg sac spider silk is indeed small. This is also in agreement with the known high contribution of serine residues that are known to destabilize α-helices because of the polar side chain that is able to be involved in a hydrogen bond. However, it is possible that more stable helical conformations are formed in egg sac spider silk.

The extension that is observed for egg sac seems to be variable, as is seen for the two egg sacs in Figure 9.6. It is not clear if this variability is due to the different mass that was difficult to control or to the variable structure of both egg sacs.

As for dragline, also egg sac spider and *B. mori* silk show an abrupt increase, but at a higher temperature of about 300 °C. It is attributed to melting or degradation of the crystallites, causing rapid deterioration in fibre strength [Cao & Bhoyro 2001].

Cao & Bhoyro [2001] reported that increasing the temperature leads to two competing processes: softening of the sample due to increased molecular mobility (physical process resulting in extension under stress) and forming a harder material due to thermal pyrolysis (chemical process resulting in contraction). The latter becomes dominant at higher temperatures, so that further increases in sample length stop and the sample contracts.

Furthermore, a few experiments were stopped early (at about 250 °C) to see if the transitions in the neighbourhood of 200 °C were due to pyrolysis of the silks. The fibres measured until 320 °C became black due to pyrolysis, this was not the case when stopped early. It is suggested that for Tussah and dragline indeed a conformational transition of the α-helices takes place which makes the fibres less thermally stable.

9.4. CONCLUSION

The DSC experiments on the regenerated and methanol treated samples confirmed that for *B. mori*, the methanol treatment indeed induced the conformational transition to β-sheet. For the Tussah sample, the used procedure for obtaining an "amorphous" sample was indeed not successful, as also observed in the DRIFTS experiments.

The TGA experiments lead to the conclusion that the thermal degradation temperature of the Tussah and egg sac fibres is higher than for the other silks. All silks show a two-phase degradation behaviour.

As far as the TMA results concerned, it should be firstly remarked that there is a clear force-dependence for all silk fibres.

The thermal stability when strained is higher for *Bombyx mori* and egg sac spider silk. It is suggested that the lower α-helical content explains this behaviour. This is confirmed by the shrinkage observed for Tussah and dragline silk, but not for the *B. mori* and egg sac silk fibres.

The relatively high thermal stability of egg sac spider silk is suggested to be due to the fraction of short-chain β-sheets and especially β-turns, with adjacent fibroin chains more tightly aggregated within the amorphous regions and stabilized by an intramolecular network of hydrogen bonds. This feature led to a restriction of the thermally induced molecular motion of the fibroin chains, as demonstrated by the relatively high thermal stability.

Further relations to the structure of these silks will be discussed in Chapter 10.

9.5. REFERENCES

Cao J. & Bhoyro A.Y., Structural characterization of Wool by Thermal Mechanical Analysis of Yarns, Text. Res. J. 71(1):63-66 (2001)

Freddi G., Kato H., Tsukada M., Allara G., Shiozaki H., Physical properties and dyeability of NaOH-treated silk fibers, J. Appl. Polym. Sci. 55:481-487 (1995)

Freddi G, Monti P, Nagura M, Gotoh Y, Tsukada M , Structure and molecular conformation of Tussah silk fibroin films: Effect of heat treatment, J. Polym. Sci. Pt. B-Polym. Phys. 35(5):841-847 (1997)

Freddi G., Pessina G., Tsukada M., Swelling and dissolution of silk fibroin (*Bombyx mori*) in N-methyl morpholine N-oxide, Int. J. Biol. Macromol. 24:251-263 (1999)

Guess K.B. & Viney C., Thermal analysis of major ampullate (drag line) spider silk: the effect of spinning rate on tensile modulus, Thermochimica Acta 315 (1):61-66 (1998)

Kweon H.Y., Um I.C., Park Y.H., Thermal behavior of regenerated *Antheraea pernyi* silk fibroin film treated with aqueous methanol, Polymer 41(20):7361-7367 (2000)

Kweon H.Y., Um I.C., Park Y.H., Structural and thermal characteristics of *Antheraea pernyi* silk fibroin/chitosan blend film, Polymer 42:6651-6656 (2001a)

Kweon H.Y., Woo S.O., Park Y.H., Effect of heat treatment on the structural and conformational changes of regenerated *Antheraea pernyi* silk fibroin films, J. Appl. Polym. Sci. 81(9):2271-2276 (2001b)

Li M.Z., Lu S.Z., Wu Z.Y., Yan H., Mo J., Wang L., Study on porous silk fibroin materials. I. Fine structure of freeze dried silk fibroin, J. Appl. Polym. Sci. 79(12):2185-2191 (2001)

Li M.Z., Tao W., Lu S.Z., Kuga S., Compliant film of regenerated *Antheraea pernyi* silk fibroin by chemical crosslinking, Int. J. Biol. Macromol. 32(3-5):159-163 (2003)

Magoshi J. & Nakamura S., Studies on physical properties and structure of silk. Glass transition and crystallization of silk fibroin, J. Appl. Polym. Sci. 19(4):1013-1015 (1975)

Magoshi J., Mizuide M., Magoshi Y., Takahashi K. Kubo M., Nakamura S., Physical properties and structure of silk. VI. Conformational changes in silk fibroin induced by immersion in water at 2 to 130°C, J. Polym. Sci. Pt. B-Polym. Phys. 17:515-520 (1979)

Magoshi J., Magoshi Y., Becker M.A., Kato M., Han Z., Tanaka T., Inoue S., Nakamura S., Crystallization of silk fibroin from solution, Thermochimica Acta, 352:165-169 (2000)

McCrum N.G., Buckley C.P., Bucknall C.B., Principles of Polymer Engineering, 2nd Edition, Oxford University Press, USA (1997)

Motta A., Fambri L., Migliaresi C., Regenerated silk fibroin films: Thermal and dynamic mechanical analysis, Macromolecular Chemistry and Physics 203:1658-1665 (2002)

Nakamura S., Magoshi J., Magoshi Y., Thermal properties of silk proteins in silkworms, In: Silk polymers: Material science and biotechnology, ACS Symposium Series 544, Washington DC, 210-221 (1994)

Tanaka T., Magoshi J., Magoshi Y., Lotz B., Inoue S.-I., Kobayashi M., Tsuda H., Becker M.A., Han Zh., Nakamura Sh., Spherulites of Tussah silk fibroin: structure, thermal properties and growth rates, Journal of Thermal Analysis and Calorimetry 64:645-650 (2001)

Tanaka T., Magoshi J., Magoshi Y., Inoue S., Kobayashi M., Tsuda H., Becker M.A., Nakamura Sh., Thermal properties of *Bombyx mori* and several wild silkworm silks, J. Therm. Anal. Calorim. 70:825-832 (2002)

Tsukada M., Freddi G., Crighton J.S., Structure and compatibility of poly(vinyl alcohol)-silk fibroin (PVA/SF) blend films, J. Polym. Sci. Pt. B-Polym. Phys. 32:243-248 (1994a)

Tsukada M., Freddi G., Kasai N., Physical properties and phase separation structure of *Antheraea pernyi*/*Bombyx mori* silk fibroin blend films, J. Polym. Sci. Pt. B-Polym. Phys. 32:1175-1182 (1994b)

Tsukada M., Freddi G, Gotoh Y, Kasai N, Physical and chemical properties of Tussah silk fibroin films, J. Polym. Sci. Pt. B-Polym. Phys. 32(8):1407-1412 (1994c)

Tsukada M., Freddi G, Minoura N., Changes in the fine structure of silk fibroin fibers following gamma irradiation, J. Appl. Polym. Sci. 51:823-829 (1994d)

Tsukada M., Obo M., Kato M., Freddi G., Zanetti F., Structure and dyeability of *Bombyx mori* silk fibers with different filament sizes, J. Appl. Polym. Sci, 60:1619-1627 (1996)

Tsukada M., Freddi G., Kasai N., Monti P., Structure and molecular conformation of Tussah silk fibroin films with water-methanol solutions: Dynamic mechanical and thermomechanical behavior, J. Polym. Sci. 36:2717-2724 (1998)

Um I.C., Kweon H.Y., Perk Y.H., Hudson S., Structural characteristics and properties of the regenerated silk fibroin prepared from formic acid, Int. J. Biol. Macromol. 29(2):91-97 (2001)

10

STRUCTURE-PROPERTY CORRELATIONS OF SILKS

Defining the structure and property correlations of the silk class of structural proteins is in its early stages because of the difficulties encountered with large, insoluble, repetitive proteins. Our knowledge of functional correlations for most of the spider silk materials is very limited, with the exception of the major ampullate gland fibres and to some extent the viscid silk fibres produced by the flagelliform gland.

In order to identify further structure-property correlations for the studied silks, in this chapter, the structural models (or tertiary structure) of the silks proposed in literature are discussed. Further aspects of the morphology of the silks are reviewed, since it is known that also the micro- or nano-fibrillar structure of fibres plays a role in their mechanical performance. For egg sac spider silk, a fractographic analysis was added. This is followed by a discussion of the structural basis for the physical properties for the studied silks. To be complete, the phenomenon of supercontraction is discussed. Finally, based on the performed experiments, a more detailed structural model is proposed for egg sac spider silk.

10.1. STRUCTURAL MODEL FOR FIBRES

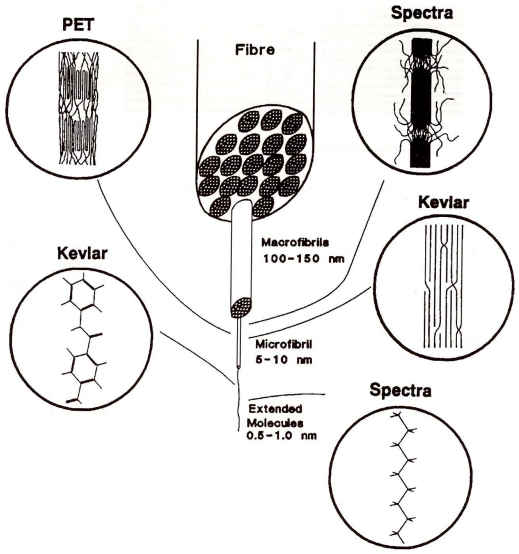

Figure 10.1 - Structural elements observed in fibres [Prevorsek 1996]

A generalized structural model representing the key characteristics of fibrous materials is shown in Figure 10.1. All fibres consist of a multitude of structural elements. Their arrangements in the fibre super-structure, and their dimensions are well-defined and for man-made fibres do not vary a great deal from fibre to fibre. The microfibrils consist of alternating crystallites and amorphous regions. The axial connection between the crystallites is accomplished by intrafibrillar tie molecules inside each microfibril. The adjacent microfibrils may be interconnected by interfibrillar tie molecules. It is believed that the mechanical properties of fibres are to a large degree controlled by the structure of the microfibrils [Fakirov 1996].

It is generally accepted that fibres contain small but highly ordered crystalline entities embedded in an amorphous matrix. Furthermore, since the molecules are much longer than these "micelles" or crystallites, the individual molecules pass through a number of crystallites, alternating with segments in the amorphous or disordered regions and thus provide integrity to the system. These features were the basis of the fringed-micelle model which was proposed around 1930 [Fakirov 1996, Gupta 2000]. As a natural consequence of this model, the roles played by the two phases were understood more clearly: cohesion, stability, strength and durability were provided by crystals while the non-crystalline regions were mainly responsible for extensibility, recovery, toughness and a path for diffusion.

The fringed-micelle model is today considered unrealistic except for polymers of exceptionally low crystallinity [McCrum *et al*. 1997]. The random arrangement of adjacent crystals in the fringed-micelle model does not accord with evidence obtained from microscopy. Most, if not all, textile and industrial fibres are highly oriented, and they are characterized by a fibrillar microstructure (Figure 10.1).

Consequently, the fringed-fibril structural model was developed to model fibre structure, it is shown in Figure 10.3. Fibrils are clusters of partially aligned molecules. Microfibrils, the most elementary fibrils, consist of alternating layers of ordered (crystalline) and disordered (noncrystalline) regions along the fibril length.

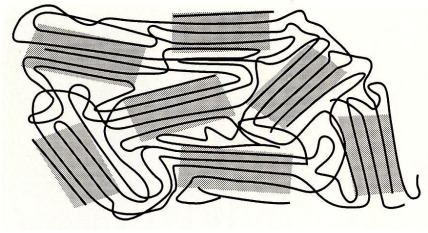

Figure 10.2 - The fringed-micelle model [Warner 1995]

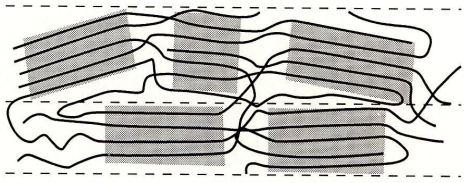

Figure 10.3 – The fringed-fibril model [Warner 1995]

In the late fifties, direct evidence for folded chains in polymer samples was provided [Warner 1995, Gupta 2000]. To accommodate this observation, the fringed-micelle model was modified so that a single molecule, besides passing alternatively through crystalline and amorphous regions in oriented fibre, could also fold back and forth, this is shown in Figure 10.4. Though extended chain crystals have the lowest free energy, the chains prefer to crystallize by folding because in this way crystallization is rapid; thus the considerations are kinetic in nature rather than equilibrium. Consequently, the lamellar crystals with folded chains are not in their most stable state but will tend towards it whenever they have a chance, e.g. on subsequent heating. The presence of folds in fibres results in an interruption of chain continuity along the fibre length. This modified fringed-micelle model is a reasonable model of unoriented semicrystalline polymers [Warner 1995].

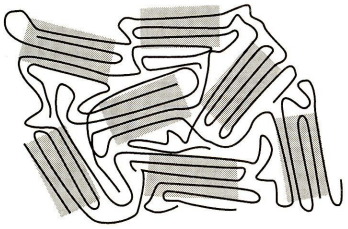

Figure 10.4 – The modified fringed-micelle model [Warner 1995]

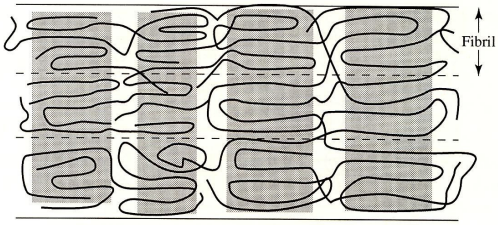

Figure 10.5 – The Peterlin model [Warner 1995]

For the structure of drawn polymers, the Peterlin model was developed [Warner 1995], as is shown in Figure 10.5. In this model, crystals are highly oriented, and material in the noncrystalline regions is also rather highly oriented.

Although semi-crystalline polymer materials are traditionally regarded as two-phase systems, the three-phase fibre structural model is nowadays also an accepted model for semi-crystalline polymers such as poly(ethylene terephtalate), nylon 6, …. The three-phase fibre structural model proposed by Prevorsek [1996] for meltspun fibres consists of microfibrils separated by intermicrofibrillar domains (Figure 10.6). The microfibrils consist of a series of crystalline and amorphous domains that alternate along the microfibril. Further, at least some of the intermicrofibrillar domains are

filled with highly extended molecules parallel to the fibre direction. As such a distinction is made between two types of amorphous domains, those separating the adjacent crystallites in the microfibril and those separating the microfibrils.

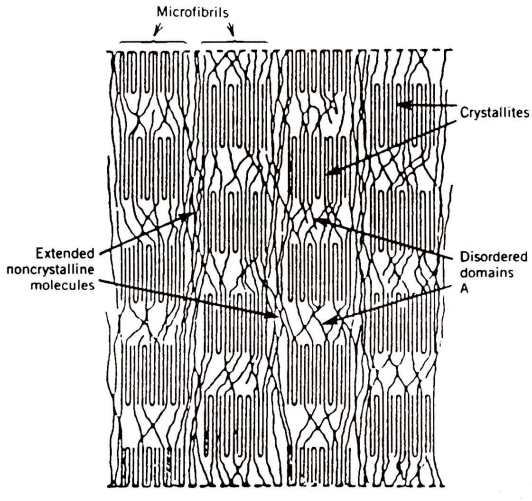

Figure 10.6 – The three-phase model proposed by Prevorsek [1996]

10.2. TERTIARY STRUCTURE OF SILKS

10.2.1. SILKWORM SILKS

10.2.1.1. Bombyx mori

The molecules in the crystalline region of silk are present as fully extended chains. The molecules are quite well oriented along the fibre axis and the degree of crystallinity is quite high though its exact measurement is difficult. However, *B. mori* silk is believed to have a three-phase structure [Tsukada *et al.* 1992]. The highly ordered, crystalline phase contributes for 60% to the fibre structure, 10% is disordered (amorphous) and the remaining part (30%) is an imperfectly ordered, oriented amorphous phase.

Silk II fibres consist of both quasi-crystalline and amorphous domains. The primary structure of *B. mori* silk contains multiple repeats of $(Ala\text{-}Gly\text{-}Ser\text{-}Gly\text{-}Ala\text{-}Gly)_n$ which make up about 55% of the total fibre and form the insoluble quasi-crystalline Cp-fraction after chymotrypsin cleavage. The remaining sequence of fibroin is rich in Tyr and constitutes the amorphous part of the fibre.

The structure of Silk II was characterized first by Marsh *et al.* [1955a] as a regular array of antiparallel β-sheets. Figure 10.7 shows a three-dimensional representation of the β-pleated sheet crystals with chemically distinct faces [Kaplan *et al.* 1994] as proposed for the *B. mori* fibre [Marsh *et al.* 1955a] (more in detail described in Chapter 5). The β-sheet crystals, occupy 40-50% of the total volume of the silk fibre [Iizuka 1965], with the remainder being occupied by protein chains having a much less ordered, possibly amorphous, structure. Iizuka [1965] believes that in the

amorphous or less crystalline regions the glycine-X unit is also present but the fraction of perturbations or completely different sequences containing bulkier residues, is higher.

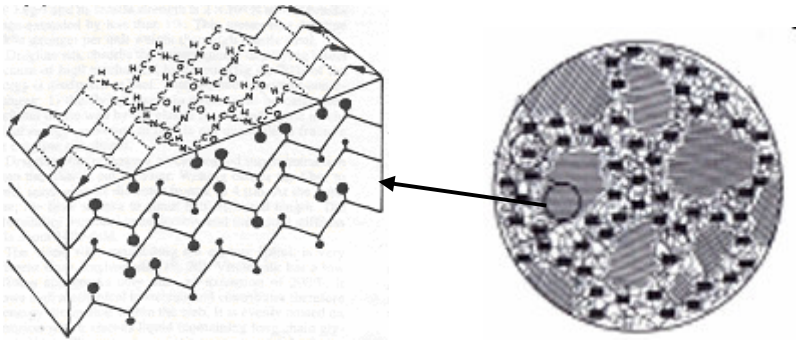

Figure 10.7 - Fibroin structure of the silk of *Bombyx mori* – Right: Crystal of antiparallel β-sheet – Left: Three-phase structure

More recently, Takahashi *et al.* [1999] reported a more detailed X-ray diffraction analysis of *B. mori* silk fibroin. They proposed that two antipolar-antiparallel β-sheet structures are statistically stacked with different relative orientations. Thus, in this model the methyl groups of alanine residues alternately point to both sides of the sheet structure along hydrogen bonding direction, differing from the crystal structure model proposed by Marsh *et al.* [1955a], as represented in Figure 10.8. The two different kinds of intersheet stacking occur at a ratio of 1:2. This was confirmed by Asakura *et al.* [2002a] by means of solid-state NMR.

The polar conformation of sheets in which methyl groups of adjacent strands point to opposite sides of the sheet is also referred to as "out-of-register". The antipolar conformation in which all methyl groups point to the same side of the sheet is also called "in-register".

Zhou *et al.* [2001] suggested that the β-sheets may be parallel, rather than antiparallel. In the polar-parallel assembly (Figure 10.8), all the GAGAGS hexapeptides are at one end of the β-sheet, all the large side chains are clustering together at the other end, and a regular packing is expected.

So, even now there is no consensus with respect to the manner the different β-sheets are packed. Unfortunately, the experiments performed in this work also did not allow providing further information.

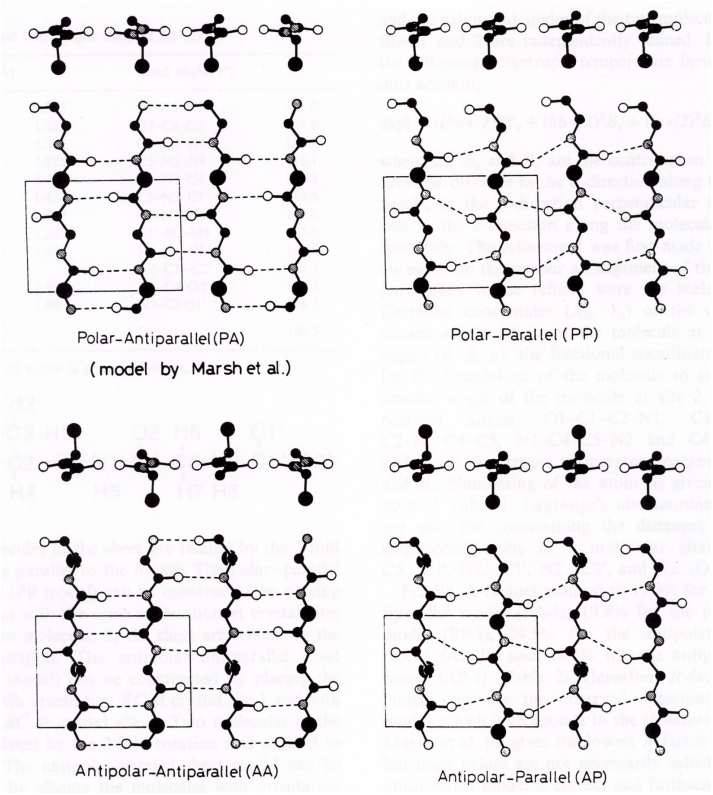

Figure 10.8 - Four models for the sheet structure formed by hydrogen bonds

10.2.2. MAJOR AMPULLATE (DRAGLINE) SILK

10.2.2.1. Introduction

The different attempts to characterize the (hierarchical) molecular order in spider silk have resulted in a number of microstructural models that are similar in concept although differing in detail. These models can be used to explain the various aspects of the mechanical behaviour of spider silk.

10.2.2.2. Two-phase models

Termonia [1994] proposed that spider dragline silk is a semicrystalline material made of amorphous flexible chains reinforced by tiny, virtually undeformable, crystals. These crystals are composed of poly-alanine sequences arranged into β-sheets parallel to the fibre axis. The amorphous part, on the other hand, is composed of chains rich in glycine that are entangled and linked together through hydrogen bonds, as schematically represented in Figure 10.9.

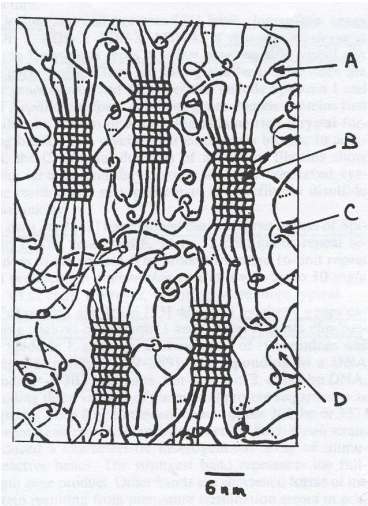

Figure 10.9 - Model as proposed by Termonia (A: amorphous chain; B: β-pleated sheet; C: entanglement; D: hydrogen bonds) [Termonia 1994, Heslot 1998]

Gosline *et al.* [1999] stated that the difference in proline content between *Nephila clavipes* MA silk (± 3%) and *Araneus diadematus* MA silk (±16%) has major consequences for the two MA silks. *N. clavipes* MA silk is apparently made primarily of the proline-free fibroin (Nc-MA-1), and the proposals for the presence of ordered structures in the glycine-rich domains [Simmons *et al.* 1994] are reasonable (see also 10.2.2.3 Three-phase model). *A. diadematus* MA silk contains fibroins with high proline content, and this should prevent the formation of similar ordered structures in the *A. diadematus* silk network. Thus Gosline *et al.* [1999] stated that the simple two-phase (amorphous + crystalline) network model for *A. diadematus* (Figure 10.9) is probably correct for *A. diadematus*, but it probably does not apply to *N. clavipes* MA silk. This difference is also suggested to explain the greater initial modulus, a lower extensibility but the similar strength of *N. clavipes* MA silk compared to the properties of *A. diadematus* MA silk.

Reported repeating sequence motifs [Guerette *et al.* 1996] for fibroins from the spider *A. diadematus* show that the pattern of small crystal-forming blocks alternating with larger "amorphous" blocks is a feature of spider silk fibroins produced in at least three silk glands, the major ampullate (MA) gland, the minor ampullate (MI) gland and the cylindrical (CYL) or tubuliform gland. The proportions of crystal-forming and amorphous sequence elements, imparting different tendencies for the formation of crystals in their silk fibres, are however different. For example, the two fibroins found in *A. diadematus* MA silk have similar proportions to those produced by *N. clavipes*, with crystal-forming elements occupying approximately one-quarter of the repeat block. The *A. diadematus* MI fibroin has a much larger fraction of crystal-forming blocks (68%) and very short amorphous blocks (32%), a pattern that has been documented recently for *N. clavipes* MI silk [Colgin & Lewis 1998]. The high crystal-forming content of MI silk fibroins probably accounts for the fact that spider MI silks are more birefringent

than MA silks and that MI silks do not supercontract when they are immersed in water [Work 1977], properties that reflect a high crystal content.

10.2.2.3. Three-phase model

The most accepted structural model at the moment is that the poly-alanine regions form β-sheets which stack to form crystals in an amorphous glycine-rich matrix [Lewis 1992]. Moreover, there is broad agreement that three phases are present in the solid state of spider major ampullate silk of *N. clavipes*: an amorphous matrix and two types of ordered phase. Studies based on different experimental techniques all show that one of the ordered phases comprises molecules with a high degree of alignment relative to the fibre axis and occupying a crystalline lattice, while the other ordered phase consists of less highly aligned molecules that do not occupy a well-defined lattice. The terms non-periodic lattice (NPL) crystals [Thiel *et al.* 1997], protocrystals [Simmons *et al.* 1996] and oriented amorphous material [Grubb & Jelinski 1997] have been coined to describe the latter structures.

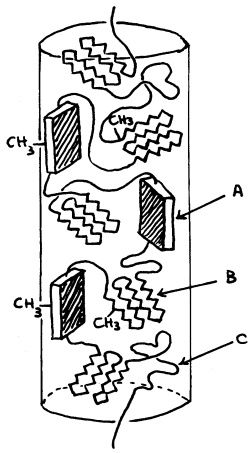

Rectangles A: highly oriented Ala crystals of β-sheets

Canted sheet-like structures B: weakly oriented yet crystalline unaggregated sheets

Curved lines C: Gly-rich matrix

Figure 10.10 - Model as proposed by Simmons *et al.* [1996]

Simmons *et al.* [1996] and Tirrell [1996] concluded from deuterium NMR spectra that the crystalline fraction of dragline silk consists of two types of alanine-rich regions. One population, representing about 40% of the alanine residues, is composed of highly oriented alanine-rich crystals. The other population (60%) consists of poorly oriented and less densely packed 'protocrystals', probably preformed β-sheets. The internal structure of such a fibre may resemble that depicted in Figure 10.10. Moreover, they believe that glutamine and other bulky residues limit the growth of β-sheets and force the formation of loops and tie chains that link crystals to one another and to the surrounding amorphous matrix.

Furthermore, the alanine methyl groups found in the highly oriented domains are preferentially oriented at 90° to the fibre axis, as would be observed for alanine in β-sheets with the chain axis parallel to the fibre axis [Simmons *et al.* 1996].

Simmons *et al.* [1996] stated that the poorly oriented crystallites may be important in effectively coupling the highly oriented crystalline domains and the amorphous regions, thereby producing a biomaterial with exceptional toughness.

The three-phase model shows similarities with the proposed three-phase model for PET, as shown in Figure 10.6. The stress-strain curve of dragline silks (see Chapter 2) shows some similarities with that of PET-yarns: it also shows two maxima in the modulus (slope). Vandenheuvel *et al*. [1993] studied the molecular changes of PET yarns during stretching. The first modulus marks the breakdown of the amorphous entanglement network and the start of molecular uncoiling. Molecular fracture of short taut-tie molecules between crystals causes the modulus to pass through a second maximum.

10.2.3. FLAGELLIFORM (VISCID OR SPIRAL) SILK

Gosline *et al.* [1994, 1995] have tried to model frame (also secreted by the major ampullate glands) and viscid silk from the spider *Araneus diadematus*, as represented in Figure 10.11. Frame silk contains a short chain network (15-20 amino acid residues) cross-linked by β-sheet crystals. Flagelliform or viscid silk appears to have fewer cross-linking crystals and longer chains (on the average, 40 amino acid residues). He showed that the amorphous regions can behave as rubber networks and exhibit rubber-like or entropy elasticity.

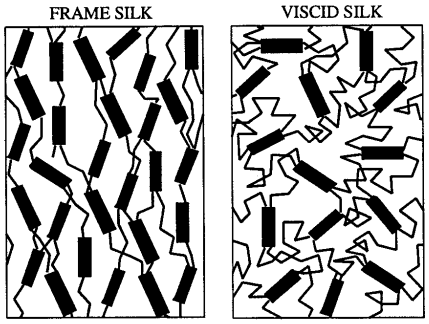

Figure 10.11 - Models for frame and viscid silks [Gosline *et al.* 1994]

The flagelliform silk contains only three motifs repeated many times in the same order. The largest of the protein's three motifs, $(Gly\text{-}Pro\text{-}Gly\text{-}Gly\text{-}X)_n$, may form a β-spiral or helix composed of a large number of β-turns arranged end-to-end, as observed in elastin [Urry 1984]. These can then act as springs, which are bond together by hydrogen bonding at the X-residues to form a highly elastic network [Hayashi *et al.* 1999, Vollrath & Knight 2001]. This particular model for the β-spiral formed by the GPGGSGPGGY segment of flagelliform silk is shown in Figure 10.12.

Interestingly, it has been determined that flagelliform silk has at least 43 continuous motifs in the spiral, whilst ampullate silk consists of 9 uninterrupted motifs. A correlation between extensibility and the number of sequential motifs has been suggested [Gosline *et al*. 1994].

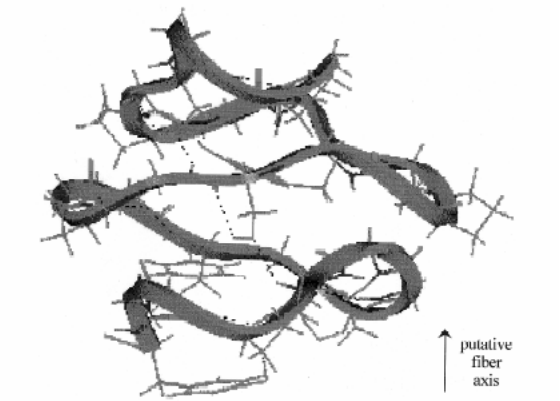

Figure 10.12 - Proposed structure for flagelliform [Hayashi *et al.* 1999]

10.2.4. MINOR AMPULLATE SILK (*NEPHILA CLAVIPES*)

Few structural analyses have been performed on minor ampullate silk primarily due to the lack of sequence information. The only secondary structure, detected by FT-IR analysis and fibre X-ray diffraction, is β-sheet oriented parallel to the fibre axis [Dong *et al.* 1991, Parkhe *et al.* 1997, Liivak *et al.* 1997].

Based on deduced amino acid sequence [Colgin & Lewis 1998] and biophysical data [Parkhe *et al.* 1997], a working model for minor ampullate spider silk has been developed. Multiple β-strands form sheets that are stacked to form the crystalline regions similar to those described for *Bombyx mori* fibroin and dragline silk. These sheets involve both inter- and intra-molecular interactions. Each repeat unit has two domains of about 15 residues that participate in β-sheets. Each β-strand domain is separated by a GGX domain. Repetitive regions, each composed of about 20 β-sheet forming domains, are flanked by 137 amino acid spacer regions. Spacers may serve as a matrix for embedding the crystalline regions.

Based on the examination of the β-sheet side chain spacing of known sequences measured by X-ray diffraction, Colgin & Lewis [1998] concluded that neither spacer regions nor GGX (X=Y, Q or R) domains participate in β-sheets because the side chain spacing eliminates the inclusion of larger residues in the sheets. Although the minor ampullate silk proteins have short alanine regions, the flanking glycine-alanine stretches also likely form β-sheets. The GAGA domains are similar to silkworm fibroin crystalline regions. Based on diffraction data and extrapolation of NMR data from *B. mori* and major ampullate silk, the $(GA)_y(A)_z$ domains of minor ampullate silk primarily form β-sheets that comprise the crystalline regions of the fibre. Structures of the spacer regions and GGX domains have not been determined because the only detected overall structure has been β-sheet.

10.2.5. EGG SAC SILK

Guerette *et al*. [1996] believed that the dominantly repeated crystallisable motifs in *Araneus diadematus* egg sac silk (Figure 10.13) are $(\text{-A-})_m$ ($m \leq 8$) and $(\text{-Gly-Gly-X})_n$ ($n \leq 4$; X = Ala, Leu, Gln or Tyr). These are similar to the motifs that form β-sheet crystals in major ampullate (MA) silk spun by *Nephila clavipes* spiders [Thiel *et al.* 1997, Xu & Lewis 1990, Hinman & Lewis 1992], however the values of m and n for *A. diadematus* are somewhat smaller than the corresponding values for *N. clavipes* MA silk.

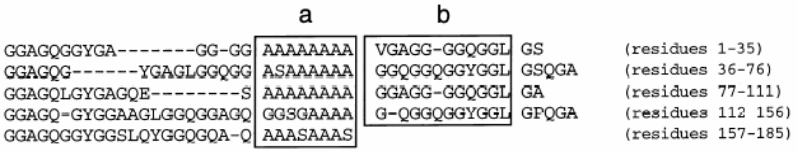

Figure 10.13 - Amino acid sequence of *A. diadematus* [Guerette *et al.* 1996] egg sac silk, aligned to highlight the dominantly repeated crystallisable motifs: (a) $(\text{-Ala-})_m$; (b) $(\text{-Gly-Gly-X-})_n$ [Barghout *et al.* 1999]

Since the amino acid composition of egg sac spider silk is known to consist of a high percentage of serine, the motifs found by Guerette *et al.* [1996] are doubtful to be the only motifs. Recently, Tian & Lewis [2006] found new amino acid motifs such as $(\text{Ser})_n$, $(\text{Ser-Ala})_n$, $(\text{Ser-Gln})_n$, and Gly-X (X represents Gln, Asn, Ile, Leu, Ala, Val, Tyr, Phe, Asp). However, the structure of these motifs is unknown.

X-Ray diffraction studies [Parkhe *et al.* 1997] on major ampullate, minor ampullate and egg sac spider silk revealed that in contrast to the other spider silks, egg sac β-sheets show no clear orientation.

Furthermore, the structure has been modelled as twisted β-sheet (NPL) crystals based on the results from transmission electron microscopy [Barghout *et al.* 1999]. Polypeptide chains with a β-strand conformation can exhibit a spontaneous right-handed twist (see Figure 5.7 in Chapter 5). In turn, this means that individual β-pleated sheets as well as β-sheet crystals built from these strands also exhibit a right-hand twist. A crystal with such a twisted morphology is shown schematically in Figure 10.14. This twist, parallel to the chain direction, has not been observed in (*N. clavipes*) dragline, a structurally superior silk, suggesting a correlation with decreased silk strength and stiffness. It is known that the initial lengthening of the fibre is the result of the degree to which polymers can be moved into alignment with the axis of deformation [Hatch 1993]. However, in the initial region the amorphous regions, or the flexible chains between crystalline domains, will be firstly affected, so it is doubtful that the β-sheets situated in the crystalline regions will be straightened in this initial region and thus would result in a lower modulus and thus stiffness. Furthermore, there are so many factors determining fibre strength such as the number of crystals, the size of the crystals, the number of inter- and intra-molecular bonds so that it is doubtful that the twist of the β-sheet crystals plays a large role in it.

Moreover, the tensile experiments described in Chapter 2 revealed that the stiffness or initial modulus of egg sac spider silk is higher than that of dragline silk for the *A. diadematus* spider.

Barghout *et al.* [2001] further found that transverse sections of *A. diadematus* spider egg sac silk fibres exhibit significant microstructural anisotropy. This anisotropy is not observed in transverse sections of MA silk produced by the same species of spider.

Figure 10.15 helps to explain what is meant by multistructural anisotropy. It shows the significant directions of a randomly-chosen β-sheet crystal within an egg sac silk fibre. Z is parallel to the fibre axis. X is an arbitrary but consistently chosen direction lying in the transverse section of the fibre. X_H is the projection of the hydrogen bond direction onto the transverse section. The angle α between X_H and X is defined within the transverse section; the angle β defines the tilt of the chain direction relative to Z. Neighbouring crystals would be characterized by values of α and β similar to those exhibited by the example shown. Crystals further away would still exhibit similar values of α, but their values of β would vary more widely.

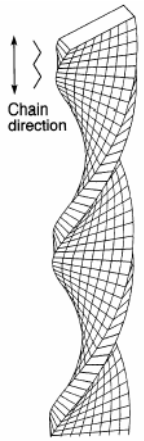

Figure 10.14 - Schematic illustration of twisted β-sheet crystal morphology [Barghout *et al.* 1999]

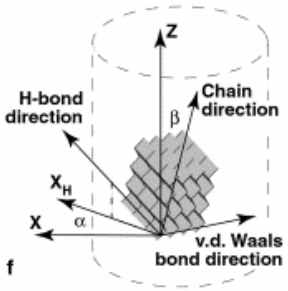

Figure 10.15 - Multistructural anisotropy of egg sac silk [Barghout *et al.* 2001]

Egg sac silk is used to construct a tangled mat of material that surrounds and protects the eggs. At any point along its length, the egg sac fibre must be able to bend easily in one plane but otherwise resist bending and stretching; a multiaxially anisotropic microstructure can impart these mechanical properties. In the contrary, the principal role of MA spider silk is to carry tensile loads, in which case there is no need for transverse anisotropy.

10.3. QUATERNARY STRUCTURE OF SILKS

10.3.1. SILKWORM SILKS

10.3.1.1. *Bombyx mori* silk

The silk spun by *Bombyx mori* is the product of three genes. The first identified silk gene encodes for a very large, insoluble protein designated as the heavy chain fibroin (called Fhc or H-chain, 200-500 kDa). Two additional genes, the light chain fibroin (L-chain) (25 kDa designated as Fl) and the P25 glycoprotein (about 30 kDa), encode two subunits of the *B. mori* fibre. The heavy and light chains are linked by a disulfide bond, as represented in Figure 10.16 [Mita *et al.* 1994, Zhou *et al.* 2000, Inoue *et al*. 2000], and P25 associates with these chains by noncovalent interactions, mainly by hydrophobic interactions with the H-chain [Inoue *et al.* 2000]. The carboxy terminus of *B. mori* contains three Cys residues. The two residues closest to the end are engaged in an intramolecular disulphide bond, while the third Cys is used to link the end of the protein to the L-fibroin through a disulphide bridge [Tanaka *et al.* 1999, Tanaka & Mizuno 2001, Bini *et al*. 2004]. These Cys residues may play a role in linking H- and L-fibroin molecules, which together with two differentially glycosylated P25 components, are thought to form a quaternary complex [Bini *et al.* 2004]. This complex may represent the soluble mesogenic units thought to be present in the stored silk dope. The highly hydrophilic nature of the L-fibroin may help to make the quaternary complex soluble and mesogenic. Homologues of L-fibroin and P25 are not found in *Antheraea* [Tanaka & Mizuno 2001], suggesting that the quaternary complex is not essential for spinning.

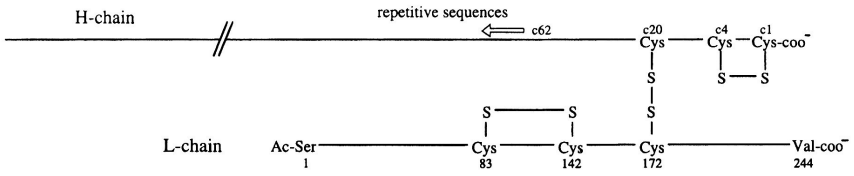

Figure 10.16 - Inter- and intermolecular disulfide bonds in the fibroin H-L complex of *B. mori*

The molar ratios of the heavy chain, light chain, and P25 are 6:6:1, both in cocoons and in fibroin secreted into the lumen of posterior silk gland [Inoue *et al.* 2000].

From the amino acid sequence [Yamaguchi *et al.* 1989], the L-chain cannot be considered to be associated with the crystalline region of silk. The rather regular part of the H-chain, Cp fraction, which is obtained by chymotrypsin treatment of the fibroin solution, is considered to be associated with the crystalline region [Warwicker 1954].

The GX-rich regions in the H-chain form 12 crystalline domains, distributed into about six subdomains beginning with a stretch of GAGAGS hexapeptides and usually ending with a GAAS sequence [Zhou *et al*. 2001]. In total, the heavy chain comprises some 64 subdomains. Zhou *et al*. [2001] suggested that each subdomain form a β-strand (about 66 residues long), connected by a 4-residue β-turn at the GAAS boundary tetrapeptide. These β-strands are much longer than in globular

proteins, where they rarely exceed 15 residues. A crystalline domain will then comprise either one β-sheet or two β-sheets packing on top of each other. Each one of these domains could constitute a structural unit made of two layers of three-stranded β-sheets. A thicker and broader structure can then be created by packing domains side by side and layer by layer both within and between fibroin chains.

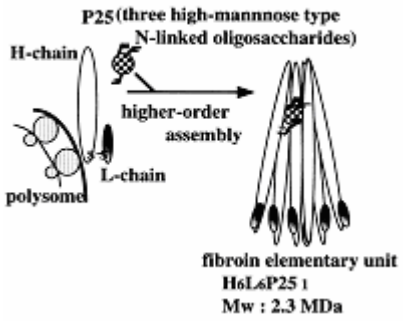

Figure 10.17 - A model showing the assembly of the elementary unit of fibroin [Inoue *et al.* 2000]

The P25 component is a glycoprotein containing Asn-linked oligosaccharide chains [Bini *et al.* 2004]. The P25 appears to be the only N-glycosylated protein in the silk complex composed of H-fibroin, L-fibroin and P25 [Inoue *et al.* 2000]. Glycosylation of the P25 may contribute to the solubility, amphiphilicity and assembly of the complex. P25 seems to form a compact structure containing possibly four intramolecular disulfide bonds [Inoue *et al.* 2000].

Based on biochemical analysis, Inoue *et al*. [2000] presented a full model, shown in Figure 10.17, in which a single molecule of P25 with its three N-linked oligosaccharide chains associates with six sets of the disulfide-linked H-L heterodimer by noncovalent interactions. The H-L dimers and N-glycosylated P25 assemble into $H_6L_6P25_1$ complex through hydrophobic interactions between P25 and H-chains and by hydrogen bonding between N-linked oligosaccharide chains of P25 and H-chains. A single molecule of P25 is located internally and plays an important role in maintaining integrity of the complex.

B. mori also produces sericin, a protein glue that ensures that the fibroin cocoon threads adhere to one another. Five sericin genes have been cloned and partially sequenced [Grzelak 1995]. The sericin fraction (25%) contains 37% serine, 17% glycine and 16% aspartate [Garel 1982].

10.3.1.2. *Antheraea pernyi* or Tussah silk

In contrast to *Bombyx mori*, homologues of L-fibroin and P25 are not found for *Antheraea* [Tanaka & Mizuno 2001]. The three Cys residues present in *Antheraea* species occupy different positions than in *B. mori*. This difference may correlate with the apparent absence of L-fibroin in this genus [Bini *et al.* 2004].

10.3.2. SPIDER SILKS

Bini *et al*. [2004] showed that silk proteins consist of conspicuously hydrophilic terminal domains flanking a very long central portion constructed from hydrophobic blocks separated by hydrophilic ones. The hydrophobic blocks dominate the protein and form intermolecular β-sheets. There is currently a gap in understanding how the distribution of hydrophilic and hydrophobic blocks and other features of the primary sequence of silk proteins determine secondary, tertiary and quaternary structure of the protein [Bini *et al.* 2004]. Some preliminary studies [Jin & Kaplan 2003] indicate how in heavy chain fibroin a conspicuously hydrophilic terminal peptide and a large central predominantly hydrophobic region might help to initiate micelle formation. The alternation of hydrophilic and hydrophobic blocks in silk proteins has been suggested to form lamellar liquid crystal phases [Knight & Vollrath 2002] by phase separation of the hydrophobic from the hydrophilic blocks as in certain synthetic main chain liquid crystal polymers.

Lombardi & Kaplan [1990] noted that disulfide bridges do not appear to play a role in maintaining the structural integrity of silk for two reasons: (1) the overall absence of cysteine (< 0.50%) in the amino acid analysis, and (2) the insolubility of the silk in mercaptoethanol. *Methionine* also appears to have little influence on the secondary structure, since the total amount of this amino acid (< 0.50%) is too small and methionine is not implicated in cross-linking in any characterized protein. Thus, bonds between molecules are secondary bonds, specifically the rather strong ionic and hydrogen bonds. Undoubtedly, the inter- and intra-molecular bonding is somehow responsible for the high performance of the fibre. However, based on a quantitative cysteine analysis of the MA gland protein, Mello *et al.* [1994] found a cysteine content of 0.36% and thus suggested that the two peptide chains available in *N. clavipes* MA silk are held together by 3-5 disulphide bonds.

10.4. MORPHOLOGY OF SILKS

10.4.1. INTRODUCTION

As opposed to the term “structure” which refers to fine structure at the smallest level and includes parameters like intermolecular distances, interplanar distances, molecular orientation, etc., the term “morphology“ refers to the relatively larger entities forming the coarser structure and includes features like crystallite size, arrangement of crystalline and amorphous regions, fibrillar entities, etc.

The common morphological entity in all textile fibres, both natural and manufactured, is the fibril, which is an assembly of molecules. The molecules generally aggregate in the form of a periodic structure of alternating ordered crystalline lamellar blocks and disordered non-crystalline regions stacked vertically in long narrow columns along the fibre length (Figure 10.2).

10.4.2. SILKWORM SILKS

Scanning electron microscopy (SEM) has revealed that the macrostructure of silk fibres are characterized by long, thin, parallel (ribbon-like) microfibrils [Marsh *et al.* 1955a]. More recently, bundles of nanofibrils, helical features and a layered structure with fibrils on different layers at a cross angle were observed for different silkworm silks (*Bombyx mori, Antheraea pernyi, Antheraea yamamai, Attacus Atlas*) [Putthanarat *et al.* 2000, Poza *et al*. 2002].

Yang *et al*. [2005] looked at the fracture surfaces of a *Nephila edulis* silk and *B. mori* silkworm silk broken at very low temperatures. Unlike most other polymeric materials, the fracture of spider MA silk is ductile and therefore tough rather than brittle, even at liquid-nitrogen temperatures. In contrast, silkworm silk gave a very coarse transverse break in liquid nitrogen, clearly revealing its microfibril structure. The latter may indicate a weaker bonding of nanofibrils to the inter-nanofibrillary matrix in *B. mori* compared to spider MA silk.

According to Höhnel [Huber 1947] the fibrils in wild silk are only 0.3 to 1.5 μm in diameter; they run parallel to each other through the fibre and are rather more dense in the outer portion of the fibre than in the inner part. To his opinion there is really no difference in kind between the structure of wild silk and that of the cultivated silk; that is to say, the fibroin fibre of the latter is also composed of structural fibrils but they fuse into one another in a more homogeneous manner on emerging from the silk glands, thus rendering it more difficult to recognize them.

10.4.3. SPIDER SILKS

10.4.3.1. Major ampullate silk

The fibrillar structure of dragline silk had been proved by means of scanning electron microscopy (SEM) [Mahoney *et al*. 1994], transmission electron microscope (TEM) [Thiel *et al.* 1994, 1997] and atomic force microscopy (AFM) images [Mahoney *et al*. 1994, Li *et al.* 1994, Gould *et al*. 1999, Pan *et al.* 2004], Raman spectroscopy [Pan *et al.* 2004, Yeh & Young 1999, Shao & Vollrath 1999, Sirichaisit *et al.*1999], and X-Ray diffraction [Grubb & Jelinski 1997, Riekel *et al.* 1999]. These microfibrillar structures are believed to evenly distribute any applied stress.

A group at the University of Washington [Thiel *et al.* 1994, 1997] has characterized individual crystallites within the amorphous matrix for MA silk by means of TEM. They are irregularly shaped, approximately 70-100 nm in diameter, and uniformly distributed through the matrix. Other authors [Grubb & Jelinski 1997, Riekel *et al.* 1999] found that the domains organise into microcrystals with much smaller sizes of at least 2 × 5 × 7 nm. Pan *et al.* [2004] used AFM to determine average fibril diameters of dragline silk (*Araneus Ventricosus*) and found values of 100-400 nm depending on the spinning speed and method the silk was obtained.

A group at Dupont de Nemours [Li *et al.* 1994] has observed a highly organized skin-core structure for the dragline silk fibre of *Nephila clavipes* with AFM. The core consists of pleated fibril-like structures, which are arranged in two concentric cylinders. This basic structure is later confirmed by other authors [Vollrath *et al.*

1996, Frische *et al.* 1998]. Vollrath *et al.* [1996] further propose that the tube or skin seems to consist of twisted bands of microfibrils and is covered by an outer waterproof coating. Also an inner membrane between skin and core would be present [Vollrath *et al.* 1996], as presented in Figure 10.18.

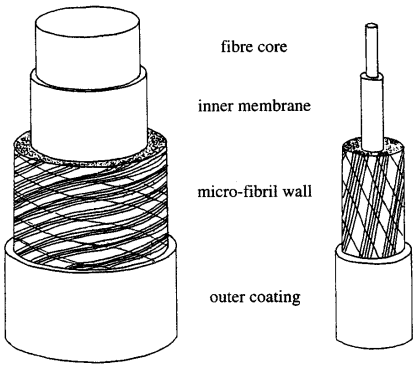

Figure 10.18 - Skin-core model as proposed by Vollrath *et al.* [1996]

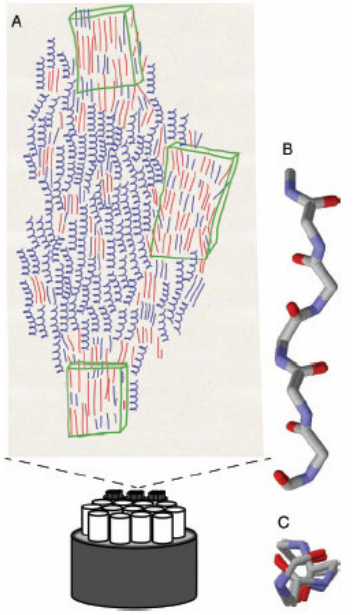

Figure 10.19 - Model as proposed by van Beek *et al.* [2002] with β-sheet regions interconnected with predominantly 3_1 helical parts

Van Beek *et al.* [2002] postulated a model, based on 2-D solid state NMR, consisting of a skin–core organisation, with a multitude of fibrillar substructures and covered by a hard skin, forming the fibre. The molecular structure (see Figure 10.19) consists of β-sheet regions, containing alanine and glycine, interleaved with predominantly 3_1-helical parts (curls), which do not contain alanine. All chains tend to be parallel. The crystallites are irregular and strongly depend on processing.

Depending on the method, larger or smaller ordered domains can be identified as crystalline (boxes). B and C are side and top projections of a repetitive model peptide to show the approximate 3-fold symmetry (3_1 helical parts). This model is confirmed by other authors [Putthanarat *et al.* 2000, Augsten *et al.* 2000]. Peptide chains of the Nc-MA-1 and Nc-MA-2 proteins are highly oriented along the fibre direction, possibly induced by the elongational flow inside the duct during spinning. The majority of the alanine residues is incorporated in regular β-sheet structures, which predominantly form microcrystalline domains, which include glycine residues, tentatively assigned to be the GGX regions. The remaining glycine-rich parts were found to predominantly have preserved a well-defined 3_1-helical secondary structure.

10.4.3.2. Egg sac silk

Fibrils randomly distributed in a matrix within the fibre are suggested in the egg case of *Argiope aurantia* [Li *et al.* 1994].

The cylindrical gland silk fibres of *Pugettia producta* seem to exhibit, at least occasionally, longitudinally bands along the fibre axis, whereas those of *Uloborus walckenaerius* show spheres in a matrix [Li *et al.* 1994].

X-ray diffraction experiments were performed on an *Argiope keyserlingi* egg sac and clear structural differences were observed within the egg sac [Riekel *et al*. 2003]. The inner part of the egg sac is made of *Bombyx mori*-type poly(alanylglycine) silk, while the outer part is composed of MA-type poly(alanine) silk. It is not known, however, whether the cylindrical glands produce both types of silks. Probably, the mechanical properties of egg sac silks may be optimized to maximize stiffness and stretch resulting in a protective shield for the eggs [Riekel *et al.* 2003].

10.4.4. EXPERIMENTS FOR EGG SAC SPIDER SILK

10.4.4.1. Materials and methods

The morphology of fibres is often determined by means of a fractographic analysis. A Scanning Electron Microscope (JEOL JSM-5600 LV, SEM) was used to make pictures of the fracture surfaces of egg sac spider silk fibres broken on the tensile tester (FAVIMAT) at different speeds. The samples were mounted on stubs and coated with gold (JEOL JFC –1200 Fine coater, 8 nm).

10.4.4.2. Results and discussion

Figure 10.20, Figure 10.21 and Figure 10.22 show some SEM pictures of fibres broken at resp. 1 mm/min, 20 mm/min and 100 mm/min.

It is confirmed that the egg sac silk fibres have a circular cross-section. Also longitudinal bands along the fibre axis are seen, as also observed by Li *et al.* [1994] for other cylindrical gland silk fibres.

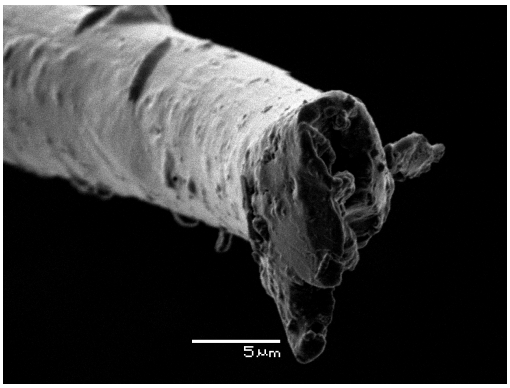

Figure 10.20 – SEM photo of fracture surface (broken at 1 mm/min)

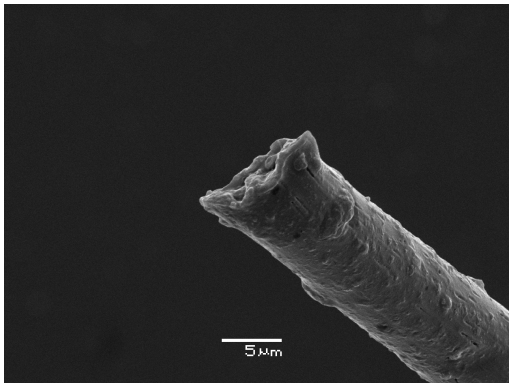

Figure 10.21 - SEM photo of fracture surface (broken at 20 mm/min)

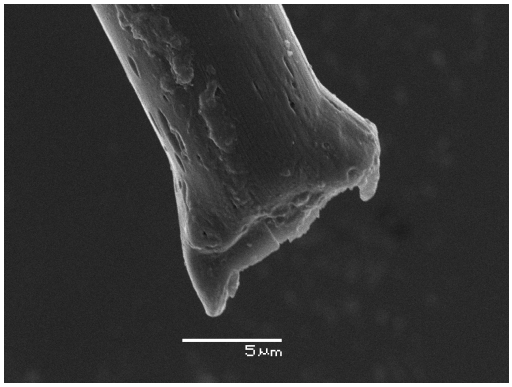

Figure 10.22 - SEM photo of fracture surface (broken at 100 mm/min)

Different photos reveal that egg sac spider silk shows a skin-core structure, as also observed for MA silk [Li *et al*. 1994, Vollrath *et al.* 1996, Frische *et al*. 1998, van Beek *et al.* 2002, Poza *et al*. 2002] and *B. mori* silk [Marsch *et al*. 1955a, Putthanarat *et al*. 2000, Poza *et al*. 2002, Yang *et al*. 2005]. Moreover, the skin shows a more plastic behaviour than the core. This structure is in accordance with

the microstructural anisotropy in a cross-section that is observed by Barghout *et al.* [2001].

Even at low testing speed (Figure 10.20), although some bulk material is protruding the fracture surface, no circular fibrils are visible and thus no fibrillar structure is proposed as observed for *B. mori* or dragline spider silk. At higher speeds, the fracture becomes more brittle, resulting in a featureless fracture surface, although again the skin is a little more plastically deformed than the core.

The plastic deformation of the skin can be the result of the higher shear forces at the surface when the threads are secreted by the spinning glands.

10.5. STRUCTURAL BASIS FOR MECHANICAL PROPERTIES

10.5.1. INTRODUCTION

The ability of a fibre to withstand and recover from mechanical forces is largely determined by its fine structure: degree of orientation, crystallinity, molecular weight, bonding between polymers, chain continuity, etc. In the case of natural fibres, aspects of their macroscopic and microscopic structure also play a significant role [Hatch 1993, Gupta 2000].

Guerette *et al.* [1996] have identified silks as follows: "Silks are macromolecular composites of amorphous protein domains that are cross-linked and reinforced by β-sheet microcrystals; the degree of crystalline cross-linking and reinforcement largely determines functionally important mechanical properties. Factors that influence the formation and size of the crystals include the primary and secondary structure of the proteins, control of the genes that encode these proteins, and the chemical and mechanical processing of the proteins during spinning."

Most structural models indicate that silks are semicrystalline proteins, with substantial portions of their polypeptide chains forming crystallites of stacked β-pleated sheets, explaining the exceptional strength of dragline spider silk [Simmons *et al.* 1994, Hayashi *et al.* 1999, Jelinski *et al.* 1999]. However, the extensibility of silk is attributed to the non-crystalline or 'amorphous' (on X-ray diffraction) regions [Simmons *et al.* 1996]. The mechanical properties and macromolecular conformations of these amorphous regions have been the subject of much speculation, but little direct experimentation.

10.5.2. FACTORS DETERMING TENSILE PROPERTIES

10.5.2.1. Molecular weight

For most fibre-forming polymers, fibre formation becomes possible at a molecular weight of about 5,000 g/mol and at values of 10,000 g/mol commercial fibres can be made [Gupta 2000]. Both silkworm and spider silks all have very high molecular weights ranging from 100,000 to 200,000 g/mol for silkworm silks [Cook 1984] to 200,000 to 300,000 g/mol [Foelix 1996] for MA spider silk (*Nephila*). The large

molecule explains partly the high fracture resistance since it is more difficult to separate chain segments from their neighbours. Furthermore, at high strains the cumulative bonding forces contribute to strength enhancement.

The long chain contributes to a finite extensibility of 5-10% on application of load and recovery on release of the load. The extension results from bond deformation and hindered rotation around the single covalent bonds in those regions of the fibres which are not highly ordered [Gupta 2000].

10.5.2.2. Molecular orientation and crystallinity

Higher orientation means greater resistance to deformation, greater breaking load and tensile stiffness and relatively lower extension to break compared to that for the unoriented or less oriented fibre [Gupta 2000]. The role of molecular orientation of the long polymer chains in enhancing intermolecular cohesion is of paramount importance in textile fibres. As is previously found and described in the structural models (see 10.1), the fibre system is not just a mixture of crystalline and amorphous components, mechanically connected together in a very special way [Treloar 1970]. It is obvious that longer chains would thread through more crystallites compared with shorter chains and would also be more entangled in the amorphous regions; both these factors would contribute to enhancement of some mechanical properties.

Molecular orientation may not always result in crystallization but in an enhancement of order when the various types of bonds such as hydrogen bonds and other weak interatomic forces can contribute to a property enhancement. Individually each bond may be quite weak but if many weak bonds connect a single long chain to its neighbours, then the total force holding the chain in place will be high.

Bombyx mori silk, with its extremely long crystal sequences and high crystallinity, does not match MA spider silk for stiffness, strength or extensibility, and also the highly crystalline MI silk is not stronger than MA silk. As a consequence, it seems that crystallinity is not the only important feature of network design in spider MA silks [Gosline *et al.* 1999]. Amorphous chains that allow deformation and viscoelastic energy dissipation are equally important features of MA silk designs.

X-ray studies have evidenced that the silk crystals or micelles of *B. mori* silk are extended to the maximum possible in the normal state; so when the fibres are stretched, extension can take place for the most part only by means of internal slipping, i.o.w. the micelles slip over one another [Huber 1947]. This structural feature restricts the possible extension in *B. mori* silk.

10.5.2.3. Chemical structure

10.5.2.3.1. Introduction

The fact that only a few polymers have succeeded as commodity fibres is indicative of the severe demands made on them both from processability (for manufactured fibres) and properties point of view, which includes an interplay of an optimum molecular weight with adequate intermolecular forces and the capacity for

orientational reinforcement of the structure through molecular alignment [Gupta 2000]. In cases where intermolecular forces are weak, a stiff backbone containing a rigid unit (such as having a ring structure) and the capacity to orient will be assets.

In natural fibres, such as silk, the intermolecular forces are quite intense. As a consequence, for these fibres the glass transition temperature (Tg) and melting temperature (Tm) are often above its decomposition temperature.

In proteins, the functional properties are known to be determined highly by its primary and secondary structure.

10.5.2.3.2. Primary structure

Silks are consisting of proteins and it is well known that the properties of proteins depend primarily on the summation of the properties of the active groups present, together with the properties due to the large size of the molecule [Howitt 1953].

Dragline silks spun by three species of *Nephila* and two species of *Argiope* have similar amino acid compositions [Gatesy *et al.* 2001], suggesting that differences in the mechanical properties of the proteins are due to the structural configuration of the molecules [Kishore *et al.* 2002]. Hayashi *et al.* [1999] proposed that the tremendous diversity of spider silks has evolved through the modification and rearrangement of a few amino acid motifs. This shuffling of protein modules directly corresponds to the array of mechanical properties exhibited by these silks.

In Chapter 5, we mentioned that the primary structure of silk proteins often consists of an alternation of hydrophobic and hydrophilic blocks in the central or core region. The function of this alternation has been suggested to help to produce a lamellar phase-separated structure within the prespun silk molecules similar to that seen in amphiphilic block co-polymers [Craig & Riekel 2002] and this in turn gives rise to a lamellar liquid crystal elastomeric structure in the final silk [Knight & Vollrath 2002]. The variation in lengths of both the hydrophobic and hydrophilic blocks seen in most silk proteins may prevent the formation of large and perfect crystals, which would make silk too stiff and brittle [Bini *et al.* 2004]. Variation in the block lengths would also serve to vary the extension of the polypeptide backbone from block to block in the nanofibril with further implications for the mechanical properties.

The predominately hydrophobic nature of the silk proteins is essential to exclude water and thus produces the high packing density and β-crystallinity required for mechanical function [Bini *et al.* 2004]. It is also important to resist swelling and dissolution to enable silks to function in wet or humid environments. In addition, the hydrophilic domains may assist in the plasticisation by water important in the function of spider silks.

Fedic *et al.* [2003] tried to find a correlation between fibroin amino acid sequence and physical silk properties of different moths: wax moth (*Galleria mellonella*), European flour moth (*Ephestia kuehniella*), and Indian meal moth (*Plodia interpunctuella*). Despite different repeat structure, the silks of *G. mellonella* and *E. kuehniella* exhibit similar tensile strength as the *Bombyx* and *Antheraea* silks. The silk of *G. mellonella* was considerably more extensible and somewhat stronger than

the silks of *B. mori* and *A. pernyi*. The H-fibroins of moths show a high proportion of large amino acids. They concluded that silk strength in moths is correlated with the regularity of H-fibroin repeats.

10.5.2.3.3. Secondary structure

Major ampullate silk

Parkhe *et al.* [1997] stated that the local regions of crystalline β-sheets are playing a key role in the tensile strength of the fibres as the large number of hydrogen bonds, combined with the hydrophobic forces due to the absence of water in these regions, provides a large force preventing the silk molecules from separating.

Kümmerlen *et al.* [1996] speculated that the extremely strong mechanical properties of silk may be related to the presence of the 3_1 helical structures because they are able to form interhelix hydrogen bonds cross-linking the helices. The existence of 3_1 helices [Kümmerlen *et al.* 1996, Dong *et al.* 1991] in the GGX repeats are believed to serve as a transition or link between crystalline β-sheet regions and less rigid protein structures. Also, neighbouring GGX helices may interact to maintain alignment among adjacent protein molecules in the fibre.

Flagelliform gland silk

Looking at the sequence information for a fibroin from the flagelliform gland (Figure 5.12 in Chapter 5) [Hayashi & Lewis 1998], no obvious crystal-forming domains like present in the other silks can be found. Gosline *et al.* [1999] proposed that its exceptional strength should be explained by the available cross-linking in the glycine-rich amorphous domains.

Different authors [Hinman & Lewis 1992, Hayashi & Lewis 1998] believe that Nc-MA-2 and flagelliform silk are composed of β-turn structures in the proline-rich regions GPGXX alternating with β-sheet regions formed by the poly-alanine segments. Under tension, the linked β-turns may form a β-turn spiral or extend an already present spiral, as β-turns are known to possess a degree of structural flexibility. This would be similar to an elastic mechanism proposed for elastin, β-turn spirals acting as springs. The β-spiral spring could easily serve as the elastic mechanism of the fibre. The proline residue would be the focal point for the retraction energy after stretching. By forcing the proline bonds to torque in response to extension, a large force can be generated for retraction [Hayashi *et al.* 1999]. The second feature of the proposed model by Hayashi *et al.* [1999] is the positioning of the hydroxyls in serine (Ser) and tyrosine (Tyr) for hydrogen bonding with downstream glycine residues. The long Tyr side chains will stabilise the tight β-turns and the shorter Ser side chains stabilise the layers of coils. The importance of these bonds is supported by the strong tendency for Tyr and Ser residues to regularly alternate in flagelliform silk [Hayashi & Lewis 1998]. As further support of the GPGXX motif providing the elasticity mechanism, there is a correspondence between the number of tandemly arrayed GPGXX repeats and the different extensibilities of the two silks. Major ampullate silk with up to 35% extension has

at most nine β-turns in a row before interruption by another motif [Colgin & Lewis 1998]. Flagelliform silk with 200% extensibility has at least 43 contiguously linked β-turns in its spring-like spirals [Hayashi & Lewis 1998].

Minor ampullate spider silk

Liivak *et al.* [1997] compared the structure and mechanical properties of major and minor ampullate silk of *Nephila clavipes*. They speculated that the lower stress and modulus correlate with the appearance of populations of alanines that are not all in β-sheet conformations. Secondly, the existence of conformations other than pure β-sheet conformation could increase the maximum strain of the silk.

Minor ampullate silk displays a higher maximum strain than that of major ampullate gland silk. This strain is not reversible and thus represents deformation, not elasticity. The irreversible extension of the spacer regions in minor ampullate gland silk is also suggested to contribute to its strain properties [Colgin & Lewis 1998, Liivak *et al.* 1997].

Colgin & Lewis [1998] stated that the large number of β-sheets formed by the interaction of many Nc-MI-proteins may account for the relatively high tensile strength of the minor ampullate silk fibre.

10.5.2.3.4. Packing density

Silkworm fibroin, minor and major ampullate silks all have similar types of crystalline β-sheets and all have tensile strengths of the same order of magnitude. Colgin & Lewis [1998] suggested that these high tensile strengths can be attributed to the additive effect of large numbers of hydrogen bonds formed by stacked stacks of β-sheets. The additional hydrophobic interactions of the alanine residues in major ampullate silk may be responsible for its higher tensile strength [Colgin & Lewis 1998, Hayashi *et al.* 1999].

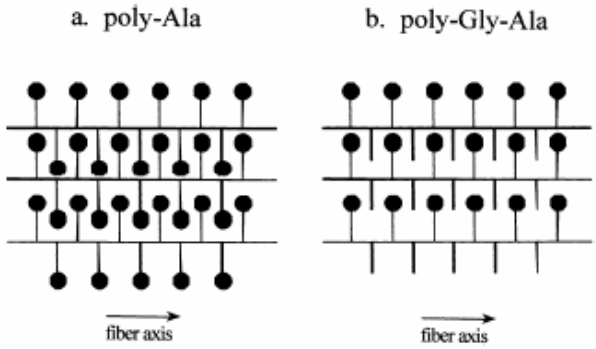

Figure 10.23 - Ball and stick diagrams showing the intercalation of (a) poly-Ala and (b) poly-Gly-Ala β-sheet regions [Hayashi *et al.* 1999]

In case of β-sheets formed by poly-Ala, the successive alanine residues are placed on alternate sides of a backbone. Each chain can then interlock with an adjacent chain via hydrophobic interactions (Figure 10.23a). The poly-Gly-Ala regions can form a similar structure (Figure 10.23b). However, regardless of which type of β-sheet the poly-Gly-Ala regions form, the glycine side of the polypeptide chain will be unable to have the same hydrophobic interactions hypothesised for poly-Ala. With fewer interactions, the poly-Gly-Ala regions have a lower binding energy than poly-Ala β-sheets. This is in agreement with the lower tensile strength of minor ampullate silk (with poly-Gly-Ala) relative to major ampullate silk (with poly-Ala). Parkhe *et al.* [1997] also attributed the lower strength for minor ampullate silk to the composition of both Gly-Ala and poly-Ala repeats in the β-sheet regions of this silk. Moreover, they stated that the larger Ala residues in the β-sheet regions of MA silk can cause the sheet to pucker resulting in a different mechanical behaviour.

The possible hydrophobic interactions are also related to the packing density in the β-sheet structure, and thus the presence of small amino acid residues, may affect the mechanical properties, such as strength. A feature of the pleated-sheet structures is that the bonds between the α-carbon atoms in the main polypeptide chains and the adjoining β-carbon atoms of the side chains are oriented approximately perpendicular to the plane of the sheet. Moreover, within each polypeptide chain, the side chains of adjacent amino acid residues protrude from opposite sides of the β-sheet. As a consequence, the way in which adjacent sheets are packed together is determined almost entirely by the sizes and shapes of the side chains of the component amino acid residues [Marsh *et al.* 1955a]. Pleated sheets containing only glycine residues, in which β-carbon atoms are replaced by hydrogen atoms, would be expected to pack together much more closely than would pleated sheets consisting of alanine or of larger amino acid residues. Indeed, construction of accurate scale models [Pauling & Corey 1953] of antiparallel-chain pleated sheets shows that two sheets consisting solely of glycine residues may pack together at a distance of about 3.5 Å, whereas sheets containing only alanine or serine residues may pack together efficiently at a distance of about 5.7 Å; larger amino acid residues require larger packing distances [Marsh *et al.* 1955a].

10.5.2.4. Morphology

The common morphological entity in all textile fibres, both natural and manufactured, is the fibril, which is an assembly of molecules. The conformation of the molecules and their spatial arrangement into the fibrils differ from fibre to fibre and determine to a high extent its mechanical behaviour [Gupta 2000]. For example, if the crystalline and amorphous phases are connected in series along the long axis of the fibre, the mechanical properties will be dominated by the amorphous phase. However, if they are connected in parallel, the mechanical properties will be dominated by the crystalline phase.

Both spider silk and silkworm silks are supposed to consist of a nanofibrillar structure (see also 10.4). A multifibrillar fibre with weak bonding between fibrils offers a number of possible mechanical advantages over a solid fibre of the same total cross sectional area. One is that the fibre will have greater flexibility so that it requires a lower moment to bend through a given radius of curvature [Hull 1995].

Another related advantage is that the fibre can be bent to a smaller minimum radius of curvature before failing occurs in tension on the outside of the bend or in compression on the inside of the bend [Hull 1995]. Both of these are related to the fact that the shear involved in bending a solid fibre can be accommodated with little stress in the weakly bonded inter-fibril boundaries of a nanofibrillar fibre. The advantage concerning failure might be the explanation for the lack of failure in the dragline silk of *N. clavipes* under a very sharp bend [Mahoney *et al.* 1994, Cunniff *et al.* 1994].

Also it can be noted that if the crossing fibrils are arranged in a helical or zig-zag manner in the fibre, they could extend the strain to failure in tension and compression significantly. The former could occur because these non-straight fibrils would straighten parallel to the fibre as the originally "straight" ones extend and break. The latter could occur because the non-straight fibrils would compress in the manner of a spring as the "straight" ones undergo buckling or shear failure. Both effects could contribute to the lack of failure under a sharp bend in the dragline silk of *Nephila clavipes* [Mahoney *et al.* 1994, Cunniff *et al.* 1994]. The tensile effect could contribute to the reported large tensile strains of spider silks at failure.

Finally, it can be observed that if a void or other flaw is the size of the fibril diameter, only the fibril will fail. On the contrary, if the void were in a solid fibre which behaved in a brittle fashion, the whole fibre could fail at a critical stress [Hull 1995].

Ko [1997] suggested that the high level of strength and modulus of the spider silk derive from the well-organised, highly ordered liquid crystalline fibrils together with a substantial number of inter-fibrillar bonds. The high level of breaking elongation, normally concomitant to high strength, is attained by the helicity of the fibrils.

Poza *et al*. [2002] reported a comprehensive investigation of the fracture surfaces for silks of two silkworms *Attacus Atlas*, representative for the wild silkworms, and *Bombyx mori* and mooring lines (MA silk) of one spider (*Argiope trifasciata*) and made a correlation with the mechanical behaviour. *A. atlas* was formed of bunches of microfibrils (about 1 µm in diameter) embedded in a soft matrix, which were pulled out from the matrix during fracture. The large volume fraction of matrix is in agreement with the reduced elastic modulus of the fibre, as compared to *B. mori*, The large strain-to-break also correlates well with the fibre pull-out mechanisms of the fracture surfaces, which is typical of composites with non-linear behaviour prior to failure. *B. mori* were made up of two brins of irregular shape embedded in a proteinaceous coating. Failure occurred by fracture of the brins, whose fracture surface presented a fine globular structure corresponding to the ends of the nanofibrils (1-2 µm in length, about 100 nm in diameter). The total absence of pull-out within the brin fracture surface is supposed to be indicative of a strong bonding between the nanofibrils, which would also be responsible for the high stiffness and strength of the *B. mori* fibres. *A. trifasciata* fibres were circular and exhibited a defined core-skin structure, also found for *N. clavipes* MA silk [Li *et al*. 1994, Vollrath *et al*. 1996, Frische *et al*. 1998]. The skin fracture surface was featureless while the core showed a globular structure similar to that of *B. mori* although a slightly longer average diameter of the fibrils is observed in silkworm silk. The features correspond to a microfibrillar structure similar to that observed by AFM in *N. clavipes* dragline silk [Li *et al*. 1994]. The fracture surfaces did not provide any

explanation of the differences in the strain to break between spider silk (± 30%) and silkworm silk (± 15%).

10.6. EXPLANATION OF SUPERCONTRACTION

A common feature of typical dragline (MA) spider silks, in contrast to minor ampullate spider silk, is their apparent ability to "supercontract" when submerged in aqueous solvents [Work 1977, 1981, Work & Morosoff 1982]. There are man-made polymers which exhibit supercontraction in organic solvents or when heated, but virtually none which will supercontract in pure water at room temperature [Shao & Volrath 1999].

When the MA fibres are in contact with aqueous media, they swell about twice in cross-section and shrink to about half of its original length [Work 1981, Work & Morosoff 1982]. Supercontraction in water is accompanied with a large reduction in material stiffness and larger strain-to-break [Work 1977, Termonia 1994, Shao & Vollrath 1999], i.o.w. it behaves like an elastomer. However, on re-stretching the mechanical properties are largely recovered [Work 1981, Shao & Vollrath 1999, Shao *et al.* 1999].

Several researchers [Shao & Vollrath 1999, Shao *et al.* 1999, Gosline *et al.* 1999] tried to find a structural explanation of supercontraction of dragline spider silks in water and other solvents. A more detailed explanation of the supercontraction behaviour is given by Gosline *et al.* [1999] by use of the model shown in Figure 10.24.

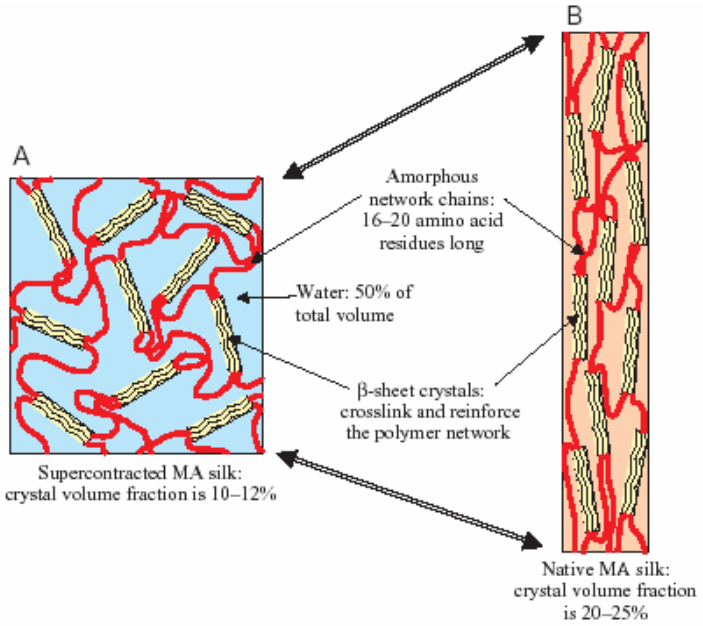

Figure 10.24 - Gosline model for the molecular architecture of *Araneus diadematus* MA gland silk

The native MA silk contains a crystal-crosslinked and crystal-reinforced polymer network. The amorphous chains interconnect the crystals (± 16-20 amino acid residues long). The water absorbed during supercontraction is associated primarily with these amorphous chains. The rubber-like elasticity of the hydrated network arises from the large-scale extension of these coiled amorphous chains. The amorphous chains are extended, and the polymer crystals are rotated during the stretching and shrinking to produce a strongly preferred molecular orientation parallel to the fibre axis. The physical state of the extended, amorphous chains remains to be determined, but Gosline *et al.* [1999] proposes that they form a rigid, extended polymeric glass phase, creating a highly oriented, fibre-reinforced polymer network.

This reorientation, such that the polymer crystals are no longer parallel to the fibre axis, is confirmed by diffraction data performed by Parkhe *et al.* [1997]. However, minor ampullate silk of which it is known that it does not supercontract, also shows this reorientation so that a more complex mechanism should be considered. Parkhe *et al.* [1997] suggested that the reorientation of the β-sheets regions in MA silk affects other structural regions which together result in the contraction. Egg sac silk showed very little β-sheet orientation in the natural state and there were no detectable changes in the diffraction pattern upon wetting [Parkhe *et al.* 1997].

A small experiment performed by Gellynck [2006] of wetting egg sac spider silk under a light microscope revealed that egg sac spider silk only swells in diameter in water (Figure 10.25) and does not contract (Figure 10.26), confirming the observation of Parkhe *et al*. [1997]. In Figure 10.26 an egg sac fibre is mounted between two clamps in the photo above, in the photo below some droplets of water are put on the fibre. The clamps kept their position since no shrinkage occurs.

Gosline *et al.* [1999] further noted that the glycine-rich motifs in both MA silks of *Araneus diadematus* contain numerous polar glutamine residues (glutamine Q), and these are suggested to explain the tendency of MA silk to absorb water and supercontract. The content of glutamine (Glx) residues is comparable for MA and egg sac spider silk, so this suggestion is doubtfull.

Also *Bombyx mori* silkworm silk is known to show no supercontraction phenomenon [Pérez-Rigueiro *et al.* 2000, Guinea *et al.* 2003]. A swelling (18%) of the fibre is reported after immersion in water [Kawahara *et al.* 1996]. Furthermore, a significant reduction of the elastic modulus after immersion in water and a slight increase in elastic modulus after immersion in ethanol are observed [Pérez-Rigueiro *et al.* 2001]. Immersion in water results in the substitution of interprotein hydrogen bonds by water-protein hydrogen bonds without a significant change in the conformation of the protein. Ethanol is suggested to desiccate the material, increasing the number of interprotein hydrogen bonds.

To conclude, although several aspects are mentioned to explain the supercontraction phenomenon, its explanation is still not completely found.

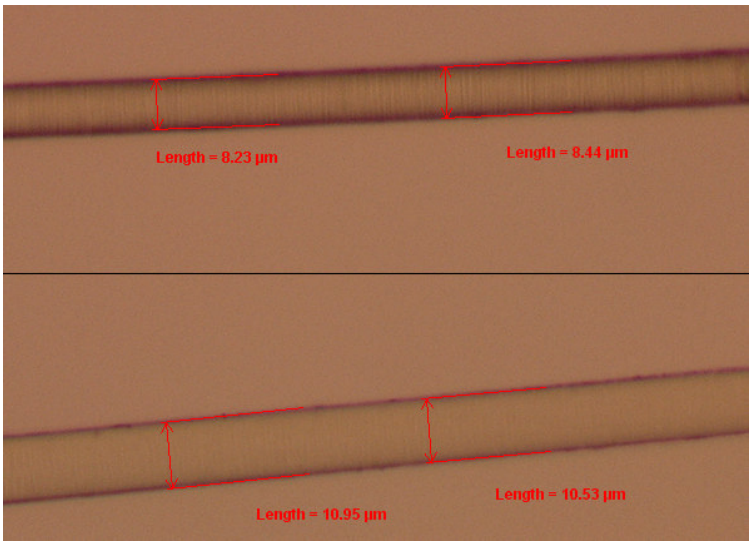

Figure 10.25 – Swelling of egg sac spider silk in water (photo above before and photo below after water immersion, "Length" indicates the diameter) [Gellynck 2006]

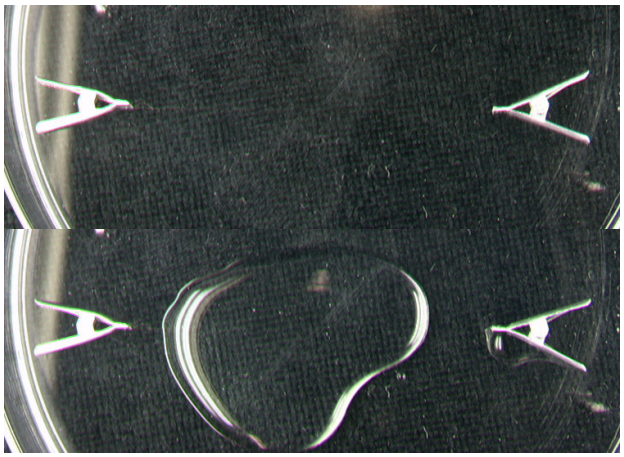

Figure 10.26 – Egg sac spider silk does not supercontract in water (photo above before and photo below after water immersion)

10.7. STRUCTURAL MODEL FOR EGG SAC SPIDER SILK

10.7.1. SUMMARY OF KNOWN INFORMATION

The physical properties of egg sac spider silk differentiate from those of the other silks in the following features, as deduced from Chapters 2, 3 and 9:

- A rubber-like behaviour characterized by a plateau in the stress-strain curve beyond the yield point, with limited strain hardening zone;
- A lower strength and the same or even higher strain as dragline silk;
- Worse elastic recovery and resilience behaviour at higher strain values, however comparable with Tussah silk;
- Higher creep;
- Significant strain-rate dependency;
- No observable supercontraction in water;
- A high thermal stability (unstrained) comparable with Tussah silk;
- No thermal shrinkage (comparable with *B. mori*) when heated under an applied force.

As far as the amino acid composition concerned (see Chapter 4), it is important to note that the percentage of serine is high compared to the other silks, compensated by a much lower glycine content. Also the high contribution of amino acid residues with hydrophobic or polar, voluminous side chain, is worth to be mentioned.

With respect to the secondary structure of egg sac spider silk, the vibrational and NMR spectroscopic experiments (Chapters 6 and 8) revealed that egg sac spider silk:

- only contains limited amounts of, possibly small, β-sheet structures, and in which Ala and Ser residues are involved;
- is dominated by β-turn structures and random coil structures;
- further includes a limited amount of α-helical structures, although they were difficult to confirm; possibly these helical regions are of another, more thermally stable, helical form.

The fractographic analysis reveals that no microfibrils can be detected, even after straining at very low testing speeds. It reveals that the structure of egg sac spider silk is highly dominated by the amorphous regions. Furthermore, a skin-core structure is detected in which the properties of the skin are more plastic than the core.

10.7.2. DISCUSSION

From the measured and known amino acid composition of silk proteins secreted by the tubuliform glands of different species and from the amino acid sequence found in the article of Tian & Lewis [2006], shown in Figure 10.27, it can be concluded that the structure of egg sac spider silk of different spider species will be similar.

The serine residues in different tubuliform gland silk fibroins reside in $(Ser)_n$, $(Ser\text{-}Ala)_n$, $(Ser\text{-}Gln)_n$ motifs in the primary sequence of egg sac spider silks [Tian & Lewis 2006]. Furthermore, Gly-X regions are found, in which X represents Gln, Asn, Ile, Leu, Ala, Val, Tyr, Phe, Asp. The egg sac spider silks of different species are differing in the presence or absence of e.g. Gln-Gln motifs or stretches of Thr.

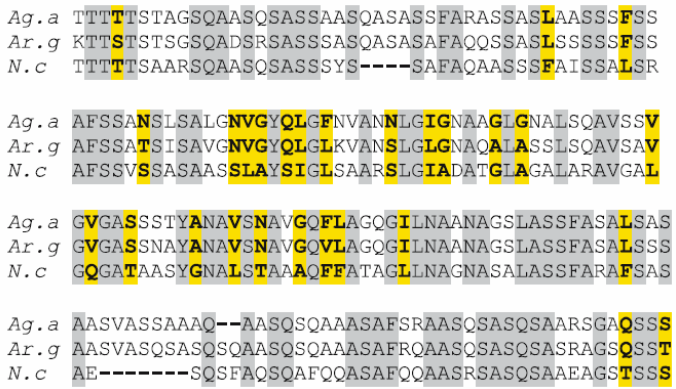

Figure 10.27 – Amino acid sequence alignment of the tubuliform silk protein repeat units among *Argiope aurantia* (Ag. a), *Araneus gemmoides* (Ar. g), and *Nephila clavipes* (N. c). Darkly shaded regions indicate identical amino acids. Lightly shaded regions with bold letters indicate similar amino acids [Tian & Lewis 2006]

Although the structure of the motifs is not clear, β-sheet crystals twisted parallel to the chain direction were proposed by Barghout *et al*. [1999] in *Araneus diadematus* egg sac silk. The X-ray diffraction pattern of egg sac spider silk of *Nephila clavipes* revealed that the β-sheets show no clear orientation with respect to the fibre axis [Parkhe *et al*. 1997]. Both features are in contrast to what is found in MA or dragline spider silk. Moreover, the dimensions of the orthorhombic unit cell indicate that some bulky residues are involved in the β-sheet structures [Parkhe *et al*. 1997].

In order to get a β-sheet structure at least 3 residues are required. Moreover, amino acid residues that are mostly involved in a β-sheet structure are: Ala, Gly, Ser, Leu, Thr, Ile, and Val. However, Ala, Leu, Ile and Val are also good α-helix formers. The hydrophobic residues are stabilising both secondary structures by means of hydrophobic interactions. Polar residues are often flanking β-sheet structures since they stabilize the structure by means of hydrogen bonding, however these residues will force the structure to turn. So, it is not likely that two consecutive Ser residues both reside in the β-sheet structure. However, consecutive serine residues are found often in β-turn structures [Hutchinson & Thornton 1994].

As a consequence, it is suggested that only the Ala-Ala-Ala (AAA), flanked by Ser (S) of Gln (Q) are involved in β-sheet crystals. The presence of Gln and Ser is suggested to force the β-sheet crystals to turn, explaining the twist that is observed. Also in MA silk, the β-sheet domains are flanked by glutamine residues and are suggested, along with the GGX sequences that appear beside them (which are not stable β-formers), to prevent further growth of the β-sheet in the chain direction [Simmons *et al.* 1996], as is seen in Figure 10.28. The β-sheet crystals are thus suggested to be small (only 5 residues long) compared to what is observed in dragline (MA) silk (11-13 residues) [Simmons *et al*. 1996]. Furthermore, looking at the sequences in Figure 10.27, domains containing QAAAS, or SAAAQ are uncommon, although combinations of Ala and Ser (ASASS, ASSAS, AASSS, SASAAS) are more frequently occurring.

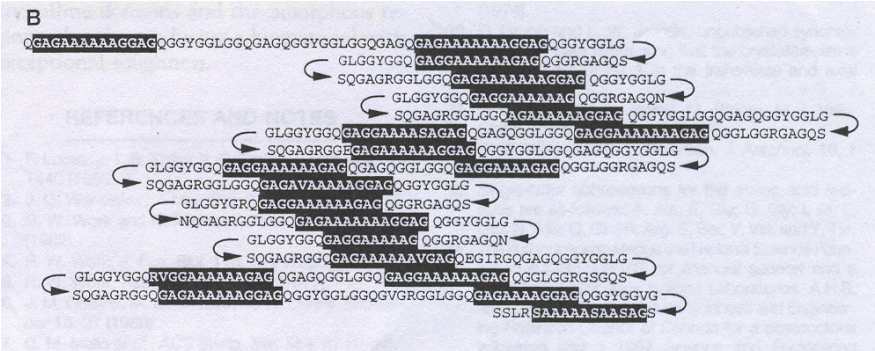

Figure 10.28 - Proposed folding of molecule into alanine-rich β-sheet (highlighted) domains and glycine-rich amorphous regions [Simmons *et al.* 1996]

This provides evidence that the crystalline domains in egg sac spider silk are small. The high amount of bulky residues and/or the presence of a high amount of polar serine residues are responsible for the limitations in the growth of the β-sheet crystals and force the formation of loops and tie chains that link crystals to one another and to the surrounding amorphous matrix. Residues with big, bulky or asymmetric side groups cannot be incorporated into tightly packed, regular structures and thus restrict the packing density in the crystalline domains. Apart from explaining the lower tensile strength, the small β-sheet crystals also result in the worse visco-elastic behaviour of egg sac spider silk.

Furthermore, the egg sac spider silk is indeed dominated by β-turn structures. Several authors [Asakura *et al*. 2001, Okabayashi *et al*. 2002, Peng *et al*. 2005] believe β-turn structures are formed as intermediate structures during the conformational transition from random coil (in spinning gland) to β-sheet structure (in the fibre). The spider seems to control the amino acid sequence so that the β-sheet structures cannot fully develop.

However, amino acids with side chains that can H-bond (Ser, Asp, and Asn) are known to destabilize α-helices. Furthermore, also amino acids with more voluminous branches such as Val and Ile destabilize the α-helix due to steric interactions. The above mentioned amino acid residues are highly represented in

egg sac spider silk and explains why no α-helical conformation could be proved in this silk. However, it is suggested that helical conformations are formed by linked β-turns accounting for the relative high strain-at-break. α-helix structures are known to be normally flexible and elastic. The presence and combination of β-turns as helical structures may result in the worse elastic behaviour.

Lewis and co-workers [Hinman & Lewis 1992, Hayashi & Lewis 1998] believe that a strain-at-break larger than 5-10% is explained by the presence of β-turns (GPGXX motif), which are linked together into β-spirals, like observed in elastin [Urry 1984]. Egg sac spider silk shows a strain value of more than 30%, but no GPGXX motifs are found till now in its primary structure. Moreover, the fractions of glycine and proline are small. In flagelliform and MA spider silk, it is the positioning of the Tyr and Ser residues that are thought to result in the formation of β-turns. Also Tyr is only for a small amount known to be present in egg sac spider silk.

Tatham & Shewry [2000] also reported that elastomeric proteins often contain β-turns as a structural motif, apart from intermolecular cross-links. It is suggested that apart from serine residues also other residues, possibly asparagine (N), are responsible for these β-turns. Asparagine residues are particularly favoured in turns [Hutchinson & Thornton 1994]. The reason for the presence of these polar residues in turns, is that these residues have side chains that can act as hydrogen bond acceptors; these stabilize the turn by forming a hydrogen bond between the oxygen atoms on their side chains and the main chain amide of another residue in the turn. It is suggested that in the case of a succession of Ala and Ser of only 3 residues, the probability is higher that successive β-turns are formed than extensive β-sheets.

Furthermore, it has been reported that a β-turn rich conformation can be stabilized by hydrophobic interactions between aromatic residues (e.g. Tyr - Y, Phe - F) and by hydrogen bonding between amino and carboxy groups of glutamine (Q) residues with other glutamine residues and possibly the peptide backbone [Tatham *et al.* 1985]. Egg sac spider silk contains a high amount of hydrophobic amino acid residues, such as Ala (25-30%), Val (6-10%), Leu (6-8%), Phe (3-4%) which makes the contribution of hydrophobic interactions plausible. It is also noted that the presence of lysine is much higher in egg sac spider silk than in the other silks. Lysine is known to participate in the cross-linking of neighbouring molecules [Hartgerink 2004], as is observed in collagen and elastin [Urry 1982]. Moreover, the positively charged side chains of the lysine residues are expected to engage in electrostatic interactions with the negatively charged side chains of glutamic acid (E) and aspartic acid (D) residues, which interestingly, also appear to occur more frequently in egg sac spider silk than in other silks (Table 4.7).

The high number of intramolecular hydrogen bonds and hydrophobic interactions in the possibly linked β-turn structures act as cross-linkers, possibly in combination with lysine, and help to resist for a long time the force applied, resulting in a high deformation (strain) for a small increase in stress. These interactions lead to a plastic behaviour and also result in unfavourable visco-elastic properties. These intramolecular hydrogen bonds also explain the high thermal stability of egg sac spider silk (Chapter 9). By heating, the mobility of the molecules is increased, this can result in a breakage of hydrogen bonds but at the same time, new ones are formed preventing thermal decomposition.

The flattened region in the stress-strain curve would indicate that the intrafibre bonding within egg sac spider silk is weak [Hatch 1993]. Shao *et al.* [1999] interpreted the plateau in the stress-strain curves (in MA silk) as indicating that disoriented and coiled molecular chains reorient under the stretching force as pre-shrunk (after immersion in water) MA silk displayed larger plateaus. The flat hardening region in the stress-strain curve of egg sac spider silk revealed that the mechanical behaviour is dominated by the amorphous regions since strain hardening would be due to a conversion of amorphous regions from a rubber state to a glassy or crystal state [Vollrath & Porter 2006]. Amorphous chains can lose virtually all their mobility, but retain the ability to be uncoiled under very high loads. Such deformations are resisted by strong frictional forces between segments in the polymer chain, and the network exhibits extremely high mechanical hysteresis, as is found in Chapter 3. Under these conditions, amorphous polymer networks are very difficult to break [Gosline *et al.* 1986]. Since the mechanical properties are highly determined by the amorphous fraction, we would expect that the crystalline and amorphous domains are connected in series along the long axis of the fibre [Gupta 2000].

Because of the observed skin-core structure, we expect that the crystals are not randomly distributed into the amorphous phase. Furthermore, the size of the β-sheet crystals is too limited to lead to the formation of microfibrils.

There are several structural aspects explaining the lower tensile strength of egg sac spider silk compared to the other silk fibres:

- The lower crystalline β-sheet content and smaller crystals, as proven by the spectroscopic observations;
- The higher heterogeneity of the repeats [Fedic *et al*. 2003], as is evidenced by the broader Amide I bands in the DRIFTS experiments (Chapter 6) and is seen in the known primary structure of egg sac spider silk (Chapter 5).

The relative high strain-at-break and limited strain hardening can be explained by:

- the β-turn structures that are possibly linked into helical structures, and possibly explaining the twist in β-sheet crystals that is observed in egg sac spider silk [Barghout *et al*. 1999];
- the lysine, hydrophobic and hydrogen bond interactions that are acting as cross-links, similar as in rubbers.

10.7.3. CONCLUSION

A structural model for egg sac spider silk is proposed in which the crystalline and amorphous phases are connected in series along the long axis of the fibre. Furthermore, the crystalline fraction is small compared to the amorphous fraction and is not highly oriented. The crystalline fraction consists of β-sheet crystals of a limited length connected with loop or β-turn structures to the amorphous regions. Furthermore, it is suggested that, in the more amorphous fraction, β-turn structures are linked resulting in helical structures. Finally, the crystals are not at random

distributed in the amorphous fraction such that a skin-core structure is formed without a microfibrillar structure.

10.8. REFERENCES

Asakura T., Ashida J., Yamane T., Kameda T., Nakazawa Y., Ohgo K., Komatsu K., A repeated beta-turn structure in poly(Ala-Gly) as a model for Silk I of *Bombyx mori* silk fibroin studied with two-dimensional Spin-diffusion NMR under Off Magic Angle Spinning and Rotational Echo Double Resonance, J. Mol. Biol. 306:291-305 (2001)

Asakura T., Yao J., Yamane T., Umemura K., Ulrich A.S., Heterogeneous structure of silk fibers from *Bombyx mori* resolved by C-13 solid-state NMR spectroscopy, J. Am. Chem. Soc. 124:8794-8795 (2002a)

Augsten K., Mühlig P., and Herrmann C., Glycoproteins and skin-core structure in *Nephila clavipes* spider silk observed by light and electron microscopy, Scanning 22:12-15 (2000)

Barghout J.Y.J., Thiel B.L., Viney C., Spider (*Araneus diadematus*) cocoon silk: a case of non-periodic lattice crystals with a twist?, Int. J. Biol. Macromol. 24:211-217 (1999)

Barghout J.Y.J., Czernuszka J.T., Viney C., Multiaxial anisotropy of spider (*Araneus diadematus*) cocoon silk fibres, Polymer 42:5797-5800 (2001)

Bini E, Knight D. P., Kaplan D. L., Mapping domain structures in silks from insects and spiders related to protein assembly, J. Mol. Biol. 335(1):27-40 (2004)

Colgin M.A. & Lewis R.V., Spider minor ampullate silk proteins contain new repetitive sequences and highly conserved non-silk-like “spacer regions”, Protein science 7:667-672 (1998)

Cook J.G., Handbook of textile fibres – Natural fibres, Merrow Publishing Co. Ltd., Durham, UK, 144-165 (1984)

Craig C.L. & Riekel Chr., Comparative architecture of silks, fibrous proteins and their encoding genes in insects and spiders, Comp. Biochem. Physiol. B 133:493-507 (2002)

Cunniff P.M., Fossey S.A., Auerbach M.A., Song J.W., Mechanical properties of major ampulate gland silk fibers extracted from *Nephila clavipes* spiders, In: Silk polymers: Material science and biotechnology, ACS Symposium Series 544, Washington DC, 234-251 (1994)

Dong Z., Lewis R.V., Middaugh C.R., Molecular mechanism of spider silk elasticity, Arch. Biochem. Biophys. 284:53-57 (1991)

Fakirov S. (Ed.), Oriented Polymer Materials, Hüthig & Wepf Verlag, Heidelberg (1996)

Fedic R., Zurovec M., Sehnal F., Correlation between fibroin amino acid sequence and physical silk properties, J. Biol. Chem. 278(37):32255-35264 (2003)

Foelix R.F., Chapter 5 - Biology of spiders, 2nd Edition, Oxford University Press, Georg Thieme Verlag, New York, 110 (1996)

Frische S., Maunsbach A.B., Vollrath F., Elongate cavities and skin-core structure in *Nephila* spider silk observed by electron microscopy, Journal of Microscopy 189(1):64-70 (1998)

Garel J.P., The silkworm, a model for molecular and cellular biologists, TiBS 105-108 (1982)

Gatesy J., Hayashi C., Dagmara M., Woods J., Lewis R., Extreme diversity, conservation, and convergence of spider silk fibroin sequences, Science 291:2603-2605 (2001)

Gellynck K., Zijde en spinrag in weefselengineering – Silk and spider silk in tissue engineering, Thesis submitted to obtain the degree of Doctor of Applied Sciences, option Material Sciences, Promotor Prof. Dr. P. Kiekens (2006)

Gosline J.M., DeMont M.E., Denny M.W., The structure and properties of spider silk, Endeavor 10(1):37-43 (1986)

Gosline J.M., Pollak C.C., Guerette P.A., DeMont M.E., Denny M.W., Elastomeric network models for the frame and viscid silks from the orb-web of the spider *Araneus diadematus*. In: Silk polymers: Materials science and biotechnology, Kaplan D., Adams W.W., Farmer B., Viney C. (Eds.), Am. Chem. Soc. 329-341 (1994)

Gosline J., Nichols C., Guerette P., Cheng A., Katz S., The macromolecular design of spider silks. In: Biomimetics. Design and processing of materials, Sarikaya M., Aksay I.A. (Eds.), AIP Press, 237-261 (1995)

Gosline J.M., Guerette P.A., Ortlepp C.S., Savage K.N., The mechanical design of spider silks: From fibroin sequence to mechanical function, J. Exp. Biol. 22(23):3295-3303 (1999)

Gould S.A.C., Tran K.T., Spagna J.C., Moore A.M.F., Shulman J.B., Short and long range order of the morphology of silk from *Latrodectus hesperus* (Black Widow) as characterized by Atomic Force Microscopy, Int. J. Biol. Macromol. 24:151-157 (1999)

Grzelak K., Control of expression of silk protein genes, Comparative Biochemistry and Physiology B-Biochemistry & Molecular Biology 110 (4):671-681 (1995)

Grubb D.T. & Jelinski J.W., Fiber morphology of spider silk: the effects of tensile deformation, Macromolecules 30:2860-2867 (1997)

Guerette P.A., Ginzinger D.G., Weber B.H.F., Gosline J.M., Silk properties determined by gland specific expression of spider fibroin gene family, Science 272:112-114 (1996)

Guinea G.V., Elices M., Pérez-Rigueiro J., Plaza G., Self-tightening of spider silk fibers induced by moisture, Polymer 44: 5785-5788 (2003)

Gupta V.B., Structure of textile fibres and structural dependence of their mechanical properties, In: Progress in textiles: science & technology, Kothari V.K (Ed.), Vol. 2, IAFL Publications, India, 11-118 (2000)

Hartgerink J.D., Covalent capture: a natural complement to self-assembly, Current Opinion in Chemical Biology 8 (6):604-609 (2004)

Hatch K.L., Chapter 8 – Fibre properties and identification, In: Textile fibers, West Publishing Company, USA, 109-118 (1993)

Hayashi C.Y. & Lewis R.V., Evidence from flagelliform silk cDNA for the structural basis of elasticity and modular nature of spider silks, J. Mol. Biol. 275:773-784 (1998)

Hayashi C.Y., Shipley N.H., Lewis R.V., Hypotheses that correlate the sequence, structure and mechanical properties of spider silk proteins, Int. J. Biol. Macromol. 24:271-274 (1999)

Heslot H., Artificial fibrous proteins: A review, Biochimie 80:19-31 (1998)

Hinman M.B. & Lewis R.V., Isolation of a Clone Encoding a Second Dragline Silk Fibroin, J. Biol. Chem. 267:19320-19324 (1992)

Howitt F.O., Proteins – Silk, In: The structure of textile fibres, Urquhart A.R., Howitt F.O. (Eds.), The Textile Institute, Manchester, 59-68 (1953)

Huber C.J., Chapter XVII - The silk fibers, In: Matthew's Textile Fibres – Their physical, microscopical and chemical properties, Mauersberger H.R. (Ed.), 5th edition, John Wiley & Sons Inc., New York, 679-729 (1947)

Hull D., An introduction to composite materials, Cambridge University Press, Cambridge, Chapters 2 and 3 (1995)

Hutchinson E.G. & Thornton J.M., A revised set of potentials for β-turn formation in proteins, Protein Science 3:2207-2216 (1994)

Iizuka E., Degree of crystallinity and modulus relationships of silk threads from *Bombyx mori*, Biorheology 3:1-8 (1965)

Inoue S., Tanaka K., Arisaka F., Kimura S., Ohtomo K., Mizuno S., Silk fibroin of *Bombyx mori* is secreted, assembling a high molecular mass elementary unit consisting of H-chain, L-chain, and P25, with 6:6:1 molar ratio, J. Biol. Chem. 275(51):40517-40528 (2000)

Jelinski L.W., Blye A., Liivak O., Michal C., LaVerde G., Seidel A., Shah N., Yang Z., Orientation, structure, wet-spinning, and molecular basis for supercontraction of spider dragline silk, Int. J. Biol. Macromol. 24(2-3):197-201 (1999)

Jin H.-J. & Kaplan D.L., Mechanism of silk processing in insects and spiders, Nature 424:1057-1061 (2003)

Kaplan D., Adams W.W., Farmer B., Viney C., Silk polymers: Materials science and biotechnology, Am.Chem. Soc., Washington DC (1994)

Kawahara Y., Shioya M. Takaku A., Influence of swelling of noncrystalline regions in silk fibers on modification with methacrylamide, J. Appl. Polym. Sci. 59:51-56 (1996)

Kishore A.I., Herberstein M.E., Craig, C.L., Separovic F., Solid-state NMR relaxation studies of Australian spider silks, Biopolymers 61:287-297 (2002)

Knight D.P. & Vollrath F., Biological liquid crystal elastomers, Phil. Trans. Roy. Soc. Ser. B 357:155-163 (2002)

Ko F.K., Spider silk, Textile Asia, April, 38-43 (1997)

Kümmerlen J., van Beek J.D., Vollrath F., Meier B.H., Local structure in spider dragline silk investigated by two-dimensional spin-diffusion nuclear magnetic resonance, Macromolecules 29:2920-2928 (1996)

Lewis R.V., Spider silk: the unraveling of a mystery, Accts. Chem. Res. 25:392-397 (1992)

Li S.F.Y, McGhie A.J., Tang S.L., New internal structure of spider dragline silk revealed by Atomic Force Microscopy, Biophys. J. 66(4):1209-1212 (1994)

Liivak O., Flores A., R. Lewis, Jelinski L.W., Conformation of the polyalanine repeats in minor ampullate gland silk of the spider *Nephila clavipes*, Macromolecules 30:7127-7130 (1997)

Lombardi S.J. & Kaplan D.L., The amino acid composition of major ampullate gland silk (dragline) of *Nephila clavipes* (Araneae, Tetragnathidae), J. Arachnol. 18:297-306 (1990)

Mahoney D.V., Vezie D.L., Eby R.K., Adams W.W., Kaplan D., Aspects of the Morphology of Dragline Silk of *Nephila clavipes*, In: Silk polymers: Material science and biotechnology, ACS Symposium Series 544, Washington DC, 196-209 (1994)

Marsh R.E., Corey R.B., Pauling L., An investigation of the structure of silk fibroin, Biochim. Biophys. Acta 16:1-34 (1955a)

McCrum N.G., Buckley C.P., Bucknall C.B., Principles of polymer engineering, 2nd Edition, Oxford University Press, USA (1997)

Mello C.M., Senecal K., Yeung B., Voudros P., Kaplan D., In: Silk polymers – Materials science and biotechnology, Kaplan D., Adams W.W., Farmer B., Viney C. (Eds.), American Chemical Society: Washington DC, 67-79 (1994)

Mita K., Ichimura S., James T.C., Highly repetitive structure and its organization of the silk fibroin gene, J. Mol. Evol. 38:583-592 (1994)

Okabayashi H., Ishida M., Tamaoki H., Masuda H., O'Connor C.J., Fourier transform IR study of aggregational behavior of N-acetyl-L- and N-butyloxycarbonyl-L-glutamic acid oligomeric benzyl esters in dioxane and benzene: beta-turn -> antiparallel beta-sheet transition, Biopolymers 65:81-88 (2002)

Pan Z.J., Li C.P., Xu Q., Active control on molecular conformations and tensile properties of spider silk, J. Appl. Polym. Sci. 92:901-905 (2004)

Parkhe A.D., Seeley S.K., Gardner K., Thompson L., Lewis R.V., Structural studies of spider silk proteins in the fiber, J. Mol. Recognit. 10:1-6 (1997)

Pauling L. & Corey .R.B., Two Pleated-Sheet Configurations of Polypeptide Chains Involving Both Cis and Trans Amide Groups, Proc. Nat. Acad. Sci. U S A, 39(4):247–252 (1953)

Peng X., Shao Z., Chen X., Knight D.P., Wu P., Vollrath F., Further investigation on potassium-induced conformation transition of *Nephila* spidroin film with two-dimensional infrared correlation spectroscopy, Biomacromolecules 6:302-308 (2005)

Pérez-Rigueiro J., Viney C., Llorca J., Elices M., Mechanical properties of silkworm silk in liquid media, Polymer 41:8433-8439 (2000)

Pérez-Rigueiro J., Elices M., Llorca J., Viney C., Tensile properties Of *Attacus Atlas* silk submerged in liquid media, J. Appl. Polym. Sci. 82(1):53-62 (2001)

Poza P., Pérez-Rigueiro J., Elices M., Llorca J., Fractographic analysis of silkworm and spider silk, Engineering Fracture Mechanics 69(9):1035-1048 (2002)

Prevorsek D.C., Structural aspects of damage tolerance of Spectra fibres and composites, In: Oriented Polymer Materials, Fakirov S. (Ed.), Hüthig & Wepf Verlag, Heidelberg, 444-465 (1996)

Putthanarat S., Stribeck N., Fossey S.A., Eby R.K., Adams W.W., Investigation of the nanofibrils of silk fibers, Polymer 41:7735-7747 (2000)

Riekel C., Bränden C., Craig C., Ferrero C., Heidelbach F., Müller M., Aspects of X-Ray diffraction on single spider fibers, Int. J. Biol. Macromol. 24:179-186 (1999)

Riekel C., Chapter 3 - The mechanical functions of silks and their correlated structural properties, In: Spider webs and silk – Tracing evolution from molecules to genes to phenotypes, Craig C. L. (Ed.), Oxford University Press, USA, 51-83 (2003)

Shao Z. & Vollrath F., The effect of solvents on the contraction and mechanical properties of spider silk, Polymer 40:1799-1806 (1999)

Shao Z., Vollrath F., Sirichaisit J., Young R.J., Analysis of spider silk in native and supercontracted states using Raman spectroscopy, Polymer 40(10):2493-2500 (1999)

Simmons A., Ray E., Jelinski L.W., Solid state ^{13}C NMR of *N. clavipes* dragline silk establishes structure and identity of crystalline regions, Macromolecules 27:5235-5237 (1994)

Simmons A., Michal C.A., Jelinski L.W., Molecular orientation and two-component nature of the crystalline fraction of spider dragline silk, Science 271:84-87 (1996)

Sirichaisit S., Young R.J., Vollrath F., Molecular deformation in spider dragline silk subjected to stress, Polymer 41:1223-1227 (1999)

Takahashi Y., Gehoh M., Yuzuriha K., Structure refinement and diffuse streak scattering of silk (*Bombyx mori*), Int. J. Biol. Macromol. 24(2-3):127-138 (1999)

Tanaka K., Kajiyama N., Ishikura K., Waga S., Kukuchi A., Ohtomo K., Takagi T., Mizuno S., Determination of the site of disulfide linkage between heavy and light chains of silk fibroin produced by *Bombyx mori*, Biochim. Biophys. Acta 1432:92-103 (1999)

Tanaka K. & Mizuno S., Homologues of fibroin L-chain and P25 of *Bombyx mori* are present in *Dendrolimus spectabilis* and *Papilio xuthus* but not detectable in *Antheraea yamamai*, Insect Biochem. Mol. Biol. 31:665-677 (2001)

Tatham A.S., Drake A.F., Shewry P.R., A conformational study of a glutamine- and proline-rich cereal seed protein, C hordein, Biochem. J. 226:557-562 (1985)

Tatham A.S. & Shewry P.R., Elastomeric proteins: biological roles, structures and mechanisms, TiBS 25(11):567-571 (2000)

Termonia Y., Molecular modeling of spider silk elasticity, Macromolecules 27:7378-7381 (1994)

Thiel B.L., Kunkel D.D., Viney C., Physical and chemical microstructure of spider dragline: a study by analythical transmission electron microscope, Biopolymers 34:1089-1097 (1994)

Thiel B.L., Guess K.B., Viney Chr., Non-periodic lattice crystals in the hierarchical microstructure of spider (major ampullate) silk, Biopolymers 41:703-719 (1997)

Tian M. & Lewis R.V., Tubuliform silk protein: A protein with unique molecular characteristics and mechanical properties in the spider silk fibroin family, Applied Physics 82(2):265-273 (2006)

Tirrell D.A., Putting a new spin on spider silk, Nature 271:39-40 (1996)

Treloar L.R.G.; Introduction to polymer science, Wykeham Publications (London) Ltd. (1970)

Tsukada M., Freddi G., Nagura M., Ishikawa H., Kasai N., Structural changes of silk fibers induced by heat treatment, J. Appl. Polym. Sci. 46:1945-1953 (1992)

Urry D.W., Characterization of soluble peptides of elastin by physical techniques, Methods Enzymol. 82:673-716 (1982)

Urry D.W., Protein elasticity based on conformations of sequential polypeptides – the biologic elastic fibre, J. Prot. Chem. 3:403-436 (1984)

van Beek, J.D., Hess, S., Vollrath, F., Meier, B.H., The molecular structure of spider dragline silk: Folding and orientation of the protein backbone, Proc. Nat. Acad. Sci. 99(16):10266-10271 (2002)

Vandenheuvel C.J.M., Heuvel H.M., Faassen W.A., Veurink J., Lucas L.J., Molecular-changes of PET yarns during stretching measured with rheooptical infrared-spectroscopy and other techniques, J. Appl. Polym. Sci. 49(5): 925-934 (1993)

Vollrath F., Holtet T., Thogersen H., Frische S., Structural organization of spider silk, Proc. R. Soc. Lond. Ser. B-Biol. Sci. 263:147-151 (1996)

Vollrath F. & Knight D., Liquid crystalline spinning of spider silk, Nature 410:541-548 (2001)

Vollrath F. & Porter D., Spider silk as a model biomaterial, Applied Physics 82(2):205-212 (2006)

Warner S.B., Fibre science, Prentice Hall, Engelwood Cliffs, New Jersey, 11-66 (1995)

Warwicker J.O., The crystal structure of silk fibroin, Acta Cryst. 7:565-573 (1954)

Work R.W., Dimensions, birefringence and force-elongation behaviour of major and minor ampullate silk fibres from orb-web spinning spiders, Text. Res. J. 47:650-662 (1977)

Work R.R., A comparative study of the supercontraction of major ampullate silk fibers of orb-web-building spiders (*Araneae*), J. Arachnol. 9:299-308 (1981)

Work R.W. & Morosoff N., A physico-chemical study of the supercontraction of spider major ampullate silk fibers, Text. Res. J. 52:349-356 (1982)

Xu M. & Lewis R.V., Structure of a protein superfiber: Spider dragline silk, Proc. Nat. Acad. Sci. USA 87:7120-7124 (1990)

Yamaguchi K., Kikuchi Y., Takagi T., Kikuchi A., Oyama F., Shimura K., Mizuno S., Primary structure of the silk fibroin light chain determined by cDNA sequencing and peptide analysis , J. Mol. Biol. 210:127-139 (1989)

Yang Y., Chen X., Shao Z., Zhou P., Porter D., Knight D.P., Vollrath F., Toughness of Spider Silk at High and Low Temperatures, Adv. Mater. 17(1):84-88 (2005)

Yeh W.-Y. & Young R.J., Molecular deformation processes in aromatic high modulus polymer fibres, Polymer 40:857-870 (1999)

Zhou C.-Z., Confalonieri F., Medina N., Zivanovic Y., Esnault C., Yang T., Jacquet M., Janin J., Duguet M., Perasso R. and Li Z.-G., Fine organisation of *Bombyx mori* heavy chain gene, Nucleic Acids Research 28(12):2413-2419 (2000)

Zhou C.-Z., Confalonieri F., Jacquet M., Perasso R., Li Z.-G., Janin J., Silk fibroin: Structural implications of a remarkable amino acid sequence, Proteins: Structure, Function, and Genetics 44:119-122 (2001)

11

CONCLUSIONS

11.1. ACHIEVEMENTS

Spiders produce a variety of high-performance structural fibres with mechanical properties unmatched in the natural world and comparable with the very best synthetic fibres produced by modern technology. The remarkable combination of strength and deformability in spider silk makes the molecular origin of these properties very interesting to material scientists. As a result, there is a considerable interest in the design of these materials as a guide to the commercial production of protein-based fibrous biopolymers through genetic engineering. To understand the design of silks, we must understand the correlation between structure and properties. The aim of this thesis is to help in this approach by studying the structure-property relations of two types of spider silks in comparison to silkworm silks.

Araneus diadematus was selected as spider species since most of the known structural information is based on information of the spider species *Nephila clavipes* whereas knowledge of function is based on experiments with *A. diadematus* spider silk. Furthermore, apart from the most investigated dragline spider silk, the main focus was on the egg sac spider silk because of limited research available.

To help in obtaining structural aspects of the spider silks, a comparison was made with the silk of the domestic silkworm *Bombyx mori* and silk of the wild silkworm, *Antheraea pernyi*, better known as Tussah silk. The structure of *B. mori* silk is dominated by the antiparallel β-sheet structure, whereas in Tussah silk also α-helical structures are known to be present.

Uni-axial tensile experiments were performed, apart from the silkworm silks, on dragline and egg sac spider silks of different spider species. It was concluded that the egg sac spider silks show a completely different stress-strain behaviour than the dragline silks. The tensile behaviour of the egg sac spider silks is characterized by a flat plastic region resulting in a comparable strain value and a tenacity value that is 2 to 3 times lower than those for the *Araneus* dragline silks. The tensile behaviour of the *Araneus* dragline silks shows more similarities with that of the silkworm silks despite of its different function in nature. Unfortunately, the variability within the results for the dragline silk of the *A. diadematus* spider was much higher than those for the egg sac silk. Also the extreme fineness of the dragline spider silk resulted in some difficulties in the measurement. So, it was decided to focus further on the egg sac spider silk.

The stress-strain curve of the egg sac spider silk was further successfully simulated by means of the standard linear solid (SLS) model. A cluster analysis on the parameters of the SLS model for five different egg sacs resulted in the detection of two significantly different fibre populations. These fibre populations are associated to the different layers in the egg sac, although also the origin, secreted by a different tubuliform spinning gland, can be an explanation.

Silks are semi-crystalline and visco-elastic materials. The visco-elastic nature leads to time-dependent phenomena such as an effect of strain rate or testing speed, hysteresis and creep behaviour.

The resilience and elastic recovery of dragline spider silk was found to be significantly better than those of egg sac spider silk and the silkworm silks, in spite of its higher variability. Dragline spider silk shows a much smaller permanent deformation and less energy dissipation in a loading-unloading cycle. The results of resilience and elastic recovery in function of the preset strain showed that the behaviour of egg sac and Tussah silk was not significantly different up to strains of 10%. It is suggested that in Tussah silks some structures, probably extended β-sheets, are present responsible for strain hardening which are lacking in egg sac spider silk. The resilience and elastic recovery curves for *B. mori* silk exceeded more quickly their constant value. This result is suggested to be explained by the lack of helical structures in *B. mori* silk.

As far as the creep behaviour is concerned, egg sac spider silk shows a much higher creep than dragline spider silk and the silkworm silks. It is suggested that the lower crystalline content, the twist observed in the β-sheet crystals and the higher content of β-turns are responsible for it.

The effect of testing speed was investigated for dragline and egg sac spider silk. The results for dragline silks showed too much variability in stress-strain behaviour for making any conclusion. For egg sac spider silk, it is proved that the tenacity logarithmically increases with testing speed, whereas the post-modulus linearly decreases with testing speed. With respect to the initial modulus, this parameter increased significantly up to a speed of 20 mm/min, after which it decreases again. It is suggested that at lower speeds, a certain amount of plastic or unrecoverable deformation takes place during the time of the test itself, which can not occur with high testing speeds. When the stress-strain behaviour is simulated by means of the SLS model, higher testing speeds result in a higher level of the plastic or hardening

region, in a shift of the yield region to higher strain values and in a more horizontal behaviour of the hardening region. A speed of 20 mm/min could be considered as a saturation point, at higher speeds the effect of speed decreases.

The amino acid composition was determined for the silkworm silks and dragline and egg sac silk of different spider species. In all cases, the small amino acids glycine, alanine and serine were the most abundant ones, reaching 85 % of the total composition for the silkworm silks and about 60 % for the spider silks. Although the total amount of these amino acids is reported to be representative for the crystallization potential of proteins, this amount could only explain the higher stiffness and strength of the *N. clavipes* draglines. In the case of the other silks, it seems that a comparable crystallization potential does not evidently result in a higher strength. The amino acid composition of *Araneus* dragline silks was similar and characterized by high amounts of glycine (24-27%), alanine (21-23%), proline (13-18%) and glutamic acid or glutamine (11-14%). The different stress-strain behaviour of *N. clavipes* dragline silk could partly be explained by its different amino acid composition: a higher amount of glycine (37%) and arginine (8% vs. 1-2%), a lower amount of proline (4%) and tyrosine (3% vs. 5%).

When the amino acid composition of dragline is compared to that of egg sac spider silk, alanine, serine and amino acids with large side chains, such as valine, leucine, threonine and phenylalanine, are more abundant in the egg sac fibres, whereas glycine, tyrosine, glutamine and/or glutamic acid and proline are more available in draglines. The presence of a high fraction of amino acids with a large side chain explains the clearly lower strength of egg sac spider silk compared to the other silks since these large residues prevent the formation of compact β-sheet crystals. The amino acid composition of the silkworm silks mostly differs from that of the spider silks in its lower fraction of Glx (glutamine or glutamic acid).

The secondary structure of the different silks was investigated by means of vibrational spectroscopy and nuclear magnetic resonance (NMR) spectroscopy. In these techniques, in the conformation sensitive regions certain maxima can be assigned to a different secondary structure. Moreover, from NMR spectroscopy the local secondary structure of the most important amino acids (alanine, glycine, serine) can be deduced.

Different infrared techniques, in transmission as well as in reflection mode, and Raman spectroscopy were tried. Raman spectroscopy was not found to be a reliable technique to estimate secondary structure because of fluorescence of the silks. The spectra recorded in the infrared transmission mode were too low in resolution, especially in the conformation sensitive regions. The best spectra were obtained by means of the less known Diffuse Reflection Infrared spectroscopy (DRIFTS) and Attenuated Total Reflection (ATR-FTIR) spectroscopy. However, for both techniques, shifts of the maxima in some regions were observed in the spectra compared to literature on infrared spectroscopy of proteins and silks. Moreover, the DRIFT spectra show a much higher resolving power compared to ATR-FTIR spectroscopy. Some experiments were done to find a reason for the shifts in the DRIFT spectra, however none of the studied factors could explain them. It is supposed that specular reflection played a role in this. It is suggested that this newer spectroscopic sampling technique could also be useful for detecting the secondary structure of other solid proteins.

In order to justify the assignment to secondary structure, a conformational transition of silkworm silk fibroins was performed. For *B. mori* and Tussah silk, it was tried to obtain amorphous silk by dissolution of the silk, followed by dialysis of the salt and freeze-drying. From literature, it is known that by treating these regenerated silk fibroins with a methanol solution, a transition takes place from random coil and/or helical structures to β-sheet structures. The conformational transition of the regenerated samples was confirmed by NMR spectroscopy and differential scanning calorimetry (DSC). From the DRIFTS analysis, we could conclude that it is a valuable technique for a qualitative evaluation of the secondary structure, resulting in more details than with other infrared modes. In the conformation-sensitive regions, absorption maxima are associated to secondary structure, such as β-sheet, α-helix, β-turn and random coil conformations. Furthermore, a link between wave number and the length of the β-sheet structures is suggested. However, some uncertainty remains with respect to the presence of α-helical structures.

It is suggested that also an identification of the Silk III structure, a third structure found at the air-water interface of *B. mori* silk, is possible with DRIFTS.

For a quantitative evaluation of the secondary structure, however, more research will be required in order to reduce the degrees of freedom in the curve-fitting procedure.

The DRIFT spectra of the different silks differentiate substantially. The generally known structure of *B. mori* and Tussah silk was confirmed from different conformation-sensitive regions. For *B. mori*, β-sheet and random coil structures are clearly detected, whereas for Tussah silk also features of the α-helix structure were observed. This difference allowed the identification of the secondary structure of the spider silks.

Absorption peaks in the conformation-sensitive regions further revealed that egg sac spider silk of the *A. diadematus* spider shows only limited amounts of, probably small, β-sheet structures and is dominated by a random coil and helical conformation, apart from β-turn structures. The presence of β-turn structures are suggested that do not take part in extended β-sheet structures. The linked β-turns possibly form helical structures, such as a β-spiral, which could explain the twist in the β-sheet crystals, as observed in literature.

The investigated dragline spider silk seems to be dominated by β-turn structures as well, although also evidence of helical structures was found.

The NMR spectroscopy gave some complementary information about the secondary structure of egg sac spider silk. It was concluded that the alanine residues, as well as the serine residues, are involved in a β-sheet related conformation. Also a high amount of β-turn structures, as detected in FT-IR spectroscopy, is confirmed.

Finally, the thermal behaviour of the silks was studied with thermogravimetry (TGA) and a thermal mechanical analysis (TMA).

From the TGA experiments, it could be concluded that the thermal degradation temperature of Tussah and egg sac spider silk is higher than for the other silks studied. A 20% weight loss was reached for Tussah and egg sac spider silk at about 300°C, whereas for *B. mori* and dragline spider silk this temperature of thermo-

oxidative stability was only 280°C. All silks show a two-phase degradation behaviour.

The thermal stability when strained, as found by TMA, is higher for *B. mori* and egg sac spider silk. It is suggested that the lower α-helical content explains this behaviour. The presence of an α-helical structure is observed as a shrinkage in the TMA curves of Tussah and dragline spider silk.

The relatively higher thermal stability of egg sac spider silk is suggested to be due to the higher fraction of smaller β-sheets, with adjacent chains more tightly aggregated within the amorphous regions and stabilized by an intermolecular network of hydrogen bonds. These features lead to a restriction of the thermally induced molecular motion of the fibroin chains, as demonstrated by the relatively high thermal stability.

To conclude, it is clear that a major part of the physical properties, such as stress-strain behaviour, creep, elastic behaviour and thermal properties can be explained by the amino acid composition of the silks. The high fraction of residues with a larger side chain prevents in egg sac spider silk the growth of the β-sheet crystals resulting in a less crystalline structure, which in turn explains the lower strength of egg sac spider silk. Also the flat post-yield behaviour, the high creep and low resilience is suggested to be caused by these large residues and the presence of β-turns in extended amorphous regions. As a consequence, the amorphous phase is characterized by a high number of intramolecular interactions: hydrogen, hydrophobic and electrostatic bonds, resulting in a higher plastic deformation before fibre break.

The structural model of egg sac spider silk is suggested to be composed of small regions of β-sheet structures forming small crystallites embedded in extended amorphous domains. The amorphous fraction is dominated by β-turn structures that possibly form linked helical structures. Furthermore, on the basis of the fractographic analysis a non-microfibrillar skin-core structure is suggested.

11.2. OUTLOOK

In order to get a more detailed structural model for the spider silks, further research is required on, among others, the orientation, quantification of the secondary structure and determination of the size of the crystals. The possible quantification of secondary structure, based on DRIFT spectra, will require recording spectra of solid proteins with a well-known structure (e.g. deduced with other reliable techniques). Furthermore, subtraction of water vapour absorption should be considered. With respect to orientation, polarization studies may be useful. X-ray diffraction (SAXS) or Atomic Force Microscopy (AFM) studies could reveal information about the size of the nanofibrils and/or crystals.

However, it is expected that this research on silk proteins is helpful in the characterization of other solid proteins, in the selection of amino acid sequences for the production of protein-based polymers and in finding an explanation for the disappointing results of artificial spider silk.

Annex

VIBRATIONAL SPECTROSCOPY

The first methods that were used to study the secondary structure of the silks are vibrational spectroscopy, especially FT-IR and FT-Raman spectroscopy.

FT-Raman and FT-IR spectroscopy are powerful tools for studying proteins at a molecular level, because they provide information on the peptide backbone structure, as well as on conformational transitions and changes in the side chain environment.

Since the determination of the structure in this PhD thesis is mainly based on these techniques, in this annex the principles of both spectroscopic techniques, sampling methods and differences between both are discussed.

Furthermore, the significance of vibrational spectroscopy (FT-IR and FT-Raman) for proteins is discussed. Moreover, the assignments of absorption maxima to a certain secondary structure are given that will be helpful in deducing the secondary structure for the silk proteins studied.

1. INTRODUCTION TO VIBRATIONAL SPECTROSCOPY

Molecules are atoms kept together by chemical bonds. In a first approximation, the force required to realise a small change of bond length or a small change in angle between two bonds is proportional to the produced change. Also the torsion required to turn a part of the molecule over a small angle around the bond in relation to the rest of the molecule is approximately proportional with the torsion angle. As a result, a molecule consists of a series coupled harmonic oscillators and when they are brought out of balance, the molecule will vibrate in such a way that the movement can be considered as a superposition of a number of single harmonic vibrations. These vibration modes can be studied with infrared and Raman spectroscopy.

A vibrating molecule can interact in two ways with electromagnetic radiation with suitable frequency [Bower & Maddams 1992]:

1) If the radiation has the same frequency as one of the normal vibrational modes, this radiation is possibly absorbed by the molecule. Infrared (IR) spectroscopy is based on this interaction.

2) The radiation can also be scattered, with or without frequency change. Scattering without frequency change is called Rayleigh scattering, the one with frequency change is called Raman scattering. Raman spectroscopy is based on the latter type of scattering.

Generally, some but not all vibrational modes of a certain type of molecule can be observed by infrared or Raman spectroscopy. The vibrational modes are infrared and/or Raman active, depending on the symmetry of the particular molecule under consideration through the selection rules.

Raman and infrared spectroscopy provide complementary information concerning the structure and conformation of biopolymers [Painter & Koenig 1975].

2. INFRARED (IR) SPECTROSCOPY

2.1. INFRARED SPECTRAL REGIONS

The electromagnetic radiation can be split up in different regions. The energy of most molecular vibrations corresponds to that of the infrared region of the electromagnetic spectrum. The complete IR region extends over the region 12500 to 10 cm^{-1}. The infrared region can be subdivided into the near-, middle- and far-infrared radiation [Skoog 1985]. The region between 12800 and 4000 cm^{-1} is called the near IR region. The middle IR region is the region between 4000 and 200 cm^{-1}. The most characteristic absorptions are taking place in this region. Finally, the far IR region is situated between 200 and 10 cm^{-1}. The range in an infrared spectrum used mostly is the region between 4000 and 400 cm^{-1} [Skoog 1985].

2.2. SELECTION RULES

In order to absorb infrared radiation, a molecule must undergo a net change in dipole moment as a consequence of its vibrational or rotational motion [Skoog 1985]. Only under these circumstances can the alternating electrical field of the radiation interact with the molecule and cause changes in the amplitude of one of its motions. The dipole moment is determined by the magnitude of the charge difference and the distance between the two centers of charge. As a diatomic molecule, such as hydrogen chloride, vibrates longitudinally, a regular fluctuation in dipole moment occurs, and a field is established which can interact with the electrical field associated with radiation. If the frequency of the radiation matches a natural vibrational frequency of the molecule, there occurs a net transfer of energy that results in a change in the amplitude of the molecular vibration; absorption of the radiation is the consequence. Similarly, the rotation of asymmetric molecules around their centers of mass results in a periodic dipole fluctuation; again, interaction with radiation is possible. No net change in dipole moment occurs during the vibration or rotation of homonuclear species such as O_2, N_2 or Cl_2; consequently, such compounds cannot absorb in the infrared.

The dipole moment is a vector quantity and has components in the x, y, z direction, where z is conventionally taken as the polymer backbone axis [Painter & Koenig 1975]. Any vibration that transforms under the symmetry operations of the polymer in the manner of a unit vector in the x, y or z direction will be infrared active. Vibrations that transform like the z unit vector are said to have parallel polarization since they absorb radiation strongest when the electric vector of the radiation lies parallel to the z or chain axis. Similarly, vibrations that transform according to the x and y unit vectors have perpendicular polarization. By measuring infrared band intensities of oriented polymer samples with perpendicular and parallel polarized infrared radiation, the symmetry species to which the band belongs may be assigned; in the case of fibrous proteins the conformation of the polypeptide backbone may be determined.

2.3. TYPES OF MOLECULAR VIBRATIONS

The relative positions of atoms in a molecule are not exactly fixed but instead fluctuate continuously as a consequence of a multitude of different types of vibrations [Skoog 1985]. For a simple diatomic or triatomic molecule, it is easy to define the number and nature of such vibrations and relate these to energies of absorption. An analysis of this kind becomes difficult if not impossible for molecules made up of several atoms, not only because of the large number of vibrating centers, but also because interactions among several centers occur and must be taken into account. Vibrations fall into the basic categories of stretching and bending. A stretching vibration involves a continuous change in the interatomic distance along the axis of the bond between two atoms. Bending vibrations are characterized by a change in the angle between two bonds and are of four types: scissoring or bending, rocking, wagging and twisting. The various types of vibrations of the methylene group are shown schematically in Figure 1.

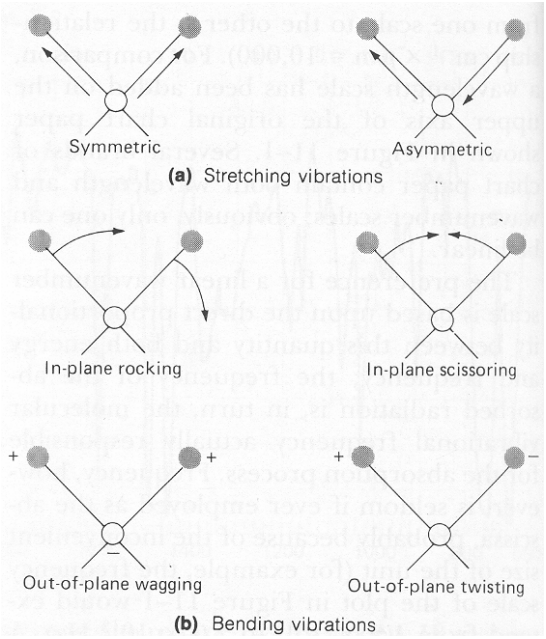

Figure 1 - Types of molecular vibrations (+ indicates motion from the page toward the reader; - indicates motion away from the reader) [Skoog 1985]

The IR spectrum can be split into two complementary regions [Williams & Fleming 1995]:

1) the region above 1500 cm^{-1} showing absorption bands assignable to a number of functional groups and
2) the region below 1500 cm^{-1} that is characteristic of the compound in question, this is also called the fingerprint region.

Figure 2 gives an overview of the regions in which the most important functional groups absorb.

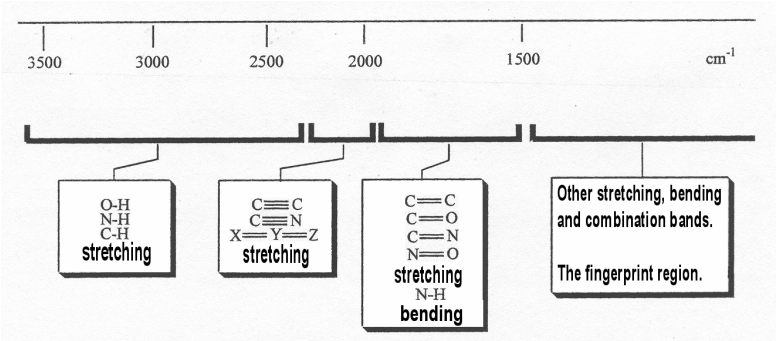

Figure 2 - Absorption wave numbers of the most important functional groups

The stretching vibrations of single bonds to hydrogen give rise to absorption at the high wave number end of the spectrum as a result of the low mass of the hydrogen

atom [Williams & Fleming 1995]. Thereafter, the order of stretching wave numbers follows the order: triple bonds at higher wave number than double bonds and double bonds higher than single bonds. On the whole, the greater the strength of the bond between two similar atoms, the higher the wave number of the vibration will be. Bending vibrations are of much lower wave number and usually appear in the fingerprint region below 1500 cm^{-1}. An exception is the N-H bending vibration which appears around 1600 cm^{-1}.

2.4. THE FOURIER TRANSFORM IR SPECTROMETER

2.4.1. Introduction

There are two types of IR spectrometers for the study of polymers

1) The dispersive IR spectrometer. The radiation of an IR source is monochromated; the monochromatic beam interacts with the sample and the non-absorbed fraction is measured. A spectrum results from a number of measurements at different wave numbers.

2) The Fourier transform IR (FT-IR) spectrometer. Polychromatic IR radiation interacts with the sample after passing an interferometer. A spectrum results from processing the interferogram with an algorithm.

2.4.2. Principle

Light covering the complete wave number range (4000-400 cm^{-1}), is split into two beams [Williams & Fleming 1995]. Either one beam is passed through the sample, or both are passed, but one beam is made to traverse a longer path than the other. Recombination of the two beams produces an interference pattern that is the sum of all the interference patterns created by each wavelength in the beam. By systematically changing the difference in the two paths, the interference patterns change to produce a detected signal varying with optical path difference. This pattern is known as the interferogram. Fourier transformation of the interferogram converts it into a plot of absorption against wave number which resembles the usual spectrum obtained by the traditional method.

The FT-IR spectrometer is based on the Michelson interferometer [Koenig 1992], its set-up is shown in Figure 3.

A parallel light beam covering the whole IR range is sent from the source to the interferometer consisting of 2 mirrors (M_1 and M_2) and a beam splitter (Figure 3). The beam splitter is a plate of IR transparent material (usually KBr) coated with germanium so that exactly 50% of the incident IR radiation intensity is reflected to mirror M_2. The other 50% is transmitted to mirror M_1. These two beams are reflected by their respective mirrors back to the beam splitter where they merge again. Mirror 1 is movable so that an optical path length difference can be created between the two beams.

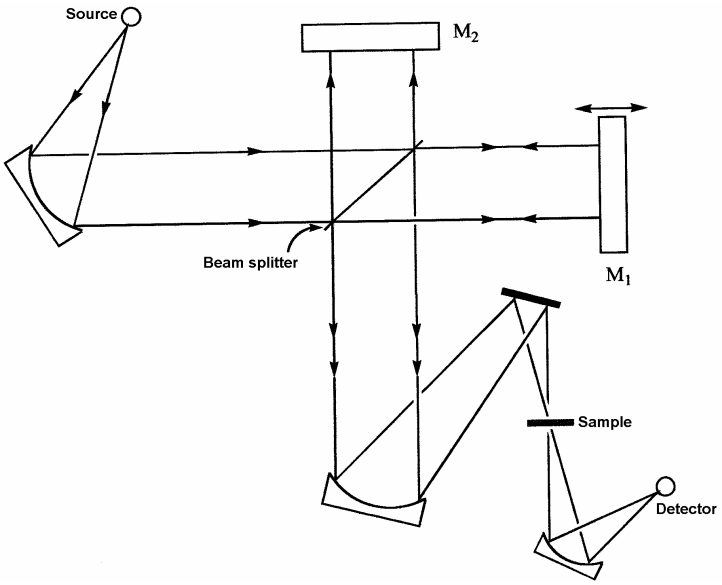

Figure 3 - Instrument set-up of a FT-IR spectrometer [Bower & Maddams 1992]

The merged beam is then sent through the sample, which partly absorbs it, and finally reaches the detector. For transmission measurements, the intensity of the light decreases according to the law of "Beer" [Bower & Maddams 1992]:

$$I = I_0 \, 10^{-abc} \qquad (1)$$

With : a: absorptivity, i.o.w. the specific absorption power of a certain component in the sample

c: concentration of this component in the sample

b: distance traveled by the light in the sample

The ratio I/I_0 is called the transmission T of the thickness b. The amount $A = \log I_0/I = abc$ is called the absorbance of the thickness b [Bower & Maddams 1992].

2.4.3. Advantages of FT-IR

Because it is not necessary to scan each wave number successively, a complete spectrum is obtained in a relatively short time. Because it is not dependent upon a slit and a prism or grating, high resolution in FT-IR is easier to obtain without sacrificing sensitivity. FT-IR is especially useful for examining small samples (several scans can be added together) and for recording the spectrum of compounds produced in the outflow of a chromatograph [Williams & Fleming 1995].

2.5. IR SAMPLING TECHNIQUES

Over the years, several IR analyzing techniques have been developed. The purpose of new techniques is mostly to obtain accurate high quality spectra, on the one hand, and to facilitate and shorten the sample preparation, on the other hand.

The radiation of the incident IR beam is partly or not absorbed, depending on the wave number. The remainder of the radiation intensity can be reflected, scattered or just transmitted by the sample. Mathematically this can be represented as follows:

$$I_0 = I_a + I_t + I_r + I_s \quad (2)$$

With I_0 : the intensity of the incident beam

I_a : the intensity of the absorbed radiation

I_t : the intensity of the transmitted radiation

I_r : the intensity of the reflected radiation

I_s : the intensity of the scattered radiation

Either the reflected, scattered, or transmitted radiation can be used to obtain the spectrum of a sample. Each of these types of radiation is associated to a certain analyzing technique in which the direction of the incident beam in relation to the sample is determinative for the dominating type of radiation. The IR spectroscopic analyzing techniques can be subdivided into two groups:

- Transmission techniques
- Reflection techniques, further subdivided into:
  - Diffuse reflection (DRIFTS)
  - Attenuated total reflection (ATR)

Vibrational spectra can also be obtained using photo-acoustic and emission spectroscopy [Koenig 1992, Coleman 1993, Smith 1996], but since they are not applied in this doctoral study, they will not be discussed further.

2.5.1. Transmission techniques

2.5.1.1. Principle

This technique, where the IR beam passes directly through the sample, is the most popular way to obtain IR spectra. The incident beam makes an angle of 90° with the sample. As a result, almost no reflection occurs.

The percentage transmission is measured as function of the wave number. Afterwards, software allows the transformation into an absorbance spectrum that is often more easily interpreted. This transformation is based on the following equation:

$$A = \log I_0 / I = \log 1/T \quad (3)$$

With: A: absorbance value

I_0 : intensity of the incident beam

I: intensity after passing the sample

T: transmission value of the sample

Further, on the basis of the law of Beer the following relation exists between the absorbance and the concentration c, which makes a link between the peak height and the concentration [Smith 1996]:

$$A = abc \quad (4)$$

With: a: absorptivity, that is, the specific absorption power of a certain component in the sample

b: distance traveled by the radiation in the sample

c: concentration of the component in the sample

2.5.1.2. Sampling techniques

For transmission measurement of solids, pressed KBr-disks are often used. KBr is an IR transparent material that is used as support and diluant. Firstly, the material is grinded to a fine powder and dispersed into a matrix. Between 1 and 3 mg of ground material needs to be mixed thoroughly with about 350 mg of ground KBr. The mixture is then transferred to a die and pressed at around 12000 psi for 1 to 2 minutes. Re-crystallization of the KBr results in a clear glassy disk about 1 mm thick. This disk is then inserted into the sample holder of the FT-IR instrument.

Liquids are traditionally analyzed as thin films in cells, a cell consisting of two IR transparent windows. A Teflon© spacer is generally used to produce a film of the desired thickness or pathlength. The sample is then injected in this cell.

For samples with very restricted dimensions, such as fibres, IR spectra can be obtained by use of an FT-IR optical bench coupled with a microscope. After positioning of the sample on the microscope, the IR beam is passed through the microscope instead of a visible light beam [Perkin Elmer 1998a].

Often transmission studies of fibres suffer from inevitable reproducibility issues given the complexity of sample preparation and presentation.

2.5.2. Diffuse reflectance infrared spectroscopy

2.5.2.1. Introduction

Diffuse reflectance infrared spectroscopy (DRIFTS) was originally developed for UV-VIS spectroscopic inspection of materials used in the paper and textiles industries. It was subsequently applied as a general method for IR analysis of rough surfaced materials and powders. Today, many of those samples are examined by ATR due to more straightforward sample handling and data interpretation.

Unlike internal (ATR) or specular reflection, diffuse reflection spectroscopy lacks an exact theoretical description [Milosevic & Berets 2002]. This is due to the

complexity of the problem rather than a lack of understanding the fundamental underlying mechanisms and phenomena. The complexity of the exact description stems from the fact that powders (and fibres) are inhomogeneous on a scale comparable to the wavelength of light. This results in scattering in addition to absorption when the incident radiation interacts with the medium. Scattering alters the effective path length of the light through the medium. This diffuse reflection depends not only on the properties that govern the interaction of light with materials but also the scattering characteristics of a particular sample. Due to the nature of inhomogeneous materials, only approximate theoretical descriptions of diffuse reflectance exist. Of these, The Kubelka-Munk model is the most widely accepted.

2.5.2.2. Principle

Diffuse reflection occurs when the incident angle of the IR beam is fixed whereas the angles of the reflected radiation vary between -90° and 90° relative to the normal to the sample surface. Since the sample (powder or fibre) is internally inhomogeneous, the radiation penetrating into the sample scatters from numerous points and thus the reflected light leaves the sample in different directions. This is the key to the theoretical description of diffuse reflection [Milosevic & Berets 2002]. Figure 4 shows the difference between the internal or specular (as in ATR) reflected light and the diffusely reflected radiation.

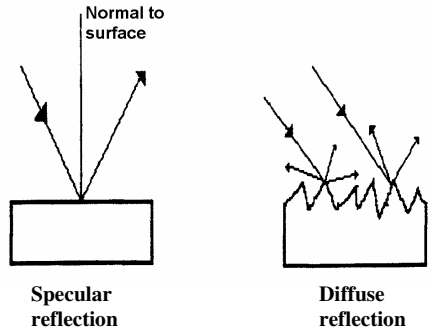

Figure 4 - Difference between specular and diffuse reflection

The DRIFT accessoire in the Perkin Elmer GX 2000 FT-IR instrument that is used in the experiments in this thesis, is shown in Figure 5 [Perkin Elmer 1996]. As can be seen, an ellipsoid mirror is used to detect the diffuse reflection.

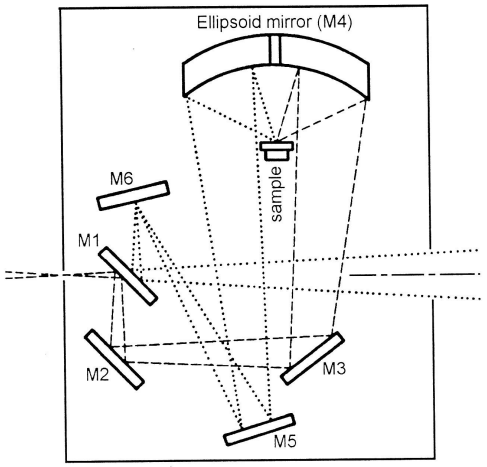

Figure 5 – The DRIFT accessoire in the Perkin Elmer GX 2000

The Kubelka-Munk model assumes that the scattering process can be described in a similar manner to the absorption process. Instead of describing diffuse reflection using the amplitude of radiation, it is described by the intensity of light propagating through the randomly inhomogeneous medium. After some calculations, Kubelka and Munk found the following relation between the concentration and peak heights, known as the Kubelka-Munk transform [Smith 1998, Coleman 1993, Milosevic & Berets 2002]:

$$KM = \frac{(1 - R_\infty)^2}{2 \cdot R_\infty} = \frac{k}{s} \qquad (5)$$

with KM: ordinate value in Kubelka-Munk units

R_∞: reflection of an infinite thick sample (infinite in relation to the penetration depth of the IR beam)

k: absorption coefficient

s: scattering factor

The absorption coefficient is defined as follows [Smith 1998, Coleman 1993]:

$$k = 2.303\ a\ c \qquad (6)$$

With a: absorptivity

c: concentration

Substituting Equation (6) in Equation (5) results in:

$$KM = \frac{2.303 \cdot a \cdot c}{s} \qquad (7)$$

In practice, the R_∞ reflection values are measured for the different wave numbers and by means of Equation (5) the DRIFTS spectrum is converted with suitable

software to the so-called Kubelka-Munk spectrum (expressed in Kubelka-Munk units).

The scattering factor s is amongst others dependent on the refractive index, particle size and packing density of the sample [Milosevic & Berets 2002], e.g. for powdered samples. In case of fabrics or yarns, the fabric structure and the degree of stretching also play a role.

The Kubelka-Munk model ignores the effects of front surface or specular reflectance. Front surface reflectance causes spectral anomalies, ranging from simple offsets in the measured values to severely distorted bands depending on the strength of the absorption index.

The penetration depth in diffuse reflection is defined as follows [Milosevic & Berets 2002]:

$$d_p = \frac{1}{\sqrt{k \cdot (k + 2 \cdot s)}} \tag{8}$$

Thus stronger scattering and absorption coefficients result in shorter penetration depths. This relationship between the penetration depth and the absorption coefficient is responsible for the extremely high sensitivity of diffuse reflectance to weak absorbers.

The Kubelka-Munk model incorporates several requirements regarding the sample. These assumptions [Milosevic & Berets 2002] are that the scattering coefficient is essentially constant throughout the sample (sample thoroughly mixed and homogeneous), the front surface reflectance is minimized, the sample is infinity thick (>> 3 × penetration depth), and the illumination of the sample is isotropic (readily handled by most spectrometers).

2.5.3. Attenuated total reflection (ATR)

2.5.3.1. Introduction

ATR techniques are well established for the direct measurement of solid and liquid samples without sample preparation. Traditionally IR spectrometers have been used to analyze solids, liquids and gases by means of transmitting the infrared radiation through the sample. Where the sample is in a liquid or solid form the intensity of the spectral features is determined by the thickness of the sample and typically this sample thickness cannot be more than a few tens of microns. The technique of ATR has in recent years revolutionized sold and extended to liquid sample analyses because it combats the most challenging aspects of infrared analyses, namely sample preparation and spectral reproducibility.

Principle

ATR spectroscopy uses the phenomenon of total internal reflection (Figure 6) [Perkin Elmer 2004]. An infrared beam is directed onto an optically dense crystal with a high refractive index at a certain angle. The internal reflectance creates an

evanescent wave that extends beyond the crystal surface into the sample (0.5-5 µm) held in contact with the crystal. The penetration depth depends on the material being used. The evanescent wave which is formed decays rapidly from the crystal surface, consequently, a good contact between the crystal and the sample must be maintained when performing ATR measurements. In regions of the IR spectrum where the sample absorbs energy, the evanescent wave will be attenuated or altered. The attenuated energy from each evanescent wave is passed back to the IR beam, which then exits the opposite end of the crystal and is passed to the detector in the IR spectrometer. The system then generates an infrared spectrum.

The penetration depth for ATR is a function of the wavelength, refractive index of the crystal being used and the angle of incident of the beam. It can be calculated with the following formula [Perkin Elmer 1998a]:

$$d_p = \frac{\lambda}{2 \cdot \pi \cdot n_1 \cdot \sqrt{\sin^2 \theta - n_{21}^2}} \qquad (9)$$

With: λ : the wavelength of the radiation

θ : the angle of incidence of the beam

n_{21}: the ratio of the refractive indices of the sample and the ATR crystal

Different materials can be used for the ATR crystal. The crystal used needs to have a higher refractive index than the sample being measured. Germanium, diamond, KRS-5 (thallium-bromoiodide), silicon and zinc selenide are some of the materials with a high refractive index that are used.

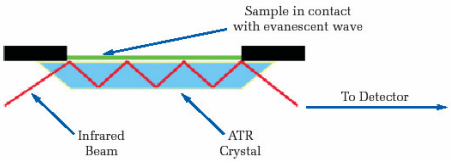

Figure 6 - A multiple reflection ATR system

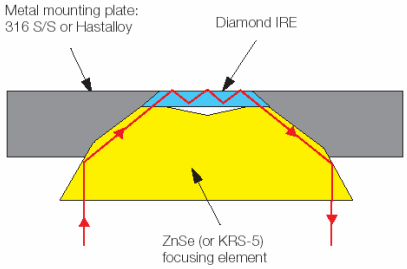

Figure 7 - Schematic of a universal-ATR top plate

The most common arrangement for an ATR is a top-mounted prism (Figure 7) that will allow the analysis of solids, liquids and pastes.

Attenuated total reflection (ATR), have been applied to study structural aspects of membrane proteins and to measure the orientation of membrane components through the use of polarized IR radiation [Arrondo & Goni 1999]. This sampling technique was developed by Harrick [1967] and later applied to membranes by Fringeli & Günthard [1981]. Various recent reviews have been published on the use of ATR in studying membrane protein structure and orientation [Goormaghtigh & Ruysschaert 1990, Axelsen & Citra 1996, Tamm & Tatulian 1997, Arrondo & Goni 1999]

3. RAMAN SPECTROSCOPY

3.1. INTRODUCTION

In 1928, the Indian physicist C.V. Raman discovered that the wavelength of a small fraction of the radiation scattered by certain molecules differs from that of the incident beam and furthermore that shifts in wavelength depend upon the chemical structure of the molecules responsible for the scattering [Skoog 1985].

The theory of Raman scattering shows that the phenomenon results from the same type of vibrational changes that are associated with infrared absorption [Skoog 1985]. Thus, the difference in wavelength between the incident and scattered radiation, also known as Raman shift, corresponds to wavelengths in the mid-infrared region. Indeed, the Raman scattering spectrum and infrared absorption spectrum for a given species often resemble one another quite closely. There are, however, enough differences between the kinds of groups that are infrared and Raman active to make the techniques complementary rather than competitive.

3.2. PRINCIPLE

Raman spectra are obtained by irradiating a sample with a powerful source of visible monochromatic radiation, often high-intensity gas or solid lasers are used [Skoog 1985]. During irradiation, the spectrum of the scattered radiation is measured at some angle (usually 90°) with a suitable visible region spectrometer.

The scattered radiation, observed at 90° to the incident beam, is of three types, namely Stokes, anti-Stokes, and Rayleigh [Skoog 1985], as shown in Figure 8. The latter, of which the wavelength is exactly that of the excitation source, is significantly more intense than either of the other two types. In Raman spectra, the abscissa is usually expressed in the Raman shift $\Delta\sigma$, which is defined as the difference in wave numbers (cm^{-1}) between the observed radiation and that of the source. The Rayleigh scattering is then observed at $\Delta\sigma = 0$. Superficially, the appearance of Raman spectral lines at lower energies (longer wavelengths) is analogous to the Stokes shifts found in a fluorescence experiment; for this reason, negative Raman shifts are called Stokes shifts. Shifts towards higher energies are termed anti-Stokes; quite generally, anti-Stokes lines are appreciably less intense than the corresponding Stokes lines. For this reason only, the Stokes part of a spectrum is generally used. Furthermore, the abscissa of the plot is often labeled simply frequency in cm^{-1} rather than wave number shift $\Delta\sigma$; the negative sign is also dispensed with. It is noteworthy that fluorescence may interfere seriously with the observation of Stokes shift but not with anti-Stokes. With fluorescing samples, anti-Stokes signals may, therefore, be more useful despite their lower intensities.

Raman spectroscopy is an inelastic scattering measurement [Painter & Koenig 1975]. The energy differences between the incident radiation and scattered photons equal the vibrational energy of the normal modes. Raman activity requires that the vibration induce a change in the molecular polarizability. The Raman scattered light from a random array of molecules is polarized for vibrations that are completely

symmetric. A symmetric vibration is one that is transformed into itself by operation of each symmetry element of the molecules. All other Raman active vibrations depolarize the scattered light.

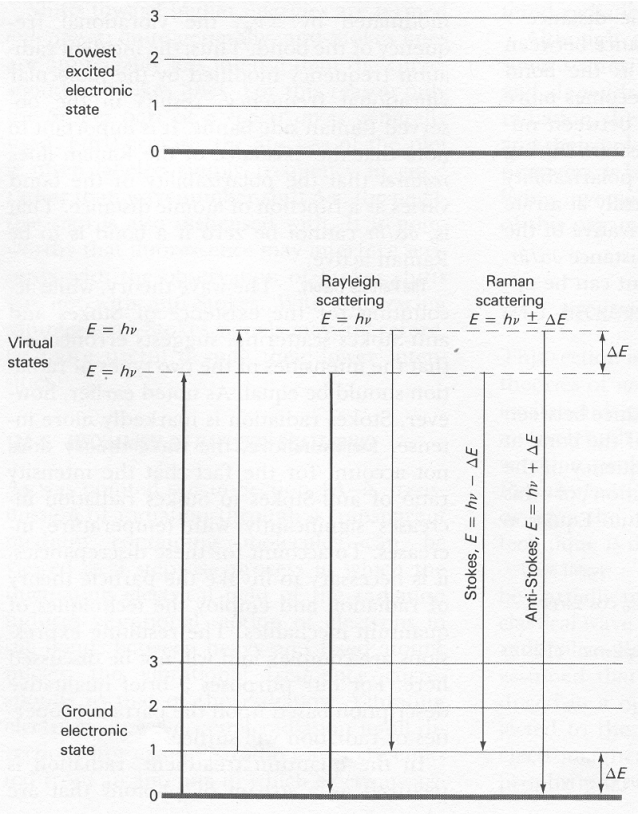

Figure 8 - Origin of Rayleigh and Raman scattering

3.3. THE FT-RAMAN SPECTROMETER

3.3.1. Introduction

Although the Raman effect was discovered in 1928 and the first Raman spectrum of a polymer was obtained in 1932, Raman spectroscopy took off only after laser sources became available in the sixties [Bower & Maddams 1992].

In analogy with IR-spectrometers, two types of instrument can be distinguished:

1) The dispersive Raman spectrometer
2) The Fourier Transform Raman spectrometer (FT-Raman)

The dispersive Raman spectrometer can be further subdivided in one- and multicanal spectrometers depending on the type of detector used. Such instrument was not used in this work. A further description can be found in literature [Koenig 1992].

3.3.2. Instrument set-up for f the FT-Raman spectrometer

In Raman spectroscopy, the intensity of the Stokes radiation that is emitted by the sample is plotted against the Raman shift, expressed in cm^{-1}. Figure 9 shows the way a Raman spectrum is obtained. The scattered radiation is collected parallel to the incident laser beam, i.o.w. the angle between the incident radiation and the scattered radiation equals 180°. This principle is also called "back scattering". Most modern Raman systems are designed to analyse light scattered either at 90° to the input direction, or at 180°, as shown in Figure 9.

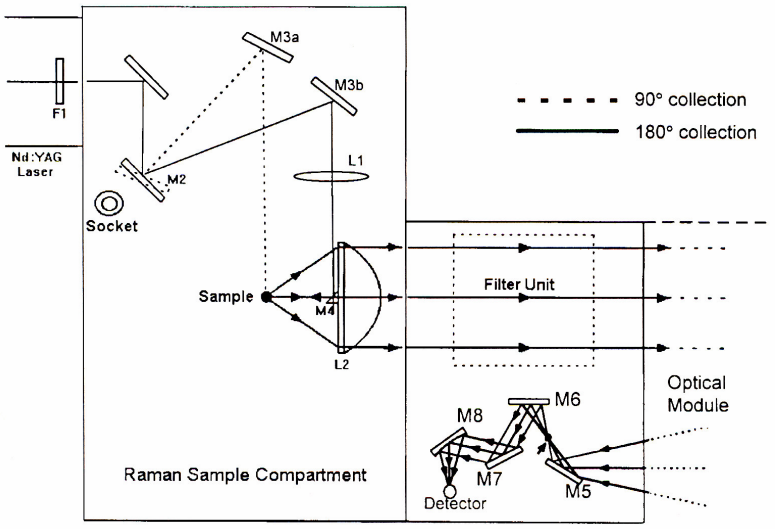

Figure 9 - Set-up for taking Raman spectra [Perkin Elmer 1998b]

Figure 9 shows a schematic representation of the FT-Raman instrument. The main components are [Koenig 1992]:

- A laser source: a Nd:YAG (yttrium aluminium garnet crystal doped with triply-ionized neodymium) laser with primary emission in the near IR at 1064 µm (9398 cm^{-1}). A second laser with emission in the visual region (often a He:Ne laser) is used to align the sample in the Nd:YAG beam and for the projection of the collected radiation on the entry port of the interferometer.
- An FT-interferometer equipped with a beam splitter and detector for the near-IR region.
- A sample room with scattering optics positioned to guide the Stokes radiation towards the entry aperture of the FT-interferometer.
- An optical filter to remove the very intense Rayleigh scattering.

3.3.3. Raman sampling techniques

As in FT-IR spectroscopy, apart from taking spectra of samples mixed into KBr disks, bundles of fibres or fabrics can be directly irradiated. The Raman spectrometer can also be coupled with a microscope, hence Raman microscopy.

4. POLARIZATION EFFECTS

The material that is investigated is often oriented, e.g. as a consequence of a stretching treatment. A partial alignment of the molecules in the drawing direction is then observed. As a result, the spectrum will not be independent of the orientation of the incident radiation's polarization vector [Bower & Maddams 1992, Koenig 1992]. This anisotropy manifests itself in the IR absorption or Raman spectrum because the contribution of each segment of the molecule to the total absorption of the sample at the frequency of a certain normal mode is dependent on the angle between the electrical field vector of the incident beam and the dipole moment vector of the molecular segment. Only the component of the electrical field parallel to the dipole moment has effect. The contribution will be maximal when electrical field and dipole moment are parallel, and zero when they are perpendicular to each other. The absorbance of the sample for radiation polarized parallel to the drawing direction, $A_{//}$, will be, for each peak, different than that for radiation polarized perpendicular to the drawing direction, $A_{\perp}$.

Practically, in IR spectroscopy a polarizer is introduced into the optical system and the spectra are studied with the sample oriented in different ways with respect to the polarizer.

In IR experiments, a dichroic ratio of the sample is defined as [Bower & Maddams 1992]:

$$D = A_{//} / A_{\perp} \tag{10}$$

In Raman experiments, the term depolarization ratio is more used and defined as:

$$p = \frac{I_{\perp}}{I_{//}} = \frac{I_{x(zx)y}}{I_{x(zz)y}} \tag{11}$$

The symbols outside the parentheses in Equation (11) are the directions of the incident (left) and scattered radiation (right). The symbols inside denote the polarization directions of the incident (left) and scattered light (right). The experimental set-up is often as depicted in Figure 10, in which Iij refers to the measured Raman intensity for scattered radiation polarized parallel to the i axis of the sample system, with incident radiation polarized parallel to the j axis. The depolarization ratio is readily obtained by inserting a Nicol analyzer prism between the sample and the monochromator. Spectra are then obtained with the prism oriented parallel with first the xz and then the xy plane shown.

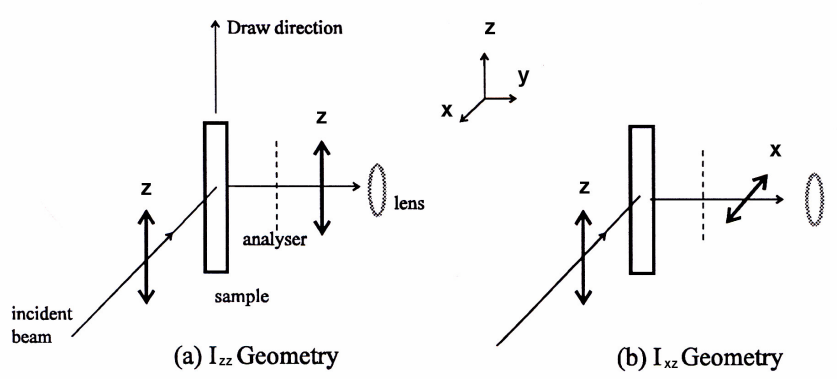

Figure 10 - Scattering geometry often employed in Raman studies of oriented samples

The measurement of dichroism can reveal useful information with respect to the orientation degree of polymer samples. For more details, it is referred to the literature [Bower & Maddams 1992, Koenig 1992, Siesler *et al*. 1996].

5. SPECTROSCOPY OF PROTEINS

5.1. INTRODUCTION

The amide group of proteins and polypeptides presents characteristic vibrational modes (Amide modes) that are sensitive to the protein conformation [Krimm & Bandekar 1986, Surewicz *et al.* 1993, Bramanti *et al.* 1997b].

However, two difficulties have mainly to be overcome in protein conformation studies [Bramanti *et al.* 1997a]:

(a) the recognition of the different spectral components of conformation-sensitive amide bands (particularly Amide I and III bands) due to the resulting overlap of bands originating from the different secondary structures, such as α-helix, β-sheets, turns, and random structure, which constitute different protein domains;

(b) the assignment of the amide component bands to different types of secondary structures. The assignment of Amide I components, which are very often used in secondary structure analysis, has been widely reported in literature [Krimm & Bandekar 1986, Byler & Susi 1986]. The Amide II and III regions, too, could be useful in protein conformation analysis, but due to the simultaneous absorptions of amino acid side chains in this region, only a qualitative analysis can be performed.

5.2. ADVANTAGES AND DISADVANTAGES

5.2.1. FT-IR spectroscopy

A particular feature [Haris & Chapman 1992] of the technique of FT-IR spectroscopy for the study of proteins is that high-quality spectra can be obtained quickly with relative ease with very small amounts of protein (1 mM or 100 µg) in a

variety of environments, such as aqueous solution, lipids, crystals, and organic solvents.

There are no problems associated with background fluorescence, light scattering or the size of the molecule [Haris & Chapman 1992].

5.2.2. FT-Raman spectroscopy

A disadvantage of Raman spectroscopy is that it is often difficult to obtain spectra of high signal-to-noise ratio because of interfering luminescence background [Haris & Chapman 1992]. It results in spectra with strong backgrounds and consequently poor spectral quality. Even FT-Raman spectroscopy can give spectra of proteins which are dominated by that of the chromophore rather than that of the protein itself [Bennett *et al.* 1990].

A further limitation of this technique is that of fluorescence, resulting in an increase of the baseline to the lower wave number side. Good quality spectra can not be obtained for many polymeric samples due to the curtain of fluorescence that hides them.

The advantage of Raman spectroscopy for biological applications [Xue 1994] are primarily the low interference of water, the availability of the low frequency modes which are highly sensitive to conformation and the sensitivity to homonuclear bonds such as S-S, N-N, C-C, C=C, and aromatic groupings. In addition, Raman spectroscopy is a non-invasive technique since usually no change in the sample or its environment occurs during structural characterization.

5.3. GENERAL FEATURES OF VIBRATIONAL SPECTRA

A broader band in spectra indicates that a wider distribution of hydrogen bond distances and geometries are available [Painter & Koenig 1975, Sun *et al.* 1997], in other words it reflects the uniformity of chain conformation.

Often a shift of the Amide I peak to lower frequencies is observed. Because the C=O stretching mode does not couple significantly to backbone vibrations, such shifts to lower frequencies are widely considered to be the “acid test” of the formation of hydrogen bonds [Painter & Koenig 1975, Sun *et al.* 1997]. In other words, this shift implies intermolecular interactions involving e.g carbonyl groups and the proton donors of the protein, such as the amide groups, the hydroxyl groups, and the amine groups, etc and thus stronger interactions than that of free carbonyl groups (not hydrogen bonded carbonyl groups).

5.4. AMIDE AND SKELETAL MODES OF POLYPEPTIDES

5.4.1. Introduction

Proteins consist of a kaleidoscope of possible amino acid sequences and this complicates the analysis of spectra. Detailed analysis of the vibrational spectra of macromolecules, especially homopolypeptides, has provided a deeper understanding

of structure and interactions in proteins and helped to establish structure-frequency correlations [Painter & Koenig 1975]. An important advance in this direction for proteins came with the determination of the peptide group in N-methylacetamide [Miyazawa *et al.* 1958], the simplest molecule containing a trans peptide group analogous to that in a polypeptide chain. This was followed by the characterisation of several specific amide vibrations in polypeptide systems [Miyazawa 1962, 1967]. Extensive use has been made of the spectra-structure correlations based on some of these amide modes, including attempts to determine secondary structure compositions in proteins.

The vibrational modes sensitive to backbone conformation are those of the amide group.

The peptide group, the structural repeat unit of proteins, gives up to 9 characteristic bands named Amide A, B, I, II ... VII. The most important amide bands for structural studies are visualized in Figure 11. The Amide A band (about 3500 cm^{-1}) and Amide B (about 3100 cm^{-1}) originate from a Fermi resonance between the first overtone of Amide II and the N-H stretching vibration. Amide I and Amide II bands are two major bands of the protein infrared spectrum. The Amide I band (between 1600 and 1700 cm^{-1}) is mainly associated with the C=O stretching vibration (70-85%) and is directly related to the backbone conformation. Amide II results from the N-H bending vibration (40-60%) and from the C-N stretching vibration (18-40%). This band is conformationally sensitive. Amide III and IV are very complex bands resulting from a mixture of several coordinate displacements. The out-of-plane motions are found in Amide V, VI and VIII.

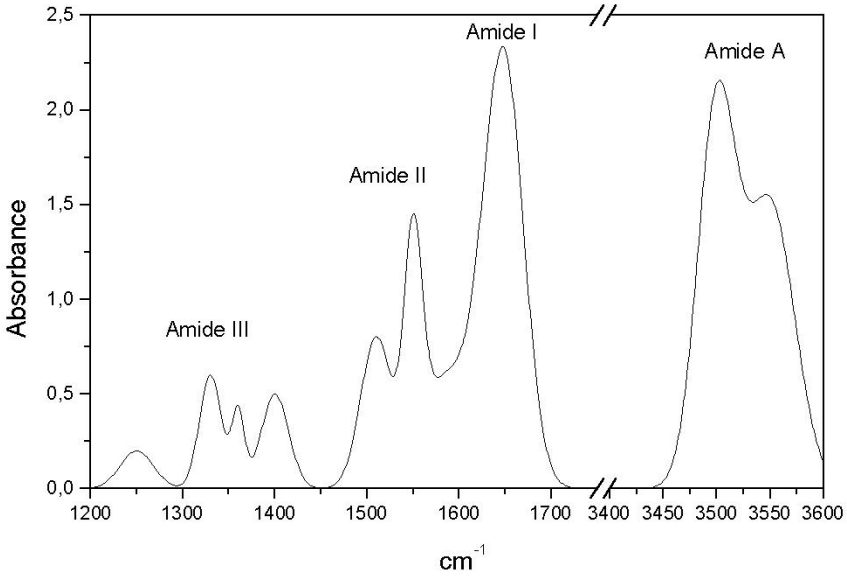

Figure 11- The Amide vibrations [Jabs 2000] seen by FT-IR

5.4.2. NH stretch mode

The Amide A mode is with more than 95% due to the N-H stretching vibration. This mode of vibration does not depend on the backbone conformation but is very sensitive to the strength of a hydrogen bond. It has wave numbers between 3225 and 3280 cm^{-1} for hydrogen bond lengths between 2.69 to 2.85 Å [Krimm & Bandekar 1986].

5.4.3. Amide I mode

The Amide I mode in polypeptides is primilary governed by the stretching vibrations of the C=O (70-85%) and C-N groups (10-20%), but it can also contain significant contributions from $C^{\alpha}CN$ deformation and minor contributions from $C^{\alpha}C$ stretching, CNC^{α} deformation, H^{α} bending, and NH in-plane bending [Krimm & Bandekar 1986].

It is the most intense absorption band in proteins. Its frequency is found in the range between 1600 and 1700 cm^{-1}. The Amide I absorption is essentially determined by the backbone conformation and independent of the amino acid sequence, its hydrophilic or hydrophobic properties and charge. The exact band position is determined by the backbone conformation and the hydrogen bonding pattern. Studies with model polypeptides have shown that there is a good correlation between the Amide I band frequency and the type of secondary structure present [Susi & Byler 1986]. Specific assignments to secondary structure are further discussed in section 5.6.

5.4.4. Amide II mode

Amide II is found in the 1510 and 1580 cm^{-1} region and it is more complex than Amide I. Amide II derives mainly from N-H in-plane bending (40-60% of the potential energy). The rest of the potential energy arises from the C-N (18-40%) and the C-C (about 10%) stretching vibrations and much smaller contributions from C=O in-plane bending and $N\text{-}C^{\alpha}$ stretching [Krimm & Bandekar 1986].

This mode is always strong in the IR spectrum and weak or absent in the Raman spectrum.

The Amide II region presents absorptions due both to the peptide bond formation in the different secondary structures and to the absorptions of amino acid side chains. The effect of amino acid side chains on the spectrum is discussed in section 5.4.9.

5.4.5. Amide III mode

Although the so-called Amide III mode has been described as the localized counterpart to Amide II, and contains N-H in-plane bending and C-N stretching in N-methylacetamide, the situation is in fact much more complex for the polypeptide chain [Krimm & Bandekar 1986]. The Amide III mode mainly consists of the in-phase combination of NH in-plane bending and CN stretching with contributions from C-C stretching and C=O in-plane bending [Bandekar 1992]. The main point is

that N-H in-plane bending is a significant component of a number of modes in the ~1400 to 1200 cm^{-1} region, mixing differently in different parts of this region and as a function of the side chain structure. It is therefore not possible to expect a simple general relationship between such a frequency and the backbone conformation [Hsu *et al.* 1976].

However, Amide III analysis is used as a complementary method to Amide I analysis in protein structural studies [Bramanti *et al.* 1997a]. The intensity of this band is lower than that of Amide I and II, and consequently it is preferred for the analysis of secondary structure in cases where Amide I has absorbance values higher than unity. A way of assigning Amide III components to the different secondary structures has been developed by Fu *et al.* [1994]. This is further discussed in section 5.6.

5.4.6. Skeletal stretch mode

In addition to the amide modes, all polypeptide chain conformations appear to have a characteristic skeletal stretching mode [Krimm & Bandekar 1986] that is relatively common origin and that give rise to a strong Raman and IR band, generally in the region 960-880 cm^{-1}. The counterpart skeletal stretch mode, found near 1100 cm^{-1} in N-methylacetamide, does not show up as a characteristic band in polypeptides; rather its NC^{α} stretching contribution is distributed broadly in the region ~1180-920 cm^{-1}, depending on the side chain composition.

For side chains longer than CH_3, there is mixing of backbone and side chain stretching motions that depends on the "extension" of the backbone [Krimm & Bandekar 1986]. However, the frequency of this mode can be an indicator of backbone conformation, as is observed for $(Glu)_n$ in different conformations [Sengupta & Krimm 1987].

5.4.7. Amide V mode

The Amide V mode is situated in the 600-750 cm^{-1} wave number range. This mode in N-methylacetamide consists of C-N twisting plus N-H out-of-plane bending, although C=O out-of-plane bending can make a small contribution. In the polypeptide chain, C-N twisting and N-H out-of-plane bending are also the main components but other coordinates contribute significantly. Thus, the frequency of this mode depends not only on the strength of the hydrogen bond, but also on the side chain structure [Krimm & Bandekar 1986].

5.4.8. Other Amide modes and skeletal deformations

For N-methylacetamide Krimm & Bandekar [1986] defined C=O in-plane bending (Amide IV), C=O out-of-plane bending (Amide VI), C-N twisting (Amide VII), and $C^{\alpha}CN$ deformation and CNC^{α} deformation as characteristic modes. Such a classification is too simplistic for a polypeptide chain, where many of these modes, together with $NC^{\alpha}C$ deformation and C^{β} bending, mix strongly and very differently depending on the main chain conformation and the side chain structure.

5.4.9. Contribution of side chain modes

Amino acid side chains, particularly those with aromatic groups, exhibit characteristic frequencies. Although the amino acid residue absorption can affect the protein secondary structure estimation, the knowledge of amino acid residues absorption is useful in probing the local environment of the group in the protein [Krimm & Bandekar 1986] or in the study of structural transitions in proteins upon variation of pH, temperature, or upon binding of ligands and substrates [Jabs 2000]. The Amide I and II modes are hardly affected by the side chains, but significant changes are seen for Amide III modes [Krimm & Bandekar 1986], as summarised in Table 1. Since we do not expect significant side chain contributions for amino acid residues that are present in the silks for less than 5%, this table is limited to the most important ones for the silks studied.

In the following, only the side chain vibrations of amino acids that are highly represented in the studied silks, are further discussed.

All hydrophobic amino acid side chains present characteristic absorptions in the 1500-1330 cm^{-1} range; in the same region, absorptions due to the COO^- symmetrical stretching of acid amino acids are present at 1410 and 1391 cm^{-1}.

For side chains composed of aliphatic groups, such as alanine, valine, leucine and isoleucine, the most prominent characteristic frequencies will be those associated with the CH_2 and CH_3 groups (Table 1). The CH_3 symmetric bending mode shows up as a characteristic IR band at 1375 ± 5 cm^{-1} for a single group, and as a doublet at 1395-1385 and 1365-1360 cm^{-1} when the CH_3 groups are bonded to the same C atom [Krimm & Bandekar 1986] .

The hydroxyl group of serine and threonine should have a characteristic deformation mode (see table) [Krimm & Bandekar 1986]. In β-$(Ser)_n$ it has been assigned to a Raman band at 1399 cm^{-1}. Since this mode is likely to be mixed with other backbone vibrations, it is probably a poor group frequency.

The COOH groups of aspartic and glutamic acids have characteristic frequencies depending on the state of ionization [Krimm & Bandekar 1986]. A shoulder at about 1620 cm^{-1} has been assigned to absorption of glutamine side chain amides [van Dijk *et al*. 1997] in cyclic peptides.

Table 1 - Characteristic side chain wave numbers [Krimm & Bandekar 1986] (s stretch, as antisymmetric stretch, ss symmetric stretch, b bend, ab antisymmetric bend, sb symmetric bend, d deformation, r rock)

		Wave number (cm^{-1})			
Residue	**Group**	**Raman**	**Infrared**	**Assignment**	**References**
Ala	CH_2	1465 ± 20	1465 ± 20	CH_2 b	Bellamy 1975
Val	CH_3	1450 ± 20	1450 ± 20	CH_3 ab	Bellamy 1975
Leu - Ile	CH_3		1375 ± 5	CH_3 sb	Bellamy 1975
Ser - Thr	OH	1399	1350-1250	OH d	Bellamy 1975
Asp	COOH	1720	1720	CO s	Sengupta & Krimm 1985
			1716±2	COOH s	Venyaminov & Kalnin 1990
			1713		Chirgadze *et al.* 1975, in heavy water
			1574±2	CO_2^- as	Venyaminov & Kalnin 1990
			1584		Chirgadze *et al.* 1975, in heavy water
Glu	COO^-		1712±2	COOH s	Venyaminov & Kalnin 1990
			1706		Chirgadze *et al.* 1975, in heavy water
			1560±3	CO_2^- as	Sengupta *et al.* 1984, Venyaminov & Kalnin 1990
			1567		Chirgadze *et al.* 1975, in heavy water
		1425	1415	CO_2^- ss	Sengupta & Krimm 1985
Asn	$CONH_2$	1650	1650	CO s	Bellamy 1975
			1648		Chirgadze *et al.* 1975, in heavy water
	CO		1678±3	CO s	Venyaminov & Kalnin 1990
	NH_2		1622±2	NH_2 b	Venyaminov & Kalnin 1990
Gln		1615	1615	NH_2 b	Naik & Krimm 1984
			1635		Chirgadze *et al.* 1975, in heavy water
	CO		1670±4	CO s	Venyaminov & Kalnin 1990
	NH_2		1610±4	NH_2 b	Venyaminov & Kalnin 1990
Arg	$CN_3H_5^+$		1673±3	$CN_3H_5^+$ as	Venyaminov & Kalnin 1990
			1633±3	$CN_3H_5^+$ ss	Venyaminov & Kalnin 1990
			1608		Chirgadze *et al* .1975, in heavy water
			1586		Chirgadze *et al.* 1975, in heavy water
Tyr	Phenyl	1600	1600	Ring	Lord & Yu 1970
		1590		Ring	Lord & Yu 1970
			1450	Ring	Lord & Yu 1970
		850, 830		Ring	Lord & Yu 1970

In tyrosine, the doublet at 850/830 cm^{-1} has been assigned to a Fermi resonance between a ring breathing mode and the overtone of an out-of-plane ring bending vibration [Siamwiza *et al.* 1975, Takeuchi *et al*. 1989]. The intensity ratio of the two components is related to the environment of the tyrosine side chain [Dunker *et al.* 1979] and in particular to the manner of hydrogen bonding of the phenolic OH group [Yu *et al.* 1973, Siamwiza *et al.* 1975]. If the tyrosine is "buried" the phenolic OH group acts as strong hydrogen bond donor to an electronegative acceptor (such as carboxyl oxygen) and the intensity of the 830 cm^{-1} band is higher than that of 850 cm^{-1} band. In fact, the $\mathbf{I_{850} / I_{830}}$ ratio achieves its minimum value of about 0.3. When Tyr is deprotonated at elevated pH to form a phenoxide ion, the $\mathbf{I_{850} / I_{830}}$ ratio is approximately 0.7. When the tyrosine residue is on the surface of a protein in aqueous solution ("exposed"), the phenolic OH group acts as both a donor and an acceptor of moderate or weak hydrogen bonds and the doublet bands exchange their intensities and the intensity ratio can reach a value of 1.25. Hence, the $R_{tyr} = I_{853}/I_{830}$ becomes a spectral marker of tyrosine hydrogen bonding strength. When the phenoxyl oxygen is the acceptor of a strong hydrogen bond from an electronegative group (such as lysyl NH3+ group) and does not participate in significant hydrogen bond donation, the $\mathbf{I_{850} / I_{830}}$ ratio approaches the presumed maximum value of 2.5 [Siamwiza *et al.* 1975].

The tyrosyl spectra-structure correlation of Siamwiza *et al.* [1975], as well as the proposed equations, does not explain satisfactorily the behaviour of nonglobular proteins. In fact, these authors based their proposal on the assumption that the phenoxyl group is always hydrogen bonded. The existing correlation for hydrogen bonded tyrosine residues was extended and refined by Thomas and coworkers [Wen *et al.* 1999, Thomas 2002]. They observed much higher intensity ratios than 2.5 (reaching even 6.7), and interpreted this as indicative of a highly hydrophobic local environment for each tyrosine residue, a state not represented in any previously studied globular protein.

This ratio is now also extensively used as an indicator of tyrosine interactions in non-globular (such as polypeptides), their assemblies and their degree of exposure to water [Siamwiza *et al.* 1975, Monti *et al.* 1998, Shao *et al.* 1999, Taddei *et al.* 2004, Rousseau *et al.* 2004].

However, Thomas [2002] looked for the characteristic Raman markers for tyrosine and proved that the peak at 827 cm^{-1} found in the spectra of p-cresol (in vapor phase) is not attributed to vibrations of the tyrosine residue but due to vibrations of the phenylalanine residues. p-Cresol in the vapor phase was investigated as a model for the non-hydrogen bonded state tyrosyl side chain. They found a Fermi doublet consisting of a very strong 839 cm^{-1} component and a very weak 812 cm^{-1} component ($I_2/I_1 = 6.7$) in lieu of the canonical Fermi doublet ($0.30 < I_2/I_1 < 2.5$) associated with phenoxyl hydrogen bonding [Siamwiza *et al.* 1975]. Because $I_2 >> I_1$ when phenoxyl hydrogen bonding is absent, it is suggested that the Raman signature diagnostic of the non-hydrogen bonded tyrosyl side chain appears in fact as a singlet rather than a doublet.

The results of any quantitative analysis may be significantly distorted by the contribution into the Amide I region of the spectrum of the amino acid side chain

absorption [Chirgadze *et al.* 1975, Surewicz *et al.* 1993]. Amino acids with by far the highest absorption coefficients in the 1600-1700 cm^{-1} region are asparagine and glutamine. Other residues that give rise to infrared bands overlapping the Amide I region include side chains of arginine and, to a lesser extent, tyrosine, aspartic acid, glutamic acid, and lysine. Quantitative contribution of side chain absorption to the spectrum of the Amide I spectrum depends on the amino acid composition of a particular protein. The typical contribution may be estimated as 15-20% of the total band intensity between 1600 and 1700 cm^{-1} [Chirgadze *et al.* 1975, Surewicz *et al.* 1993], although it may be higher if the protein is particularly rich in amino acids such as Asn or Gln.

It is clear that the presence of bands arising from amino acid side chains must be recognized before attempting to extract structural information from the shapes of Amide I and Amide II bands.

5.4.10. Hydration effect

Sample molecules in the solution deform the water H-bond network and change the water spectrum [Jabs 2000]. The hydration effect in the spectra can be described by an absorption band with the parameters[1]: v_0 = 1652 cm^{-1} - FWHH = 50 cm^{-1} - f_G = 0.5.

5.5. AMIDE AND SKELETAL MODES FOR PROTEINS

The globular and fibrous proteins differ from the simple polypeptides in at least two basic regards [Painter & Koenig 1975]. First, proteins are complicated copolymers containing approximately 20 different amino residues that have aromatic, aliphatic, and reactive functional groups as side chains. Several of these side chain vibrations scatter strongly in the Raman spectrum and to a much lesser degree in the infrared spectrum. Fortunately, these lines do not appear with strong intensity in the conformationally sensitive regions of the Raman spectrum, i.e., the Amide I and III regions. The Raman lines due to side chains are themselves of interest because of their sensitivity to the local environment of the side chain. Some of the amino acid residues are part of enzyme active sites such as tryptophan and tyrosine and have strong conformationally sensitive Raman lines. A second major difference between the polypeptides and proteins is the distribution of secondary structures found in the latter. A typical globular proteinlike lysozyme will contain a mixture of α-helical, β-sheet, and disordered chains. Usually the ordered chain conformations in proteins are not very extensive but are short and often distorted relative to the homopolypeptides (and fibrous proteins). Defects in the ordered structure are frequently occurring. Here the term defect refers to non-linear hydrogen bonds, distorted helices, breaks in a helical segment to accommodate the cornering of folding of the polypeptide chain, and other similar features. The selection rules for the normal vibrations of the ordered polypeptide structures were derived assuming zero defects and infinitely long structures. Relaxation of either assumption implies a

[1] V_0 = band position – FWHH = band half width - f_G = band shape parameter

loss of symmetry; therefore frequency shifts, line broadening, and the appearance of new lines are possible consequences.

Nevertheless, the characteristic frequencies and intensities of the conformationally sensitive lines of proteins correlate reasonably well with the corresponding lines of polypeptides for molecules that have similar conformations.

5.6. ASSIGNMENT OF WAVE NUMBERS TO SECONDARY STRUCTURE

5.6.1. Introduction

In a protein with n amino acids forming n-1 amide bonds, the amide frequencies of each single bond depend on specific properties of its environment. In particular hydrogen bonding, steric situations, and dielectric properties of the solvent are known to influence the frequency of the amide vibrations. However, because the secondary structure in proteins is characterised by repetitive, very typical sterical and hydrogen bonding environments of the amide bonds, peptide groups belonging to one specific element of the secondary structure absorb at very similar frequencies.

Band position reflects the conformation of the structural element under study. From the canonical band positions, it can be inferred that only large changes ($\geq$10 cm^{-1}) in band position indicate variations in the secondary structure, whereas small shifts ($\leq$6 cm^{-1}) reflect local changes in a given conformation [Arrondo & Goni 1999].

The determination of secondary structure in proteins from FT-IR spectra really started with studies of Byler & Susi [1986] and Krimm & Bandekar [1986]. In the following sections, the assignment to secondary structure of frequencies in different regions in the vibrational (FT-IR or FT-Raman) spectrum is described.

5.6.2. The assignment of secondary structure for polypeptides

Krimm & Bandekar [1986] made a spectroscopic study of polypeptides with different secondary structure (APRS = antiparallel rippled β-sheet structure, APPS = antiparallel pleated β-sheet structure, Aib = Poly(α-aminoisobutyric acid)). The results are summarised in Table 2 [Krimm & Bandekar 1986].

Based on the study of Krimm & Bandekar [1986], it can be concluded that associating characteristic frequency ranges with conformation should be done with caution when we observe that bands of comparable intensities are found in comparable regions for different secondary structures (e.g. β-$(GluCa)_n$ at 1260 cm^{-1} and α-$(Ala)_n$ at 1265 cm^{-1}).

Table 2 - Observed frequencies of backbone modes of polypeptides (Raman bands: italic, IR and Raman bands: bold, IR band: regular)

Structure	APRS	APPS	APPS	3_1 helix	α-helix	α-helix	3_{10}-helix
Molecule	$(Gly)_n$ I	β-$(Ala)_n$	β-$(GluCa)_n$	$(Gly)_n$ II	α-$(Ala)_n$	α-$(GluH)_n$	3_{10}-$(Aib)_n$
Amide I	1685	1694	1693	*1654*	1658	1653	1656
	1674	*1669*	**1665**	1640	*1655*	*1652*	*1647*
	1636	1632	1624				
Amide II	1517	1555	**1597**	**1560**	1545	1550	1545
	1515	*1538*	**1568**	1550	1516	1510	*1531*
		1524	1560				
Amide	*1410*	*1399*	**1260**	**1380**	*1338*	*1340*	*1339*
III	1408	1402	1225	**1333**	*1278*	*1296*	*1313*
	1295	**1333**	**1223**	**1283**	1270	**1283**	**1280**
	1220	*1243*			1265		
	1214	**1224**					
	1162						
Skeletal	*884*	*909*	*956*	*884*	*908*	*924*	*908*
Amide V	708	706	*705*	740	658	670	694
		698		*673*	618	*618*	680

5.6.3. Summary of assignments for proteins

The assignments of wave numbers to secondary structure for proteins are summarised in Table 6.1 and Table 6.2 in Chapter 6.

5.7. FIBROUS PROTEINS VERSUS GLOBULAR PROTEINS

Most studies on the quantification of secondary structure are based on globular proteins (often recorded in solution) of which the secondary structure can be much different from that of fibrous proteins, such as silk fibroin. Fibrous proteins, unlike globular proteins, contain repetitive amino acid sequences, giving rise to very regular secondary protein structures [Wilson *et al.* 2000]. In addition, fibrous proteins in many cases exhibit α-helical and/or β-sheet conformations, but also can assume other conformations not observed in globular proteins, such as the β-spiral and polyglycine II 3-fold helix. Because these conformations are not well represented in standard spectroscopic data sets, they are difficult to infer from a typical spectroscopic characterization of secondary structure. The predominant helical conformation adopted by the repetitive sequences in fibrous proteins can incorporate most of the protein molecule such that fibrous proteins tend to exhibit one dominant structure. Therefore, it may be possible to identify spectroscopic trends that distinguish more of the subtleties of these conformations and to examine interconversion of these conformations to determine how it might occur. These

results may also provide insights into conformational transition and folding pathways in globular proteins.

6. REFERENCES

Arrondo J.L.R. & Goni F.M., Structure and dynamics of membrane proteins as studied by infrared spectroscopy, Prog. Biophys. Mol. Biol. 72:367-405 (1999)

Axelsen P.H. & Citra M.J., Orientational order determination by internal reflection infrared spectroscopy, Progr. Biophys. Mol. Biol. 66:227-253 (1996)

Bandekar J., Amide modes and protein conformation, Biochim. Biophys. Acta 1120:123-143 (1992)

Bellamy L.J., In: The infrared spectra of complex molecules, 3rd Ed., Chapman & Hall, London (1975)

Bennett R., Cutler D.J., Mould H.M., Chapman D., An observation of resonance Raman in the near-infrared, J. Raman Spectrosc. 21(10):699-702 (1990)

Bower D.I. & Maddams W.F, The vibrational spectroscopy of polymers, Cambridge University, USA (1992)

Bramanti E., Benedetti E., Sagripanti A., Papineschi F., Benedetti E., Determination of secondary structure of normal fibrin from human peripheral blood, Biopolymers 41(5):545-553 (1997a)

Bramanti E., Benedetti E., Nicolini C., Berzina T., Erokhin V., D'Alessio A., Benedetti E., Qualitative and quantitative analysis of the secondary structure of cytochrome C Langmuir-Blodgett films, Biopolymers 42(2):227-37 (1997b)

Byler D.M. & Susi H., Examination of the secondary structure of proteins by deconvolved FT-IR spectra, Biopolymers 25:469-487 (1986)

Chirgadze Y.N., Fedorov O.V., Trushina N.P., Estimation of amino acid residue side-chain absorption in the infrared spectra of protein solutions in heavy water, Biopolymers 14:679-694 (1975)

Coleman P.B., Practical sampling techniques for infrared analysis, CRC Press LLC, USA (1993)

Dunker A.K., Williams R.W., Peticolas W.L., Ultraviolet and laser Raman investigation of the buried tyrosined in FD Phage, J. Biol. Chem. 254(14):6444-6448 (1979)

Fringeli U.P. & Günthard Hs.H., Infrared membrane spectroscopy, In: Membrane spectroscopy, Grell E. (Ed.), Springer, Berlin, 270-332 (1981)

Fu F.-N., De Oliviera D.B., Trumble W.R., Sarkar H.K., Secondary structure estimation of proteins using the Amide III region of Fourrier transform-infrared spectroscopy: Application to analyze calcium binding-induced structural changes in calsequestrin, Applied Spectroscopy 48(11):1432-1441 (1994)

Goormaghtigh E. & Ruysschaert J.M., Polarized attenuated total reflectance infrared spectroscopy as a tool to investigate the conformation and orientation of membrane

components, In: Molecular description of biological membranes by computer aided conformational analysis, vol. I, CRC Press, Boca Raton, 285-329 (1990)

Haris, P.I. & Chapman D., Does Fourier-transform infrared spectroscopy provide useful information on protein structures?, TiBS 17:328-333 (1992)

Harrick N.J., Internal reflection spectroscopy, Wiley/Interscience, New York (1967)

Hsu S.L., Moore W.H., Krimm S., Vibrational spectrum of unordered polypeptide chain – Raman study of feather keratin, Biopolymers 15(8):1513-1528 (1976)

Jabs A., Determination of secondary structure in proteins by Fourier transform infrared spectroscopy (FTIR), IMB Jena, Germany, http://www.imb-jena.de/ImgLibDoc/ftir/IMAGE_FTIR.html (2000)

Koenig J.L., Spectroscopy of polymers, American Chemical Society, Washington DC (1992)

Krimm S. & Bandekar J., Vibrational spectroscopy and conformation of peptides, polypeptides, and proteins, Advances in Protein Chemistry 38:81-364 (1986)

Lord R.C. & Yu N.T., Laser-excited Raman spectroscopy of biomolecules. I. Native lysozyme and its constituent amino acids, J. Mol. Biol. 50:509-524 (1970a)

Lord R.C. & Yu N.T., Laser-excited Raman spectroscopy of biomolecules. II. Native ribonuclease and α-chymotrypsin, J. Mol. Biol. 51:203-213 (1970b)

Milosevic M. & Berets S.L., A review of FT-IR diffuse reflection sampling considerations, Applied Spectroscopy Reviews 37(4):347-364 (2002)

Miyazawa T., Shimanouchi T., Mizushima S., Normal vibrations of N-methylacetamide, J. Chem. Phys. 29:611-616 (1958)

Miyazawa T., In: Polyamino acids, polypeptides, and proteins, M.A. Stahmann (Ed.), University of Wisconsin Press, Madison, 201-217 (1962)

Miyazawa T., In: Poly-α-amino acids, G.D. Fasman (Ed.), Dekker, New York, 69-103 (1967)

Monti P., Freddi G., Bertoluzza A., Kasai N., Tsukada M., Raman spectroscopic studies of silk fibroin from *Bombyx mori*, J. Raman Spectrosc. 29(4):297-304 (1998)

Naik V. M. & Krimm S., Vibrational analysis of peptides, polypeptides and proteins XVII. Normal modes of crystalline Pro-Leu-Gly-NH2, a type II β-turn, Int. J. Pept. Protein Res. 23:1-24 (1984)

Painter P.C. & Koenig J.L., Raman spectroscopy of polypeptides and proteins, In: Handbook of biochemistry and molecular biology, Fasman G.D. (Ed.), 575-580 (1975)

Perkin Elmer, Manual of the Perkin Elmer spectrometer GX 2000: FTIR spectroscopy AutoIMAGE Microscope Techniques and Maintenance Guide, Perkin-Elmer Cooperation (1998a)

Perkin Elmer, Manual of the Perkin Elmer spectrometer GX 2000: Spectrum GX Raman FTIR User's Guide, Perkin Elmer Cooperation (1998b)

Perkin Elmer, Manual of the Perkin Elmer spectrometer GX 2000: Diffuse Reflectance Accessory User's Guide, Perkin Elmer Ltd. (1996)

Perkin Elmer, FT-IR Spectroscopy – Attenuated Total Reflectance, Perkin Elmer technical note, http://las.perkinelmer.com/content/manuals/007024a-ftirspectroscopyatr-technicalnote.pdf (2004)

Perkin Elmer, ATR Accessories – An overview, Perkin Elmer technical note, http://las.perkinelmer.com/content/manuals/007024_01_app1.pdf (2004)

Rousseau M.-E., Lefèvre T., Beaulieu L., Asakura T., Pézolet M., Study of protein conformation and orientation in silkworm and spider silk fibers using Raman microspectroscopy, Biomacromolecules 5:2247-2257 (2004)

Sengupta P.K. & Krimm S., Hsu S.L., Vibrational analysis of peptides, polypeptides and proteins. 21. Beta-calcium-poly(L-Glutamate), Biopolymers 23(8):1565-1594 (1984)

Sengupta P. & Krimm S., Vibrational analysis of peptides, polypeptides and proteins. 32. Alpha-poly(L-glutamic acid), Biopolymers 24(8):1479-1491 (1985)

Sengupta P. & Krimm S., Vibrational analysis of peptides, polypeptides and proteins. 36. Raman and normal-mode studies of the extended-helix conformation in polypeptide chains, Biopolymers 26(S0):S99-S107 (1987)

Shao Z., Vollrath F., Sirichaisit J., Young R.J., Analysis of spider silk in native and supercontracted states using Raman spectroscopy, Polymer 40(10):2493-2500 (1999)

Siamwiza M.N., Lord R.C., Chen M.C., Takamatsu T., Harada I. Matsuura H., Shimanouchi T., Interpretation of doublet at 850 and 830 cm^{-1} in Raman spectra of tyrosyl residues in proteins and certain model compounds, Biochemistry 14: 4870-4876 (1975)

Siesler H.W., Characterization of polymer deformation by vibrational spectroscopy, In: Oriented polymer materials, Fakirov S. (Ed.), Hüthig & Wepf Verlag, Heidelberg (1996)

Skoog D.A., Principles of Instrumental Analysis, Saunders College Publishing, Florida, USA, 3rd edition (1985)

Smith B.C., Fundamentals of Fourier Transform Infrared spectroscopy, CRC Press LLC, Florida, USA (1996)

Sun Y., Shao Z., Hu P., Yu T., Hydrogen bonds in silk fibroin-poly(acrylonitrile-co-methyl acrylate) blends: FT-IR study, J. Polym. Sci. Pt. B-Polym. Phys. 35:1405-1414 (1997)

Surewicz W.K., Mantsch H.H., Chapman D., Determination of protein secondary structure by Fourier transform infrared spectroscopy: A critical assessment; Biochemistry 32(2):389-394 (1993)

Susi H. & Byler D.M., Resolution-enhanced Fourier transform infrared spectroscopy of enzymes, Methods Enzymol. 130:290-311 (1986)

Taddei P., Asakura T., Yao J., Monti P., Raman study of poly(alanine-glycine)-based peptides containing tyrosine, valine, and serins as model for the semicrystalline domains of *Bombyx mori* silk fibroin, Biopolymers 75(4):314-324 (2004)

Takeuchi H., Watanabe N., Satoh Y., Harada H., Effects of hydrogen bonding on the tyrosine Raman bands in the 1300-1150 cm^{-1} region, J. Raman Spectrosc. 20:233-237 (1989)

Tamm L.K. & Tatulian S.A., Infrared spectroscopy of proteins and peptides in lipid bilayers, Q. Rev. Biophys. 30:365-429 (1997)

Thomas G.J., Jr., New structural insights from Raman spectroscopy of proteins and their assemblies, Biopolymers (Biospectroscopy) 67:214-225 (2002)

Van Dijk A., Van Wijk L., Van Vliet A., Haris P., Van Swieten E., Tesser G., Robillard G., Structure characterization of the central repetitive domain of high molecular weight gluten proteins. I. Model studies using cyclic and linear peptides, Protein Science 6:637-648 (1997)

Venyaminov S.Y. & Kalnin N.N., Quantitative IR spectrophotometry of peptide compounds in water (H_2O) solutions. I. Spectral parameters of amino acid residue absorption bands, Biopolymers 30(13-14):1243-57 (1990)

Wen Z.Q., Armstrong A., Thomas G.J., Jr., Demonstration by ultraviolet resonance Raman spectroscopy of differences in DNA organization and interactions in filamentous viruses Pf1 and fd†, Biochemistry 38:3148-3156 (1999)

Williams D.H. & Fleming I., Spectroscopic methods in organic chemistry, 5th Edition, McGraw-Hill (1995)

Wilson D., Valluzzi R., Kaplan D., Conformational transitions in model silk peptides, Biophys. J. 78(5): 2690-2701 (2000)

Xue G., Laser Raman spectroscopy of polymeric materials, Progr. Polym. Sci. 19:317-388 (1994)